Du manteau au système géothermal de haute température : Dynamique de subduction et anomalies thermiques en Méditerranée orientale

Vincent Roche

ÉCOLE DOCTORALE
ENERGIE, MATERIAUX, SCIENCES DE LA TERRE ET DE L'UNIVERS

ISTO / BRGM

THÈSE présentée par :

Vincent ROCHE

soutenue le : 29 janvier 2018

pour obtenir le grade de :

Docteur de l'université d'Orléans

Discipline / Spécialité : Sciences de la Terre et de l'Univers / Géodynamique

Du manteau au système géothermal de haute température : dynamique de subduction et anomalies thermiques en Méditerranée orientale

THÈSE dirigée par :

Laurent GUILLOU-FROTTIER	Ingénieur-Chercheur, HDR, BRGM
Laurent JOLIVET	Professeur, Université Pierre et Marie Curie

RAPPORTEURS :

Inga MOECK	Professeure, Institut de Géophysique Appliquée de Leibniz
Philippe YAMATO	Professeur, Université de Rennes 1

JURY :

Bruno SCAILLET	Directeur de Recherches, ISTO (Président)
Christian TEYSSIER	Professeur, University of Minnesota
Michael RESSEL	Assistant Professeur, Nevada Bureau of Mines and Geology
Inga MOECK	Professeure, Institut de Géophysique Appliquée de Leibniz
Philippe YAMATO	Professeur, Université de Rennes 1
Laurent GUILLOU-FROTTIER	Ingénieur-Chercheur, HDR, BRGM
Laurent JOLIVET	Professeur, Université Pierre et Marie Curie

Manuscrit de Thèse

Vincent ROCHE

Du manteau au système géothermal de haute température : dynamique de subduction et anomalies thermiques en Méditerranée orientale

THÈSE dirigée par :

Laurent GUILLOU-FROTTIER Ingénieur-Chercheur, HDR, BRGM
Laurent JOLIVET Professeur, Université Pierre et Marie Curie

REMERCIEMENTS

3 ans et quelques mois pour terminer par le commencement : les remerciements… et malgré cela les mots me manquent car il y a tant de personnes à remercier. On s'en remet donc aux glorieux anciens, qui ont déjà réfléchi à la question, et on lit, relit… Mais au final, l'un des meilleurs moyen est de se laisser guider par son ressenti ! Je m'excuse d'avance pour les oublis.

Malgré le manque d'originalité, il faut bien le reconnaître, mes premières pensées vont vers mes deux directeurs de thèse :

- *Joueur de tennis aguerri et fin stratège sur la modélisation numérique en 2D, mais également en **3D,** alias Laurent Guillou-Frottier. Un grand merci pour ta confiance et ta patience que tu m'as accordé. Tu fais preuve d'une très grande pédagogie et je te remercie chaleureusement pour ta disponibilité. Tu as toujours su me recadrer dans les méandres de mes textes en allant à l'essentiel. J'aurais pu te remercier en une seule phrase mais pour une fois j'ai suivi tes conseils.*
- *Chanteur émérite et président d'une certaine ligue, alias Laurent Jolivet. Je te remercie sincèrement pour tout : ta confiance, ton énergie débordante sur le terrain, tes connaissances et tes disponibilités à toute heure. Je te dois beaucoup et c'est avant tout tes qualités humaines que j'aimerais souligner. Tout a commencé en août 2012 lorsque j'ai reçu un coup de téléphone à Peyrins. Au final cette collaboration aura duré quelques années pour aboutir à la rédaction de ce manuscrit.*

Mes pensées et remerciements vont ensuite vers Vincent Bouchot, Johann Tuduri et Laurent Beccalotto. On ne se connaissait pas au départ mais quelques jours en Turquie nous ont permis de tisser des liens et d'officialiser cela avec nos fameux teeshirts, que j'espère vous voir porter le jour de ma soutenance. Merci pour vos connaissances que vous m'avez enseigné sur la géothermie mais également sur la métallogénie.

Un merci particulier à Romain et Hugues pour leur bonne humeur permanente à la fac mais également sur le terrain.

Merci également aux argonautes endurcis et aux apprentis. Un immense merci à Stéphane Scaillet qui a monté un superbe labo Argon, à Laurent Perdereau, Quentin Thibault et plus particulièrement à Florian Duval qui m'a permis de finir dans les temps ce manuscrit…

Je profite pleinement de ce moment pour remercier les membres du jury et particulièrement les deux rapporteurs, Ingoa Moeck et Philippe Yamato qui ont accepté de lire ces quelques pages afin d'apporter leurs critiques bénéfiques.

Merci à ceux qui ont facilité le déroulement de cette thèse : le directeur de l'université Ary Bruand, le Labex (particulièrement Bruno Scaillet) et le BRGM. Merci à Marlène Lallemand, Martine

Bodusseau, Virginie Lancelot, Olivier Gaudefroy, Nathalie Pothier, Catherine Giffault, Catherine Leroy, Marie-Noëlle Pailhès, Lucile Esnee, Laurent Catherine et Yohann Brossard.

Merci à ceux qui ont participé de près ou de loin à ces travaux. Je pense notamment aux litholamelleurs Sylvain Janiec et Jean-Gabriel Badin, à Patricia Benoist-Julliot (malgré l'oubli persistant sur les métallisations des lames), Ida Di Carlo pour les analyses à la microsonde électronique et les séances MEB et Abdeltif Lahfid pour son aide sur le Raman. Jerem et Philippe pour les datations U-Pb. Merci également à Marielle Aton pour toutes les petites choses du quotidien. Une pensée également à Morgan et à Clément.

Merci à ceux qui ont fait en sorte que ces années orléanaises, loin d'Anaïs, se passent bien. Je pense évidemment à mes amis Valou et sa femme Nolwenn (☺), Dustin (alias Tiphaine pour les intimes), Joanna, La praline, Justine, Maxou, Armel, Eloïse, Anaëlle. Puis à tous les autres : Hugo, Sarah dont j'ai eu le plaisir de partager mon bureau au BRGM, Thomas, Kévin, Chloé, Mohammed, David, Yann, Malcom, Adoum, Xin, Leila, Colin, Rabi, Florent, Thomas, Adrien, Benoit, Marie-Laure, Carlos, Amélie, Zineb, Morgane, Fabien, Nicolas, Clément, Julie mais également les plus anciens Jacques, Gulia et Cam, Pietro, Alexandre, Emeline. Une pensée également aux collègues du BRGM : Seb, Mathieu, Gaëtan, Guillaume, Anne-Sophie, Laurent, Nicolas, Eric…

Un grand merci à mes proches qui ont su m'aider et me soutenir notamment lors de cette dernière année. Un merci tout particulier à ma mère pour la relecture, à mon frère pour son coup de pouce sur la bibliographie et à Sony pour son niveau d'anglais irréprochable. Et surtout à Anaïs, qui m'a soutenu pendant toutes ces années malgré les 6000 km qui nous séparaient et qui m'a enfin rejoint sur Orléans, sans elle la mise en page aurait été désastreuse… De nouvelles aventures nous attendent.

Bonne lecture.

INTRODUCTION : Raison d'être de la thèse.....11

CHAPITRE I : Contexte scientifique et motivations 15

CHAPITRE II : Contrôle structural et lithologique sur l'activité géothermique actuelle dans la province du Menderes (partie occidentale de la Turquie) 75

CHAPITRE III : Evolution structurale de l'île de Leros (Dodécanèse) : implication géologique dans l'Est de la Méditerranée 137

CHAPITRE IV : Evolution géodynamique de la région Est-Méditerranéenne.....179

CHAPITRE V : Evolution structurale et thermique du Massif du Menderes du Crétacé à l'actuelle (Turquie).....257

CHAPITRE VI : Rôle de la subduction dans la localisation des dômes métamorphiques et des champs géothermaux 345

SYNTHESE - DISCUSSION - PERSPECTIVES & ABRIDGED ENGLISH VERSION 385

SYNTHESIS AND DISCUSSION - abridged English version.....416

CONCLUSION GENERALE 431

ANNEXES 447

INTRODUCTION : Raison d'être de la thèse....11

CHAPITRE I : Contexte scientifique et motivations....15

I.1. La géothermie : la chaleur de la Terre....17

I.1.1. Des ressources naturelles et quasiment inépuisables....17

I.1.2. Les types de ressources géothermales....20

I.1.3. Les classifications de systèmes géothermaux selon des champs de références....21

I.1.4. Définition d'un système géothermal magmatique de haute température....23

I.2. Contextes géodynamiques favorables aux développements de systèmes géothermiques de HT : le cas de la subduction....27

I.2.1. Les systèmes géothermaux en contexte de subduction : magmatique vs. amagmatique....28

I.2.1.1. Les systèmes magmatiques d'arc ou d'arrière-arc : actifs vs. fossiles....29

a. Les systèmes magmatiques actifs....29

b. Les systèmes magmatiques fossiles....32

I.2.1.2. Les systèmes géothermaux amagmatiques : actifs vs. fossiles....35

a. Les systèmes amagmatiques actifs....35

b. Les systèmes amagmatiques fossiles....41

I.2.2. Systèmes géothermaux de HT : la particularité du domaine arrière-arc....42

I.3. Dynamique des zones de subduction....43

I.3.1. Généralité sur la subduction....43

I.3.2. Les principales forces impliquées....45

I.3.3. Les différents modèles géodynamiques....47

I.3.3.1. Le modèle classique de la plaque supérieure....48

I.3.3.2. Le modèle du slab roll-back....49

I.3.3.3. Le rôle des flux mantelliques....49

I.3.4. Thermicité dans les zones de subduction : évolution de la plaque supérieure....52

I.4. Intérêts de la zone d'étude....55

I.4.1. Contexte géothermal de l'Anatolie occidentale....55

I.4.1.1. Une région anormalement chaude....55

I.4.1.2. Une région marquée par de nombreux gisements métalliques....57

I.4.2. Contexte géodynamique et géologique....58

I.5. Question scientifique, objectifs de la thèse et démarche adoptée....60

I.6. Références....62

CHAPITRE II : Contrôle structural et lithologique sur l'activité géothermique actuelle dans la province du Menderes (partie occidentale de la Turquie)....75

II.1. Introduction....83

II.2. Geological setting....84

II.2.1. The eastern Mediterranean region 84
II.2.2. The Menderes Massif 85
II.3. Geothermal setting in the Menderes Massif 88
II.3.1. Thermal anomalies at different scales 88
II.3.2. Synthesis of fluids and isotopes 89
II.3.2.1. Studies on oxygen and hydrogen isotopes of the main geothermal fluids 89
II.3.2.2. Helium isotopic signature 90
II.4. Analysis of the tectonic and structural settings of geothermal fields in the Menderes Massif at local and regional scale 93
II.4.1. Structural features of the Salihli geothermal field 95
II.4.2. Structural features of the Alaşehir geothermal field 97
II.4.3. Structural features of the Salavatlı and Germencik geothermal fields 101
II.4.4. Structural features of the Salavatlı and Germencik geothermal fields 105
II.5. Discussion 108
II.5.1. The Menderes Massif Core complex and associated geothermal fields 108
II.5.1.1. Crustal-scale: the role of detachments 108
II.5.1.2. Basin-scale: the N-S transfer faults 111
II.5.2. Possible fluid pathways in the Menderes Massif: from the mantle to the geothermal reservoir 112
II.5.2.1. Source to sink 112
II.5.2.2. A long-lived duration geothermal Province 116
II.5.3. Origin of heat source in the Menderes Massif 116
II.5.4. An underestimated geothermal potential? 117
II.6. Conclusion 118
II.7. Acknowledgements 119
II.8. Appendix 120
II.8.1. The Alaşehir graben 120
II.8.1.1. Stratigraphy and structure 120
II.8.1.2. The main geothermal fields: Salihli and Alaşehir 121
II.8.2. The Büyük Menderes graben 122
II.8.2.1. Stratigraphy and structure 122
II.8.2.2. The main Büyük Menderes geothermal fields: Salavatlı and Germencik 122
II.8.3. Cumaovası basin 123
II.8.3.1. Stratigraphy and structure 123
II.8.3.2. The Seferihisar geothermal field 124
II.9. References 125

CHAPITRE III : Evolution structurale de l'île de Leros (Dodécanèse) : implication géologique dans l'Est de la Méditerranée 137

III.1. Introduction 144

III.2. Geological setting 144

III.2.1. The Cyclades Archipelago 144

III.2.2. The southwestern part of Turkey 146

III.2.3. The Dodecanese Archipelago 148

III.3. A new structural map of Leros 150

III.4. Kinematics of deformation 152

III.4.1. Ductile deformation 152

III.4.2. Brittle deformation 155

III.5. Metamorphic record and P-T estimates in metamorphic units 157

III.5.1. Conventional metamorphic petrology observations 158

III.5.2. RSCM thermometry 161

III.6. Discussion 163

III.6.1. Structural and metamorphic evolution 163

III.6.2. Large-scale correlations 165

III.6.3. Tectonic implications in the Eastern Aegean domain 167

III.7. Conclusion 167

III.8. Acknowledgements 168

III.9. Appendix 169

III.10. References 173

CHAPITRE IV : Evolution géodynamique de la région Est-Méditerranéenne 179

IV.1. Introduction 185

IV.2. Geological and Geodynamic setting 186

IV.2.1. Aegean domain and continental Hellenides 189

IV.2.1.1. Pelagonian Nappe 189

IV.2.1.2. Pindos Nappe 190

IV.2.1.3. Cycladic Blueschist Unit 190

IV.2.1.4. Gavrovo Nappe-Tropolitza 191

IV.2.1.5. Phyllite-Quartzite Nappe 191

IV.2.1.6. Ionan and Paxos Nappes 192

IV.2.2. Western Turkey 193

IV.2.2.1. Afyon and Ören metamorphic domain 193

IV.2.2.2. Cycladic Blueschist Unit 194

IV.2.2.3. Menderes Massif 194

IV.2.3. Eastern Aegean Islands 195
IV.2.3.1. Samos 196
IV.2.3.2. Fourni and Thymaena Islands 199
IV.2.4. Dodecanese islands 199
IV.3. New field observations 203
IV.3.1. Fourni and Thymaena Islands 203
IV.3.2. Dodecanese islands 204
IV.4. Metamorphism 204
IV.4.1. Samos 204
IV.4.2. Fourni and Thymaena islands 206
IV.4.3. Dodecanese islands 206
IV.5. Ductile shearing 209
IV.5.1. Samos 209
IV.5.2. Fourni and Thymaena islands 212
IV.5.3. Dodecanese 215
IV.6. Brittle deformation 221
IV.7. Discussion 225
IV.7.1. Correlations between Western Anatolia and the Aegean region 225
IV.7.1.1. Fourni, Samos, western Anatolia and the Cyclades 226
IV.7.1.2. Dodecanese, Menderes cover and Amorgos Island 231
IV.7.2. Tectonic evolution of the Aegean-Anatolia region 234
IV.7.2.1. Kinematic of deformation from the Cretaceous to the Oligocene 236
a. Prograde deformation 236
b. Syn-orogenic deformation 236
IV.7.2.2. An overall NNE-SSW gradient of extension during Oligo-Miocene to Present 237
IV.7.3. Slab tearing: which consequences in the overriding plate? 239
IV.8. Conclusion 240
IV.9. Acknowledgements 241
IV.10. References 242
CHAPITRE V : Evolution structurale et thermique du Massif du Menderes du Crétacé à l'actuelle (Turquie) 257
V.1. Introduction 265
V.2. Geological setting 266
V.2.1. The Lycian Nappes and the Cycladic Blueschist Unit (CBU) 267
V.2.2. The Menderes MCC (MMCC) 268
V.2.2.1. Lithology of the MMCC 268

V.2.2.2. Structure and metamorphism of the MMCC: the main controversies 269
V.3. Structural analysis of the Menderes MCC from new field data 271
V.3.1. Alaşehir detachment: Salihli, Alaşehir and Urganlı areas 273
V.3.2. The Bozdağ - Birgi areas 276
V.3.3. Halıköy - Sultanhisar and Salavatlı areas 276
V.3.4. SMM area: from Kurudere to Çine 280
V.4. Quantitative T and age constraints 283
V.4.1. ^{40}Ar-^{39}Ar dating in the CMM and SMM 283
V.4.1.1. CMM area 289
V.4.1.2. The Bozdağ - Birgi areas 289
V.4.1.3. Halıköy - Sultanhisar areas 291
V.4.1.4. SMM area: from Çine to Kurudere 292
V.4.2. U-Pb dating in the CMM 296
V.4.3. RSCM T_{max} results 298
V.5. Discussion 303
V.5.1. Tectonic contacts in the CMM and SMM 303
V.5.2. Distribution of T_{max} (RSCM) 307
V.5.3. Metamorphism and deformation across the Menderes Massif 308
V.5.3.1. HP-LT metamorphism 308
V.5.3.2. HT-LP Metamorphism and deformation before and during the Alpine orogeny 312
V.5.3.3. HT-LP Metamorphism and deformation during the Oligo-Miocene in the CMM 313
V.5.4. A possible evolution of the Menderes Massif 315
V.6. Conclusion 317
V.7. Acknowledgements 317
V.8. Appendix 318
V.8.1. Analytical methods 318
V.8.1.1. ^{40}Ar-^{39}Ar Geochronology 318
V.8.1.2. U-Pb method 319
V.8.1.3. RSCM (Raman Spectroscopy on Caronaceous Materials) 321
V.8.2. Sample distribution and results of ^{40}Ar-^{39}Ar and U-Pb ages 322
V.8.3. Representative microprobe analyses 331
V.8.4. Geochronological data 333
V.9. References 337
CHAPITRE VI : Rôle de la subduction dans la localisation des dômes métamorphiques et des champs géothermaux 345
VI.1. Introduction 351

VI.2. Geodynamic and geothermal settings of the Menderes Massif 353

VI.3. 3-D thermal evolution of subduction 354

VI.3.1. Model set-up 355

VI.3.2. Results 357

VI.3.2.1. Thermo-mechanical instabilities 357

VI.3.2.2. Slab dynamics and shear heating 358

VI.4. From subcrustal thermal anomalies to geothermal systems: 2-D model of fluid circulation 362

VI.4.1. Model setup 362

VI.4.2. Results 364

VI.4.2.1. Role of basement and detachment permeabilities 364

VI.4.2.2. Fluid flow field and temperature profiles 365

VI.5. Discussion 367

VI.5.1. Large-scale thermo-mechanical boudinage, and emplacement of MCC in Western Anatolia 367

VI.5.2. Detachments and localization of HEGRs in Western Anatolia 369

VI.5.3. Subduction dynamics and localization of HERSs: the Larderello (Tuscany) and the Basin and Range (Western United States) areas 370

VI.6. Conclusion 371

VI.7. Acknowledgements 371

VI.8. Appendix 373

VI.8.1. Supplementary Figures 373

VI.8.2. Supplementary Materials 376

VI.8.2.1. 3-D Numerical approach 376

VI.8.2.2. 2-D Numerical approach 379

VI.9. References 381

SYNTHESE - DISCUSSION - PERSPECTIVES & ABRIDGED ENGLISH VERSION 385

VII.1. Évolution de la dynamique de subduction dans la partie orientale de la Méditerranée : conséquences tectoniques et thermiques 388

VII.1.1. Crétacé Supérieur à Éocène inférieur : un gradient métamorphique HP-BT sur l'ensemble de la région 389

VII.1.2. Éocène: un paradoxe entre HP-BT et HT-BP 389

VII.1.3. Oligocène au Miocène : un gradient métamorphique HT-MP sur l'ensemble de la région 393

VII.1.3.1. Conséquences thermiques de cette dynamique 397

VII.1.4. Miocène à Actuel : une activité tectonique encore présente 398

VII.1.4.1. Conséquences thermiques de cette dynamique 401

VII.2. Les systèmes hydrothermaux amagmatiques actifs vs. fossiles en contexte d'arrière-arc : vers un modèle conceptuel général 402

VII.2.1. Caractéristiques des systèmes géothermaux amagmatiques actifs de HT 404

VII.2.2. Caractéristiques des systèmes hydrothermaux amagmatiques fossiles de HT 406

VII.3. Perspectives 409

VII.3.1. Evolution de la zone de subduction : localisations des systèmes géothermaux HT 409

VII.3.2. Fenêtres mantelliques & zone de transfert : le cas particulier du Basin & Range... 412

VII.3.3. La dynamique de subduction : un contrôle de premier ordre sur la distribution des systèmes de HT ? 414

VII.4. Synthesis and Discussion - abridged English version 416

VII.4.1. The Menderes geothermal Province 416

VII.4.1.1. Thermal evolution of the Menderes Massif 416

VII.4.1.2. Amagmatic fossil vs. active geothermal systems in the Menderes Massif 418

a. Active geothermal systems 419

b. Fossil geothermal systems 420

VII.4.2. Subduction dynamics: a first order control on the distribution of high-enthalpy geothermal systems (HEGS)? 422

VII.4.2.1. The complexity of Larderello geothermal system (Italy) 422

VII.4.2.2. The case of the mantle windows (e.g. the Basin & Range, West America) 423

VII.4.2.3. Subduction dynamics and others HEGS 424

VII.5. Références 425

CONCLUSION GENERALE 431

LISTE DES FIGURES 435

LISTE DES TABLES 443

ANNEXES 447

Annexe A : Lexique 449

Annexe B : Anatomy of the Cycladic Blueschist Unit on Sifnos Island (Cyclades, Greece) 451

Annexe C : Migration of geothermal fluids in extensional MCC: a long-lived hydrothermal (mineral and geothermal) system? 479

INTRODUCTION : Raison d'être de la thèse

Cette introduction a pour but d'exposer les motivations de ce travail de thèse en précisant :

- la question scientifique de la thèse (problématique)
- l'objectif de la thèse visant à répondre à la question
- la démarche adoptée pour atteindre cet objectif

La question principale de la thèse est la suivante :

Pourquoi **la province géothermale du Massif du Menderes** (Anatolie occidentale, Turquie), qui fait l'objet d'un rush depuis 2010 (production en hausse de 336% en 5 ans [Bertani, 2015]), est-elle considérée comme une province haute température de taille mondiale avec un potentiel de capacité installée estimé à 20000[1] MWe*, alors qu'elle est exempte d'activité volcanique comparé à l'est du pays ?

Afin de répondre à cette question, nous focaliserons notre étude sur les liens entre la dynamique de subduction et les anomalies thermiques. Plus exactement, les processus mantelliques et crustaux, qui contrôlent la distribution spatiale et temporelle des anomalies thermiques de grandes longueur d'onde seront analysés à l'échelle de la Méditerranée Orientale, et plus particulièrement dans la région de l'Anatolie occidentale (Turquie). Il s'agira de comprendre l'évolution spatio-temporelle du régime thermique de la lithosphère anatolienne entre 50 Ma et aujourd'hui. A travers un contexte géodynamique particulier de retrait et déchirure du panneau plongeant, les phénomènes de conduction* et de convection* thermique seront intégrés afin d'améliorer la compréhension de la Province géothermale du Massif du Menderes jusqu'à celle du système géothermal* de haute température en position d'arrière-arc.

Pour discuter et apporter des nouvelles contraintes sur cette problématique, ce manuscrit s'articule en 6 chapitres :

(i) Le premier chapitre est dédié au contexte général et scientifique, au sens large. Les notions abordées sont principalement basées sur les classifications et les modèles génétiques des systèmes géothermaux de haute-température dans la littérature. La répartition spatiale des champs géothermaux actifs et fossiles dans un contexte de subduction sera brièvement abordée. Par ailleurs, une présentation synthétique sur la dynamique de subduction sera également exposée. Enfin, une dernière partie est vouée à

[1] https://www.german-energy-solutions.de/GES/Redaktion/DE/Publikationen/Praesentationen/2015/2015-10-01-iv-tuerkei-02-schiffer-consult.pdf?__blob=publicationFile&v=7

* Définition du terme en *Annexe A. Lexique*

l'intérêt de la zone d'étude. Ce chapitre a donc pour but d'exposer les principales motivations de ce travail ainsi qu'une familiarisation avec le sujet.

(ii) Le second chapitre est entièrement consacré à la circulation actuelle des fluides dans la croûte. La mise en place des gisements géothermaux de haute température dans un contexte d'arrière-arc de zone de subduction (*i.e.* le Massif du Menderes) sera discutée.

(iii) Le troisième chapitre est dédié à l'étude structurale et thermique des roches d'une île du Dodécanèse (Leros), localisée à l'aplomb d'une possible déchirure du panneau plongeant.

(iv) Le quatrième chapitre est dédié à l'évolution géodynamique de la région Anatolienne. Cette étude se concentre particulièrement sur la région de Dodécanèse dans l'est de la Mer Egée, sous laquelle une déchirure du panneau plongeant africain est supposée avoir lieu. Paradoxalement, très peu d'études de la cinématique de la déformation et du métamorphisme ont été menées dans cette région.

(v) Le cinquième chapitre est dédié à l'évolution thermique et tectonique du *Metamorphic Core Complex* (MCC*) du Massif du Menderes (localisé à l'ouest de la Turquie) depuis 50 Ma, une nécessité puisque nous nous intéressons entre autres aux grandes longueurs d'onde de la structure thermique de la région. Basée principalement sur des études de terrain et géochronologiques (*e.g.* $^{40}Ar/^{39}Ar$; U-Pb), et sur des compilations de données (*e.g.* traces de fissions sur zircon et apatite), un modèle évolutif de mise en place du MCC sera proposé.

(vi) Le sixième chapitre traite à la distribution spatiale et temporelle des anomalies thermiques de grandes longueurs d'ondes sur une échelle de temps similaire à celle de la dynamique de subduction. En utilisant une approche numérique en 3D et 2D, les liens entre dynamique mantelliques (*e.g. shear heating*, flux mantelliques) et crustales (*e.g.* convection dans les détachements*) seront détaillés.

(vii) Le dernier chapitre est consacré à une discussion générale sur cette province géothermale. Des perspectives sur une classification des systèmes de haute température dans les zones de subduction seront brièvement abordées.

CHAPITRE I : Contexte scientifique et motivations

I.1. La géothermie : la chaleur de la Terre

I.1.1. Des ressources naturelles et quasiment inépuisables

Face à l'explosion démographique observée depuis quelques décennies et aux conséquences de l'hyperconsommation croissante de matières énergétiques, la question de la raréfaction, voire de l'épuisement de ces ressources énergétiques fossiles donc non renouvelables (*i.e.* pétrole, gaz, charbon), constitue aujourd'hui un sujet de débat et un enjeu de société encourageant à produire plus avec moins.

Concernant ces énergies fossiles, un consensus semble se dégager suggérant que le scénario de l'épuisement de ces ressources est improbable à l'horizon 2100 mais qu'il serait possible dès les prochains siècles. On sait par ailleurs que la consommation des charbons et hydrocarbures fossiles aggrave le réchauffement de l'atmosphère par la production de gaz à effet de serre et la communauté internationale s'oriente de plus en plus vers des sources d'énergie décarbonées. Bien que de nombreuses inconnues persistent sur l'avenir du pétrole, les ressources de gaz naturel sont abondantes et représentent plus de 120 années de consommation [selon l'IFP, Institut Français du Pétrole[2]]. Les experts prévoient une forte croissance de la demande et de la production dans les années futures même si le gaz naturel ne peut prétendre se substituer massivement au pétrole. De même pour le nucléaire, l'uranium utilisé dans les réactions de fission nucléaire est une ressource abondante et relativement bien répartie sur l'ensemble de la planète. Selon l'Agence Internationale de l'Energie Atomique (AIEA), les ressources mondiales répertoriées représentent à ce jour plus de 5,9 millions de tonnes (Mt) d'uranium, soit l'équivalent d'un siècle de consommation au rythme actuel. Par ailleurs, des études estiment à 10,6 Mt le potentiel des ressources considérées comme spéculatives, avec des futurs gisements qui pourraient voir le jour dans les prochaines décennies.

Cependant l'accès à ces ressources fossiles sera de plus en plus difficile considérant que les futurs gisements seront plus difficiles à découvrir (profonds et/ou cachés), nécessitant plus d'investissements et que leur exploitation sera bien plus énergivore. Ainsi, l'augmentation programmée de la consommation énergétique de l'industrie extractive, et par conséquent de toute la chaine de valeur manufacturière rentrera en confrontation avec la lutte contre le changement climatique. Prenons comme exemple la combustion d'hydrocarbures dans les 100 prochaines années qui continuera à accroitre l'effet de serre et qui représentera encore ~75 à 80 % de l'énergie utilisée par les activités humaines. Selon le rapport du GIEC [2014] (Groupe d'Experts Intergouvernemental sur l'Evolution du Climat), cette combustion ainsi que d'autres émissions futures engendreront une augmentation de la concentration de CO_2 dans l'atmosphère de 500 à 1500 ppm, et une augmentation de la température de 0,3 à 4,8 °C en 2100, entrainant une fonte rapide des glaces, et par conséquent une augmentation du niveau marin de 26

[2] http://www.ifpenergiesnouvelles.fr/Espace-Decouverte/Les-grands-debats/Quel-avenir-pour-le-gaz-naturel/Reserves-production-et-consommation#1

à 98 cm sur la même période. Il est important de préciser que tous les scénarii potentiels d'émission sont basés d'une part sur les tendances socio-économiques plausibles et d'autre part sur l'incertitude du modèle climatique utilisé pour les calculer. Dans tous les cas, il est important de noter que tous les modèles s'accordent sur (i) une augmentation de la teneur en CO_2, (ii) une élévation de la température moyenne mondiale et donc (iii) une hausse du niveau de la mer dans le siècle à venir. Même si l'écosystème qui nous protège est extrêmement complexe, et sûrement très adaptable, il est devenu évident que le niveau d'activité aujourd'hui atteint constitue une perturbation non négligeable et non réversible.

Ainsi, les énergies renouvelables considérées comme inépuisables, composées de toutes les énergies issues de manière directe ou indirecte du soleil (*i.e.* énergies solaire, éolienne, hydraulique et les bioénergies), doivent être développées pour les besoins présents et futurs de notre société [Bal & Chabot, 2001]. En outre, l'explosion démographique des pays émergeants ainsi que l'évolution de notre mode de vie, impliquent un accroissement continu de la demande en énergie. Tous ces éléments montrent la nécessité de la diversification et du développement des énergies renouvelables qui représentent aujourd'hui moins de 15 % de la production énergétique mondiale selon l'AIE (Agence international de l'énergie).

Dans cette gamme d'énergies naturelles, la géothermie, du grec géo (la terre) et thermos (la chaleur), est probablement l'une des plus anciennes exploitées par l'homme. Bien avant l'exploitation industrielle de « masse », de nombreux vestiges préhistoriques ont été découverts proches des manifestations naturelles (sources chaudes, geysers…) où la population locale utilisait ces émergences à des fins pratiques (chauffage, cuisson et bain). De manière plus sophistiquée, au Moyen-Âge, la commune de Chaudes-Aigues (Cantal, massif Central) a développé le premier système de chauffage collectif par le biais d'un circuit d'eau chaude alimenté par plusieurs sources naturelles (82 °C). Le 4 juillet 1904, en allumant symboliquement cinq ampoules avec une turbine à vapeur géothermale à Larderello en Toscane (Italie), le prince italien Piero Ginori Conti lançait la production d'électricité à partir de la géothermie[3].

De nos jours, la géothermie se développe rapidement, et mute principalement vers des applications de production d'électricité et de chauffage (pisciculture, aquaculture, pompes à chaleur…). En 30 ans la production mondiale d'énergie géothermique a quasiment doublé passant de 38,035 à 73,549 GWh* (Fig. I.1) [Bertani, 2015]. Cette tendance se traduit par le développement de dizaines de centrales géothermiques pour la production d'électricité (*i.e.* les centrales en activité depuis 2010 comme Nga Awa Purua en Nouvelle-Zélande, 132 MWe ; Jersey Valley aux USA, 19,4 MWe ; Olkaria II au Kenya, 35 MWe). Les prévisions de cette production pour 2020, basées sur un recensement précis de tous les projets existants à un stade opérationnel, conduisent à une augmentation importante de la

[3] (http://www.faiteslepleindavenir.com/2015/02/05/111-ans-geothermie/)

capacité installée atteignant les 21,4 GWe* (Fig. I.1). Une telle tendance montre donc l'intérêt que peut susciter la géothermie à l'échelle mondiale.

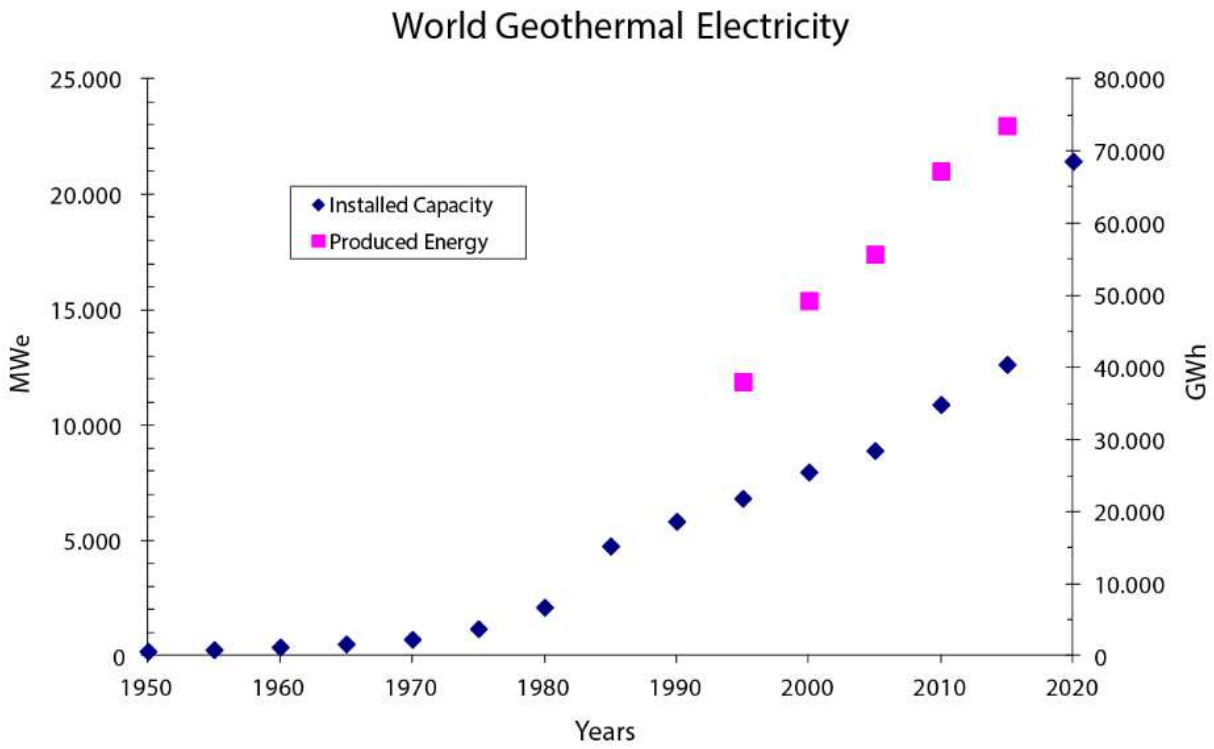

Figure I.1 : évolution de la capacité mondiale d'électricité géothermique installée (en MWe) et produite (en GWh) depuis 1950 d'après Bertani [2015].

Par ailleurs, Dickson & Fanelli [2003] ont estimé la quantité totale d'énergie géothermique sur Terre à $12{,}6 \times 10^{12}$ EJ*, et dans les ordres de $5{,}4 \times 10^{9}$ EJ dans la croûte. Sachant que la consommation mondiale actuelle est estimée à 0,432 EJ pour toutes les activités humaines confondues selon l'AIE, la géothermie offre alors l'opportunité de subvenir complètement à nos besoins énergétiques, à condition d'avoir accès à ces ressources. Depuis 1950, le regain d'intérêt pour cette source de chaleur et la technologie qui vise à l'exploiter sont donc directement liés aux enjeux sociaux-économiques et au coût du potentiel de production, moins élevé que d'autres énergies (*e.g.* l'énergie solaire). En effet, certains atouts comme les faibles émissions de gaz à effet de serre pour produire cette énergie, ou le fait que la « recharge du système » peut être alimentée par des eaux usées (*i.e.* le cas d'un geyser rechargé artificiellement par les eaux usées de Santa Rosa en Californie via un pipeline car le champs se situe en milieu désertique), démontrent les multiples intérêts d'utiliser cette ressource. Afin d'optimiser l'exploitation de cette ressource énergétique, des études sur l'exploration (*i.e.* prédire les zones de haut potentiel, réduire le risque de puits non productifs et utiliser une meilleure technologie afin de minimiser les coûts de production pour caractériser la géométrie du réservoir*), sur la construction de nouvelles centrales géothermiques et sur la rentabilité économique de ces systèmes, doivent être encore développées.

I.1.2. Les types de ressources géothermales

Considérée comme renouvelable par les agences internationales de l'énergie, cette géoressource est continuellement alimentée par un flux de chaleur induit principalement par le gradient géothermal terrestre qui est lui-même sujet aux variations (i) du noyau, (ii) du manteau et (iii) de la désintégration radioactive de certains minéraux (*e.g.* uraninite) présents dans les roches de la croûte. À l'échelle planétaire, ce gradient de température peut néanmoins, dans certains contextes géologiques, changer drastiquement. En terme de gradient « normal », les boucliers archéens et paléoprotérozoïques ainsi que les bassins sédimentaires d'avant-pays ou intracontinentaux, ont respectivement des gradients de température de l'ordre de 2 °C/100 m et 3 °C/100 m, similaire à la valeur moyenne en France qui est de 3 °C/100 m [Lucazeau & Vasseur, 1989 ; Bonté *et al.*, 2010]. À l'inverse, les limites de plaques lithosphériques (zones de rifting, zones de subduction, et chaîne de collision) sont marquées par des instabilités thermiques importantes : les plus élevées peuvent atteindre plus de 140 °C/100 m dans les domaines d'arrière-arcs (au niveau des failles à faible pendage [Mulch *et al.*, 2006 ; Gottardi *et al.*, 2011]). Par conséquent, la géodynamique qui se définit par l'étude de la dynamique du globe et de ses différentes enveloppes, et donc, entre autres l'étude des mouvements des plaques, a une influence fondamentale sur la distribution des systèmes géothermaux puisqu'elle modifie directement le régime thermique et donc le flux de chaleur. Les ressources géothermales se définissent (1) par des anomalies positives de températures, qui découlent directement d'un flux de chaleur anormalement élevé à faible profondeur, et (2) par la présence de fluides (*e.g.* météorique, magmatique et/ou métamorphique) dans un milieu perméable. Ces anomalies peuvent de fait permettre le développement de réservoirs géothermiques (> 200 °C) à des profondeurs (kilométrique) d'exploitation économiquement rentable.

De fait, la répartition des ressources géothermiques est inégalement répartie à l'échelle mondiale. Actuellement, les 12 champs les plus importants sont localisés aux Etats-Unis (The Geysers, 1585 MWe ; Salton Sea, 388 MWe ; Coso, 270 MWe), aux Philippine (1870 MWe), en Italie (Larderello, 785 MWe), au Mexique (Cerro Prieto, 720 MWe), au Kenya (Olkaria, 581 MWe), en Indonésie (Salak, 377 MWe ; Darajat, 260 MWe ; Wyang Windu, 227 MWe), en Islande (Hellisheidi, 303 MWe) et en Nouvelle-Zélande (Wairakei, 232 MWe dans la « Taupo Volcanic Zone » TVZ) [Bertani, 2015]. Ces 12 champs représentent 46% de la capacité totale installée pour la production d'électricité. A titre de comparaison, le champ de Kızıldere en Turquie (Menderes Massif) à une capacité installée de 107 MWe [Bertani, 2015].

La figure I.2 montre la diversité des champs géothermaux en fonction de leur contexte géodynamique. Ils se situent principalement (i) au niveau des zones de subduction où l'activité de l'arc magmatique est importante (*e.g.* l'arc de La Sonde ou des Philippines), (ii) aux niveaux des zones divergentes en contexte de rifting océanique (*e.g.* Dorsale Médio-Atlantique comme les Açores) ou intracontinental (*e.g.* le Rift Est Africain), (iii) aux niveaux des zones transformantes par le biais de

failles décrochantes (*e.g.* la faille de San Andreas) et (iv) aux niveaux des points chauds (*e.g.* Islande, Hawaï, Réunion). Il existe donc une forte corrélation entre la localisation des principaux champs géothermaux mondiaux et la nature du contexte géodynamique comme le suggère Moeck *et al.* [2014]. Néanmoins, la diversité et la complexité de ces ressources, en raison des variabilités géologiques, géophysiques et thermodynamiques, rendent l'établissement d'une classification difficile. En accord avec plusieurs auteurs [Moeck *et al.*, 2014 ; Santilano *et al.*, 2015], une nouvelle nomenclature permettrait une évaluation quantitative de la production d'énergie et par conséquent, une amélioration de l'exploration géothermale, au moins dans ses premières phases (*i.e.* phase amont de l'exploration).

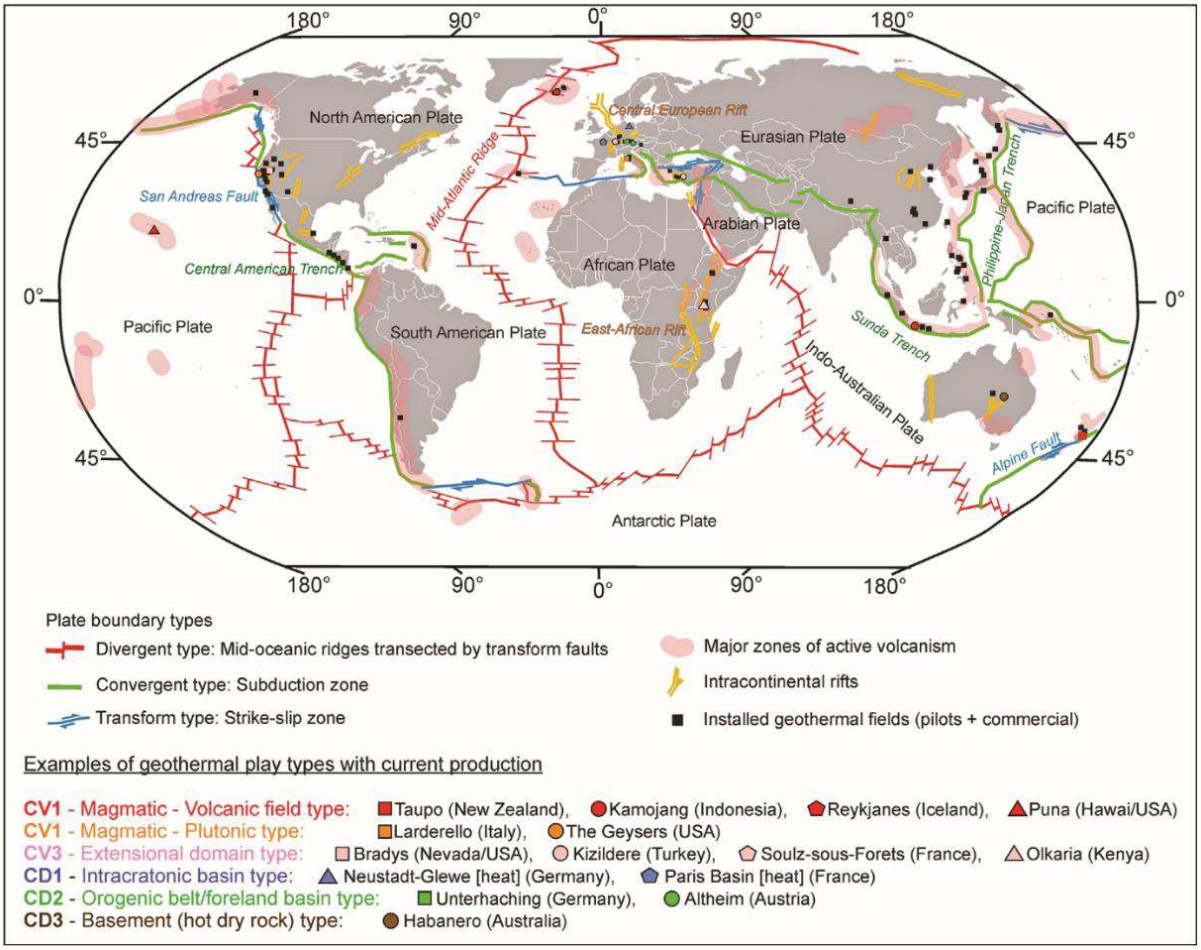

Figure I.2 : carte mondiale indiquant la localisation des champs géothermaux de références selon leurs contextes géodynamiques [Moeck, 2014], quel que soit l'usage (électricité et/ou chaleur). CV et CD représentent, respectivement, les systèmes contrôlés par des transferts de chaleur où la convection et la conduction dominent.

I.1.3. Les **classifications de systèmes géothermaux selon des champs de références**

Avant de discuter des classifications spécifiques à la géothermie Haute-Température (HT), on rappelle que les différentes nomenclatures, publiées ces 30 dernières années, sont principalement basées

sur la température des réservoirs et leurs propriétés thermodynamiques [Muffler, 1979 ; Hochstein, 1988 ; Haenel *et al.*, 1988 ; Benderitter & Cormy, 1990 ; Sanyal, 2005]. Ainsi de manière classique, les systèmes géothermaux sont divisés en trois sous-catégories (Fig. I.3) :

- les systèmes de basse température (*i.e.* les températures de réservoirs sont < 90 °C), utilisés pour du chauffage individuel et/ou collectif, la climatisation, la pisciculture...

- les systèmes de moyenne température (90 < T < 150 °C) où l'énergie produite est utilisée dans un cadre industriel comme les serres agricoles et l'extraction de produits chimiques et de métaux, mais également pour la cogénération électricité-chaleur avec des centrales adaptées

- les systèmes de haute température (T > 150 °C), utilisés principalement pour la production d'électricité.

C'est ce dernier type de géothermie qui fera l'objet de notre étude bibliographique.

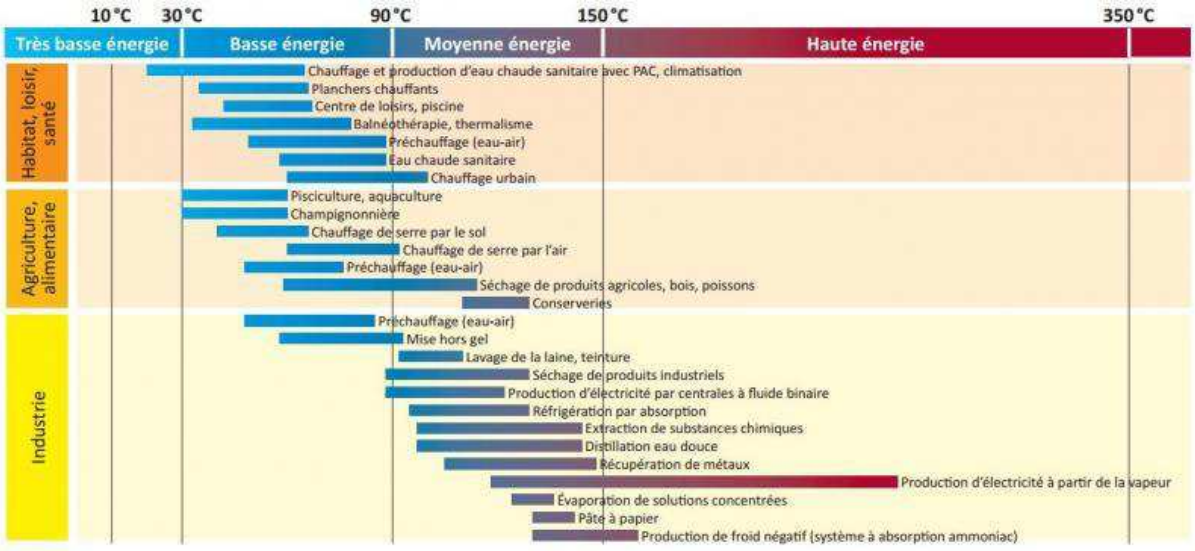

Figure I.3 : classification des systèmes géothermaux selon leurs températures de réservoir et leurs applications respectives d'après le BRGM (Bureau de recherches géologiques et minières) et ADEME (Agence de l'environnement et de la maîtrise de l'énergie). Images disponible à l'adresse suivante : http://www.geothermie-perspectives.fr/article/j-3-cop21-geothermie-comment-ca-marche-en-faire-quoi

Concernant la géothermie HT, le regain d'intérêt pour cette source d'énergie observé ces dernières années, implique l'émergence de nouvelles classifications fondées sur les mécanismes de transfert de chaleur, et/ou sur des caractéristiques géologiques [Moeck *et al.*, 2014 ; Elders *et al.*, 2014 ; Santilano *et al.* 2015]. Ces classifications semblent plus adaptées à la découverte de nouveaux gisements, mais elles diffèrent selon l'échelle à laquelle on définit le système. Par exemple, Santilano *et al.* [2015] affirment que les connaissances géodynamiques ne sont pas suffisamment claires pour les relier aux différents systèmes géothermaux ; par conséquent ils utilisent une approche locale pour décrire ces systèmes. En se basant sur l'étude de trois principaux champs géothermaux HT, Larderello et Monte

Amiata (Italie), The Geysers (USA) et Kızıldere (Turquie), ils identifient deux types de système avec des sous-catégories : (i) les systèmes convectifs (l'intérêt de cette étude) et (ii) les systèmes conductifs.

Les systèmes convectifs regroupent principalement les systèmes de HT. Ils se localisent préférentiellement aux limites de plaques tectoniques, où le magmatisme est récent (< 500 000 ans) et où la déformation est importante (Fig. I.2) [Faulds *et al.*, 2009 ; 2010 ; Deon *et al.*, 2012 ; Nukman & Moeck, 2013]. Dans cette configuration, les eaux d'origine météorique ou marine (*i.e.* recharge) peuvent migrer jusqu'à la transition fragile/ductile [*e.g.* Famin *et al.*, 2004] et vont ensuite se réchauffer sous l'influence d'une source de chaleur plus ou moins profonde (magma, intrusif…). Ces fluides géothermaux vont alors transporter la chaleur des niveaux les plus profonds vers la proche surface avant d'être bloqués à faible profondeur par une couverture imperméable. Ainsi, les contrôles structuraux et lithologiques vont jouer un rôle déterminant sur la perméabilité des réservoirs, et donc sur la circulation et l'émergence de ces fluides. Bien que cette récente classification contraigne bien les mécanismes physico-chimiques à l'origine de ces systèmes géothermaux, elle n'explique que de manière parcellaire (i) l'évolution temporelle de ces systèmes et (ii) la localisation des grandes provinces géothermales comme le Basin & Range, suggérant des processus d'échelle crustale et lithosphérique différents. Cette classification ne peut donc être utilisée pour guider l'exploration géothermale. Or, comme indiqué précédemment, le contexte géodynamique a une influence majeure sur la distribution du flux de chaleur en surface et donc sur l'évolution spatio-temporelle de l'anomalie thermique à différentes profondeurs (*i.e.* du manteau à la croûte). Cet aspect est par conséquent crucial car il peut influencer l'évolution des systèmes géothermaux depuis le manteau, jusqu'à la surface. Ainsi, la classification de Moeck [2014], qui se définit par un ensemble de contextes géodynamiques favorables au développement des systèmes géothermaux de HT, parait plus adaptée (Fig. I.2). En effet, l'auteur dans un premier temps prend en compte les relations de transfert de chaleur (convection vs. conduction) à différentes échelles, et dans un second temps, aborde l'évolution spatio-temporelle des systèmes géothermiques en fonction du contexte géodynamique. Cependant, cette classification reste simplifiée puisqu'elle ne prend pas en compte des dynamiques particulières telles que la dynamique d'arrière-arc associée au retrait et/ou à la déchirure du panneau plongeant.

I.1.4. Définition d'un système géothermal magmatique de haute température

Avant de présenter les différents contextes géodynamiques associés aux systèmes de HT, il est important de définir la notion de « système géothermal » qui se différencie de celle du « champ géothermal* ». Alors que la première notion correspond à un ensemble d'objets géologiques indispensables au bon fonctionnement du système, allant de la source de chaleur jusqu'aux expressions géothermales de surface (Figs. I.4a et I.5), la seconde représente uniquement les manifestations visibles

depuis la surface à savoir les sources (*i.e.* eau), les activités fumeroliennes (*i.e.* gaz) et éventuellement des zones d'altération (Fig. I.4a).

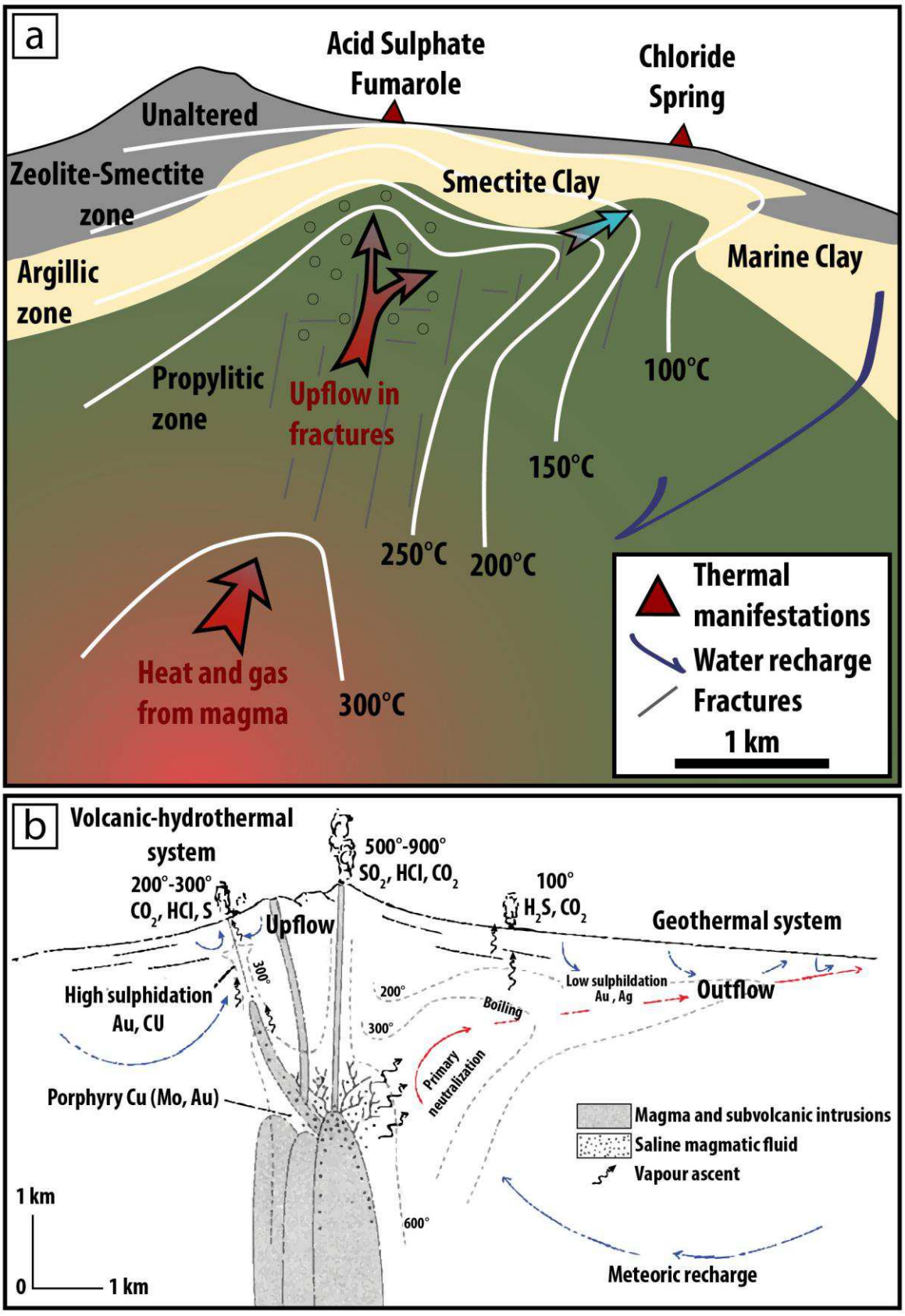

Figure I.4 : similitudes entre les modèles conceptuels actifs et fossiles de systèmes géothermaux magmatiques de HT. (a) Modèle actif modifié d'après Cumming [2009]. Un réservoir à 250 °C localisé dans les roches fracturées. (b) Modèle avec relief d'un système porphyrique et épithermale modifié d'après Hedenquist & Lowenstern, [1998].

Afin de guider l'exploration géothermale, Cumming [2009] présente un modèle conceptuel où les températures de réservoirs sont comprises entre 150 °C et 350 °C. Basé principalement sur des observations de terrain et des données géophysiques (*i.e.* magnétotellurie), il définit à la base une source de chaleur d'origine magmatique (*i.e.* chambre en cours de refroidissement diffusant de la chaleur par conduction), suivi d'un réservoir perméable capé par une zone non perméable dénommée par les anglo-saxons « cap rock* » (roche couverture) favorisant le développement d'un système de convection hydrothermale (Fig. I.4a). Précisément, la source de chaleur localisée dans la croûte supérieure (entre 3 – 10 km dans le cas d'un pluton) active la circulation des fluides profonds qui sont généralement d'origine météorique (*i.e.* recharge). Le réservoir, lieu d'exploitation des ressources HT, se définit par une forte perméabilité (*e.g.* ~$5x10^{-15}$ m^2), qui peut être primaire (*i.e.* matricielle) et/ou secondaire (*i.e.* acquise par fracturation). La perméabilité primaire peut être soit intra-formationnelle (*i.e.* encaissant de type ignimbrite, grès), soit inter-formationnelle (*i.e.* entre différentes formations lithologiques) alors que la secondaire est principalement causée par l'activité tectonique (*i.e.* encaissant fracturé) et/ou hydrothermale (*i.e.* altération). Cette zone perméable et chaude permet alors aux cellules de convection de se développer, grâce à la présence d'eau météorique ou marine issue de la recharge (Fig. I.4a). La roche couverture empêche alors la remontée des fluides hydrothermaux vers la surface et permet la circulation des fluides chauds dans le réservoir. Elle est généralement définie par une couche imperméable (*e.g.* ~ $5x10^{-18}$ m^2), composée d'argiles d'origine sédimentaire (*e.g.* argile lacustre des champs de la Taupo Volcanic Zone en Nouvelle-Zélande) et/ou plus fréquemment d'argiles d'origine hydrothermale de type smectite résultant de l'interaction des fluides géothermaux avec la roche encaissante.

Un système géothermal HT concerne donc un volume limité de roche, caractérisé par la circulation de fluides dont les températures sont comprises entre 150 °C et 350 °C. Bien qu'il soit difficile d'obtenir un consensus général sur l'origine des fluides selon le type de systèmes de HT, les fluides hydrothermaux présentent de nombreux points communs. En règle générale, le fluide est d'origine météorique avec dans certains cas, une composante marine (cas de Bouillante : jusqu'à 50 %) et/ou magmatiques (fluides riches en gaz H_20, HCl, SO_2, CO_2 et salins dans certains cas, comme à Bouillante). Il est essentiel de préciser qu'un système géothermal peut être actif ou fossile. En ce sens, les gîtes épithermaux acides (*high-sulfidation deposit types*) et neutres (*low-sulfidation deposit types*) correspondent à des systèmes hydrothermaux fossiles constituant l'apex volcanique des systèmes porphyriques (*i.e.* localisés immédiatement au-dessus de la chambre magmatique) [Hedenquist & Lowenstern, 1994]. Ainsi, les processus de mise en place des systèmes hydrothermaux actifs et fossiles

sont généralement similaires et reflètent respectivement l'état thermique actuel et passé de la croûte au-dessus des zones de subduction (Fig. I.4b) (*cf. I.2.1.1.b.*).

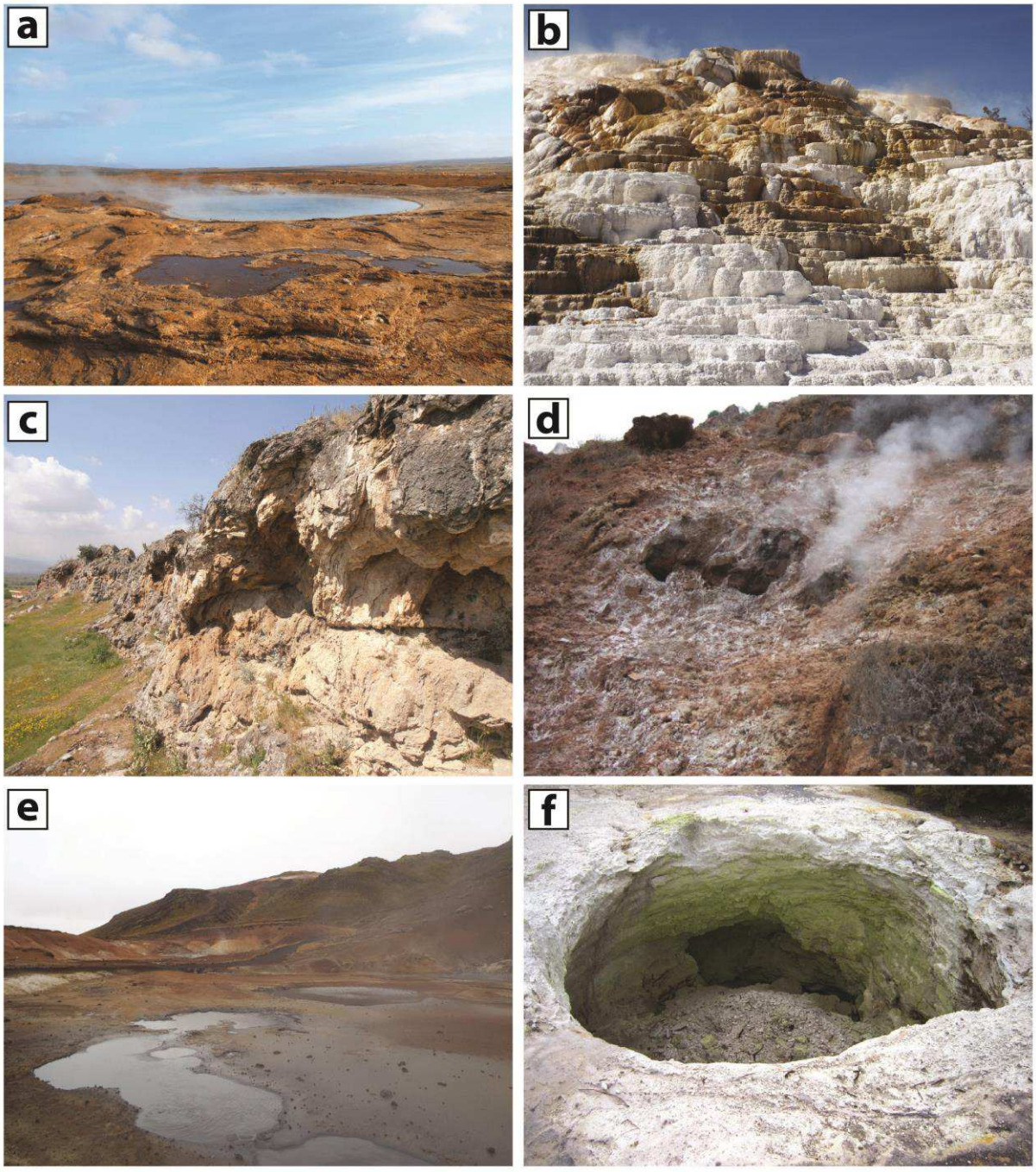

Figure I.5 : différents phénomènes géothermaux. (a) Activité géothermale montrant le rôle des archéobactéries dans la coloration des sources et des geysers au parc du Yellowstone. (b) Travertins (précipitation de carbonate) formant des marches d'escalier au parc du Yellowstone aux Etats-Unis. (c) Travertins indiquant la présence d'une faille récente dans le Massif du Menderes en Turquie (champ géothermal d'Urganlı). (d) Activité fumerolienne dans le Massif du Menderes en Turquie (Kızıldere). (e) Solfatare marquée par la présence de bulles de CO_2 à la surface en Islande. (f) Cratère d'effondrement résultant de l'érosion chimique provoquée par les condensats acides au-dessus de l'aquifère dans la zone vadose (champ géothermal de Wai-O-Tapu en Nouvelle-Zélande).

I.2. Contextes géodynamiques favorables aux développements de systèmes géothermiques de HT : le cas de la subduction

La géothermie à l'échelle mondiale s'est rapidement développée au XX^{ème} siècle, malgré une stagnation dans les années 2000 (*i.e.* manque d'investissement dans ces géo-ressources) ; l'activité depuis ces dernières années est en forte augmentation. En 2015, les estimations de la capacité installée de cette ressource énergétique sont proches de 519 MWe [Bertani, 2015]. Il est important de noter qu'une large proportion des ressources géothermiques de HT se répartit principalement le long des zones de subduction et plus particulièrement au niveau des arcs volcaniques (*e.g.* Indonésie, Philippines, Japon…) et dans les domaines arrière-arcs (*e.g.* Nouvelle-Zélande, Etats-Unis, Turquie…) (Fig. I.6). Ces zones ont donc un intérêt économique majeur puisqu'elles concentrent l'essentiel de la production d'électricité géothermique mondiale. Par exemple, le Japon est une des régions volcaniques les plus actives au monde avec environ 200 édifices volcaniques qui apportent une chaleur importante favorisant le développement de l'industrie géothermale depuis les années 1920. Ces volcans, généralement associés à du volcanisme d'arc, se distribuent de manière homogène dans tout le pays. Paradoxalement, bien que la région du Basin & Range localisée dans la partie ouest des Etats-Unis présente de nombreux champs géothermaux regroupés dans différentes zones (*e.g.* les champs regroupés dans l'ouest et dans la partie centrale du Nevada : le champ de Dixie Valley dans la ceinture de Humboldt, les champs de Wasatch dans l'ouest de l'Utah [Faulds *et al.*, 2012]), l'activité volcanique dans cette zone a cessé entre 10 Ma et 3 Ma [Faulds *et al.*, 2012]. Même si des discussions sur le rôle possible d'intrusions magmatiques sous certains de ces systèmes géothermaux sont encore actives [Faulds *et al.*, 2012], à l'échelle d'une province géothermique (plusieurs milliers de km²), une autre source de chaleur est nécessaire pour expliquer l'anomalie du flux de chaleur régionale dans cette région. Ainsi, l'origine de la chaleur de ces systèmes pourrait être associée à une source plus profonde, impliquant probablement des processus géodynamiques à grande échelle tels que la dynamique de subduction (*i.e.* la subduction de la plaque Farallon sous le Basin & Range). Nous reviendrons par la suite sur les particularités de cette province dont la capacité électrique actuelle atteint jusqu'à ~100 MWe selon la localité du champ (*e.g.* Dixie Valley) [Faulds *et al.*, 2012].

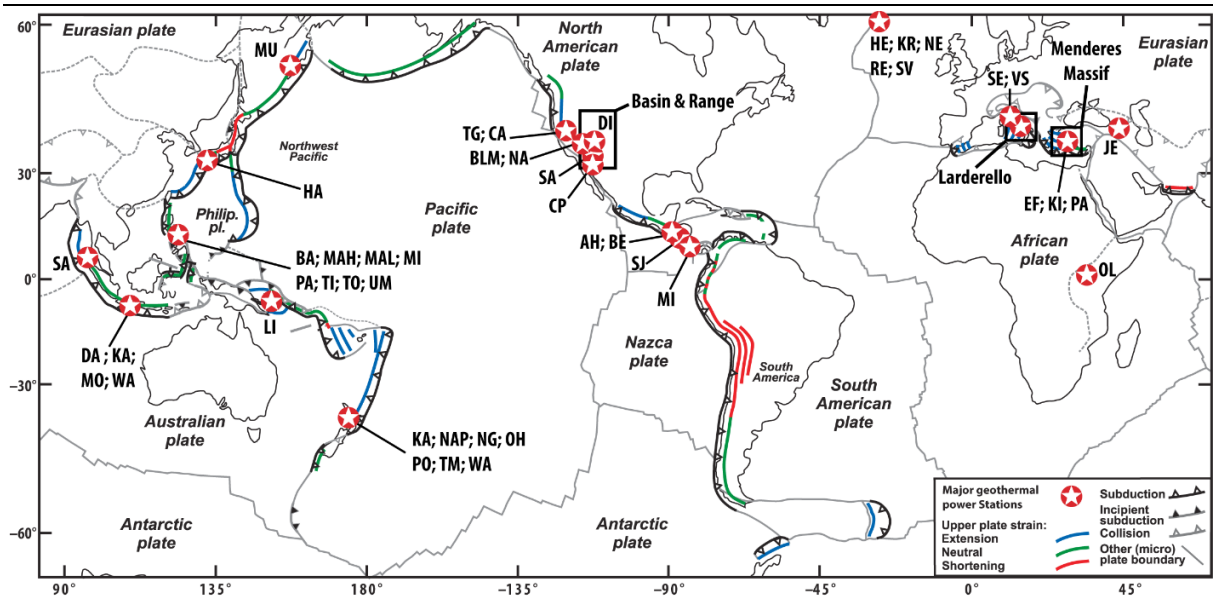

Figure I.6 : carte montrant la corrélation entre les principaux champs géothermaux de HT en activité et en construction (étoile blanche et rond rouge) et les principales zones de subduction dans le monde, modifié d'après Schellart et al. [2007]. JE, Jermaghbyur (Arménie); Mi, Miravalles (Costa Rica); AH, Ahuachapán, BE, Berlín (Le Salvador); HE, Hellisheidi, KR, Krafla, NE, Nesjavellir, RE, Reykjanes, SV, Svartsengi (Islande); DA, Darajat, KA, Kamojang, MO, Mount Salak, SA, Sarulla, WA, Wayang Windu (Indonésie) ; LA, Larderello, SE, Serrazzano, VS, Valle Secolo (Italie) ; HA, Hatchobaru (Japon); OL, Olkaria (Kenya); CP, Cerro Prieto (Mexique); KA, Kawerau, NAP, Nga Awa Purua, NG, Ngatamariki, OH, Ohaaki, PO, Poihipi, TM, Te Mihi, WA, Wairakei (Nouvelle-Zélande); SJ, San Jacinto Tizate (Nicaragua); LI, Linhir (Nouvelle-Guinée); BA, Bacman I, MAH, Mahanagdong, MAL, Malitbog, MI, Mindanao I-II, PA, Palinpinon I-II, TI, Tiwi A-B-C, TO, Tongonan 1, UM, Upper Mahiao (Philippines); MU, Mutnovskaya, Russia; EF, Efeler, KI, Kızıldere, PA, Pamukören (Turquie); BLM, CA, Calistoga, DV, Dixie Valley, NA, Navy, SA, Salton Sea, TG, The Geysers (Etats-Unis).

Par ailleurs, comme pour la localisation des champs géothermaux, les zones de subduction sont également reconnues pour la grande diversité des gîtes minéraux qui leur sont associés (*e.g.* gîtes porphyriques et épithermaux, breccia pipes, skarns, mantos, voire des gîtes de sulfures massifs en contexte arrière-arc) et pour la suite d'éléments associés composé de métaux de base (Cu, Pb, Zn, Mo) et de métaux précieux (Au, Ag (±Pt)) [Menant *et al.*, 2016a]. Ainsi, la communauté scientifique a mené de nombreuses études sur les minéralisations en contexte de subduction [Solomon, 1990 ; Hedenquist & Lowenstern, 1994 ; Sillitoe, 1997 ; 2010 ; Tosdal & Richards, 2001 ; Richards, 2003 ; 2005 ; 2009 ; Sillitoe & Hedenquist, 2003 ; Cooke *et al.*, 2005 ; Williams-Jones & Heinrich, 2005 ; Seedorff *et al.*, 2005 ; Groves & Bierlein, 2007 ; Wilkinson, 2013 ; Bertrand *et al.*, 2014].

I.2.1. Les systèmes géothermaux en contexte de subduction : magmatique vs. amagmatique

De ce fait, des modèles conceptuels détaillés ont été proposé pour décrire les principaux processus de circulation actifs et fossiles en lien avec la géodynamique. Il s'agit (i) des systèmes actifs dominés par une activité magmatique (*i.e.* volcanisme actif ou chambre magmatique profonde) comme aux Etats-Unis (*i.e.* The Geysers, [Hulen & Nielson, 1996 ; Dalrymple *et al.*, 1999]), en Nouvelle-Zélande (*i.e.*

The Taupo Volcanic Zone, [Wilson & Rowland, 2016]) et en Italie (*i.e.* Larderello, [Baldi *et al.*, 1994]) ou (ii) des systèmes hydrothermaux fossiles localisés depuis la surface de la plaque chevauchante, jusqu'au coin mantellique sus-jacent à la lithosphère subduite.

Il existe à contrario peu d'études sur les provinces géothermales considérées comme « amagmatiques » (*i.e.* dont l'origine thermique n'est pas reliée à la présence de magma). En effet, il est clair que la présence de magma à faible profondeur (*i.e.* chambre magmatique et/ou pluton récent) génère des anomalies thermiques exploitables sur des faibles distances, alors que les anomalies thermiques amagmatiques restent peu comprises. D'une part parce que ces dernières impliquent un saut d'échelle important (une province géothermale de plusieurs milliers de km²) comparé aux études des systèmes magmatiques, suggérant une implication d'une source de chaleur profonde d'origine mantellique (ou base de croûte) et d'autre part, parce que la dynamique de la subduction est un processus complexe, qui évolue dans le temps, et qui engendre aussi bien de la compression que de l'extension. Ainsi, on s'attend à ce que les anomalies thermiques évoluent en fonction de la dynamique de subduction. Alors que les systèmes géothermaux actifs restent difficiles à explorer, faute de modèles conceptuels encore réellement adaptés, les systèmes fossiles sont mieux caractérisés [*e.g.* Groves *et al.*, 1998 ; 2003]. Afin de mieux comprendre les mécanismes physico-chimiques à l'origine de ces systèmes amagmatiques et d'éviter les amalgames avec les systèmes classiques magmatiques, il est nécessaire de mieux caractériser les provinces amagmatiques pour guider l'exploration géothermale et améliorer la connaissance sur ces paléo-systèmes.

I.2.1.1. Les systèmes magmatiques d'arc ou d'arrière-arc : actifs vs. fossiles

a. Les systèmes magmatiques actifs

Deux grands modèles conceptuels de systèmes géothermaux de HT basés sur la topographie, sont décrits dans la littérature : les systèmes en dépression (*i.e.* bassin et zone d'arrière-arc) et les systèmes à fort relief (*i.e.* arc insulaire et stratovolcan) (Fig. I.7a et I.7b). Les systèmes en dépression sont caractérisés uniquement par des remontées verticales de fluides géothermaux (*upflows*), impliquant en surface la formation de sources thermales chlorurées sodiques à l'aplomb du système magmatique (Fig. I.7a). A contrario, les systèmes à fort relief exercent un contrôle topographique important sur la circulation des fluides hydrothermaux. Ils se localisent principalement dans les régions d'arc volcanique avec des compositions basaltique à andésitiques (*i.e.* le long de l'arc insulaire de Java [Deon *et al.*, 2012]). Cet effet de topographie empêche les fluides d'atteindre la surface à l'aplomb de la chambre magmatique et de plus modifie le gradient hydraulique. Ce dernier permet alors aux fluides de s'écouler latéralement sur des longues distances (~10 km jusqu'à 50 km dans de rare cas) vers les bas-reliefs [Byrdina *et al.*, 2013], avant de précipiter sous la forme de sinters siliceux (*i.e.* silica sinters) si la

température est suffisante ou sous la forme de travertins si elle ne l'est pas. On utilise donc le terme de *"upflow"* pour les zones de remontées de fluides géothermaux situées à l'aplomb de la chambre magmatique en cours de refroidissement depuis plusieurs centaines de milliers d'années et le terme de *"outflow"* lorsque les fluides épousent la pente du stratovolcan (Fig. I.7b) [Hoschtein, 1988].

Les systèmes marqués par la présence d'un intrusif proche de la surface en cours de refroidissement (700 °C à > 1000 °C, *e.g.* le champ géothermal de Larderello [Santilano *et al.*, 2015]) (Fig. I.7a), sont également intéressants pour la géothermie puisque leur cristallisation va engendrer une libération importante de chaleur. La source de chaleur d'origine magmatique est généralement située dans la croûte supérieure (3–10 km) sous la forme de grandes chambres magmatiques. Ainsi, le développement d'un système de grande taille et de longue durée est favorisé par (i) la présence de multiples intrusions dans la croûte, par (ii) l'âge de mise en place du magmatisme et (iii) par sa profondeur. Ces trois paramètres contrôlent donc directement la quantité de chaleur du système géothermal qui se localise généralement à l'aplomb de ce dernier. C'est le cas par exemple à Larderello ou au Monte Amiata (Italie) où les anomalies du flux de chaleur atteignent localement 1000 $mW.m^{-2}$ [Baldi *et al.*, 1994] à l'aplomb des intrusions. Alors que la première est datée à 3,8–1,3 Ma [Dini *et al.*, 2005], les secondes, indiquées par des études géophysiques sous le Mont Amiata [Bernabini *et al.*, 1995 ; Manzella *et al.*, 1998 ; Finetti, 2006], sont plus jeunes et correspondent en surface à l'activité volcanique datée à 0,3–0,2 Ma [Gianelli & Puxeddu, 1994]. Des études similaires sur le champ géothermal de Geysers (Etats-Unis) [Dalrymple *et al.* 1999] confirment ainsi la présence d'un batholite récent (1,18 Ma) localisé à faible profondeur avec un volume d'environ 100 km^3. Ce dernier est à l'origine du développement des systèmes de HT. Il est intéressant de noter qu'il peut exister un écart temporel (n x 100 000 ans) entre la fin du magmatisme et la mise en place du système géothermal. Cette particularité est fortement débattue par la communauté scientifique.

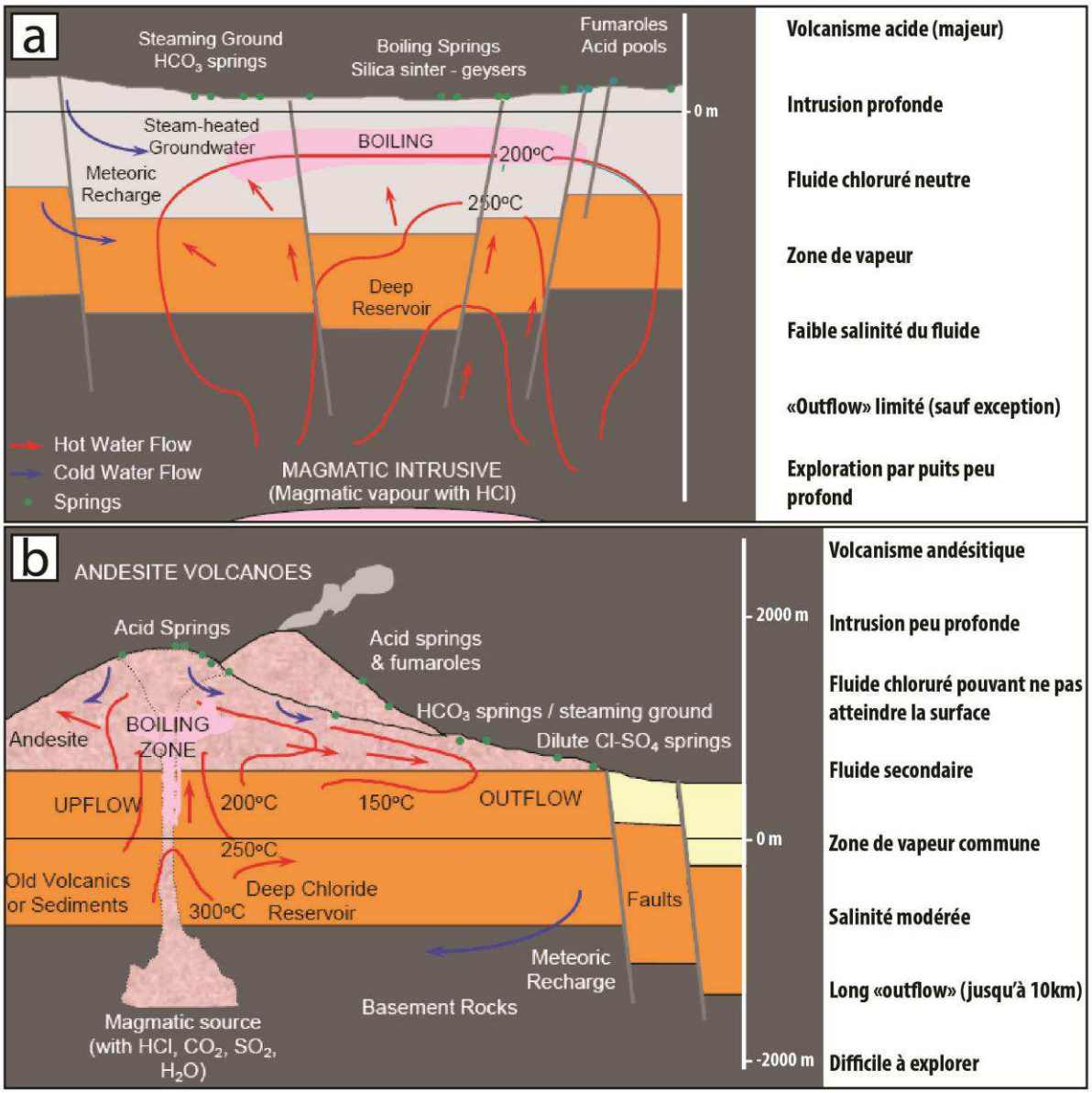

Figure I.7 : modèles conceptuels actifs de systèmes géothermaux magmatiques de HT. (a) Modèle sans relief, en dépression, typique du domaine arrière-arc modifié d'après KML [1995]. (b) Modèle avec relief, typique des arcs insulaires modifié d'après KML [1995].

Dans les deux types de systèmes, le fluide une fois homogénéisé dans le réservoir, est généralement caractérisé par une composition chlorurée-sodique (NaCl) à pH neutre à légèrement acide (5 à 7) en présence de gaz dissous (notamment CO_2 et H_2S). Il présente également de faibles teneurs en sel de l'ordre de 1 à 3 $g.l^{-1}$, sauf dans certains cas comme à Bouillante (20 $g.l^{-1}$). Ainsi, selon la nature du fluide et de la roche encaissante, différentes expressions de surface sont observées. Par exemple, des sources chaudes chlorurées-sodiques associées à des dépôts siliceux de type silica-sinters (principalement composé d'opale, calcédoine et/ou quartz) présentant parfois des concentrations élevés en As (100 $mg.kg^{-1}$) et des métaux tels que la Sb, Tl, Hg, [Corbett & Leach, 1993] témoignent de températures de réservoirs supérieures à 175 °C (Figs. I.5a, b et c). Lorsqu'une partie du réservoir atteint l'ébullition, d'autres expressions plus acides (allant jusqu'à un pH ~2.5), comme les fumerolles, les

cratères d'effondrements et les piscines de boue, appelées « mud-pots » (Figs. I.5d, e et f) se développent et se localisent à l'aplomb du réservoir en cours d'ébullition en relation avec l'émission de gaz H_2S (Fig. I.7). En effet, l'ébullition des eaux chlorurées au toit du réservoir produit des fluides biphasés, liquide neutre et vapeurs acides enrichies en H_2S (gaz). Les vapeurs acides se condensent par la suite bien plus haut au-dessus du réservoir (dans la zone *vadose)*, où l'oxydation du H_2S produit de l'acide sulfurique H_2S0_4 et des eaux sulfatées. Ces condensats acides (100–150 °C, pH 2 à 4) vont corroder la roche encaissante pour former des cratères de dissolution et produire des boues acides (Figs. I.5e et I.5f). Ces expressions de surface sont donc généralement accompagnées par des altérations de l'encaissant de type kaolinite, et représentent de bons guides pour l'exploration géothermale. En général, la chaleur est ensuite évacuée par l'intermédiaire de structures associées à la mise en place de l'appareil volcanique (*e.g.* caldeira, stratovolcans, bassin arrière-arc) et/ou par la néotectonique dans le cas d'un intrusif. Les réservoirs sont intrinsèquement perméables car ils se composent de roches volcaniques fracturées (perméabilité de fracture) et/ou se caractérisent par une perméabilité matricielle comme les ignimbrites poreuses des champs de Nouvelle-Zélande. Il est important de noter que les fluides des systèmes géothermaux magmatiques sont caractérisés par une forte composante mantellique, qui est indiquée par le ratio élevé (> 4–5 Ra) du rapport isotopique de $^3He/^4He$. Ce ratio est généralement utilisé pour contraindre les circulations de fluides hydrothermaux à l'échelle crustale [Kennedy & van Soest, 2005 ; 2006].

b. Les systèmes magmatiques fossiles

Magmatisme et transfert des métaux : magma d'arc vs. magma post-collision et arrière-arc

Il est important ici de souligner que la formation d'une concentration métallique nécessite une source, un transport et un dépôt [Routhier, 1963]. Les fluides hydrothermaux (une saumure sur-salée et un fluide volatil) transportent les métaux, et les facteurs tels que la baisse de la pression, de la température ou encore l'interaction avec la roche encaissante ou avec d'autres fluides (*e.g.* météoriques), favorisent la précipitation de phases minérales dans des environnements variés et dans différents contextes géodynamiques (Fig. I.8). Les éléments et le fluide qui les transporte dépendent alors de la perméabilité de la roche encaissante. L'eau à l'état liquide est généralement très chargée en sel (environ 40 % pds Eq. NaCl) comparé au fluide volatil, et donne lieu à des minéralisations au toit des intrusions magmatiques, appelés porphyres* cuprifères (Fig. I.4b). Des gîtes épithermaux acides puis neutres (ou « low sulfidation ») sont donc formés à l'aplomb de ces systèmes porphyriques (Fig. I.4b).

Magmatisme et transfert des métaux : magma d'arc vs. magma post-collision et arrière-arc

Comme pour les systèmes actifs, les modèles conceptuels sont généralement développés au niveau des arcs magmatiques fossiles, là où la variabilité et les teneurs en métaux sont les plus importantes, et par conséquent les plus rentables. Ces zones sont généralement caractérisées par des magmas silicatés issus directement de la fusion partielle du manteau [Gill, 1981], induit par une déshydratation du slab (*i.e.* panneau plongeant). Stocké en base de croûte sous la forme d'un complexe de sills [Herzberg *et al.*, 1983] dans la zone appelée la « melting-assimilation-storage-homogenization » zone (*i.e.* MASH zone) ou zone chaude (Fig. I.8a) [Hildreth & Moorbath, 1988 ; Annen, 2006], le magma primaire va progressivement se différencier grâce à des processus de cristallisation fractionné et d'assimilation de la croûte inférieure encaissante. Pendant cette phase de cristallisation, le magma s'appauvrit en certains métaux (*e.g.* Au et éléments sidérophiles) qui sont piégés dans des minéraux sulfurés néoformés [Hedenquist & Lowenstern, 1994 ; Zajacz *et al.*, 2012]. Mais il s'enrichit localement en cuivre [Richards, 2009] et en certains métaux d'affinité crustale comme le plomb, le zinc, l'argent et possiblement le molybdène [Richards, 2011]. Néanmoins, la réinjection d'un magma primaire chaud peut déstabiliser cette tendance, d'une part en remobilisant les minéraux sulfurés néoformés qui contiennent de l'or et des éléments sidérophiles, et d'autre part en réapprovisionnant en métaux cette zone MASH [Richards, 2009 ; Wilkinson, 2013]. Une fois différencié, le magma andésitique à dacitique s'accumule dans une chambre magmatique dans la croûte supérieure par l'intermédiaire de nombreux dykes [Annen, 2006]. Au cours de cette remontée, les conditions de pression et de température diminuent. Ces variations génèrent alors une baisse de la solubilité de l'eau et une saturation progressive du magma en éléments volatils, favorisant ainsi le mécanisme d'exsolution entre 500 et 600 °C. Ce mécanisme est crucial pour le fractionnement et la concentration des métaux [Hedenquist & Lowenstern, 1994 ; Candela & Piccoli, 2005 ; Scaillet, 2010 ; Wilkinson, 2013].

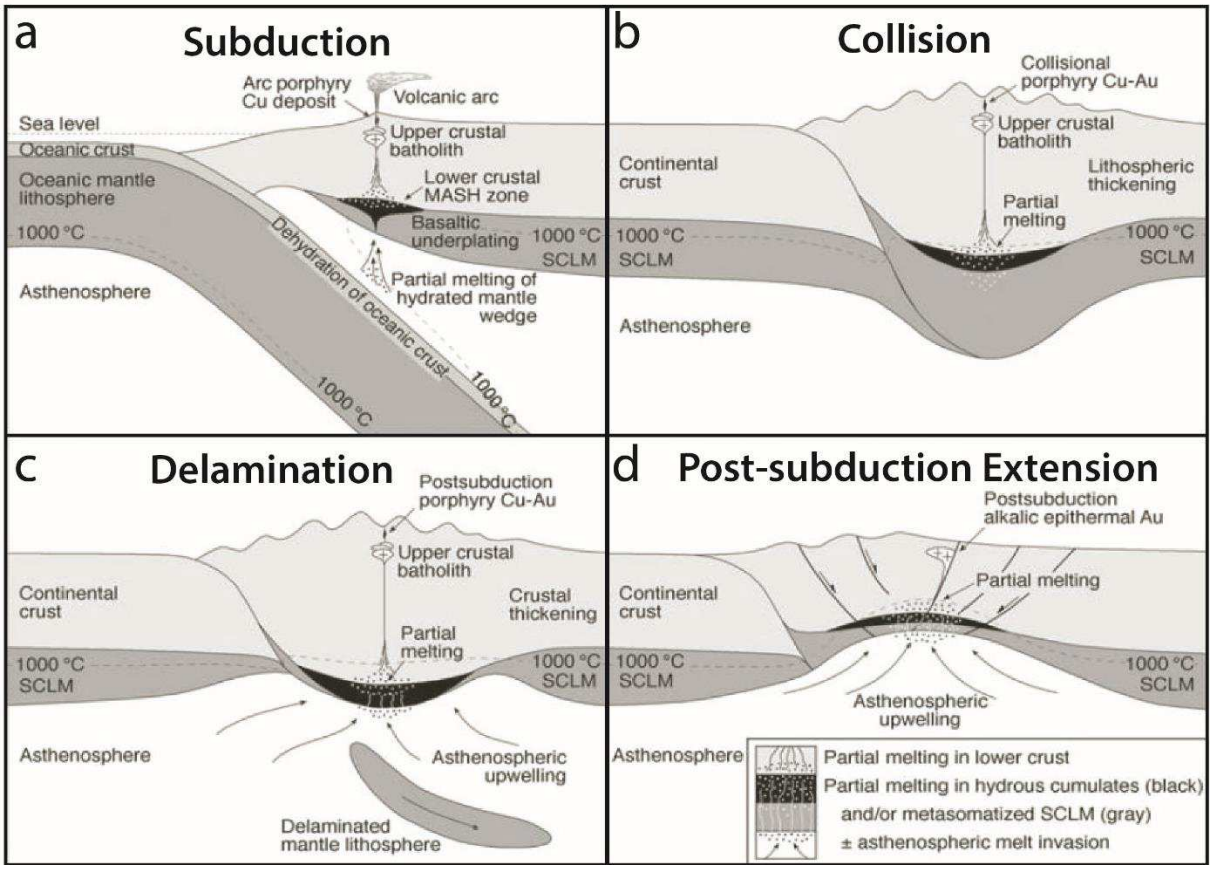

Figure I.8 : schémas conceptuels (a) d'une zone de subduction, (b) de collision, (c) de post-collision et (d) d'extension arrière-arc montrant les principaux processus, systèmes magmatiques et hydrothermaux qui peuvent s'y développer d'après Richards [2009].

Dans les domaines « post-collision » et « d'arrière-arc » (Figs. I.8c et I.8d), le magmatisme peut être généré par différents processus comme (i) la rééquilibration thermique, (ii) l'épaississement lithosphérique, (iii) la délamination lithosphérique ou (iv) l'extension lithosphérique. Ces magmas considérés comme hérités, se localisent en quantité limitée dans la croûte supérieure [Davies & von Blankenburg, 1995 ; Jiang *et al.*, 2006]. Ils présentent également un enrichissement en Au comparé aux magmas d'arc, qui s'explique par la présence de sulfures résiduels enrichis en éléments sidérophiles dans la base de la croûte inférieure et dans le manteau lithosphérique [Richards, 2005]. Facilité par une densité moins importante que l'encaissant et par des structures crustales perméables, jouant le rôle de drain, ces magmas remontent rapidement dans la croûte supérieure [Richards *et al.*, 1990].

Hydrothermalisme et précipitation des métaux : l'exemple des épithermaux neutres*

Les systèmes hydrothermaux actifs d'arcs présentent de nombreux points communs avec les systèmes fossiles (notamment les épithermaux neutres à Au-Ag …) (Figs. I.7b et I.4c). D'ailleurs, l'activité fumerolienne de certains volcans actifs (*e.g.* le Mérapi et le Kawah Ijen sur l'ile de Java en Indonésie) constitue l'analogue moderne des gîtes épithermaux acides. Plus en détail, basé sur des

comparaisons et des compilations de données entre des systèmes géothermaux actifs (*e.g.* Bouillante, Guadeloupe ; Awibengkok et Kamojang, Indonésie), et des gîtes minéraux fossiles épithermaux neutres (*e.g.* Cirotan et Lebong Tandai, Indonésie), Bouchot & Genter [2009] mettent en évidence des similitudes (i) sur la signature magmatique, (ii) sur les contrôles structuraux (*i.e.* failles décrochantes, pull-aparts…), (iii) sur les délais de mise en place de l'activité hydrothermale, compris entre 1 Ma et 500 000 ans après l'intrusion et/ou le volcanisme (même si cette période dépend du volume du magma, de sa profondeur de mise en place, et de l'aspect épisodique de la mise en place), (iv) sur la présence de sinters et de breccia pipes indiquant des informations sur la qualité du réservoir. Néanmoins, il est intéressant de noter que les conditions P-T du réservoir géothermique diffèrent pour les systèmes actifs et fossiles. Alors que l'ébullition peut parfois se produire dans les systèmes actifs (Fig. I.7b), elle semble se produire plus généralement dans les gisements fossiles (Fig. I.4c), dans la mesure où l'ébullition est considérée comme un facteur essentiel à la précipitation des métaux et notamment de l'or.

Les minéralisations des épithermaux neutres se caractérisent généralement par des veines rubanées à gangue de quartz, calcédoine, adulaire, calcite, minéraux de manganèse (*i.e.* rhodochrosite et rhodonite), où peuvent se concentrer des métaux précieux comme l'or ou l'argent (notamment sous la forme de tellures), mais également des métaux de base tels que le plomb (*i.e.* galène), le zinc (*i.e.* sphalérite) et le cuivre (*i.e.* chalcopyrite). En réagissant de manière significative avec la roche encaissante et les eaux météoriques, le fluide minéralisateur se neutralise progressivement au cours de son transport [White & Hedenquist, 1990 ; Hedenquist & Lowenstern, 1994], favorisant la précipitation des métaux. Ces systèmes fossiles présentent de nombreuses similitudes avec les systèmes actifs, et leur compréhension apporte donc de nouvelles contraintes sur le fonctionnement des systèmes actifs (*cf. chapitre VII et Annexe C*).

I.2.1.2. Les systèmes géothermaux amagmatiques : actifs vs. fossiles

a. Les systèmes amagmatiques actifs

En l'état de la connaissance, les systèmes amagmatiques sont principalement localisés dans les régions arrière-arc des zones de subduction où l'activité tectonique importante semble déconnectée d'une activité volcanique récente, comme c'est le cas dans le Basin & Range (Etats-Unis) ou dans le Massif du Menderes (Turquie) [Faulds *et al.*, 2009]. C'est d'ailleurs dans la première région citée que, dans les années 1970, ce type de système a été décrit pour la première fois. Différents auteurs [*e.g.* Benoit, 1999 ; Blackwell *et al.*, 2000] soulignent l'absence de volcanisme récent dans cette région (*i.e.* absence dans la croûte supérieure) et expliquent par conséquent la localisation des nombreux champs géothermaux de HT (*i.e.* 280 °C à 3 km de profondeur, Dixie Valley [Blackwell *et al.*, 2000] ; Fig. I.9a),

par la présence d'anomalies de température profonde, localisées dans la croûte inférieure. Des études sur la géochimie isotopique de l'hélium confirment également que ces systèmes sont amagmatiques [Kennedy *et al.*, 2000]. Ces signatures isotopiques particulières (*i.e.* caractérisés par 2 à 15 % d'hélium mantellique) impliquent que les niveaux de décollement/détachement à l'échelle crustale semblent connectés avec le manteau supérieur [Pik & Marty, 2009]. Plus récemment, Wannamaker *et al.* [2006a ; b] ont réalisé différents profils magnétotelluriques au travers de cette province (Fig. I.9b). L'un d'entre eux, qui traverse d'est en ouest le Basin & Range (300 km de long), indique la présence d'une anomalie conductrice localisée dans la partie inférieure de la croûte entre 20 et 25 km profondeur. Selon ces auteurs, cette anomalie correspond à une source de chaleur profonde, interprétée comme du sous-plaquage magmatique. Néanmoins, ces différentes études confirment que l'anomalie thermique dans la région est de grande longueur d'onde. L'activité tectonique récente associée à ces anomalies de température de grande profondeur, contrôle alors la circulation des fluides dans la croûte supérieure et donc l'émergence de sources chaudes en surface [Caskey *et al.*, 2000].

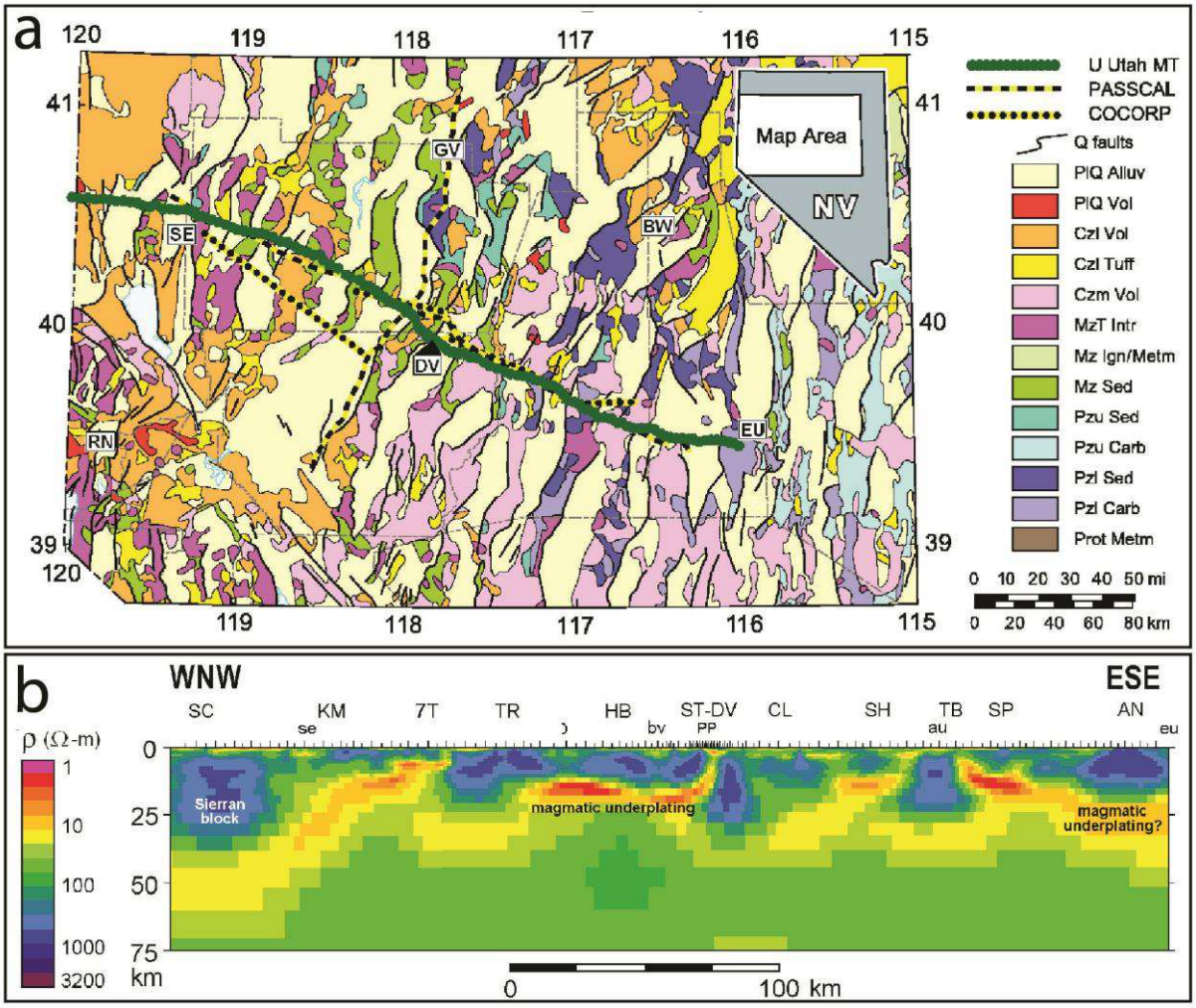

Figure I.9 : Profil MT à travers le Basin & Range d'après Wannamaker et al. [2006b]. (a) Carte géologique de la partie nord-ouest de l'état du Nevada. Le tracé vert indique les stations ou le profil MT a été réalisé. Dixie Valley (DV), Reno (RN), Grass Valley (GV), San Emidio (SE), Beowawe (BW) et Eureka (EU). (b) Profil 2D non linéaire MT. Smoke Creek (SC), les sources chaudes de San Emidio (se), Kumiva Peak (KM), Seven Troughs Range (7T), Trinity Range (TR), Humboldt Range (HB), Buena Vista Valley (bv), Stillwater Range-Dixie Valley system (ST-DV), Centrale électrique (PP), Clan Alpine Range (CL), Shoshone Range (SH), ville d'Austin (au), Toiyabe Range (TB), Simpson Park Range (SP), Antelope Range (AN),et la ville d'Eureka (eu).

Il est important de noter que la dynamique de subduction semble être reliée à la formation d'anomalies de températures pluri-décakilométriques en profondeur par le l'intermédiaire de différents processus comme, par exemple, une remontée asthénosphérique [Moeck, 2014], une croûte inférieure anormalement chaude... En effet, à l'opposé des systèmes volcaniques ($^3He/^4He$ >4–5 Ra), le rapport isotopique de $^3He/^4He$ est faible ($^3He/^4He$ ~1 Ra) indiquant à la fois une composante crustale dominante et mantellique limitée. Les différents types de faille (*i.e.* normales à faible et fort pendage, décrochantes) qui accommodent l'extension dans la plaque supérieure, jouent également un rôle déterminant dans la circulation des fluides. Ces zones perméables se comportent comme des conduits et/ou comme des barrières (*i.e.* gouge de faille) [Caine *et al.*, 1996 ; Bense & Person, 2006], et permettent alors aux fluides hydrothermaux de remonter vers la surface (Fig. I.10). Ces fluides sont généralement bicarbonatés, plus rarement chlorurés (en cas d'influence marine comme à Seferihisar à l'ouest du massif du Menderes en

Turquie), et les températures des réservoirs mesurées sont comprises entre 150 et 287 °C. On notera que des températures très élevées (*i.e.* ~280 °C) peuvent être atteintes à de faibles profondeurs (2750 m) comme à Alaşehir (Turquie) [Baba *et al.*, 2015] ou à Dixie Valley (USA, voir ci-dessus). A ce titre les températures sont comparables à celles reliée à un système magmatique qui dépassent exceptionnellement les 300 °C. D'autres paramètres importants comme le champ de contrainte de la croûte, le taux de déformation associé à l'extension et/ou transtension (*e.g.* taux de déformation de 10–100 ns.y^{-1} pour la région de Walker Lane dans le Basin & Range [Kreemer *et al.*, 2009]), la topographie, les processus de dissolution et de karstification vont également influencer la circulation des fluides et la localisation des réservoirs.

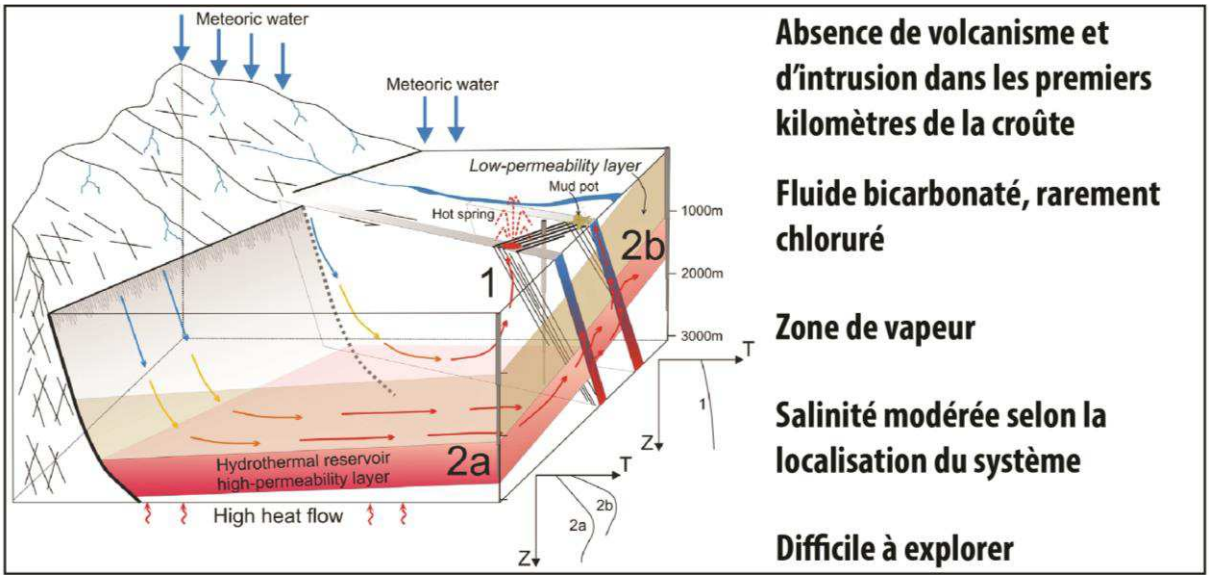

Figure 1.10 : représentations schématiques de systèmes géothermaux associés à une activité tectonique. Modifié d'après Moeck [2014].

Par ailleurs, ces régions sont généralement caractérisées par une tectonique extensive induite par la dynamique de subduction. Elle se caractérise par un amincissement crustal de la pile tectonique et l'exhumation de dômes métamorphiques (MCCs), accommodée par la formation de failles normales à faible pendage appelées détachements. Ces dômes à fort relief topographique, décrits pour la première fois à la fin des années 70 dans la province du Basin & Range [Davis & Coney, 1979 ; Crittenden *et al.*, 1980 ; Wernicke & Burchfiel, 1982], se définissent par (i) une partie centrale (le cœur du dôme) composée de roches plutoniques (*e.g.* granitoïdes, migmatites…) et/ou métamorphiques de haute température (*e.g.* métasédiments, schistes) et (ii) une bordure, définie par une faille à faible pendage où la déformation atteint son paroxysme. Cette zone porte également les marques d'un hydrothermalisme intense, comme le suggère la présence importante de veines de quartz syn-tectoniques durant l'évolution de la déformation depuis le domaine ductile jusqu'au domaine fragile (*e.g.* la zone de cisaillement de Tinos, Grèce [Famin *et al.*, 2004]). Ainsi ce système, qui comprend une déformation fragile en

prolongement d'une zone de cisaillement ductile, représente un contrôle majeur sur la circulation des fluides (paléo et actuels) à l'échelle crustale. Selon Famin *et al.* [2004], la circulation dans un détachement est générée, dans l'ordre croissant de la profondeur, par la convection thermique, par les cycles sismiques (au niveau de la transition fragile/ductile) et par la migration diffuse dans la croûte inférieure (Fig. I.11a). En somme, ces zones perméables marquées par une déformation intense (*e.g.* formation des plis en fourreaux, de mylonites et d'ultra-cataclasites) et active sur plusieurs Ma, accommodant l'exhumation des MCCs, représentent un contexte favorable pour le développement et la localisation de systèmes hydrothermaux actuels et fossiles de HT.

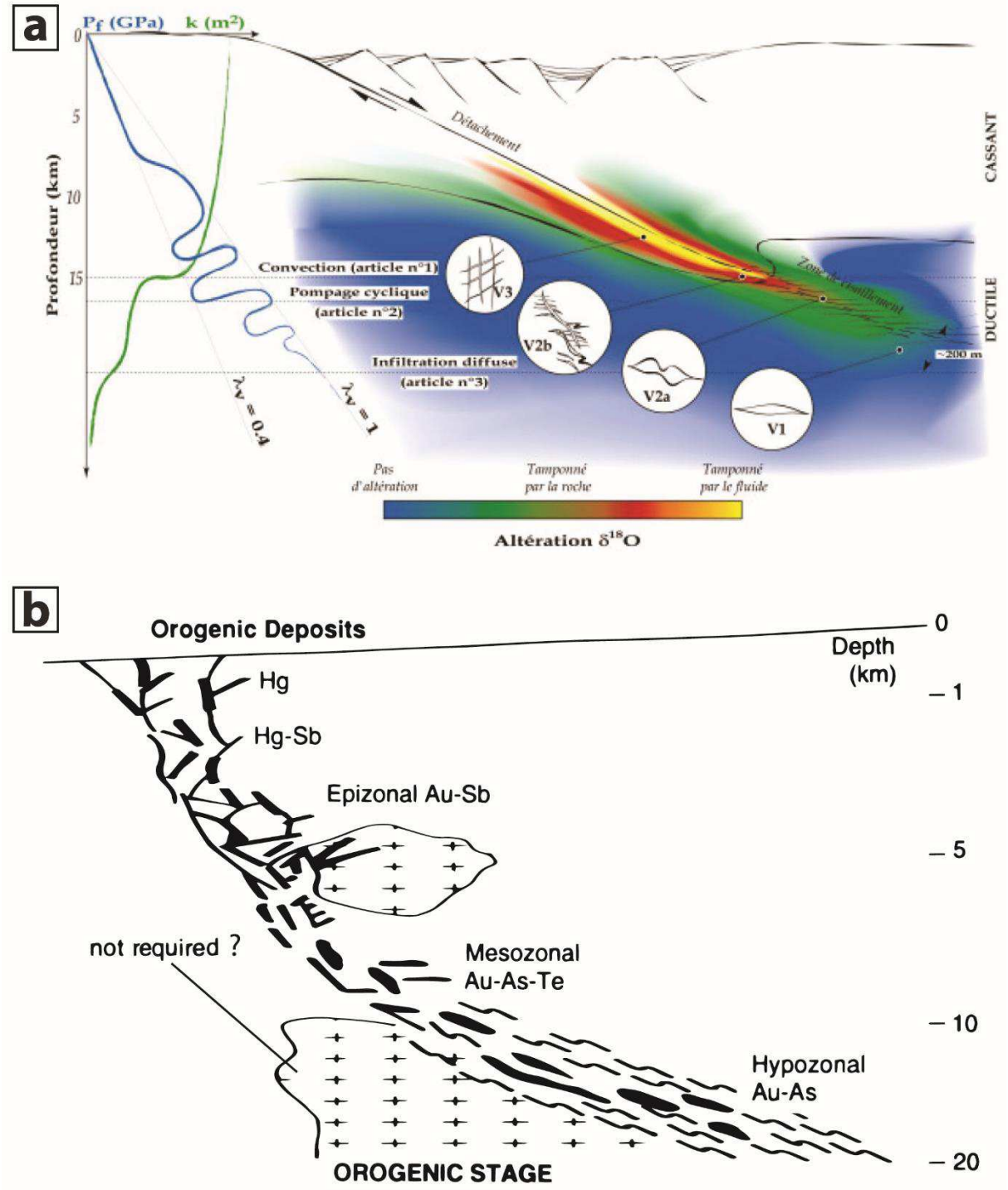

Figure I.11 : les circulations au sein d'une zone de cisaillement. Il est important de noter les similitudes entre les deux modèles. (a)Modèle extensif montrant les mécanismes de circulations dans une faille à faible pendage, ainsi que les profils de pression et de perméabilité en fonction de la profondeur [Famin, 2014]. (b) Représentation schématique des trois sous-types de gisement d'or orogénique dans un contexte compressif modifié d'après Groves et al. [1998].

b. Les systèmes amagmatiques fossiles

Les gisements d'or orogénique se forment majoritairement aux niveaux des zones de collision, mais également dans des contextes tardi-orogéniques et post-orogéniques [*e.g.* Goldfarb *et al.*, 2001 ; Groves *et al.*, 2003 ; 2005]. Dans ce sens, Bonev *et al.* [2013] montrent dans le Massif du Rhodope (sud-ouest de la Bulgarie) que des failles crustales à faible pendage, se développant dans les premiers stades d'extension, contrôlent les minéralisations à or. Bien qu'il existe une relation temporelle entre le magmatisme (*i.e.* les granitoïdes) et ces minéralisations, aucune évidence spatiale n'a été réellement démontrée [Groves *et al.*, 2003]. De ce fait, le contrôle structural des gisements mésothermaux orogéniques est primordial [*e.g.* Sibson, 1987 ; Sibson *et al.*, 1988]. Ainsi, les zones de déformation importante (*i.e.* zones de cisaillement) générées par la dynamique de subduction (*e.g.* collision, extension dans la plaque supérieure) représentent des endroits favorables aux circulations de fluides dans la croûte. Il est intéressant de noter que le système minéralisé se développe également dans des failles de second et de troisième ordre (*e.g.* failles kilométriques pour une puissance de 10 à 100 m [Colvine *et al.*, 1988]). Selon Groves *et al.* [1998], il existe trois types de gisements orogéniques (Fig. I.11b) : (i) les gisements épizonaux localisés entre 0 et 6 km de profondeur, formés à des températures de 150 °C, (ii) les gisements mésozonaux localisés entre 6 et 12 km de profondeur, formés à des températures comprises entre 300 et 475 °C, (iii) les gisements hypozonaux localisés à plus de 12 km de profondeur, formés à des températures supérieures 475 °C.

Ce type de gisements aurifères se caractérise généralement par des veines à quartz et carbonates incluant des sulfures en faible quantité (3 à 5%). Ces sulfures de fer se présentent sous la forme de pyrite, arsénopyrite et pyrrhotite, et sont accompagnés par de l'or sous la forme d'électrum. Le fluide minéralisateur a une origine profonde (*i.e.* métamorphique) et pourraient être issus des processus de granutilisation et/ou de la fusion du slab subducté en profondeur [*e.g.* Groves *et al.*, 2005]. En réagissant de manière significative avec la roche encaissante, le fluide minéralisateur se neutralise progressivement au cours de son transport [White & Hedenquist, 1990 ; Hedenquist & Lowenstern, 1994]. Différentes altérations comme la carbonatisation (apparition de magnésite, ankérite-dolomite-calcite), la sulfuration (apparition de pyrite, arsénopyrite et/ou pyrrhotite), la silicification (localisée à proximité des veines) et la chloritisation (encaissant mafique) sont couramment observées mais varient fortement spatialement [Gloaguen, 2006].

En résumé, qu'elles soient compressives et/ou extensives, les zones de cisaillement crustales représentent des structures perméables permettant aux fluides minéralisateurs de circuler facilement dans la croûte. Lors de leurs remontées vers la surface, la chute rapide de la pression et le mélange avec d'autres fluides (*e.g.* météoriques) favorisent la baisse de la solubilité des métaux en solution et donc leur précipitation. Si on considère que la croûte est précédemment enrichie en or et autres métaux sidérophiles, ces zones qui s'enracinent à des profondeurs importantes joueraient un rôle fondamental dans la formation de ces systèmes à l'échelle crustale.

I.2.2. Systèmes géothermaux de HT : la particularité du domaine arrière-arc

Alors que les gîtes fossiles (*i.e.* de type épithermal* neutre) se localisent principalement au niveau des zones d'arc, les gisements géothermaux actifs sont en domaine d'arc et également regroupés dans le domaine arrière-arc et/ou post-orogénique. Dans le Basin & Range, pour partie en arrière de l'arc volcanique des Cascades et de la Faille de San Andreas, les champs actifs s'alignent généralement sur des failles crustales qui se développent perpendiculairement à la direction principale d'extension et à proximité des failles bordières qui contrôlent la mise en place des bassins. La distribution spatiale de ces systèmes s'étend donc sur plusieurs dizaines de kilomètres. Par ailleurs, comme indiqué ci-dessus, l'anomalie conductrice localisée dans la partie inférieure de la croûte pourrait être attribuée à du sous-plaquage magmatique (Fig. I.9b) [Wannamaker *et al.*, 2006a ; b]. De ce fait, ces anomalies thermiques de grande longueur d'onde résultent probablement de processus associés à la dynamique de subduction (*i.e.* remontée mantellique liée à l'extension). Ainsi, le nombre élevé de sources thermales dans ces régions reflètent probablement ces processus profonds (*i.e.* associés à la dynamique mantellique), qui peuvent être néanmoins difficiles à expliquer en raison du manque d'observations directes (*e.g.* géométrie de la lithosphère subduite, processus mantelliques).

Bien que les études citées précédemment expliquent les mécanismes physico-chimiques à l'origine des gisements fossiles et actifs [*e.g.* Groves *et al.*, 1998 ; Sillitoe & Hedenquist, 2003 ; Richards, 2005 ; 2009 ; Cumming, 2009], notamment dans les domaines d'arcs magmatiques, il n'existe aucun consensus, et par conséquent aucun modèle conceptuel clair sur les systèmes amagmatiques post-orogénique. Comme indiqué précédemment, ces régions sont caractérisées par une activité tectonique importante et par une absence quasi-totale de volcanisme dans la croûte supérieure (*e.g.* le Basin & Range). Paradoxalement, elles présentent de nombreuses évidences de circulations de fluides hydrothermaux ou de nombreux paramètres incluant par exemple la perméabilité des zones de cisaillement, la lithologie et la géométrie des réservoirs, qui peuvent influencer et modifier cette circulation sur des échelles de temps peu connues. Les similitudes entre ces systèmes (*cf. I.2.1.2.*, Fig. I.11) offrent par conséquent l'opportunité d'apporter de nouvelles contraintes temporelles sur la dynamique des circulations des fluides dans la croûte. Des modèles conceptuels complets à l'échelle de la subduction, montrant les relations entre les systèmes actifs et fossiles (*e.g.* les zones de cisaillement aurifères associées à l'exhumation de MCCs), permettraient une meilleure compréhension de l'évolution thermique d'une région, et plus particulièrement dans les zones d'arrière-arc où le flux de chaleur est anormalement élevé sur une durée de plusieurs dizaines de millions d'années (*e.g.* ~30 Ma dans la région Egéenne).

Bien que ces études montrent l'importance de ces processus tectoniques sur la mise en place de gisements potentiellement exploitables, l'évolution géodynamique de la subduction doit être reconsidérée au vue des changements majeurs qu'elle peut induire sur la dynamique crustale et mantellique, et donc sur les mécanismes de genèse des champs géothermaux et des gisements

métalliques. En effet, la complexité tridimensionnelle (3D) des zones de subduction est de plus en plus étudiée, numériquement et analogiquement [Buiter *et al.*, 2002 ; Funiciello *et al.*, 2003 ; Govers & Wortel, 2005 ; Jadamec & Billen, 2010 ; Bertrand *et al.*, 2014 ; Sternai *et al.*, 2014 ; Menant *et al.*, 2016a ; b]. Dès lors que les panneaux plongeants peuvent se déchirer ou se détacher, l'évolution géométrique et mécanique du panneau plongeant va fortement changer [Sternai *et al.*, 2014]. Cette dynamique contribue également à la migration spatio-temporelle du magmatisme [Menant *et al.*, 2016b]. Bien que de nombreuses études aient discuté des aspects thermiques de la subduction en 2D [Deal *et al.*, 1999 ; van Keken & King, 2005 ; Arcay *et al.* 2007], les processus thermiques en 3D sont rarement étudiés. Quand ils le sont, les études se focalisent sur les zones de fusion partielle [Menant *et al.* 2016b], qui présentent un fort intérêt économique avec la présence de gisements à Au, Ag, Mo, et Cu (*e.g.* porphyres et épithermaux).

I.3. Dynamique des zones de subduction

I.3.1. Généralité sur la subduction

La convection mantellique est un phénomène physique reconnu par la communauté qui permet à la chaleur interne de la Terre de s'évacuer. Cette convection se manifeste en surface et en profondeur par les variations du géoïde, le changement de vitesse des ondes sismiques à l'échelle du manteau, ou encore par les anomalies bathymétriques. Cette composante est essentielle puisqu'elle fait partie intégrante de la théorie de la tectonique des plaques. En ce sens, l'une des conséquences majeures de ces mouvements mantelliques est la subduction. Par définition, les zones de subduction représentent des zones de convergence entre les plaques tectoniques où l'une des deux plaques plonge vers les profondeurs du manteau (Fig. I.12a) sous l'autre. Alors que la subduction océanique se définit par des propriétés physico-chimiques différentes (*e.g.* densité différente) entre les deux plaques, la subduction continentale, qui met en contact des lithosphères de densité proches, engendre généralement la formation d'une chaîne de montagnes (*i.e.* à cause de sa forte flottabilité). Ainsi à l'échelle du globe, la convection mantellique génère des courants ascendants (*i.e.* panaches mantelliques) et des courants descendants dont les zones de subduction en sont les marqueurs. Ces zones denses et froides constituent des hétérogénéités les plus visibles au sein du manteau [*e.g.* Bijwaard, 1999].

Comme l'indique les différentes géométries des fosses en surface [Jarrard, 1986 ; Heuret & Lallemand, 2005 ; Lallemand *et al.*, 2005 ; Schellart *et al.*, 2007], il existe actuellement une grande diversité des zones de subduction actives à travers le monde. Ces zones se caractérisent par des longueurs variables (entre 250–7400 km) et par des géométries variées (Fig. I.12b). Par exemple, la subduction andine est caractérisée par un slab à tendance rectiligne, alors qu'à contrario, la subduction associée à la plaque de Scotia ou les subductions méditerranéennes sont courbes. De même, une grande

diversité dans les vitesses de retrait et d'avancée des fosses est observée. En effet, dans certains cas les vitesses atteignent des valeurs de 15 cm.an^{-1} (*e.g.* retrait de la Fosse des Tonga) alors que dans d'autres cas, les vitesses sont plus faibles de l'ordre de 0.6 cm.an^{-1} (*e.g.* retrait de la Fosse des Aléoutiennes) (Fig. I.12b). Enfin, la déformation dans la plaque supérieure diffère également d'un endroit à l'autre (Fig. I.12b). Dans la plupart des zones de subduction matures, il existe une multitude de régimes tectoniques comme l'expansion océanique qui induit la création de bassin arrière-arc (régime extensif ; *e.g.* Mariannes, Tonga) ou comme la formation de chaînes de montagnes (régime compressif ; *e.g.* Amérique du Sud) (Fig. I.12b).

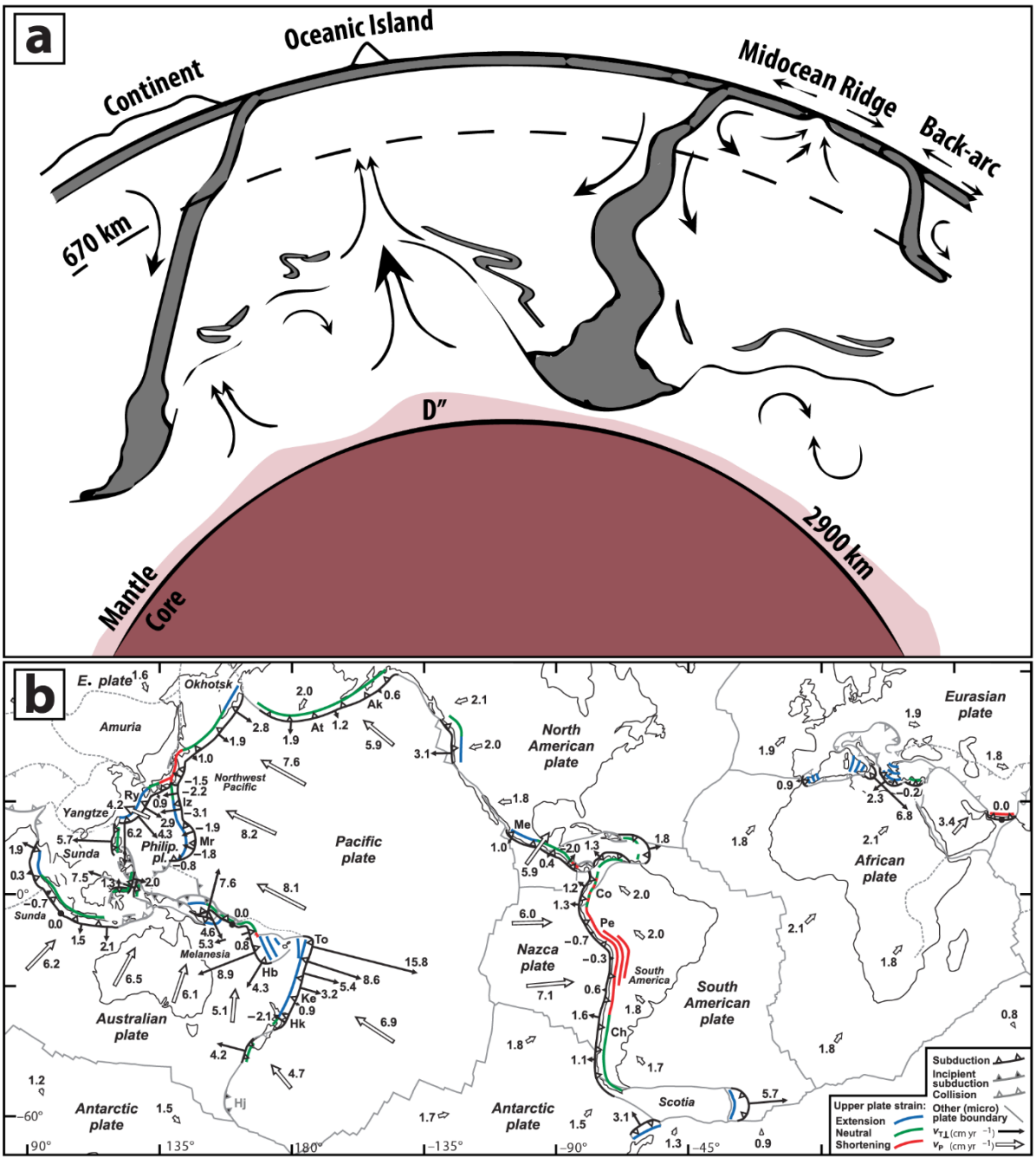

Figure I.12 : schéma conceptuel et répartition des zones de subduction à l'échelle mondiale. (a) schéma partiel du manteau convectif terrestre modifié d'après Kellogg et al. [1999]. Les zones de subduction sont représentées en gris foncé, et correspondent aux courants descendants qui animent le manteau. (b) carte recensant les principales zones de subduction dans le monde. Les abréviations correspondent à la figure B : Ak, Alaska; At, Aleutian; Ch, Chile; Co, Colombia; Hb, New Hebrides; Hk, Hikurangi; Iz, Izu-Bonin; Ke, Kermadec; Ku, Kuril; Jp, Japan; Me, Mexico; Mr, Mariana; Pe, Peru; Ry, Ryukyu; To, Tonga. Les vitesses des plaques tectoniques sont marquées par les flèches blanches alors que les flèches noires indiquent les vitesses de migration des fosses océaniques [Schellart et al., 2007].

En outre, la résolution croissante des modèles de tomographie sismique et des modèles numériques 2D fournit de nouveaux concepts sur la dynamique des slabs. De nombreuses études montrent que, dans certains cas, les panneaux plongeants peuvent pénétrer le manteau inférieur sur plusieurs milliers de kilomètres. A contrario, ils s'enracinent parfois au niveau de la transition manteau supérieur – manteau inférieure à 670 km (Fig. I.12a). Cette discontinuité, qui est marquée par l'apparition de la perovskite, peut déformer de manière significative la géométrie du slab [*e.g.* Kincaid & Olson, 1987 ; Guillou-Frottier *et al.*, 1995 ; Royden & Husson, 2009]. Même si les mécanismes contrôlant ces différentes dynamiques sont de mieux en mieux compris, le nombre croissant des modèles géodynamiques permet de formuler différentes hypothèses sur les paramètres clefs qui contrôlent la manière dont le slab s'écoule dans le manteau sur une échelle de plusieurs dizaines de millions d'années [*e.g.* Van der Hilst & Seno, 1993 ; Van der Lee & Nolet, 1997 ; Van der Voo *et al.*, 1999a ; Wortel & Spakman, 2000 ; Faccenna *et al.*, 2001a ; 2001b ; Fukao *et al.*, 2001]. En ce sens, il y a un commun accord pour dire que les slabs agissent passivement lorsque les panneaux plongeants sont ancrés dans le manteau profond. Dans ce contexte, la déformation arrière-arc accommode le mouvement vers l'arrière ou vers l'avant de la plaque supérieure par rapport à la fosse. A l'inverse, les slabs agissent activement lorsque la force de traction est importante (Fig. I.13a). Dans ce cas, un raccourcissement de la fosse est généralement observé (*e.g.* la fosse des Mariannes, Fig. I.12a).

Par ailleurs, il est essentiel de noter que tous les modèles précédents (*e.g.* numériques et/ou analogiques) sont généralement en 2D. Or, la subduction est un processus 3D complexe qui va influencer et modifier le comportement des panneaux plongeants (*i.e.* retrait et éventuellement déchirure). Ainsi, en considérant l'existante de tels mouvements dans le manteau, on peut se questionner sur les effets thermiques engendrés par ces dynamiques. Comprendre les mécanismes de transfert de chaleur du manteau à la croûte dans les régions extensives arrière-arcs est un des enjeux majeurs de cette étude. Avant de présenter brièvement les différents modèles géodynamiques, il est important de rappeler les principales forces impliquées dans les zones de subduction.

I.3.2. Les principales forces impliquées

Les forces influencent à la fois la cinématique et donc la dynamique des plaques et la déformation dans une zone de subduction (Fig. I.13). Classiquement, ces forces sont divisées en deux catégories : les

forces internes correspondant à la plaque subduite et le panneau plongeant, et les forces externes qui se définissent par des interactions entre le manteau environnant et la plaque supérieure. Parmi ces différentes forces on identifie généralement :

(i) la force de traction également appelée "*slab pull* ", qui se définie par un excès de masse du slab par rapport au manteau environnant (Fig. I.13a) ; cette force verticale et motrice est fonction de la différence de densité moyenne entre l'asthénosphère et le slab et du volume du slab [Heuret, 2005 ; Faccenna *et al.*, 2012].

(ii) la force de résistance du manteau lors de l'enfouissement du slab (*i.e.* les mouvements d'avancés et de reculs, "*anchor forces*" sur la figure I.13a).

(iii) les forces associées aux couplages entre les deux plaques ; elles incluent les forces de friction et de pression à l'interface des plaques mais également les forces de pressions ainsi que les mouvements de flexion du slab (Fig. I.13a) ; ces forces de frottement sont généralement exercées le long de la zone sismogénique.

(iv) la résistance visqueuse du manteau lors de la pénétration du slab dans le manteau (Fig. I.13a).

D'autres types de forces difficiles à estimer, néanmoins importantes, agissent également lors de la dynamique de subduction. La combinaison de ces forces génère des contraintes mécaniques et thermiques dans la plaque supérieure mais également dans la plaque subduite. En conséquence, ces dernières peuvent par exemple modifier la déformation intrinsèque de la plaque plongeante. D'autres facteurs comme la présence de flux mantelliques régionaux associées à une dynamique particulière (*i.e.* le retrait du slab ou l'absence de slab) influent également sur la dynamique de subduction.

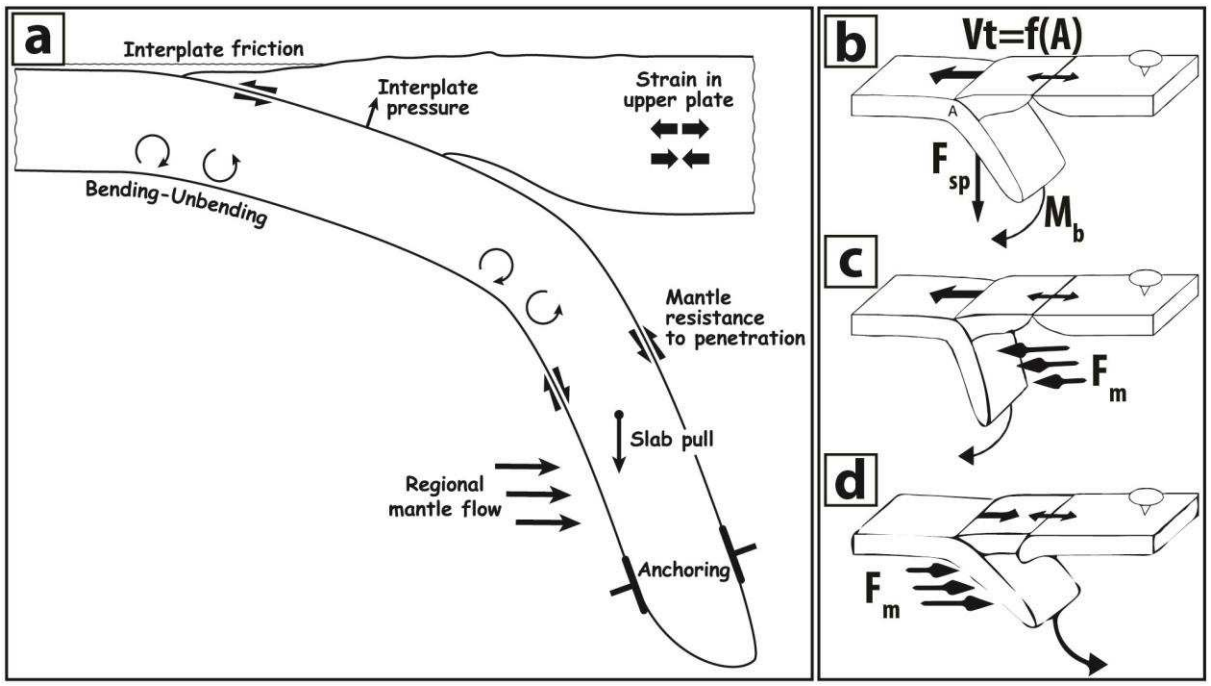

Figure I.13 : les principales forces à l'œuvre et les modèles géodynamiques associés. (a) les forces majeures d'une zone de subduction d'après Lallemand et al. [2005]. (b) le modèle du retrait du panneau plongeant. V_t : mouvement absolu de la fosse ; F_{sp} : force associée au slab pull ; M_b : flexion A : l'âge du slab modifié d'après Heuret & Lallemand [2005]. (c) et (d) le modèle contrôlé par la dynamique mantellique modifié d'après Heuret & Lallemand [2005]. Dans le premier cas, les flux poussent le panneau plongeant du côté du coin mantellique, favorisant ainsi le retrait et de l'extension arrière-arc alors que dans le second cas, les flux poussent la plaque subduite, favorisant alors l'avancée de la fosse et la compression dans la plaque supérieure. F_m : force générée par les flux mantelliques.

I.3.3. Les différents modèles géodynamiques

Même si les observations détaillées ci-dessus confirment que la dynamique de subduction est un phénomène complexe, de nombreuses études [*e.g.* Uyeda & Kanamori, 1979 ; Shemenda, 1994 ; Lallemand *et al.*, 2005 ; Schellart *et al.* 2007] proposent des modèles conceptuels sur le comportement des slabs. Il est couramment admis par la communauté scientifique que la déformation de la plaque supérieure est directement liée à la géométrie du slab (*i.e.* son pendage). Alors que les subductions à faible pendage se caractérisent généralement par une déformation compressive dans la plaque supérieure [*e.g.* Barazangi & Isacks, 1976 ; Jordan *et al.*, 1983 ; Ruff & Kanamori, 1980], les subductions à fort pendage sont corrélées avec une déformation extensive dans la plaque supérieure. Dans le détail, des études récentes basées sur une approche statistique [*e.g.* Boutelier *et al.*, 2003 ; Lallemand *et al.*, 2005] montrent que les « back-arcs compressifs » sont associés à des valeurs de pendage inférieure à 30°, alors qu'a contrario, les « back-arcs extensifs » se développent principalement dans les zones où le pendage est supérieur à 50°. Néanmoins, aucun consensus sur le paramètre contrôlant cette géométrie n'existe. En effet, la plupart des auteurs [*e.g.* Uyeda & Kanamori, 1979] supposent que le pendage du slab est principalement contrôlé par la force de traction. Cette corrélation semble se vérifier dans certains cas,

comme par exemple dans le cas de la subduction de Nankai ou des Mariannes. Cependant, il existe de nombreux contre-exemples comme celui de la subduction Hellénique dans le domaine méditerranéen. En réalisant une étude sur plus de 159 transects de zone de subduction, Lallemand *et al.* [2005] concluent que l'angle du slab ne peut être corrélé à la magnitude de la force de traction. Ils ne notent également aucune corrélation entre l'angle du slab et (i) l'âge la lithosphère subduite, (ii) la thermicité de la plaque plongeante, (iii) le taux de convergence et (iv) la polarité de la subduction. Cette étude confirme d'une part la complexité de la géométrie 3D des zones de subduction, qui induisent nécessairement des évolutions géodynamiques différentes se répercutant à la fois sur la dynamique crustale et mantellique. Elle montre d'autre part, que le mouvement absolu de la plaque supérieure joue un rôle déterminant sur cette dynamique, notamment lorsque le slab atteint la discontinuité à 670 km. Basé sur les relations « fosses et dynamique du slab », Heuret & Lallemand [2005] proposent une classification que nous détaillons par la suite.

I.3.3.1. Le modèle classique de la plaque supérieure

Dans ce modèle, la courbure du panneau plongeant est contrôlée par le mouvement de la plaque supérieure à travers deux types de forces : (i) les forces de friction et de pression à l'interface des plaques et par (ii) la force de résistance visqueuse du manteau lors de la pénétration du slab (Fig. I.13a). Ainsi, la déformation dans le domaine arrière-arc dépend principalement du mouvement absolu de la plaque supérieure à condition que la position de la fosse soit plus ou moins fixe dans l'espace et dans le temps [Heuret & Lallemand, 2005]. Dans ces conditions, un mouvement de retrait dans la plaque supérieure induit une extension arrière-arc alors qu'un mouvement en avancée (*i.e.* en direction de la fosse) implique de la compression dans cette dernière. Il existe donc de manière générale une bonne corrélation entre le mouvement de la plaque supérieure et la déformation associée (*i.e.* extension arrière-arc lors du retrait de la plaque supérieure et vice-versa). Cependant, il est intéressant de relever que dans plusieurs cas le mouvement absolu de la plaque supérieure ne correspond ni (i) à la déformation enregistrée dans la plaque supérieure ni (ii) aux mouvements de la fosse (*e.g.* Tonga, New Hebrides). Afin d'expliquer ces dynamiques particulières, la prise en compte des aspects tridimensionnels impliquant l'existence de flux mantelliques particuliers semble nécessaire. En exerçant une surpression sur l'une des bordures du slab, ces flux peuvent alors entrainer une migration vers l'avant ou vers l'arrière de la plaque supérieure par rapport à l'arc.

I.3.3.2. Le modèle du slab roll-back

De nombreuses études réalisées dans les années 1990, montrent que le couplage entre la force associée au *"slab pull"* et celle associée à la courbure du slab, peut générer une migration vers l'arrière du panneau plongeant (appelé également *"roll-back"*) [*e.g.* Molnar & Atwater, 1978 ; Dewey, 1980 ; Garfunkel *et al.*, 1986]. Ce mouvement de recul engendre alors la localisation d'une déformation extensive dans la plaque supérieure (Fig. I.13b). Ces études offrent donc un aperçu de la complexité de la dynamique de subduction. Néanmoins, ces approches sont généralement réalisées en deux dimensions. En effet, pour une meilleure compréhension de cette dynamique, qui s'exprime à travers de multiples processus (*e.g.* migration de la fosse, déformation de la plaque supérieure…), il est nécessaire de regarder la subduction comme (i) une structure limitée spatialement (*i.e.* la longueur varie entre 250–7400 km) et (ii) une géométrie tridimensionnelle complexe qui évolue dans le temps. Récemment, en utilisant des simulations analogiques ou numériques tridimensionnelles, Faccenna *et al.* [1997 ; 2001a], Funiciello *et al.* [2003 ; 2006], Piromallo *et al.* [2006] ou Schellart *et al.* [2007] montrent que la largeur de la subduction exerce un contrôle de premier ordre sur la courbure des slabs, et donc sur leurs tendances à reculer à travers le temps. En effet, leurs résultats indiquent d'une part que le taux de migration de la fosse est inversement lié à la largeur du slab et d'autre part, que le *roll-back* est facilité à proximité d'un bord latéral du slab par l'intermédiaire des flux mantelliques. Comme le montre la Figure I.14b, ces résultats sont compatibles avec les vitesses de retrait constatées à l'échelle mondiale, avec une vitesse maximale (6–16 cm.yr-1) observée seulement près des bordures des slabs. Les zones de subductions étroites (≤ 1.500 km) sont les témoins de retraits rapides et développent une géométrie concave, orientée du côté du coin mantellique (Fig. I.14a). A contrario, les slabs (≥ 4000 km) sont presque stationnaires au centre et développent une géométrie convexe (Fig. I.14a).

I.3.3.3. Le rôle des flux mantelliques

Selon Heuret & Lallemand [2005], il existe 3 types de flux mantelliques qui peuvent agir et modifier la dynamique des slabs : à l'échelle globale, un flux venant de l'est associé à la dérive vers l'ouest de la lithosphère (Fig. I.14b) [*e.g.* Nelson & Temple, 1972 ; Doglioni, 1993] ; les flux régionaux comme le montre le mouvement du manteau supérieur sub-Pacifique [*e.g.* Garfunkel *et al.*, 1986 ; Lallemand, 1998] ou encore le mouvement du point chaud des Afars (Fig. I.14c) [Faccenna *et al.*, 2013] ; et enfin des flux localisés à proximité des zones de retrait et/ou des déchirures du slab (Fig. I.14d) [*e.g.* Alvarez, 1982 ; Russo & Silver, 1994 ; Yogodzinski *et al.*, 2001 ; Menant *et al.*, 2016b]. Dans ce sens, plusieurs études sismologiques et géochimiques ont démontré que le matériel du manteau s'écoule des bordures vers le coin mantellique au niveau des zones de subduction [*e.g.* Russo & Silver, 1994 ; Peyton *et al.*, 2000 ; Pearce *et al.*, 2001]. Ainsi, les flux asthénosphériques sont considérés comme des flux de

retour induits par le retrait du panneau plongeant. Il est intéressant de noter que les composantes toroïdales et poloïdales ce ces flux favorisent également son retrait [Kiraly *et al.*, 2017]. Or il est important de souligner que dans certains cas, ces flux mantelliques peuvent être moteur ; la force additionnelle (notée F_m) peut alors engendrer une migration parallèle à la fosse (Fig. I.13d).

Par ailleurs, un certain nombre d'observations géologiques dans des contextes extensifs (*e.g.* comme les domaines d'arrière-arcs avec la mer Égée, la mer du Tyrrhénienne septentrionale et le domaine d'Alboran) souligne l'existence d'un fort couplage entre les flux asthénosphériques et la déformation enregistrée dans la croûte de la plaque supérieure [Jolivet *et al.*, 2013 ; 2015 ; Sternai *et al.*, 2014 ; Menant *et al.*, 2016b]. Cette déformation se distribue généralement sur de larges zones, accommodées par des failles de cisaillement à faible pendage peu profondes (*i.e.* zone de cisaillement et détachements). Selon Jolivet *et al.* [soumis], ces zones d'échelle crustale sont caractérisées par une forte asymétrie traduisant une composante de cisaillement simple à l'échelle de la lithosphère. Cette dernière est favorisée principalement par un couplage visqueux entre les flux asthénosphériques sous-jacent et la croûte (*e.g.* traction ou compression basale), et dans une moindre mesure par les hétérogénéités dans la croûte et la lithosphère (*i.e.* héritage tectonique).

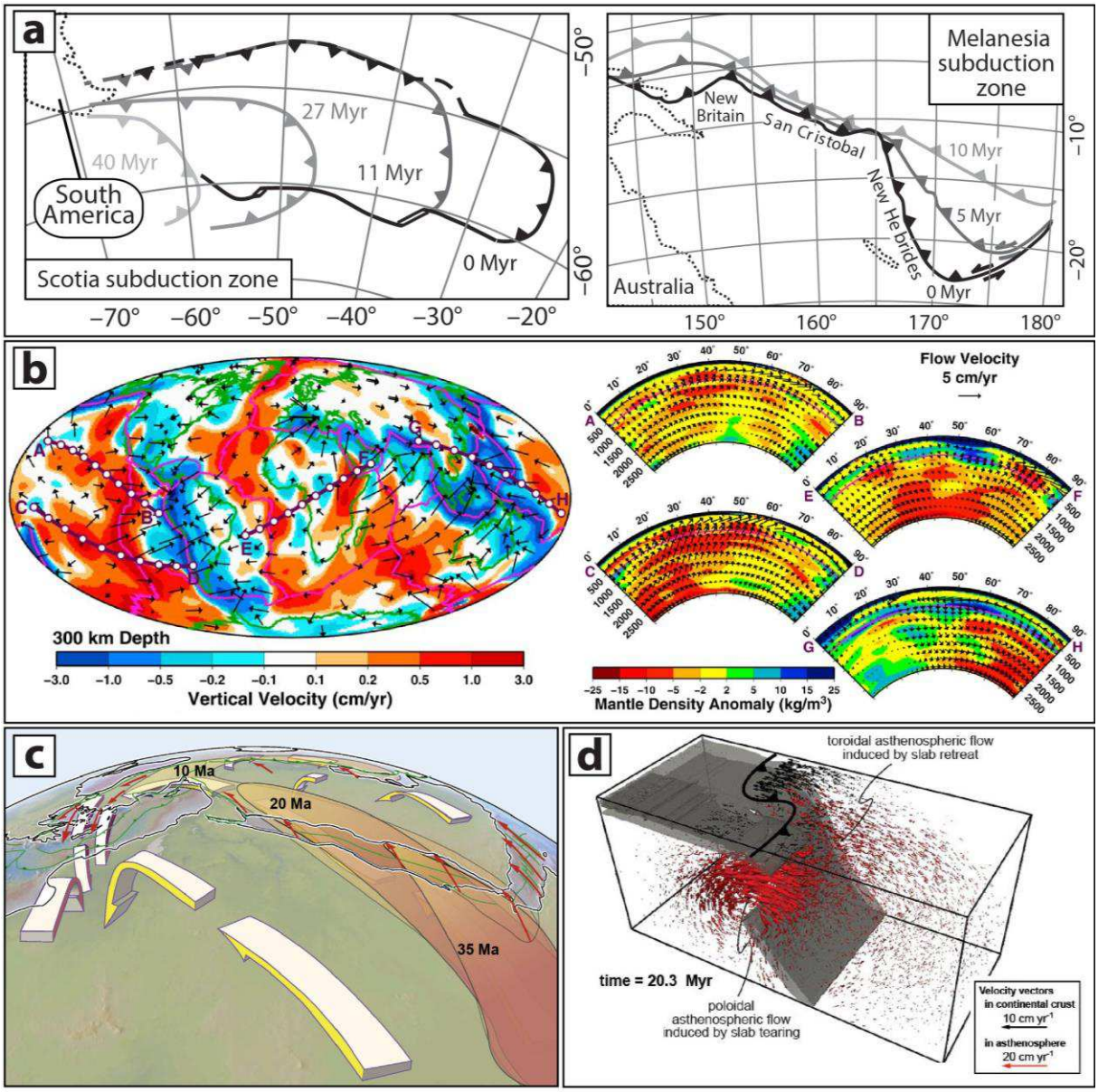

Figure I.14 : zones de subduction et flux mantelliques à différentes échelles. (a) Evolution progressive de deux de zones de subduction dont la largeur varie selon l'endroit modifiée d'après Schellart et al. [2007]. La figure de gauche montre l'évolution de la zone de subduction de Scotia dont la longueur est estimée à 800 km, et la droite correspond à la zone de subduction Malaisienne dont la longueur est estimée à 4400 km. (b) Modèle global des flux mantelliques à 300 km de profondeur, contraint par des observations basées sur l'anisotropie sismique d'après Conrad & Behn [2010]. Les couleurs et les flèches noires indiquent les mouvements verticaux et horizontaux dans l'asthénosphère, respectivement. Les profiles, indiqués sur la figure de gauche, montrent les anomalies de densité dans le manteau ainsi que le champ de vitesse associée, représenté par les flèches noires. (c) Figure conceptuelle indiquant les mouvements mantelliques à cinématique nord associées à la dynamique du point chaud des Afars d'après Faccenna et al. [2013]. (d) Modèle numérique montrant une vue 3D d'une zone de subduction d'après Menant et al. [2016b]. Les flux mantelliques sont représentés par les flèches rouges. Il est important de noter les composantes poloïdale et toroïdale associées à ces flux.

I.3.4. Thermicité dans les zones de subduction : évolution de la plaque supérieure

Il est important de rappeler que les bassins arrière-arcs sont généralement caractérisés par des anomalies élevées du flux de chaleur, comme l'atteste certaines températures qui atteignent localement jusqu'à 800 °C au Moho [Currie & Hyndman, 2006]. Différentes hypothèses sont proposées dans la littérature afin expliquer ces anomalies, mais aucun véritable consensus n'est établi, probablement à cause de la complexité de la dynamique de subduction. Par exemple, selon Brown [2006], les températures anormalement élevées dans les zones d'arrière-arcs sont principalement liées à une production de chaleur radioactive importante en réponse à une phase de collision continentale. Dans cette continuité, Hyndman *et al.* [2005] suggèrent que les anomalies thermiques présentes dans les domaines de back-arcs résultent principalement d'un flux de chaleur anormal orogénique marqué principalement par la présence de plutons syn-orogéniques et par du métamorphisme de haut grade (Fig. I.15a). A contrario, des modèles numériques simples remettent en question cette hypothèse. Prenons comme exemple l'étude de Clark *et al.* [2011]. En surestimant les températures dans leur modèle (à cause d'absence de mouvement latéral car le modèle ne prend en compte que des mouvements verticaux), leurs résultats montrent qu'avec une croûte épaisse (~70 km), une production de chaleur de 2 $\mu W.m^{-3}$ dans la croûte supérieure et un taux d'érosion de 0,7 $mm.y^{-1}$, il est impossible de générer des roches de ultra haute température (UHT ~800–900 °C). Il faut donc envisager un autre mécanisme couplé au précédent pour apporter la chaleur nécessaire à la formation de ce type de métamorphisme.

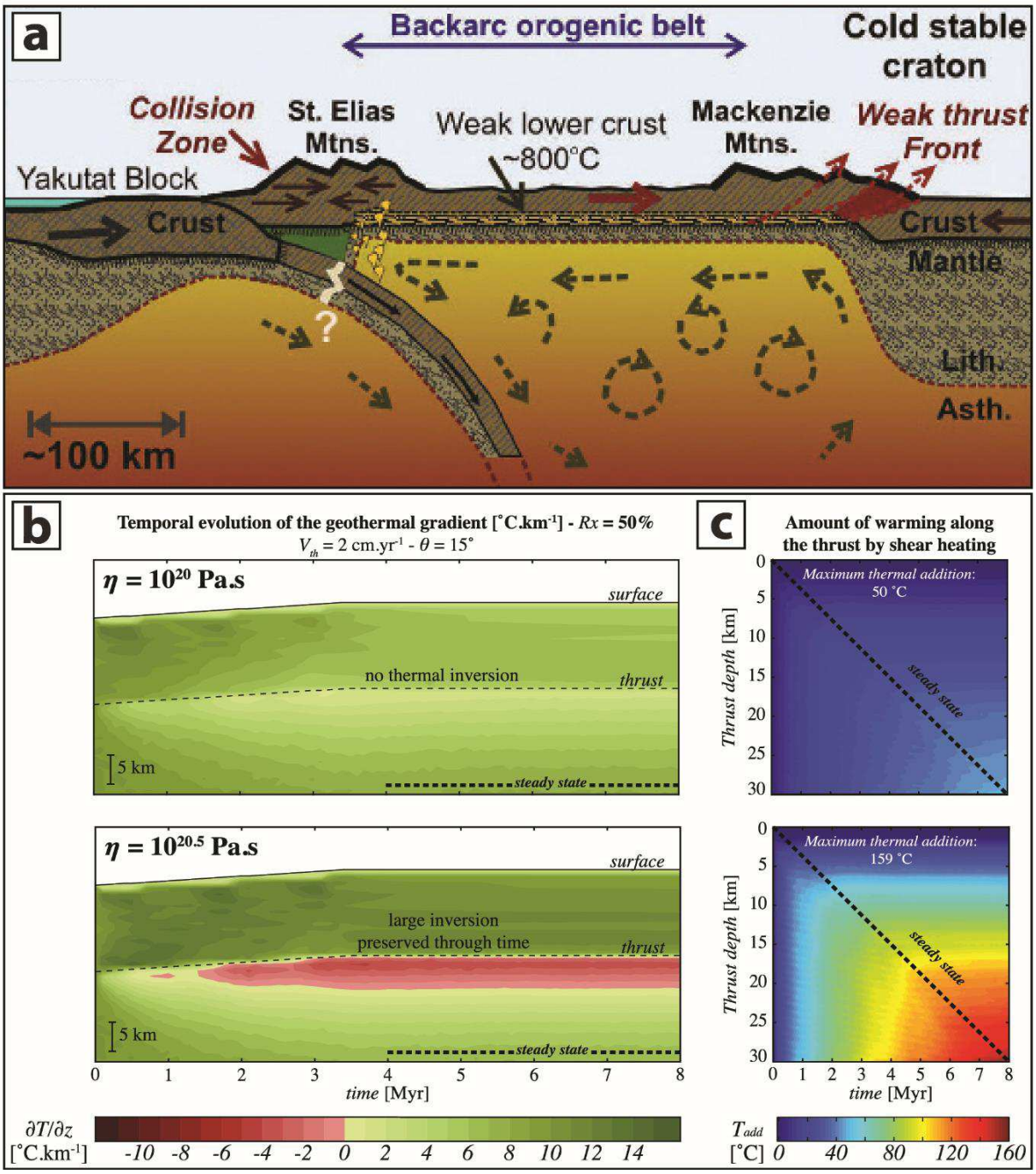

Figure I.15 : flux de chaleur orogénique et anomalies thermiques. (a) Modèle conceptuel d'un back-arc considéré comme mobile d'après Hyndman et al. [2005]. (b) et (c) Influence du shear heating sur le gradient géothermique d'après Duprat-Oualid et al. [2013]. Profil vertical d'un modèle numérique 2D à un instant donné montrant une large inversion thermique pour des valeurs de viscosité de l'ordre de $10^{20.5}$ Pa.s. La figure de droite montre les profils thermiques associés. Il est important de noter que la production de chaleur par shear heating est importante le long du chevauchement, comme le témoigne les températures anormalement élevées (159 °C à 30 km de profondeur).

Il existe de nombreuses discussions sur les quantités de chaleur produites par « mécanisme de chauffage » dans la croûte. Ce mécanisme appelé *"shear heating"* (noté H_s) correspond au produit entre le taux de déformation ($\dot{\varepsilon}$) et la contrainte de cisaillement (τ). Même s'il est évident que ce mécanisme est présent lors des phases d'épaississement (*i.e.* chevauchement) et d'amincissement crustal (*i.e.*

détachements), aucun consensus sur son influence sur le degré de métamorphisme n'est établi dans la littérature [*e.g.* Nabelek *et al.*, 2010]. En effet, pour certains, sa contribution est significative et permet d'expliquer par exemple la superposition d'une unité de haut grade métamorphique sur une unité de bas grade dans les chaînes de collision (Figs. I.15b et I.15c) ou encore du métamorphisme de UHT [*e.g.* Nicolas *et al.,* 1977 ; Scholz, 1980 ; Molnar & England, 1990 ; Leloup *et al.*, 1999 ; Duprat-Oualid *et al.*, 2013] alors que pour d'autres, elle est négligeable [Brun & Cobbold, 1980 ; Fleitout & Froidevaux, 1980]. Dans ce sens, Clark *et al.* [2011] suggèrent que le *shear heating* augmente temporairement la production de chaleur dans les premiers stades du fonctionnement de la zone de cisaillement. Cependant sa contribution diminue avec le temps puisque les températures augmentent à cause de l'épaississement crustal (*i.e.* production radiogénique). Dans tous les cas, ces études montrent bien que la production de chaleur est associée (i) à la production radiogénique lors de l'épaississement crustal et (ii) au *shear heating* (en plus faible proportion). Ces deux mécanismes peuvent en partie expliquer le métamorphisme de HT dans les domaines arrière-arc, mais également les anomalies de températures en surface (*i.e.* la relaxation thermique de ces orogènes s'exprime sur plusieurs millions d'années).

Cependant, les précédentes observations détaillées ci-dessus (*cf. I.4.3.3.*) confirment l'importance de la dynamique mantellique dans les zones de subduction. Qu'ils soient moteurs ou passifs, ces flux génèrent des anomalies thermiques de grande longueur d'onde qui affectent principalement les roches de la plaque supérieure. De nombreuses études géochimiques et géodynamiques témoignent dans ce sens. D'une part, un magmatisme calco-alcalin riche en potassium est observé dans les domaines arrière-arcs [Johnson *et al.*, 1978 ; Hawkesworth *et al.*, 1995]. Ce dernier est directement lié à l'amincissement et à la délamination de la lithosphère, induisant alors une fusion partielle (i) de la croûte inférieure et (i) du manteau lithosphérique sous-jacent [Tatsumi *et al.*, 1989 ; Hawkesworth *et al.*, 1995 ; Pe-Piper & Piper, 2006]. D'autre part, Curie *et al.* [2006] notent que le manteau supérieur de la plaque supérieure est également caractérisé par des températures anormalement élevées qui s'étendent de l'arc jusqu'au domaine arrière-arc. En compilant différents jeux de données sur des arcs du Pacifique (*e.g.* vitesse sismique, flux de chaleur, thermobarométrie sur des xénolites), ces auteurs montrent que les températures de 1200 °C sont atteintes seulement à 60 km de profondeur. Leurs résultats mettent en évidence que les mouvements convectifs mantelliques jouent un rôle prépondérant sur la transmission de la chaleur vers la base de la croûte lors de l'extension arrière-arc.

Pour résumer, il existe dans les domaines arrière-arcs différents types d'anomalies thermiques de grandes longueurs d'ondes. Elles sont généralement associées à (i) la production de chaleur radiogénique, (ii) au *shear heating* et (iii) aux flux mantelliques. Ces anomalies favorisent d'une part, le développement du métamorphisme de HT–UHT et du magmatisme, et d'autre part, elles sont responsables des anomalies en surface actuelles (*e.g.* flux de chaleur anormal avec des valeurs ~100 $mW.m^{-2}$ dans le Basin & Range et dans le massif du Menderes). Cependant, le rôle de la part de chaque mécanisme sur la production de chaleur reste à éclaircir, et c'est l'un des objectifs de ce travail. A

l'image de la dynamique de subduction, l'évolution spatio-temporelle de la thermicité de la plaque supérieure est un phénomène complexe, qui change selon l'endroit étudié.

I.4. Intérêts de la zone d'étude

I.4.1. Contexte géothermal de l'Anatolie occidentale

I.4.1.1. Une région anormalement chaude

La région orientale de la méditerranée et plus particulièrement l'Anatolie occidentale en Turquie possède un potentiel géothermique considérable, dont la capacité installée actuelle est de 820,9 MWe[4], la plaçant au 6ème rang mondial et au 2ème rang européen après l'Italie (916 MWe) [Bertani, 2015]. En Anatolie occidentale, aujourd'hui, cette capacité installée cumule l'exploitation des champs géothermaux de Kızıldere, Germencik, Sultanisar et Alaşehir. A titre de comparaison, la capacité installée à Bouillante en 2012 (Guadeloupe, France) est de l'ordre 15 MWe.

Outre son potentiel remarquable en sources chaudes (Fig. I.16a) et en champs géothermaux, l'Anatolie occidentale est une province géothermale importante marquée par des anomalies du flux de chaleur. Des études récentes [Erkan, 2014 ; 2015] indiquent des valeurs comprises entre 85 – 90 $mW.m^{-2}$ allant jusqu'à 120 $mW.m^{-2}$, proche de grabens comme ceux d'Alaşehir (nomé aussi Gediz) et le Büyük Menderes dans le Massif du Menderes. Cette province est considérée comme atypique dans la mesure où la source de chaleur des champs géothermaux est très débattue. En effet, la majorité des modèles géothermiques turcs suggèrent l'existence d'intrusions magmatiques cachées dans la croûte supérieure [Simsek, 1985 ; Filiz *et al.*, 2000 ; Karamanderesi & Helvaci, 2003 ; Yilmazer *et al.*, 2010 ; Bülbül *et al.*, 2011 ; Özen *et al.*, 2012 ; Özgür *et al.*, 2015] comme c'est le cas à Larderello. Cependant, pour certains auteurs, l'absence de volcanisme actuel dans la région, à l'exception du magmatisme non différencié de Kula (Fig. I.16a), implique que l'origine des systèmes géothermaux de HT serait associée à une source de chaleur très profonde, sans avoir à invoquer des chambres magmatiques dans le croûte supérieure (0 à 5 km) [Faulds *et al.*, 2010 ; Haizlip *et al.*, 2013 ; Kocyigit, 2015 ; Kaya, 2015 ; Haklidir *et al.*, 2015]. De récentes études sur la profondeur de l'isotherme de Curie (correspondant à la température à laquelle les minéraux ferro- et ferrimagnétiques perdent leur aimantation permanente) [Aydin *et al.*, 2005 ; Bilim *et al.*, 2016] montrent une anomalie de grande longueur d'onde localisée dans la croûte sous le Massif du Menderes. Cette anomalie de 580 °C est observée à de faibles profondeurs de l'ordre de ~ 8 à 10 km dans cette région (Fig. I.16b). Une anomalie thermique de cette

[4] http://www.nortonrosefulbright.com/knowledge/publications/149911/geothermal-electricity-generation-in-turkey-large-potential-awaiting-investors

dimension ne peut être entièrement liée à des intrusions dans la croûte, surtout dans une région peu magmatique, et doit nécessairement trouver sa source plus profondément, donc dans le manteau.

Tous ces éléments confirment la présence d'anomalies thermiques régionales à différentes profondeurs selon les provinces qui font certainement appel à des processus d'ampleur régionale (*i.e.* lithosphère, asthénosphère…) impliquant donc des processus géodynamiques. Dans ces conditions particulières, l'activité tectonique dans la croûte supérieure va jouer un rôle fondamental dans la circulation des fluides géothermaux, permettant ainsi à la chaleur de s'évacuer au travers des zones perméables. En ce sens, l'Anatolie occidentale présente des analogies avec le Basin & Range aux USA, qui constitue une province géothermale importante [Faulds *et al.*, 2009 ; 2012]. Nous reviendrons dans le *chapitre II* sur ce point central qui définit l'originalité de la thèse.

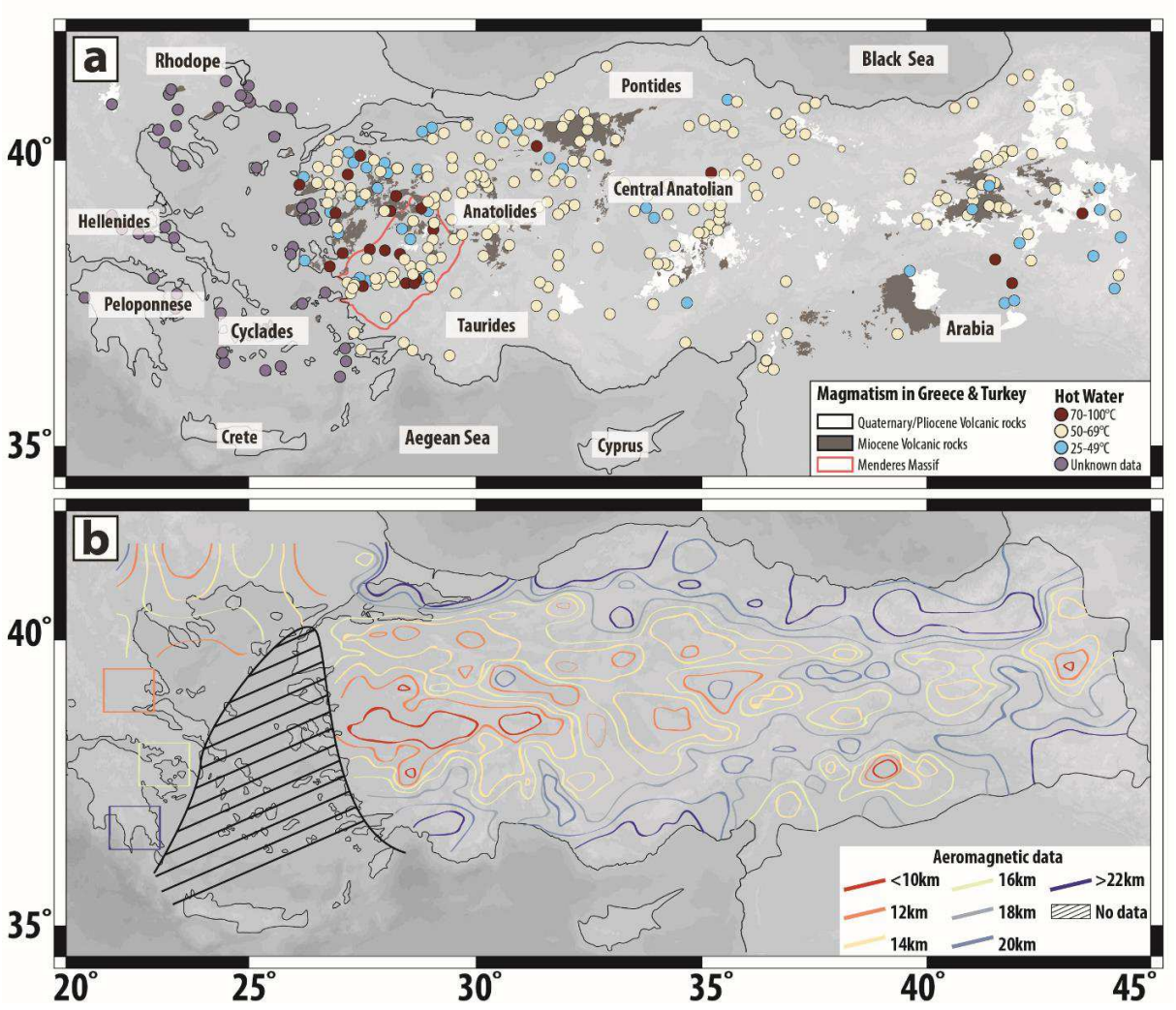

Figure I.16 : cartes de la Méditerranée orientale. (a) Compilation des sources thermales comprises entre 25 et 100 °C projetées sur une carte de la zone d'étude montrant l'activité magmatique depuis le Miocène jusqu'à l'actuel. (b) profondeur de l'isotherme de Curie, correspondant à une température de 580 °C. Ces données résultent d'une compilation de plusieurs études [Tselentis, 1991 ; Stampolidis & Tsokas, 2002 ; MTA, 2005 ; Aydin et al., 2005 ; Mendrinos et al., 2010 ; Andritsos et al., 2015].

I.4.1.2. Une région marquée par de nombreux gisements métalliques

La région Méditerranéenne a connu une histoire géodynamique complexe (voir ci-dessous), marqués par différentes provinces magmatiques [*e.g.* Pe-Piper & Piper, 1989 ; 2006 ; Altherr & Siebel, 2002 ; Keskin, 2003 ; Marchev *et al.*, 2004a ; Harangi *et al.*, 2006 ; Agostini *et al.*, 2007 ; Dilek & Altunkaynak, 2009 ; Stouraiti *et al.*, 2010 ; Bolhar *et al.*, 2010 ; Seghedi *et al.*, 2013 ; Ersoy & Palmer, 2013]. Ces différents épisodes magmatiques ont généré la formation de plusieurs provinces métallifères [*e.g.* Janković, 1997 ; Berza *et al.*, 1998 ; Heinrich & Neubauer, 2002 ; Skarpelis, 2002 ; Marchev *et al.*, 2005 ; von Quadt *et al.*, 2005 ; Yigit, 2009 ; 2012], dont les relations avec la dynamique de subduction ont fait l'objet de plusieurs études ces dernières années [Richards, 2014 ; Menant *et al.*, 2016a ; b]. En effet, Menant *et al.* [2016a ; b] montrent que les processus mantelliques et crustaux, liés à cette dynamique tridimensionnelle (3D) de la subduction hellénique, favorisent la genèse de concentrations métalliques (*i.e.* Au et Cu). A partir de reconstructions cinématiques de cette région et de modèles numériques, ces auteurs décrivent la succession des contextes métallogéniques en relation avec l'histoire des événements géodynamiques en 3D : (i) une province riche en cuivre, qui s'est développée dans un environnement d'arc au Crétacé supérieur (Fig. I.17a) ; (ii) à l'Oligocène-Miocène, une province riche en plomb-zinc puis en or, s'est également mise en place dans un contexte d'arrière-arc (Figs. I.17b et I.17c). Ces épisodes fertiles sont principalement contrôlés par le retrait du panneau plongeant, qui favorise le développement d'un domaine aminci arrière-arc dans la lithosphère par le biais de flux asthénosphériques complexes en 3D et par la déchirure du slab induisant des vitesses de recul différentes selon la portion de slab. Bien que ces études apportent de nouvelles contraintes sur les processus thermiques en 3D, elles se focalisent principalement sur l'évolution du magmatisme et des ressources minérales (*e.g.* gisements fossiles comme les porphyres/épithermaux). Mais très peu d'études font le lien avec les ressources géothermales actives, et donc sur l'évolution thermique sur le long terme et le court terme d'une zone de subduction marquée par une dynamique 3D complexe. C'est l'objet principal de cette thèse.

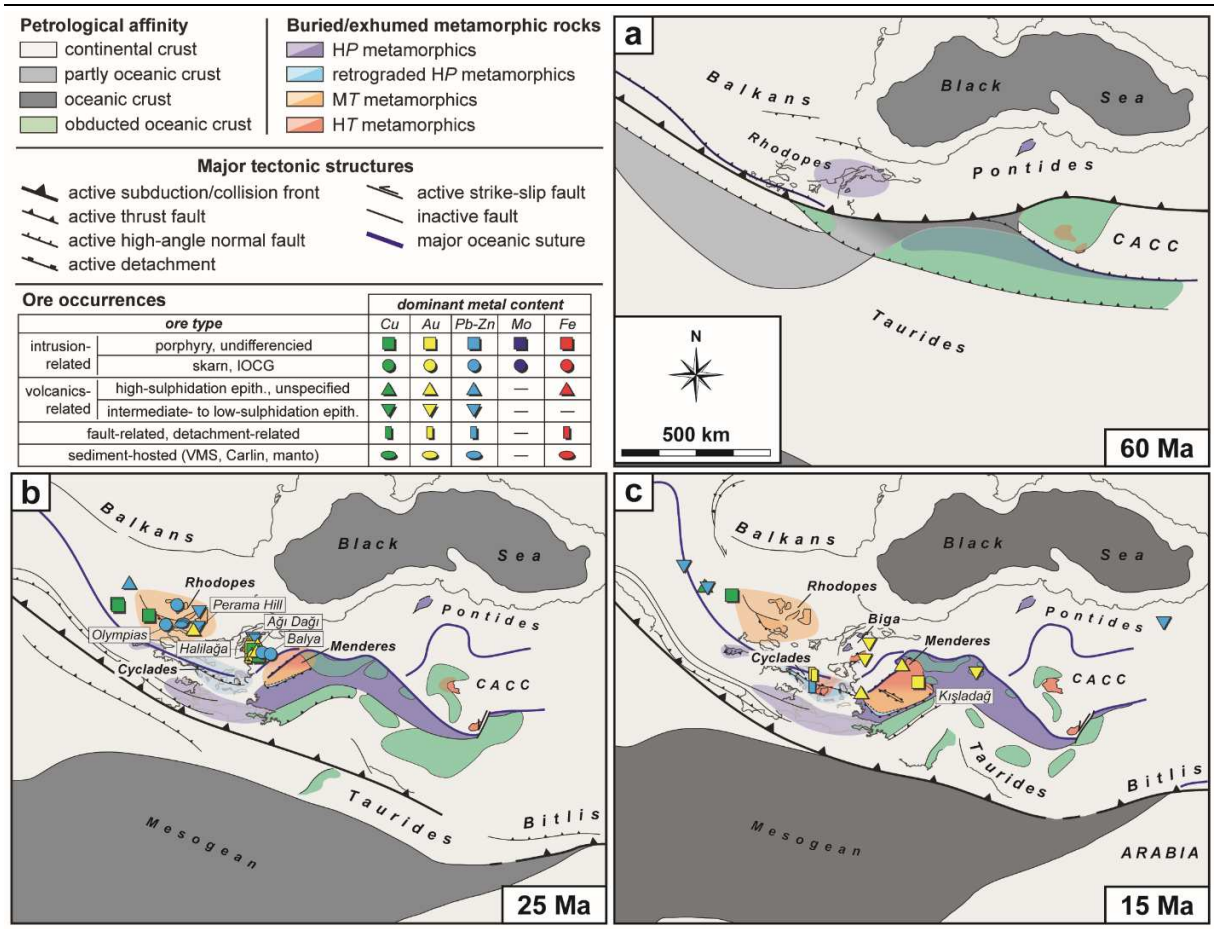

Figure I.17 : cartes paléotectoniques de la Méditerranée orientale extraites du modèle de reconstruction cinématique de Menant et al. [2016a], mettant en évidence la distribution spatiale et temporelle des occurrences minéralisées depuis le Crétacé supérieur jusqu'au Miocène. CACC : Central Anatolian Crystalline Complex.

I.4.2. Contexte géodynamique et géologique

Par ailleurs, l'engouement scientifique suscité par la dynamique de subduction, qui présente une évolution tectonique et magmatique complexe, a donné lieu à de très nombreuses études dans le domaine oriental méditerranéen, mais également en Anatolie occidentale. Ainsi, ces études se traduisent par une base de données exceptionnelle, tant du point de vue de la géodynamique que de la connaissance de la structure du manteau (*i.e.* tomographie sismique, anisotropie sismique, épaisseur de la croûte …) ou de la cinématique actuelle (GPS) ou passée (reconstructions) [*e.g.* Biryol *et al.*, 2011 ; Reilinger & McClusky, 2011 ; Becker *et al.*, 2012 ; Karabulut *et al.*, 2013 ; Vanacore *et al.*, 2013 ; Faccenna *et al.*, 2014 ; Jolivet *et al.*, 2013 ; Menant *et al.*, 2016a ; b].

Le contexte géodynamique de la zone appartient au système téthysien qui se caractérise par une zone de subduction océanique à vergence nord sous l'Eurasie. Durant cette période, plusieurs blocs continentaux se sont successivement accrétés (*i.e.* l'Apulie, l'Arabie et l'Inde), impliquant des épisodes de subductions et/ou de collisions continentales qui ont engendré la formation de nombreuses chaines

orogéniques comme les Alpes et le Zagros. La région méditerranéenne, plus particulièrement sa partie orientale, témoigne de ces épisodes successifs ou plusieurs écailles crustales se sont accrétées formant un prisme orogénique (*i.e.* la chaîne des Hellénides-Taurides) [Le Pichon & Angelier, 1979 ; Bonneau & Kienast, 1982 ; Jolivet *et al.*, 2003 ; Van Hinsbergen *et al.*, 2005 ; Brun & Sokoutis, 2010 ; Jolivet & Brun, 2010]. Suite à un changement drastique des conditions limites de la dynamique de subduction vers 35 Ma, un mouvement rétrograde de la lithosphère subductée se développe dans l'asthénosphère, permettant ainsi le développement d'un large domaine d'arrière-arc anormalement chaud [*e.g.* Jolivet & Brun, 2010]. En réponse à ce retrait, les contraintes extensives ont engendré l'effondrement partiel de la chaîne dont la région du Menderes et des Cyclades reflètent la morphologie (Fig. 1.18a). Cette extension post-orogénique orientée N-S à NE-SW est assistée par des failles normales à faible pendage qui permettent l'exhumation de roches métamorphiques sous la forme de dômes [Lister *et al.*, 1984 ; Urai *et al.*, 1990 ; Gautier *et al.*, 1993 ; Sokoutis *et al.*, 1993 ; Bozkurt, 2001 ; Bozkurt & Oberhänsli, 2001 ; Vanderhaeghe, 2004 ; Bonev *et al.*, 2006 ; Brun & Sokoutis, 2007 ; Brun & Faccenna, 2008 ; Gessner *et al.*, 2013 ; Jolivet *et al.*, 1994 ; 1999 ; 2004 ; 2013]. Un second épisode majeur, correspondant à une probable déchirure du panneau plongeant égéen sous l'Anatolie, est suggéré dans la littérature (voir localisation dans la figure I.18b). Bien que l'âge de cette déchirure soit débattu (Eocène pour l'étude de Govers *et al.* [2016] et Miocène pour l'étude de Menant *et al.* [2016a]), les images issues de la tomographie sismique [De Boorder *et al.*, 1998 ; Piromallo & Morelli, 2003 ; Govers & Wortel, 2005 ; Li *et al.*, 2008 ; Biryol *et al.*, 2010 ; Salaün *et al.*, 2012 ; Delph *et al.*, 2015], la distribution spatiale et temporelle du magmatisme, ainsi que son évolution géochimique [Dilek & Altunkaynak, 2009 ; Jolivet *et al.*, 2015 ; Menant *et al.*, 2016a] sont des marqueurs majeurs en faveur de son existence. Selon Wortel & Spakman, [2000], cette fenêtre mantellique favoriserait la migration de matériau chaud et profond associé à l'asthénosphère vers la base de la lithosphère et/ou de la croûte. Nous reviendrons dans le *chapitre IV* sur la géométrie de cette déchirure.

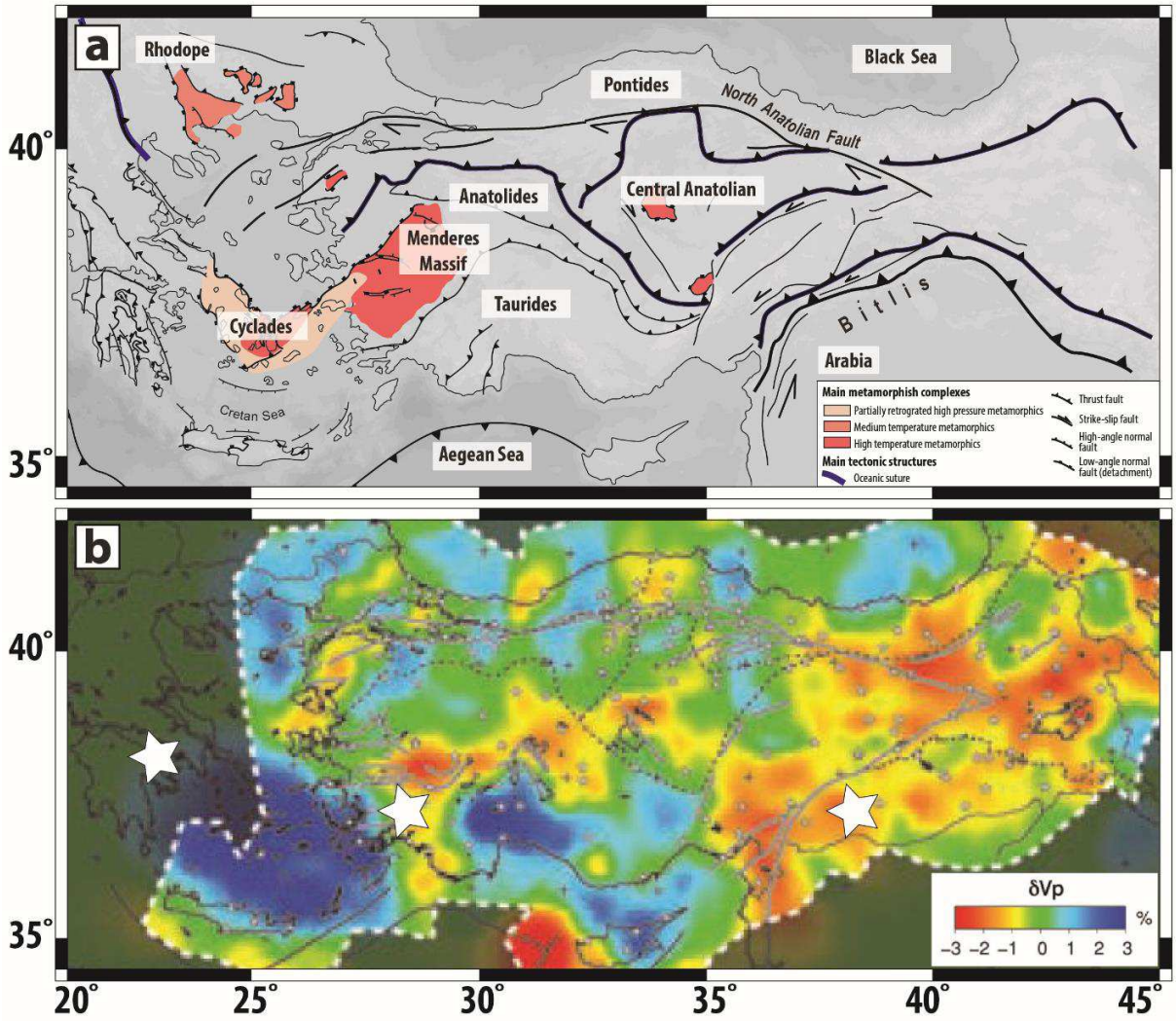

Figure I.18 : cartes de la Méditerranée orientale. (a) carte tectonique et métamorphique de la Méditerranée orientale montrant les principales structures actives, extensives à faible pendage, chevauchantes constituant la chaîne des Hellénides et des Taurides (lignes noires) et les principales zones de suture océanique (lignes épaisses bleues). Les principaux dômes métamorphiques de HT sont également représentés. Modifiée d'après Jolivet et al. [2013]. (b) carte de variations de vitesses des ondes sismiques P à 200 km de profondeur [Biryol et al., 2011]. Dans le domaine Anatolien, les étoiles blanches représentent les anomalies de vitesse négative (rouge) pouvant être interprétées comme des déchirures ou détachement des lithosphères subduites.

I.5. Question scientifique, objectifs de la thèse et démarche adoptée

La question scientifique principale est la suivante : quelles sont les conséquences thermiques de la dynamique de subduction dans les domaines arrière-arcs ? Afin de répondre à cette question, nous focaliserons notre étude sur la partie orientale de l'Anatolie, plus précisément sur le Massif du Menderes. Ce massif a la particularité de présenter (i) de nombreux champs géothermaux actuels, qui définiront peut-être de futurs gisements métalliques, mais également (ii) des gisements épithermaux fossiles (connus dans la littérature et observés sur le terrain), (iii) une histoire tectono-métamorphique complexe (épisode de haute-pression et de haute-température) suggérant des rééquilibrages thermiques rapides et

importants à l'échelle de la subduction. Il s'agira en particulier de comprendre l'évolution spatio-temporelle du régime thermique de la lithosphère anatolienne entre 50 Ma et aujourd'hui en s'appuyant sur une approche globale multidisciplinaire basée sur la géologie, la géophysique, la thermicité, la géochimie et la modélisation, de la zone de subduction à la province géothermale. Pour tracer l'histoire d'une anomalie thermique de grande longueur trouvant sa source très probablement dans le manteau, il est en effet nécessaire de travailler sur des constantes de temps suffisantes, en l'occurrence plusieurs dizaines de millions d'années.

Dans le détail, l'exploitation de l'ensemble des données et des reconstructions cinématiques issues de la littérature obtenus lors de ces années, devrait mener à un modèle génétique. Ce dernier pourra être testé par des simulations numériques (3D et 2D), examinant d'une part le comportement thermique et mécanique de la lithosphère, et s'intéressant d'autre part aux circulations hydrothermales dans la croûte supérieure. Ainsi, de nouvelles contraintes sur les mécanismes de production et de transfert de chaleur dans les zones de subductions à différentes échelles seront discutées.

Une autre question également essentielle sera abordée : quelle est la géométrie (*i.e.* tuyauterie) du système (circulation de la chaleur par conduction puis des fluides chauds par convection) entre le manteau et les expressions de surface ? Cette deuxième question importante traitera des circulations des fluides chauds jusqu'à la surface compte tenu d'une anomalie thermique régionale en profondeur. Il s'agira notamment de positionner en profondeur cette dernière et d'identifier les drains crustaux principaux permettant la mise en place des systèmes géothermaux actuels. En ce sens, il faudra précisément établir le rôle de ces drains dans l'alimentation du réservoir où les circulations de fluides permettent l'homogénéisation de la température sur plusieurs dizaines voire centaines de mètres.

La finalité d'une telle étude pourrait s'appliquer à d'autres zones de subduction dans le monde (*e.g.* la zone de subduction des Cascades aux Etats-Unis et son arrière-arc) afin d'une part d'améliorer l'exploration géothermale spécifique aux systèmes amagmatiques en développant de nouveaux modèles conceptuels spécifiques, et d'autres part utiliser les données géothermales disponibles sur une région précise afin de mieux contraindre l'évolution thermique de cette zone de subduction.

I.6. Références

Agostini, S., Doglioni, C., Innocenti, F., Manetti, P., Tonarini, S., & Savaşçin, M. Y. (2007). The transition from subduction-related to intraplate Neogene magmatism in the Western Anatolia and Aegean area. Geological Society of America Special Papers, 418, 1-15.

Altherr, R., & Siebel, W. (2002). I-type plutonism in a continental back-arc setting: Miocene granitoids and monzonites from the central Aegean Sea, Greece. Contributions to Mineralogy and Petrology, 143(4), 397-415.

Alvarez, W. (1982). Geological evidence for the geographical pattern of mantle return flow and the driving mechanism of plate tectonics. Journal of Geophysical Research: Solid Earth, 87(B8), 6697-6710.

Andritsos, N., Dalambakis, P., Arvanitis, A., Papachristou, M., & Fytikas, M. (2015). Geothermal developments in Greece–Country update 2010-2014. In Proceedings World Geothermal Congress 2015 (pp. 19-24).

Annen, C. (2009). From plutons to magma chambers: Thermal constraints on the accumulation of eruptible silicic magma in the upper crust. Earth and Planetary Science Letters, 284(3), 409-416.

Arcay, D., Tric, E., & Doin, M. P. (2007). Slab surface temperature in subduction zones: Influence of the interplate decoupling depth and upper plate thinning processes. Earth and Planetary Science Letters, 255(3), 324-338.

Aydın, İ., Karat, H. İ., & Koçak, A. (2005). Curie-point depth map of Turkey. Geophysical Journal International, 162(2), 633-640.

Baba, A. (2015). Application of geothermal energy and its environmental problems in Turkey. International Journal of Global Environmental Issues, 14(3-4), 321-331.

Bal, J. L., & Chabot, B. (2001). Les énergies renouvelables. État de l'art et perspectives de développement. Comptes Rendus de l'Académie des Sciences-Series IIA-Earth and Planetary Science, 333(12), 827-834.

Baldi, P., Bertini, G., Cameli, G. M., Decandia, F. A., Dini, I., Lazzarotto, A., & Liotta, D. (1994). Tettonica distensiva post-collisionale nell'area geotermica di Larderello (Toscana meridionale). Stud. Geol. Camerti, 1, 183-193.

Barazangi, M., & Isacks, B. L. (1976). Spatial distribution of earthquakes and subduction of the Nazca plate beneath South America. Geology, 4(11), 686-692.

Becker, T. W., Lebedev, S., & Long, M. D. (2012). On the relationship between azimuthal anisotropy from shear wave splitting and surface wave tomography. Journal of Geophysical Research: Solid Earth, 117(B1).

Benderitter, Y., & Cormy, G. (1990). Possible approach to geothermal research and relative costs. Small geothermal resources: A guide to development and utilization, UNITAR, New York, 59-69.

Benoit, D. (1999). Conceptual models of the Dixie Valley, Nevada geothermal field. Transactions-Geothermal Resources Council, 505-512.

Bense, V. F., & Person, M. A. (2006). Faults as conduit-barrier systems to fluid flow in siliciclastic sedimentary aquifers. Water Resources Research, 42(5).

Bernabini, M., Bertini, G., Cameli, G. M., Dini, I., & Orlando, L. (1995). Gravity interpretation of Mt. Amiata geothermal area (Central Italy). In Proceedings of the World Geothermal Congress (pp. 859-862).

Bertani, R. (2015). Deep geothermal energy for heating and cooling. Renewable Heating and Cooling: Technologies and Applications, 67.

Bertrand, G., Guillou-Frottier, L., & Loiselet, C. (2014). Distribution of porphyry copper deposits along the western Tethyan and Andean subduction zones: Insights from a paleotectonic approach. Ore Geology Reviews, 60, 174-190.

Berza, T., Constantinescu, E., & VLAD, S. N. (1998). Upper Cretaceous magmatic series and associated mineralisation in the Carpathian–Balkan Orogen. Resource Geology, 48(4), 291-306.

Bijwaard, H. (1999). Seismic travel-time tomography for detailed global mantle structure. Faculteit Aardwetenschappen.

Bilim, F., Akay, T., Aydemir, A., & Kosaroglu, S. (2016). Curie point depth, heat-flow and radiogenic heat production deduced from the spectral analysis of the aeromagnetic data for geothermal investigation on the Menderes Massif and the Aegean Region, western Turkey. Geothermics, 60, 44-57.

Biryol, C. B., Zandt, G., Beck, S. L., Ozacar, A. A., Adiyaman, H. E., & Gans, C. R. (2010). Shear wave splitting along a nascent plate boundary: the North Anatolian Fault Zone. Geophysical Journal International, 181(3), 1201-1213.

Biryol, B.C., Beck, S. L., Zandt, G., & Özacar, A. A. (2011). Segmented African lithosphere beneath the Anatolian region inferred from teleseismic P-wave tomography. Geophysical Journal International, 184(3), 1037-1057.

Blackwell, D. D., Golan, B., & Benoit, D. (2000). Thermal regime in the Dixie Valley geothermal system. Geothermal Resources Council Transactions, 24, 223-228.

Bolhar, R., Ring, U., & Allen, C. M. (2010). An integrated zircon geochronological and geochemical investigation into the Miocene plutonic evolution of the Cyclades, Aegean Sea, Greece: Part 1: Geochronology. Contributions to Mineralogy and Petrology, 160(5), 719-742.

Bonev, N., Burg, J. P., & Ivanov, Z. (2006). Mesozoic–Tertiary structural evolution of an extensional gneiss dome—the Kesebir–Kardamos dome, eastern Rhodope (Bulgaria–Greece). International Journal of Earth Sciences, 95(2), 318-340.

Bonev, N., Ovtcharova-Schaltegger, M., Moritz, R., Marchev, P., & Ulianov, A. (2013). Peri-Gondwanan Ordovician crustal fragments in the high-grade basement of the Eastern Rhodope Massif, Bulgaria: evidence from U-Pb LA-ICP-MS zircon geochronology and geochemistry. Geodinamica Acta, 26(3-4), 207-229.

Bonneau, M., & Kienast, J. R. (1982). Subduction, collision et schistes bleus; l9exemple de l9Egee (Grece). Bulletin de la Société geologique de France, 7(4), 785-791.

Bonté, D., Guillou-Frottier, L., Garibaldi, C., Bourgine, B., Lopez, S., Bouchot, V., Lucazeau, F. (2010). Subsurface temperature maps in French sedimentary basins : new data compilation and interpolation. Bulletin de la Société Géologique de France 181, 377-390

Bouchot, V., & Genter, A. (2009). Exploration guides for active high-temperature geothermal systems as modern analogs for paleo-epithermal systems. Geothermal Resources Council Transactions, 33, 447-453.

Boutelier, D., Chemenda, A., & Burg, J. P. (2003). Subduction versus accretion of intra-oceanic volcanic arcs: insight from thermo-mechanical analogue experiments. Earth and Planetary Science Letters, 212(1), 31-45.

Bozkurt, E. (2001). Neotectonics of Turkey–a synthesis. Geodinamica acta, 14(1-3), 3-30.

Bozkurt, E., & Oberhänsli, R. (2001). Menderes Massif (Western Turkey): structural, metamorphic and magmatic evolution-a synthesis. International Journal of Earth Sciences, 89(4), 679-708.

Brun, J. P., & Cobbold, P. R. (1980). Strain heating and thermal softening in continental shear zones: a review. Journal of Structural Geology, 2(1-2), 149-158.

Brun, J. P., & Sokoutis, D. (2007). Kinematics of the southern Rhodope core complex (North Greece). International Journal of Earth Sciences, 96(6), 1079-1099.

Brun, J. P., & Faccenna, C. (2008). Exhumation of high-pressure rocks driven by slab rollback. Earth and Planetary Science Letters, 272(1), 1-7.

Brun, J. P., & Sokoutis, D. (2010). 45 my of Aegean crust and mantle flow driven by trench retreat. Geology, 38(9), 815-818.

Buiter, S. J., Govers, R., & Wortel, M. J. R. (2002). Two-dimensional simulations of surface deformation caused by slab detachment. Tectonophysics, 354(3), 195-210.

Bülbül, A., Özen, T., Tarcan, G. (2011). Hydrogeochemical and hydrogeological investigations of thermal waters in the Alasehir-Kavaklidere area (Manisa-Turkey). Afr. J. Biotechnol. 10, 17223–17240.

Byrdina, S., Ramos, D., Vandemeulebrouck, J., Masias, P., Revil, A., Finizola, A., ... & Macedo, O. (2013). Influence of the regional topography on the remote emplacement of hydrothermal systems with examples of Ticsani and Ubinas volcanoes, Southern Peru. Earth and Planetary Science Letters, 365, 152-164.

Caine, J. S., Evans, J. P., & Forster, C. B. (1996). Fault zone architecture and permeability structure. Geology, 24(11), 1025-1028.

Candela, P. A., & P. M. Piccoli (2005), Magmatic processes in the development of porphyry-type ore systems, Econ. Geol., 100th Anniversary Volume, 25–37.

Cannell, J., Cooke, D. R., Walshe, J. L., & Stein, H. (2005). Geology, mineralization, alteration, and structural evolution of the El Teniente porphyry Cu-Mo deposit. Economic Geology, 100(5), 979-1003.

Caskey, S. J., & Wesnousky, S. G. (2000). Active faulting and stress redistributions in Dixie Valley, Beowawe, and Bradys geothermal fields: Implications for geothermal exploration in the Basin and Range: 25th workshop on Geothermal Reservoir Engineering. In Proceedings, 25th Workshop on Geothermal Reservoir Engineering (pp. 24-26).

Čermák, V., & Haenel, R. (1988). Geothermal maps. In Handbook of Terrestrial Heat-Flow Density Determination (pp. 261-300). Springer Netherlands.

Clark, C., Fitzsimons, I. C., Healy, D., & Harley, S. L. (2011). How does the continental crust get really hot?. Elements, 7(4), 235-240.

Colvine, A. C. (1988). Archean lode gold deposits in Ontario (Vol. 139). Ontario Ministry of Northern Development and Mines.

Conrad, C. P., & Behn, M. D. (2010). Constraints on lithosphere net rotation and asthenospheric viscosity from global mantle flow models and seismic anisotropy. Geochemistry, Geophysics, Geosystems, 11(5).

Crittenden, M. D., Coney, P. J., Davis, G. H., & Davis, G. H. (Eds.). (1980). Cordilleran metamorphic core complexes (Vol. 153). Geological Society of America.

Cumming, W. (2009). Geothermal resource conceptual models using surface exploration data. In Proceedings.

Currie, C. A., & Hyndman, R. D. (2006). The thermal structure of subduction zone back arcs. Journal of Geophysical Research: Solid Earth, 111(B8).

Dalrymple, G. B., Grove, M., Lovera, O. M., Harrison, T. M., Hulen, J. B., & Lanphere, M. A. (1999). Age and thermal history of the Geysers plutonic complex (felsite unit), Geysers geothermal field, California: a 40 Ar/39 Ar and U–Pb study. Earth and Planetary Science Letters, 173(3), 285-298.

Davis, G. H., & Coney, P. J. (1979). Geologic development of the Cordilleran metamorphic core complexes. Geology, 7(3), 120-124.

Davies, J. H., & von Blanckenburg, F. (1995). Slab breakoff: a model of lithosphere detachment and its test in the magmatism and deformation of collisional orogens. Earth and Planetary Science Letters, 129(1-4), 85-102.

De Boorder, H., Spakman, W., White, S. H., & Wortel, M. J. R. (1998). Late Cenozoic mineralization, orogenic collapse and slab detachment in the European Alpine Belt. Earth and Planetary Science Letters, 164(3), 569-575.

Deal, M. M., & Nolet, G. (1999). Slab temperature and thickness from seismic tomography: 2. Izu-Bonin, Japan, and Kuril subduction zones. Journal of Geophysical Research: Solid Earth, 104(B12), 28803-28812.

Delph, J. R., Zandt, G., & Beck, S. L. (2015). A new approach to obtaining a 3D shear wave velocity model of the crust and upper mantle: An application to eastern Turkey. Tectonophysics, 665, 92-100.

Deon, F., Moeck, I., Sheytt, T., & Jaya, M. S. (2012). Preliminary assessment of the geothermal system of the Tiris volcanic area, East Java, Indonesia. In 74th EAGE Conference and Exhibition incorporating EUROPEC 2012.

Dewey, J.F., (1980). Episodicity, sequence and style at convergent plate boundaries. In: D., Strangway, (Ed.). The Continental Crust and Its Mineral Deposits. Geol. Assoc. Can., Spec. Pap. 20, pp.553–573.

Dickson, M. H., & Fanelli, M. (2013). Geothermal energy: utilization and technology. Routledge.

Dilek, Y., & Altunkaynak, Ş. (2009). Geochemical and temporal evolution of Cenozoic magmatism in western Turkey: mantle response to collision, slab break-off, and lithospheric tearing in an orogenic belt. Geological Society, London, Special Publications, 311(1), 213-233.

Dini, A., Gianelli, G., Puxeddu, M., & Ruggieri, G. (2005). Origin and evolution of Pliocene–Pleistocene granites from the Larderello geothermal field (Tuscan Magmatic Province, Italy). Lithos, 81(1), 1-31.

Doglioni, C. (1993). Some remarks on the origin of foredeeps. Tectonophysics, 228(1-2), 1-20.

Duprat-Oualid, S., Yamato, P., & Pitra, P. (2013). Major role of shear heating in intracontinental inverted metamorphism: Inference from a thermo-kinematic parametric study. Tectonophysics, 608, 812-831.

Elders, W. A., Friðleifsson, G. Ó., & Albertsson, A. (2014). Drilling into magma and the implications of the Iceland Deep Drilling Project (IDDP) for high-temperature geothermal systems worldwide. Geothermics, 49, 111-118.

Erkan, K. (2014). Crustal heat flow measurements in western Anatolia from borehole equilibrium temperatures. Solid Earth Disc, 6(1), 403-426.

Erkan, K. (2015). Geothermal investigations in western Anatolia using equilibrium temperatures from shallow boreholes. Solid Earth, 6(1), 103.

Ersoy, E. Y., & Palmer, M. R. (2013). Eocene-Quaternary magmatic activity in the Aegean: implications for mantle metasomatism and magma genesis in an evolving orogeny. Lithos, 180, 5-24.

Faccenna, C., Mattei, M., Funiciello, R., & Jolivet, L. (1997). Styles of back-arc extension in the central Mediterranean. Terra Nova, 9(3), 126-130.

Faccenna, C., Funiciello, F., Giardini, D., & Lucente, P. (2001a). Episodic back-arc extension during restricted mantle convection in the Central Mediterranean. Earth and Planetary Science Letters, 187(1), 105-116.

Faccenna, C., Becker, T. W., Lucente, F. P., Jolivet, L., & Rossetti, F. (2001b). History of subduction and back arc extension in the Central Mediterranean. Geophysical Journal International, 145(3), 809-820.

Faccenna, C., Becker, T. W., Lallemand, S., & Steinberger, B. (2012). On the role of slab pull in the Cenozoic motion of the Pacific plate. Geophysical Research Letters, 39(3).

Faccenna, C., Becker, T. W., Jolivet, L., & Keskin, M. (2013). Mantle convection in the Middle East: Reconciling Afar upwelling, Arabia indentation and Aegean trench rollback. Earth and Planetary Science Letters, 375, 254-269.

Famin, V., Philippot, P., Jolivet, L., & Agard, P. (2004). Evolution of hydrothermal regime along a crustal shear zone, Tinos Island, Greece. Tectonics, 23(5).

Faulds, J. E., Bouchot, V., Moeck, I., & Oguz, K. (2009). Structural controls on geothermal systems in western Turkey: a preliminary report. Geothermal Resources Council Transactions, 33, 375-382

Faulds, J. E., Hinz, N., Kreemer, C., & Coolbaugh, M. (2012). Regional patterns of geothermal activity in the Great Basin Region, Western USA: correlation with strain rates. Geothermal Resources Council Transactions, 36, 897-902.

Filiz, S., Tarcan, G., & Gemici, U. (2000). Geochemistry of the Germencik geothermal fields, Turkey. In Proceedings of WGC-2000 World Geothermal Congress (Vol. 28, pp. 1115-1120).

Finetti, I. R. (2006). Basic regional crustal setting and superimposed local pluton-intrusion-related tectonics in the Larderello-M. Amiata geothermal province, from integrated CROP seismic data. Bollettino della Società geologica italiana, 125(1), 117-146.

Fleitout, L., & Froidevaux, C. (1980). Thermal and mechanical evolution of shear zones. Journal of Structural Geology, 2(1-2), 159-164.

Fukao, Y., Widiyantoro, S., & Obayashi, M. (2001). Stagnant slabs in the upper and lower mantle transition region. Reviews of Geophysics, 39(3), 291-323.

Funiciello, F., Faccenna, C., Giardini, D., & Regenauer-Lieb, K. (2003). Dynamics of retreating slabs: 2. Insights from three-dimensional laboratory experiments. Journal of Geophysical Research: Solid Earth, 108(B4).

Funiciello, F., Moroni, M., Piromallo, C., Faccenna, C., Cenedese, A., & Bui, H. A. (2006). Mapping mantle flow during retreating subduction: Laboratory models analyzed by feature tracking. Journal of Geophysical Research: Solid Earth, 111(B3).

Garfunkel, Z., Anderson, C. A., & Schubert, G. (1986). Mantle circulation and the lateral migration of subducted slabs. Journal of Geophysical Research: Solid Earth, 91(B7), 7205-7223.

Gautier, P., Brun, J. P., & Jolivet, L. (1993). Structure and kinematics of upper Cenozoic extensional detachment on Naxos and Paros (Cyclades Islands, Greece). Tectonics, 12(5), 1180-1194.

Gessner, K., Gallardo, L. A., Markwitz, V., Ring, U., & Thomson, S. N. (2013). What caused the denudation of the Menderes Massif: Review of crustal evolution, lithosphere structure, and dynamic topography in southwest Turkey. Gondwana Research, 24(1), 243-274.

Gianelli, G., Manzella, A., & Puxeddu, M. (1997). Crustal models of the geothermal areas of southern Tuscany (Italy). Tectonophysics, 281(3-4), 221-239.

Gill, J. B. (1981), Orogenic andesites and plate tectonics, Minerals and rocks 16, Springer-Verlag, Berlin ; New York.

Gloaguen, E. (2006). Apports d'une étude intégrée sur les relations entre granites et minéralisations filoniennes (Au et Sn-W) en contexte tardiorogénique (Chaîne Hercynienne, Galice centrale, Espagne) (Doctoral dissertation, Université d'Orléans).

Goldfarb, R. J., Groves, D. I., & Gardoll, S. (2001). Orogenic gold and geologic time: a global synthesis. Ore geology reviews, 18(1), 1-75.

Goldfarb, R., Baker, T., Dube, B., Groves, D. I., Hart, C. J., & Gosselin, P. (2005). Distribution, character and genesis of gold deposits in metamorphic terranes. Society of Economic Geologists.

Gottardi, R., Teyssier, C., Mulch, A., Vennemann, T. W., & Wells, M. L. (2011). Preservation of an extreme transient geotherm in the Raft River detachment shear zone. Geology, 39(8), 759-762.

Govers, R., & Wortel, M. J. R. (2005). Lithosphere tearing at STEP faults: response to edges of subduction zones. Earth and Planetary Science Letters, 236(1), 505-523.

Govers, R., & Fichtner, A. (2016). Signature of slab fragmentation beneath Anatolia from full-waveform tomography. Earth and Planetary Science Letters, 450, 10-19.

Groves, D. I., & Bierlein, F. P. (2007). Geodynamic settings of mineral deposit systems. Journal of the Geological Society, 164(1), 19-30.

Groves, D. I., Goldfarb, R. J., Gebre-Mariam, M., Hagemann, S. G., & Robert, F. (1998). Orogenic gold deposits: a proposed classification in the context of their crustal distribution and relationship to other gold deposit types. Ore geology reviews, 13(1), 7-27.

Groves, D. I., Goldfarb, R. J., Robert, F., & Hart, C. J. (2003). Gold deposits in metamorphic belts: overview of current understanding, outstanding problems, future research, and exploration significance. Economic geology, 98(1), 1-29.

Groves, D. I., Condie, K. C., Goldfarb, R. J., Hronsky, J. M., & Vielreicher, R. M. (2005). 100th Anniversary Special Paper: secular changes in global tectonic processes and their influence on the temporal distribution of gold-bearing mineral deposits. Economic Geology, 100(2), 203-224.

Guillou-Frottier, L., Buttles, J., & Olson, P. (1995). Laboratory experiments on the structure of subducted lithosphere. Earth and Planetary Science Letters, 133(1-2), 19-34.

Haizlip, J. R., Haklidir, F. T., & Garg, S. K. (2013). Comparison of reservoir conditions in high noncondensible gas geothermal systems. In Proceedings, Thirty-Eighth Workshop on Geothermal Reservoir Engineering, Stanford University.

Haklidir, M., & Haklidir, F. T. (2015). Fuzzy control of calcium carbonate and silica scales in geothermal systems. In Proceedings World Geothermal Congress.

Harangi, S., Downes, H., & Seghedi, I. (2006). Tertiary-Quaternary subduction processes and related magmatism in the Alpine-Mediterranean region. Geological Society, London, Memoirs, 32(1), 167-190.

Hawkesworth, C., Turner, S., Gallagher, K., Hunter, A., Bradshaw, T., & Rogers, N. (1995). Calc-alkaline magmatism, lithospheric thinning and extension in the Basin and Range. Journal of Geophysical Research: Solid Earth, 100(B6), 10271-10286.

Hedenquist, J. W., & Lowenstern, J. B. (1994). The role of magmas in the formation of hydrothermal ore deposits. Nature, 370(6490), 519-527.

Heinrich, C. A., & Neubauer, F. (2002). Cu–Au–Pb–Zn–Ag metallogeny of the Alpine–Balkan–Carpathian–Dinaride geodynamic province.

Herzberg, C. T., Fyfe, W. S., & Carr, M. J. (1983). Density constraints on the formation of the continental Moho and crust. Contributions to Mineralogy and Petrology, 84(1), 1-5.

Heuret, A. (2005). Dynamique des zones de subduction: étude statistique globale et approche analogique (Doctoral dissertation, Université Montpellier II-Sciences et Techniques du Languedoc).

Heuret, A., & Lallemand, S. (2005). Plate motions, slab dynamics and back-arc deformation. Physics of the Earth and Planetary Interiors, 149(1), 31-51.

Hildreth, W., & Moorbath, S. (1988). Crustal contributions to arc magmatism in the Andes of central Chile. Contributions to mineralogy and petrology, 98(4), 455-489.

Hochstein, M. P. (1988). Assessment and modelling of geothermal reservoirs (small utilization schemes). Geothermics, 17(1), 15-49.

Hulen, J. B., & Nielson, D. L. (1996). The Geysers felsite (No. CONF-960913--). Geothermal Resources Council, Davis, CA (United States).

Hyndman, R. D., Currie, C. A., & Mazzotti, S. P. (2005). Subduction zone backarcs, mobile belts, and orogenic heat. GSA Today, 15(2), 4-10.

Jadamec, M. A., & Billen, M. I. (2010). Reconciling surface plate motions with rapid three-dimensional mantle flow around a slab edge. Nature, 465(7296), 338.

Janković, S. (1997). The Carpatho-Balkanides and adjacent area: a sector of the Tethyan Eurasian metallogenic belt. Mineralium Deposita, 32(5), 426-433.

Jarrard, R. D. (1986). Relations among subduction parameters. Reviews of Geophysics, 24(2), 217-284.

Jiang, Y. H., Jiang, S. Y., Ling, H. F., & Dai, B. Z. (2006). Low-degree melting of a metasomatized lithospheric mantle for the origin of Cenozoic Yulong monzogranite-porphyry, east Tibet: geochemical and Sr–Nd–Pb–Hf isotopic constraints. Earth and Planetary Science Letters, 241(3), 617-633.

Johnson, R. W., & Arculus, R. J. (1978). Volcanic rocks of the Witu Islands, Papua New Guinea: The origin of magmas above the deepest part of the New Britain Benioff zone. Bulletin of Volcanology, 41(4), 609-655.

Jolivet, L., & Brun, J. P. (2010). Cenozoic geodynamic evolution of the Aegean. International Journal of Earth Sciences, 99(1), 109-138.

Jolivet, L., Daniel, J. M., Truffert, C., & Goffé, B. (1994). Exhumation of deep crustal metamorphic rocks and crustal extension in arc and back-arc regions. Lithos, 33(1-3), 3-30.

Jolivet, L., Maluski, H., Beyssac, O., Goffé, B., Lepvrier, C., Thi, P. T., & Van Vuong, N. (1999). Oligocene-Miocene Bu Khang extensional gneiss dome in Vietnam: geodynamic implications. Geology, 27(1), 67-70.

Jolivet, L., Faccenna, C., Goffé, B., Burov, E., & Agard, P. (2003). Subduction tectonics and exhumation of high-pressure metamorphic rocks in the Mediterranean orogens. American Journal of Science, 303(5), 353-409.

Jolivet, L., Famin, V., Mehl, C., Parra, T., Aubourg, C., Hébert, R., & Philippot, P. (2004). Strain localization during crustal-scale boudinage to form extensional metamorphic domes in the Aegean Sea. Geological Society of America Special Papers, 380, 185-210.

Jolivet, L., Faccenna, C., Huet, B., Labrousse, L., Le Pourhiet, L., Lacombe, O., ... & Philippon, M. (2013). Aegean tectonics: Strain localisation, slab tearing and trench retreat. Tectonophysics, 597, 1-33.

Jolivet, L., Faccenna, C., Agard, P., Frizon de Lamotte, D., Menant, A., Sternai, P., & Guillocheau, F. (2015). Neo-Tethys geodynamics and mantle convection: from extension to compression in Africa and a conceptual model for obduction. Canadian journal of earth sciences, 53(11), 1190-1204.

Jolivet, L., Menant, A., Clerc, C., Sternai, P., Ringenbach, J-C., … & Gorini, C. (submitted). Extensional crustal tectonics and crust-mantle coupling, a view from the geological record.

Jordán, T. E., Isacks, B. L., Allmendinger, R. W., Brewer, J. A., Ramos, V. A., & Ando, C. J. (1983). Andean tectonics related to geometry of subducted Nazca plate. Geological Society of America Bulletin, 94(3), 341-361.

Karabulut, H., Paul, A., Afacan Ergün, T., Hatzfeld, D., Childs, D. M., & Aktar, M. (2013). Long-wavelength undulations of the seismic Moho beneath the strongly stretched Western Anatolia. Geophysical Journal International, 194(1), 450-464.

Karamanderesi, İ. H., & Helvaci, C. (2003). Geology and hydrothermal alteration of the Aydın-Salavatlı geothermal field, western Anatolia, Turkey. Turkish Journal of Earth Sciences, 12(2), 175-198.

Kaya, A. (2015). The effects of extensional structures on the heat transport mechanism: An example from the Ortakçı geothermal field (Büyük Menderes Graben, SW Turkey). Journal of African Earth Sciences, 108, 74-88.

Kellogg, L. H., Hager, B. H., & van der Hilst, R. D. (1999). Compositional stratification in the deep mantle. Science, 283(5409), 1881-1884.

Kennedy, B. M., & Van Soest, M. C. (2005). Regional and Local Trends in helium isotopes, basin and range province, western North America: Evidence for deep permeable pathways. Lawrence Berkeley National Laboratory.

Kennedy, B. M., & van Soest, M. C. (2006). A helium isotope perspective on the Dixie Valley, Nevada, hydrothermal system. Geothermics, 35(1), 26-43.

Kennedy, B. M., Fischer, T. P., & Shuster, D. L. (2000). Heat and helium in geothermal systems. In a Proceedings of the Twenty-fifth Workshop on Geothermal Reservoir Engineering (pp. 167-173).

Keskin, M. (2003). Magma generation by slab steepening and breakoff beneath a subduction-accretion complex: An alternative model for collision-related volcanism in Eastern Anatolia, Turkey. Geophysical Research Letters, 30(24).

Kincaid, C., & Olson, P. (1987). An experimental study of subduction and slab migration. Journal of Geophysical Research: Solid Earth, 92(B13), 13832-13840.

Király, Á., Capitanio, F. A., Funiciello, F., & Faccenna, C. (2017). Subduction induced mantle flow: Length-scales and orientation of the toroidal cell. Earth and Planetary Science Letters, 479, 284-297.

Kivelä, S. M., Friberg, M., Wiklund, C., & Gotthard, K. (2017). Adaptive developmental plasticity in a butterfly: mechanisms for size and time at pupation differ between diapause and direct development. Biological Journal of the Linnean Society.

Koçyiğit, A. (2015). An overview on the main stratigraphic and structural features of a geothermal area: the case of Nazilli-Buharkent section of the Büyük Menderes Graben, SW Turkey. Geodinamica Acta, 27(2-3), 85-109.

Kreemer, C., Blewitt, G., & Hammond, W. C. (2009). Geodetic constraints on contemporary deformation in the northern Walker Lane: 2. Velocity and strain rate tensor analysis. Geological Society of America Special Papers, 447, 17-31.

Lallemand, S., Heuret, A., & Boutelier, D. (2005). On the relationships between slab dip, back-arc stress, upper plate absolute motion, and crustal nature in subduction zones. Geochemistry, Geophysics, Geosystems, 6(9).

Le Pichon, X., & Angelier, J. (1979). The Hellenic arc and trench system: a key to the neotectonic evolution of the eastern Mediterranean area. Tectonophysics, 60(1), 1-42.

Leach, T. M., & Corbett, G. J. (1993). Porphyry-related carbonate base metal gold systems: the transition between the epithermal and porphyry environments. Abstr Vol Geological Society of Australia 2nd Natl Meet, Armidale, Abstr, 34, 39-40.

Leloup, P. H., Ricard, Y., Battaglia, J., & Lacassin, R. (1999). Shear heating in continental strike-slip shear zones: model and field examples. Geophysical Journal International, 136(1), 19-40.

Li, C., van der Hilst, R. D., Engdahl, E. R., & Burdick, S. (2008). A new global model for P wave speed variations in Earth's mantle. Geochemistry, Geophysics, Geosystems, 9(5).

Lister, G. S., & Snoke, A. W. (1984). SC mylonites. Journal of Structural Geology, 6(6), 617-638.

Lucazeau, F., & Vasseur, G. (1989). Heat flow density data from France and surrounding margins. Tectonophysics, 164(2-4), 251-258.

Luhr, J.F., (1997). Extensional tectonics and the diverse primitive volcanic rocks in the western Mexican volcanic belt: Canadian Mineralogist, v. 35, p. 473–500.

Mancktelow, N., Zwingmann, H., & Mulch, A. (2016). Timing and conditions of clay fault gouge formation on the Naxos detachment (Cyclades, Greece). Tectonics, 35(10), 2334-2344.

Manzella, A., Mackie, R., & Fiordelisi, A. (1999). A MT survey in the Amiata volcanic area: A combined methodology for defining shallow and deep structures. Physics and Chemistry of the Earth, Part A: Solid Earth and Geodesy, 24(9), 837-840.

Marchev, P., Raicheva, R., Downes, H., Vaselli, O., Chiaradia, M., & Moritz, R. (2004). Compositional diversity of Eocene–Oligocene basaltic magmatism in the Eastern Rhodopes, SE Bulgaria: implications for genesis and tectonic setting. Tectonophysics, 393(1), 301-328.

Marchev, P., Arai, S., & Vaselli, O. (2006). Cumulate xenoliths in Oligocene alkaline basaltic and lamprophyric dikes from the eastern Rhodopes, Bulgaria: Evidence for the existence of layered plutons under the metamorphic core complexes. Geological Society of America Special Papers, 409, 237-258.

McGrath, A., Stouraiti, C., & Windley, B. (2017). Geochemistry of mylonitic gneisses from the Cycladic Basement Unit (Paros and Serifos, Aegean Sea): implications for protoliths of the high-grade gneisses. International Journal of Earth Sciences, 106(6), 2067-2089.

Menant, A., Jolivet, L., Augier, R., & Skarpelis, N. (2013). The North Cycladic Detachment System and associated mineralization, Mykonos, Greece: Insights on the evolution of the Aegean domain. Tectonics, 32(3), 433-452.

Menant, A., Jolivet, L., & Vrielynck, B. (2016a). Kinematic reconstructions and magmatic evolution illuminating crustal and mantle dynamics of the eastern Mediterranean region since the late Cretaceous. Tectonophysics, 675, 103-140.

Menant, A., Sternai, P., Jolivet, L., Guillou-Frottier, L., & Gerya, T. (2016b). 3D numerical modeling of mantle flow, crustal dynamics and magma genesis associated with slab roll-back and tearing: The eastern Mediterranean case. Earth and Planetary Science Letters, 442, 93-107.

Mendrinos, D., Choropanitis, I., Polyzou, O., & Karytsas, C. (2010). Exploring for geothermal resources in Greece. Geothermics, 39(1), 124-137.

Moeck, I. S. (2014). Catalog of geothermal play types based on geologic controls. Renewable and Sustainable Energy Reviews, 37, 867-882.

Molnar, P., & Atwater, T. (1978). Interarc spreading and Cordilleran tectonics as alternates related to the age of subducted oceanic lithosphere. Earth and Planetary Science Letters, 41(3), 330-340.

Molnar, P., & England, P. (1990). Temperatures, heat flux, and frictional stress near major thrust faults. Journal of Geophysical Research: Solid Earth, 95(B4), 4833-4856.

Muffler, L. J. P. (1979). Assessment of geothermal resources of the United States, 1978 (No. USGS-CIRC-790). Geological Survey, Reston, VA (USA). Geologic Div..

Nabelek, P. I., Whittington, A. G., & Hofmeister, A. M. (2010). Strain heating as a mechanism for partial melting and ultrahigh temperature metamorphism in convergent orogens: Implications of temperature-dependent thermal diffusivity and rheology. Journal of Geophysical Research: Solid Earth, 115(B12).

Nelson, T. H., & Temple, P. G. (1972). Mainstream mantle convection: a geologic analysis of plate motion. AAPG Bulletin, 56(2), 226-246.

Nicolas, A., & Le Pichon, X. (1980). Thrusting of young lithosphere in subduction zones with special reference to structures in ophiolitic peridotites. Earth and Planetary Science Letters, 46(3), 397-406.

Nukman, M., & Moeck, I. (2012). Field based geothermal exploration: Structural controls in the Tarutung Basin/North Central Sumatra (Indonesia). In EGU General Assembly Conference Abstracts (Vol. 14, p. 10009).

Özen, T., Bülbül, A., & Tarcan, G. (2012). Reservoir and hydrogeochemical characterizations of geothermal fields in Salihli, Turkey. Journal of Asian Earth Sciences, 60, 1-17.

Özgür, N., & Karamenderesi, I. H. (2015). An update of the geothermal potential in the continental rift zone of the Büyük Menderes, Western Anatolia, Turkey. In Proceedings, Thirty-Ninth Workshop on Geothermal Reservoir Engineering Stanford University, Stanford, California.

Paquette, J. L., Ménot, R. P., Pin, C., & Orsini, J. B. (2003). Episodic and short-lived granitic pulses in a post-collisional setting: evidence from precise U–Pb zircon dating through a crustal cross-section in Corsica. Chemical Geology, 198(1), 1-20.

Pearce, J. A., Leat, P. T., Barker, P. F., & Millar, I. L. (2001). Geochemical tracing of Pacific-to-Atlantic upper-mantle flow through the Drake Passage. Nature, 410(6827), 457.

Pe-Piper, G., & Piper, D. J. (2006). Unique features of the Cenozoic igneous rocks of Greece. Geological Society of America Special Papers, 409, 259-282.

Peyton, V., Levin, V., Park, J., Brandon, M., Lees, J., Gordeev, E., & Ozerov, A. (2001). Mantle flow at a slab edge: seismic anisotropy in the Kamchatka region. Geophysical Research Letters, 28(2), 379-382.

Pik, R., & Marty, B. (2009). Helium isotopic signature of modern and fossil fluids associated with the Corinth rift fault zone (Greece): implication for fault connectivity in the lower crust. Chemical Geology, 266(1), 67-75.

Piromallo, C., & Morelli, A. (2003). P wave tomography of the mantle under the Alpine-Mediterranean area. Journal of Geophysical Research: Solid Earth, 108(B2).

Piromallo, C., Becker, T. W., Funiciello, F., & Faccenna, C. (2006). Three-dimensional instantaneous mantle flow induced by subduction. Geophysical Research Letters, 33(8).

Reilinger, R., & McClusky, S. (2011). Nubia–Arabia–Eurasia plate motions and the dynamics of Mediterranean and Middle East tectonics. Geophysical Journal International, 186(3), 971-979.

Richards, J. P. (2005), Cumulative factors in the generation of giant calc-alkaline porphyry Cu deposits, in Super Porphyry Copper & Gold Deposits: A Global Perspective, vol. 1, pp. 7–25, Porter T. M., Adelaide, Australia.

Richards, J. P. (2009). Postsubduction porphyry Cu-Au and epithermal Au deposits: Products of remelting of subduction-modified lithosphere. Geology, 37(3), 247-250.

Richards, J. P. (2011). High Sr/Y arc magmas and porphyry Cu±Mo±Au deposits: just add water. Economic Geology, 106(7), 1075-1081.

Routhier, P. (1964). Rapport de synthèse. Developments in Sedimentology, 2, 167-176.

Royden, L. H., & Husson, L. (2009). Subduction with variations in slab buoyancy: models and application to the Banda and Apennine systems. Subduction Zone Geodynamics, 35-45.

Ruff, L., & Kanamori, H. (1980). Seismicity and the subduction process. Physics of the Earth and Planetary interiors, 23(3), 240-252.

Russo, R. M., & Silver, P. G. (1994). Trench-parallel flow beneath the Nazca plate from seismic anisotropy. science-new york then washington-, 1105-1105.

Salaün, G., Pedersen, H. A., Paul, A., Farra, V., Karabulut, H., Hatzfeld, D., ... & SIMBAAD Team. (2012). High-resolution surface wave tomography beneath the Aegean-Anatolia region: constraints on upper-mantle structure. Geophysical Journal International, 190(1), 406-420.

Santilano, A., Manzella, A., Gianelli, G., Donato, A., Gola, G., Nardini, I., ... & Botteghi, S. (2015). Convective, intrusive geothermal plays: what about tectonics?. Geothermal Energy Science, 3(1), 51-59.

Sanyal, S. K. (2005). Cost of geothermal power and factors that affect it. In Proceedings world geothermal congress (pp. 24-29).

Scaillet, B. (2010). Economic geology: Volatile destruction, Nat. Geosci., 3(7), 456–457, doi:10.1038/ngeo908.

Schellart, W. P., Freeman, J., Stegman, D. R., Moresi, L., & May, D. (2007). Evolution and diversity of subduction zones controlled by slab width. Nature, 446(7133), 308.

Scholz, C. H. (1980). Shear heating and the state of stress on faults. Journal of Geophysical Research: Solid Earth, 85(B11), 6174-6184.

Seedorff, E., Dilles, J. H., Proffett, J. M., Einaudi, M. T., Zurcher, L., Stavast, W. J. A., ... & Barton, M. D. (2005). Porphyry deposits: Characteristics and origin of hypogene features. Economic Geology 100th anniversary volume, 29, 251-298.

Seghedi, I., Ersoy, Y. E., & Helvacı, C. (2013). Miocene–Quaternary volcanism and geodynamic evolution in the Pannonian Basin and the Menderes Massif: A comparative study. Lithos, 180, 25-42.

Shemenda, A.I., 1994. Subduction: Insights from Physical Modeling. Kluwer Academic Publishers, Dordrecht.

Sibson, R. H. (1987). Earthquake rupturing as a mineralizing agent in hydrothermal systems. Geology, 15(8), 701-704.

Sibson, R. H., Robert, F., & Poulsen, K. H. (1988). High-angle reverse faults, fluid-pressure cycling, and mesothermal gold-quartz deposits. Geology, 16(6), 551-555.

Sillitoe, R. H. (1997). Characteristics and controls of the largest porphyry copper-gold and epithermal gold deposits in the circum-Pacific region. Australian Journal of Earth Sciences, 44(3), 373-388.

Sillitoe, R. H., & Hedenquist, J. W. (2003). Linkages between volcanotectonic settings, ore-fluid compositions, and epithermal precious metal deposits. Special Publication-Society of Economic Geologists, 10, 315-343.

Sillitoe, R. H., Perelló, J., & García, A. (2010). Sulfide-bearing veinlets throughout the stratiform mineralization of the Central African Copperbelt: temporal and genetic implications. Economic Geology, 105(8), 1361-1368.

Şimşek, Ş. (1985). Geothermal model of Denizli, Sarayköy-Buldan area. Geothermics, 14(2-3), 393-417.

Skarpelis, N. (2002). Geodynamics and evolution of the Miocene mineralization in the Cycladic-Pelagonian belt, Hellenides. Bull. Geol. Soc. Greece, 34(6), 2191-2206.

Sokoutis, D., Brun, J. P., Van Den Driessche, J., & Pavlides, S. (1993). A major Oligo-Miocene detachment in southern Rhodope controlling north Aegean extension. Journal of the Geological Society, 150(2), 243-246.

Solomon, M. (1990). Subduction, arc reversal, and the origin of porphyry copper-gold deposits in island arcs. Geology, 18(7), 630-633.

Stampolidis, A., & Tsokas, G. N. (2002). Curie point depths of Macedonia and Thrace, N. Greece. Pure and Applied Geophysics, 159(11), 2659-2671.

Sternai, P., Jolivet, L., Menant, A., & Gerya, T. (2014). Driving the upper plate surface deformation by slab rollback and mantle flow. Earth and Planetary Science Letters, 405, 110-118.

Tatsumi, Y., Otofuji, Y. I., Matsuda, T., & Nohda, S. (1989). Opening of the Sea of Japan back-arc basin by asthenospheric injection. Tectonophysics, 166(4), 317-329.

Tosdal, R. M., & Richards, J. P. (2001). Magmatic and structural controls on the development of porphyry Cu±Mo±Au deposits. Reviews in Economic Geology, 14, 157-181.Richards, J. P. (2003). Tectono-magmatic precursors for porphyry Cu-(Mo-Au) deposit formation. Economic Geology, 98(8), 1515-1533.

Tselentis, G. A. (1991). An attempt to define Curie point depths in Greece from aeromagnetic and heat flow data. pure and applied geophysics, 136(1), 87-101.

Urai, J. L., Schuiling, R. D., & Jansen, J. B. H. (1990). Alpine deformation on Naxos (Greece). Geological Society, London, Special Publications, 54(1), 509-522.

Uyeda, S., & Kanamori, H. (1979). Back-arc opening and the mode of subduction. Journal of Geophysical Research: Solid Earth, 84(B3), 1049-1061.

van der Hilst, R., & Seno, T. (1993). Effects of relative plate motion on the deep structure and penetration depth of slabs below the Izu-Bonin and Mariana island arcs. Earth and Planetary Science Letters, 120(3-4), 395-407.

van der Lee, S., & Nolet, G. (1997). Seismic image of the subducted trailing fragments of the Farallon plate. Nature, 386(6622), 266.

Van der Voo, R., Spakman, W., & Bijwaard, H. (1999). Mesozoic subducted slabs under Siberia. Nature, 397(6716), 246.

Van Hinsbergen, D. J. J., Hafkenscheid, E., Spakman, W., Meulenkamp, J. E., & Wortel, R. (2005). Nappe stacking resulting from subduction of oceanic and continental lithosphere below Greece. Geology, 33(4), 325-328.

van Keken, P. E., Currie, C., King, S. D., Behn, M. D., Cagnioncle, A., He, J., ... & Wang, K. (2008). A community benchmark for subduction zone modeling. Physics of the Earth and Planetary Interiors, 171(1), 187-197.

Vanacore, E. A., Taymaz, T., & Saygin, E. (2013). Moho structure of the Anatolian Plate from receiver function analysis. Geophysical Journal International, 193(1), 329-337.

Vanderhaeghe, O. (2004). Structural development of the Naxos migmatite dome. Geological Society of America Special Papers, 380, 211-227.

von Quadt, A., Moritz, R., Peytcheva, I., & Heinrich, C. A. (2005). 3: Geochronology and geodynamics of Late Cretaceous magmatism and Cu–Au mineralization in the Panagyurishte region of the Apuseni–Banat–Timok–Srednogorie belt, Bulgaria. Ore Geology Reviews, 27(1), 95-126.

Wannamaker, P. E., Doerner, W. M., & Hasterok, D. P. (2006a). Cryptic Faulting and Multi-Scale Geothermal Fluid Connections in the Dixie Valley-Central Nevada Seismic Belt Area; Implications from MT Resistivity Surveying. In 31st Workshop on Geothermal Reservoir Engineering, Stanford University, Stanford, CA.

Wannamaker, P. E., Hasterok, D. P., & Doerner, W. M. (2006b). Possible magmatic input to the Dixie Valley geothermal field, and implications for district-scale resource exploration, inferred from magnetotelluric (MT) resistivity surveying. In GRC 2006 Annual Meeting: Geothermal Resources-Securing Our Energy Future.

Wernicke, B., & Burchfiel, B. C. (1982). Modes of extensional tectonics. Journal of Structural Geology, 4(2), 105-115.

White, N. C., & Hedenquist, J. W. (1995). Epithermal gold deposits: styles, characteristics and exploration. SEG newsletter, 23(1), 9-13.

Wilkinson, J. J. (2013). Sediment-Hosted Zinc-Lead Mineralization: Processes and Perspectives: Processes and Perspectives.

Williams-Jones, A. E., & Heinrich, C. A. (2005). 100th Anniversary special paper: vapor transport of metals and the formation of magmatic-hydrothermal ore deposits. Economic Geology, 100(7), 1287-1312.

Wilson, C. J., & Rowland, J. V. (2016). The volcanic, magmatic and tectonic setting of the Taupo Volcanic Zone, New Zealand, reviewed from a geothermal perspective. Geothermics, 59, 168-187.

Wortel, M. J. R., & Spakman, W. (2000). Subduction and slab detachment in the Mediterranean-Carpathian region. Science, 290(5498), 1910-1917.

Yigit, O. (2012). A prospective sector in the Tethyan Metallogenic Belt: Geology and geochronology of mineral deposits in the Biga Peninsula, NW Turkey. Ore Geology Reviews, 46, 118-148.

Yilmazer, Ö., Yilmazer, Ö., Özvan, A., Leventeli, Y., & Yilmazer, I. (2010). Earthquake is Manmade Catastrophe Rather than a Natural Disaster: Turkey. In Survival and Sustainability (pp. 383-389). Springer Berlin Heidelberg.

Yogodzinski, G. M., Lees, J. M., Churikova, T. G., & Dorendorf, F. (2001). Geochemical evidence for the melting of subducting oceanic lithosphere at plate edges. Nature, 409(6819), 500.

Zajacz, Z., Candela, P. A., Piccoli, P. M., Wälle, M., & Sanchez-Valle, C. (2012). Gold and copper in volatile saturated mafic to intermediate magmas: Solubilities, partitioning, and implications for ore deposit formation. Geochimica et Cosmochimica Acta, 91, 140-159.

CHAPITRE II : Contrôle structural et lithologique sur l'activité géothermique actuelle dans la province du Menderes (partie occidentale de la Turquie)

Comme brièvement introduit dans la partie *I.5*, nous avons vu que la partie orientale de la Méditerranée est reconnue comme une zone à fort potentiel géothermal caractérisée par des valeurs de flux de chaleur élevées [Erkan, 2014 ; 2015]. Dans ce domaine d'arrière-arc (Fig. II.1), les activités magmatiques et volcaniques récentes sont peu développées, en particulier dans le Massif du Menderes où cette activité (comprise entre 2 – 0.2 millions d'années) se localise uniquement dans la province volcanique de Kula [Richardson-Bunbury, 1996 ; Bunbury *et al*., 2001]. Paradoxalement, la majorité des modèles géothermiques suggèrent l'existence de probable(s) intrusion(s) magmatique(s) dans la croûte supérieure comme source de chaleur (Fig. II.2a) [Simsek, 1985 ; Filiz *et al.*, 2000 ; Karamanderesi & Helvaci, 2003 ; Yilmazer *et al.*, 2010 ; Bülbül *et al.*, 2011 ; Özgür *et al.*, 2015]. A contrario, faute de volcanisme actif, de nouvelles études considèrent cette activité comme amagmatique. Dans ces conditions, l'activité tectonique joue un rôle fondamental dans la propagation des anomalies de températures vers la surface (Fig. II.2b) [Tarcan & Gemici, 2003 ; Faulds *et al.*, 2010 ; Haizlip *et al.*, 2013 ; Kaya, 2015 ; Haklidir *et al.*, 2015 ; Gessner *et al.*, 2017]. Il est important de noter qu'aucune de ces études ne discute réellement de l'apport de chaleur qui fait probablement appel à des processus d'ampleur géodynamique (*cf.* anomalies de grandes longueurs d'ondes données par les températures de Curie ; Fig. I.16b).

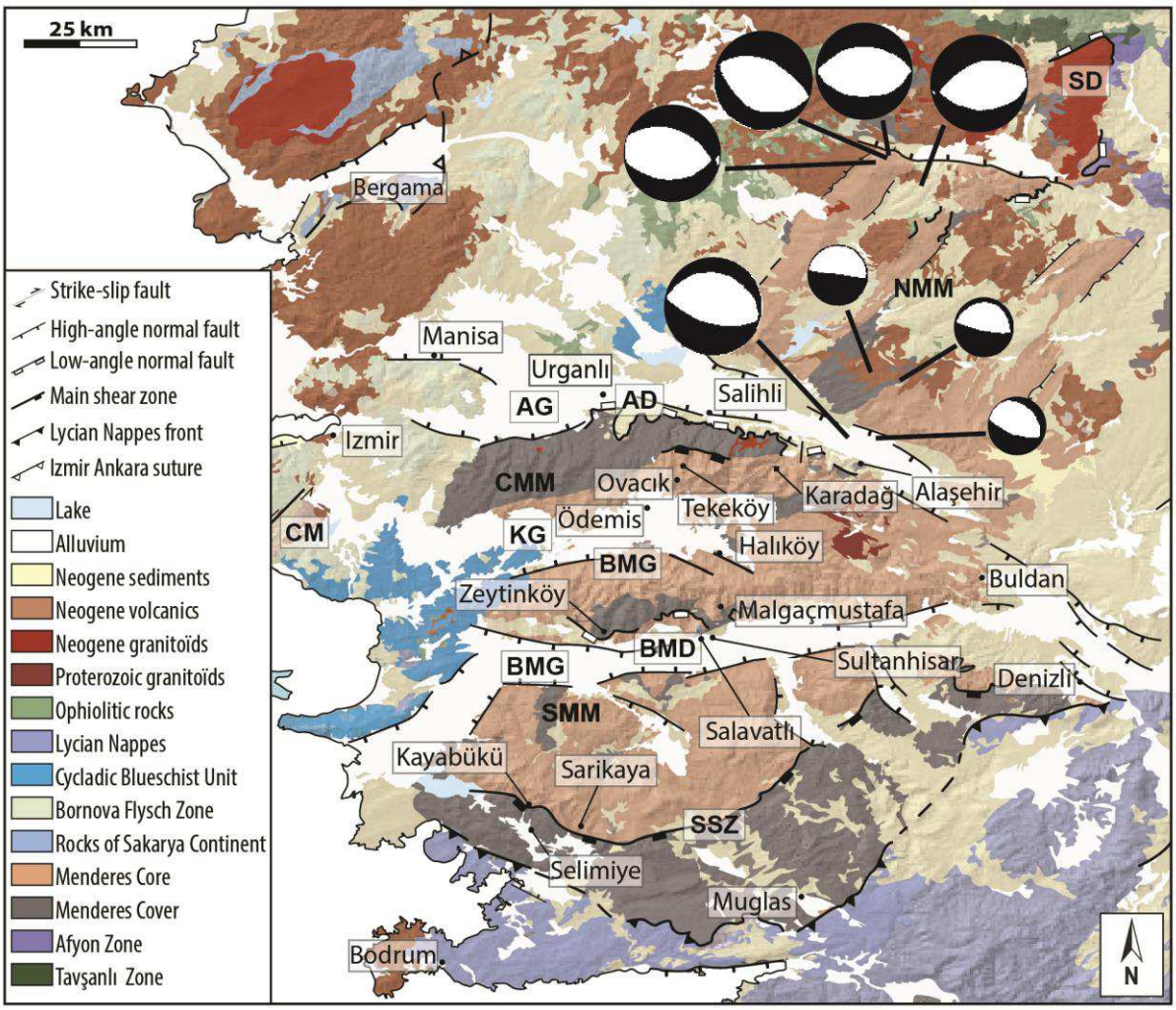

Figure II.1: carte tectonique du Massif du Menderes simplifiée montrant les principaux domaines géologiques modifiée d'après le MTA (Mineral Research & Exploration General Directorate) soit l'équivalent du BRGM et d'après Jolivet et al. [2013]. Les mécanismes au foyer représentés par les cercles noirs et blancs proviennent de l'étude d'Eyidogan & Jackson [1985]. Les grandes sphères correspondent à des données acquises sur des périodes longues alors que les petites sphères représentent un événement ponctuel. Les structures principales et les grabens sont indiqués par les abréviations suivantes : BMD (Büyük Menderes detachment) ; BMG (Büyük Menderes Graben) ; CM (Cumaovası Basin) ; AD (Alaşehir detachment) ; AG (Alaşehir Graben) ; KG (Küçük Menderes Graben) ; CMM (Central Menderes Massif ; SD (Simav detachment) ; SMM (Southern Menderes Massif) ; SSZ (Selimiye shear zone).

Afin de lever l'incertitude quant à l'origine de la chaleur et de mieux caractériser les relations entre les différents types de failles qui contrôlent la circulation des fluides actuelles (*i.e.* failles à fort et faible pendage, failles décrochantes), nous avons utilisé une approche régionale basée sur l'étude de différents champs géothermaux, qui se localisent dans la province géothermale du Menderes. Ce travail est donc principalement basé sur une compilation bibliographique concernant principalement le Massif du Menderes. Cette synthèse regroupe des données publiées dans la littérature sur les anomalies de températures en surface correspondant aux sources de chaleur, ainsi que des données de températures de réservoirs mesurées ou estimées à l'aide de géothermomètres (*i.e.* Na-K, SiO_2, Na-K-Ca…). D'autres

compilations sur le rapport isotopique de l'hélium et sur la signature isotopique de l'oxygène et de l'hydrogène ont également été réalisées afin de mieux comprendre les circulations des fluides géothermaux à différentes échelles [Güleç, 1988 ; Filiz *et al.*, 2000 ; Özgür, 2002 ; Güleç *et al.*, 2002 ; Tarcan & Gemici, 2003 ; Simsek, 2003 ; Güleç & Hilton, 2006 ; Mutlu *et al.*, 2008 ; Pik & Marty, 2009 ; Özen *et al.*, 2012 ; Karakuş, 2015]. Par ailleurs, de nouvelles données structurales acquises lors de deux missions de terrain en Turquie, apportent de nouvelles contraintes sur la circulation des fluides dans la croûte.

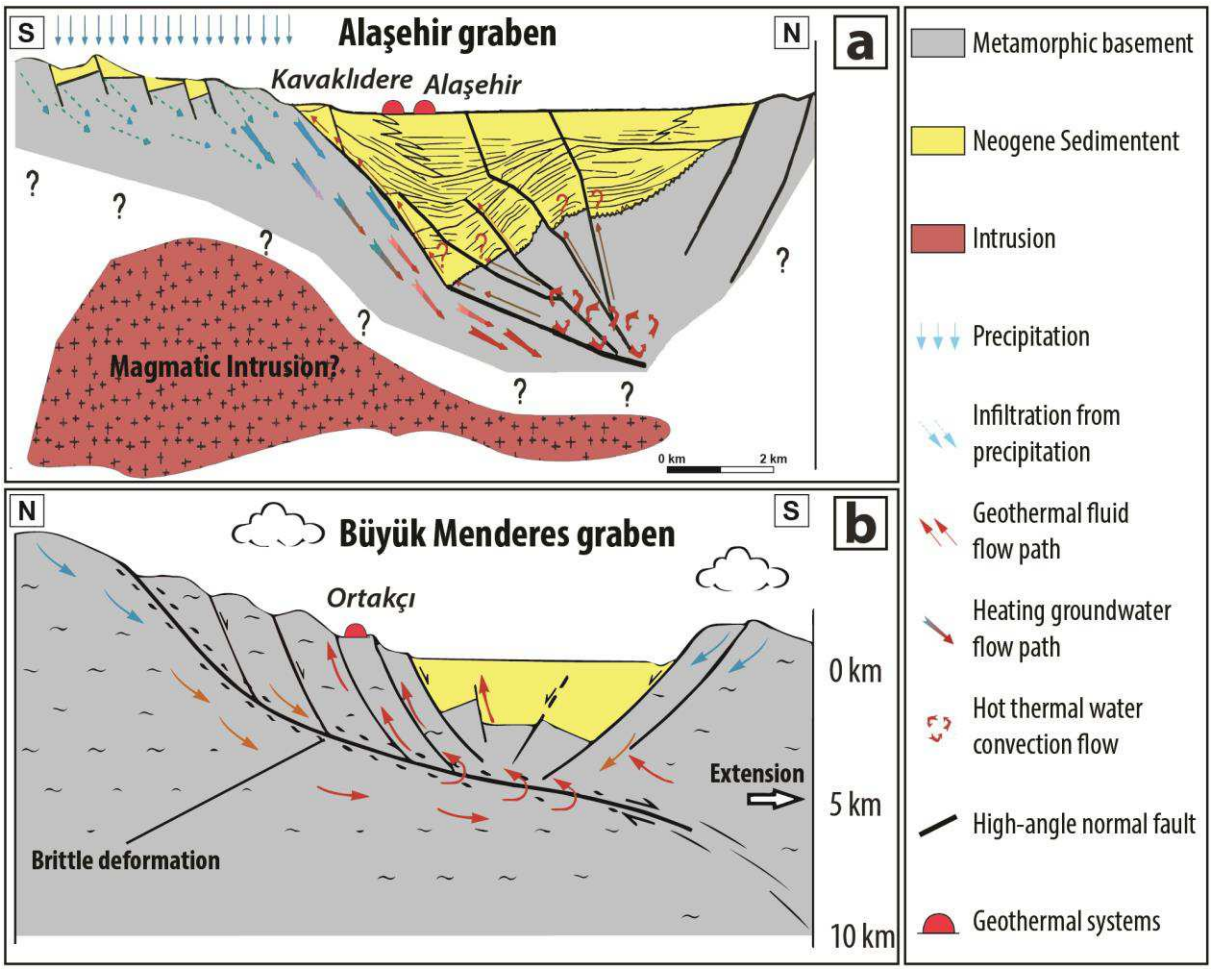

Figure II.2: représentations schématiques de systèmes géothermaux dans le Massif du Menderes associés à (a) une activité volcanique modifié d'après Bülbül et al. [2011] et à (b) une activité tectonique modifié d'après Kaya [2015]. A noter que la première figure correspond au graben d'Alaşehir (nord) alors que la seconde au graben du Büyük Menderes (sud). Dans les deux cas la source de chaleur diffère.

Principaux résultats :

Les principaux résultats suggèrent que les anomalies thermiques régionales ne résultent pas nécessairement d'un magmatisme sous-jacent mais que des processus de plus grande échelle interviennent. Il pourrait s'agir comme on le verra plus loin de l'évolution thermique de la zone de

subduction. Dans le détail, cet article présente les principales structures qui favorisent la circulation des fluides à différentes échelles. A l'échelle du bassin, des failles de transfert N-S contrôlent la circulation des fluides et expliquent en partie la localisation des sources de part et d'autre des grabens. A l'échelle crustale, les détachements, qui s'enracinent profondément dans la croûte, contrôlent la circulation ascendante et/ou descendante des fluides. Ces systèmes sont considérés comme des zones d'échanges thermiques où l'écoulement du fluide et la déformation jouent un rôle central dans le transport de chaleur des niveaux profonds de la croûte vers la surface [*e.g.* Mulch *et al.*, 2006 ; Famin *et al.*, 2004]. Finalement, nous proposons une possible évolution du massif qui se résume comme suit :

(i) Un épisode extensif important qui est induit d'une part, par le retrait rapide du panneau plongeant vers le sud, et d'autre part, par la déchirure de ce dernier sous l'ouest de l'Anatolie au Miocène (Fig. I.18b). Cette extension, accommodée par la formation de failles à faible pendage d'échelle crustale (*e.g.* le détachement de Simav, le détachement d'Alaşehir et le détachement du Büyük Menderes) [Hetzel *et al.*, 1995a ; 1995b ; Bozkurt, 2001 ; Gessner *et al.*, 2001b ; Sözbilir, 2001 ; 2002 ; Işık *et al.*, 2003 ; Bozkurt & Sözbilir, 2004 ; Hetzel *et al.*, 2013], permet l'exhumation du MCC du Menderes. Par ailleurs, la mise en place de migmatites contemporaines à l'extension post-orogénique dans ce massif [Catlos & Cemen, 2005 ; Cenki-Tok *et al.*, 2016], mais également dans le domaine Egéen, localisées à proximité du Massif du Menderes [Duchêne *et al.*, 2006 ; Beaudoin *et al.*, 2015 ; Laurent *et al.*, 2015 ; Jolivet *et al.*, 2015], confortent la présence d'anomalies thermiques de grandes longueurs d'onde à faible profondeur. Durant cette période, l'activité des détachements continue et des failles de transfert décrochantes liées soit à (i) la courbure de la fosse, (ii) des différences de vitesse d'extension au sein même du massif et/ou à (iii) la rotation de la partie centrale du Menderes lors de son exhumation (25 – 30° d'après Van Hinsbergen *et al.* [2010]), ont également affecté les détachements créant localement des espaces en ouverture, appelés jogs. Ces structures, générées par une différence de rhéologie (*i.e.* socle et bassin) vont faciliter l'écoulement et la remontée des fluides vers la surface.

(ii) Comme l'indique la présence des séismes sur la Figure II.2, la région du Menderes est encore active. Des failles normales à fort pendage orientées E-W contrôlent la géométrie des bassins comme celui d'Alaşehir, du Büyük Menderes ou encore du Simav. Même s'il est évident que certaines de ces failles recoupent le détachement, il est important de noter que dans d'autre cas ces failles s'aplatissent en profondeur (*i.e.* faille listrique) [Eyidogan & Jackson, 1985]. Ainsi, ces failles dont le mécanisme au foyer est compatible avec un jeu normal semblent être associées au jeu du détachement en profondeur. Ces différents épisodes d'intense fracturation favorisent d'une part la circulation d'eau météorique et d'autre part la formation de réservoir dans le socle du massif (*e.g.* gneiss). Les intersections entre le détachement, les failles de transferts N-S et certaines failles E-W généreront des ouvertures (*i.e.* jogs) qui favoriseront l'émergence des sources chaudes.

Structural, lithological and geodynamic controls on geothermal activity in the Menderes geothermal Province (Western Anatolia, Turkey)

Vincent ROCHE[1, 2, 3*], Vincent BOUCHOT[3, 1, 2], Laurent BECCALETTO[3, 1, 2], Laurent JOLIVET[1, 2, 3] Laurent GUILLOU-FROTTIER[3, 1, 2], Johann TUDURI[3, 1, 2], Erdin BOZKURT[4, 5], Kerem OGUZ[6], and Bülent TOKAY[5]

[1] *Université d'Orléans, ISTO, UMR 7327, 45071, Orléans, France*

[2] *CNRS/INSU, ISTO, UMR 7327, 45071 Orléans, France*

[3] *BRGM, ISTO, UMR 7327, BP 36009, 45060 Orléans, France*

[4] *Center for Global Tectonics & State Key Laboratory of Geological Processes and Mineral Resources, China University of Geosciences, Wuhan, 388 Lumo Road, Hongshan District, Wuhan 430074, Hubei Province, China*

[5] *Middle East Technical University, Department of Geological Engineering, Ankara, Turkey*

[6] *Municipality of Salihli, Salihli, Turkey*

(Cet article a été publié au journal IJES)

Abstract

Western Turkey belongs to the regions with the highest geothermal potential in the world, resulting in significant electricity production from geothermal resources located predominantly in the Menderes Massif. Although geothermal exploitation is increasingly ongoing, geological and physical processes leading to the emplacement of geothermal reservoirs are hitherto poorly understood. Several studies on the Menderes Massif led to different interpretations of structural controls on the location of hot springs and of the heat source origin. This paper describes geological evidence showing how heat is transmitted from the abnormally hot mantle to the geothermal reservoirs. On the basis of field studies, we suggest that crustal-scale low-angle normal faults convey hot fluids to the surface and represent the first-order control on geothermal systems. At the basin-scale, connected on low-angle normal faults, kilometric high-angle transfer faults are characterized by dilational jogs, where fluids may be strongly focused. In addition, favourable lithologies in the basement (*e.g.* karstic marble) could play a critical role in the localization of geothermal reservoirs. Finally, a compilation of geochemical data at the scale of the Menderes Massif suggests an important role of the large mantle thermal anomaly, which is related to the Hellenic subduction. Heat from shallow asthenospheric mantle is suggested to be conveyed toward the surface by fluid circulation through the low-angle faults. Hence, geothermal activity in the Menderes Massif is not of magmatic origin but rather associated with active extensional tectonics related to the Aegean slab dynamics (*i.e.* slab retreat and tearing).

II.1. Introduction

The high heat flow driving active geothermal systems is often believed to find its source in portions of crust invaded by magmas, but some of significant geothermal provinces are considered amagmatic namely not of magmatic origin in terms of heat source (*i.e.* no magmatic intrusions in the upper crust). In this case, large-scale processes (*e.g.* slab dynamics) inducing large-scale thermal anomalies are favoured, as for the Basin & Range Province in the Western US. In this extensional context, geothermal systems have been described as amagmatic in origin [*e.g.* Benoit, 1999; Blackwell *et al.*, 2000; Faulds *et al.*, 2004; 2011]. The exact origin of heat remains debated and, for instance, magmatic underplating under the overriding plate [Wannamaker *et al.*, 2006] and/or shear heating in the mantle in actively deforming area [*e.g.* Roche *et al.*, 2018] are some hypothesis of heat source possibilities. Despite the well-documented existence of large-scale seismic velocity anomalies in the mantle of the Eastern Mediterranean region [*e.g.* De Boorder *et al.*, 1998], very few studies have actually considered such amagmatic geothermal provinces in their large-scale geodynamic contexts [*e.g.* Roche *et al.*, 2015; 2016; 2018; Gessner *et al.*, 2017]. The path of heat transport from mantle to surface, either conductive or through advection of hot fluids, remains to be described in such environments. The Menderes Massif is one of the best examples where such a description can be done, from the mantle to the actively extending crust, up to the geothermal reservoirs.

The Menderes Massif is recognized as an active geothermal area where extensional or transtensional tectonics is accompanied by elevated heat flow values (~ 100 mW m^{-2}), which appear to extend to almost the entire Aegean domain [Erkan, 2014; 2015]. There, high heat flow estimated by Jongsma [1974] may correspond to the low *P*- wave seismic velocity zone described by Piromallo and Morelli [2003]. Surprisingly, magmatic activity and related volcanism have been very sparse there in the recent period (*i.e.* Pliocene and Quaternary); the unique volcanic activity occurred in the Kula volcanic field during the Quaternary between 2 and 0.2 Ma [*e.g.* Richardson-Bunbury, 1996; Bunbury *et al.*, 2001; Maddy *et al.*, 2017] where geothermal activity is absent. Existing models suggest probable magmatic reservoirs in the upper crust as heat source of the geothermal system in this area, more or less connected with the Kula basaltic activity [*e.g.* Simsek, 1985; Filiz *et al.*, 2000; Karamanderesi & Helvaci, 2003; Yilmazer *et al.*, 2010; Bülbül *et al.*, 2011; Özen *et al.*, 2012; Özgür *et al.*, 2015; Ozdemir *et al.*, 2017; Alçiçek *et al.*, 2018]. Nonetheless, others authors have also suggested a deeper and larger heat source triggered by slab dynamics (*i.e.* astenospheric mantle flow due to slab rollback and tearing [*e.g.* Kaya, 2015; Roche *et al.*, 2015; 2016; 2018; Gessner *et al.*, 2017]). It is then worth studying the consequences of these processes on the distribution of heat at the surface. In this case, recent tectonic activity and related graben structures have a major interest because they could control the fluid flow processes [*e.g.* Tarcan & Gemici, 2003; Faulds *et al.*, 2010; Haizlip *et al.*, 2013; Kocyigit, 2015; Kaya, 2015; Haklidir *et al.*, 2015].

Consequently, this study is dedicated to a multi-scale analysis of the different identified features of several geothermal fields of the Menderes Massif. We present a detailed structural analysis of main geothermal fields (*i.e.* Salihli, Alaşehir, Salavatlı and Seferihisar, Kızıldere, Germencik) to better characterize the fluid flow pattern. It is critical to evaluate which type of faults and which parts of them are most favourable for focusing geothermal activity. Our results are then discussed at different scales including that of the "Menderes geothermal Province". At the scale of lithosphere-mantle interactions, we use a broad compilation of mantle-He and oxygen-hydrogen isotopic data to propose and discuss a new conceptual model explaining the regional thermal anomaly with reference to geodynamic processes.

II.2. Geological setting

II.2.1. The eastern Mediterranean region

During the Cenozoic, the eastern Mediterranean region (Fig. II.3a) has undergone a two-step tectono-metamorphic evolution. Firstly, in the late Cretaceous-Eocene, the convergence of Africa and Eurasia has led to the closure of the Izmir-Ankara Ocean and to the accretion of subducting continental and oceanic lithospheres [Bonneau & Kienast, 1982; Dercourt *et al*., 1986; Jolivet & Brun, 2010]. Secondly, since the Oligo-Miocene, the kinematics in Mediterranean region has been mainly controlled by the southward retreat of the African slab responsible for back-arc extension [*e.g.* Malinverno & Ryan, 1986; Jolivet & Faccenna, 2000; Jolivet & Brun, 2010; Ring *et al*., 2010]. The Oligo-Miocene geological evolution of the Aegean region, including the Menderes Massif and the Cyclades, results from this episode of slab roll-back [*e.g.* Seyitoglu & Scott, 1991; Seyitoğlu *et al*., 1992; Seyitoglu & Scott, 1996; Jolivet *et al*., 1996]. In addition, recent studies based on geochemical analyses [*e.g.* Dilek & Altunkaynak, 2009; Ersoy *et al*., 2010; Prelevic *et al*., 2012], on tomographic models [*e.g.* De Booder *et al*., 1998; Biryol *et al*., 2011; Salaün *et al*., 2012] and on tectonic and magmatic evolution in this area [Dilek & Altunkaynak, 2009; Jolivet *et al*., 2015; Menant *et al*., 2016; Govers & Fichtner, 2016] invoke the particular slab dynamics beneath western Turkey, which would be characterized by a slab tear since the Miocene [Jolivet *et al*., 2015] (Fig. II.3a). The complex geometry of subduction zones and the tight arcs characterizing the Mediterranean region as a whole are direct consequences of slab retreat and slab tearing [Wortel & Spakman, 2000; Spakman & Wortel, 2004; Faccenna *et al*., 2004; Govers & Wortel, 2005; Faccenna *et al*., 2006]. Beside the heat wave caused by the advection of hot asthenosphere to shallow depths during retreat, slab tearing tends to efficiently localize deformation, and to facilitate high-temperature metamorphism, crustal melting, granitic intrusions and fluid circulations [Jolivet *et al*., 2015; Menant *et al*., 2016; Roche *et al*., 2018]. Therefore, magmatic activity during the Miocene was intense in western Turkey, but it has significantly decreased since 12 Ma [*e.g.* Ersoy *et al*., 2010]. In addition, this slab dynamics has a direct consequence on Moho depth, estimated only at ~ 25 – 30 km

in the Menderes Massif (based on geophysical data such as receiver functions computed from teleseismic earthquakes from Karabulut *et al.* [2013]; deep seismic reflection data from Cifci *et al.* [2011]; Bouguer gravity data from Altinoğlu *et al.* [2015] and conductivity data from Bayrak *et al.* [2011]).

The current tectonic evolution in this region is mainly controlled by the westward motion of Anatolia [Reilinger *et al.*, 2006] and by N-S extension, both consequences of the same slab roll-back process complicated by several episodes of slab tearing [*e.g.* Faccenna *et al.*, 2006; Jolivet *et al.*, 2013; 2015]. This direction of extension is also well constrained by the orientation of regional-scale anisotropic fabrics, suggesting a large-scale viscous flow in the lower crust and lithospheric mantle since the Miocene [Endrun *et al*., 2011].

II.2.2. The Menderes Massif

The Menderes Massif is located in the back-arc domain of the Hellenic subduction zone in the western part of Turkey (Figs. II.3a and II.3b), and constitutes a part of the Anatolide-Tauride block. After a first episode of nappe stacking and crustal thickening [*e.g.* Collins & Robertson, 1998; Ring *et al.,* 1999; Gessner *et al.,* 2001a], the thickened crust of the Menderes Massif has undergone a NNE-SSW post-orogenic extension stage since the Oligo-Miocene [*e.g.* Seyitoglu & Scott, 1991; Seyitoglu *et al.,* 1992; Bozkurt & Oberhänsli, 2001; Bozkurt *et al.,* 2011]. Considered as a single large metamorphic core complex, this massif has recorded a controversial two-stage exhumation process. According to Ring *et al.* [2003], these two stages are symmetrical, first along the south-dipping Lycian and north-dipping Simav detachments on the southern and northern edges of the massif, and then located in the Central Menderes Massif (CMM) along the Alaşehir and the Büyük Menderes detachments (Fig. II.3b). But Seyitoglu *et al.* [2004] challenged the first stage of exhumation suggesting that this massif was exhumed initially as an asymmetric core complex in the Early Miocene. In any case, this post-orogenic extension has led to the exhumation of three submassifs, from north to south: the Gördes, Ödemiş (corresponding to the CMM) and Çine submassifs. These submassifs are separated by E-W striking half-grabens that are seismically active. The northern part of the Gördes submassif is limited in the north by the Simav graben, the Ödemiş submassif by the Alaşehir graben (also known as Gediz graben) to the north, and by the Büyük Menderes graben to the south (Fig. II.3b, see more details in the *Appendix II.8.* for the studied grabens).

Post-orogenic extension was thus accommodated by three main detachment faults (*i.e.* low-angle normal faults) in the central and northern submassifs, namely:

(i) the Büyük Menderes detachment along the northern margin of the Büyük Menderes graben with top-to-the-S kinematic criteria [Fig. II.3b; *e.g.* Emre & Sözbilir, 1997; Gessner *et al.,* 2001b; Ring *et al.,* 2003];

(ii) the Alaşehir detachment (also named Gediz detachment, Lips *et al.* [2001]) along the southern margin of the Alaşehir graben with top-to-the-N sense of shear [Fig. II.3b; *e.g.* Emre, 1992; Hetzel *et al.,* 1995a; 1995b; Gessner *et al.,* 2001b; Sözbilir, 2001; Seyitoglu *et al.,* 2002; Işık *et al.,* 2003; Bozkurt & Sözbilir, 2004; Hetzel *et al.,* 2013] and

(iii) the Simav detachment, later cut by the high angle Simav normal fault that bounds to the south the Simav graben with top-to-the-NE kinematic indicators [Fig. II.3b; *e.g.* Seyitoglu, 1997; Isik *et al.,* 1997; Isik & Tekeli, 2001; Işık *et al.,* 2004].

However, the exhumation history of the Menderes Core complex and the multi-staged activity of the detachments remain matters of debate. Several authors suggest that the Alaşehir graben formation is controlled by (i) low-angle normal faults that have been active since the inception of the basin, and then by (ii) more recent high-angle faults crosscutting the earlier-ones [*e.g.* Hetzel *et al.,* 1995a; 1995b; Emre & Sozbilir, 1997; Sozbilir, 2001; Oner & Dilek, 2011]. For others, the initiation of the graben involved high-angle normal faults that gradually became low angle with time [*e.g.* Gessner *et al.,* 2001b; Bozkurt, 2001; Seyitoğlu *et al.,* 2002; Purvis & Robertson, 2005; Çiftçi & Bozkurt, 2009a; 2010; Demircioğlu *et al.,* 2010; Seyitoğlu *et al.,* 2014]. According to Seyitoğlu and Işik [2015], this last hypothesis may explain the large range values of ages from the Alaşehir detachment, explaining a continuum of deformation since Early Miocene in the framework of a rolling hinge model [Buck, 1988] for the formation of the grabens and exhumation of the CMM [*e.g.* Gessner *et al.,* 2001b; Seyitoglu *et al.,* 2002; 2014]. Note that syn-extensional Miocene granitoid intrusions are also recorded in the footwall of the Alaşehir and Simav detachments [*e.g.* Hetzel *et al.,* 1995b; Isik *et al.,* 2003; 2004].

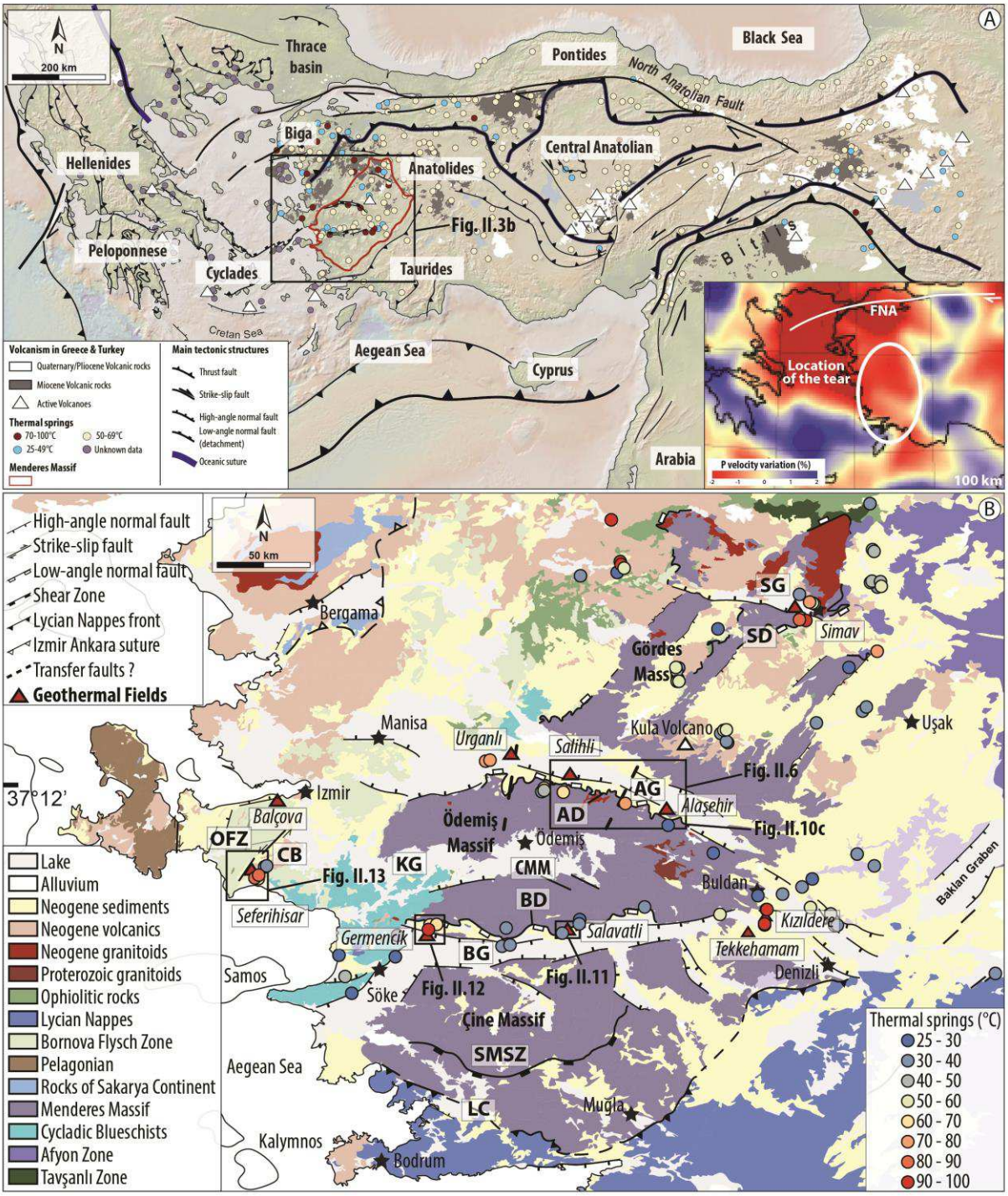

Figure II.3: Tectonic map of eastern Mediterranean region highlighting the main tectono-metamorphic domains and showing location of the study area. Modified from Jolivet et al. [2013]. (a) Simplified tectonic map showing major thermal occurrences based on a compilation of several data sources [Akkuş et al., 2005; Bayram and Simsek 2005, Mendrinos et al., 2010 and Andritsos et al., 2015] and spatial distribution of Upper Terciary-Quaternary volcanics rocks (from the geological map of the MTA). Note that white triangles indicates active volcanoes. Base maps made with GeoMapApp (https://www.geomapapp.org). Tomographic model of Piromallo and Morelli [2003] showing the Vp anomalies at the ~ 100 km depth in the bottom right corner of this Figure. The white circle illustrates the schematized position of the slab tearing. (b) Tectonic and geological map of the Menderes Massif modified from the geological map of the MTA and Bozkurt et al. [2011]. Red triangles represent main geothermal areas of the Menderes Massif, from Faulds et al. [2010] and Kaya [2015]. Thermal spring locations correspond to our study, and to the studies from Akkuş et al. [2005] and Bayram and Simsek [2005]. Also indicated is the position of the Figure II.6, II.10c, II.11, II.12 and II.13. Main structures and grabens are indicated in

abbreviations: AD (Alaşehir detachment); AG (Alaşehir graben); BD (Büyük Menderes detachment); BG (Büyük Menderes graben); CB (Cumaovası basin); CMM (Central Menderes Massif); KG (Küçük Menderes graben); LC (Lycian contact); OFZ (Orhanlı fault zone); SMSZ (Southern Menderes shear zone); SD (Simav detachment) and SG (Simav graben).

The early Miocene evolution of the Menderes Massif is dominated by high-angle E-W striking normal faults that root into [Seyitoglu *et al.,* 2002] or cut the current low-angle normal faults [*e.g.* Koçyigit *et al.,* 1999; Yılmaz *et al.,* 2000], and control basin sedimentation (*i.e.* the initiation of the Alaşehir and Büyük Menderes grabens formation [*e.g.* Seyitoglu, 1997; Seyitoglu *et al.,* 2002]). During Pliocene-Quaternary times, another set of high-angle normal faults is recorded, controlling the youngest grabens such as the Küçük Menderes and Simav grabens [Seyitoglu *et al.,* 2004] and the current geometry of the basin [Bozkurt & Sozbilir, 2004; Kent *et al.,* 2016]. Furthermore, an additional distributed strike-slip tectonics with a normal component is well observed in the Alaşehir graben with high-angle N-S striking faults crosscutting the Neogene sediments [*e.g.* Çiftçi & Bozkurt, 2010; Yilmazer *et al.,* 2010; Oner & Dilek, 2011] and affecting the basement of the Menderes Massif (see black dotted line in the Alaşehir graben in Figure II.3b). Similar strike-slip faults are observed in the Büyük Menderes graben, which can be interpreted as transfer faults [*e.g.* Çifçi *et al.,* 2011].

II.3. Geothermal setting in the Menderes Massif

II.3.1. Thermal anomalies at different scales

At first glance, there is a strong correlation between the distribution of hot springs and geothermal fields with the location of detachments (Fig. II.3b). According to recent studies [*e.g.* Roche *et al.,* 2015; 2016; 2018; Kaya, 2015; Gessner *et al.,* 2017], these large-scale structures may represent the primary control on geothermal fields in this massif. In that instance, Gessner *et al.* [2017] showed that most of hotter thermal springs are located in areas of structural complexity. Similar correlations between high heat flow values and complex graben structures are emphasized by many studies [Tezcan 1995; Pfister *et al.,* 1998; Erkan, 2014; 2015]. For instance, Erkan [2014] estimated heat flow values of 85 – 90 mW m^{-2}, locally higher than 100 mW m^{-2} in the northeastern part of the Alaşehir graben. These data are in accordance with locations of several hot springs of interest, but also with shallow Curie-point depth (CPD) published in the Menderes Massif area [Aydin *et al.,* 2005; Dolmaz *et al.,* 2005; Bilim *et al.,* 2016]. According to Bilim *et al.* [2016], the average of CPD in the whole Menderes area (assumed to represent the depth of the 580 °C isotherm [Schlinger, 1985; Ross *et al.*, 2006]) is *ca.* 9.5 km with a shallowest point at 6.21 km around the Kula basaltic area. A thermal anomaly thus encompasses the whole Menderes Massif. The same authors also suggest that locations of hot springs belonging to the

Büyük Menderes Graben area coincide with the lowest values of the magnetic intensity, which are aligned along the boundary fault of the graben. Furthermore, using the magnetotelluric method through the northern part of the Menderes Massif, Ulugergerli *et al.* [2007] showed a large partial melting zone located at ~ 12 km depth and deep intrusions (*i.e.* ~ 15 km depth) located below the Simav graben and the Kula volcano, therefore suggesting abnormal high temperature values.

To sum up, all these studies confirm that thermal anomalies in the Menderes Massif are observed with different wavelengths (*i.e.* crustal-scale to geothermal field-scale), thus different depths. The short wavelength anomalies result from shallow depth processes and those with long wavelength (crustal-scale) from deep processes, and thus large-scale dynamics [*e.g.* Roche *et al.,* 2015; 2016; 2018; Gessner *et al.,* 2017]. However, the circulation pathways of such hot crustal fluids are not yet properly understood.

II.3.2. Synthesis of fluids and isotopes

II.3.2.1. Studies on oxygen and hydrogen isotopes of the main geothermal fluids

Many studies on the isotopic composition of water samples in the CMM area have been performed (Fig. II.4) [Filiz *et al.,* 2000; Özgür, 2002; Tarcan & Gemici, 2003; Özen *et al.,* 2012; Baba *et al.,* 2014]. To the first order, they show that most of the data from the Alaşehir and the Büyük Menderes grabens are close to the global meteoric water line (GMWL) thus indicating a meteoric origin for most of the geothermal fluids (Figs. II.4b and II.4c). Indeed, the distribution of isotopic compositions of the thermal waters in Salihli, Aydin-Germencik, Salavatlı and Denizli-Kızıldere geothermal fields shows a meteoric origin. However, some variations in isotopic distributions can be noted. There is a clear $\delta^{18}O$ shift from the MMWL (Mediterranean Meteoric Water Line) and cold-water values (empty symbols in Figure II.4b) that indicate strong water-rock interaction for all geothermal fields (Figs. II.4b and II.4c). For example, the isotopic distribution of hot waters in Kurşunlu and in greenhouses well is located below the GMWL, which suggests a probable mixing of deep and shallow thermal waters [Özen *et al.,* 2012]. Bülbül *et al.* [2011] reported a similar observation from the Alaşehir geothermal field, suggesting that thermal water reservoirs are fed by ground waters of dominant meteoric origin. They estimated cold-water contributions to thermal waters ranging from 75 to 95%. Moreover, the Seferihisar geothermal field, in the Cumaovası basin, shows additional variations in isotopic compositions (Fig. II.4d): isotopic values approach the isotopic value of Agean sea water, implying a mixing with seawater related to the proximity of the Mediterranean Sea [Tarcan & Gemici, 2003]. Similar signatures are observed in the Söke geothermal field [Simsek, 2003], with slight deviations from the MMWL line of isotopic distribution, implying an evaporation effect on cold-waters (Fig. II.4d). The isotopic composition of

thermal waters indicates that they are of meteoric origin and then mixed with seawater in the western part of Söke, particularly near the coast.

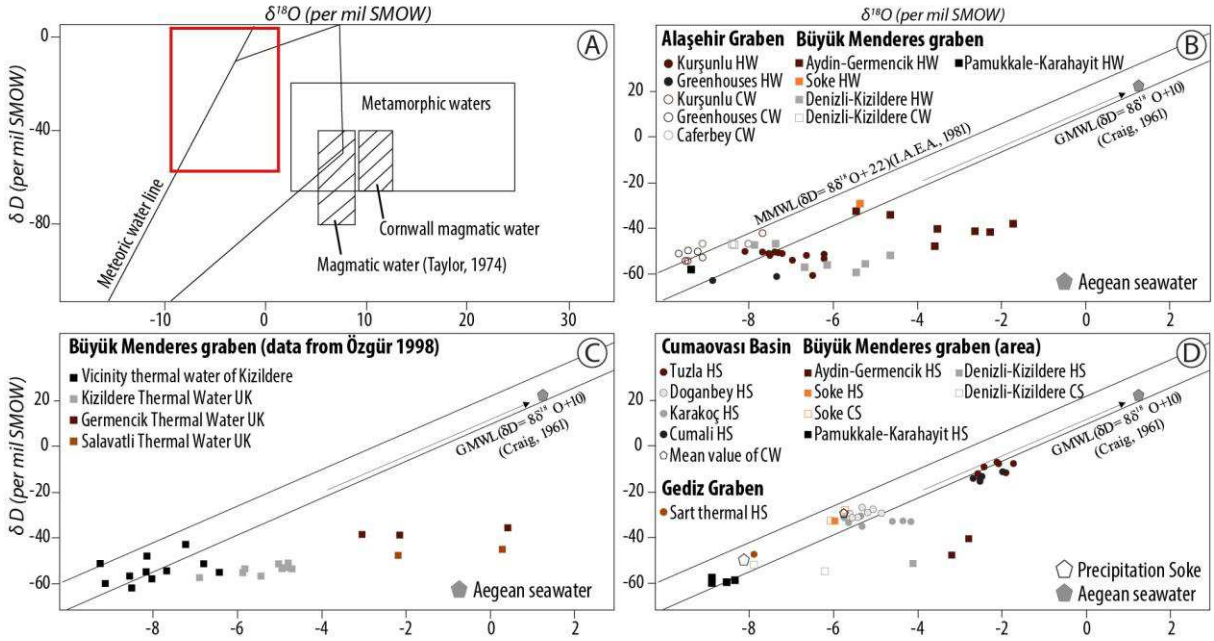

Figure II.4: δD vs δ18O diagrams. (a) Plot of δD vs δ18O diagram for different water types. The field of magmatic water and formation waters are taken from Taylor [1974]. The field for magmatic waters from the granites of Cornwall is from Sheppard [1977]. The meteoric water line is from Epstein et al. [1965]. The metamorphic water field combines the values of Taylor [1974] and Sheppard [1981]. Red rectangle indicates the field of all isotopic data from the Menderes Massif. (b) Stable isotope compositions of the geothermal reservoir fluids in the studied areas showing hot and cold waters wells. Abbreviations: HW (Hot water well), CW (Cold water well). (c) Stable isotopes of different geothermal fields in the Büyük Menderes Graben. Abbreviation: UK (unknow sampling locations). (d) Stable isotopes of springs in three main basins. Abbreviations: HS (Hot spring), CS (Cold spring). Compilation of data from Filiz et al. [2000], Özgür [2002], Tarcan and Gemici [2003], Simsek [2003] and Özen et al. [2012].

II.3.2.2. Helium isotopic signature

In a tectonically active continental setting, the presence or the absence of mantle helium (^{3}He) in hydrothermal fluids can constrain the relationships between tectonics, magmatism and fluid circulation in faulted settings [O'Nions & Oxburgh, 1988; Marty *et al.,* 1992; Kennedy *et al.,* 1997; Kulongoski *et al.,* 2005; Pik & Marty, 2009]. It has been established that the ^{3}He/^{4}He ratio can be used as tracer of the competing influence of crustal vs. mantle volatiles in various tectonic settings [Mutlu *et al.,* 2008]. Based on the analyses of water and gas samples, and/or fluid inclusion trapped in calcite, many studies have discussed the isotopic composition of He in the eastern Mediterranean region [Güleç, 1988; Güleç *et al.,* 2002; Shimizu *et al.,* 2005; Güleç & Hilton, 2006; Mutlu *et al.,* 2008; Pik & Marty, 2009; Karakus, 2015]. Below, we present a new compilation of recent isotopic studies using the classification of Pik and Marty [2009] (Fig. II.5).

In the Aegean domain, the Corinth rift shows a crustal signature while the Hellenic volcanic arc is characterized by high values of $^{3}He/^{4}He$ ratio, Ra (> 15% of mantle-He) suggesting a mantle origin (Fig. II.5a). In addition, estimated $^{3}He/^{4}He$ ratios of samples normalized to the atmospheric $^{3}He/^{4}He$ ratio range from 0.10 to 1.44 in the western part of Anatolia (Figs. II.5a and II.5b). These values are significantly higher than the crustal production value of 0.05 [Mutlu *et al.,* 2008]. Karakuş [2015] added new data on the $^{3}He/^{4}He$ ratios for the Simav geothermal field (values range from 1.36 to 1.57). The highest values of helium ratio correspond to the Quaternary alkaline activity of Kula volcano and to the Pliocene Denizli volcanics (2.52) along the Alaşehir and the eastern segment of the Büyük Menderes grabens (Fig. II.5b). These results reveal a mixed origin for helium between mantle and continental crust components.

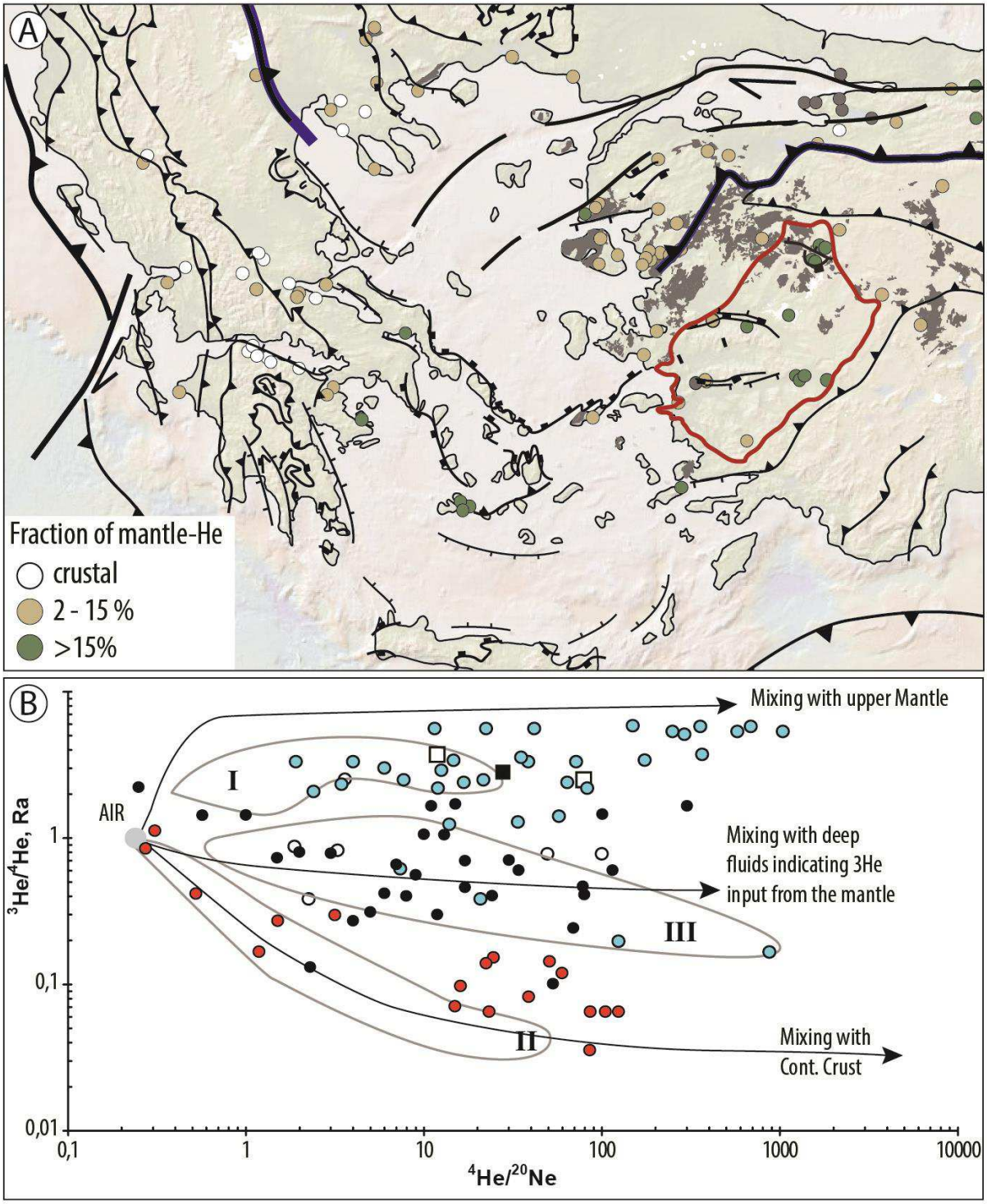

Figure II.5: Isotopic composition of Helium. (a) Fraction of mantle-He in hydrothermal fluids from the Aegean Anatolian domains computed from helium isotopic data, assuming mixing between a crustal component (0.04 Ra) and a mantle component (8 Ra), modified from Pik and Marty [2009]. Helium isotopic data are from Pik and Marty [2009] and Karakuş [2015]. (b) R/Ra diagram for the eastern Mediterranean region from Güleç [1988], Güleç et al. [2002], Güleç and Hilton [2006], Mutlu et al. [2008], Pik and Marty [2009] and Karakuş [2015]. Black dots showing data of the west Anatolian domain, red dots data of the gulf of Corinth, Blue dots data of the magmatic arc and white dots data of the back arc region in Greece. In addition, white and black squares indicate respectively the Denizli and Kula areas which are located in the Menderes Massif. The fields of the three groups of hydrothermal fluids [Pik & Marty 2009], are also presented: I = arc magmatic fluids (>15% mantle-He), II = crustal signature (<1% mantle-He), III = other intermediate fluids (2–15% mantle-He).

II.4. Analysis of the tectonic and structural settings of geothermal fields in the Menderes Massif at local and regional scale

In this chapter, we summarize the structural framework of several geothermal fields, in order to identify the main conduits for geothermal fluid flow and related reservoirs. Our field survey consisted of (i) field mapping in order to complement the existing geological and geothermal maps and (ii) structural data acquisition and (iii) general cross-sections. We have first focus on the Alaşehir graben (Fig. II.3b), where numerous geothermal wells have been drilled by MTA (General Directorate of Mineral Research and Exploration of Turkey) or by private companies since the 1980s, and where two most important geothermal fields are recognized (Salihli and Alaşehir, Fig. II.6a). We will then focus on the Germencik and Salavatlı geothermal fields located along the northern margin of the Büyük Menderes half-graben (Fig. II.3b). Finally, the structural framework of the Seferihisar geothermal field is also provided (Fig. II.3b). A brief description of all these geothermal systems is presented in the *Appendix II.8*. They are generally characterized by medium- to high-enthalpy, with reservoir temperature values ranging from 120 to 287 °C [*e.g.* Karamanderesi, 2013; Baba *et al.,* 2015].

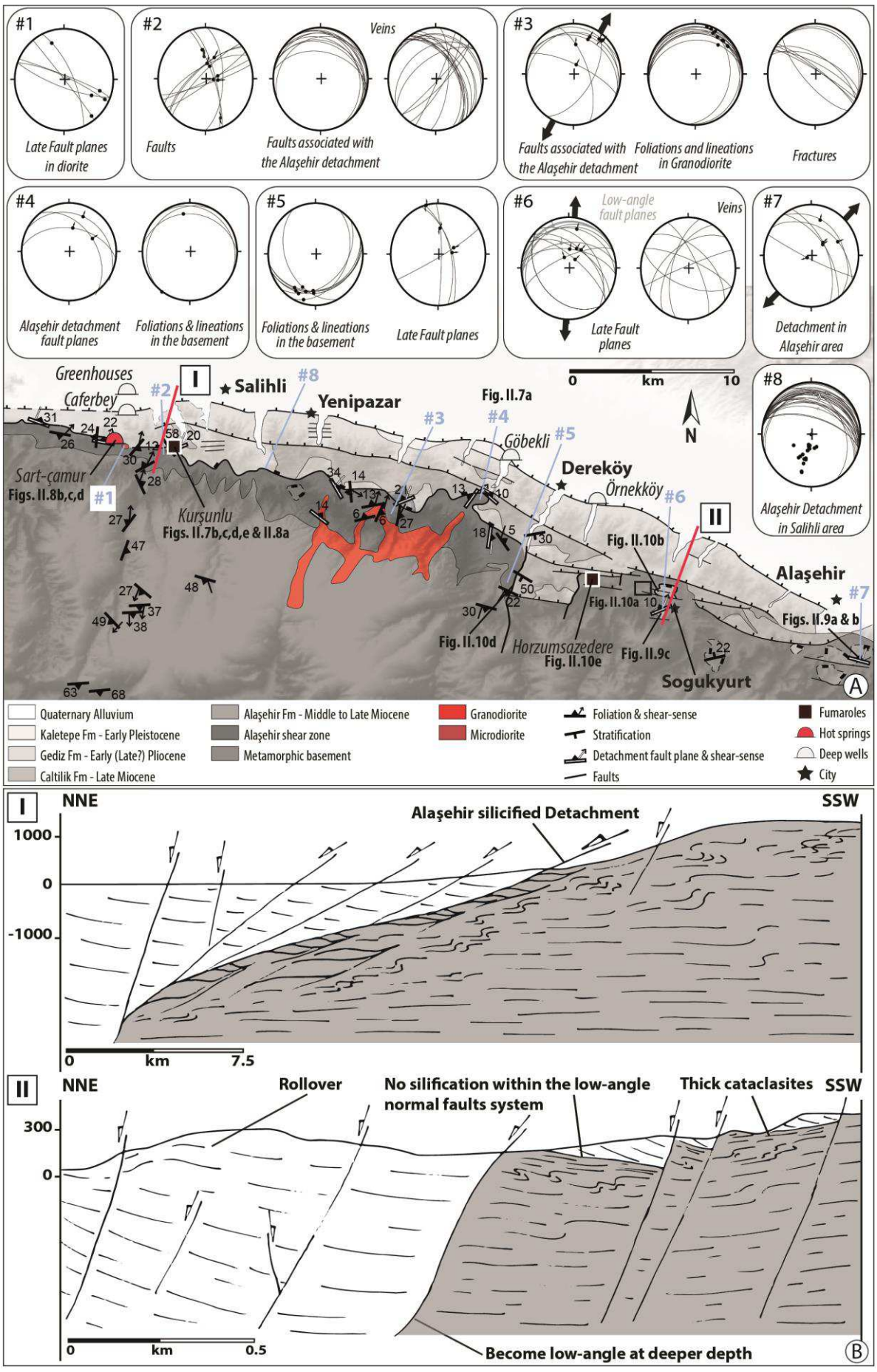
#1
Late Fault planes in diorite
#2
Faults
Veins
Faults associated with the Alaşehir detachment
#3
Faults associated with the Alaşehir detachment
Foliations and lineations in Granodiorite
Fractures
#4
Alaşehir detachment fault planes
Foliations & lineations in the basement
#5
Foliations & lineations in the basement
Late Fault planes
#6
Low-angle fault planes
Veins
Late Fault planes
#7
Detachment in Alaşehir area
#8
Alaşehir Detachment in Salihli area
Greenhouses
Caferbey
Salihli
Yenipazar
Fig. II.7a
Göbekli
Dereköy
Örnekköy
Sart-çamur
Figs. II.8b,c,d
Kurşunlu
Figs. II.7b,c,d,e & II.8a
Fig. II.10b
Alaşehir
Figs. II.9a & b
Fig. II.10a
Fig. II.10d
Horzumsazedere
Fig. II.10e
Fig. II.9c
Sogukyurt
0 km 10
N
Quaternary Alluvium
Kaletepe Fm - Early Pleistocene
Gediz Fm - Early (Late?) Pliocene
Caltilik Fm - Late Miocene
Alaşehir Fm - Middle to Late Miocene
Alaşehir shear zone
Metamorphic basement
Granodiorite
Microdiorite
Foliation & shear-sense
Stratification
Detachment fault plane & shear-sense
Faults
Fumaroles
Hot springs
Deep wells
City
NNE
SSW
Alaşehir silicified Detachment
1000
0
-1000
0 km 7.5
Rollover
No silification within the low-angle normal faults system
Thick cataclasites
300
0
0 km 0.5
Become low-angle at deeper depth

Figure II.6: Geological and tectonic map of the Alaşehir graben modified from Asti [2016]. (a) Map showing main structures: the Alaşehir low-angle normal fault, E-W striking high-angle normal faults and N-S striking high strike-slip faults which are described by Çiftçi and Bozkurt [2010]. Thermal springs and fumarole activity are also located in the map. Brittle structures, foliation, veins and fractures are presented in Schmidt's lower hemisphere equal-area projection. Detailed results of the fault slip data inversion are also presented using the Win-Tensor software [Delvaux & Sperner, 2003]. Also indicated is the position of the Figures II.7, II.8, II.9 and II.10. (b) Cross-sections through the northern part of the Ödemiş Massif. Sections are all roughly parallel to the tectonic transport. To draw the shape of stratification, we used the bedding data of the Neogene sediments from Asti [2016]. Colours show different rock types. Cross-sections are indicated by red solid lines in Figure II.6a.

II.4.1. Structural features of the Salihli geothermal field

At regional-scale, the Alaşehir detachment is one of the best-preserved crustal structure in the study area (Fig. II.7a). Both metamorphic rocks and Miocene intrusions in the footwall of the detachment present a pervasive network of kilometric to millimetric structures developed from the ductile-brittle transition to the brittle field during extension and exhumation (Fig. II.6b) [*e.g.* Emre, 1992; Hetzel *et al.,* 1995a; 1995b; Isik *et al.,* 2003]. Close to the main contact between the Menderes basement rocks and Neogene sediments, the foliation of basement rocks strikes E-W with low to moderate dip values toward the north and carries a N-S trending stretching lineation (Fig. II.6). Most ductile kinematic indicators are top-to-the-NNE. All lithologies are deformed by asymmetric structures and folds at various scales consistent with top-to-the-NNE shear sense such as asymmetric boudinaged quartz veins within tight overturned folds indicating a top-to-the-NE sense of shear (Fig. II.7b). On the other hand, ductile-brittle fault system corresponds to listric and gently dipping centimetric to decametric faults within schist and marble layers that may reactivate and (or) cross-cut low-angle ductile shear zones (Fig. II.7c). This brittle stage is also associated with slickenlines and kinematic indicators indicating top-to-the-NNE motion (Fig. II.6a, #2). Finally, the brittle detachment fault plane is well observed in the landscape (Fig. II.7a), controlling the present-day topography of the CMM at regional scale and strikes E-W with a moderate dip toward the north (Fig. II.6a, #8). It is associated with a thick (approximately 50 cm to 3 m) zone of cataclasites or a thick quartz-breccia vein (Fig. II.7d), which locally hosts Sb-Hg(-Au) ore deposits [Larson & Erler, 1993]. Fault plane and associated striae (*e.g.* Fig. II.6a, #3 and #4) are consistent with a NNE-SSW extension. In addition, vein networks mostly filled by calcite or quartz in the footwall of the detachment (Fig. II.7e) present an approximately NW-SE (*i.e.* parallel to the detachment) and NE-SW preferred orientations (*i.e.* perpendicular to the detachment) (Fig. II.6a, #2). This shows evidence of a significant older fluid circulation in the fault plane during the exhumation of the deeper parts of the Menderes Massif.

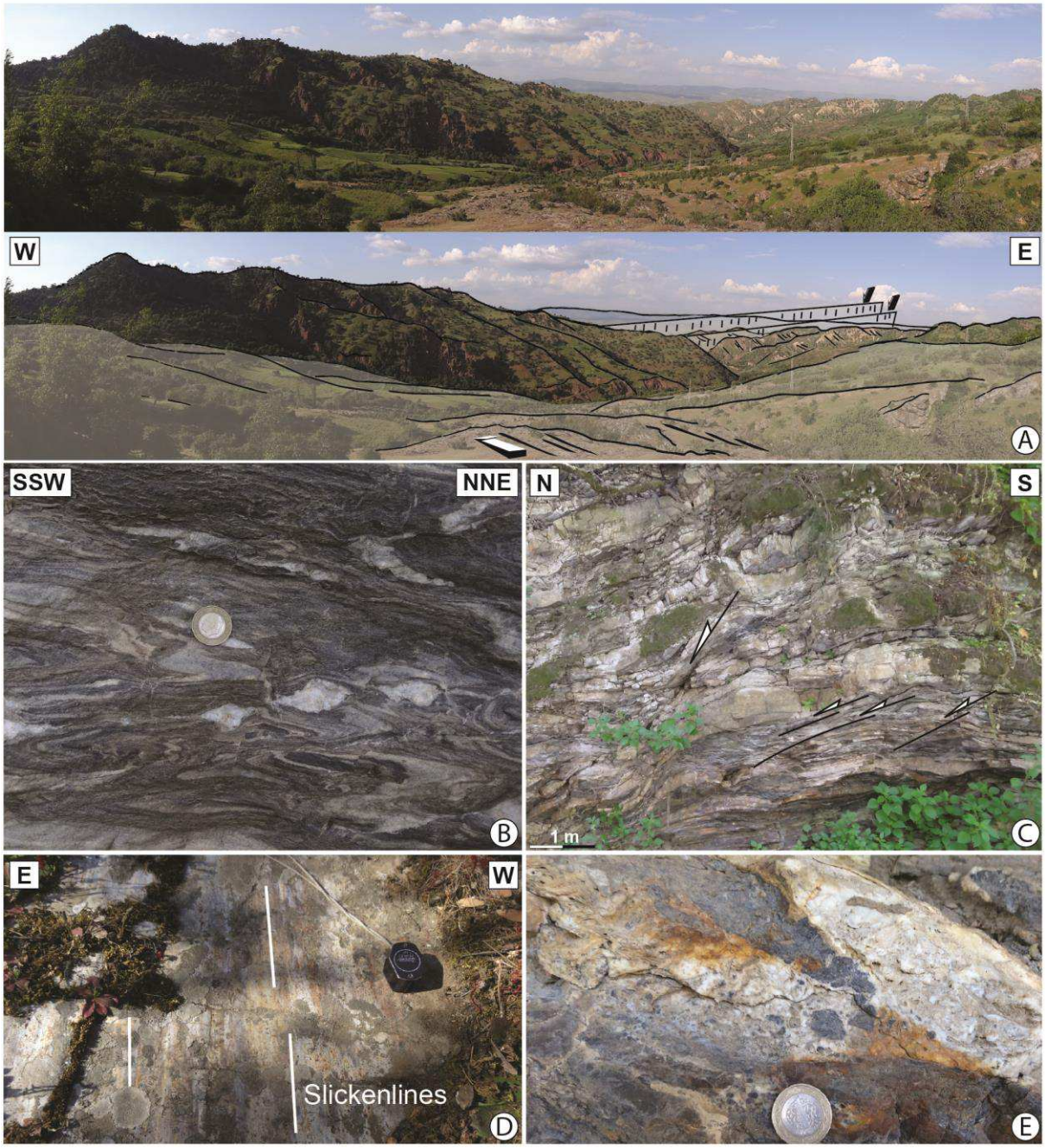

Figure II.7: Kinematic of deformation associated with the Alaşehir detachment. (a) Large-scale view of the Alaşehir detachment surface close to Salihli area. (b) Asymmetric boudins compatible with top-to-the-NNE ductile deformation in marbles layers. (c) Representative outcrop recognized as demonstrative of a brittle stage subsequently developed after the ductile one where shear zones are locally reactivated in the brittle field. (d) Fault plane of the Alaşehir detachment with slickenlines. (e) Calcite and quartz vein parallel to the bedding, located few meters below the main fault plane. The position of the pictures is indicated in Figure II.6a.

In the entire studied area, faults that are particularly abundant play a major role in the formation and development of longitudinal and transverse valleys (*e.g.* Kurşunlu valley, Alaşehir graben). Three types of plurimetric to kilometric faults, particularly frequent in this area, are observed in the field (Fig. II.6a). The first one is characterized by NNE-dipping normal faults and the second one is defined by sub-vertical N-S striking strike-slip faults (Figs. II.6a, #2; II.8a and II.8b). In the second case,

slickenlines are gently plunging consistently 15 to 30°N (Figs. II.8a and II.8c) and kinematic indicators indicate a main dextral movement with a slight normal component. Locally, these faults are accompanied with a cluster of calcite veins as dilational jog structures (Fig. II.8d). The third type of faults consists in a set of conjugate faults strikes NE-SW and dips with an approximately 60° mean dip angle, is well developed in quartzite levels in the Kurşunlu valley (Fig. II.6a, #2). The different fault sets, including the detachment and the associated high-angle E-W conjugate normal faults and the N-S strike-slip faults to NE-SW faults, are compatible with N-S extension, where strike-slip faults act as transfer zones between extensional blocks. All these faults affect the basement and the Neogene sediments, but the chronologic relationships are not clear in the field.

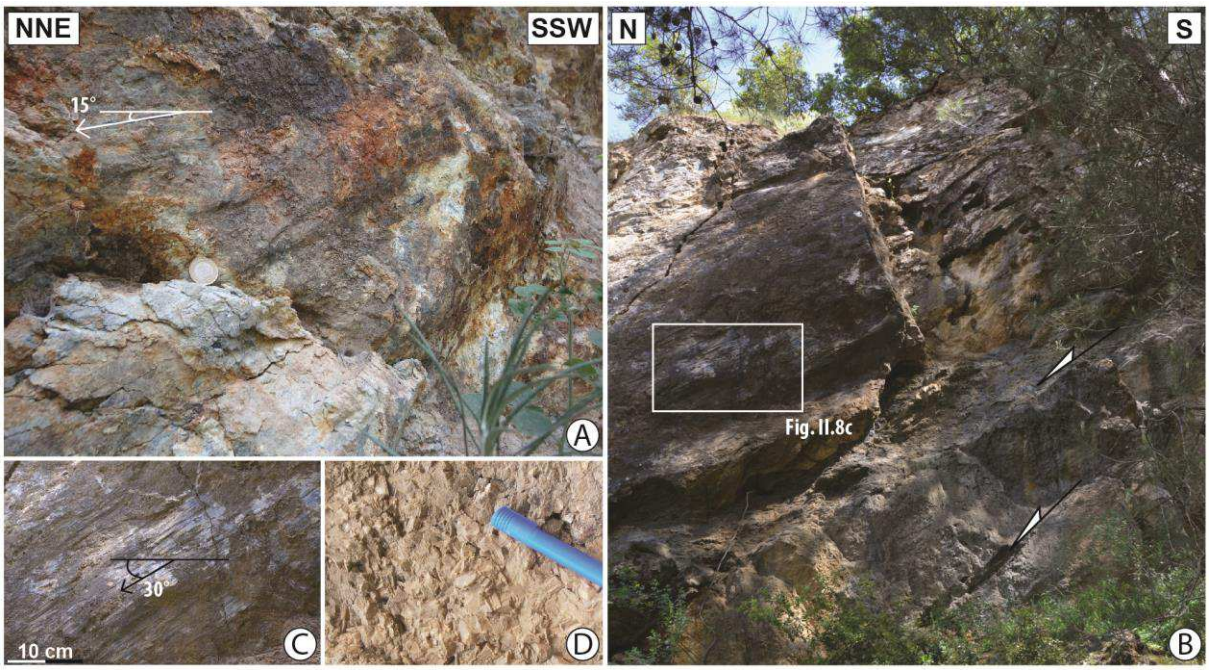

Figure II.8: Brittle deformation in the Salihli area. (a) N-S strike-slip fault in the Kurşunlu valley. (b) E-W striking normal faults are cross-cut by N-S strike-slip fault. (c) Close-up view of a slip-plane in the basement of the Menderes indicating nearly horizontal with a normal component slickenlines. (d) Calcite indicating fluid circulation close to the strike-slip fault. The position of the pictures is indicated in Fig. II.6a.

II.4.2. Structural features of the Alaşehir geothermal field

The Alaşehir geothermal field is located between Alaşehir and Salihli in the eastern part of Alaşehir graben. It is one of the most important geothermal areas characterized by the highest reservoir temperature (287 °C) ever reached in Turkey (in a deep well, 2750 m, from Baba *et al.* [2015], Table II.1). As for the Salihli geothermal field, the recent tectonic activity is assumed to control the location of the thermal springs and related geothermal reservoirs [Bülbül *et al.,* 2011]. In this area, the detachment fault plane is attested by the development of a thick zone (~ 1 m) of cataclasites (Fig. II.9a).

It consists of yellow and red foliated cataclasites directly overlain by unaltered Neogene sediments (Fig. II.9b). Similar to the kinematics recorded in the area of Salihli, striae are compatible with a NE-SW extension (Figs. II.9a and II.6, #7). Additional low-angle normal faults in the hanging-wall of the detachment are observed between 1 metre-thick cataclasites and sediments (Figs. II.9c, II.9d and II.9e). Locally pseudotachylytes are observed (Fig. II.9f) and medium-angle normal faults in sediments merge with the main fault plane (Fig. II.9g). According to Hetzel *et al.* [2013], this brittle deformation stage observed in the Alaşehir detachment system was active from ~ 9 Ma to 4 – 3 Ma. This may be consistent with rapid Pliocene cooling inferred from published thermochronological data [Gessner *et al.,* 2001b; Ring *et al.,* 2003]. While the Alaşehir detachment is well defined in the landscape at Salihli, it is however often crosscut by a set of E-W high-angle north-dipping normal faults in the Alaşehir area (Figs. II.6b and II.10a). Brittle structures, shallow- and steeply-dipping faults present a marked consistency of the extension direction (Fig. II.6a, #6). Locally, fluid circulation occurs along fault planes (Fig. II.10b), suggesting that these faults may also control meteoric fluid circulations. The absence of any hot springs close to the E-W striking faults suggest that these faults are recharge zones for reservoirs at depth.

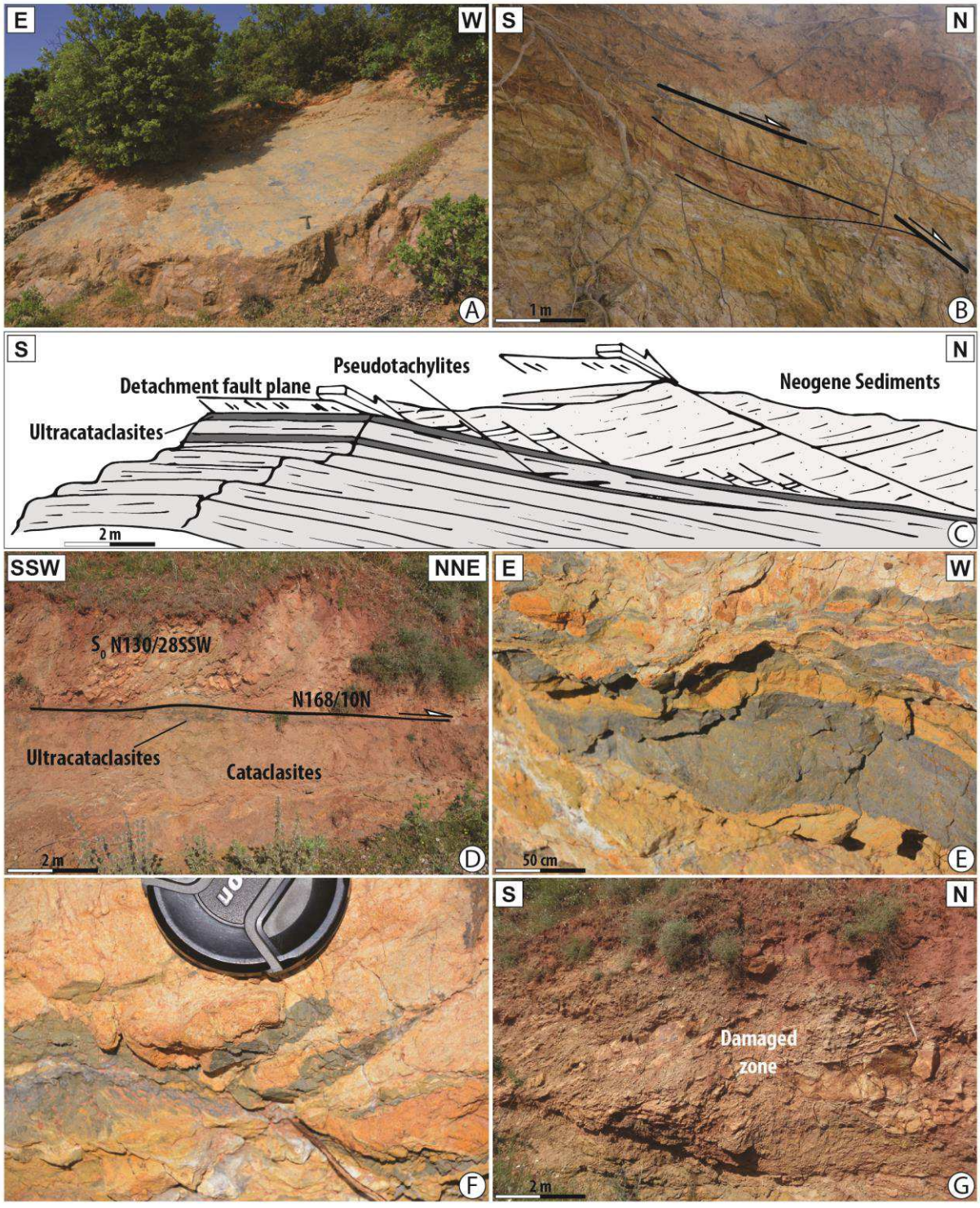

Figure II.9: Brittle deformation associated with the Alaşehir detachment in the Alaşehir area. (a) Detachment surface marked by a thick zone of cataclasites. (b) Foliated cataclasites below the main fault plane. Note that the shearing is toward the north. (c) Sketch depicting the relationships between the detachment fault plane and Neogene sediments in the NNW of Kara Kirse. (d) Low-angle contact between metamorphic rocks (augen gneiss unit) and Neogene sediments. (e) and (f) Close-up view of ultracataclasites and centimetric pseudotachylytes, respectively. (g) Metric damaged zone in sediments. The position of the pictures is indicated in Fig. II.6a.

Furthermore, another set of faults is observed at some places. At landscape-scale, in the south-east of Alaşehir, we identified triangular facets within synrift sediments due to NW-SE trending high-

angle normal fault (Fig. II.10c). The latter are horizontally offset from 2 km toward the south in the Narlıdere area, defining a NE-SW transfer fault (Figs. II.10c and II.3b for the location). Similar features are also observed in the Dereköy traverse valley, close to the Horzum Turtleback structure described by Seyitoglu *et al.* [2014]. There, we identified a N-S striking high-angle fault (Fig. II.10d). Fault kinematics indicates a first sinistral movement followed by normal movement (Figs. II.6a, #5 and II.10d). The synrift sediments are offset southward and face the Paleozoic basement of the detachment footwall across the valley, indicating the presence of left-lateral strike-slip fault in the vicinity of the Horzumsazdere geothermal system (black line in Fig. II.6a). Close to the detachment and to these N-S strike-slip faults, a weak fumarole activity associated with a probable acidic alteration (with the typical H_2S smell) affects Neogene sediment deposits (Fig. II.10e). Down in the valley, several thermal springs (medium temperatures ranging around 25 and 30 °C) reach the surface in Neogene sediments where they form travertines.

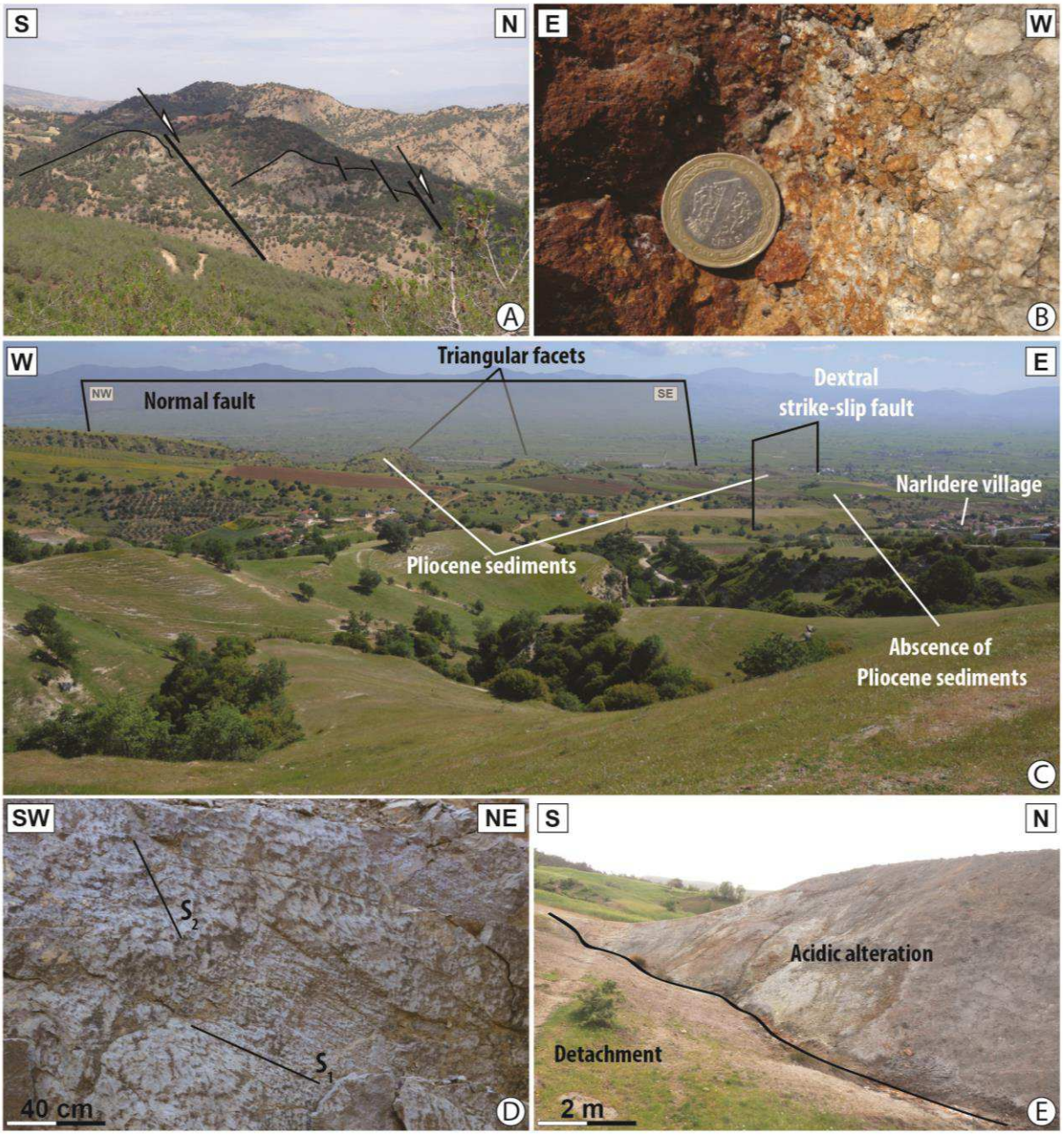

Figure II.10: Brittle deformation in the Alaşehir area. (a) Large-scale E-W high-angle normal faults. Outcrop shows hanging wall displacements toward the north. (b) Close-up view of E-W striking fault showing centimetric and angular blocs (i.e. cataclase). Note also the alteration of the basement rocks implying a probable meteoric fluid circulation during fault activity. (d) Land-scape view of triangular facets in the eastern part of Alaşehir. Note the probable position of strike-slip fault. This fault is also mapped by Oner and Dilek [2013]. (d) Fault plane and associated striae (two generations) of N-S striking strike-slip fault. Note that stereographic projection of striated fault planes corresponds to the number #5 in Fig. II.6a. (e) Picture showing an acidic alteration related to fumarole activity. See Fig. II.6a for the location of pictures.

II.4.3. Structural features of the Salavatlı and Germencik geothermal fields

South of the CMM, the Salavatlı and Germencik geothermal fields (Table II.1 for more information) are respectively located on the northern flank of the Büyük Menderes graben between

Sultanhisar and Köşk (Figs. II.3b and II.11), and at 20 km west of Aydin (Figs. II.3b and II.12). Similar to the previous geothermal systems, both Salavatlı and Germencik geothermal systems are located close to the Büyük Menderes detachment (Fig. II.3b). Even though the age of top-to-the-north ductile deformation is still controversial [*e.g.* Bozkurt, 2001; Gessner *et al.,* 2001a; Seyitoglu & Işik, 2015], all studies indicate a second top-to-the-south ductile-brittle shearing event [*e.g.* Hetzel *et al.,* 1995a; 1995b; Gessner *et al.,* 2001b; Bozkurt & Sözbilir, 2004].

In details, the geological sequence of the Salavatlı geothermal field is composed of Neogene sediments deposited over schist-marble sequences and augen gneiss unit (Fig. II.11a). Even though the major structural feature does not clearly outcrop in this area due to strong neo-tectonic overprint, the Büyük Menderes detachment was identified in two different drill holes [Karamanderesi & Helvaci, 2003]. According to this study, the marble sequences in the Menderes massif at ~ 800 m depth host the geothermal reservoirs. Our new observations suggest that the general structure and the topography are mainly induced by a set of major normal- to strike-slip faults. These faults control the first-order distribution of lithologies of the two main units (augen gneiss and schist-marble sequences, Fig. II.11a). The first ones are NW-SE trending faults with opposite dips (Figs. II.11b and II.11c), showing kinematic indicators of a normal movement. Here, kinematic indicators are compatible with a top-to-SW motion. The second ones are the most important and they strike N-S (Fig. II.11c). These high-angle faults are characterized by a thick fault gouge and crosscut all earlier structures, such as NW-SE trending faults, and the detachment (see the profile of Karamanderesi and Helvaci [2003]). Locally, slickenlines are well preserved and indicate a sinistral movement. Close to these main structures, hot springs are often observed (Fig. II.11a), suggesting a first-order control on the emergence of thermal fluids. In addition, the presence of N-S to NE-SW trending travertine and travertine-sulphur deposits in higher altitudes [Karamanderesi & Helvaci, 2003] confirm the key role of such structures.

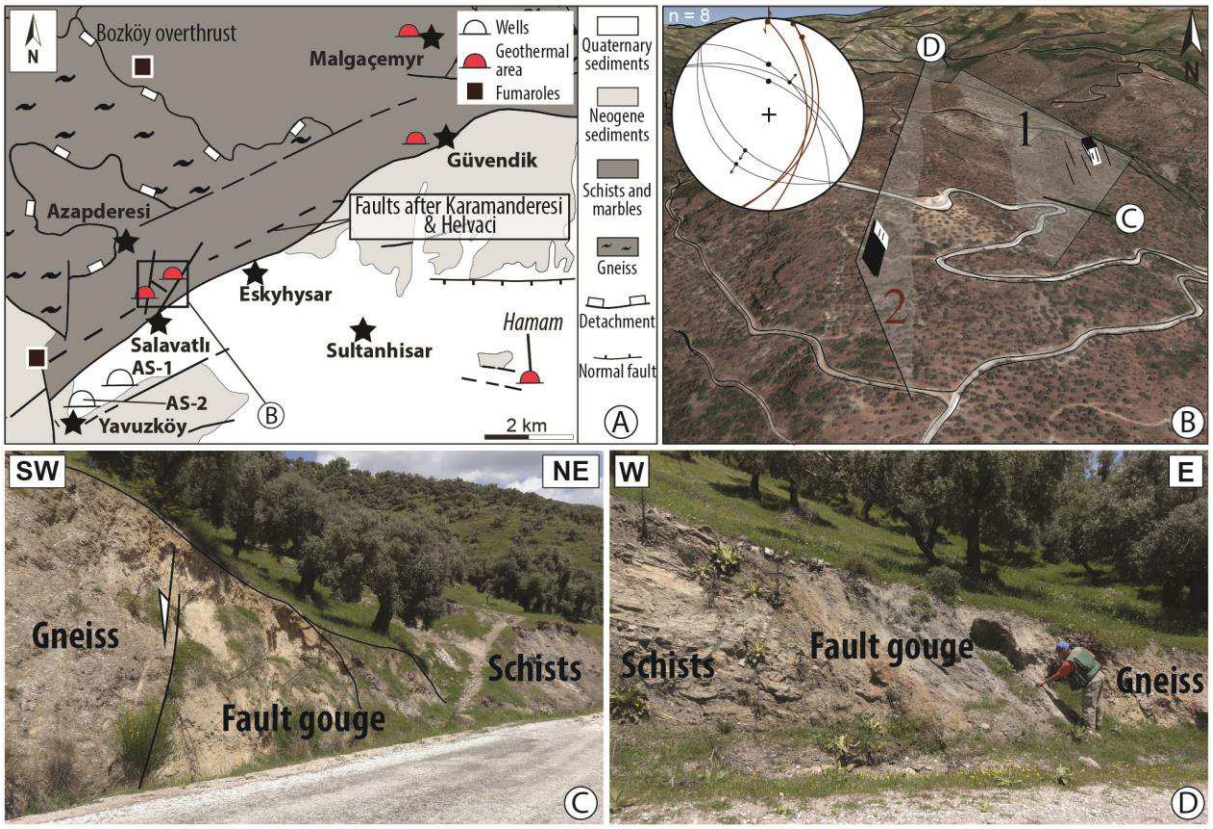

Figure II.11: Brittle deformation in the Salavatlı area. (a) Simplified geological map of Salavatlı geothermal field modified from [Karamanderesi & Helvaci, 2003]. (b) Google earth view of the area. Main structures and stereographic projections of faults systems are indicated. Location is indicated in Figure II.11a. (c) NW-SE trending normal fault between gneiss and schists. (d) N-S trending faulted contact between schists/marbles sequences and gneiss. Note the metric fault breccia between these both units.

The Germencik geothermal field is characterized by numerous fumaroles, hot springs, travertines and widespread hydrothermal alterations (*e.g.* Çamurlu and Bozköy hot springs; Fig. II.12a). The Menderes basement rocks are mainly composed of Paleozoic metamorphic rocks such as the augen gneiss and schist-marble sequences, overlain by Neogene sediments. North of Çamurlu hot spring (Fig. II.12a), the main foliation of metamorphic units strikes E-W and the Neogene sediments dip slightly toward the north (Fig. II.12a). Locally, travertines are located close to this contact (Fig. II.12a), showing that it acts as a major drain for fluid circulation. In addition, in the vicinity of Bozköy, the main foliation of metamorphic units strikes NW-SE with a low dip values (~ 5 – 10°) (Fig. II.12b), whereas the Neogene sediments dips to the south (Fig. II.12c). Such an unexpected change of dip direction may suggest a fault drag area and the possible presence of a N-S high-angle strike-slip transfer fault (Fig. II.12a). Here again, the occurrence of geothermal vents suggests that this type of faults favors fluid circulation (Fig. II.12d). More recent tectonic features are also well expressed and consist in the development of E-W striking high-angle normal faults (Figs. II.12a and II.12f). Some of them are characterized by dip values (reaching ~ 60°; Fig. II.12e). When such faults root in the Büyük Menderes detachment at depth (Fig. II.12e), others dip steeper (~ 80°) and crosscut it. This latter set of faults has

allowed for instance the exhumation of the Kızılcagedik Horst. This area is also characterized by numerous deep wells (see location of Ömerbeyli in Figure II.12a), and the highest temperatures were reached in the Büyük Menderes graben (~ 230 °C at a depth of 975 m and 1196 m [Filiz *et al.*, 2000]). Here, the E-W trending high-angle faults generate a wide fractured zone.

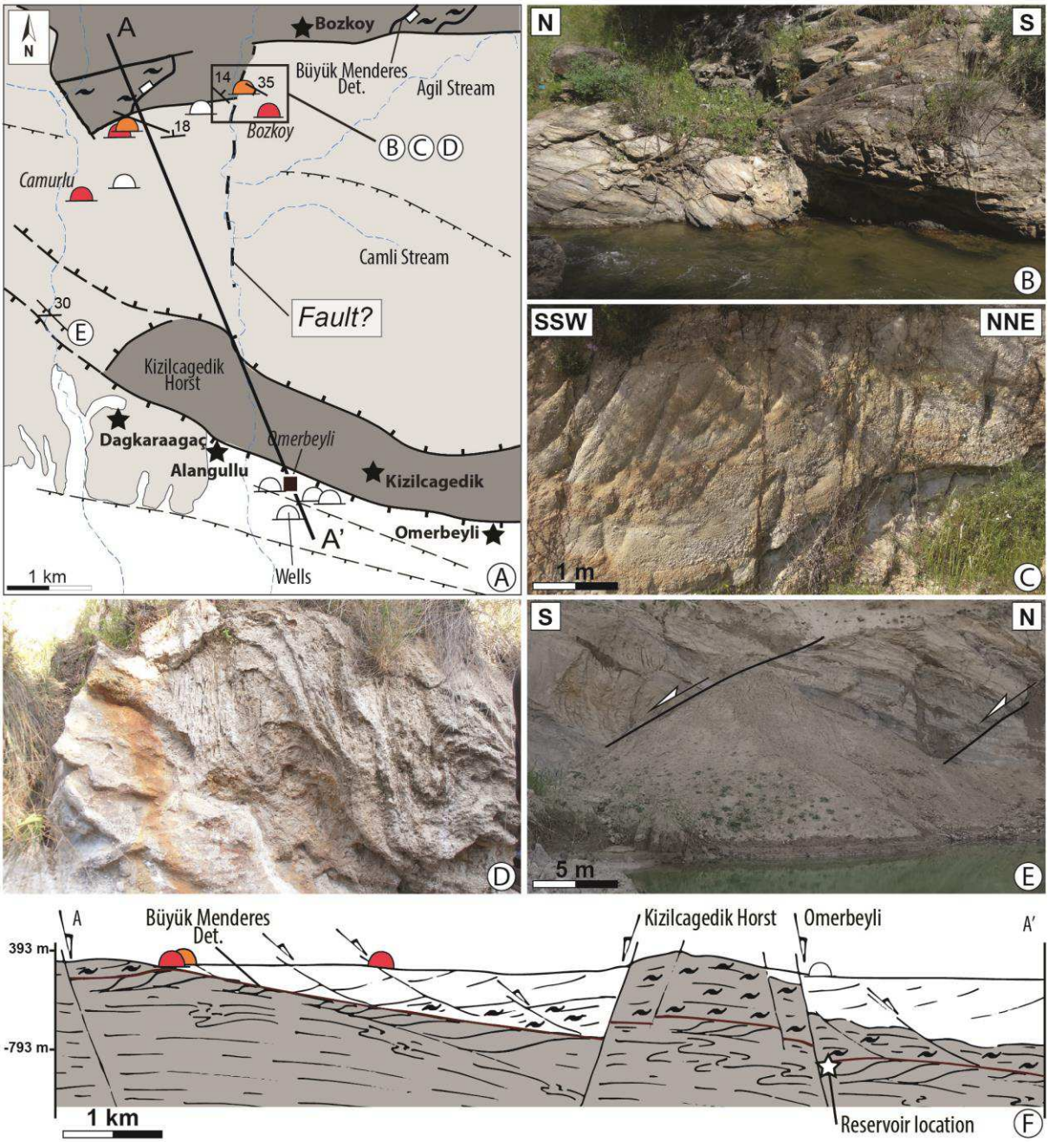

Figure II.12: Structures and geothermal activities in the Germencik geothermal field. (a) Simplified geological map of Germencik area modified from Karamanderesi [2013], showing thermal springs and fumaroles locations. (b) Shallow dipping E-W trending foliation in the basement of the Menderes units. (c) Dip inversion of the bedding in Neogene sediments close to the basement. (d) Travertine indicating fluid circulation. (e) Sallow dipping E-W striking fault in Neogene sediments of the Büyük Menderes graben. (f) Simplified cross-section of the Germencik area (see location on Figure II.12a).

II.4.4. Structural features of the Salavatlı and Germencik geothermal fields

The Seferihisar geothermal field (Table II.1 for more information) is located in the northern flank of the Büyük Menderes graben between Sultanhisar and Köşk (Figs. II.3b and II.13a). The basement of the Menderes Massif in this area is made of metamorphic rocks such as schists, marbles and local phyllite intercalations [*e.g.* Dora *et al.,* 1990; Güngör & Erdoğan, 2002] topped by the Bornova flysch mélange. This area is similar to the central part of the Menderes Massif, but shows some differences such as lower topography and a hidden tectonic contact localized between the Bornova flysch mélange and the Menderes Massif as suggested by Erdoğan [1990]. We briefly present below the relationships between hot spring locations and faults, and we refer the reader to the study of Ring *et al.* [2017] for more information about the Miocene-to-Present tectonic evolution. Field observations show that hot springs are generally located close to NE to SW striking strike-slip faults (Figs. II.13a, II.13b and II.13c). Kinematic indicators suggest a dextral strike-slip movement with lineation pitch ranging from 10°S to 22°S (Fig. II.13d). In addition, these faults are characterized by multi-metric damaged zones, locally strongly altered, attesting for recent fluid circulation. Dextral strike-slip movement is associated with dilational jogs and pull-apart structures (Fig. II.13a), probably close to the intersection zones between N-S strike-slip fault and the early contact between the Bornova mélange and the Menderes basement rocks (*i.e.* the tectonic contact descibed by Erdoğan [1990]). Furthermore, in places, E-W trending fault corridors cut these first faults (Fig. II.13e). These later sub-vertical faults show several sub-vertical and sub-horizontal slickenlines, with plunging values ranging from 85°W to 49°E and 24°E to 4°W, respectively (Fig. II.13e). The calculated paleo-stress analysis suggests that kinematic indicators are compatible with a NW-SE extension (Fig. II.13a). All along the main road between Cumhuriyet and Orhanlı (Fig. II.13a), sandstones of Bornova mélange usually display a strong alteration. Hence, it seems reasonable to assume the existence of others faults, which would be parallel to the previous one in this area.

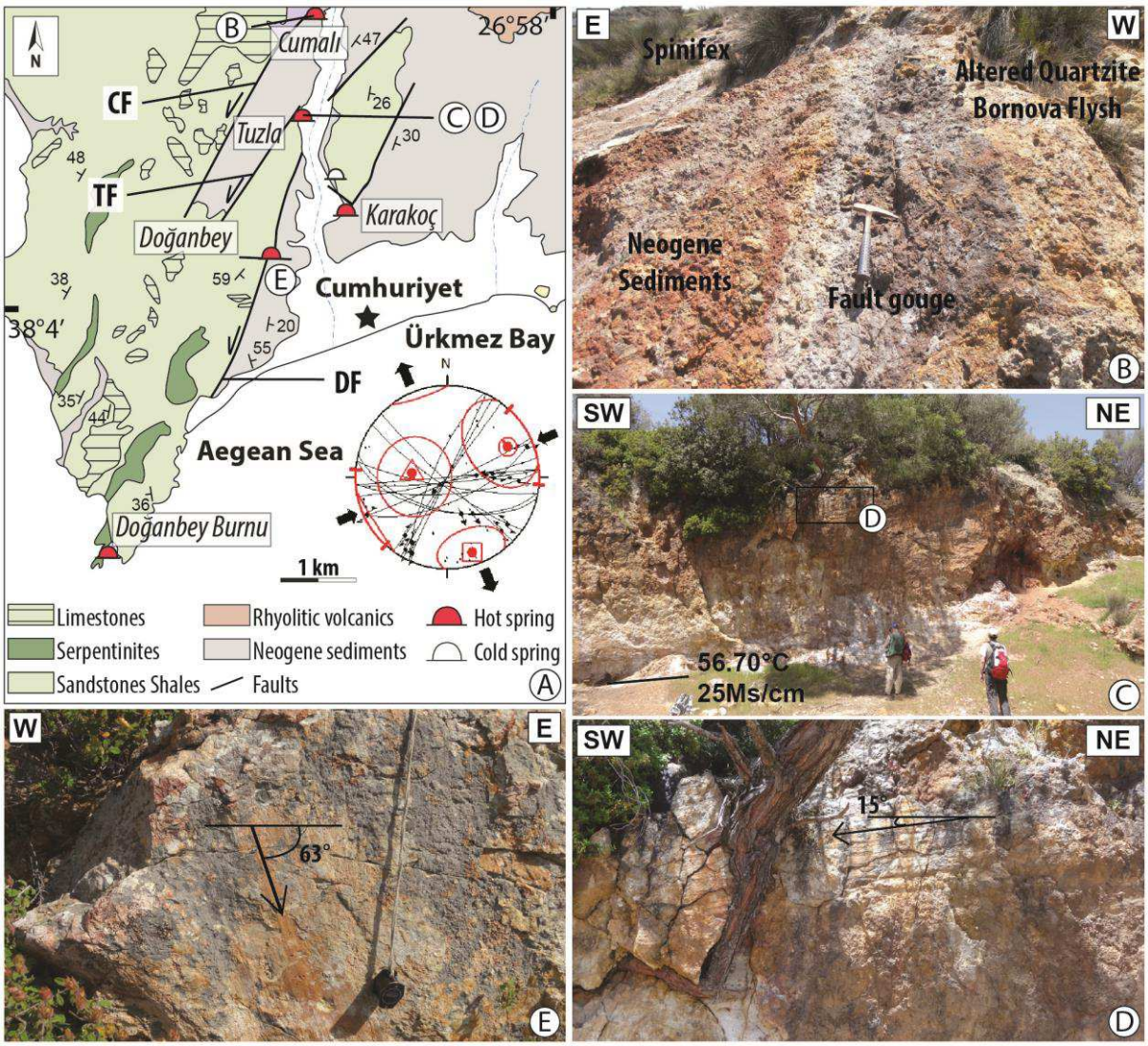

Figure II.13: Brittle deformation in the Seferihisar area. (a) Simplified tectonic and geological map of Seferihisar geothermal areas showing main structures: the Cumalı Fault (CF), the Tuzla Fault (TF) and the Doğanbey Fault (DF). Modified from Genç et al. [2001] and Drahor and Berge [2006]. Also are represented stereographic projections of striations and kinematics of the main fault planes. (b) CF showing the altered contact between the basement and Neogene sediments. (c) Field photograph of TF plane in the Bornova mélange showing a NNE-SSW trending. Note the strong alteration at the foot of the fault implying the presence of hot spring. (d) Close-up view of the fault plane showing well-preserved slickenlines. (e) Fault plane and associated striae belonging to the E-W trending normal fault. See Figure II.13a for location.

	Geothermal fields	*Depth & Thickness*	*Flow & Discharge rates*	*Measured temperatures*	*Chemical geothermometers*	*Lithology*	*Capfault and caprock*
Alaşehir graben	*Salihli*	Reservoir depth varies from 40–400 m	20 L/s (K-1) and 40 to 80 L/s (other wells in Kurşunlu area)	83–94°C	80° to 250°C (with vrariability of geothermometers e.g., SiO_2; Quartz Steam Loss; Na-K-C)	Karstified and fractured marbles of the basement; Çaltılık Formation	Siliceous ADFP and Gediz Formation
		Reservoir depth from 950–1500 m	30 to 35 L/s	90–92°C			
	Alaşehir	Reservoir depth from 1150 m and 1600 m	12 L/s (KG-1) and 6,74 L/s (Ak-2)	215°C (A5-2)		Karstified and fractured marbles of the basement; Çaltılık Formation	Siliceous ADFP and Gediz Formation
		Reservoir depth from 1750 to 2750 m	5–90 L/s	159–287,5°C			
	Urganlı-Turgutlu	Reservoir depth at 460 m	20 L/s	62°C		-	-
Büyük Menderes graben	*Germencik*	Shallow reservoir depth in sediments (around 285 m)	Average flow rate rate 300 tph	203–217°C	150–250°C (Na-K & Na-K-Ca)	Miocene conglomerates and Fractured rocks of the basement	Neogene clastic sediment such as clayey levels
		Deeper reservoir in basement changes depending on the locality from 965 to 2432 m depth		191–276°C			
	Salavatlı	Reservoir depth from 750–1923 m	Average flow rate 1480 tph	148–176°C	160–175°C (Giggenbach, 1986)	Fissures and fractures zones of the basement	-
		Reservoir depth at 3224 m	-	211°C	-		-
	Kızıldere	First reservoir depth at 400 m	Average flow rate 1400–1500 tph	148–198°C	-	Sazak Formation (Pliocene sediments) and quaztites, marbles, gneiss of the basement	Pliocene impermeable clayey
		Second reservoir depth from 1100 m to 1200 m		200–212°C			
		Just below the second		242°C	250–260°C (SiO_2; Na-K-Ca)		
		Fourth reservoir depth unknow	-	>250°C	-	-	-
Cumaovası basin	*Seferihisar (Tuzla)*	Reservoir depth from 333–553 m	Total discharge rates of 130 tph	174–176°C	-	Fractured mafic submarine volcanics and fractured rocks of Bornova mélange; Marbles of Menderes?	Clay-rich zones of the Neogene sediments
Simav graben	*Simav*	First reservoir shallow depth, 85 m	-	105°C	83 to 182°C (SiO_2) and 148 to 163°C (Na-K-Ca-Mg)	Neogene sediments: Naşa basalt, Budağan limestone, Arıkaya and Balıkbası formations; Menders units?	Clayey level of Eynal, Akdağ and Sarıcasu Formations
		Second reservoir: around 725 m		162°C			

Table II.1: Catalogue of hot springs and geothermal fields associated with the metamorphic core complex formation in the Menderes Massif. ADFP: Alaşehir detachment fault plane. Compilation data from Simşek [1984; 2003], Simsek and Demir [1991], Yılmazer and Karamanderesi [1994], Karamanderesi [1997; 2013], Özgür et

al. [1998a; 1998b], Tarcan et al. [2000]; Gemeci and Tarcan [2002], Tarcan and Gemici [2003], Yildirim et al. [2005], Kose [2007], Faulds et al. [2010], Kindap et al. [2010], Tekin and Akin [2011], Özen et al. [2012], Baba et al. [2014 ; 2015], Akin et al. [2015] and Tureyen et al. [2016].

II.5. Discussion

II.5.1. The Menderes Massif Core complex and associated geothermal fields

The genesis of a geothermal system requires source of high temperatures, reservoirs of large quantity of hot fluids (permeable structures and lithology) and its caprock. All of these features are present in the Menderes Massif, thus explaining the geothermal potential. As seen previously, thermal anomalies show different wavelengths at different depths in the Menderes Massif (*i.e.* crustal-scale to geothermal field-scale). Whereas the short wavelength anomalies result from shallow depth processes and may be associated with N-S transfer faults, the long wavelength (i.e. crustal-scale or mantle-scale) result from deep processes and may be associated with detachments activity. Therefore, as for many geothermal fields in western Turkey and abroad, faults appear to represent a first-order control on fluid flow and heat transport, and thus on the location of reservoirs at depth and hot springs at the surface as leak of reservoir (Fig. II.14a). In the following, we first focus on detachments at crustal-scale, then we highlight the role of N-S transfer faults at basin-scale.

II.5.1.1. Crustal-scale: the role of detachments

At the scale of the Menderes Massif, the presence of numerous hot springs close to E-W striking, northward and/or southward dipping low-angle normal fault (Fig. II.3b) confirms that detachments control fluid circulations. These latter are controlled by the current global structure of the Menderes core complex resulting from a multi-staged activity of the detachments since the Miocene. Indeed, ongoing tectonic lets the detachment systems active, and meanwhile, (i) detachment faults became incrementally split into many sections separated by transfer faults and (ii) different sets of faults (*i.e.* E-W striking faults) merge at depth into the detachments [see Seyitoglu *et al.*, 2002]. This complex tectonic evolution thus induces an intense hydrothermal activity (*e.g.* silicified detachment in some areas), for instance within thick damage zone (*e.g.* up to 10 m of cataclasites associated with the Alaşehir detachment are present in the hanging-wall and the footwall of the detachment, Fig. II.9) reaching ~ 10 km (containing the ductile-brittle deformation associated with the detachment) according to Bozkurt [2001]. One can question whether such detachment fault systems have acted as important conduits for fluid circulations since the Miocene. In any case, these structures generate zones of high fracture density and permeability that host significant fluid flows in the upper crust. They are also connected with most superficial

structures (*i.e.* N-S transfer faults) and probably seem highly effective for heat transport and fluid circulation at deeper depth toward specific reservoirs (Figs. II.14a and II.14b).

Many studies on fluid compositions [Famin *et al.*, 2004; Mulch *et al.*, 2007; Gottardi *et al.*, 2011; Hetzel *et al.*, 2013; Quilichini *et al.*, 2015] suggest that low-angle detachments permit pervasive meteoric fluid flow downward and/or upward along detachment fault planes, reaching depths of 10 – 15 km. In addition, isotopic studies show the presence of small amounts of deep CO_2, H_2S, B and He in thermal waters (see our compilation, section II.3.2). We thus suggest that large-scale detachment faults may represent the conduits allowing the escape of helium to the surface in the Menderes Massif. In others words, fault-controlled circulation of meteoric fluids is the dominant mechanism to explain the migration of mantle volatiles from the ductile-brittle transition zone to the near-surface (Fig. II.14b) [Mutlu *et al.*, 2008; Jolie *et al.*, 2016]. Brittle fault systems are thus probably connected at depth with ductile shear zones (Fig. II.14b).

Ductile shear zones may indeed represent efficient pathways for hydrothermal fluids [*e.g.* Oliver, 1996; Taillefer *et al.*, 2017]. Two main mechanisms explain the fluid migration in the deeper part of the crust: deformation-driven flow [Oliver, 1996] and thermally-driven flow (*i.e.* buoyancy-driven) through the crust, which is favoured by the high (i) permeability of detachments that collect and bring up deep hot fluids and (ii) temperature induced by the shear heating mechanism. This latter term refers to the generation of heat from the mechanical work of tectonic processes [Scholz, 1980]. It thus increases with slip rate, friction coefficient and stiffness of materials [Leloup *et al.*, 1999; Souche *et al.*, 2013]. Considered as a most rapidly deforming regions [*e.g.* Reilinger *et al.*, 2006], western Anatolia domain would favour the development of such mechanism at crustal-scale. Indeed, neo-tectonic activity in the Menderes Massif is characterized by earthquakes occurring in the shallow crust, with the mean depth being shallower in the Simav domain (9.7 km) compared to the western domain (11.9 km) and the central Menderes (11.2 km) domain [Gessner *et al.*, 2013]. Brittle deformation is still active (*e.g.* the Gediz detachment, Buscher et al. [2013]) and may locally occur under high temperatures conditions (*e.g.* 580 °C at ~ 10 km [Bilim *et al.*, 2016]), probably close to the ductile-brittle transition zone. The numerous ductile shear zones may have had (and perhaps still have [*e.g.* Ring *et al.*, 2017]) a strong and continuous thermal effect at depth, explaining also the anomalously shallow position of Curie-point depths. Hence, in these areas heat could also be generated by tectonic processes, probably along the brittle-ductile shear zones in the upper levels of the continental crust (Fig. II.14b) [Scholz, 1980]. Although the contribution of shear heating at crustal scale is debated [Lachenbruch & Sass, 1992], more studies would be needed to explore this possibility. In particular, the amount of heat produced and the time constants of such heat production should be addressed.

	Geothermal fields	Structural setting	Structural characteristics	Main controls
Alaşehir graben	Salihli	HW and FW of the south side of the graben	Intersections between N-dipping detachment, N-S trending strike-slip faults and sometimes E-W trending normal faults	KC, FC, FRC
	Alaşehir	HW and FW of the south side of the graben	Intersections between N-dipping detachment, N-S trending strike-slip faults and sometimes E-W trending normal faults	
	Urganlı-Turgutlu	HW and FW of the north side of the graben	Intersections between N-dipping detachment, N-S trending strike-slip faults in the basin	FC
Büyük Menderes graben	Germencik	HW and FW of the north side of the graben	Intersections between S-dipping detachment, N-S trending strike-slip faults and E-W trending normal faults	FC, FRC
	Salavatlı	HW and FW of the north side of the graben	Intersections between NNE-SSW trending strike-slip faults and SE-NW striking normal faults	
	Kızıldere	HW and FW of the north side of the graben	Eastern termination of major normal fault; Intersections between N-S trending strike-slip faults and E-W striking normal fault	
Cumaovası basin	Seferihisar	HW and FW of the contact between BM/MU	Intersections between N-S transfer faults and the contact between BM/MU	FC
Simav graben	Simav	HW and FW of the north side of the graben	N-dipping detachment and intersections between N-S striking transfer fault and S-dipping normal fault	FC

Table II.2: Main controls on geothermal fields in the Menderes Massif. BD: Büyük Menderes detachment, BM: Bornova Mélange, FC: Fault controlled, FRC: Fracture controlled, FW: Foot wall, AD: Alaşehir detachment, HW: Hanging wall, KC: Karstic controlled, MU: Menderes Unit, NF: Normal fault.

Furthermore, using a numerical model of coupled fluid flow and heat transport processes, Magri *et al.* [2010] showed that temperature patterns in the Seferihisar-Balçova area result from both interaction of convective flow (*i.e.* buoyancy-driven flow) and meteoric recharge induced by the horst

(*i.e.* mixed convection) in the shallower crust. Recently, Roche *et al.* [2018] showed that high temperatures at 6 km depth (300 – 350 °C) are sufficient to allow a high fluid density contrast, permitting upward flow along the low-angle fault, using also 2-D numerical models (see Figure 8 in their study). This implies that buoyancy-driven flow is superimposed to topography-driven flow in some places. This case is, for instance, well observed in the Seferihisar geothermal systems where the topographic gradient related to the formation of MCC appears to be negligible. This implies that the observed temperature patterns result mainly from the thermally driven flow within permeable faults. In all cases, hot fluids in the detachments will further enhance temperature increase in the upper part of the fault zone, thus generating high thermal gradients in these areas. For instance, Gottardi *et al.* [2011] estimated high temperature gradient of ~ 140 °C/100 m across the Miocene Raft River shear zone in the United States, as revealed by isotope thermometry. There, the geotherm is quasi-stable over a long time duration. As a consequence, it raises the question whether similar geothermal fields in the Menderes Massif could have been active during millions of years.

Additionally, it is clear that permeability related to fault zones architecture is a first-order control on fluid flow in the upper crust [*e.g.* Caine *et al.*, 1996]. Our study shows that the thick siliceous microbreccia of the Alaşehir detachment fault plane (Table II.2) acts as cap fault of the fluid circulating below this plane. Thus, depending on the area, the detachment can be considered at kilometric-scale as a combined "conduit-barrier" and as a "localized conduit" [Caine *et al.*, 1996], where the conduit corresponds to the thick shear zone and the barrier is associated with the fault plane and/or with the hanging wall of the detachment. Depending on the pressure gradients, the flow within the detachment may be characterized by horizontal-flow according to normal kinematic and related dilatancy (Fig. II.14a). In both cases, the high permeability in the shear zone favours fluid circulation (*e.g.* in marbles levels through karstification process in the Menderes Massif) and thus generates secondary reservoirs (Fig. II.14a).

II.5.1.2. Basin-scale: the N-S transfer faults

Based on our structural observations, we highlight that strike-slip faults control many geothermal reservoirs in depth, related to hot springs and travertine deposits at the surface. In terms of geometry, for instance, Çiftçi and Bozkurt [2010] suggested, from a seismic profile interpretation, the existence of two kilometric transfer faults with a large normal component in the Alaşehir graben (Fig. II.6a). These transfer faults correspond to the location of several travertines oriented NW-SE and NE-SW and hot springs at the surface, which are respectively associated with the Urganlı [Temiz & Eikenberg, 2011] and Alaşehir geothermal field (Fig. II.6a). Kaya [2015] also suggests that the Tekkehamam geothermal field (located in the southern part of the Büyük Menderes graben, Fig. II.3b) is associated with a N-S transfer fault that cuts both the basement and Neogene sediments. Thus, this set of faults is a good

candidate to act as conduit for fluid circulation when hot springs and related travertines are located far from the detachment (Fig. II.14a; Table II.2). Here, horse-tail termination of these strike-slip faults (see more details in Faulds *et al.* [2011]), generates many closely spaced faults that locally increase permeability, favouring the growth of reservoirs.

Although no clear chronology between detachments and the N-S strike-slip transfer zones can be observed in the field, we favour a contemporaneous and ongoing development of these faults systems during the development of the sedimentary basin according to Oner and Dilek [2013]. They are mainly found at the foothills of the main Menderes mountains, crosscutting the detachments in high topographic zones. Nonetheless, we suggest that these faults may also root to detachments at deeper depth (Fig. II.14a). There, pull-apart structures, *en échelon* and relay-ramp faults may be locally developed, generating dilational jogs with vertical pitch that focus fluid circulation and thus geothermal upflow (Fig. II.8d and Fig. II.13c). In addition, reservoirs are commonly focused at the dilational junction between detachments and nearby N-S strike-slip faults or within the strike-slip faults (*e.g.* Cumalı fault, Fig. II.13a and II.14a).

To sum-up, these faults define several hundred meters wide relay zones where faults are considered as "distributed conduits" [Caine *et al*., 1996]. They are characterized by multiple minor faults, connected with major structures where fluids can flow through highly fractured metamorphic rocks thanks to the seismic pumping mechanism [*e.g.* Sibson *et al*., 1975; McCaig, 1988; Famin *et al*., 2005]. Consequently, we refer hereafter to these sinistral or dextral strike-slip faults as the "geothermal transverse and transfer faults" related to main reservoirs (Fig. II.14a). Hence, these faults should be used as a main guide for geothermal exploration. This hypothesis is opposed to the idea of Gessner *et al*. [2017], suggesting that NNE-SSW-orientated lineaments do not have a significant role in fluid flow pattern.

II.5.2. Possible fluid pathways in the Menderes Massif: from the mantle to the geothermal reservoir

II.5.2.1. Source to sink

Based on structural analyses of field data and isotopic distribution of waters, we suggest similar pathways of fluids for the Alaşehir and the Büyük Menderes half-grabens, that could also extend to the Simav graben and Cumaovası basin: meteoric cold waters and/or sea waters (*i.e.* for the Seferehisar case) circulate downwards along E-W high-angle to listric normal faults (*e.g.* Salihli and Alaşehir geothermal systems), implying that such faults control the meteoric recharge of deeper reservoirs (Fig. II.14a). More generally, meteoric water infiltration along fractured rocks of the basement of the

Menderes Massif is controlled by (i) the footwall topography gradient induced by MCC exhumation, and by (ii) the stress regime in the crust, allowing recharge and hydrothermal fluid circulation. Then, temperature of fluids increases progressively. Hot fluids can circulate along the main detachments (*i.e.* Simav, Alaşehir and Büyük Menderes detachments) within karstified marbles or/in fractured rocks of the basement. During this stage, the geochemical properties of meteoric waters are modified and their composition (*e.g.* Na-HCO_3 type) is mainly controlled by calcite dissolution in the marbles layers of the Menderes Massif under high temperature conditions. Locally, some exchange with mantle-He, CO_2, B and H_2S isotopes could occur in deep parts of the crust in the ductile-brittle transition zone (Fig. II.14b). Through a seismic pumping mechanism [*e.g.* Sibson *et al.*, 1975; McCaig, 1988; Famin *et al.*, 2005], hydraulic gradients may force fluid downward across the ductile-brittle transition using the high permeability of microcrack networks (*e.g.* after earthquake rupture). After a complex deep fluid pathway, thermal waters may then recharge reservoirs of the metamorphic rocks of the Menderes at depth (Figs. II.14a and II.14b).

Different lithologies may behave as reservoirs (Table II.1). Reservoirs are herein defined by highly fractured but also by karstified carbonate layers of the CMM (*e.g.* Salihli, Alaşehir, Germencik, Salavatlı… [Tarcan *et al.*, 2000]). For instance, the high-temperature geothermal reservoir observed in Alaşehir, is located in the upper section of the Paleozoic basement, with feeder zones in the upper Paleozoic carbonates at approximately 1150m and 1600m of depth [Akin *et al.*, 2015]. Fractured metamorphic rocks such as quartzite can also act as an aquifer for geothermal fluid (*e.g.* Kızıldere [Simsek, 2003]). In both cases, the main reservoirs are located just below the detachments, which is in some places silicified. There, blind geothermal reservoirs may also form. Indeed, according to Magri *et al.* [2010], when hydrothermal plumes reach the upper impermeable boundary (*e.g.* the Alaşehir detachment), over-pressured blind geothermal reservoirs are formed. This implies that other geothermal systems in the Menderes Massif are yet to be discovered. In order to fully understand these geothermal systems, stress modelling related to faulting is necessary to bring new constraints on the evolution of fluid pathways [Moeck *et al.*, 2009]. In addition, other reservoir types may be developed in the hanging-wall of detachments. For example, in the Cumaovası basin, it is made of fractured submarine volcanics of the Bornova mélange [Tarcan & Gemici, 2003]. Because of the high permeability units in Neogene continental silicoclastic rocks, secondary aquifers may also occur (Fig. II.14a). Indeed, Neogene sediments may have highly variable permeability, but they usually rather display mega-cap rocks related to underlying geothermal system (*e.g.* the Alaşehir geothermal system [Tarcan *et al.*, 2000]).

After a short time of residence (around 20 – 50 years, [Simsek, 2003]) in different kinds of reservoirs, hot thermal fluids can flow along the dilational intersections or junction between the N-S strike-slip faults and the detachment, and then emerge at the surface (*e.g.* Kurşunlu, Sart-Çamur, Germencik hot springs) (Fig. II.14a). In this case, the direction of flow is mainly determined by the prevailing permeability and by the regional stress field. Similar features of fluid flow pattern are

observed in the Cumaovası basin where the NE-SW trending strike-slip faults affected also the detachment, forming dilational jogs and favoring hot water circulation from karstic and fractured reservoirs to the surface (*e.g.* Figs. II.13b and II.13c).

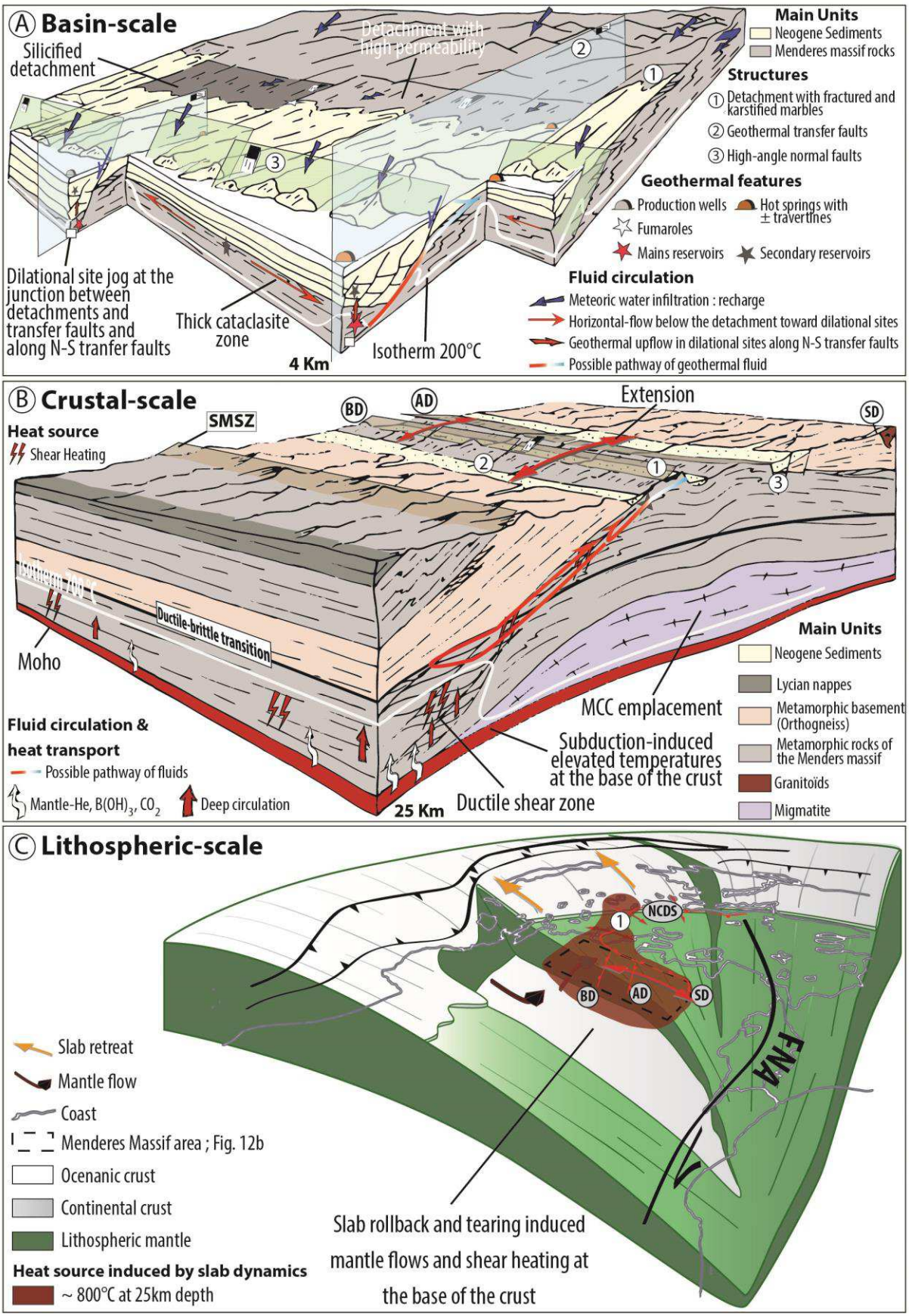

Figure II.14: Conceptual models at different scales showing the heat source origin and main structural controls on fluid flows in the Menderes Massif. (a) Synthetic simplified block diagram of the Alaşehir graben showing the relationships between these faults. Hot springs, reservoirs and fluid circulation are also indicated. (b) Role of the

detachment on deep circulation in the Menderes Massif. Numbers show different type of faults, see Fig. II.14 for more details. Main structures are indicated in abbreviations: AD (Alaşehir detachment); BD (Büyük Menderes detachment); SD (Simav detachment) and SMSZ (Southern Menderes shear zone). (c) Tentative 3D reconstruction and flow directions in the mantle (red arrows) of the Aegean region before the recent slab tear below the Corinth Rift and after. Red line and red arrows show the main detachments and kinematic of extension in this region, respectively. Yellow arrows indicate the slab retreat in the Aegean domain. Main structures are indicated in abbreviations: AD (Alaşehir detachment), BD (Büyük Menderes detachment) and SD (Simav detachment).

II.5.2.2. A long-lived duration geothermal Province

Hetzel *et al.* [2013] suggested that the Alaşehir and Büyük Menderes detachments recorded a long-lived brittle deformation from around 22 Ma until 4 – 3 Ma. Hence, the low-angle crustal normal faults were (still) active over a long period of time. We thus suggest that detachments control magma ascent (*e.g.* Salihli granodiorite, Egrigöz granite) as well as fluid circulation in the Menderes Massif during the Miocene. Nonetheless, the presence of Kursunlu Sb-Hg(-Au) deposit [Larson & Erler, 1993] located within the Alaşehir detachment system, implies a drastic change in the fluid pathway evolution compare to the Miocene. Indeed, according to Larson and Erler [1993], Alaşehir detachment conveyed deep circulation of shallow hydrothermal fluids (*i.e.* meteoric origin) with a minor component of crustal and mantellic origin, thus similar to the present-day hot springs. Hence, the mineralizing fluid seems to be not related to the Miocene intrusions. To better characterize this evolution, a detailed study of such deposit would be useful, bringing new constraints on the structural control of the mineralization and the timing of mineralizing processes. This imply that detachments control fluid pathways over millions years (episodic or continuous mineralized pulse(s)?).

II.5.3. Origin of heat source in the Menderes Massif

At geodynamic-scale, the origin of the thermal anomalies propagating all the way to the surface could reflect both slab-rollback and slab tear below western Turkey. Heat can be generated by many processes, including anomalous mantle heat flow mainly due to asthenospheric flow and shear heating (Fig. II.14c) [Roche *et al.*, 2018]. Based on heat conduction, the time scale t_{diff} is defined by the following equation:

$t_{diff} = L^2/ \kappa$

where L is Moho depth (meter) and κ is the thermal diffusivity ($m^2\ s^{-1}$). Considering a Moho depth of ~ 25 km under the Menderes Massif [*e.g.* Karabulut *et al.*, 2013] and taking a thermal diffusivity (κ) of $10^{-6}\ m^2\ s^{-1}$, the current thermal anomaly observed at the surface (shown by the presence of numerous sources and gas events) could reflect the thermal expression of a 20 Ma old slab tear at Moho depth. In other words, the heat source at the base of the crust coupled to the exhumation of the MCC is induced by slab dynamics since the Miocene as suggested by previous authors [*e.g.* Jolivet *et al.*, 2015; Menant

et al., 2016; 2018; Roche *et al.*, 2018]. This increase of temperature recorded in the mantle and in the crust favours the emplacement of a large zone of migmatization and/or magmatic underplating at the base of the crust. This hypothesis is also consistent with:

(i) the presence of high temperatures (~ 580 °C) at shallow depths (~ 10 km under the Menderes; [Aydin *et al.*, 2005; Bilim *et al.*, 2016]);

(ii) the current models of Miocene slab tearing in this region [Jolivet *et al.*, 2015].

(iii) the enrichment of mantle-He [Mutlu *et al.*, 2008], B and sometimes high content of CO_2 and H_2S within all thermal waters [Vengosh *et al.*, 2002]; for instance, mantle-He values suggest that helium is probably transferred to the lower crust by degassed fluids from deep mantle melts [Mutlu *et al.*, 2008]; these values comparable to that observed in hydrothermal fluids from the western part of the Basin & Range Province (4 – 25% mantle-He) where active volcanism is also absent [Kennedy & Soest, 2007].

To sum-up, the lack of significant magmatic activity in this area shows that the upper crust and related magmatic bodies is not a direct heat source for these geothermal systems [Faulds *et al.,* 2010]. Nevertheless, based on 3-D Vp imaging of the upper crust beneath the Denizli geothermal field, Kaypak and Gökkaya [2012] showed that intrusive magmatic bodies may also explain the heat source of few geothermal systems in this area. According to this study and others [*e.g.* Faulds *et al.*, 2010; Kaya, 2015; Gessner *et al.*, 2017] the spatial distribution of hot springs and fumaroles is associated with the tectonic activity. Using the classification of Moeck [2014], the "geothermal Province" of the Menderes Massif can be considered as a fault controlled system in an extensional domain, where convection occurs along fault systems. Although most of existing models of geothermal heat source suggest a probable magmatic intrusion in the upper crust, this study confirms that the tectonic activity induced by subduction dynamics controls the spatial distribution of heat in the Menderes massif (Fig. II.14) [*e.g.* Kaya, 2015; Gessner *et al.*, 2017; Roche *et al.*, 2018]. We thus think that this area may be used as a reference case to better understand the amagmatic geothermal systems.

II.5.4. An underestimated geothermal potential?

It is clear that dense fracturing caused by tectonic activity implies a modification of the regional fluid flow, which is controlled by the state of stress in the crust, and influences the localization and the typology of reservoirs. Reilinger *et al.* [2006] have estimated fault-slip rates in a block model consisting of 19 plates/blocks and using M>4.5 earthquakes above 35 km. Based on GPS-derived velocity field data, they suggested a total extension of approximately 25 mm/yr corresponding to 10.9 ± 0.3 mm/yr for the left lateral strike-slip component and 14.5 ± 0.3 mm/yr of pure extension. This rapid relative motion is twice the rate reported from the Basin & Range Province where Bennett *et al.* [2003] estimate relative motion of 9.3 ± 0.2 mm/yr with high strain rates, using the same method (*i.e.* GPS-derived

velocity field data). Faulds *et al.* [2012] showed that the regional pattern of geothermal activity in the same area is directly correlated with strain rates. If we compare, for instance, the total discharge of the Seferihisar geothermal field (*e.g.* 100 – 150 L/s to 300 L/s according to Tarcan and Gemici [2003]), located in a seismically active zone (*e.g.* see compilation from Özkaymak *et al.* [2013]) is twice to four times that of the Salihli geothermal field (2 – 80 l/s; [Özen *et al.*, 2012]), which is a less active zone. Paradoxically, the topography is less steep in Seferihisar area than in Salihli area. Therefore, we suggest that active deformation could affect fluid velocity in the upper crust, improving the flow rates of a geothermal system.

Furthermore, the Basin & Range Province is quite similar to the Menderes Province because MCCs are exhumed along low-angle normal faults, and represent a favourable setting for amagmatic high enthalpy geothermal resources [Roche *et al.*, 2018]. In addition, the origin of the heat of these systems may be also associated with a deeper source induced by subduction dynamics (*i.e.* magmatic underplating under the overriding plate; [Wannamaker *et al.*, 2006]). Because of the similarities between these both geothermal Provinces, we suggest that the geothermal potential in the Menderes is probably underestimated (~ 820 MWe, Geothermal Resource Association). Indeed, the current geothermal installed capacity of the Basin & Range province is estimated at ~ 2349 MWe [Bertani, 2016].

II.6. Conclusion

Our work is based on a multiscale study and on a compilation of geothermal and structural observations in the whole Menderes Massif. It provides a new vision on the role of a large-scale thermal anomaly below the Menderes Massif and more generally in the Eastern Mediterranean region. We suggest that such regional thermal anomalies at the origin of the Menderes geothermal Province result from the tectono-thermal evolution of the Aegean subduction zone at depth. This Province is characterized by an intense hydrothermal activity, favoured by both a high elevation area and a neo-tectonic activity in absence of magmatic input. Such proxies are related to the Menderes Core Complex evolution, which is structured by three main detachments. We also have identified, at crustal-scale, the essential role of the low-angle normal faults, corresponding to a permeable channelized fluid flow systems for ascending fluid flows. N-S transfer faults then control the position of geothermal systems and should be used as a main guide for geothermal exploration. In addition, we emphasize that the lithological control is determinant for understanding the location of geothermal reservoirs, and may have a strong influence in the fluid circulation pattern of thermal waters. Eventually, we highlight that an episodic model (*e.g.* seismic pumping) and / or a continuous model seem possible over several million years in the Menderes Massif.

II.7. Acknowledgements

This work has received funding from the Labex Voltaire (ANR-10-LABX-100-01) homed at Orléans University and BRGM, the French geological survey. The paper benefited from relevant revisions by Inga Moeck, Klaus Gessner and Gürol Seyitoğlu.

II.8. Appendix

In the following, we present briefly the geological and geothermal settings of studied areas.

II.8.1. The Alaşehir graben

II.8.1.1. Stratigraphy and structure

The Alaşehir graben trends WNW-ESE (Fig. II.3b). The thickness of its sedimentary filling changes laterally from west to east and also from south to north. The graben is asymmetric: its northern margin has a more subdued topography than the southern margin which steeply rises from 50 m to more than 2000 m a.s.l. The stratigraphy of the Alaşehir graben has been studied by several authors [İztan & Yazman, 1990; Seyitoglu, 1992; Cohen *et al.*, 1995; Yilmaz *et al.*, 2000; Sarica, 2000; Seyitoglu *et al.*, 2002; Purvis & Robertson, 2004; 2005]. In 2009a, Çiftçi and Bozkurt proposed a new stratigraphic nomenclature and defined five lithostratigraphic formations, from top to bottom: (i) Quaternary alluvium; (ii) post-Miocene Kaletepe and Bintepeler formations merge in the Sart formation (e.g. Seyitoglu *et al*. 2002), with alluvial fan to fluvial affinities; (iii) the Gediz Formation also with alluvial fans, fluvial to lacustrine affinities; (iv) the Çaltılık Formation with alluvial to lacustrine affinities; (v) the Early-Middle Miocene Alaşehir Formation, the oldest Neogene unit exposed along the southern margin of the Alaşehir graben.

It is developed above a major low-angle extensional structure [*e.g.* Hetzel *et al*., 1955a; 1995b; Emre & Sözbilir, 1997] intruding by syn-tectonic granitoïds [*e.g.* Salihli granodiorite at 15.0 ± 0.3 Ma after Glodny and Hetzel [2007]) (red body in Figure II.6a) that separates the high-grade metamorphic rocks (*i.e.* schists, marbles, gneisses) of the Menderes Massif from sedimentary strata in the hanging wall. According to most of studies, the initiation of the graben started with high-angle normal fault which gradually became low angle with time [*e.g.* Gessner *et al*., 2001c; Seyitoğlu *et al*., 2002; Purvis &Robertson, 2005; Ciftci & Bozkurt, 2009b; 2010]. Based on E-W seismic reflection profile, Çiftçi and Bozkurt [2010] proposed the existence of two sub-basins comprising 3000 m of sediments (Salihli and Alaşehir sub-basins) separated by a possible relay ramps [Seyitoglu *et al*., 2002], starting since the Miocene. Contemporaneous with this displacement, a rapid exhumation of the footwall of the Alaşehir detachment in the Miocene to Pliocene until ~ 4 – 2 is recorded (*e.g.* Gessner *et al*., 2001c; Seyitoglu *et al*., 2002; Buscher *et al.*, 2013; Hetzel *et al*., 2013]. Even if this continuum of extension is still controversial [*e.g.* Koçyiğit *et al*., 1999; Yılmaz *et al*., 2000; Bozkurt & Sözbilir, 2004; Purvis & Robertson, 2004; Emre & Sözbilir, 2007; Kaya *et al*., 2007], it clear that extension since the Miocene controls the exhumation of the Menderes MCC and associated basins. Finally, post-Miocene formation

corresponds to the development of E-W trending high-angle normal faults that control the current geometry of the basin [*e.g.* Bozkurt & Sozbilir, 2004; Purvis & Robertson, 2004; Kent *et al.*, 2016]. This fault is segmented into three strands [Çiftçi & Bozkurt, 2007; 2009b], which possibly have disturbed both the graben sedimentary fill and the metamorphic basement rocks. It is noteworthy that steeply N-S trending strike-slip faults cut and dissect the massif [*e.g.* Yilmazer *et al.*, 2010; Oner & Dilek, 2011].

II.8.1.2. The main geothermal fields: Salihli and Alaşehir

The Salihli geothermal field is located along the southern margin of the graben (Fig. II.3b) and is mainly used for district heating. Two groups of hot springs are identified: (i) the westerly Sart-Çamur thermal springs (52°C [Özen *et al.*, 2012]); (ii) the easterly Kurşunlu geothermal spring group, related to 20 shallow wells, up to 400 m in depth, indicating temperatures ranging from 83 to 94 °C and by discharge flow rates ranging from 40 to 80 L/s [Özen *et al.*, 2012] (Table II.1). In addition, further north, a high temperature of 155 °C has been measured in the Caferbey well at a depth of 1189 m [Karamanderesi, 1997], but with a low discharge flow rate of 2 L/s. In the Greenhouses geothermal area, the temperature of thermal water is around 85 °C between 1000 to 1189 m depth in Neogene sediments [Özen *et al.*, 2012]. Moreover, three new wells, whose depths range from 2500 m to 3000 m, have been drilled at the same location with high temperatures but low flow rates. In the Kurşunlu valley, the presence of a shallow reservoir in marbles is described by Yılmazer and Karamanderesi [1994]. Based on empirical chemical geothermometers and mixing models applied to the thermomineral waters, Tarcan *et al.* [2000] suggested that reservoir temperature varies between 150 °C and 230 °C, so that it could be used to produce electricity.

The Alaşehir geothermal field is located between Alaşehir and Salihli (Figs. II.3b and II.6a). It is one of the most important geothermal areas of Turkey. Four main groups from west to east are identified: (i) the Göbekli geothermal system, which is characterized by high reservoir temperatures around 182 °C confirmed by drilling to 1500 m depth [Yildirim *et al.*, 2005]; (ii) the Örnekköy area, which was investigated by Turkeler in 2011, reflecting the existence of a large reservoir below the basin; (iii) the Horzumsazdere spring, located in the south of the previous area; (iv) the Alaşehir Ilica spa, located in Alaşehir city. The highest reservoir temperature (287 °C) ever reached in Turkey was measured within this reservoir at 2750 m in a deep well [Baba *et al.*, 2015] (Table II.1). This high temperature geothermal fluid is located in the upper section of the permeable Paleozoic basement, with the major feed zones in the upper Paleozoic carbonaceous metamorphic rocks (marble) at approximately 1150 m and 1600 m at depths [Akin *et al.*, 2015] (Table II.1).

II.8.2. The Büyük Menderes graben

II.8.2.1. Stratigraphy and structure

The Büyük Menderes (150 km x 5 – 15 km) graben is bounded to the north and to the south by the high-grade metamorphic rocks of the Menderes Massif. It trends approximately E-W from Buldan to Germencik and changes drastically to a SW direction to the west (Fig. II.3b). The thickness of the Büyük Menderes graben is lower than that of the Alaşehir graben, with values ranging from 1000 to 1500 m. The stratigraphy has been defined by four sedimentary sequences that overly the metamorphic Menderes rocks [*e.g.* Sozbilir & Emre, 1990; Sen & Seyitoğlu, 2009]. They are, from top-to bottom: (i) Quaternary alluvium; (ii) late Pliocene–Pleistocene (based on micromammalian fossils [Ünay *et al*., 1995]) Asartepe formation with alluvial fan affinities which unconformably overlies the following units [Sozbilir & Emre, 1990; Sen & Seyitoğlu, 2009]; (iii) late Miocene alluvial to fluvial Gökkırantepe formation consists of red conglomerates, sandstones and mudstones, conformably overlying the Hasköy formation [Sozbilir & Emre, 1990] and (iv) the Early-Middle Miocene [*e.g.* Sozbilir & Emre, 1990; Seyitoglu & Scott, 1992; Akgun & Akyol, 1999] Hasköy Formation consists of conglomerates, sandstones and mudstones with lignite levels [Sozbilir & Emre, 1990]. This formation includes also E-W trending normal growth faults [Sozbilir & Emre, 1990].

The geometry of the graben is similar that of the Alaşehir half-graben in the sense that a S-dipping low-angle normal fault, named the Büyük Menderes detachment [*e.g.* Hetzel *et al*., 1995a; Gessner *et al*., 2001c], separates the graben from metamorphic rocks of the basement. The graben is also bordered by well-developed south dipping normal fault systems which juxtaposed Neogene sediments above the Menderes Massif. Based on N-S seismic reflection data Çifçi *et al*. [2011] showed that some of the E-W normal faults have acted as growth faults during the beginning of the basin formation. They also interpreted two generations of N-S striking faulting in E-W seismic profile. Some of these faults intersect the graben filling, hence postdating the graben whereas others are syn-sedimentary attesting by lens-shaped geometry of Haskoy and Gökkırantepe formations. In addition, same major controversy as the Alaşehir basin remain unresolved: a continuum of extension [*e.g.* Seyitoglu & Isik, 2015] vs. episodic manner separated by compression events and/or tectonic quiescence [*e.g.* Koçyigit *et al*., 2000; Gürer *et al*., 2009].

II.8.2.2. The main Büyük Menderes geothermal fields: Salavatlı and Germencik

The Salavatlı geothermal field is located on the northern flank of Büyük Menderes graben between Sultanhisar and Köşk (Fig. II.3b). In 1987 and 1988, two wells were drilled to 1510 m (AS-1)

and 962 m depth (AS-2), with temperatures values of 169.5 ° and 172 °C, respectively (see locations of wells in Figure II.11a [Karamanderesi & Helvaci, 2003; Serpen *et al*., 2015]). At the surface, hot springs at 32 °C close to Malgaçemir village confirm the present geothermal activity [Karamanderesi, 2013]. In 2006, a third well was drilled to produce electricity and several wells were drilled to the east of Sultanhisar (5 – 8 km away from the main area). Low temperature values around 120 °C were measured at 1000 m depth, implying a temperature decrease from west to east [Serpen *et al*., 2015]. These authors suggested that the volume of the Salavatlı-Sultanhisar geothermal field could reach up to 56 km^3 at depth.

The Germencik geothermal field is located in the northwestern part of the Büyük Menderes graben. Owing to detailed studies from nine deep (235 – 2398 m depth) wells, two high temperatures reservoirs were found. The first one resides in Miocene conglomerates with temperature around 203 – 217 °C [Simsek, 2003] (Table II.1). The second deeper one is located in marble levels of the Menderes units with estimated temperatures around 191 – 232 °C (Table II.1). Currently, more than 70 wells have been drilled with temperature reservoir reaching locally 276 °C [Tureyen *et al*., 2016]. Tekin and Akin [2011] suggested that permeability of the deeper reservoir is mainly due to fracturation of rocks formed during the brittle tectonic deformation. Currently, the reservoir is considered to be the primary target for power generation with a potential estimated around 232 MWe [Tureyen *et al*., 2016].

II.8.3. Cumaovası basin

II.8.3.1. Stratigraphy and structure

The Cumaovası basin (~ 35 km x 5 – 17 km, also known as the Çubukludağ graben) is bounded by the western end of the Alaşehir and Küçük grabens and trends approximately NNE-SSW (Fig. II.3b). The stratigraphy of the Cumaovası basin has been defined by two main sedimentary sequences that overly the metamorphic Menderes rocks. Firstly, the most recent filling deposits are characterized by plio-quaternary units, which consist of two terrestrial successions that are separated by an angular unconformity [Uzel & Sözbilir, 2008]; the younger deposits corresponds to the recent alluvium of the Görece formation. Secondly, the earlier filling is defined by Neogene volcano-sedimentary units which can be divided into five major lithostratigraphic units (see Genç *et al*. [2001] and Uzel and Sözbilir [2008], for more details). From bottom to top, one can distinguish: the Çatalca formation which is assumed to correspond to lateral equivalent of the Alaşehir formation of the Alaşehir graben [Koçyiğit *et al*., 1999; Yılmaz *et al*., 2000; Sözbilir, 2001; 2002; Seyitoğlu *et al*., 2002; Bozkurt & Sözbilir, 2004]. The basin basement is made of metamorphic rocks (i.e. schists, marbles and local phyllite intercalations) of the Menderes Massif [Dora *et al*., 1990; Güngör & Erdoğan, 2002] which are overlain by Cretaceous-Paleocene rocks of the Bornova mélange [Başarır & Konuk, 1981; Erdoğan, 1990].

The geometry of this graben changes from the Alaşehir and the Büyük Menderes half-grabens in the sense that the disposition of the sedimentary basin is controlled by strike-slip faults and oblique normal faults. Indeed, Uzel and Soezbilir [2008] suggest a polyphase evolution of the Cumaovası basin with change from transpressional to transtensional tectonics at the Pleistocene. They link the first event to NE-SW extension and NW-SE shortening, associated with sinistral NNE-SSW strike-slip faults. The younger event indicates a mixture of normal and strike-slip movement in a transtensional tectonic regime. According to Ring *et al*. [2017], even if faultslip data are heterogeneous, they indicate a constant N- to NNE-directed extension. This event is also well-defined by the recent earthquake activity which occurs to the south of Izmir Bay region [Uzel & Soezbilir, 2008] and by others located in the Seferihisar area [Tan *et al*., 2008; Özkaymak *et al*., 2012]. According to Uzel and Soezbilir [2008], these successive extensional events may be related to the westward escape and southwestward motion of western Anatolia along the North Anatolian Fault Zone. In any case, this youngest set of normal faults is still active and seems to be associated with detachment faulting in the Menderes Massif [Özkaymak *et al*., 2013; Ring *et al*., 2017].

II.8.3.2. The Seferihisar geothermal field

The Seferihisar geothermal field is located 40 km southwest of Izmir and is one of the most important geothermal areas in western Anatolia. Five groups of natural thermal springs are identified (red dots in Figure II.13a). Their temperatures vary from 30 to 82.5 °C (for Tuzla) and the springs have a total discharge rates of 100 – 150 L/s [Tarcan & Gemici, 2003]. In deep geothermal wells (up to 2000 m), a total discharge rate of about 300 L/s was found in the reservoir. Reservoir temperatures varies between 62 and 178 °C according to empirical chemical geothermometers (Table II.1) and locally, downhole temperature indicate 153 °C at 225 m in depth [Tarcan & Gemici, 2003]. In this geothermal system, the reservoir is mainly made of the fractured submarine volcanics of the Bornova mélange [Tarcan & Gemici, 2003]. Locally, limestones and serpentinites of Bornova mélange and Neogene terrestrial sediments can also behave as aquifers due to high permeability. In addition, hydrogeochemical assessment indicates that thermal waters were mixed with cold seawater before and/or after heating at depth. At the seashore in the south of the studied area, the shallow aquifer consists of Holocene alluvial deposits [Tarcan & Gemici, 2003].

II.9. References

Akgün, F., & Akyol, E. (1999). Palynostratigraphy ofthe coal-bearing Neogene deposits graben in Büyük Menderes Western Anatolia. Geobios, 32(3), 367-383.

Akin, S., Yildirim, N., Yazman, M., Karadag, M., Seçkin, C., Tonguç, E., Gürel, E., & Yarim, H. (2015). Coiled Tubing Acid Stimulation of Alaşehir Geothermal Field, Turkey.

Akkus, I., Akıllı, H., Ceyhan, S., Dilemre, A., & Tekin, Z. (2005). Türkiye jeotermal kaynakları envanteri. MTA Genel Müdürlügü Yayınları, Envanter Serisi, 201.

Altinoğlu, F.F., Sari, M., & Aydin, A. (2015). Detection of Lineaments in Denizli Basin of Western Anatolia Region Using Bouguer Gravity Data. Pure Appl. Geophys. 172, 415–425.

Andritsos, N., Dalambakis, P., Arvanitis, A., Papachristou, M., & Fytikas, M. (2015). Geothermal developments in Greece–Country update 2010-2014. In Proceedings World Geothermal Congress 2015 (pp. 19-24).

Asti, R. (2016). A source-to-sink history of supradetachment Gediz Graben (W Turkey): from exhumation of the Central Menderes Massif through the Gediz Detachment Fault to sedimentation in the graben.

Aydın, İ., Karat, H. İ., & Koçak, A. (2005). Curie-point depth map of Turkey. Geophysical Journal International, 162(2), 633-640.

Baba, A., Bundschuh, J., & Chandrasekharam, D. (2014). Geothermal systems and energy resources: Turkey and Greece. CRC Press.

Baba, A., Şimşek, C., Gündüz, O., Elçi, A., & Murathan, A. (2015). Hydrogeochemical Properties of Geothermal Fluid and Its Effect on the Environment in Gediz Graben, Western Turkey.

Bayrak, M., Serpen, Ü., & İlkışık, O.M. (2011). Two-dimensional resistivity imaging in the Kızıldere geothermal field by MT and DC methods. J. Volcanol. Geotherm. Res. 204, 1–11.

Bayram, A. F., & Simsek, S. (2005). Hydrogeochemical and isotopic survey of Kütahya-Simav geothermal field. In Proceedings of World Geothermal Congress, Antalya, Turkey (pp. 24-29).

Beaudoin, A., Augier, R., Laurent, V., Jolivet, L., Lahfid, A., Bosse, V., ... & Menant, A. (2015). The ikaria high-temperature metamorphic core complex (Cyclades, Greece): geometry, kinematics and thermal structure. Journal of Geodynamics, 92, 18-41.

Bennett, R. A., Wernicke, B. P., Niemi, N. A., Friedrich, A. M., & Davis, J. L. (2003). Contemporary strain rates in the northern Basin and Range province from GPS data. Tectonics, 22(2).

Benoit, D. (1999). Conceptual models of the Dixie Valley, Nevada geothermal field. Transactions-Geothermal Resources Council, 505-512.

Bense, V. F., & Person, M. A. (2006). Faults as conduit-barrier systems to fluid flow in siliciclastic sedimentary aquifers. Water Resources Research, 42(5).

Bertani, R. (2016). Geothermal power generation in the world 2010–2014 update report. Geothermics 60, 31–43.

Bilim, F., Akay, T., Aydemir, A., & Kosaroglu, S. (2016). Curie point depth, heat-flow and radiogenic heat production deduced from the spectral analysis of the aeromagnetic data for geothermal investigation on the Menderes Massif and the Aegean Region, western Turkey. Geothermics, 60, 44-57.

Biryol, C.B., Beck, S.L., Zandt, G., & Özacar, A.A. (2011). Segmented African lithosphere beneath the Anatolian region inferred from teleseismic P-wave tomography. Geophys. J. Int. 184, 1037–1057.

Blackwell, D. D., Golan, B., & Benoit, D. (2000). Thermal regime in the Dixie Valley geothermal system. Geothermal Resources Council Transactions, 24, 223-228.

Bonneau, M. & Kienast, J.R. (1982). Subduction, collision et schistes bleus: exemple de l'Egée, Grèce. Bull. Soc. géol. France, 7: 785-791.

Bozkurt, E. (2001). Late Alpine evolution of the central Menderes Massif, western Turkey. Int. J. Earth Sci. 89, 728–744. doi:10.1007/s005310000141

Bozkurt, E. & Oberhänsli, R. (2001). Menderes Massif (Western Turkey): structural, metamorphic and magmatic evolution–a synthesis. Int. J. Earth Sci. 89, 679–708.

Bozkurt, E., & Sözbilir, H. (2004). Tectonic evolution of the Gediz Graben: field evidence for an episodic, two-stage extension in western Turkey. Geol. Mag. 141, 63–79.

Bozkurt, E., Satır, M., & Buğdaycıoğlu, Ç. (2011). Surprisingly young Rb/Sr ages from the Simav extensional detachment fault zone, northern Menderes Massif, Turkey. J. Geodyn. 52, 406–431.

Buck, W. R. (1988). Flexural rotation of normal faults. Tectonics, 7(5), 959-973.

Bülbül, A., Özen, T., & Tarcan, G. (2011). Hydrogeochemical and hydrogeological investigations of thermal waters in the Alasehir-Kavaklidere area (Manisa-Turkey). Afr. J. Biotechnol. 10, 17223–17240.

Bunbury, J. M., Hall, L., Anderson, G. J., & Stannard, A. (2001). The determination of fault movement history from the interaction of local drainage with volcanic episodes. Geological Magazine, 138(2), 185-192.

Buscher, J. T., Hampel, A., Hetzel, R., Dunkl, I., Glotzbach, C., Struffert, A., ... & Rätz, M. (2013). Quantifying rates of detachment faulting and erosion in the central Menderes Massif (western Turkey) by thermochronology and cosmogenic 10Be. Journal of the Geological Society, 170(4), 669-683.

Caine, J. S., Evans, J. P., & Forster, C. B. (1996). Fault zone architecture and permeability structure. Geology, 24(11), 1025-1028.

Catlos, E. J., & Cemen, I. (2005). Monazite ages and the evolution of the Menderes Massif, western Turkey. International Journal of Earth Sciences, 94(2), 204-217.

Cenki-Tok, B., Expert, M., Işık, V., Candan, O., Monie, P., & Bruguier, O. (2016). Complete Alpine reworking of the northern Menderes Massif, western Turkey. International Journal of Earth Sciences, 105(5), 1507-1524.

Çifçi, G., Pamukçu, O., Çoruh, C., Çopur, S., & Sözbilir, H. (2011). Shallow and deep structure of a supradetachment basin based on geological, conventional deep seismic reflection sections and gravity data in the Buyuk Menderes Graben, western Anatolia. Surveys in Geophysics, 32(3), 271-290.

Ciftci, N. B., & Bozkurt, E. (2007). Anomalous stress field and active breaching at relay ramps: a field example from Gediz Graben, SW Turkey. Geological Magazine, 144(4), 687-699.

Çiftçi, N. B., & Bozkurt, E. (2009a). Evolution of the Miocene sedimentary fill of the Gediz Graben, SW Turkey. Sedimentary Geology, 216(3-4), 49-79.

Çiftçi, N. B., & Bozkurt, E. (2009b). Pattern of normal faulting in the Gediz Graben, SW Turkey. Tectonophysics, 473(1-2), 234-260.

Çiftçi, N.B., & Bozkurt, E. (2010). Structural evolution of the Gediz Graben, SW Turkey: temporal and spatial variation of the graben basin. Basin Res. 22, 846–873.

Cohen, H. A., Dart, C. J., Akyüz, H. S., & Barka, A. (1995). Syn-rift sedimentation and structural development of the Gediz and Büyük Menderes graben, western Turkey. Journal of the Geological Society, 152(4), 629-638.

Collins, A.S., & Robertson, A.H.F. (1998). Processes of Late Cretaceous to Late Miocene episodic thrust-sheet translation in the Lycian Taurides, SW Turkey.

De Boorder, H., Spakman, W., White, S. H., & Wortel, M. J. R. (1998). Late Cenozoic mineralization, orogenic collapse and slab detachment in the European Alpine Belt. Earth and Planetary Science Letters, 164(3), 569-575.

Delvaux, D., & Sperner, B. (2003). New aspects of tectonic stress inversion with reference to the TENSOR program. Geological Society, London, Special Publications, 212(1), 75-100.

Demircioğlu, D., Ecevitoğlu, B., & Seyitoğlu, G. (2010). Evidence of a rolling hinge mechanism in the seismic records of the hydrocarbon-bearing Alaşehir graben, western Turkey. Petroleum Geoscience, 16(2), 155-160.

Dercourt, J., Zonenshain, L.P., Ricou, L.E., Kuzmin, V.G., Le Pichon, X., Knipper, A.L., Grandjacquet, C., Sbortshikov, I.M., Geyssant, J., Lepvrier, C., Pechersky, D.H., Boulin, J., Sibuet, J.C., Savostin, L.A., Sorokhtin, O., Westphal, M., Bazhenov, M.L., Lauer, J.P. & Biju-Duval, B. (1986). Geological evolution of the Tethys belt from the Atlantic to the Pamir since the Lias. Tectonophysics, 123: 241-315.

Dilek, Y., & Altunkaynak, Ş. (2009). Geochemical and temporal evolution of Cenozoic magmatism in western Turkey: mantle response to collision, slab break-off, and lithospheric tearing in an orogenic belt. Geol. Soc. Lond. Spec. Publ. 311, 213–233.

Dolmaz, M. N., Ustaömer, T., Hisarli, Z. M., & Orbay, N. (2005). Curie point depth variations to infer thermal structure of the crust at the African-Eurasian convergence zone, SW Turkey. Earth, planets and space, 57(5), 373-383.

Dora, O.Ö., Kun, N., & Candan, O. (1990). Metamorphic history and geotectonic evoultion of the Menderes Massif. IESCA Proc2:102-115.

Drahor, M.G., & Berge, M.A. (2006). Geophysical investigations of the Seferihisar geothermal area, Western Anatolia, Turkey. Geothermics 35, 302–320..

Duchene, S., Aissa, R., & Vanderhaeghe, O. (2006). Pressure-temperature-time evolution of metamorphic rocks from Naxos (Cyclades, Greece): Constraints from thermobarometry and Rb/Sr dating. Geodinamica Acta, 19(5), 301-321.

Emre, T. (1992). Gediz grabeni'nin (Salihli-Alaflehir arasi) jeolojisi. 45. Turkiye Jeoloji Kurultayi Bildiri Ozleri, s.60.

Emre, T., & Sözbilir, H. (1997). Field evidence for metamorphic core complex, detachment faulting and accommodation faults in the Gediz and Büyük Menderes grabens, western Anatolia, in: International Earth Sciences Colloquium on the Aegean Region, Izmir-Güllük, Turkey. pp. 73–93.

Endrun, B., Lebedev, S., Meier, T., Tirel, C., & Friederich, W. (2011). Complex layered deformation within the Aegean crust and mantle revealed by seismic anisotropy. Nature Geoscience, 4(3), 203.

Epstein, S., Sharp, R. P., & Gow, A. J. (1965). Six-year record of oxygen and hydrogen isotope variations in South Pole firn. Journal of Geophysical Research, 70(8), 1809-1814.

Erdoğan, B. (1990). İzmir-Ankara Zonu'nun, İzmir ile Seferihisar arasındaki bölgede stratigrafik özellikleri ve tektonik evrimi. TPJD Bül. 2, 1–20.

Erkan, K. (2014). Crustal heat flow measurements in western Anatolia from borehole equilibrium temperatures. Solid Earth Discuss. 6, 403–426.

Erkan, K. (2015). Geothermal investigations in western Anatolia using equilibrium temperatures from shallow boreholes. Solid Earth, 6(1), 103.

Ersoy, E.Y. Helvacı, C., & Palmer, M.R., (2010). Mantle source characteristics and melting models for the earlymiddle Miocene mafic volcanism in Western Anatolia: implications for enrichment processes of mantle lithosphere and origin of K-rich volcanism in postcollisional settings. Journal of Volcanology and Geothermal Research, 198, 112–128.

Eyidoğan, H., & Jackson, J. (1985). A seismological study of normal faulting in the Demirci, Alaşehir and Gediz earthquakes of 1969–70 in western Turkey: Implications for the nature and geometry of deformation in the continental crust. Geophysical Journal International, 81(3), 569-607.

Faccenna, C., Piromallo, C., Crespo-Blanc, A., Jolivet, L. & Rossetti, F. (2004). Lateral slab deformation and the origin of the Western Mediterranean arcs. Tectonics, 23: doi:10.1029/2002TC001488.

Faccenna, C., Bellier, O., Martinod, J., Piromallo, C., & Regard, V. (2006). Slab detachment beneath eastern Anatolia: A possible cause for the formation of the North Anatolian fault. Earth and Planetary Science Letters, 242(1-2), 85-97.

Famin, V., Philippot, P., Jolivet, L., & Agard, P. (2004). Evolution of hydrothermal regime along a crustal shear zone, Tinos Island, Greece. Tectonics 23.

Famin, V., Hébert, R., Philippot, P., & Jolivet, L. (2005). Ion probe and fluid inclusion evidences for co-seismic fluid infiltration in a crustal detachment. Contrib. Mineral. Petrol., 150(3): 354-367, DOI 10.1007/s00410-005-0031-x.

Faulds, J. E., Coolbaugh, M., Blewitt, G., & Henry, C. D. (2004). Why is Nevada in hot water? Structural controls and tectonic model of geothermal systems in the northwestern Great Basin. Geothermal Resources Council Transactions, 28, 649-654.

Faulds, J., Coolbaugh, M., Bouchot, V., Moek, I., & Oguz, K. (2010). Characterizing Structural Controls of Geothermal Reservoirs in the Great Basin, USA, and Western Turkey: Developing Successful Exploration Strategies in Extended Terranes. Presented at the World Geothermal Congress 2010, p. 11 p.

Faulds, J. E., Hinz, N. H., Coolbaugh, M. F., Cashman, P. H., Kratt, C., Dering, G., ..., & McLachlan, H. (2011). Assessment of favorable structural settings of geothermal systems in the Great Basin, western USA. Geothermal Resources Council Transactions, 35, 777-783.

Faulds, J. E., Hinz, N., Kreemer, C., & Coolbaugh, M. (2012). Regional patterns of geothermal activity in the Great Basin Region, Western USA: correlation with strain rates. Geothermal Resources Council Transactions, 36, 897-902.

Filiz, S., Tarcan, G., & Gemici, U. (2000). Geochemistry of the Germencik geothermal fields, Turkey, in: Proceedings of the World Geothermal Congress. pp. 1115–1120.

Gemici, Ü., & Tarcan, G. (2002). Hydrogeochemistry of the Simav geothermal field, western Anatolia, Turkey. Journal of Volcanology and Geothermal Research, 116(3-4), 215-233.

Genç, C. Ş., Altunkaynak, Ş., Karacık, Z., Yazman, M., & Yılmaz, Y. (2001). The Çubukludağ graben, south of İzmir: its tectonic significance in the Neogene geological evolution of the western Anatolia. Geodinamica Acta, 14(1-3), 45-55.

Gessner, K., Piazolo, S., Güngör, T., Ring, U., Kröner, A., & Passchier, C.W. (2001a). Tectonic significance of deformation patterns in granitoid rocks of the Menderes nappes, Anatolide belt, southwest Turkey. Int. J. Earth Sci. 89, 766–780.

Gessner, K., Ring, U., Johnson, C., Hetzel, R., Passchier, C.W., & Güngör, T. (2001b). An active bivergent rolling-hinge detachment system: Central Menderes metamorphic core complex in western Turkey. Geology 29, 611–614.

Gessner, K., Gallardo, L. A., Markwitz, V., Ring, U., & Thomson, S. N. (2013). What caused the denudation of the Menderes Massif: Review of crustal evolution, lithosphere structure, and dynamic topography in southwest Turkey. Gondwana Research, 24(1), 243-274.

Gessner, K., Markwitz, V., & Güngör, T. (2017). Crustal fluid flow in hot continental extension: tectonic framework of geothermal areas and mineral deposits in western Anatolia. Geological Society, London, Special Publications, 453, SP453-7.

Glodny, J., & Hetzel, R. (2007). Precise U–Pb ages of syn-extensional Miocene intrusions in the central Menderes Massif, western Turkey. Geological Magazine, 144(2), 235-246.

Gottardi, R., Teyssier, C., Mulch, A., Vennemann, T. W., & Wells, M. L. (2011). Preservation of an extreme transient geotherm in the Raft River detachment shear zone. Geology, 39(8), 759-762.

Govers, R. & Wortel, M.J.R. (2005). Lithosphere tearing at STEP faults: Response to edges of subduction zones. Earth and Planet. Sci. Lett., 236 505– 523.

Govers, R. & Fichtner, A. (2016). Signature of slab fragmentation beneath Anatolia from full-waveform tomography. Earth and Planetary Science Letters 450 10–19; http://dx.doi.org/10.1016/j.epsl.2016.06.014.

Güleç, N. (1988). Helium-3 distribution in western Turkey. Miner. Res Expl Bull 108, 35–42.

Güleç, N., & Hilton, D.R. (2006). Helium and heat distribution in western Anatolia, Turkey: Relationship to active extension and volcanism. Geol. Soc. Am. Spec. Pap. 409, 305–319.

Güleç, N., Hilton, D.R., & Mutlu, H. (2002). Helium isotope variations in Turkey: relationship to tectonics, volcanism and recent seismic activities. Chem. Geol. 187, 129–142.

Güngör, T., & Erdoğan, B. (2002). Tectonic significance of mafic volcanic rocks in a Mesozoic sequence of the Menderes Massif, West Turkey. International Journal of Earth Sciences, 91(3), 386-397.

Gürer, Ö. F., Sarica-Filoreau, N., Özburan, M., Sangu, E., & Doğan, B. (2009). Progressive development of the Büyük Menderes Graben based on new data, western Turkey. Geological Magazine, 146(5), 652-673.

Haizlip, J. R., Haklidir, F. T., & Garg, S. K. (2013). Comparison of Reservoir Conditions in High Noncondensible Gas Geothermal Systems. In proceedings, 38th Workshop on Geothermal Reservoir Engineering (pp. 11-13).

Haklidir, F. T., Sengun, R., & Haizlip, J. R. (2015). The Geochemistry of the Deep Reservoir Wells in Kizildere (Denizli City) Geothermal Field (Turkey). Geochemistry, 19, 25.

Hetzel, R., Passchier, C.W., Ring, U., & Dora, Ö.O. (1995a). Bivergent extension in orogenic belts: the Menderes Massif (southwestern Turkey). Geology 23, 455–458.

Hetzel, R., Ring, U., Akal, C., & Troesch, M. (1995b). Miocene NNE-directed extensional unroofing in the Menderes Massif, southwestern Turkey. J. Geol. Soc. 152, 639–654.

Hetzel, R., Zwingmann, H., Mulch, A., Gessner, K., Akal, C., Hampel, A., Güngör, T., Petschick, R., Mikes, T., & Wedin, F. (2013). Spatiotemporal evolution of brittle normal faulting and fluid infiltration in detachment fault systems: A case study from the Menderes Massif, western Turkey. Tectonics 32, 364–376.

Isik, V., Tekeli, O., & Cemen, I. (1997). Mylonitic fabric development along a detachment surface in northern Menderes massif, western Anatolia, Turkey. In Geol. Soc. America, Abstracts with Programs.

Işik, V., & Tekeli, O. (2001). Late orogenic crustal extension in the northern Menderes Massif (western Turkey): evidence for metamorphic core complex formation. Int. J. Earth Sci. 89, 757–765.

Işık, V., Seyitoğlu, G., & Cemen, I. (2003). Ductile–brittle transition along the Alaşehir detachment fault and its structural relationship with the Simav detachment fault, Menderes Massif, western Turkey. Tectonophysics 374, 1–18.

Isik, V., Tekeli, O., & Seyitoglu, G. (2004). The 40Ar/39Ar age of extensional ductile deformation and granitoid intrusion in the northern Menderes core complex: implications for the initiation of extensional tectonics in western Turkey. Journal of Asian Earth Sciences, 23(4), 555-566.

İztan, H., & Yazman, M. (1990). Geology and hydrocarbon potential of the Alaşehir (Manisa) area, western Turkey. In Proceedings of International Earth Sciences Congress, Aegean Region (pp. 327-333).

Jolie, E., Klinkmueller, M., Moeck, I., & Bruhn, D. (2016). Linking gas fluxes at Earth's surface with fracture zones in an active geothermal field. Geology, G37412-1.

Jolivet, L., & Faccenna, C. (2000). Mediterranean extension and the Africa-Eurasia collision. Tectonics 19, 1095–1106. doi:10.1029/2000TC900018

Jolivet, L., & Brun, J.P. (2010). Cenozoic geodynamic evolution of the Aegean. Int J Earth Sci Geol Rundsch 99, 109–138. doi:10.1007/s00531-008-0366-4Jolivet, L., Goffé, B., Monié, P., Truffert-Luxey, C., Patriat, M., Bonneau, M., 1996. Miocene detachment in Crete and exhumation P-T-t paths of high-pressure metamorphic rocks. Tectonics, 15(6), 1129-1153.

Jolivet, L., Faccenna, C., Huet, B., Labrousse, L., Le Pourhiet, L., Lacombe, O., ..., & Philippon, M. (2013). Aegean tectonics: Strain localisation, slab tearing and trench retreat. Tectonophysics, 597, 1-33.

Jolivet, L., Menant, A., Sternai, P., Rabillard, A., Arbaret, L., Augier, R., Laurent, V., Beaudoin, A., Grasemann, B., Huet, B., Labrousse, L., & Le Pourhiet., L. (2015). The geological signature of a slab tear below the Aegean. Tectonophysics, 659, 166-182. doi:10.1016/j.tecto.2015.08.004

Jongsma, D. (1974). Heat flow in the Aegean Sea. Geophysical Journal International, 37(3), 337-346.Karabulut, H., A. Paul, T. Afacan Ergün, D. Hatzfeld, D. M. Childs, M. Aktar, 2013. Long-wavelength undulations of the seismic Moho beneath the strongly stretched Western Anatolia, Geophys. J. Int. , 194, 450–464; doi: 410.1093/gji/ggt1100.

Karakuş, H. (2015). Helium and carbon isotope composition of gas discharges in the Simav Geothermal Field, Turkey: Implications for the heat source. Geothermics, 57, 213-223.

Karamanderesi, İ.H. (1997). Salihli-Caferbey (Manisa Ili) jeotermal sahası potansiyelive gelecegi. Dunya Enerji Konseyi Turk Milli Komitesi, Turkiye 7. Enerji Kongresi teknik oturum bildiri metinleri, pp. 247–261 (in Turkish).

Karamanderesi, İ.H. (2013). Characteristics of Geothermal Reservoirs in Turkey. IGA Academy Report 0102-2013.

Karamanderesi, İ.H., & Helvaci, C. (2003). Geology and hydrothermal alteration of the Aydın-Salavatlı geothermal field, western Anatolia, Turkey. Turk. J. Earth Sci. 12, 175–198.

Kaya, A. (2015). The effects of extensional structures on the heat transport mechanism: An example from the Ortakçı geothermal field (Büyük Menderes Graben, SW Turkey). J. Afr. Earth Sci. 108, 74–88.

Kaya, O., Ünay, E., Göktaş, F., & Saraç, G. (2007). Early Miocene stratigraphy of Central West Anatolia, Turkey: implications for the tectonic evolution of the Eastern Aegean area. Geological Journal, 42(1), 85-109.

Kaypak, B., & Gökkaya, G. (2012). 3-D imaging of the upper crust beneath the Denizli geothermal region by local earthquake tomography, western Turkey. Journal of Volcanology and Geothermal Research, 211, 47-60.

Kennedy, B. M., & Van Soest, M. C. (2007). Flow of mantle fluids through the ductile lower crust: Helium isotope trends. Science, 318(5855), 1433-1436.

Kennedy, B. M. Kharaka, Y. K., Evans, W. C., Ellwood, A., DePaolo, D. J., Thordsen, J., ..., & Mariner, R. H., (1997). Mantle fluids in the San Andreas fault system, California. Science, 278(5341), 1278-1281.

Kent, E., Boulton, S. J., Stewart, I. S., Whittaker, A. C., & Alçiçek, M. C. (2016). Geomorphic and geological constraints on the active normal faulting of the Gediz (Alaşehir) Graben, Western Turkey. Journal of the Geological Society, jgs2015-121.

Kindap, A., Kaya, T., Haklıdır, F.S.T., & Bükülmez, A.A. (2010). Privatization of Kizildere Geothermal Power Plant and New Approaches for Field and Plant, in: Proceedings World Geothermal Congress.

Koçyiğit, A. (2015). An overview on the main stratigraphic and structural features of a geothermal area: the case of Nazilli-Buharkent section of the Büyük Menderes Graben, SW Turkey. Geodinamica Acta, 27(2-3), 85-109.

Koçyigit, A., Yusufoglu, H., & Bozkurt, E. (1999). Discussion on evidence from the Gediz Graben for episodic two-stage extension in western Turkey. Journal of the Geological Society, London, 156, 1240-1242.

Koçyiğit, A., Unai, E., & Saraç, G. (2000). Episodic graben formation and extensional neotectonic regime in west Central Anatolia and the Isparta Angle: a case study in the Akşehir-Afyon Graben, Turkey. Geological Society, London, Special Publications, 173(1), 405-421.

Kose, R. (2007). Geothermal energy potential for power generation in Turkey: a case study in Simav, Kutahya. Renewable and Sustainable Energy Reviews, 11(3), 497-511.

Kulongoski, J. T., Hilton, D. R., & Izbicki, J. A. (2005). Source and movement of helium in the eastern Morongo groundwater Basin: the influence of regional tectonics on crustal and mantle helium fluxes. Geochimica et cosmochimica Acta, 69(15), 3857-3872.

Lachenbruch, A.H., & Saas, J. H. (1992). Heat flow from Cajon Pass, fault strength, and tectonic implications. J. Geophys. Res 97, 4995-5015.

Larson, L. T., & Erler, Y. A. (1993). The epithermal lithogeochemical signature—a persistent characterization of precious metal mineralization at Kursunlu and Örencik, two prospects of very different geology in western Turkey. Journal of Geochemical Exploration, 47(1-3), 321-331.

Laurent, V., Beaudoin, A., Jolivet, L., Arbaret, L., Augier, R., Rabillard, A., & Menant, A. (2015). Interrelations between extensional shear zones and synkinematic intrusions: The example of Ikaria Island (NE Cyclades, Greece). Tectonophysics, 651, 152-171.

Leloup, P.H., Ricard, Y., Battaglia, J., & Lacassin, R. (1999). Shear heating in continental strike-slip shear zones: model and field examples. Geophys. J. Int. 136, 19–40.

Lips, A. L., Cassard, D., Sözbilir, H., Yilmaz, H., & Wijbrans, J. R. (2001). Multistage exhumation of the Menderes massif, western Anatolia (Turkey). International Journal of Earth Sciences, 89(4), 781-792.

Maddy, D., Veldkamp, A., Demir, T., van Gorp, W., Wijbrans, J. R., van Hinsbergen, D. J. J., ..., & Stemerdink, C. (2017). The Gediz River fluvial archive: A benchmark for Quaternary research in Western Anatolia. Quaternary science reviews, 166, 289-306.

Magri, F., Akar, T., Gemici, U., & Pekdeger, A. (2010). Deep geothermal groundwater flow in the Seferihisar–Balçova area, Turkey: results from transient numerical simulations of coupled fluid flow and heat transport processes. Geofluids 10, 388–405.

Malinverno, A., & Ryan, W. B. F. (1986). Extension in the Tyrrhenian Sea and shortening in the Apennines as result of arc migration driven by sinking of the lithosphere. Tectonics 5, 227–245. doi:10.1029/TC005i002p00227

Marty, B., O'nions, R. K., Oxburgh, E. R., Martel, D., & Lombardi, S. (1992). Helium isotopes in Alpine regions. Tectonophysics, 206(1), 71-78.

McCaig, A. M. (1988). Deep fluid circulation in fault zones. Geology, 16(10), 867-870.

Menant, A., Jolivet, L., & Vrielynck, B. (2016). Kinematic reconstructions and magmatic evolution illuminating crustal and mantle dynamics of the eastern Mediterranean region since the late Cretaceous. Tectonophysics, 675, 103-140.

Menant, A., Jolivet, L., Tuduri, J., Loiselet, C., Bertrand, G. & Guillou-Frottier, L. (2018). 3D subduction dynamics: A first-order parameter of the transition from copper- to gold-rich deposits in the eastern Mediterranean region. Ore Geology Reviews, 94: 118-135.

Mendrinos, D., Choropanitis, I., Polyzou, O., & Karytsas, C. (2010). Exploring for geothermal resources in Greece. Geothermics 39, 124–137.

Moeck, I. S. (2014). Catalog of geothermal play types based on geologic controls. Renewable and Sustainable Energy Reviews, 37, 867–882.

Moeck, I. S., Schandelmeier, H., & Holl, G. H. (2009). The stress regime in a Rotliegend reservoir of the Northeast German Basin. International Journal of Earth Sciences, 98(7), 1643–1654.

Mulch, A., Teyssier, C., Cosca, M. A., & Chamberlain, C. P. (2007). Stable isotope paleoaltimetry of Eocene core complexes in the North American Cordillera. Tectonics, 26(4).

Mutlu, H., Güleç, N., & Hilton, D. R. (2008). Helium–carbon relationships in geothermal fluids of western Anatolia, Turkey. Chem. Geol. 247, 305–321.

Oliver, N. H. S. (1996). Review and classification of structural controls on fluid flow during regional metamorphism. J. Metamorph. Geol.14 (4), 477–492.

O'nions, R. K., & Oxburgh, E. R. (1988). Helium, volatile fluxes and the development of continental crust. Earth and Planetary Science Letters, 90(3), 331-347.

Oner, Z., & Dilek, Y. (2011). Supradetachment basin evolution during continental extension: the Aegean province of western Anatolia, Turkey. Geological Society of America Bulletin 123, 2115–2141. http://dx.doi.org/10.1130/B30468.1.

Oner, Z., & Dilek, Y. (2013). Fault kinematics in supradetachment basin formation, Menderes core complex of western Turkey. Tectonophysics, 608, 1394-1412.

Ozdemir, A., Yasar, E., & Cevik, G. (2017). An importance of the geological investigations in Kavaklıdere geothermal field (Turkey). Geomechanics and Geophysics for Geo-Energy and Geo-Resources, 3(1), 29-49.

Özen, T., Bülbül, A., & Tarcan, G. (2012). Reservoir and hydrogeochemical characterizations of geothermal fields in Salihli, Turkey. J. Asian Earth Sci. 60, 1–17.

Özgür, N. (2002). Geochemical signature of the Kizildere geothermal field, western Anatolia, Turkey. Int. Geol. Rev. 44, 153–163.

Özgür, N., Pekdeger, A., Wolf, M., Stichler, W., Seiler, K. P., & Satir, M. (1998a). Hydrogeochemical and isotope geochemical features of the thermal waters of Kizildere, Salavatli, and Germencik in the rift zone of the

Büyük Menderes, western Anatolia, Turkey: Preliminary studies. In Proceedings of 9th International Symposium on Water-Rock Interaction, Taupo, New Zealand (Vol. 30, pp. 645-648).

Özgür, N., Vogel, M., & Pekdeger, A. (1998b). A new type of hydrothermal alteration at the Kizildere geothermal field in the rift zone of the Biiyiik Menderes, western Anatolia, Turkey.

Özgür, N., & Karamenderesi, I. H. (2015). An update of the geothermal potential in the continental rift zone of the Büyük Menderes, Western Anatolia, Turkey. In Proceedings, Fortieth Workshop on Geothermal Reservoir Engineering Stanford University (pp. 26-28).

Özkaymak, Ç., Sözbilir, H., & Uzel, B. (2013). Neogene–Quaternary evolution of the Manisa Basin: Evidence for variation in the stress pattern of the İzmir-Balıkesir Transfer Zone, western Anatolia. Journal of Geodynamics, 65, 117-135.

Pfister, M., Rybach, L., & Simsek, S. (1998). Geothermal reconnaissance of the Marmara Sea region (NW Turkey): surface heat flow density in an area of active continental extension. Tectonophysics, Heat Flow and the Structure of the Lithosphere - IV 291, 77–89. doi:10.1016/S0040-1951(98)00032-8

Pik, R., & Marty, B. (2009). Helium isotopic signature of modern and fossil fluids associated with the Corinth rift fault zone (Greece): implication for fault connectivity in the lower crust. Chemical Geology, 266(1), 67-75.

Piromallo, C., & Morelli, A. (2003). P wave tomography of the mantle under the Alpine-Mediterranean area. Journal of Geophysical Research: Solid Earth, 108(B2). https://doi.org/10.1029/2002JB001757

Prelević, D., Akal, C., Foley, S. F., Romer, R. L., Stracke, A., & Van Den Bogaard, P. (2012). Ultrapotassic mafic rocks as geochemical proxies for post-collisional dynamics of orogenic lithospheric mantle: the case of southwestern Anatolia, Turkey. Journal of Petrology, 53(5), 1019-1055.

Purvis, M., & Robertson, A. (2004). A pulsed extension model for the Neogene–Recent E–W-trending Alaşehir Graben and the NE–SW-trending Selendi and Gördes Basins, western Turkey. Tectonophysics, 391(1-4), 171-201.

Purvis, M., & Robertson, A. (2005). Sedimentation of the Neogene–Recent Alaşehir (Gediz) continental graben system used to test alternative tectonic models for western (Aegean) Turkey. Sediment. Geol. 173, 373–408.

Quilichini, A., Siebenaller, L., Nachlas, W. O., Teyssier, C., Vennemann, T. W., Heizler, M. T., & Mulch, A. (2015). Infiltration of meteoric fluids in an extensional detachment shear zone (Kettle dome, WA, USA): How quartz dynamic recrystallization relates to fluid-rock interaction. Journal of Structural Geology, 71, 71-85.

Reilinger, R., McClusky, S., Vernant, P., Lawrence, S., Ergintav, S., Cakmak, R., Ozener, H., Kadirov, F., Guliev, I., Stepanyan, R., Nadariya, M., Hahubia, G., Mahmoud, S., Sakr, K., ArRajehi, A., Paradissis, D., Al-Aydrus, A., Prilepin, M., Guseva, T., Evren, E., Dmitrotsa, A., Filikov, S.V., Gomez, F., Al-Ghazzi, R., & Karam, G. (2006). GPS constraints on continental deformation in the Africa-Arabia-Eurasia continental collision zone and implications for the dynamics of plate interactions. J. Geophys. Res. Solid Earth 111, B05411. doi:10.1029/2005JB004051

Richardson-Bunbury, J. M. (1996). The Kula volcanic field, western Turkey: the development of a Holocene alkali basalt province and the adjacent normal-faulting graben. Geological Magazine, 133(3), 275-283.

Ring, U., Gessner, K., Güngör, T., & Passchier, C. W. (1999). The Menderes Massif of western Turkey and the Cycladic Massif in the Aegean—do they really correlate?. Journal of the Geological Society, 156(1), 3-6.

Ring, U., Johnson, C., Hetzel, R., & Gessner, K. (2003). Tectonic denudation of a Late Cretaceous–Tertiary collisional belt: regionally symmetric cooling patterns and their relation to extensional faults in the Anatolide belt of western Turkey. Geol. Mag. 140, 421–441.

Ring, U., Glodny, J., Will, T., & Thomson, S. (2010). The Hellenic subduction system: high-pressure metamorphism, exhumation, normal faulting, and large-scale extension. Annual Review of Earth and Planetary Sciences, 38, 45-76.

Ring, U., Gessner, K., & Thomson, S. (2017). Variations in fault-slip data and cooling history reveal corridor of heterogeneous backarc extension in the eastern Aegean Sea region. Tectonophysics, 700, 108-130.

Roche, V., Guillou-Frottier, L., Jolivet, L., Loiselet, C., & Bouchot, V. (2015). Subduction and slab tearing dynamics constrained by thermal anomalies in the Anatolia-Aegean region. Geophysical Research Abstracts Vol. 17, EGU2015-6882, 2015 EGU General Assembly 2015.

Roche, V., Sternai, P., Guillou-Frottier, L., Jolivet, L., & Gerya, T. (2016). Location of eastern Mediterranean hot springs induced by mantle heat flow due to slab roll-back and tearing. AGU

Roche, V., Sternai, P., Guillou-Frottier, L., Menant, A., Jolivet, L., Bouchot, V., & Gerya, T. (2018). Emplacement of metamorphic core complexes and associated geothermal systems controlled by slab dynamics. Earth and Planetary Science Letters, 498, 322-333.

Ross, H. E., Blakely, R. J., & Zoback, M. D. (2006). Testing the use of aeromagnetic data for the determination of Curie depth in California. Geophysics, 71(5), L51-L59.

Salaün, G., Pedersen, H.A., Paul, A., Farra, V., Karabulut, H., Hatzfeld, D., Papazachos, C., Childs, D.M., Pequegnat, C., Team, S., & others. (2012). High-resolution surface wave tomography beneath the Aegean-Anatolia region: constraints on upper-mantle structure. Geophys. J. Int. 190, 406–420.

Sarica, N. (2000). The Plio-Pleistocene age of Büyük Menderes and Gediz grabens and their tectonic significance on N-S extensional tectonics in West Anatolia: mammalian evidence from the continental deposits. Geological Journal, 35(1), 1-24.

Schlinger, C. M. (1985). Magnetization of lower crust and interpretation of regional magnetic anomalies: Example from Lofoten and Vesterålen, Norway. Journal of Geophysical Research: Solid Earth, 90(B13), 11484-11504.

Scholz, C. H. (1980). Shear heating and the state of stress on faults. J. Geophys. Res. Solid Earth 85, 6174–6184.

Sen, S., & Seyitoğlu, G. (2009). Magnetostratigraphy of early–middle Miocene deposits from east–west trending Alaşehir and Büyük Menderes grabens in western Turkey, and its tectonic implications. Geological Society, London, Special Publications, 311(1), 321-342.

Serpen, U., Aksoy, N., & Öngür, T. (2015). Reinjection Update of Salavatli Geothermal Field in Turkey.

Seyitoglu, G. (1992). Late Cenozoic crustal extension, basin formation and volcanism in west Turkey.

Seyitoglu, G. (1997). The Simav graben: an example of young EW trending structures in the Late Cenozoic extensional system of western Turkey. Turkish Journal of Earth Sciences, 6, 135-141.

Seyitoğlu, G., & Scott, B. (1991). Late Cenozoic crustal extension and basin formation in west Turkey. Geological Magazine, 128(2), 155-166.

Seyítoğlu, G., & Scott, B. C. (1996). The cause of NS extensional tectonics in western Turkey: tectonic escape vs back-arc spreading vs orogenic collapse. Journal of Geodynamics, 22(1-2), 145-153.

Seyitoğlu, G., & Işik, V. (2015). Late cenozoic extensional tectonics in western anatolia: exhumation of the menderes core complex and formation of related basins. Bulletin Of The Mineral Research and Exploration, (151).

Seyitoğlu, G., Scott, B. C. & Rundle, C. C., (1992). Timing of Cenozoic extensional tectonics in west Turkey. Journal of the Geological Society, 149(4), 533-538.

Seyitoglu, G., Tekeli, O., Çemen, I., Sen, S., & Isik, V. (2002). The role of the flexural rotation/rolling hinge model in the tectonic evolution of the Alasehir graben, western Turkey. Geol. Mag. 139, 15–26.

Seyitoğlu, G., Işık, V., & Cemen, I. (2004). Complete Tertiary exhumation history of the Menderes massif, western Turkey: an alternative working hypothesis. Terra Nova, 16(6), 358-364.

Seyitoğlu, G., Işik, V., & Esat, K. (2014). A 3D model for the formation of turtleback surfaces: the Horzum Turtleback of western Turkey as a case study. Turkish Journal of Earth Sciences, 23(5), 479-494.

Sheppard, S. M. F. (1977). The Cornubian batholith, SW England: D/H and 18O/16O studies of kaolinite and other alteration minerals. Journal of the Geological Society, 133(6), 573-591.

Sheppard, S. M. (1981). Stable isotope geochemistry of fluids. Physics and Chemistry of the Earth, 13, 419-445.

Shimizu, A., Sumino, H., Nagao, K., Notsu, K., & Mitropoulos, P. (2005). Variation in noble gas isotopic composition of gas samples from the Aegean arc, Greece. Journal of Volcanology and Geothermal Research, 140(4), 321-339.

Sibson, R. H., Moore, J. M. M., & Rankin, A. H. (1975). Seismic pumping—a hydrothermal fluid transport mechanism. Journal of the Geological Society, 131(6), 653-659.

Şimşek, Ş. (1984). Aydin-Germencik-Omerbeyli geothermal field of Turkey. In Proc. of UN Seminar on Utilization of Geothermal Energy for Electric Power Production and Space Heating.

Simsek, S. (1985). Geothermal model of Denizli, Sarayköy-Buldan area. Geothermics 14, 393–417.

Simsek, S. (2003). Hydrogeological and isotopic survey of geothermal fields in the Buyuk Menderes graben, Turkey. Geothermics 32, 669–678.

Simsek, S., & Demir, A. (1991). Reservoir and cap rock characteristics of some geothermal fields in turkey and encountered problems based on lithology. J. Geotherm. Res. Soc. Jpn. 13, 191–204.

Souche, A., Medvedev, S., Andersen, T.B., & Dabrowski, M. (2013). Shear heating in extensional detachments: Implications for the thermal history of the Devonian basins of W Norway. Tectonophysics 608, 1073–1085.

Sözbilir, H. (2001). Extensional tectonics and the geometry of related macroscopic structures: field evidence from the Gediz detachment, western Turkey. Turk. J. Earth Sci. 10, 51–67.

Sözbilir, H., & Emre, T. (1990). Neogene stratigraphy and structure of the northern rim of the Büyük Menderes graben. In Proceedings of International Earth Science Colloquium on the Aegean Region (Vol. 2, pp. 314-322).

Spakman, W. & Wortel, R. (2004). A tomographic view on Western Mediterranean geodynamics. In: W. Cavazza, F.M. Roure, W. Spakman, G.M. Stampfli and P.A. Ziegler (Editors), The TRANSMED Atlas - The Mediterranean region from crust to Mantle. Springer, Berlin, Heidelberg, pp. 31-52.

Taillefer, A., Soliva, R., Guillou-Frottier, L., Le Goff, E., Martin, G., & Seranne, M. (2017). Fault-Related Controls on Upward Hydrothermal Flow: An Integrated Geological Study of the Têt Fault System, Eastern Pyrénées (France). Geofluids, 2017.

Tan, O., Tapirdamaz, M. C., & Yörük, A. (2008). The earthquake catalogues for Turkey. Turkish Journal of Earth Sciences, 17(2), 405-418.

Tarcan, G., & Gemici, Ü. (2003). Water geochemistry of the Seferihisar geothermal area, Izmir, Turkey. J. Volcanol. Geotherm. Res. 126, 225–242.

Tarcan, G., Filiz, S., & Gemici, U. (2000). Geology and geochemistry of the Salihli geothermal fields, Turkey. Books Proc. 1829–1834.

Taylor, H. P. (1974). The application of oxygen and hydrogen isotope studies to problems of hydrothermal alteration and ore deposition. Economic geology, 69(6), 843-883.

Tekin, S., & Akin, S. (2011). Estimation of the Formation Temperature from the Inlet and Outlet Mud Temperatures while Drilling Geothermal Formations, in: Proceedings of 36th Workshop on Geothermal Reservoir Engineering. Stanford University, Stanford.

Temiz, U., & Eikenberg, J. (2011). U/Th dating of the travertine deposited at transfer zone between two normal faults and their neotectonic significance: Cambazli fissure ridge travertines (the Gediz Graben-Turkey). Geodinamica acta, 24(2), 95-105.

Tezcan, A. K. (1995). Geothermal explorations and heat flow in Turkey. Terr. Heat Flow Geotherm. Energy Asia 23–42.

Tureyen, O., Gulgor, A., Erkan, B., & Satman, A. (2016). Recent expansions of power plants in Figuris concession in the Germencik geothermal field, Turkey. In Proceedings.

Ulugergerli, E. U., Seyitoğlu, G., Başokur, A. T., Kaya, C., Dikmen, U., & Candansayar, M. E. (2007). The geoelectrical structure of northwestern Anatolia, Turkey. Pure and Applied Geophysics, 164(5), 999-1026.

Ünay, E., Göktaş, F., Hakyemez, H. Y., Avşar, M., & Şan, Ö. (1995). Dating the sediments exposed at the northern part of the Büyük Menderes Graben (Turkey) on the basis of Arvicolidae (Rodentia, Mammalia). Geological Bulletin of Turkey, 38, 75-80.

Uzel, B., & Sözbilir, H. (2008). A First Record of a Strike-slip Basin in Western Anatolia and Its Tectonic Implication: The Cumaovası Basin. Turkish Journal of Earth Sciences, 17(3).

Van Hinsbergen, D. J. (2010). A key extensional metamorphic complex reviewed and restored: the Menderes Massif of western Turkey. Earth-Science Reviews, 102(1-2), 60-76.

Vengosh, A., Helvacı, C., & Karamanderesi, İ. H. (2002). Geochemical constraints for the origin of thermal waters from western Turkey. Appl. Geochem. 17, 163–183.

Wannamaker, P. E., Hasterok, D. P., & Doerner, W. M. (2006). Possible magmatic input to the Dixie Valley geothermal field, and implications for district-scale resource exploration, inferred from magnetotelluric (MT) resistivity surveying. In GRC 2006 Annual Meeting: Geothermal Resources-Securing Our Energy Future.

Wortel, M.J.R. & Spakman, W. (2000). Subduction and slab detachment in the Mediterranean-Carpathian region. Science, 290: 1910-1917.

Yildirim, N., Aydogdu, O., & Sarp, S. (2005). Constraint problems and solution alternatives for potentially available integrated geothermal energy utilization in Turkey. Proc. World Geotherm. Congr. April 24–29.

Yilmaz, Y., Genç, Ş. C., Gürer, F., Bozcu, M., Yilmaz, K., Karacik, Z., ..., & Elmas, A. (2000). When did the western Anatolian grabens begin to develop?. Geological Society, London, Special Publications, 173(1), 353-384.

Yılmazer, S., & Karamanderesi, İ. (1994). Kurşunlu jeotermal alanının (Salihli-Manisa) jeolojisi ve jeotermal potansiteli. Dünya Enerji Konseyi Türkiye 6, 17–22.

Yılmazer, S., Pasvanoğlu, S., & Vural, S. (2010). The relation of geothermal resources with young tectonics in the Gediz graben (West Anatolia, Turkey) and their hydrogeochemical analyses. In Proceedings World Geothermal Congress (pp. 1-10).

CHAPITRE III : Evolution structurale de l'île de Leros (Dodécanèse) : implication géologique dans l'Est de la Méditerranée

Après avoir décrit dans le *chapitre II*, les différentes structures qui contrôlent la circulation des fluides à plusieurs échelles (*i.e.* les détachements, les failles de transfert) et abordé brièvement la possibilité d'une source de chaleur d'origine mantellique dans cette province géothermale, ce chapitre est dédié à l'étude structurale et métamorphique d'une île du Dodécanèse. Cette dernière se localise à l'aplomb de la déchirure du panneau plongeant qui est en partie responsable de l'anomalie thermique observée dans le Menderes. Par ailleurs, bien que l'évolution géodynamique des unités du Massif du Menderes (sud-ouest de la Turquie) et des Cyclades ait été étudiée par la communauté depuis ces dernières années [*e.g.* Bozkurt, 2001 ; Jolivet & Brun, 2010 ; Jolivet *et al.*, 2010 ; 2013 ; Pourteau *et al.*, 2016], ces deux régions possèdent des unités tectono-métamorphiques différentes (*e.g.* HP-BT dans les Cyclades à l'Eocène et HT-BP dans le Massif du Menderes à cette même période). De ce fait, peu d'études proposent des corrélations entre ces deux domaines [Ring *et al.*, 1999 ; Jolivet *et al.*, 2004], et les liens entre les différentes unités sont par conséquent difficiles à interpréter. Ainsi, l'archipel du Dodécanèse, située entre ces deux zones, représente un point essentiel dans la compréhension de l'évolution géodynamique dans la région de la Méditerranée orientale. Paradoxalement, très peu d'études ont été consacrées aux îles du Dodécanèse [Franz & Okrush, 1998 ; Katagas & Sapountzis, 1980 ; Franz *et al.*, 2005] et aucune ne se focalise sur la cinématique de la déformation. Avant d'aborder l'évolution géodynamique de la région (*chapitre IV*), une étude locale a été menée sur l'île de Leros (une des îles du Dodécanèse). Cette île semble propice à une étude structurale dont les données permettraient d'apporter de nouveaux éléments sur l'évolution géodynamique de la région.

L'île de Leros fait partie de l'archipel du Dodécanèse, et présente au premier regard, des unités tectono-métamorphiques variées, regroupées en deux unités principales. L'unité de Marina se compose d'une unité de haut grade métamorphique comprenant des amphibolites massives et des micaschistes à grenat (*i.e.* représentant le socle Paléozoïque) ainsi que d'une couverture non métamorphique définie par des sédiments permo-triasiques et des marbres jurassiques de bas grade. L'unité de Temenia, localisée structuralement sous l'unité de Marina, se compose principalement de schistes, de quartzites et de marbres. Malgré la présence d'amphibole bleue, les conditions métamorphiques ne semblent pas dépasser les 8 kbar [Katagas & Sapountzis, 1980 ; Franz *et al.*, 2005].

La majeure partie de ce travail a donc consisté à décrire et comprendre les relations tectoniques entre les différentes unités (*e.g.* structure, cinématiques de la déformation, nature des contacts). L'étude structurale a principalement été menée dans l'unité de Temenia dont les marqueurs de HP-BT ont été observés. Une autre partie a été dédiée à l'étude des conditions métamorphiques des différentes unités, en cherchant à estimer, dans la mesure du possible, les conditions de pression et de température qu'elles ont enregistrées. De ce fait une approche RSCM (Raman Spectroscopy on Carbonaceous Materials) a été utilisée. Cette méthode est basée sur les relations entre le degré d'organisation de la matière organique (MO) et la température. Ainsi, l'augmentation de la température se traduit par une augmentation du degré d'organisation. La graphitisation est un phénomène irréversible, par conséquent les températures obtenues représentent les températures issues du pic du métamorphisme (T_{max}). Cette

méthode a été calibrée par Beyssac *et al.* [2002] à partir d'échantillons naturels dont les conditions P-T avaient été déterminées par des méthodes indépendantes (*i.e.* thermo-barométrie classique). Elle est donc valable pour des gammes de températures comprises entre 330 et 640 °C. Les incertitudes absolues (*i.e.* liées à la calibration donnée par les estimations P-t) sont estimées à ± 50 °C et les incertitudes relatives associées à la méthode, ne dépassent généralement pas les 15 °C sauf dans de certains cas (*e.g.* MO héritée, gradient de déformation à l'échelle de la lame mince).

Principaux résultats :

Même si la cinématique est parfois difficilement indentifiable sur le terrain à cause des unités lithologiques (*e.g.* marbres et quartzites), cette étude a démontré que l'ensemble de l'unité de Temenia a été affectée par une déformation top-NE. Cette déformation est visible à différentes échelles, principalement marquée par du boudinage asymétrique et des bandes de cisaillement. A l'approche du contact principal entre l'unité de Marina et l'unité de Temenia, la déformation apparait plus intense suggérant l'existence d'un contact tectonique majeur à cinématique vers le NE. A l'échelle régionale, cette cinématique est compatible avec les structures post-orogéniques décrites dans les Cyclades (*e.g.* NCDS [Jolivet *et al.*, 2010]). Il est intéressant de noter que le socle de l'unité de Marina a également enregistré une déformation pénétrative pré-alpine. Par ailleurs, une déformation plus localisée affecte également les deux unités. Cette dernière est remarquable dans la partie centrale de Leros et dans sa partie sud-ouest. Les critères (*e.g.* cisaillement froids) indiquent un mouvement vers le SW, compatible avec l'extension NE-SW dans l'ensemble de la région.

Alors que l'unité de Marina ne semble pas avoir enregistré des conditions métamorphiques de HP-BT durant la phase alpine [Franz *et al.*, 2005], l'unité de Temenia présente des paragenèses HP-BT. La présence d'amphibole bleues dans les métabasites et d'aragonite dans les marbres dans la partie sud de l'île, suggèrent des conditions P-T froides. Par ailleurs, les résultats RSCM sont en accord avec ces observations. En effet, l'unité de Temenia a enregistré des températures maximales comprises entre 430 et 480 °C. A contrario, les températures du socle de l'unité de Marin sont nettement supérieures (~ 600 °C). Il est intéressant de noter que les données T_{max} acquises dans la couverture de Marina confirment également l'absence d'évènement thermique majeur dans ces unités.

En termes de lithologies et d'affinités paléogéographiques, même si le socle Paléozoïque de l'unité de Marina n'a aucun équivalent strict avec les unités du Menderes et des Cyclades, sa couverture présente des similitudes avec l'unité des Nappes Lyciennes. Cette unité, qui affleure au sud du Massif du Menderes, présente des niveaux permo-triasiques similaires à ceux observés dans la couverture de l'unité de Marina. Au contraire, l'unité de Temenia, marqué par des conditions métamorphiques de MP-BT (ré-évaluées par rapport aux précédentes estimations) semble se rapprocher de l'unité des Schistes Bleus Externes Cycladiques [Grasemann *et al.*, 2018]. En résumé, ce travail a permis d'une part,

d'apporter de nouvelles contraintes structurales locales dans cette région, et d'autre part de proposer des corrélations entre la région des Cyclades et celle du Menderes.

Tectonic evolution of Leros Island (Dodecanese, Greece) and correlations between the Aegean Domain and the Menderes Massif

Vincent Roche[1, 2, 3], Clément Conand [1, 2, 3, 4], Laurent Jolivet[5] and Romain Augier[1, 2, 3]

[1] *Université d'Orléans, Institut des Sciences de la Terre d'Orléans (ISTO), UMR7327, 45071, Orléans, France*

[2] *CNRS/INSU, ISTO, UMR7327,45071, Orléans, France*

[3] *BRGM, ISTO, UMR7327, BP36009,45060, Orléans, France*

[4] *Laboratoire Géosciences Environnement Toulouse, UMR 5563, Toulouse, France*

[5] *Sorbonne Université, CNRS-INSU, Institut des Sciences de la Terre Paris, ISTeP UMR 7193, F-75005 Paris, France*

(Cet article a été publié au journal GSL)

Abstract

The history of subduction below the Aegean region and Western Anatolia is hampered by a lack of comprehension of the correlations between the Cyclades and the Menderes Massif. The Dodecanese Archipelago, key for this discussion, has received very little attention so far. This study is focused on the island of Leros where two tectono-metamorphic units can be observed; the upper Marina unit and the lower Temenia unit. The field study, including new field mapping and structural observations, reveals that Temenia unit has been exhumed under Marina unit through a top-to-the-NE ductile shearing followed by a top-to-the-SW brittle deformation cutting the Temenia/Marina contact. The description of metamorphic aragonite and blue amphibole, complemented by RSCM thermometry, reveals that Temenia unit has been buried down to at least 20 km along a cold metamorphic gradient. In terms of lithology and paleogeographic affinities, the cover of Marina unit is similar to the Lycian Nappes that rest on top of the Menderes Massif and belong to the northern margin of the Pelagonian domain. Temenia unit can then be compared to Lower Cycladic Blueschists Nappe, which could in turn be correlated with the cover of the Menderes Massif, which has also recorded a HP-LT metamorphic overprint.

III.1. Introduction

The effects of the dynamics of subducting slabs (retreat, tearing, detachment etc.) on the tectonic evolution of the overriding plate are still highly debated [Carminati *et al.,* 1998; Wortel & Spakman, 2000; Piromallo & Morelli, 2003; Spakman & Wortel, 2004; Faccenna *et al.,* 2004; 2005; Govers & Wortel, 2005; Jolivet *et al.,* 2009; 2013; Sternai *et al.,* 2014]. The Mediterranean area is certainly the most studied and debated area thanks to the high resolution of seismic tomography data. Under the eastern part of the Aegean Sea and West Turkey all studies suggest a slab tearing well imaged by seismic tomography (Fig. III.1) [De Boorder *et al.,* 1998; Salaün *et al.,* 2012; Biryol *et al.,* 2011]. Based on the evolution and migration of the magmatic activity and the chronology of paleomagnetic rotations, Jolivet *et al.* [2015] proposed that this slab tearing happened between 20 and 8 Ma with a faster retreat between 15 and 8 Ma coeval with the fast rotation of the Hellenides revealed by paleomagnetic data [Van Hinsbergen *et al.,* 2005]. Govers & Fichtner [2016] proposed instead that the first tear was formed in the Eocene. Although the age of the tearing is still being discussed, the tectono-metamorphic record in the overriding plate has not yet been fully described, hampering a full comprehension of the coupling between crustal deformation and mantle flow that is suggested by numerical models [*e.g.* Sternai *et al.,* 2014; Menant *et al.,* 2016]. Ring *et al.* [1999], Gessner *et al.* [2013] and Jolivet *et al.* [2013; 2015] have discussed the existence of a distributed left-lateral shear zone between the Menderes Massif and the Aegean Sea, accommodating the differential motion of crustal domains above the STEP-fault, but the exact way crustal deformation accommodates this shearing is still unknown. Because of poorly understood correlations between the Aegean Sea and the Menderes Massif, discussing the tectonic evolution of the crust above the tear remains difficult. Between the Menderes Massif and the Aegean domain, the Dodecanese Archipelago (Fig. III.1a) has received very little attention so far [*e.g.* Katagas, 1980; Franz *et al*., 2005; Ring *et al.,* 2017]. This paper is focused on one of the largest islands of this Archipelago, Leros, where we have studied the contact between two units belonging to both domains, Aegean and Menderes, in order to precise the geological correlations across the STEP-fault region above the tear.

III.2. Geological setting

III.2.1. The Cyclades Archipelago

The Cyclades Archipelago belonging to the Aegean domain is located in the back-arc domain of the Hellenic subduction. This domain has recorded evidence of this subduction-related geodynamics since the Late Cretaceous. Its tectono-metamorphic evolution can be summarized in two major stages: firstly, formation of the Hellenides-Taurides orogenic belt (Late Cretaceous-Eocene) [Bonneau &

Kienast, 1982; Dercourt *et al.,* 1986; Van Hinsbergen *et al.,* 2005] and secondly post-orogenic extension associated with the retreat of the African slab [Jolivet & Faccenna, 2000; Brun & Sokoutis, 2010; Jolivet & Brun, 2010; Ring *et al.,* 2010] accommodated by different crustal-scale detachments such as the North Cycladic Detachment System (NCDS), the West Cycladic Detachment System (WCDS) or the Naxos-Paros Detachment System (Fig. III.1a) [Gautier *et al.,* 1993; Jolivet *et al.,* 2010; Grasemann *et al.,* 2012].

In details, the Cyclades Archipelago, west of the Dodecanese, shows a variety of lithologies metamorphosed under blueschist- and eclogite-facies conditions [Blake *et al.,* 1981; Bröcker, 1990; Okrusch & Bröcker, 1990; Jolivet *et al.,* 2003; 2004; Brun & Faccenna, 2008; Jolivet & Brun, 2010; Ring *et al.,* 2010] forming the Cycladic Blueschists Unit (CBU), whose formation is linked with the burial and exhumation within a subduction zone during the Eocene and subsequent exhumation during the Aegean Sea formation [Jolivet & Brun, 2010; Ring *et al.,* 2010]. Peak-pressure assemblages spectacularly crop out on the islands of Syros or Sifnos, [*e.g.* Trotet *et al.,* 2001; Groppo *et al.,* 2009; Laurent *et al.,* 2016; Roche *et al.,* 2016] but are also quite well preserved despite retrogression in many other islands [*e.g.* Avigad *et al.,* 1998; Parra *et al.,* 2002; Huet *et al.,* 2009; Augier *et al.,* 2015]. There, available P-T estimates point to a common HP-LT event at about 20 – 23 kbar and 550 °C. Recently, Grasemann *et al.* [2018] suggest the existence of two different nappes or subunits within the CBU, the Lower Cycladic Nappe for the lower pressure and the Upper Cycladic Nappe for the higher pressure parageneses. According to this study, these nappes are separated by the newly defined synorogenic Trans Cycladic Thrust (see Fig. III.1a, TCT from Grasemann *et al.* [2018]). These rocks were mainly exhumed below (1) a syn-orogenic detachment (50 – 35 Ma) cropping out on Syros [Trotet *et al.,* 2001; Laurent *et al.,* 2016; Roche *et al.,* 2016] and (2) post-orogenic detachments (after 35 Ma) such as the NCDS [Jolivet *et al.,* 2010], the WCDS [Grasemann *et al.,* 2012] or the NPFS [Urai *et al.,* 1990; Gautier *et al.,* 1993; Bargnesi *et al.,* 2013]. Most detachments show a top-to-the NE kinematics but the southwest part of the Cyclades shows an opposite top-to-the-SW sense of shear [Grasemann *et al.,* 2012]. Resting above the CBU and associated detachments, the hanging-wall Pelagonian unit did not go through an episode of subduction during the formation of the Hellenides. Finally, a late high-temperature episode is recorded during the exhumation of Metamorphic Core Complexes (MCCs) in the Middle and Late Miocene with the formation of migmatite domes in Naxos and Ikaria [Lister *et al.,* 1984; Urai *et al.,* 1990; Rabillard *et al.,* 2015; Beaudoin *et al.,* 2015]. This stage was accompanied by the emplacement of syn-tectonic Miocene I and S-type granites (*i.e.* Tinos, Mykonos, Ikaria, Naxos, Serifos or even Lavrio) [Jansen, 1973; Lee & Lister, 1992; Altherr & Siebel, 2002; Grasemann & Petrakakis, 2007; Iglseder *et al.,* 2009; Rabillard *et al.,* 2015].

III.2.2. The southwestern part of Turkey

The southwestern domain of Turkey is composed of several tectonic units. The Menderes Massif is mainly made up of basement units stacked during the Eocene [*e.g.* Ring *et al.,* 2010; Gessner *et al.,* 2001; Bozkurt & Oberhänsli, 2001; Bozkurt, 2001; Cenki-Tok *et al.,* 2016]. The core of the massif mainly shows a high-temperature overprint while the Permian-Mesozoic cover visible in the south has recorded HP-LT conditions (10 – 12 kbar and 440 °C) [Rimmelé *et al.,* 2003]. Immediately above, the Lycian Nappes, composed of a Permian-Triassic complex and Jurassic-Cretaceous marbles, overlain by the Menderes cover [Rimmelé *et al.,* 2005] and HP-LT metamorphic assemblages (8 – 10 kbar and 420 °C] are observed in the basal unit (Karaova unit or Ören unit) [Rimmelé *et al.,* 2003; Pourteau *et al.,* 2013]. A third unit, the CBU, locally occurs between the Menderes Massif and the Lycian Nappes. On its northern and eastern margins, the Menderes Massif is overthrusted by the Afyon Zone and the Tavşanlı Zone, both with HP-LT parageneses. Both units are overthrusted by the oceanic units of the Izmir-Ankara Tethyan suture zone. The Lycian Nappes root within the suture zone, as shown by the presence of klippes of HP-LT metamorphics with Fe-Mg carpholite on top of the Menderes Massif. The Menderes basement is affected by several Miocene low-angle detachments, later cut by steeply-dipping normal faults controlling the major Simav, Gediz-Alaşehir and Büyük Menderes active grabens. In the north, extension is associated with the formation of migmatites in the Early Miocene [Cenki-Tok *et al.,* 2016]. The direction of extension is NNE-SSW and bivergent [Gessner *et al.,* 2013]. Along the upper contact of the Menderes Massif, E-W and NE-SW stretching lineations and top-to-the-E/NE kinematics are documented within the basal unit of the Lycian Nappes (Ören unit or Karaova unit, see Rimmelé *et al*. [2006] and Pourteau *et al*. [2013]) suggesting the presence of a top-to-the-E/NE detachment between the Menderes Massif and the Lycian Nappes during the earlier exhumation of HP-LT rocks [Rimmelé *et al.,* 2003].

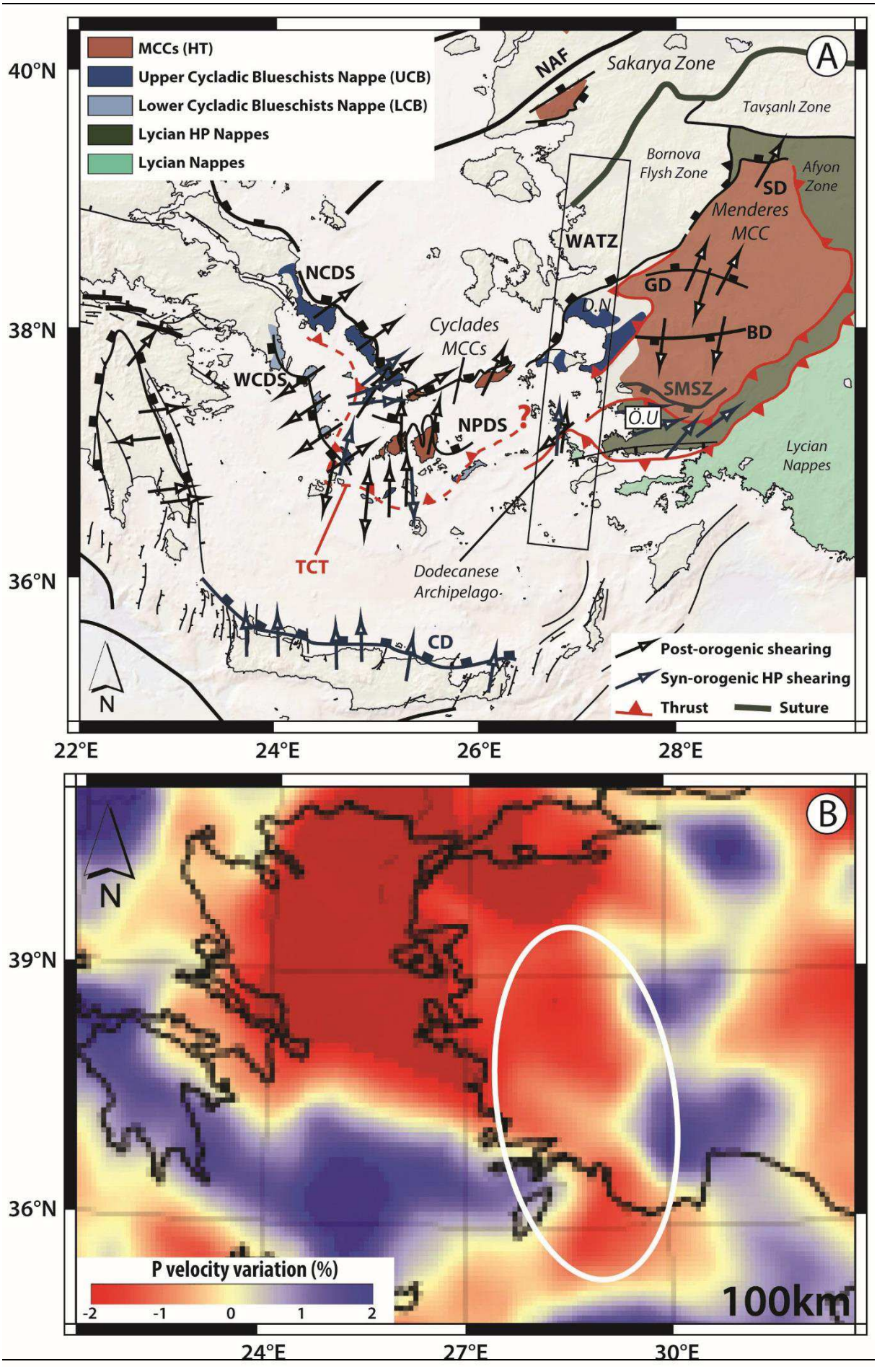
MCCs (HT)
Upper Cycladic Blueschists Nappe (UCB)
Lower Cycladic Blueschists Nappe (LCB)
Lycian HP Nappes
Lycian Nappes
NAF
Sakarya Zone
A
Tavşanlı Zone
Bornova Flysh Zone
Afyon Zone
SD
Menderes MCC
WATZ
NCDS
GD
BD
Cyclades MCCs
WCDS
SMSZ
Ö.U
NPDS
?
Lycian Nappes
TCT
Dodecanese Archipelago
CD
N
Post-orogenic shearing
Syn-orogenic HP shearing
Thrust
Suture
40°N
38°N
36°N
22°E
24°E
26°E
28°E
B
N
39°N
36°N
P velocity variation (%)
-2
-1
0
1
2
100km
24°E
27°E
30°E

Figure III.1: Upper crustal and upper mantle structures of the Eastern Agean domain and the Western Anatolia. (a) Tectonic map of the Western Mediterranean region showing the main faults and associated kinematic indicators. Data are from this study, and from earlier studies in the Cyclades (see Jolivet et al. [2013] and references therein) and in the Menderes Massif and its periphery [Rimmelé et al., 2006]. Abbreviations: BD (Büyük Menderes detachment); CD (Cretan detachment); D.N (Dilek Nappe); GD (Gediz detachment); NAF (North Anatolian Fault); NCDS (The North Cycladic detachment system); NPDS (Naxos-Paros Extensional Fault System); Ö.U (Ören unit); SD (Simav Detachment); SMSZ (southern shear zone); TCT (Trans-Cycladic Thrust); WATZ (West Anatolia Transfer Zone); WCDS (The West Cycladic detachment system). (b) Tomographic model of Piromallo and Morelli [2003]. The white circle illustrates the schematized position of the slab tearing at ~ 100 km.

III.2.3. The Dodecanese Archipelago

The Dodecanese Archipelago is mostly composed of metamorphic rocks belonging to different units that experienced very different P-T evolutions, from MT-MP conditions (*i.e.* upper greenschist to lower amphibolite-facies conditions) of probable Late Paleozoic age [Franz *et al.,* 2005] to HP-LT conditions probably coeval with the Eocene subduction history of the Cyclades on Leros, Kalymnos, Lipsi [Franz *et al.,* 2005] or on Arki [Franz & Okrusch, 1992]. These rocks are unconformably covered with shallow marine sediments of probable Miocene age [Stavropoulos & Gerolymatos, 1999]. More recent magmatic rocks are observed on Patmos and Kos [Wyers & Barton, 1986].

Very few studies were published on the geology of Leros Island. Katagas and Sapountzis [1977] distinguished four tectono-metamorphic units, which Franz *et al.* [2005] then grouped in only two, Temenia and Marina units, covered with a sedimentary unit attributed to the Miocene. Marina unit, further divided into two subunits, Panormos and Emporios [Franz *et al.,* 2005], is composed of amphibolites and garnet-micaschists (pre-Alpidic basement) and a poorly metamorphosed sedimentary cover composed of Permo-Triassic metapelites (*i.e.* siliciclastic Verrucano metasediments), metasandstones and Jurassic marbles (*i.e.* well bedded metacarbonate rocks; Fig. III.2). The pre-Alpidic basement of this unit had recorded two metamorphic episodes, a first Variscan (320 – 300 Ma K/Ar on amphiboles and white micas) characterized by high-temperature and low-pressure (MT-MP) conditions and a second one associated with the Alpine orogeny, displaying greenschist-facies metamorphic parageneses. Based on a petrological study and on the chemical composition of garnets from garnet-micaschists of Marina unit, Franz *et al.* [2005] proposed P-T conditions up to 570 – 630 °C and 6 – 8 kbar for the Variscan episode and a very weak overprint at around 300 – 350 °C at ca. 2 – 3 kbar for the Alpine episode. Temenia unit structurally underlies Marina unit through a shallow-dipping tectonic contact. It is mainly composed of schists, intercalated marble layers and rare occurrences of metabasites where HP-LT parageneses are preserved. Temenia unit also includes a thick marble layer that shapes the landscape in the southeastern part of the island. This unit has undergone an Alpine HP-LT metamorphism [Katagas & Sapountzis, 1977; Franz & Okrusch, 1992] with a peak-thermal conditions of 300 – 400 °C at 7 kbar. In most cases the basement of Marina unit rests on top of Temenia

through a shallow-dipping contact, but the cover of Marina unit is in places in direct contact with Temenia unit with no intervening basement. Otherwise, the non-metamorphic sediments (clastics and carbonates) attributed to the Miocene, rest on top of all metamorphic units. The HP-LT metamorphic parageneses of the lower unit (Temenia) and the metamorphic gap between Marina and Temenia units raise the question of potential detachments similar to the Cycladic ones, below Miocene sediments or between Temenia and Marina units.

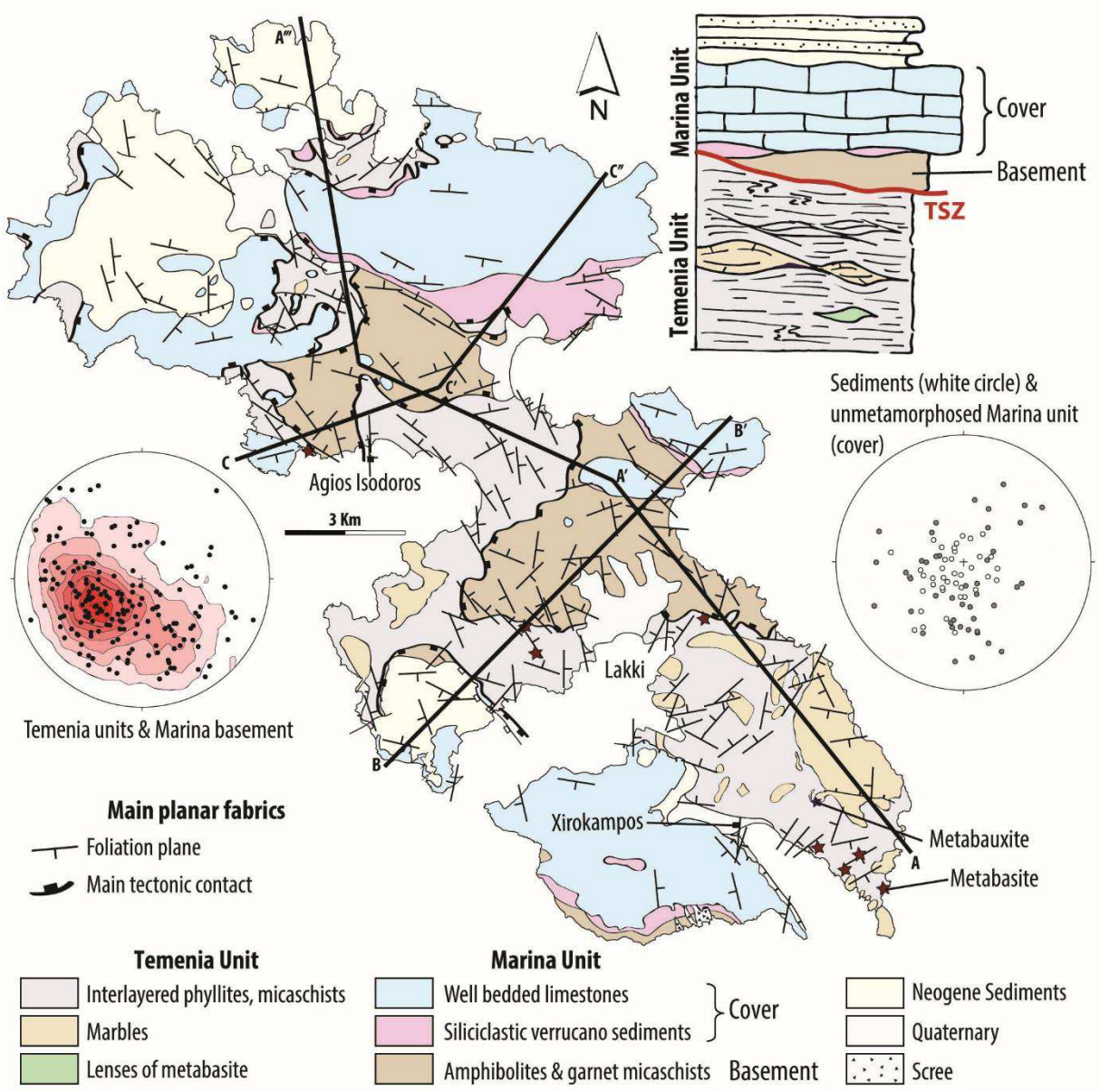

Figure III.2: New geological map of Leros Island modified from Stavropoulos and Gerolymatos [1999]. Poles of foliation and bedding in both Temenia and Marina units are presented in Schmidt's lower hemisphere equal-area projection. Black lines show the localisation of cross-sections.

III.3. A new structural map of Leros

The field survey and the satellite image analysis performed during this study allow us proposing a new geological map of Leros that complements the geologic map of Stavropoulos and Gerolymatos [1999]. Results are shown in Figures III.2 and III.3. Besides, this study brings the first tectonic map of the island including the recognition of the large-scale geometries, main structures and kinematics of deformation whether ductile or brittle. This map also indicates stretching lineations and kinematic indicators, as well as the nature of contacts and their kinematics. A tectono-stratigraphic log presents the three different units Temenia, Marina and Miocene sediments and three cross-sections complete the description of the geometrical relations between units and their deformation (Fig. III.3).

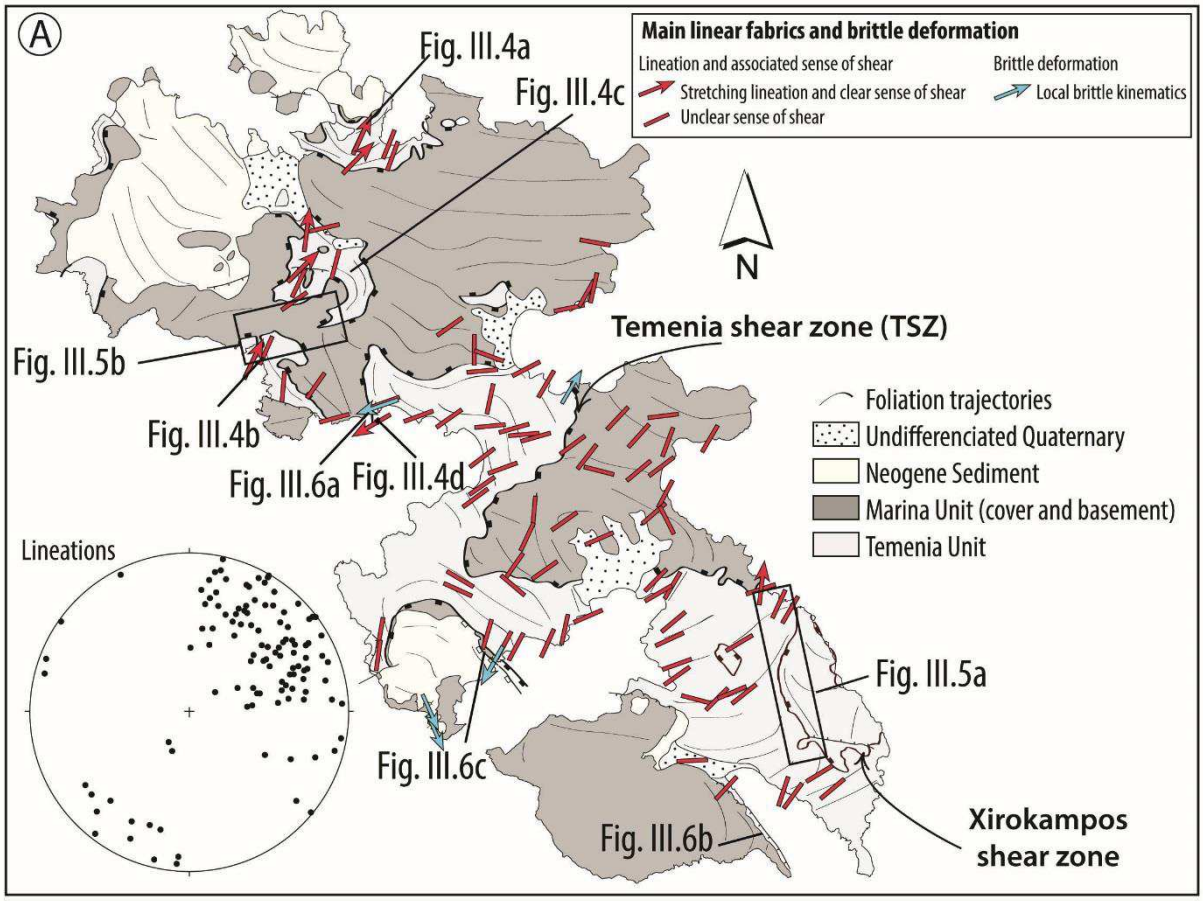
A
Main linear fabrics and brittle deformation
Lineation and associated sense of shear
Stretching lineation and clear sense of shear
Unclear sense of shear
Brittle deformation
Local brittle kinematics
N
Fig. III.4a
Fig. III.4c
Fig. III.5b
Fig. III.4b
Fig. III.6a
Fig. III.4d
Temenia shear zone (TSZ)
Foliation trajectories
Undifferenciated Quaternary
Neogene Sediment
Marina Unit (cover and basement)
Temenia Unit
Lineations
Fig. III.5a
Fig. III.6c
Fig. III.6b
Xirokampos shear zone

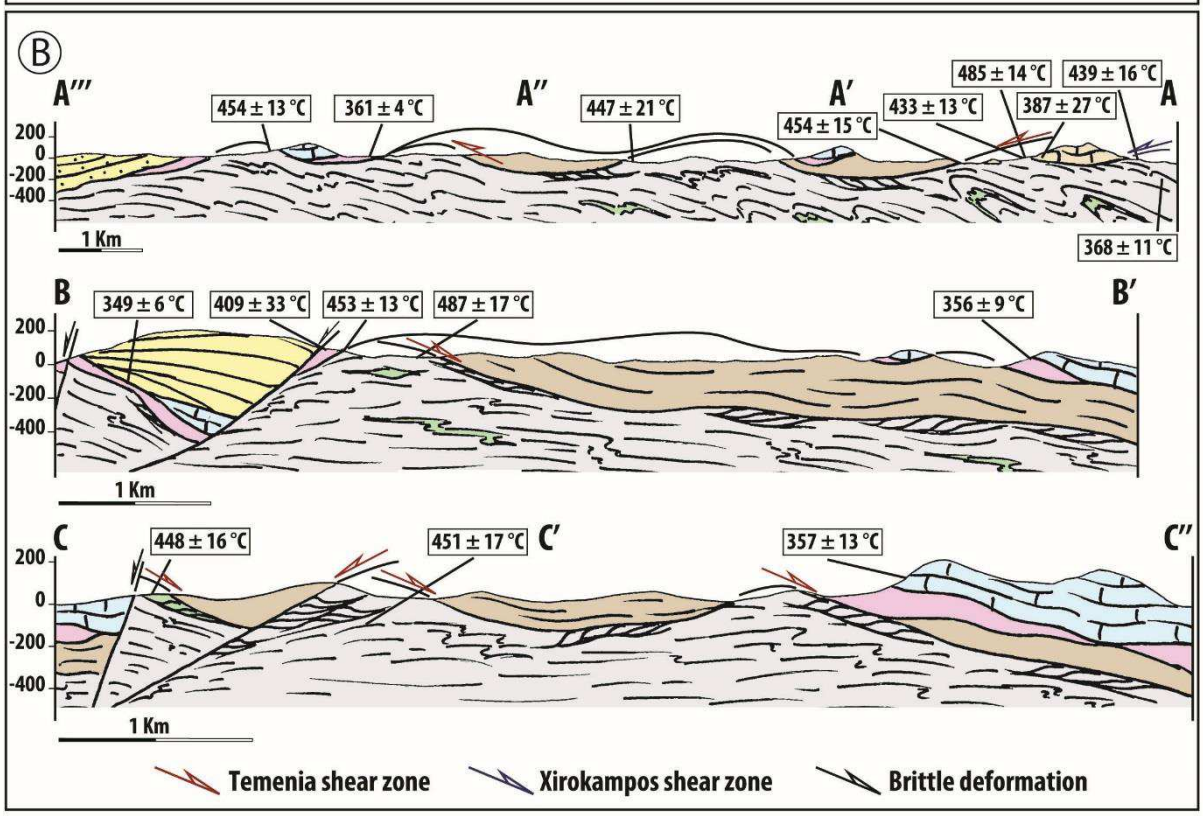
B
A'''
A''
A'
A
454 ± 13 °C
361 ± 4 °C
447 ± 21 °C
454 ± 15 °C
433 ± 13 °C
485 ± 14 °C
439 ± 16 °C
387 ± 27 °C
368 ± 11 °C
200
0
-200
-400
1 Km
B
B'
349 ± 6 °C
409 ± 33 °C
453 ± 13 °C
487 ± 17 °C
356 ± 9 °C
C
C'
C''
448 ± 16 °C
451 ± 17 °C
357 ± 13 °C
Temenia shear zone
Xirokampos shear zone
Brittle deformation

Figure III.3: Tectonic map of Leros Island with main cross-sections. (a) Main linear fabrics, foliation trajectories and the main shear zones are indicated. Note that the geometry of the main foliation remains constant across the Marina and Temenia contact. Also indicated is the position of the pictures of Figures III.4, III.5 and III.6. (b) Simplified cross-sections of Leros. Also indicated are the main results of Raman spectrometry on carbonaceous material. Black and red stars refer to and the main occurrences of index minerals.

III.4. Kinematics of deformation

III.4.1. Ductile deformation

The ductile deformation recorded in both Marina and Temenia units shows clear gradients when approaching the main contact zones identified during field mapping. Foliation and stretching lineations were systematically measured all over the island and kinematic indicators noted when present (Fig. III.4). More than 680 foliations were measured over the island in all lithologies. In average, the foliation strikes N150°E and dips about 30° toward the ENE in both units, but also shows a significant dispersion because of intense folding, as well as boudinage (Fig. III.3). For instance, the first cross-section (Fig. III.3a) indicates highly variable thickness of the pre-Alpidic basement and, more locally the lack of Permo-Triassic metasediments. Large-scale boudinage of marbles in the southeast of the island, obvious in the landscape confirms also the kilometric-scale of boudinage of Temenia unit (Fig. III.5a). In addition, this unit shows large variations in folding style and intensity with localization of folding in specific areas. The distribution of foliation poles at the scale of Temenia unit (Fig. III.2) suggests that fold axes are trending N40°E in average and dip 30° toward the NE.

Stretching lineations are marked by various types of indicators, depending upon the lithology, intensity of the deformation and P-T conditions: elongation of quartz and mica aggregates in metapelites (Temenia and Marina basement), of epidote and blue-amphiboles in HP metabasites (Temenia), hornblende in amphibolites (Marina basement) and stretched clasts in meta-conglomerates (Permo-Triassic). On most outcrops, the orientation of various types of lineation is constant. However, the strike of lineations shows a quite large dispersion, trending between N°0 and N°90 (Fig. III.3a). It is centered on an average NE direction (Fig. III.3a), with variable NE plunges in both Marina and Temenia units.

Besides systematic measurements of stretching direction, the sense of shear has been studied. Although rocks are generally pervasively deformed, reliable kinematics indicators are not very common and quite unequally distributed over the Island. In addition, we focus mainly on the study of the deformation within Temenia unit (Figs. III.3a and III.4), which presents HP-LT Alpine parageneses. Most monoclinic structures are visible in the northern part of Temenia unit close to the contact with Marina unit. Shear bands with a consistent dip deflect the foliation (Fig. III.4a) and the most competent levels are also sheared and affected by quartz veins perpendicular to the stretching direction. These structures are present at the centimetre scale (Fig. III.4a) but also pluri-metric (Figs. III.4b and III.4c),

illustrating the penetrativity of deformation. The sense of shear indicated by shear bands is top-to-the-north or top-to-the-northeast, reflecting the sense of motion along the contact between Marina and Temenia units. Opposite shear sense can be locally observed, especially near Agios Isidoros (Fig. III.2), where the observed shearing deformation is mostly accommodated by localized shear bands associated with veins evolving toward cataclasites, not by an intense penetrative deformation, suggesting conditions close to the brittle-ductile transition in these alternations of marbles and metapelites close to the contact.

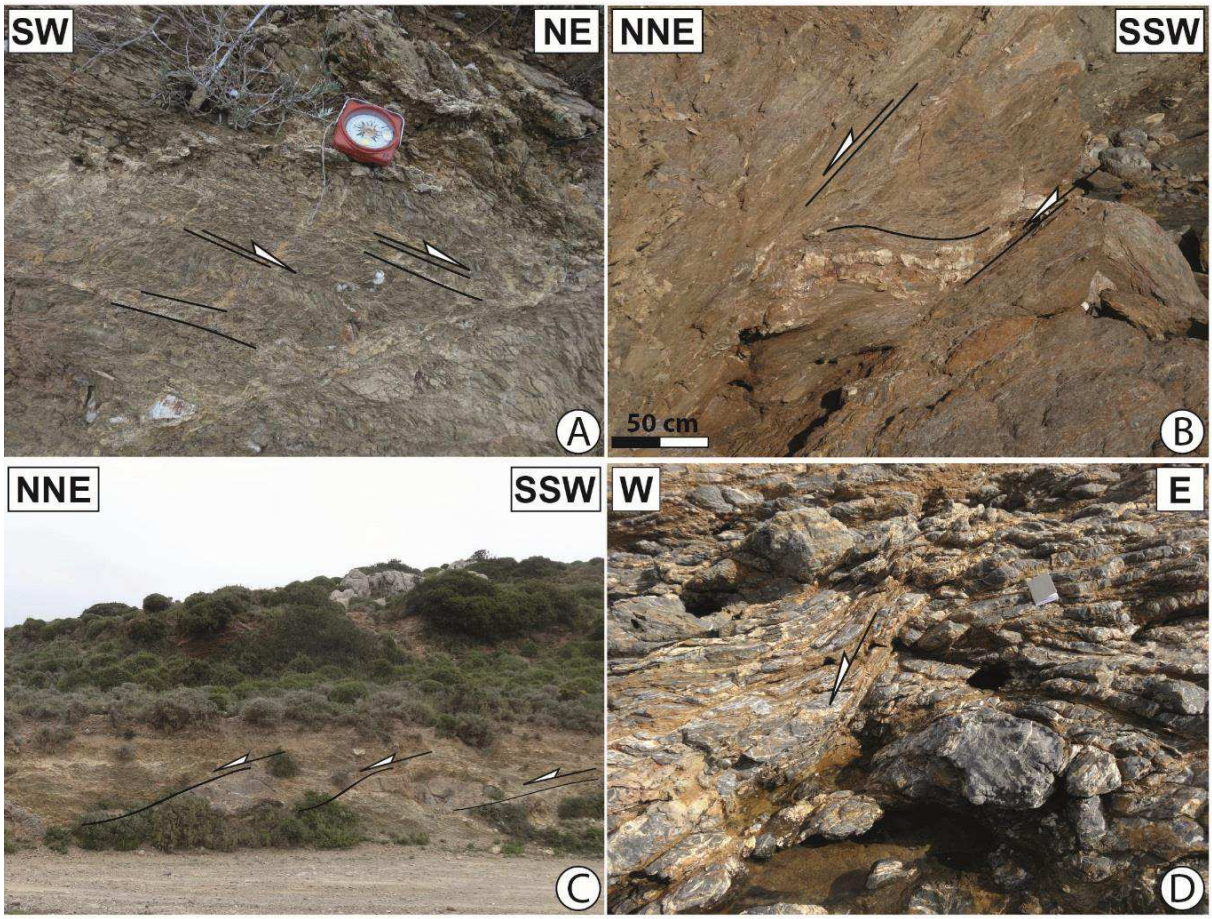

Figure III.4: Kinematics of ductile deformation in Temenia unit. (a) Detailed view of decametric top-to-the-NE shear bands in metapelites. Note that shear bands are crosscut by a SW-dipping normal fault. (b) Asymmetric quartz vein showing a top-to-the-northeast sense of shear. (c) Top-to-the-NE asymmetric boudinage of a marble layer within metapelites. (d) Metric shear bands in the metapelites and dark marble layers. Note shearing consistently top-to-the-west.

The basement of Marina unit has undergone a strong ductile deformation but shows no systematic kinematic indicators. Part of the basement has been intensely deformed under Barrovian metamorphic conditions leading to the development of a foliation and stretching lineation in amphibolites and garnet-bearing micaschists, but this deformation, closely associated with the MT-MP metamorphic conditions is related to a pre-Alpine event. On the opposite, the Mesozoic marbles of Marina unit display an intense

boudinage visible at all scales, from the centimetre to several hundreds of meters leading to large thickness variations of the Permo-Triassic formation (Fig. III.3). Further north, Figure III.5b shows the boudinaged cover of Marina resting both on Temenia unit and on the basement of Marina unit showing that boudinage has locally totally eliminated Marina basement.

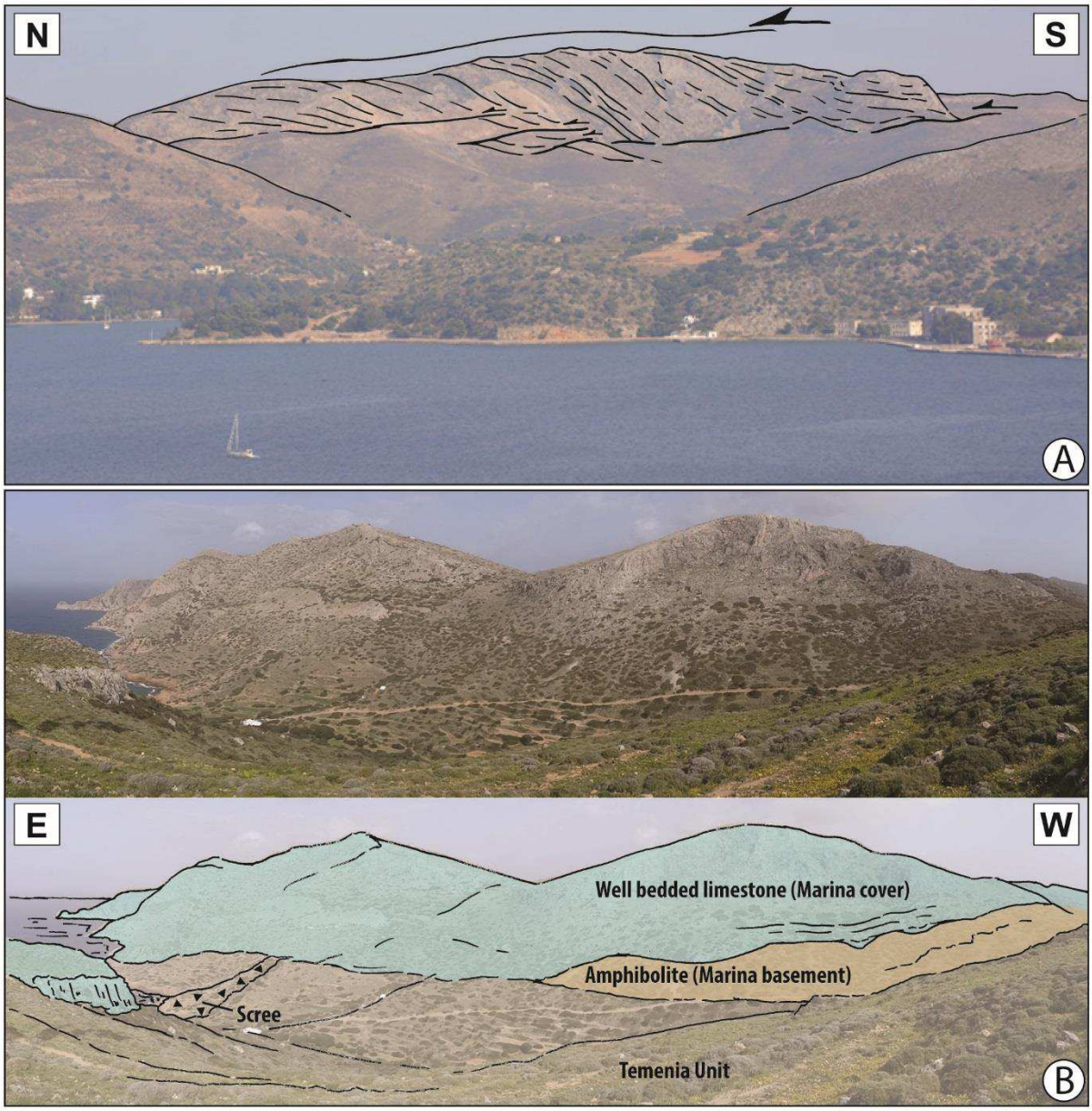

Figure III.5. Large-scale boudinage of the Temenia and Marina units. (a) Landscape view of the boudinaged marbles of Temenia. Note that some levels of marble are cross cut by the low-angle contact. (b) Landscape view of the boudinaged cover of Marina. Note the local absence of Permian-Triassic cover and the contact between Temenia unit and the limestones of Marina unit.

III.4.2. Brittle deformation

Although large-scale brittle structures are quite rare, the whole island of Leros is pervasively affected by brittle deformation (*e.g.* Fig. III.6) that post-dates ductile features. In the western part of the island (Fig. III.2), the geometrical relations between the Neogene sediments and the metamorphic units can be observed. A second deformation stage, with a top-to-the-SW kinematic, and mostly brittle, is recognized along the main contact in three main areas of the island. The first is in the area of Agios Isidoros (Fig. III.6a), where the ductile deformation within Temenia is very intense and becomes more brittle approaching the base of Marina unit with SW-dipping shear bands and faults. In addition, the contact between Temenia and Marina marbles in the village of Xirokampos (Fig. III.2) is also faulted with a steeper dip and a top-to-the-SW kinematics (Fig. III.6b). Finally, the same kinematics is observed west of Lakki (Fig. III.3), where a low-angle fault plane is observed along the contact between Neogene sediments and metamorphic units (Fig. III.6c).

There, sediments west of Lakki display a rollover geometry with a fan thickening toward the low-angle west-dipping normal fault (Fig. III.6d), showing the syn-extensional history of these deposits. These sediments, at their eastern limit, are in fault contact with a marble lens of Marina cover (Fig. III.6e) but also with Temenia schists and marbles alternation. Below the low-angle normal fault, the marbles of Marina unit are highly faulted and brecciated across a few tens of meters (Fig. III.6f). Normal faults within the breccia are generally more steeply dipping than the main fault plane, but the direction of stretching deduced from the striated fault set is compatible with the same direction of extension. All faults, small and large ones, steep or low-angle, are normal. They strike in average N130°E and dip between 10 and 70° toward the SW. The main fault shows the superimposition of two sets of striation (Fig. III.6g), the first one trending N50°E and the second one N130°E. The lower contact between the marble lens and Temenia schists is also faulted, with the same orientation as the sediment/marble contact. The first set of striation along the main plane and on smaller scale faults in the breccia is compatible with a NE-SW extension (N31°E in average) compatible with the normal throw on the main contact and with the syn-deposition tilt of the Neogene sediments. The second set of striation indicates a more N-S direction of extension (167°N in average) showing a late reactivation of the fault, still at shallow dip. In the northwest of Leros, the Neogene sediments rest with a depositional contact on the Permo-Triassic sandstones and microconglomerates and are cut by late normal faults.

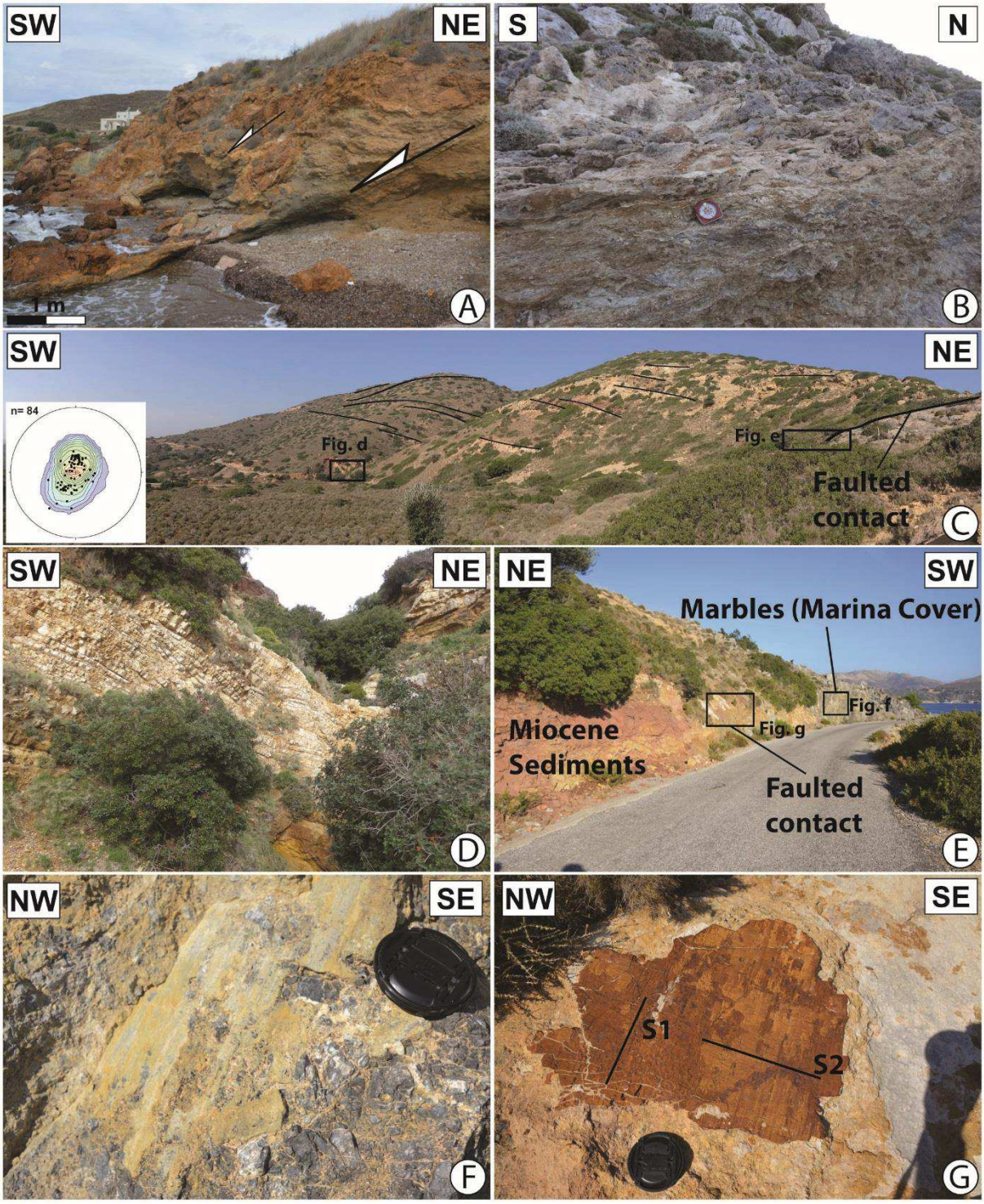

Figure III.6: Kinematic of brittle deformation in both units. (a) Metric low-angle normal faults in the Temenia unit showing top-to-the-west to -southwest deformation. (b) Fault contact between the limestones of Marina and Temenia unit near Xirokampos. Note the thickness of the cataclasites. (c) Large-scale view of the rollover geometry close to Lakki. Poles of bedding in the Neogene sediments are presented in Schmidt's lower hemisphere equal-area projection. (d) Close-up view of the deeper structural level in sediments with a dip value around ~ 40 ° toward the NE. (e) Main contact between the sediments and the metacarbonate rocks of the Marina unit. (f) Thick breccia within the marbles and associated fault plane with striae. (g) Close-up view of the main low-angle normal fault plane showing two generation of striation.

The observed Alpine structures within metamorphic units and at their contact with the Neogene sediments thus show a continuum of NE-SW stretching from ductile to brittle conditions. It starts with boudinage of all units, especially Marina that is locally partly eliminated and continues with top-to-the-NE shearing deformation within Temenia unit with a focalization along the contact between the two units. Locally, the sense of shear is opposite showing that a significant component of co-axial flow should be taken into account. The same stretching direction is observed in the first stages of brittle deformation along the contact with the sediments that are deposited during the activity of the shallow west-dipping normal fault west of Lakki. This continuum of deformation from ductile to brittle suggests that the early ductile deformation is also due to an extensional event. A late extensional event has reactivated the shallow-dipping normal fault with a more northerly direction of stretching.

III.5. Metamorphic record and P-T estimates in metamorphic units

The metamorphic record was investigated throughout Leros Island. Because most of the Island is composed by accreted sediments lacking metamorphic index minerals, except for amphibolites and garnet micaschists of the Marina unit that experienced a pre-Alpine Barrovian metamorphic event, constraints on the Alpine HP-LT metamorphic conditions remain very sparse. In a first attempt to describe the metamorphic architecture of Leros and to put constraints on the metamorphic evolution of each unit, we performed a detailed analysis of the parageneses carried by different types of lithologies present on Leros. By contrast, rocks of Leros are often rich in carbonaceous material (CM) and are therefore particularly appropriate for RSCM (Raman Spectroscopy of CM) thermometry. Results are all presented in Figure III.7 and some representative field examples are given in Figure III.8.

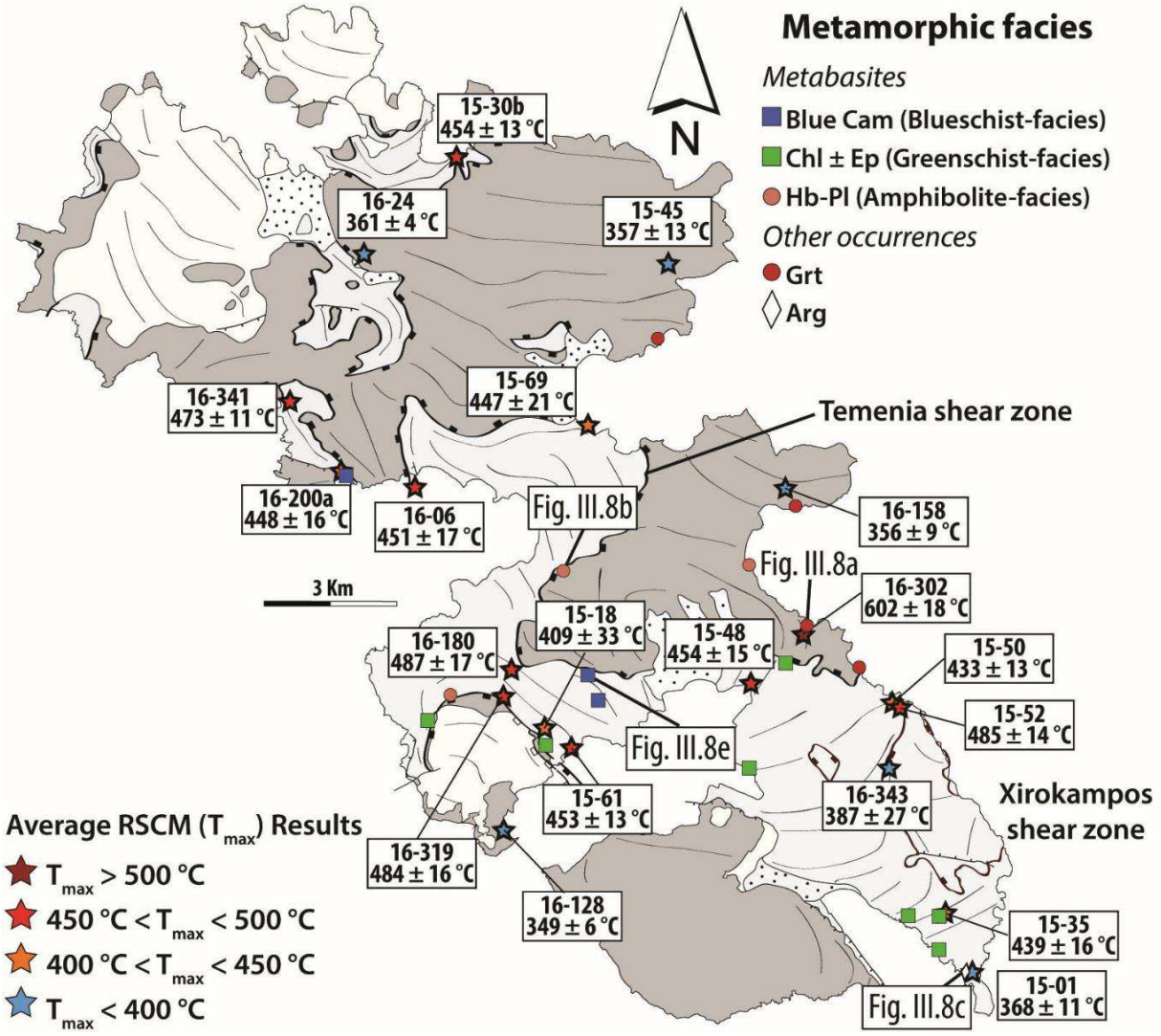

Figure III.7. RSCM distribution and metamorphic record on Leros showing the main metamorphic index minerals. Cam (clinoamphibole); Chl (chlorite); Ep (epidote); Arg (aragonite); Hb (horneblende); Grt (garnet). Abbreviations are from Whitney & Evans [2010].

III.5.1. Conventional metamorphic petrology observations

Rocks exposed on Leros show rather high variance mineral assemblages either for metacarbonate rocks or even metapelites. Parageneses in metabasites, which are a straightforward field indicator of P-T conditions, were particularly studied in the different units. This analysis was refined and strengthened by the recognition of index-minerals in other lithologies.

At a first glances, two different types of conditions are clearly recorded in Marina unit. The basement rocks of Marina unit recorded Barrovian MT-MP conditions while the cover series escaped significant Alpine imprint. In the basement, massive metabasite and micaschist are the best candidates to study metamorphic parageneses. There, hornblende and plagioclase (amphibolite facies metabasites) and garnets, muscovite and quartz (metapelites) are very common and well preserved (Figs. III.8a and

III.8b). Rocks from the cover series do not provide any reliable markers of the metamorphic grade although deformation was recorded in the ductile regime. Metacarbonate rocks show calcite recrystallization and the rare intercalations of metapelites show only the growth of phyllosilicates. In the southern part of the island, the marbles of Temenia unit locally contain a dark carbonate mineral, with a fibrous and radiating structure suggesting the presence of aragonite (Figs. III.7 and III.8c) that was validated by Raman spectroscopy (Fig. III.8d). In this unit, foliation in metabasites is mainly defined by blue amphibole needles quartz and epidote. Blue amphiboles (*Appendix III.9.*, Table III.2) show strong pleochroism without clear inclusions. Relic of crenulation cleavage marked by blue amphiboles are locally observed whereas others defined the main foliation (Fig. III.8e). They show a quite strong chemical zoning (Fig. III.8e), with a chemical core composition range from glaucophane/crossite (Na-amphiboles) to winchite (Na-Ca amphiboles) (Fig. III.8e). According to the IMA nomenclature [*e.g.* Leake *et al*., 1997], the rim of blue amphiboles are ferriwinchites (Fig. III.8f). Metamorphic assemblages present in metabasites therefore show HP-LT metamorphic conditions where the mineral assemblage recognized in the blueschists is glaucophane/crossite - chlorite - phengite - epidote - quartz ± albite ± hematite ± rutile ± titanite, conforming to the epidote-blueschist facies of Evans [1990]. This assemblage is variably overprinted into greenschist-facies conditions in which blue amphibole breaks down to chlorite. The conventional ACF diagram would indicate a cross reaction as follows: epidote + glaucophane + quartz <=> winchite + chlorite + albite. The associated greenschist-facies thus display the following paragenesis chlorite - phengite - epidote - albite - quartz - winchite - calcite - rutile. The only white micas recorded in the blueschists rocks are phengites (Fig. III.8g; *Appendix III.9.*, Table III.3) with high silica content (3.30 – 3.60 Si p.f.; Fig. III.8g). Epidote and chlorite ($X_{Mg} \approx 0.72$; *Appendix III.9.*, Tables III.4 and III.5) also have relatively homogeneous compositions. Even if our chlorite compositions are richer in magnesium that the ones described in Franz & Okrusch [1992] in blueschists from the Temenia unit of the nearby island of Arki, other mineral (*i.e.* epidote, phengite and blue-amphibole) show very similar compositions.

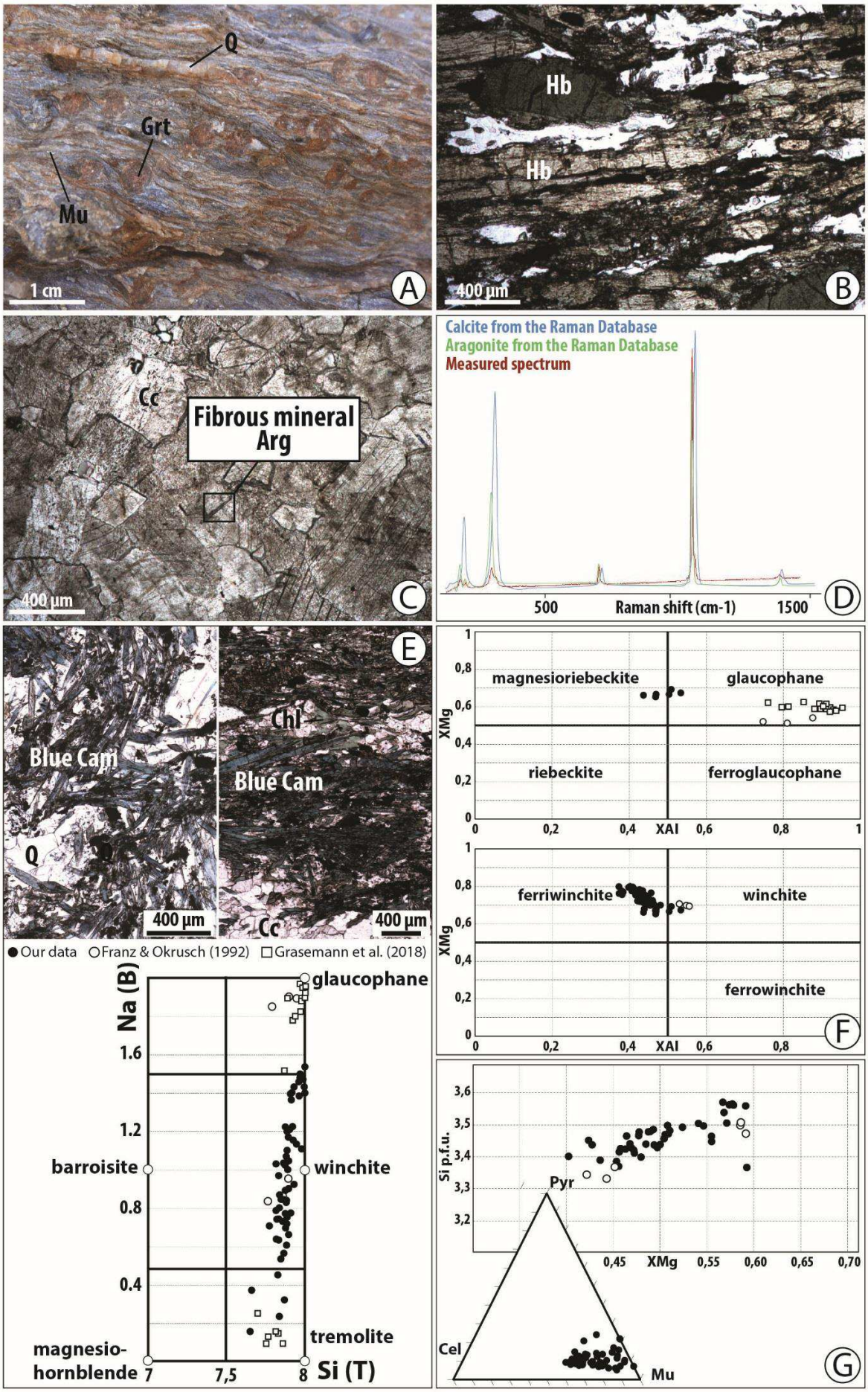
Q
Grt
Mu
1 cm
A
Hb
Hb
400 µm
B
Cc
Fibrous mineral
Arg
400 µm
C
Calcite from the Raman Database
Aragonite from the Raman Database
Measured spectrum
500
Raman shift (cm-1)
1500
D
E
Blue Cam
Q
400 µm
Chl
Blue Cam
Cc
400 µm
magnesioriebeckite
glaucophane
riebeckite
ferroglaucophane
XMg
XAl
ferriwinchite
winchite
ferrowinchite
F
Our data
Franz & Okrusch (1992)
Grasemann et al. (2018)
glaucophane
Na (B)
1.6
1.2
barroisite
winchite
0.8
0.4
tremolite
magnesio-
hornblende
7
7,5
8
Si (T)
Si p.f.u.
Pyr
XMg
Cel
Mu
G

Figure III.8. Metamorphic record on Leros and mineral chemistry. (a) Close up view of garnet bearing micaschist. Mu (muscovite); Q (quartz). (b) Thin section of massive amphibolite. (c) Marble showing locally aragonite occurrence. Cc (calcite); Arg (aragonite). (d) Selection of representative Raman spectra of aragonite. Note the good correlation between the measured spectrum and the reference spectrum. (e) Left picture indicates older-crenulation cleavage defined by blue clinoamphibole and right picture shows retrograde blue clinoamphibole and chlorite within the main foliation plane. Mineral chemistry of metabasites of amphibole plotted in tetrahedral Si versus Na at the B site. Black spots correspond to the highest values of Na (B site) which are close to the "winchchite-glaucophane" transition (i.e. Na > 1.4). (f) X_{Al} ($Al/(Fe^{3+}+Al)$) versus X_{Mg} diagrams (after Leake et al. [1997]. (g) Mineral chemistry of phengite in metabasite.

III.5.2. RSCM thermometry

Raman spectroscopy on carbonaceous material (RSCM) allows determining the maximum temperature experienced by the rock sample [Beyssac *et al.,* 2002]. The technique is based upon the observation that sedimentary carbonaceous material (CM) is progressively transformed into graphite with increasing metamorphism [Pasteris & Wopenka, 1991; Wopenka & Pasteris, 1993]. The degree of organization of the CM is quantitatively characterized by Raman spectroscopy and because of the irreversible character of graphitization, CM structure only depends on the maximum T (T_{max}) reached during metamorphism, regardless of the shape of the retrograde path during exhumation [Beyssac *et al.,* 2002]. T_{max} can be determined in the range 330 – 650 °C with an accuracy of ± 50 °C due to uncertainties on petrologic data used to calibrate the thermometer. Relative uncertainties on T attached to a series of samples are however as low as 10 – 15 °C [*e.g.* Beyssac *et al.,* 2004; Brovarone *et al.,* 2013].

Raman spectra were obtained using the Renishaw InVia Reflex system (BRGM-ISTO, Orléans). RSCM analyses were conducted on thin sections prepared on CM-rich metasediments (metapelites and marbles) cut in the structural (*i.e.* X-Z, plane orthogonal to foliation and parallel to lineation). To avoid defects on the CM related to thin section preparation, analyses were all performed below the surface of the section by focusing the laser beam beneath a transparent crystal such as quartz and calcite. Spectra were all obtained and then treated using Peakfit software following the procedure described in Beyssac *et al.* [2002].

To document the Peak-T conditions and the distribution of the Alpine metamorphic event, this thermometric study primarily focuses on Temenia unit. Samples from Marina unit (basement and cover) were also studied in order to compare the thermal evolution of the two units and the T_{max} values with P-T estimates previously published [Franz *et al.,* 2005]. However, since this method provides the maximum temperature ever experienced reached by the rock, it is impossible to obtain the conditions for a potential Alpine overprinting on Marina basement during subduction, because the temperature would not exceed the Variscan peak (570 – 630 °C) estimated by Franz *et al.* [2005].

RSCM results are all plotted on a map (Fig. III.7) and projected on the different cross-sections to locate them in the units and relative to tectonic contacts (Fig. III.3b). Detailed results, including R2 ratio, number of spectra, T_{max} and standard deviation are presented in Table III.1. 13 – 22 spectra were routinely recorded for each sample to smooth out the inner structural heterogeneity of CM within samples that is generally low.

			RSCM results			
Sample	**Unit**	**Lithology**	*Temperature (°C)*	*Standard Deviation*	*Spectrum Nb*	*1 σ*
16-128	Marina Cover	Marble	**349**	6.17	15	1.59
16-158	Marina Cover	Marble	**356**	8.56	17	2.08
15-45	Marina Cover	Marble	**357**	13.19	18	3.11
16-24	Marina Cover	Marble	**361**	4.45	17	1.08
16-343	Marina Cover	Marble	**387**	26.71	17	6.48
16-302	Marina Basement	Garnet micaschist	**602**	18.00	13	4.99
15-01	Temenia	Aragonite marble	**368**	11.00	17	2.67
15-18	Temenia	Dark marble	**409**	33.14	18	7.81
15-50	Temenia	Micaschist	**433**	13.25	15	3.42
15-35	Temenia	Micaschist	**439**	15.74	14	4.21
15-69	Temenia	Dark marble	**447**	21.47	15	5.54
16-200a	Temenia	Dark marble	**448**	15.58	16	3.90
16-01	Temenia	Dark marble	**451**	17.12	15	4.42
15-61	Temenia	Dark marble	**453**	12.87	14	3.44
15-48	Temenia	Dark marble	**454**	14.55	17	3.53
15-30b	Temenia	Micaschist	**454**	12.85	17	3.12
16-341	Temenia	Dark marble	**473**	11.33	14	3.03
16-319	Temenia	Dark marble	**484**	15.52	22	3.31
15-52	Temenia	Micaschist	**485**	13.51	14	3.61
16-180	Temenia	Dark marble	**487**	16.90	18	3.98

Table III.1: RSCM results in all units. Note that each temperature is associated with a standard deviation, a number of spectra and an error range (1σ).

Metasediments of Leros show significant variations in the structural organization of CM and then significant temperature variations (Table III.1) from one unit to another. Temperatures range from ca. 350 °C of the cover series and up to 600 °C deduced from Marina basement rocks. As a general overview, Temenia unit yielded spectra exhibiting decreasing D1 and D2 defect bands relatively to the G graphite band compared to the cover of the Marina unit [*e.g.* Beyssac *et al.*, 2003]. Such evolution can be interpreted as due to a general T decrease of one hundred degrees [*e.g.* Beyssac *et al.*, 2002]. In details, temperatures deduced from Marina cover yielded very consistent results in the narrow range of 349 ± 6 and 387 ± 27 °C. A garnet micaschist sample of Marina basement (sample 16-302) yielded a temperature of 602 ± 18 °C. This temperature falls in the range 570 – 630 °C estimated by Franz *et al.* [2005] for the peak-temperature conditions attributed to a former Variscan event. It appears therefore possible to constrain peak-temperature conditions for the Alpine events for all cover series of the Marina unit. Conversely, the intensity of Alpine events can not be constrained into the basement rocks due to

the Variscan metamorphic imprint. In Temenia unit, T_{max} values obtained in the dark marbles and micaschists fall in the range between 368 ± 11 °C and 487 ± 17 °C. The results obtained in other lithologies show a quite constant T_{max} (Fig. III.7). In addition, aragonite marbles, located in the southern part of the island (Fig. III.7), were also studied with the RSCM method to estimate T_{max}. They yielded a temperature of 368 ± 11 °C whereas the upper structural levels give a T_{max} around 439 °C in schist reaching 387 °C in the marbles (Fig. III.7).

III.6. Discussion

III.6.1. Structural and metamorphic evolution

The two main units recognized on Leros, Marina and Temenia, are superimposed through a low-angle tectonic contact. The most visible ductile deformation is associated with NE-SW stretching and a majority of top-to-the-north or -northeast kinematic indicators but, locally, even along the main contact, the opposite sense of shear can be observed (Fig. III.4d), especially during the latest increments of deformation across the brittle-ductile transition (Fig. III.6a). Almost all of these ductile shear criteria are observed in Temenia unit, close to the contact with the cover of Marina unit. In these areas, the Permo-Triassic sediments are often absent or highly thinned down to a few meters and intensely deformed, while they can reach several tens of meters elsewhere. No significant deformation is instead observed at the contact between the basement and the cover of Marina unit indicating no reactivation of this original unconformity.

A significant gap of temperature of ~ 100 °C is observed between Marina and Temenia units showing that some crustal thickness is missing across the contact, suggesting that it acted as an extensional detachment. A second-order tectonic contact between the upper marbles of Temenia containing aragonite and the lower part of the unit also shows a gap in T_{max}, further suggesting that the thinning of the nappe pile was accommodated by several yet minor shear zones. Using the RSCM T_{max} constraints together with the constraint of the occurrence of aragonite, this sample must have attained at least 8 kbar, assuming that the peak of pressure was coeval with the peak of temperature (~ 368 °C, Fig. III.9). The maximum pressure is also constrained by the presence of the celadonite-rich phengite, epidote and Na-amphiboles. According to Evans [1990], the P-T field of the epidote-blueschist-facies strongly depends on the composition of the Na-amphiboles. The Na-amphiboles of Leros range from glaucophane to crossite equivalent to Evans' grids #5 and #6. The resulting P-T range experienced by the rocks of Leros is strongly reduced by the stable occurrence of albite and aragonite and by the RSCM T_{max} temperatures for these both samples implying therefore a cold HP-LT gradient (Fig. III.9). Temenia unit was thus subducted down to at least 20 km along a HP-LT gradient compatible with an active

subduction context and later exhumed and thinned below a shallow-dipping tectonic contact with a top-to-the-NE kinematics.

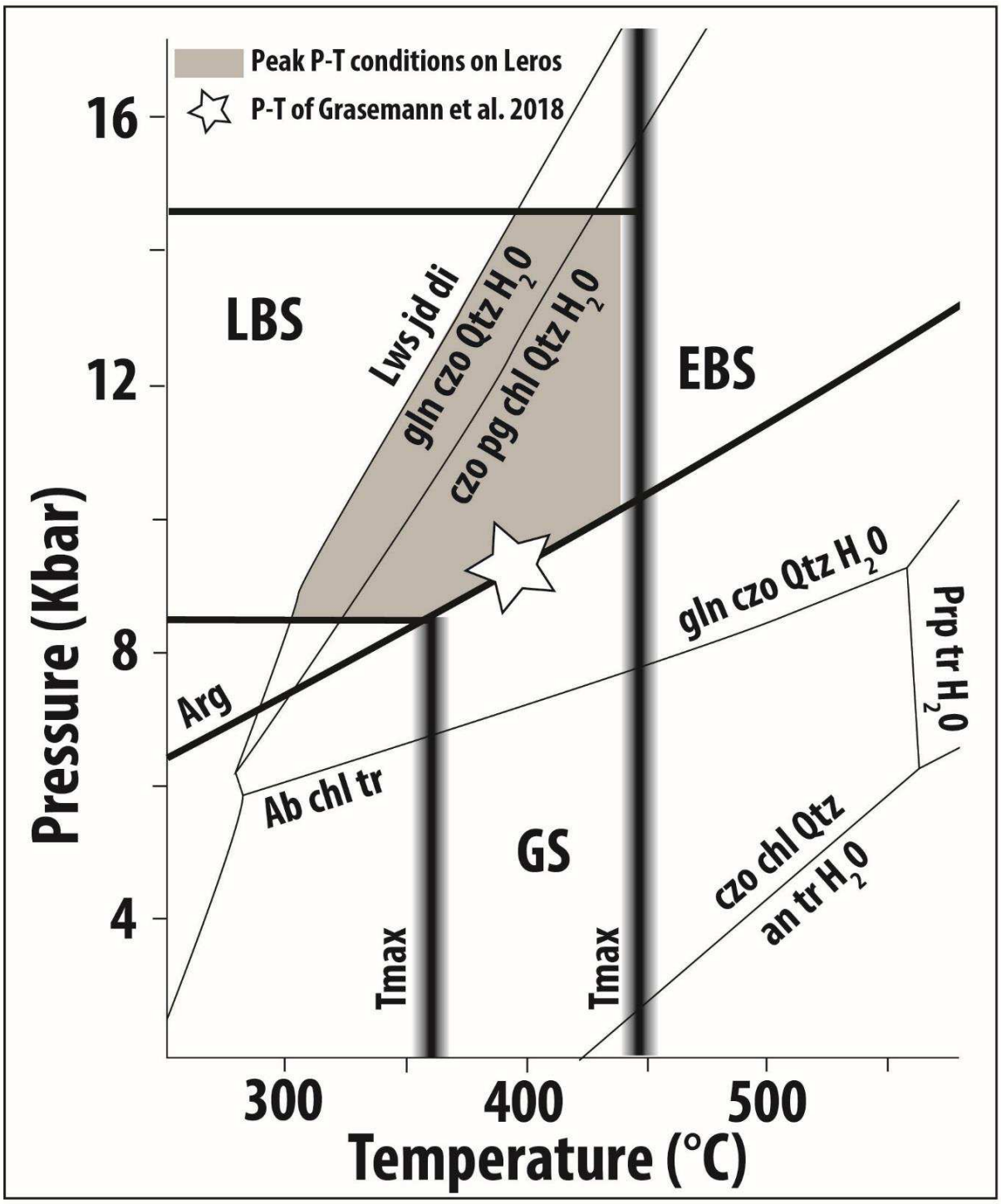

Figure III.9. P-T grid for equilibria in the system NCMASH with activity of H_20 = 0.9 showing the calculated limiting reactions for the epidote-blueschist facies for the amphibole compositions #5 after Evans [1990]. EBS = epidote-blueschist paragenesis, LBS = lawsonite-blueschist paragenesis. GS = greenschist paragenesis. The stability field of the aragonite with T_{max} estimated by the RSCM method. In the same way, we reported the T_{max} conditions of the blue amphibole sample 16-200a. The solid blue line corresponds to the mean value of T_{max} and the dotted line to the errors bars. Mineral abbreviations are indicated in the study of Evan [1990].

Furthermore, the large-scale structure reveals a boudinage of the basement of Marina unit that is locally missing between the cover and Temenia unit. Temenia marbles also show large-scale boudinage visible in the landscape. Although most of kinematic indicators are top-to-the-NE, this boudinage and the late brittle deformation shows a significant component of coaxial flow in the deformation history of both Temenia and Marina units with a progressive localization along the main contact. In the latest stage, low-angle west-dipping normal faults controlled the deposition of shallow-marine Neogene sediments. The exhumation history is in good agreement with the average direction of stretching accommodated by the main Aegean detachments during the Oligo-Miocene [Jolivet *et al.,* 2010; Grasemann *et al.,* 2012].

III.6.2. Large-scale correlations

The two tectonic units of Leros Island have recorded drastically different metamorphic histories, Marina unit having escaped a deep burial in a subduction zone and conversely preserve a strong Variscan imprint. Temenia unit instead carries unambiguous evidences of subduction but with maximum P-T conditions far less severe than the typical CBU that show higher-pressure blueschists and eclogitic conditions reaching 550 °C and 22 kbar on Syros, Sifnos or even Sikinos [*e.g.* Trotet *et al.,* 2001; Groppo *et al.,* 2009; Augier *et al*., 2015]. On Leros, P-T-conditions of the epidote-blueschist-facies did not exceed 450 °C and are quite consistent to conditions deduced by Franz & Okrusch [1992] in comparable blueschists from the Temenia unit of Arki island. These conditions are also similar to some of the more external CBU such as those observed on Folegandros for instance [Augier *et al.,* 2015] or Milos where metamorphic conditions are at 8.5 ± 2.0 kbar (Fig. III.9) [Grasemann *et al.,* 2018]. These rocks were thus buried along a common cold P-T gradient along the subduction zone but escaped the much higher conditions experienced in the subduction channel on Syros or Sifnos.

In terms of lithologies, Temenia unit shows a mixture of metapelites and marbles with minor metabasite occurrences that can also be correlated with the metamorphic sequence of Folegandros [Augier *et al.,* 2015]. Although there is a lack of massive metabasite bodies compared to the "classical" CBU, the metamorphic sequence may however represent a regional lithological variation of the same paleogeographic domain, subducted to shallower depths. It is thus possible to correlate Temenia unit with the Lower Cycladic Nappe described by Grasemann *et al.* [2018] that encompasses tectonic units belonging to the CBU but with lower maximum pressure (*i.e.* 8 – 9 kbar) than the Upper Cycladic Nappe that have recorded eclogite-facies conditions. As the Upper Cycladic Nappe is also a terminology used for the uppermost unit of the Cyclades belonging to the Pelagonian domain (devoid of any Eocene HP-LT overprint) [*e.g.* Reinecke *et al*., 1982], we prefer, in order to avoid possible confusion, to use for

these two units the "Lower Cycladic Blueschists Nappe" for the lower pressure parts and the "Upper Cycladic Blueschists Nappe" for the higher pressure ones (Fig. III.1a).

An alternative correlation of Temenia unit is with Ören unit, the lower metamorphic part of the Lycian Nappes. Peak metamorphic conditions in Ören unit are estimated at 8 kbar and 420 °C, thanks to the presence of Fe-Mg carpholite in the dark micaschists, aragonite in marbles and blue amphiboles in the overlying flysch [Rimmele *et al.,* 2003]. The sedimentary sequence of Leros is however quite different from the Ören unit that shows a more developed Permo-Triassic reddish and purple sequence and more typical metapelites with dark micaschists where Fe-Mg carpholite is present in large amounts.

Furthermore, a possible correlation with the Phyllite-Quartzite Nappe (PQN) of Crete could be envisaged. However the PQN shows ubiquitous HP-LT parageneses, characterized by the presence of Fe-Mg carpholite with maximum pressure above 16 kbar [Seidel *et al*., 1982; Theye *et al*., 1992; Jolivet *et al*., 1996; Jolivet *et al*., 2010], which is at odd with our observations on Leros. Then, the PQN is also composed of a thick pile of metapelites and meta-sandstones with minor carbonates, which makes an important additional difference with Temenia unit.

On Leros, the low-grade metamorphic Lycian Marina unit rests on top of the Lower Cycladic Blueschists Nappe. Although the metamorphic grade changes toward Western Turkey, superposition of the same broad paleogeographic units is observed with the Lycian Nappes (*i.e.* small klippes of the Ören unit) on top of the CBU [Oberhänsli *et al.,* 1998; Rimmelé *et al.,* 2006]. This unit may be thus correlated with a less metamorphosed lateral equivalent of the Lycian Nappes. One major difference between Marina unit cropping out on Leros and the Lycian Nappes is however the presence of a pre-Alpine basement always lacking in Turkey. If we accept this paleogeographic correlation with the Lycian Nappes, the origin of this basement should be looked for in the root zone of the Lycian Nappes, north of the Menderes Massif or the Afyon Zone (Fig. III.1a). Although the contact now observed has been strongly reactivated during exhumation and post-orogenic extension, there is no doubt that it was indeed originally a thrust as the Paleozoic basement of Marina unit rests on top of the Mesozoic Temenia metasediments. The difference in maximum pressure across this contact however calls for large displacements responsible for the omission of at least 10 – 15 km of the original thickness of the accretionary wedge. In addition, the Lycian Nappes are in a structural position at the top of the tectonic pile similar to that of the Pelagonian domain in the Cyclades (*i.e.* the so-called Upper Cycladic Nappe).

Furthermore, this proposed correlation raises the question of the relationships between the Lower Cycladic Blueschists Nappe and the Menderes Massif: can a lateral equivalent be observed in Western Turkey? In terms of metamorphic grade, the Kurudere Unit, resting on top of the Menderes Massif in the south [Rimmelé *et al.,* 2005], between the Menderes basement and the Lycian, has been interpreted as a lateral equivalent of the CBU [*e.g.* Ring *et al.,* 1999; Pourteau *et al.,* 2015]. In that case, it would rather correspond to the Lower Cycladic Blueschists Nappe where the metamorphic grade is lower and

garnet absent, and therefore not to the Upper Cycladic Blueschists Nappe. It would thus be a different unit from the CBU found on Dilek Peninsula that has recorded higher P-T conditions.

To sum-up, these correlations of Leros tectonic units show that the Cycladic HP-LT nappe stack can probably be extended toward the Dodecanese Archipelago and even the Menderes Massif (Fig. III.1a). Like in Western Turkey, the Lycian Marina unit rests through an original thrust contact on top of the Temenia unit. The relations between these two tectonic units should thus be studied.

III.6.3. Tectonic implications in the Eastern Aegean domain

Like in most of the Aegean Sea, this part of the CBU was exhumed below a long-angle detachment with a NE-SW direction of stretching and a predominant top-to-the NE kinematics. These kinematics of deformation during exhumation recorded on Leros can be attributed to two possible events. It can either be the same exhumation and extension as in the Cyclades, NE-SW oriented and mostly top-to-the-NE, accommodated first during syn-orogenic exhumation and then during back-arc extension [*e.g.* Jolivet *et al.,* 2010], or an earlier event, coeval with the exhumation of the metamorphic part of the Lycian Nappes (*i.e.* the Ören unit) that is in average more E-W than the Aegean extension (Fig. III.1a). The observation of a continuum of NE-SW extension on Leros which ends in the brittle field controlling the deposition of Neogene sediments is in favour of the first hypothesis.

The main direction of stretching within Temenia unit is thus related to its exhumation and clusters around NE-SW with a predominant shear sense toward the NE. This is an echo of the Aegean Oligo-Miocene back-arc extension with a progressive evolution toward more brittle conditions. One can thus notice that the main direction of extension on Leros is not significantly different from that of the Cyclades and the Menderes. This shows that the gradient of retreat between the Menderes Massif and the Cyclades, accommodated through a wide shear zone [Gessner *et al.,* 2013; Jolivet *et al.,* 2015] does not lead to a complex kinematic pattern in the crust of the overriding plate, further suggesting that the flow of mantle underneath, within the tear, is simple, as suggested by the seismic anisotropy pattern below this region [Jolivet *et al.,* 2009].

III.7. Conclusion

This first study of the tectono-metamorphic evolution of Leros Island in the Dodecanese Archipelago fills a gap in the knowledge of the Aegean region. Rough estimates on the P-T conditions in Temenia unit call for a subduction-type gradient with HP-LT conditions and a pressure around 8 – 10 kbar for a temperature ranging from 370 °C to 450 °C, whereas Marina unit does not show any strong

Alpine HP-LT overprint. The main deformation observed on Leros is related to the exhumation of both units with a preferential localization of strain along their contact with a top-to-the NE sense of shear and a large component of coaxial shear. A ca. 100 °C gap is recorded between the two units showing that the contact removed some 10 km or more of the initial thickness of the accretionary wedge. This study shows the superposition of Marina unit, correlated with the Lycian Nappes, on top of Temenia unit, a probably equivalent of the Lower Cycladic Blueschists Nappe in terms of metamorphic conditions and lithologies. This superposition of the Lycian Nappes on the CBU has already been observed in the Menderes Massif. However, a possible correlation of Temenia unit with the cover of the Menderes Massif cannot be ignored and needs to be tested by further research. Leros thus makes a link between the Cyclades and the Menderes Massif in terms of correlation of units and in terms of deformation during exhumation. With some lateral differences, the main units are found on either side of the coastline with the same vertical arrangement and some differences in the grade of metamorphism. In order to reinforce these conclusions, this study should be extended toward the north where the Dodecanese and Eastern Aegean islands of Lipsi, Arki and Fourni that have also received very little attention so far. This would also complete the kinematic pattern during back-arc extension above the slab tear and allow discussing the relations between crustal deformation and mantle flow above the tear.

III.8. Acknowledgements

This work has received funding from the Labex Voltaire homed at Orléans University and BRGM, from the European Research Council (ERC) under the seventh Framework Programme of the European Union (ERC Advanced Grant, grant agreement No 290864, RHEOLITH), and from the Institut Universitaire de France. The authors are grateful to A. Lahfid (BRGM) for assistance during the RSCM session to find the aragonite, to I. Di Carlo (ISTO) for assistance during the numerous electron microprobe sessions, and to S. Janiec and J.G. Badin (ISTO) for the preparation of thin sections. The paper benefited from relevant revisions by Bernhard Grasemann and Leander Franz.

III.9. Appendix

	Amp	Amp	Amp	Amp	Amp	Amp
SiO_2	55.274	54.895	56.041	55.714	54.916	55.191
TiO_2	0	0	0.002	0.163	0.084	0.008
Al_2O_3	4.066	3.806	3.517	0.548	2.845	1.519
FeO	15.524	15.709	14.849	9.253	15.607	11.133
MgO	12.424	12.549	13.024	18.979	14.236	17.098
CaO	1.852	2.499	2.761	11.454	5.068	9.199
MnO	0.109	0.008	0.124	0.222	0.145	0.121
Na_2O	6.306	6.2	6.167	1.132	4.836	2.466
K_2O	0	0	0	0.035	0	0.056
F	n.a.	n.a.	n.a.	n.a.	n.a.	n.a.
Total	95.555	95.666	96.485	97.501	97.738	96.791
(O,OH)	23	23	23	23	23	23
T						
Si	7.969	7.932	7.997	7.837	7.815	7.847
Al	0.031	0.068	0.003	0.091	0.185	0.153
Cr	n.a.	n.a.	n.a.	n.a.	n.a.	n.a.
Fe^{3+}	0,000	0,000	0,000	0.072	0,000	0,000
Total T	8.000	8.000	8.000	8.000	8.000	8.000
C						
Al	0.66	0.58	0.588	0,000	0.293	0.102
Cr	n.a.	n.a.	n.a.	n.a.	n.a.	n.a.
Fe^{3+}	0.604	0.613	0.572	0.28	0.6	0.427
Ti	0.000	0.000	0.000	0.017	0.009	0.001
Mg	2.67	2.703	2.771	3.98	3.02	3.624
Fe^{2+}	1.065	1,104	1.069	0.723	1.078	0.846
Mn	0.000	0.000	0.000	0.000	0.000	0.000
Total C	5.000	5.000	5.000	5.000	5.000	5.000
B						
Mg	0.000	0.000	0.000	0.000	0.000	0.000
Fe^{2+}	0.202	0.181	0.131	0.014	0.18	0.05
Mn	0.013	0.001	0.015	0.026	0.017	0.015
Ca	0.286	0.387	0.422	1.726	0.773	1.401
Na	1.498	1.431	1.432	0.233	1.03	0.534
Total B	2,000	2,000	2,000	2,000	2,000	2,000
A						
Na	0.264	0.306	0.274	0.076	0.304	0.146
K	0,000	0,000	0,000	0.006	0,000	0.01
Total A	0.264	0.306	0.274	0.082	0.304	0.156

Table III.2: Representative blue amphibole chemical analyses from Leros, Greece.

	Ph	Ph	Ph	Ph	Ph	Ph
SiO_2	53.099	49.942	50.901	52.981	51.519	49.758
TiO_2	0.064	0.241	0.081	0.055	0.264	0.197
Al_2O_3	23.18	23.608	23.64	23.032	23.177	22.824
FeO	5.395	6.12	6.164	5.532	5.828	6.085
MgO	4.18	4.279	3.589	4.18	4.354	3.841
CaO	0.008	0.128	0.022	0.066	0.036	0.124
MnO	0.063	0	0.028	0	0	0.133
Na_2O	0.067	0.163	0.146	0.154	0.11	0.12
K_2O	8.94	7.58	8.901	9.049	9.036	8.461
F	0.044	0	0.043	0.174	0.13	0
Total	95.039	92.061	93.514	95.223	94.454	91.543
(O, OH)	11	11	11	11	11	11
Si	3.565	3.464	3.498	3.563	3.506	3.493
Ti	0.004	0.013	0.005	0.003	0.014	0.011
Al	1.835	1.93	1.915	1.826	1.859	1.888
Fetot	0.303	0.355	0.355	0.312	0.332	0.358
Mn	0.004	0.000	0.002	0.000	0.000	0.008
Mg	0.419	0.443	0.368	0.419	0.442	0.402
Ca	0.001	0.01	0.002	0.005	0.003	0.01
Na	0.009	0.022	0.02	0.021	0.015	0.017
K	0.766	0.671	0.781	0.777	0.785	0.758
Total	6.902	6.906	6.941	6.921	6.952	6.941
Charge +	22	22	22	22	22	22
XMg	0.578	0.555	0.509	0.574	0.572	0.524
Al IV	0.432	0.524	0.499	0.436	0.482	0.498
Al VI	1.403	1.406	1.417	1.39	1.378	1.391
S alc.	0.775	0.693	0.8	0.797	0.799	0.774
S oct.	2.128	2.204	2.14	2.12	2.151	2.158
Na/Na+K	0.012	0.032	0.025	0.026	0.019	0.022

Table III.3: Representative phengite chemical analyses from Leros, Greece.

	Ep	Ep	Ep	Ep	Ep	Ep
SiO_2	36.33	36.713	36.376	36.856	36.534	36.591
TiO_2	0	0	0	0.046	0.064	0.114
Al_2O_3	20.015	20.723	20.591	20.232	20.512	20.525
FeO	14.188	14.511	14.9	15.072	14.273	14.393
MgO	0.002	0.007	0	0	0.009	0.004
CaO	22.124	23.002	22.466	22.439	22.633	22.63
MnO	0.217	0.015	0.248	0	0.231	0.203
Na_2O	0	0.015	0.027	0	0.027	0
K_2O	0	0	0	0	0.039	0
F	n.a.	n.a.	n.a.	n.a.	n.a.	n.a.
Total	92.876	94.986	94.608	94.644	94.322	94.461
(O, OH)	25	25	25	25	25	25
Si	6.066	6.001	5.977	6.042	6.016	6.014
Ti	0.000	0.000	0.000	0.006	0.008	0.015
Al	3.939	3.993	3.988	3.909	3.981	3.976
Fe^{+3}	1.982	1.984	2.048	2.067	1.966	1.979
Fe^{+2}						
Mn	0.031	0.003	0.035	0.035	0.033	0.029
Mg	0.001	0.002	0,000	0,000	0.003	0.001
Ca	3.958	4.029	3.956	3.956	3.993	3.985
Na	0.000	0.005	0.009	0.018	0.009	0.000
K	0.000	0.000	0.000	0.000	0.009	0.000

Table III.4: Representative epidote chemical analyses from Leros, Greece.

	Chl	Chl	Chl	Chl	Chl	Chl
SiO_2	29.104	28.321	28.912	28.027	28.012	28.699
TiO_2	0.01	0	0	0.028	0	0.048
Al_2O_3	19.155	18.653	19.559	19.006	18.502	18.728
FeO	15.109	15.251	15.547	15.384	15.252	15.766
MgO	22.689	23.81	22.868	23.581	23.324	23.5
CaO	0.118	0.03	0.058	0	0.03	0.052
MnO	0.238	0.412	0.382	0.329	0.364	0.18
Na_2O	0.044	0.024	0.055	0	0	0.036
K_2O	0	0	0	0	0.042	0.052
Total	86.466	86.501	87.382	86.354	85.526	87.059
(O, OH)	28	28	28	28	28	28
Si	5.867	5.736	5.786	5.688	5.742	5.779
Ti	0.002	0.000	0.000	0.005	0.000	0.008
Al	4.551	4.452	4.613	4.546	4.47	4.445
Fetot	2.547	2.583	2.602	2.611	2.615	2.655
Mn	0.041	0.071	0.065	0.057	0.064	0.031
Mg	6.817	7.187	6.821	7.133	7.125	7.053
Ca	0.026	0.007	0.013	0.000	0.007	0.012
Na	0.018	0.01	0.022	0.000	0.000	0.015
K	0.000	0.000	0.000	0.000	0.011	0.014
Total	19.866	20.044	19.919	20.036	20.03	20.007
Charge +	56	56	56	56	56	56
XMg	0.725	0.731	0.719	0.728	0.727	0.725

Table III.5. Representative chlorite chemical analyses from Leros, Greece.

III.10. References

Altherr, R., & Siebel, W. (2002). I-type plutonism in a continental back-arc setting: Miocene granitoids and monzonites from the central Aegean Sea, Greece. Contributions to Mineralogy and Petrology, 143(4), 397-415.

Augier, R., Jolivet, L., Gadenne, L., Lahfid, A., & Driussi, O. (2015). Exhumation kinematics of the Cycladic Blueschists unit and back-arc extension, insight from the Southern Cyclades (Sikinos and Folegandros Islands, Greece). Tectonics, 34(1), 152–185. https://doi.org/10.1002/2014TC003664

Avigad, D., Baer, G., & Heimann, A. (1998). Block rotations and continental extension in the central Aegean Sea: palaeomagnetic and structural evidence from Tinos and Mykonos (Cyclades, Greece). Earth and Planetary Science Letters, 157(1), 23-40.

Bargnesi, E. A., Stockli, D. F., Mancktelow, N., & Soukis, K. (2013). Miocene core complex development and coeval supradetachment basin evolution of Paros, Greece, insights from (U-Th)/He thermochronometry. Tectonophysics, 595–596, 165–182. https://doi.org/10.1016/j.tecto.2012.07.015

Beaudoin, A., Augier, R., Laurent, V., Jolivet, L., Lahfid, A., Bosse, V., … Menant, A. (2015). The Ikaria high-temperature Metamorphic Core Complex (Cyclades, Greece): Geometry, kinematics and thermal structure. Journal of Geodynamics, 92, 18–41. https://doi.org/10.1016/j.jog.2015.09.004

Beyssac, O., Goffé, B., Chopin, C., & Rouzaud, J. N. (2002). Raman spectra of carbonaceous material in metasediments: A new geothermometer. Journal of Metamorphic Geology, 20(9), 859–871. https://doi.org/10.1046/j.1525-1314.2002.00408.x

Beyssac, O., Brunet, F., Petitet, J. P., Goffé, B., & Rouzaud. J.-N. (2003). Experimental study of the microtextural and structural transformations of carbonaceous materials under pressure and temperature, Eur. J. Mineral., 15, 937–951.

Beyssac, O., Bollinger, L., Avouac, J. P., & Goffé, B. (2004). Thermal metamorphism in the lesser Himalaya of Nepal determined from Raman spectroscopy of carbonaceous material. Earth and Planetary Science Letters, 225(1), 233-241.

Biryol, C., Beck, S. L., Zandt, G., & Özacar, A. A. (2011). Segmented African lithosphere beneath the Anatolian region inferred from teleseismic P-wave tomography. Geophysical Journal International, 184(3), 1037–1057. https://doi.org/10.1111/j.1365-246X.2010.04910.x

Blake, M. C., Bonneau, M., Geyssant, J., Keinast, J. R., Lepvrier, C., Maluski, H., & Papanikolaou, D. (1981). A geologic reconnaissance of the Cycladic blueschist belt, Greece. Geological Society of America Bulletin, 92(5), 247. https://doi.org/10.1130/0016-7606(1981)92<247:AGROTC>2.0.CO;2

Bonneau, M., & Kienast, J. R. (1982). Subduction, collision et schistes bleus; l'exemple de l'Egee (Grece). Bulletin de La Société Géologique de France, S7–XXIV(4), 785–791. https://doi.org/10.2113/gssgfbull.S7-XXIV.4.785

Bozkurt, E. (2001). Neotectonics of Turkey – a synthesis. Geodinamica Acta, 14(1–3), 3–30. https://doi.org/10.1016/S0985-3111(01)01066-X

Bozkurt, E., & Oberhänsli, R. (2001). Menderes Massif (Western Turkey): Structural, metamorphic and magmatic evolution - A synthesis. International Journal of Earth Sciences, 89(4), 679–708. https://doi.org/10.1007/s005310000173

Bröcker, M. (1990). Blueschist-to-greenschist transition in metabasites from Tinos Island, Cyclades, Greece: Compositional control or fluid infiltration? Lithos, 25(1–3), 25–39. https://doi.org/10.1016/0024-4937(90)90004-K

Brovarone, A. V., Beyssac, O., Malavieille, J., Molli, G., Beltrando, M., & Compagnoni, R. (2013). Stacking and metamorphism of continuous segments of subducted lithosphere in a high-pressure wedge: the example of Alpine Corsica (France). Earth-Science Reviews, 116, 35-56.

Brun, J. P., & Faccenna, C. (2008). Exhumation of high-pressure rocks driven by slab rollback. Earth and Planetary Science Letters, 272(1–2), 1–7. https://doi.org/10.1016/j.epsl.2008.02.038

Brun, J.-P., & Sokoutis, D. (2010). 45 m.y. of Aegean crust and mantle flow driven by trench retreat. Geology, 38(9), 815–818. https://doi.org/10.1130/G30950.1

Carminati, E., Wortel, M. J. R., Spakman, W., & Sabadini, R. (1998). The role of slab detachment processes in the opening of the western-central Mediterranean basins: Some geological and geophysical evidence. Earth and Planetary Science Letters, 160(3–4), 651–665. https://doi.org/10.1016/S0012-821X(98)00118-6

Cenki-Tok, B., Expert, M., Işık, V., Candan, O., Monié, P., & Bruguier, O. (2016). Complete Alpine reworking of the northern Menderes Massif, western Turkey. International Journal of Earth Sciences, 105(5), 1507–1524. https://doi.org/10.1007/s00531-015-1271-2

De Boorder, H., Spakman, W., White, S. ., & Wortel, M. J. . (1998). Late Cenozoic mineralization, orogenic collapse and slab detachment in the European Alpine Belt. Earth and Planetary Science Letters, 164(3–4), 569–575. https://doi.org/10.1016/S0012-821X(98)00247-7

Dercourt, J., Zonenshain, L. P., Ricou, L. E., Kazmin, V. G., Le Pichon, X., Knipper, A. L., … Biju-Duval, B. (1986). Geological evolution of the Thethis belt from the Atlantic to the Pamirs since the Lias. Geology, 123, 241–315.

Evans, B.W. (1990). Phase relations of epidote-blueschists. Lithos, 25, 3–23.

Faccenna, C. (2005). Constraints on mantle circulation around the deforming Calabrian slab. Geophysical Research Letters, 32(6), L06311. https://doi.org/10.1029/2004GL021874

Faccenna, C., Piromallo, C., Crespo-Blanc, A., Jolivet, L., & Rossetti, F. (2004). Lateral slab deformation and the origin of the western Mediterranean arcs. Tectonics, 23(1), n/a-n/a. https://doi.org/10.1029/2002TC001488

Franz, L., & Okrusch, M. (1992). Aragonite-bearing blueschists on Arki island, Dodecanese, Greece. European Journal of Mineralogy, 4, 527–537.

Franz, L., Okrusch, M., Seidel, E., & Kreuzer, H. (2005). Polymetamorphic evolution of pre-Alpidic basement relics in the external Hellenides, Greece. Neues Jahrbuch Für Mineralogie - Abhandlungen, 181(2), 147–172. https://doi.org/10.1127/0077-7757/2005/0013

Gautier, P., Brun, J.-P., & Jolivet, L. (1993). Structure and kinematics of Upper Cenozoic extensional detachment on Naxos and Paros (Cyclades Islands, Greece). Tectonics, 12(5), 1180–1194. https://doi.org/10.1029/93TC01131

Gessner, K., Piazolo, S., Güngör, T., Ring, U., Kröner, A., & Passchier, C. W. (2001). Tectonic significance of deformation patterns in granitoid rocks of the Menderes nappes, anatolide belt, Southwest Turkey. International Journal of Earth Sciences, 89(4), 766–780. https://doi.org/10.1007/s005310000106

Gessner, K., Gallardo, L. A., Markwitz, V., Ring, U., & Thomson, S. N. (2013). What caused the denudation of the Menderes Massif: Review of crustal evolution, lithosphere structure, and dynamic topography in southwest Turkey. Gondwana Research, 24(1), 243–274. https://doi.org/10.1016/j.gr.2013.01.005

Govers, R., & Wortel, M. J. R. (2005). Lithosphere tearing at STEP faults: response to edges of subduction zones. Earth and Planetary Science Letters, 236(1–2), 505–523. https://doi.org/10.1016/j.epsl.2005.03.022

Govers, R., & Fichtner, A. (2016). Signature of slab fragmentation beneath Anatolia from full-waveform tomography. Earth and Planetary Science Letters, 450, 10–19. https://doi.org/10.1016/j.epsl.2016.06.014

Grasemann, B., & Petrakakis, K. (2007). Evolution of the Serifos metamorphic core complex. Inside the Aegean Core Complexes. Journal of the Virtual Explorer, Electronic Edition.

Grasemann, B., Schneider, D. A., Stockli, D. F., & Iglseder, C. (2012). Miocene bivergent crustal extension in the Aegean: Evidence from the western Cyclades (Greece). Lithosphere, 4(1), 23–39. https://doi.org/10.1130/L164.1

Grasemann, B., Huet, B., Schneider, D. A., Rice, A. H. N., Lemonnier, N., & Tschegg, C. (2018). Miocene postorogenic extension of the Eocene synorogenic imbricated Hellenic subduction channel: New constraints from Milos (Cyclades, Greece). GSA Bulletin.

Groppo, C., Beltrando, M., & Compagnoni, R. (2009). The P-T path of the ultra-high pressure Lago Di Cignana and adjoining high-pressure meta-ophiolitic units: insights into the evolution of the subducting Tethyan slab. Journal of Metamorphic Geology, 27(3), 207–231. https://doi.org/10.1111/j.1525-1314.2009.00814.x

Huet, B., Labrousse, L., & Jolivet, L. (2009). Thrust or detachment? Exhumation processes in the Aegean: Insight from a field study on Ios (Cyclades, Greece). Tectonics, 28(3).

Iglseder, C., Grasemann, B., Schneider, D. A., Petrakakis, K., Miller, C., Klötzli, U. S., ... & Rambousek, C. (2009). I and S-type plutonism on Serifos (W-Cyclades, Greece). Tectonophysics, 473(1), 69-83.

Jansen, J. B. H. (1973). Geological map of Naxos (1/50 000). Nation. Inst. Geol. Mining Res., Athens.

Jolivet, L., & Faccenna, C. (2000). Mediterranean extension and the Africa-Eurasia collision. Tectonics, 19(6), 1095–1106. https://doi.org/10.1029/2000TC900018

Jolivet, L., & Brun, J. P. (2010). Cenozoic geodynamic evolution of the Aegean. International Journal of Earth Sciences, 99(1), 109–138. https://doi.org/10.1007/s00531-008-0366-4

Jolivet, L., Goffé, B., Monié, P., Truffert-Luxey, C., Patriat, M., & Bonneau, M. (1996). Miocene detachment in Crete and exhumation P-T-t paths of high pressure metamorphic rocks, Tectonics, 15(6), 1129-1153.

Jolivet, L., Faccenna, C., Goffé, B., Evgenii, B., & Agard, F. (2003). Subduction tectonics and exhumation of high-pressure metamorphic rocks in the Mediterranean orogens. American Journal of Science, 303(5), 353–409. https://doi.org/10.2475/ajs.303.5.353

Jolivet, L., Rimmelé, G., Oberhänsli, R., Goffé, B., & Candan, O. (2004). Correlation of syn-orogenic tectonic and metamorphic events in the Cyclades, the Lycian nappes and the Menderes massif. Geodynamic implications. Bulletin de La Societe Geologique de France, 175(3), 217–238. https://doi.org/10.2113/175.3.217

Jolivet, L., Faccenna, C., & Piromallo, C. (2009). From mantle to crust: Stretching the Mediterranean. Earth and Planetary Science Letters, 285(1–2), 198–209. https://doi.org/10.1016/j.epsl.2009.06.017

Jolivet, L., Lecomte, E., Huet, B., Denèle, Y., Lacombe, O., Labrousse, L., … Mehl, C. (2010a). The North Cycladic Detachment System. Earth and Planetary Science Letters, 289(1–2), 87–104. https://doi.org/10.1016/j.epsl.2009.10.032

Jolivet, L., Trotet, F., Monié, P., Vidal, O., Goffé, B., Labrousse, L., Agard, P., & Ghorbal, B. (2010b). Along-strike variations of P-T conditions in accretionary wedges and syn-orogenic extension, the HP-LT Phyllite-Quartzite Nappe in Crete and the Peloponnese, Tectonophysics, 480, 133-148, doi:110.1016/j.tecto.2009.1010.1002.

Jolivet, L., Faccenna, C., Huet, B., Labrousse, L., Le Pourhiet, L., Lacombe, O., … Driussi, O. (2013). Aegean tectonics: Strain localisation, slab tearing and trench retreat. Tectonophysics, 597–598, 1–33. https://doi.org/10.1016/j.tecto.2012.06.011

Jolivet, L., Menant, A., Sternai, P., Rabillard, A., Arbaret, L., Augier, R., … Le Pourhiet, L. (2015). The geological signature of a slab tear below the Aegean. Tectonophysics, 659, 166–182. https://doi.org/10.1016/j.tecto.2015.08.004

Katagas, C. G. (1980). Mineralogy and Metamorphic Zones and Physical Conditions of Metamorphism in Leros Island , Greece ch mat of metamorphic zones (~) I of Leros. Contributions to Mineralogy and Petrology, 73, 389–402. https://doi.org/O010-7999/80/0073/0389/$02.80

Katagas, C., & Sapountzis, E. (1977). Petrochemistry of low and medium grade mafic metamorphic rocks from Leros island, Greece. TMPM Tschermaks Mineralogische Und Petrographische Mitteilungen, 24(1–2), 39–55. https://doi.org/10.1007/BF01081744

Laurent, V., Jolivet, L., Roche, V., Augier, R., Scaillet, S., & Cardello, G. L. (2016). Strain localization in a fossilized subduction channel: Insights from the Cycladic Blueschist Unit (Syros, Greece). Tectonophysics, 672–673, 150–169. https://doi.org/10.1016/j.tecto.2016.01.036

Leake, B. E., Woolley, A. R., Arps, C. E., Birch, W. D., Gilbert, M. C., Grice, J. D., ... & Linthout, K. (1997). Report. Nomenclature of amphiboles: report of the subcommittee on amphiboles of the international mineralogical association commission on new minerals and mineral names. Mineralogical magazine, 61(2), 295-321.Lee, J., & Lister, G. S. 1992. Late Miocene ductile extension and detachment faulting, Mykonos, Greece. Geology, 20(2), 121-124.

Lee, J. & Lister, G.S. (1992). Late Miocene ductile extension and detachment faulting, Mykonos, Greece. Geology, 20, 121–124.

Lister, G. S., Banga, G., & Feenstra, A. (1984). Metamorphic core complexes of Cordilleran type in the Cyclades, Aegean Sea, Greece. Geology, 12(4), 221. https://doi.org/10.1130/0091-7613(1984)12<221:MCCOCT>2.0.CO;2

Menant, A., Jolivet, L., & Vrielynck, B. (2016). Kinematic reconstructions and magmatic evolution illuminating crustal and mantle dynamics of the eastern Mediterranean region since the late Cretaceous. Tectonophysics, 675, 103–140. https://doi.org/10.1016/j.tecto.2016.03.007

Oberhänsli, R., Monie, P., Candan, O., Warkus, F., Partzch, J., & Dora, O. (1998). The age of blueschist metamorphism in the Mesozoic cover series of the Menderes Massif. Scheweiz Mineral Petrogr, 78, 309–316.

Okrusch, M., & Bröcker, M. (1990). Eclogites associated with high-grade blueschists in the Cyclades archipelago, Greece: A review. European Journal of Mineralogy, 2(4), 451–478. https://doi.org/10.1127/ejm/2/4/0451

Parra, T., Vidal, O., & Jolivet, L. (2002). Relation between the intensity of deformation and retrogression in blueschist metapelites of Tinos Island (Greece) evidenced by chlorite–mica local equilibria. Lithos, 63(1), 41-66.

Pasteris, J. D., & Wopenka, B. (1991). Raman spectra of graphite as indicators of degree of metamorphism. The Canadian Mineralogist, 29(1), 1-9.

Piromallo, C., & Morelli, A. (2003). P wave tomography of the mantle under the Alpine-Mediterranean area. Journal of Geophysical Research: Solid Earth, 108(B2). https://doi.org/10.1029/2002JB001757

Pourteau, A., Sudo, M., Candan, O., Lanari, P., Vidal, O., & Oberhänsli, R. (2013). Neotethys closure history of Anatolia: Insights from 40Ar-39Ar geochronology and P-T estimation in high-pressure metasedimentary rocks. Journal of Metamorphic Geology, 31(6), 585–606. https://doi.org/10.1111/jmg.12034

Pourteau, A., Oberhänsli, R., Candan, O., Barrier, E., & Vrielynck, B. (2015). Neotethyan closure history of western Anatolia: a geodynamic discussion. International Journal of Earth Sciences, 105(1), 203–224. https://doi.org/10.1007/s00531-015-1226-7

Rabillard, A., Arbaret, L., Jolivet, L., Le Breton, N., Gumiaux, C., Augier, R., & Grasemann, B. (2015). Interactions between plutonism and detachments during metamorphic core complex formation, Serifos Island (Cyclades, Greece). Tectonics, 34(6), 1080–1106. https://doi.org/10.1002/2014TC003650

Reinecke, T., Altherr, R., Hartung, B., Hatzipanagiotou, K., Kreuzer, H., Harre, W., ... & Böger, H. (1982). Remnants of a Late Cretaceous high temperature belt on the island of Anafi (Cyclades, Greece). N. Jb. Miner. Abh, 145(2), 157-182.

Rimmelé, G., Jolivet, L., Oberhänsli, R., & Goffé, B. (2003). Deformation history of the high-pressure Lycian Nappes and implications for tectonic evolution of SW Turkey. Tectonics, 22(2), 1–21. https://doi.org/10.1029/2001TC901041

Rimmelé, G., Parra, T., Goffé, B., Oberhänsli, R., Jolivet, L., & Candan, O. (2005). Exhumation paths of high-pressure - Low-temperature metamorphic rocks from the Lycian Nappes and the Menderes Massif (SW Turkey): A multi-equilibrium approach. Journal of Petrology, 46(3), 641–669. https://doi.org/10.1093/petrology/egh092

Rimmele, G., Oberhansli, R., Candan, O., Goffe, B., & Jolivet, L. (2006). The wide distribution of HP-LT rocks in the Lycian Belt (Western Turkey): implications for accretionary wedge geometry. Tectonic Development of the Eastern Mediterranean Region, 260(1), 447–466. https://doi.org/10.1144/gsl.sp.2006.260.01.18

Ring, U., Laws, S., & Bernet, M. (1999). Structural analysis of a complex nappe sequence and late-orogenic basins from the Aegean Island of Samos, Greece. Journal of Structural Geology, 21(11), 1575–1601. https://doi.org/10.1016/S0191-8141(99)00108-X

Ring, U., Glodny, J., Will, T., & Thomson, S. (2010). The Hellenic Subduction System: High-Pressure Metamorphism, Exhumation, Normal Faulting, and Large-Scale Extension. Annual Review of Earth and Planetary Sciences, 38(1), 45–76. https://doi.org/10.1146/annurev.earth.050708.170910

Ring, U., Gessner, K., & Thomson, S. (2017). Variations in fault-slip data and cooling history reveal corridor of heterogeneous backarc extension in the eastern Aegean Sea region. Tectonophysics, 700, 108-130.

Roche, V., Laurent, V., Cardello, G. L., Jolivet, L., & Scaillet, S. (2016). Anatomy of the Cycladic Blueschist Unit on Sifnos Island (Cyclades, Greece). Journal of Geodynamics, 97, 62–87. https://doi.org/10.1016/j.jog.2016.03.008

Salaün, G., Pedersen, H. A., Paul, A., Farra, V., Karabulut, H., Hatzfeld, D., ... & SIMBAAD Team. (2012). High-resolution surface wave tomography beneath the Aegean-Anatolia region: constraints on upper-mantle structure. Geophysical Journal International, 190(1), 406-420.

Seidel, E., Kreuzer, H., & Harre,W. (1982). The late Oligocene/early Miocene high pressure in the external hellenides, geol. Jb., E23, 165-206.

Spakman, W., & Wortel, R. (2004). A tomographic view on western Mediterranean geodynamics. The Transmed Atlas-The Mediterranean Region from Crust to Mantle, 31–52. https://doi.org/10.1007/978-3-642-18919-7_2

Stavropoulos, A., & Gerolymatos, I. (1999). Geological map of Leros, IGME.

Sternai, P., Jolivet, L., Menant, A., & Gerya, T. (2014). Driving the upper plate surface deformation by slab rollback and mantle flow. Earth and Planetary Science Letters, 405, 110–118. https://doi.org/10.1016/j.epsl.2014.08.023

Theye, T., Seidel, E., &Vidal, O. (1992). Carpholite, sudoite and chloritoid in low high-pressure metapelites from Crete and the peloponese, Greece, Eur. J. Mineral., 4, 487-507.

Trotet, F., Jolivet, L., & Vidal, O. (2001). Tectono-metamorphic evolution of Syros and Sifnos islands (Cyclades, Greese). Tectonophysics, 338(2), 179–206. https://doi.org/10.1016/S0040-1951(01)00138-X

Urai, J. L., Schuiling, R. D., & Jansen, J. B. H. (1990). Alpine deformation on Naxos (Greece). Geological Society, London, Special Publications, 54(1), 509–522. https://doi.org/10.1144/GSL.SP.1990.054.01.47

Van Hinsbergen, D. J. J., Langereis, C. G., & Meulenkamp, J. E. (2005). Revision of the timing, magnitude and distribution of Neogene rotations in the western Aegean region. Tectonophysics, 396(1–2), 1–34. https://doi.org/10.1016/j.tecto.2004.10.001

Whitney, D. L., & Evans, B. W. (2010). Abbreviations for names of rock-forming minerals. American mineralogist, 95(1), 185-187.

Wopenka, B., & Pasteris, J. D. (1993). Structural characterization of kerogens to granulite-facies graphite: applicability of Raman microprobe spectroscopy. The American Mineralogist, 78(5-6), 533-557.

Wortel, M. J. R., & Spakman, W. (2000). Subduction and Slab Detachment in the Mediterranean-Carpathian Region. Science, 290(5498), 1910–1917. https://doi.org/10.1126/science.290.5498.1910

Wyers, G. P., & Barton, M. (1986). Petrology and evolution of transitional alkaline - sub alkaline lavas from Patmos, Dodecanesos, Greece: evidence for fractional crystallization, magma mixing and assimilation. Contributions to Mineralogy and Petrology, 93(3), 297–311. https://doi.org/10.1007/BF00389389

CHAPITRE IV : Evolution géodynamique de la région Est-Méditerranéenne

Afin de mettre en évidence le contrôle ou non de la déchirure sur la localisation de ces anomalies géothermales, il convient dans un premier temps de connaitre (i) la cinématique et (ii) l'évolution métamorphique et par conséquent thermique de ces roches qui se localisent à l'aplomb de cette déchirure. Bien que des études montrent des similitudes entre le Massif du Menderes et le domaine proche des Hellenides (les Cyclades) [*e.g.* Ring *et al.*, 1999 ; Jolivet *et al.*, 2004], aucune ne prend en compte la géologie des îles localisées dans le Dodécanèse. Cette partie de la mer Egée est par conséquent très mal connue, et la quantité de données acquises pendant la thèse (*e.g.* données structurales, RSCM) permet de discuter pour la première fois du métamorphisme et de la cinématique de la déformation dans cette région.

Principaux résultats :

Dans notre interprétation, on distingue dans le prisme orogénique des unités de couverture et de socle (*i.e.* le Massif du Menderes, le socle du Dodécanèse) qui ont suivi des évolutions P-T différentes. Même si la région est de la Méditerranée a été fortement affectée par l'extension post-orogénique, la même superposition d'unités dans le domaine des Cyclades, dans le Dodécanèse et dans le Massif du Menderes a été observée. De bas en haut, on différencie (i) des unités plutôt froides comme le Menderes Massif et sa couverture, Amorgos, Folegandros, ainsi que l'unité de Ténia qui fait partie intégrante du Dodécanèse. Ces différentes unités tectono-métamorphiques ont enregistré des évolutions P-T similaires dans les conditions du faciès des schistes bleus caractérisées par des températures froides (indiqué par la présence de carpholite et d'aragonite). Structuralement au-dessus, on retrouve (ii) une unité plus interne que la précédente (*i.e.* localisée dans la partie centrale des Cyclades) qui se caractérise par des conditions P-T atteignant le faciès des éclogites. Affleurant principalement sur les îles de Syros et de Sifnos, ces unités riches en métabasites affleurent également sur Samos et dans le Massif du Menderes (notamment dans la péninsule de Dilek). Finalement, l'unité des nappes Lyciennes, localisées au Nord du Massif du Menderes, a également enregistré un évènement de HP-BT. Alors que le pic du métamorphisme est Eocène pour l'unité des Eclogites [*e.g.* Laurent *et al.*, 2016], le pic métamorphique pour ces unités d'affinité Lycienne est daté au Crétacé [*e.g.* Pourteau *et al.*, 2014]. Ainsi, ces unités ont été exhumées précocement comparé aux deux autres unités. D'autre part, une partie de ces unités a subi une translation vers le sud entre l'Eocène et l'Oligocène [Collins & Robertson, 2003 ; Pourteau *et al.*, 2015] se retrouvant donc de part et d'autre du Massif du Menderes.

Il est important de noter que certaines de ces unités ont été exhumées précocement alors que d'autres ont été affectées par un évènement thermique important. C'est le cas notamment d'une partie des unités de la nappe éclogitique dans les Cyclades, ou encore des unités du Massif du Menderes, ou le réchauffement associé à la dynamique du slab conduit à la fusion partielle pendant l'extension post-

orogénique (*e.g.* Naxos, Mykonos, Ikaria, Menderes Massif). Cette extension se caractérise par une déformation coaxiale à l'échelle crustale, comme le traduit la présence de failles kilométriques à faible pendage à cinématique opposée (*e.g.* le NCDS et le WCDS dans les Cyclades, le Gediz et Büyük détachements dans le Massif du Menderes). A contrario, l'absence de migmatites et d'intrusions magmatiques dans la région du Dodécanèse implique que cette dernière ne semble pas avoir été affectée par cet évènement thermique majeur. Par ailleurs, la déformation dans cette région est asymétrique (*e.g.* le contact entre le socle et la couverture) et le sens de cisaillement indique une déformation vers le nord-est. La présence de stries sur des plans associés à des failles à faible pendage est également compatible avec une extension fragile N-S. Il existe donc un continuum de déformation du ductile jusqu'au fragile dans cette région.

Ainsi, depuis l'Oligo-Miocène la déformation dans ces deux régions est similaire, impliquant probablement une évolution géodynamique commune. Cette supposition remet en question la récente étude de Ring *et al.* [2017], qui suggère que la déchirure du slab sous la région du Massif du Menderes engendre une évolution tectonique différente pour ces deux régions. A la suite de ce chapitre, on peut donc se questionner sur les conséquences thermiques de cette déchirure. De ce fait, le Massif du Menderes, qui est considéré comme un MCC (*Metamorhpic Core Complex*), représente le parfait candidat pour étudier ces différentes anomalies thermiques puisqu'il se localise à l'aplomb de la déchirure.

Slab fragmentation beneath the Aegean/Anatolia transition zone: insights from the tectonic and metamorphic evolution of the Eastern Aegean region

Vincent ROCHE[1, 2, 3], Laurent JOLIVET[4], Dimitrios PAPANIKOLAOU[5], Erdin BOZKURT[6], Armel MENANT[7] and Gaëtan RIMMELE[8]

[1] *Université d'Orléans, ISTO, UMR 7327, 45071, Orléans, France*

[2] *CNRS/INSU, ISTO, UMR 7327, 45071 Orléans, France*

[3] *BRGM, ISTO, UMR 7327, BP 36009, 45060 Orléans, France*

[4] *Sorbonne Universités, UPMC Univ Paris 06, CNRS, Institut des Sciences de la Terre de Paris (iSTeP), 4 place Jussieu 75005 Paris, France*

[5] *National and Kapodistrian University of Athens, Department of Dynamics Tectonics and Applied Geology, Athens, Greece*

[6] *Middle East Technical University, Department of Geological Engineering, Üniversiteler Mahallesi, Dumlupınar Bulvarı No: 1, 06800 Ankara, Turkey*

[7] *Institut de Physique du Globe, Paris, France*

[8] *TOTAL SA, La défense*

(Cet article a été soumis à Tectonophysics)

Abstract

Slab tearing below western Turkey had first-order tectonic and magmatic consequences by inducing a lateral gradient of extension in the upper plate and toroidal flow of asthenosphere that affected the typology and distribution of melts at the surface. But the coupling mechanisms between the 3D mantle flow at depth and deformation in the upper plate above a slab tear have received little attention so far. This paper is focused on the description of the distribution and kinematics of deformation in the eastern part of the Aegean Sea, within the transition zone between the Cyclades and the Menderes Massif, which have been little studied. By investigating the Dodecanese and Eastern Aegean islands, we thus complete the description of the extensional strain field in the overriding plate around the slab tear. There, extension related to slab retreat and tearing keeps a constant NNE-SSW direction accommodating the difference in finite rates of extension, without localized crustal-scale strike-slip faults and block rotations above the tear. In addition, despite the complexity involved in the Aegean-Anatolian orogenic wedge, a similar structural position is recognized through the entire region. From top to bottom, we found that (i) the Lycian units which were exhumed earlier, in the Late Cretaceous, (ii) the higher-pressure and higher-temperature units (i.e. the Upper Cycladic Blueschist Nappe), with exception of the Vourliotes nappe in Samos, and finally (iii) the colder units (merged in the Lower Blueschist Nappe, LBN) such as the Menderes and its cover before the MMM overprint, the Lower Cycladic Blueschist Nappe (e.g. Amorgos, a part of the Dodecanese and Fourni islands).

IV.1. Introduction

Slab rollback and tearing are common features in subduction zones and have a strong impact on the tectonic and metamorphic evolution of the overriding plate [e.g. Dewey, 1988; Royden, 1993; Wortel & Spakman, 2000; Govers & Wortel, 2005; Jolivet *et al*., 2013; Sternai *et al*., 2014]. One of the best examples to study consequences of this slab dynamics is located in the Eastern Mediterranean region, where numerous mantle tomography studies elucidate the deeper lithosphere structures [Bijward *et al*., 1998; De Boorder *et al*., 1998; Piromallo & Morelli, 2003; Wortel & Spakman, 2004; Li *et al*., 2008; Biryol *et al*., 2011; Salaün *et al*., 2012; Delph *et al*., 2015]. Although results show a clear ~ 200 km-depth low-velocity anomaly below western Turkey interpreted as a major tear in the Hellenic slab, there is no consensus about (i) the time-space evolution [e.g. Dilek & Altunkaynak, 2009; Jolivet *et al*., 2015a; Menant *et al*., 2016a; Gover & Fichtner 2016] and the consequences of that tearing (e.g. kinematics and metamorphism in the overriding plate, block rotations…) and (ii) the cause of the tearing remains to be understood [e.g. Papanikolaou, 2013; Gover & Fichtner 2016]. In any case, a wide sinistral lithospheric-scale shear zone accommodating different finite rates of back-arc extension due to the slab tear, named the West Anatolia Transfer Zone (WATZ) (Fig. IV.1), has been described [Ring *et al*., 1999; Gessner *et al*., 2013; Jolivet *et al*., 2015]. More recently, Ring *et al*. [2017] showed that regional variations (e.g. Samos) are controlled by the sinistral component of the WATZ that was superimposed on the regional NNE-SSW extension.

To better understand the crustal consequences of tearing, and thus the geodynamic evolution of the Eastern Mediterranean domain, it appears therefore crucial to clarify (i) the geological correlations between the Cyclades and the Menderes Massif that have often been disputed due to significant lithological differences [e.g. Ring *et al*., 1999a; Jolivet *et al*., 2004] and (ii) the distribution of kinematic indicators and the extent of metamorphic events in this region since the initiation of the tear. However, apart from the recent work of Ring *et al*. [2017] focusing on brittle deformation, very few geological studies [e.g. Franz & Okrusch, 1992; Franz *et al*., 2005; Roche *et al*., 2018a] were devoted so far to those islands located in the WATZ (e.g. Fourni, Arki, Lipsi and Leros) (Fig. IV.1). We therefore focus on these islands, by describing for the first time a complete regional scheme of ductile kinematic indicators and associated pressure-temperature (P-T) conditions. We then shed light on the possible relations between the Cyclades and the Menderes Massif and, finally, we discuss the evolution of the tear in the subducting African lithosphere and its consequences on the upper plate tectonic history.

IV.2. Geological and Geodynamic setting

Since the early Cenozoic at least, a single lithospheric slab has been continuously subducting northward below the Aegean region, accommodating most of the slow convergence between Africa and Eurasia during the closure of the Neotethys oceanic realm [e.g. Spakman *et al*., 1988; Faccenna *et al*., 2003; Jolivet *et al*., 2003; Van Hinsbergen *et al*., 2005; Jolivet & Brun, 2010; Biryol *et al*., 2011; Papanikolaou, 2013]. This area has therefore recorded the complete succession of tectonic episodes from the Late Cretaceous obduction, and Paleocene-Eocene continental accretion and crustal thickening, to the Late Oligocene to Present back-arc extension [Le Pichon & Angelier, 1981a; Bonneau, 1982; Papanikolaou, 1987; Jolivet & Faccenna, 2000; Van Hinsbergen *et al*., 2005; Jolivet *et al*., 2004a].

Before the Aegean extension started, the Vardar Ocean was sutured in the northern part of the Aegean domain until the late Cretaceous-Paleocene when the last remaining ocean was closed. The convergence between Apulia and Eurasia then continued and led to the formation of a south-verging crustal scale orogenic wedge, the Hellenides and the Taurides [Brunn, 1956; Aubouin, 1959; Brunn *et al*., 1970; Jacobshagen *et al*., 1978]. It is mainly composed of a stack of crustal slices that were decoupled from the subducting African-Adriatic lithospheric slab [Brunn *et al*., 1976; Bonneau & Kienast, 1982; Jolivet *et al*., 2003; Van Hinsbergen *et al*., 2005; Brun & Faccenna, 2008; Jolivet & Brun, 2010; Ring *et al*., 2010]. These nappes consist in coherent stratigraphic sequences and sedimentary facies, each characterizing a paleogeographic environment. Despite the importance of the post-orogenic overprint on orogenic architecture, various correlations (e.g. stratigraphy, pre-orogenic paleogeography lithologies, tectono-metamorphic history) have been proposed between Greece and Turkey in the Aegean region [Brunn *et al*., 1976; Dürr *et al*., 1978; Papanikolaou & Demirtasli, 1987; Robertson *et al*., 1991; Papanikolaou, 1996; 1997; Göncüoğlu *et al*., 1997; Ring *et al*., 1999a; Jolivet *et al*., 2004b].

The two regions show significant differences such as the age of the obduction episode, which is late Jurassic in Greece and late Cretaceous in Turkey and part of the Aegean Sea [Brunn *et al*., 1976; Bonneau, 1982; Bonneau, 1984; Robertson *et al*., 1996; Okay *et al*., 2001; Jolivet *et al*., 2004; Papanikolaou, 2009], and a variation of crustal thickness from ~ 35 km below western Turkey to ~ 26 km below the Cyclades and 18 – 15 km below the North Aegean and Cretan Sea [Makris, 1978; Le Pichon & Angelier, 1981a; 1981b; Vigner, 2002; Tirel *et al*., 2004]. More recent seismic investigations with receiver functions however showed that Moho depth below the Menderes Massif is around 26 km, a figure similar to what is observed below the Cyclades [Karabulut *et al*., 2013], suggesting that finite crustal thinning is not so different between the two regions and that the present difference in altitude is thus not the result of differential crustal thinning, except for the Cretan Sea. In both areas, nappe stacking induced the formation and exhumation of high pressure-low temperature (HP-LT) parageneses within the subduction zone at many places (e.g. during the latest Cretaceous in the

Afyon zone, during the Eocene in the Cyclades, during the Oligo-Miocene in Crete and Peloponnese) [e.g. Okay, 1986; Jolivet & Brun, 2010; Pourteau *et al*., 2016].

Since the Early Oligocene, the collapse of the Hellenides-Taurides belt and post-orogenic extension in this region have been mainly controlled by the southward retreat of the African slab [e.g. Le Pichon & Angelier, 1981b; Lister *et al*., 1984; Jolivet & Faccenna, 2000; Jolivet & Brun, 2010]. The nappe stack was cut by extensional low-angle normal faults leading to the exhumation of a series of metamorphic core complexes (MCCs) along a warmer geotherm [Lister *et al*., 1984; Avigad & Garfunkel, 1989; 1991; Gautier & Brun, 1994; Jolivet *et al*., 2004a]. For instance, in the Aegean domain, top-to-the-N detachments described in the northern part of the Cyclades link up to form the crustal-scale North Cycladic Detachment System [NCDS, Jolivet *et al*., 2010]. Top-to-the-SW kinematics was also described in the western part of the Cyclades linked into a single major detachment system named the West Cycladic Detachment System (WCDS [Grasemann *et al*., 2012]). In western Anatolia, the exhumation of the Menderes Massif Core Complex is also mainly accommodated by three detachments: (i) the top-to-the-S Büyük Menderes detachment [e.g. Hetzel *et al*., 1995a; Gessner *et al*., 2001a]; (ii) the top-to-the-NNE Gediz detachment (also named Alaşehir or Kuzey detachment) [e.g. Hetzel *et al*., 1995a; Gessner *et al*., 2001a]; and (iii) the top-to-the-NE the Simav detachment [e.g. Işık & Tekeli, 2001].

The present-day context is characterized by a more localized extension to the west in the Peloponnese and the Corinth and Volos rifts [Armijo *et al*., 1996; Rigo *et al*., 1996], to the east in the central part of the Menderes Massif [Seyitoglu *et al*., 1992; Seyitoglu & Scott, 1996; Aktug *et al*., 2009] and to the south in Crete [Angelier *et al*., 1982; Lallemant *et al*., 1994; Armijo *et al*., 1992; Flerit *et al*., 2004]. The Cyclades and the Menderes Massif (Fig. IV.1) are also part of the Anatolia-Aegean domain that is currently extruding at a fast rate along the dextral North Anatolian Fault (NAF) since 5 Ma [McKenzie, 1972; Barka, 1992; Le Pichon *et al*., 1995; McClusky *et al*., 2000; Reilinger *et al*., 2006; 2010]. In addition, instantaneous GPS velocities further show that the Aegean domain moves faster to the southwest than the Anatolian plate, the difference being accommodated by the active extension [Le Pichon *et al*., 1995; Armijo *et al*., 1999; McClusky *et al*., 2000; Jolivet, 2001]. Most of the history of this region is thus controlled by stresses imposed by the retreating subduction [Le Pichon & Angelier, 1979; Mercier *et al*., 1989; Faccenna *et al*., 2006; Sternai *et al*., 2014]. In the following, we briefly present the main units across the Aegean domain and western Turkey.

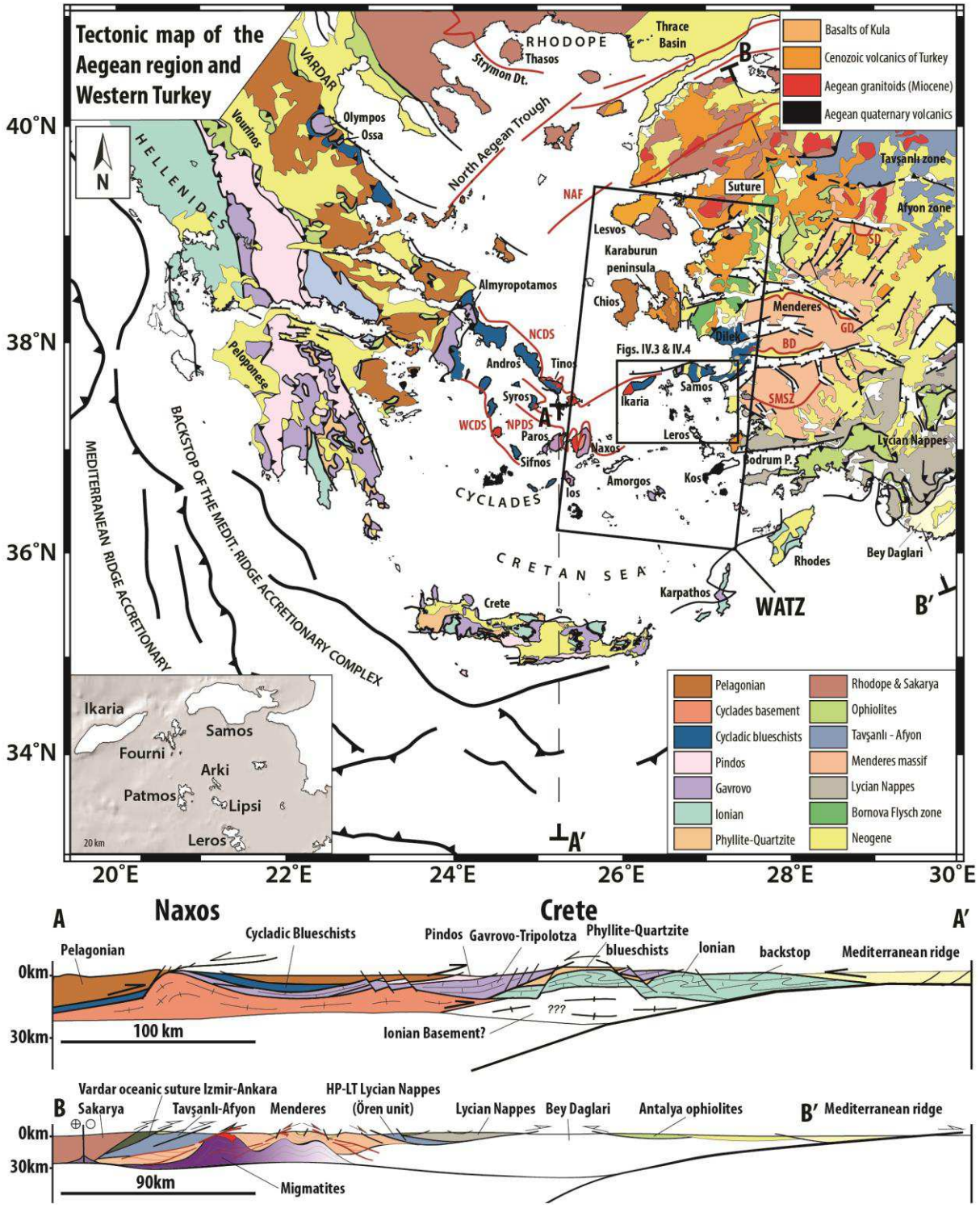

Figure IV.1: Tectonic map of the eastern Mediterranean region and the location of the study area modified from Jolivet & Brun [2010]. Note that the black rectangle corresponds to the location of the studied islands (i.e. Samos, Fourni, Arki, Lipsi and Leros), which are showed in the bottom left corner. Also indicated two N-S cross-sections, modified from Jolivet et al. [2004] and from Roche et al. [2018b]. Main extensive structures are indicated in abbreviations: BD (Büyük Menderes Detachment); GD (Gediz Detachment); NAF (North Anatolian Fault); NCDS (The North Cycladic Detachment System); NPDS (Naxos-Paros Extensional Fault System); SD (Simav Detachment); SMSZ (Southern Menderes shear zone); WATZ (West Anatolia Transfer Zone); WCDS (The West Cycladic Detachment System).

The present-day context is characterized by a more localized extension [Le Pichon *et al.*, 1995; Reilinger *et al.*, 1995; Kahle *et al.*, 2000; McClusky *et al.*, 2000]. The Cyclades archipelago is now quite stable while extension has recently concentrated to the west in the Peloponnese and the Corinth and Volos rifts [Armijo *et al.*, 1996; Rigo *et al.*, 1996], and to the east in the Main Menderes Massif [Seyitoglu *et al.*, 1992; Seyitoglu & Scott, 1996; Aktug *et al.*, 2009]. Extension is also active in Crete and further south until the Hellenic trench that represents the southernmost edge of the Aegean continental domain [Angelier *et al.*, 1982; Lallemant *et al.*, 1994; Armijo *et al.*, 1992; Flerit *et al.*, 2004]. The Cyclades and the Menderes Massif (Fig. IV.1) are part of the Anatolia-Aegean domain that is currently extruding at a fast rate along the dextral North Anatolian Fault [McKenzie, 1972; Barka, 1992; Le Pichon *et al.*, 1995; McClusky *et al.*, 2000; Reilinger *et al.*, 2006; 2010]. This westward motion started around 5 Ma [Armijo *et al.*, 1999] and can be described by a rotation about an eulerian pole located along the northern African margin near the Nile delta. In addition, instantaneous GPS velocities further show that the Aegean domain moves faster to the southwest than the Anatolian plate, the difference being accommodated by the active extension [Le Pichon *et al.*, 1995; Armijo *et al.*, 1999; McClusky *et al.*, 2000; Jolivet, 2001]. Most of the history of this region is thus controlled by stresses imposed by the subduction [Le Pichon and Angelier, 1979; Mercier *et al.*, 1989; Sternai *et al.*, 2014]. In the following, we briefly present the main units across the Aegean domain and Western Turkey.

IV.2.1. Aegean domain and continental Hellenides

IV.2.1.1. Pelagonian Nappe

The Pelagonian nappe is mainly found in continental Greece, but also in Cyclades and Crete (i.e. the so-called Upper Cycladic unit), where some remnants are observed, resting on top of the extensional metamorphic complexes (Fig. IV.1) [Reinecke *et al.*, 1982; Bonneau, 1984; Papanikolaou, 1987]. It consists of a Paleozoic basement and its Mesozoic platform sequence cover, as well as of an ophiolitic nappe obducted at the end of the Jurassic (Vourinos ophiolite) [Aubouin, 1959; Celet & Ferrière, 1978; Walcott & White, 1998]. The Pelagonian is crossing the Central Aegean from Evia to Skyros and Chios [Papanikolaou, 2013] with prolongation also in the opposite Karaburun peninsula (Fig. IV.1). Further south, the Pelagonian nappe is found above the detachments of Tinos, Syros, Paros and Mykonos, implying that it once largely covered the Aegean domain [Patzak *et al.*, 1994; Katzir *et al.*, 1996; Sanchez-Gomez *et al.*, 2002]. It also crops out further south in Crete within the Asteroussia nappe, containing various lithologies [Bonneau, 1984]. In addition, a distinct non-metamorphic unit, named Arvi nappe, is found in Crete below the Asteroussia nappe [Bonneau, 1972]. This unit consists

in late Cretaceous pillow-lava and sediments, and it has been correlated by Bonneau [1972] with the Lycian Nappes of western Turkey.

IV.2.1.2. Pindos Nappe

The Pindos nappe crops out in continental Greece, Peloponnese and Crete in a similar tectonic position as the Cycladic Blueschists Unit (CBU), immediately below the Pelagonian nappe and above the Gavrovo-Tripolitza carbonate platform (Fig. IV.1). It corresponds to a basinal area with pelagic and siliceous deposits on a thinned continental crust from the Triassic to the Eocene, overlain by an Eocene-Oligocene flysch [Brunn, 1956; Aubouin, 1959; Bonneau, 1982; Papanikolaou, 1987; Stampfli *et al*., 2003]. Similar to the CBU, some parts of the basin might have been oceanic, as attested by the occurrence of basaltic material. As a consequence, Bonneau [1982] and Papanikolaou [1987; 2013] have proposed that the Pindos nappe represents the non-metamorphosed equivalent of the CBU.

IV.2.1.3. Cycladic Blueschist Unit

The CBU crops out in most of the Cyclades (Fig. IV.1), and includes metabasic rocks interleaved with metapelites and marbles. It rests upon a continental basement that best crops out on Naxos, Paros and Ios islands [Jansen, 1973; Lister *et al*., 1984; Feenstra, 1985; Urai *et al*., 1990; Avigad, 1998; Huet *et al*., 2009]. According to Papanikolaou [1987; 2013], the Cycladic Blueschists belong to two different stratigraphic units, the Northern Cyclades representing a pelagic-oceanic environment without a pre-Alpine continental basement, contrary to the southern Cyclades which are characterized by a shallow-water carbonate platform with metabauxites and with a probable pre-alpine basement. Considered as an equivalent of the Pindos nappe [Bonneau & Kienast, 1982] forming the Pindos-Cyclades oceanic basin (i.e. terrane H2 from Papanikolaou [2013]), this unit experienced a complex alpine tectono-metamorphic evolution with (i) an early burial in blueschist- to eclogite-facies conditions during the Eocene, with a peak of pressure estimated around 20 ± 2 kbar and 550 ± 50 °C [e.g. Bröcker *et al*., 1993; Will *et al*., 1998; Keiter *et al*., 2004; Bröcker *et al*., 2013; Trotet *et al*., 2001; Groppo *et al*., 2009; Dragovic *et al*., 2012; 2015; Ashley *et al*., 2014; Augier *et al*., 2015; Laurent *et al*., 2018] (Fig. IV.2); (ii) a high temperature overprint locally reaching the amphibolite-facies and dated from the late Oligocene - early Miocene [Altherr *et al*., 1979; Altherr *et al*., 1982; Parra *et al*., 2002 ; Bröcker *et al*., 2013; Duchêne *et al*., 2006; Laurent *et al*., 2017]. Recent studies have revealed a variability in the peak metamorphic conditions in the Cycladic Blueschists. A southern fringe shows lower-pressure conditions and colder temperature as for instance on the island of Folegandros [Augier *et al*., 2015; Grasemann *et al*., 2017]. Grasemann *et al*. [2018] have thus proposed the existence of

two main nappes, showing eclogite-facies parageneses and blueschist-facies parageneses, respectively. Both nappes are renamed recently by Roche *et al*. [2018a] the "Upper Cycladic Blueschist Nappe" and the "Lower Cycladic Blueschist Nappe".

IV.2.1.4. Gavrovo Nappe-Tropolitza

The Gavrovo-Tripolitza is mainly found unmetamorphosed in the external zones of the Hellenides and in Crete [Bonneau & Kienast, 1982; Bonneau, 1984]. However, evidence of HP-LT parageneses [Schermer, 1990; Shaked *et al*., 2000] are preserved in internal tectonic windows (e.g. Olympos, Ossa, Almyropotamos, Fig. IV.1) below the Pelagonian and Cycladic Blueschists (Fig. IV.1) [Godfriaux, 1962, 1965; Godfriaux & Pichon, 1980; Godfriaux & Ricou, 1991; Schermer, 1993; Shaked *et al*., 2000]. Highly metamorphosed equivalents crops out in the Cyclades as in the core of Tinos and Naxos metamorphic domes (i.e. the so-called Cycladic Basement) [Avigad & Garfunkel, 1989; Ring *et al*., 2001; Jolivet *et al*., 2004b]. This nappe corresponds to a thick sequence of platform carbonates ranging from the Triassic to the Eocene, with a late Eocene - early Oligocene flysch in the most external domain [Aubouin, 1959]. In addition, the presence of nummulites in the metamorphic part of the flysch or in a hardground at the top of the limestones, attests that the underthrusting and HP-LT metamorphism is younger than the early Eocene [Dubois & Bignot, 1979; Godfriaux & Pichon, 1980; Godfriaux & Ricou, 1991], which is confirmed by radiometric ages [Schermer *et al*., 1990].

IV.2.1.5. Phyllite-Quartzite Nappe

The Phyllite-Quartzite (or Phyllades) complex is only found in Peloponnese and Crete (Fig. IV.1). It corresponds to a thick detrital sequence of quartzites, conglomerates and schists, with minor limestones and metabasites dated from the late Carboniferous to the Mid Triassic [Creutzburg, 1977; Greilling, 1982; Krahl *et al*., 1983; Hall *et al*., 1984]. However, this sequence has been recently challenged by Papanikolaou and Vassilakis [2010]. They demonstrated a probable distinction between the Paleozoic low-medium grade metamorphic rocks of the Arna unit and the underlying formations, such as the fossiliferous formations belonging to the Tyros/Ravdoucha Beds-base of Tripolis or to a lateral equivalent of western Crete unit. Locally, this unit also contain basement units such as in eastern Crete. It is highly metamorphosed in HP-LT conditions, with a peak of pressure dated around 25 Ma and the final exhumation around 15 Ma [Seidel, 1978; Seidel *et al*., 1982; Theye & Seidel, 1991; Theye *et al*., 1992; Theye & Seidel, 1993; Bassias & Triboulet, 1994; Jolivet *et al*., 1996; 2010;

Thomson *et al*., 1998]. All this sequence was exhumed from below the Gavrovo-Tripolitza nappe by the Cretan Detachment, active during the deposition of a supra-detachment basin [Jolivet *et al*., 1996; Van Hinsbergen *et al*., 2006; Seidel *et al*., 2007; Zachariasse *et al*., 2011]. An alternative interpretation linking syn-orogenic exhumation with continuous compression was also proposed by Chatzaras *et al*. [2006].

IV.2.1.6. Ionan and Paxos Nappes

The metamorphosed Ionian nappe (known also as Mani unit from Papanikolaou [2013]), located below the Phyllite-Quartzite nappe, crops out in the whole external domain including the Peloponnese, Crete, Karpathos and Rhodos (Fig. IV.1) [Bonneau, 1982; Bonneau & Kienast, 1982; Thiebault, 1982; Bonneau, 1984]. From base to top, this nappe is made of a neritic calcareous sequence dated from the upper Triassic to mid Liassic, a pelagic sequence from the middle Jurassic to Eocene covered with an upper Eocene to Miocene flysch [Aubouin, 1959]. Although this nappe is found unmetamorphosed in the west and in the southernmost Dodecanese islands (e.g. Karpathos and Rhodes), it instead shows HP-LT parageneses in Peloponnese and Crete with occurrences of Fe-Mg-carpholite and aragonite [Theye *et al*., 1992; Theye & Seidel, 1993]. Finally, the most external Paxos unit is made of a continuous carbonate platform dated from the Jurassic to the Miocene and covered with a Miocene to Pliocene flysch cropping out in the west in the Ionian Islands.

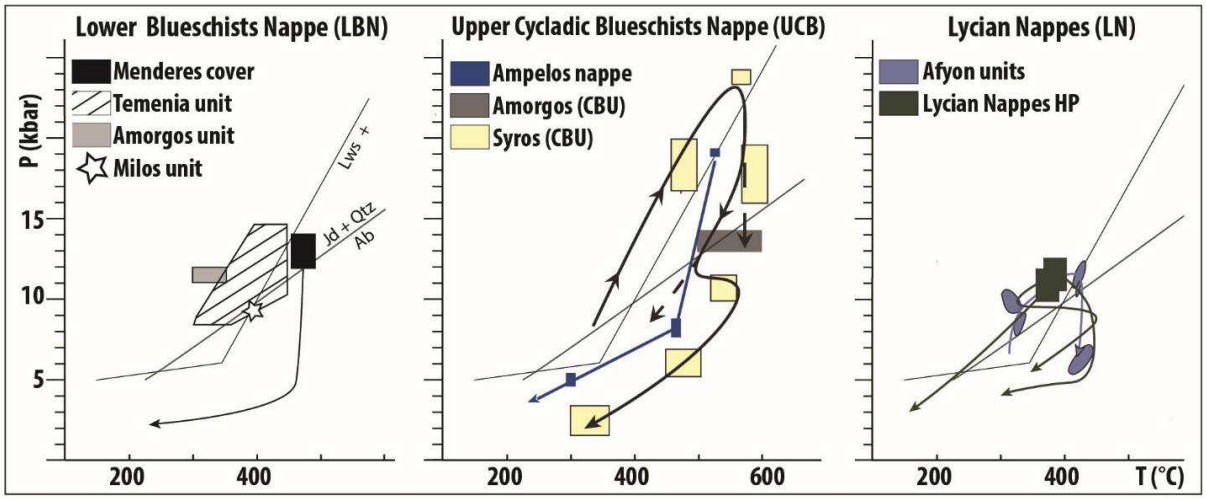

Figure IV.2: Compilation of P-T paths. Data are from Theye et al. [1997], Will et al. [1998], Rimmelé et al. [2005], Rosenbaum et al. [2007], Pourteau et al. [2014], Laurent et al. [2018] and Roche et al. [2018a].

IV.2.2. Western Turkey

Western Anatolia can be subdivided into three continental domains distinguished on the basis of structural, stratigraphic and metamorphic criteria: (i) the Eurasian margin of Istanbul Zone [Okay, 1989]; (ii) the Strandja Massif and the Sakarya Zone, which are primary Tethyan units accreted during the Jurassic [Sengör, 1984]; and (iii) the Africa-derived Anatolides-Taurides. The latter is located just south of the Izmir-Ankara suture zone and consists of a Mesozoic carbonate platform with a Precambrian - Paleozoic continental basement (Fig. IV.1) [Sengör & Yılmaz, 1981; Okay *et al*., 1996]. It recorded different P-T metamorphic conditions (i.e. Tavşanlı, Afyon and Ören units), resulting from successive late Cretaceous - early Cenozoic underthrusting events and subsequent Eocene collision and exhumation [Şengör & Yılmaz, 1981; Kaymakci *et al*., 2009; Torsvik & Cocks, 2009]. In western Turkey, these units were then partly affected by the Oligocene - Miocene post-orogenic extension [e.g. Dilek & Altunkaynak, 2009; Ersoy & Palmer, 2013].

IV.2.2.1. Afyon and Ören metamorphic domain

The Afyon Zone consists also of a coherent stratigraphic section from a Precambrian - Paleozoic continental basement dominated by micaschists, and overlain by early Triassic - early Tertiary platform to deep marine sediments with alkaline volcanic occurrences (Fig. IV.1) [Candan *et al*., 2002]. The presence of sodic amphiboles, carpholite and aragonite relics indicate blueschist-facies metamorphism [Candan *et al*., 2005; Pourteau *et al*., 2010, 2014; Scheffler *et al*., 2016]. Pourteau *et al*. [2013] correlated this unit with the Ören unit (also named Karaova unit by Rimmelé *et al*. [2003a]), which lies on the top of the CBU and the Menderes Massif.

Ören unit crops out in the southern part of the Menderes Massif and consists of Mesozoic clastic to carbonate rocks, overlain by a sedimentary mélange (Fig. IV.1) [Bernoulli *et al*., 1974; Rimmelé *et al*., 2003a]. According to several authors [e.g., Erdoğan & Güngör, 2004; Rimmelé *et al*., 2003a], the Ören unit was initially located north of the Menderes Massif, suggesting a southward translation over more than 300 km between the upper Cretaceous and the late Miocene [Hayward, 1984; Van Hinsbergen, 2010]. This unit underwent a HP-LT metamorphism event (Fig. IV.2) [Oberhänsli *et al*., 2001; Rimmelé *et al*., 2003a; 2005; Scheffler *et al*., 2014] around 62 – 59 Ma [^{40}Ar-^{39}Ar on white mica; Pourteau *et al*., 2013]. According to Papanikolaou & Demirtasli [1987], this unit is equivalent from the stratigraphic point of view to the Ionian/Mani unit with characteristic formations at the upper horizons such as the multicolored cipolines, beneath the phyllites of the metaflysch). A difference should however be pointed out. HP-LT metamorphism in these two units has been recorded at different moments. The HP-LT metamorphic event in the Ionian unit of Crete dates from the Oligocene - Miocene [Jolivet *et al*., 1996] while it goes back to the Paleocene in the Ören unit [Pourteau *et al*., 2013]. The

two units thus cannot strictly speaking belong to a single tectonic unit, although the stratigraphy in the Late Cretaceous may be similar, suggesting that the two basins were connected at this period.

IV.2.2.2. Cycladic Blueschist Unit

The Ören unit is tectonically overlain by the CBU (see above), mainly exposed in the Dilek Peninsula (Fig. IV.1). This unit shows an epidote-blueschist-facies metamorphic sequence of Permian–Mesozoic neritic carbonate, tectonically overlain by an ophiolitic mélange (e.g. metagabbro, serpentinite and marble) [Okrusch *et al*., 1984; Candan *et al*., 1997; Ring *et al*., 1999b; Çetinkaplan, 2002]. Correlation with the Aegean domain suggests peak metamorphism around 50 Ma [Ring *et al*., 1999a; Pourteau *et al*., 2013] but Oberhänsli *et al*. [1998] dated this HP-LT metamorphism in the Dilek Peninsula around 40 Ma (^{40}Ar-^{39}Ar on phengite).

IV.2.2.3. Menderes Massif

The Menderes Massif is a tectonic window exposing metamorphic rocks that were derived from the central Anatolide-Tauride continental block, originally south of the Tavşanlı suture domain and Afyon domains (Fig. IV.1) [e.g. Pourteau *et al*., 2013]. Schuiling [1962] classically subdivided the Menderes Massif into a "core" of augen gneisses, and a metasedimentary "cover". Alternatively, Gessner *et al*. [2001b] presented the Menderes Massif as a stack of nappes formed from the early Paleozoic to the Tertiary and consisting of a series of crystalline Pan-African basement and Mesozoic limestone units that underwent a complex Alpine history. Kinematics of deformation and metamorphism remain largely debated [e.g. Bozkurt & Park, 1994; Régnier *et al*., 2003; Ring *et al*., 2003; Bozkurt, 2004; 2007].

The "core" corresponds to the Çine unit that consists of a high grade metaclastic sequence, up to 6 km in thickness, deposited around 600 – 590 Ma [Candan *et al*., 2001; Koralay *et al*., 2012] and intruded by voluminous granitoids, and gabbros between 570 and 520 Ma [e.g. Hetzel & Reischmann, 1996; Gessner *et al*., 2001b; Candan *et al*., 2016]. These lithologies have a generally well-developed foliation that is regionally consistent across most of the Menderes Massif. The Çine unit experienced a regional high temperature-low pressure (HT-LP) metamorphism at 620 °C, 7 kbar [e.g. Akkök, 1983; Bozkurt & Park, 1999; Bozkurt & Oberhänsli, 2001] that locally overprints eclogitic mafic inclusions (640 °C and 15 kbar [Oberhänsli *et al*., 1997; Candan *et al*., 2001]). Both the eclogites and the metasediments provide geochronological evidence for a Pan-African metamorphism (e.g. U-Pb dating of monazite inclusions in garnet [Catlos & Çemen, 2005; Oberhänsli *et al*., 2010]).

The "cover" series well crops out in the central and southern parts of the massif. It is defined by a metasedimentary sequence, including conglomerates, graphitic schists and quartzites with carbonate beds from the upper Paleozoic to lower Mesozoic [e.g. Schuiling, 1962; Dora *et al*., 2001; Régnier *et al*., 2003; Erdoğan & Güngör, 2004]. According to different studies [e.g. Bozkurt, 2001; Gessner *et al*., 2001; Rimmelé *et al*., 2003b], this "cover" underwent two or three main metamorphic events. The first event corresponds to an Eocene HT-LP metamorphism, with metamorphic conditions evolving from 625 – 670 °C, 7 – 9 kbar to 550 °C, 6 – 8 kbar, from north to south [Whitney & Bozkurt, 2002; Schmidt *et al*., 2015; Cenki-Tok *et al*., 2016]. This metamorphism probably developed during the crustal thickening associated with the internal imbrication of the Anatolide-Taurides platform. Whereas there is a common agreement in the literature about this main HT-LP event, currently no consensus has been reached on the HP-LT event, which is well preserved in the southern part of the massif (i.e. Kurudere - Nebiler unit). Indeed, Rimmelé *et al*. [2003b] showed the presence of magnesio-carpholite, suggesting HP-LT metamorphic conditions (470 – 500 °C and 12 – 14 kbar) (Fig. IV.2). According to these authors the carpholite-bearing sequence belongs to the cover of the Menderes Massif, implying that the whole massif underwent HP-LT metamorphism. Most other studies however interpreted these metamorphic sediments as a separate nappe, tentatively correlated with the CBU [Ring *et al*., 1988; 1999a; Régnier *et al*., 2007; Pourteau *et al*., 2014; 2016]. Finally, Cenki-Tok *et al*. [2016] show young ages around 25 – 20 Ma for mylonites and migmatites in the northern part of the massif, showing that it has recorded the same HT-LP event as the Cyclades in the Late Oligocene and early Miocene.

IV.2.3. Eastern Aegean Islands

Samos and Fourni Islands are located in the eastern part of the Aegean Sea, two kilometers west of Dilek peninsula (western Turkey, Fig. IV.1). Several studies were devoted to Samos Island that occupies a key-position at the transition between Aegean domain and western Turkey [Mposkos, 1978; Papanikolaou, 1979; Theodoropoulos, 1979; Mposkos & Perdikatsis, 1984; Weidmann *et al*., 1984; Mezger & Okrusch, 1985; Okrusch *et al*., 1984; Chen, 1995; Will *et al*., 1998; Ring *et al*., 1999b; Ring *et al*., 2007]. Alternatively, no study was published on Fourni and only one on the nearby island of Thymaena [Papanikolaou, 1980]. There, the Thymaena unit consists of sandstones and red nodular limestones with mafic igneous rocks from the middle Triassic, and white dolomites and neritic limestones with megalodon from the upper Triassic. According to Papanikolaou [1980], this nappe is cut by a series of minor thrusts shown by the superposition of middle Triassic sediments on top of upper Triassic ones. In the following, we briefly present the geology on Samos Island, where several metamorphic units and large fluvial to lacustrine Miocene sedimentary basins are observed (Fig. IV.3a).

IV.2.3.1. Samos

The metamorphic succession of Samos consists of four distinct tectono-metamorphic units, from the base to the top. (i) The Kerketeas marbles crop out in the western part of the island in a tectonic window below the overlying Ampelos unit [Papanikolaou, 1979; Theodoropoulos, 1979; Ring *et al*., 1999b]. The tectonic contact between these units is named Pythagoras Thrust. The Kerketeas unit consists in a monotonous sequence of dolomitic marbles with local schist on top that can be correlated with the Cycladic basement, i.e. the Gavrovo-Tripolitza nappe; incipient HP-LT metamorphism and a subsequent greenschist overprint is recorded [Mposkos, 1978]. (ii) The Ampelos unit outcrops over the central part of the island. We include in this unit the Agios Nikolaos unit distinguished by some authors [Ring *et al*., 1999b]. It is mainly made of metasediments (e.g. schists and marbles) with minor occurrences of metabasites (Fig. IV.3a). The lower part contains slices of gneiss that provided Triassic radiometric ages on zircons and older ages (Carboniferous) are found in orthogneiss of the Agios Nikolaos unit. This unit can be correlated with the lower part of the CBU [Ring *et al*., 1999b]. The Ampelos nappe displays an Eocene blueschist-facies metamorphic event, followed by an Oligo-Miocene overprint under greenschist-facies conditions [Okrusch *et al*., 1984; Chen, 1995; Chen *et al*., 1995]. P-T estimates suggest a peak metamorphism at 520 °C and 19 kbar (Fig. IV.2) [Will *et al*., 1998] and 455 – 485 °C, 6 – 7 kbar for the greenschist-facies overprint [Chen, 1995]. (iii) The Selçuk nappe crops out in the center of the island as discontinuous outcrops of metabasites (Fig. IV.3a) [Ring *et al*., 1999b]. It is similar in terms of lithology to the ophiolitic mélange metamorphosed in HP-LT conditions in the upper part of the Cycladic Blueschists, for instance in Syros and Sifnos (Fig. IV.3a). (iv) The Vourliotes nappe crops out in the eastern part of the island where it is mainly made of schists and marbles (Fig. IV.3a). The upper marble formation has been dated as Upper Cretaceous on the basis of rudists found within the metabauxite outcrops at the eastern part of the island [Papanikolaou, 1979]. It has undergone the same metamorphic conditions as the Ampelos nappe [Ring *et al*., 1999b]. (v) The Kallithea nappe and the Katavasis Complex are only found in the westernmost part of the island, on top of Kerketeas marbles. Here, we merged these both units in the Kallithea nappe, that can be correlated with the upper Cycladic Nappe where no evidence for a Cenozoic HP-LT metamorphism are observed; the Kallithea nappe is made of sandstones, serpentinized peridotite lenses, spilite and diabase with red radiolarites and fossiliferous ammonitico rosso-type limestones overlain by an Upper Triassic to Jurassic massive limestone series [Papanikolaou, 1979; Theodoropoulos, 1979]. The underthrusted Katavasis Complex is mainly composed of marbles, amphibolites and quartzites, formed under amphibolite-facies conditions [Mezger & Okrusch, 1985; Chen, 1995]. It is locally intruded at ~ 10 Ma by igneous dykes cut by a distinct low-angle normal fault [Ring *et al*., 1999b], suggesting a younger activity of this fault that is interpreted as an extension of the NCDS [Jolivet *et al*., 2010].

A large surface of Samos is covered by Mio-Pliocene sedimentary basins [Theodoropoulos, 1979; Weidmann *et al*., 1984] (Fig. IV.3a). The basal part consists on conglomerate levels with pebbles derived from the local basement. Locally, terrestrial gastropods are preserved, showing a proximal or distal flood plain deposit. This unit is overlain by the Pythagorion formation made of thick-bedded freshwater limestones with rare occurrences of clastic horizons and tuffaceous sands. It corresponds to a shallow lacustrine environment. An interstratified volcaniclastic sequence (basalt and tuff) is also well developed in the Pythagorion formation, formed as a subaqueous flow some 11 Myrs ago. The western part of this formation corresponds to the Mavradzei beds with bituminous limestones and sands, suggesting a paludal deposition environment. Both formations were overlain by the Hora formation that consists in thick-bedded limestones grading upward into thin-bedded limestones showing slump structures in the upper levels. Just above, slumped yellow-green marls with some thin-bedded diatomaceous shales are common. Finally, the top of this formation is defined by thinly bedded limestones with some marly intervals and tuffaceous turbidite layers giving a deposition age around 9 Ma. All these formations thus defined the lower cycle formed between ~ 12 Ma and 9 Ma. The upper cycle is formed between 8.6 and 6.2 Ma. It starts with the Mytilini formation that rests unconformably above the Hora or the Pythagorion formation. Channelized gravels suggest a fluvial origin for these deposits, and the sequence then grades upward into a clastic horizon with clasts of the Hora formation. In addition, some levels of tuffaceous marls, silts and sands, with pebbles of basement are observed in this formation. Tuffaceous samples provided ages around 7 and 7.5 Ma [Weidmann *et al*., 1984]. The top of this unit consists in tuffs interbedded with marls and tuffaceous silts that provided a mean age of 6.18 Ma. The upper cycle ends with the Kokkari formation attributed to the Pliocene. It is made of thick-bedded lacustrine limestones interfingering with the upper part of the Mytilini formation.

According to Ring *et al*. [1999b], the tectono-metamorphic units of Samos have recorded five successive deformation stages. D_1 and D_2 stages are associated with the HP-LT metamorphic event and show a roughly consistent E-W orientation with bivergent sense of shear. They correspond to the thrusting of the Ampelos nappe onto the Kerketeas marbles in the western part of the island. D_3 event corresponds to the greenschist-facies metamorphism associated with crustal extension. These major events are mainly associated with ESE-WSW transport direction. However, in the core of the Ampelos nappe, D_3 stretching lineations display a N-S with top-to-the-N and top-to-the-S kinematic indicators Ring *et al*. [1999b] therefore conclude to a large component of coaxial strain during the exhumation of these units. Finally, D_4 corresponds to a short contractional event between 8.6 and 9 Ma whereas D_5 is extensional, corresponding to the formation of N-S trending normal faults.

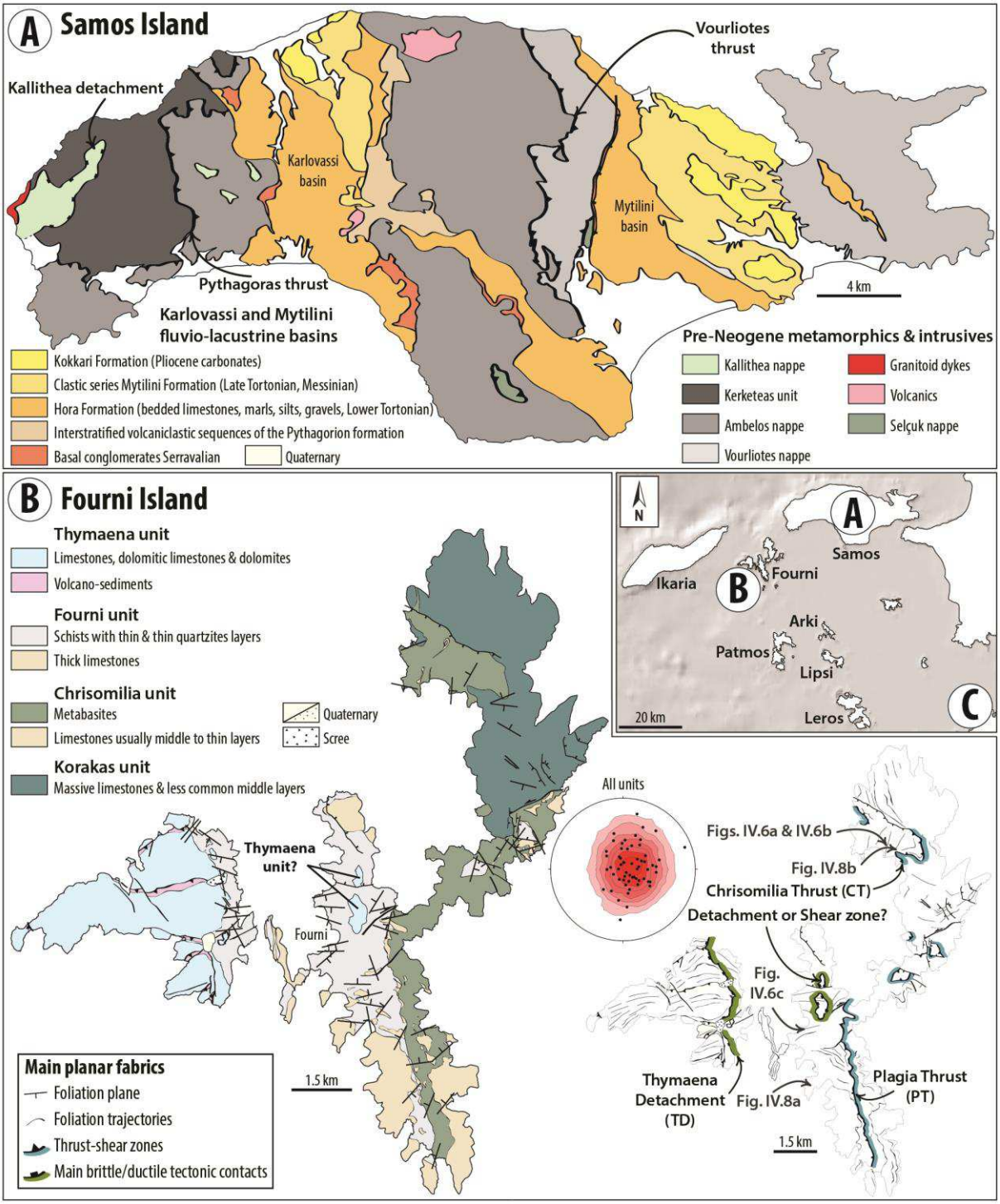

Figure IV.3: Geological and foliation maps of Samos and Fourni islands. (a) Lithologic outlines are from new field observations and from a compilation of existing maps of Samos [e.g. Theodoropoulos, 1979; Papanikolaou, 1979; 1980; Ring et al., 1999b]. (b) Simplified geological maps of Fourni and Thymaena islands showing foliation trajectories. Lithological outlines are from our field observations for Fourni Island. Traces of main shear zones and location of Figures IV.6 and IV.8 are also reported. Poles of foliation in all units are presented in Schmidt's lower hemisphere equal-area projection. (c) Location of the study area. See Figure IV.1 for location.

IV.2.3.2. Fourni and Thymaena Islands

Whereas Thymaena Island benefited from a map coverage by the study of Papanikolaou [1980], there is no geological map available of Fourni Island. In Thymaena, the non-metamorphic succession from the middle to upper Triassic consists in sandstones and red nodular limestones with mafic igneous rocks, and white dolomites and neritic limestones with megalodon. A series of north-directed thrusts affected all the sequence. According to Papanikolaou [1980], thrusting may be related to the middle-upper Miocene period (Fig. IV.3b).

IV.2.4. Dodecanese islands

Dodecanese islands (Figs. IV.1 and IV.4) were mapped by the Greek Geological Survey (IGME) [Stavropoulos & Gerolymatos, 1999]. However, the tectono-metamorphic evolution of Kalymnos, Leros, Lipsi and Arki remains fragmentary. The metamorphic succession consists in the tectonic superimposition of two distinct tectono-metamorphic units, Marina and Temenia units from the top to the base, respectively [Franz *et al*., 2005; Roche *et al*., 2018a].

Outcrops of Marina unit are well exposed in Kalimnos and Leros and locally in the southeastern part of Lipsi (Fig. IV.4). The first-order architecture of this unit is defined by crystalline rocks that are transgressively overlain by weakly metamorphosed, violet schists, conglomerates and sandstones resembling the Permo-Triassic (?) siliciclastic “Verrucano” sediments, which grade upwards into upper Triassic to Liassic dolomite and limestone. According to Papanikolaou [2013], these formations are similar to the volcano-sedimentary-type Tyros Beds at the base of the Tripolis unit below the carbonate platform, however no more precise correlation can be established. Indeed, conversely, Dürr *et al*. [1978] suggest that the sedimentary formation of Marina unit correspond to units of the Lycian Nappes in SW Turkey. It is followed by well-bedded upper Jurassic to lower Cretaceous (?) limestone with cherty replacement [Dürr, 1975; Dürr *et al*., 1978; Franz *et al*., 2005]. Crystalline rocks are represented by the Panormos and Emporios units [Franz *et al*., 2005]. The first resembles the Cretan Myrsini unit, consisting mostly in a succession of marbles, plagioclase gneisses and kyanite–staurolite–garnet micaschists with intercalations of banded epidote and garnet amphibolites. The base of this unit is formed of fine-grained schist and minor coarse-grained massive amphibolite with a thickness of about 100 m. The overlying Emporios unit is made of albite gneisses and chloritoid–biotite schists, and corresponds to the Cretan Chamezi unit [Franz *et al*., 2005]. Like on Crete, the basement rocks of the Dodecanese islands experienced a polyphase deformation (i.e. Variscan and Alpine). K-Ar dating of these basement slices suggest Variscan ages partially reset by a very low-grade Alpine overprint [Franz *et al*., 2005].

The underlying Temenia unit is mainly exposed in Arki, Lipsi and Leros (Fig. IV.4) and consists of late Paleozoic to Mesozoic sediments affected by an Alpine HP-LT metamorphism [Franz & Okrusch, 1992]. It consists of interlayered phyllites, micaschists, quarzites and marbles with rare occurrences of metabasites. The presence of Mg-riebeckite, glaucophane and aragonite in Leros and Arki islands [Katagas, 1980; Franz & Okrusch, 1992; Roche *et al*., 2018a], implies a subduction-related metamorphism with a minimum pressure of ~ 8 kbar (Fig. IV.2). Roche *et al*. [2018a] show that glaucophane/Mg-riebeckite is locally preserved and may destabilize into winchite, suggesting a decrease in pressure and temperature. The blueschist-facies event was thus followed by a greenschist-facies overprint. In addition, new data from this study suggest T_{max} conditions around 368 to 487 °C for this unit (using Raman spectroscopy on carbonaceous material, RSCM) [Roche *et al*., 2018a]. Dürr [1975] considers this unit as an equivalent of the Kara Dag unit in the Lycian Nappes of western Turkey (Fig. IV.1). However, Roche *et al*. [2018a] challenge this hypothesis, suggesting that this unit belongs to the Lower Cycladic Blueschist Nappe.

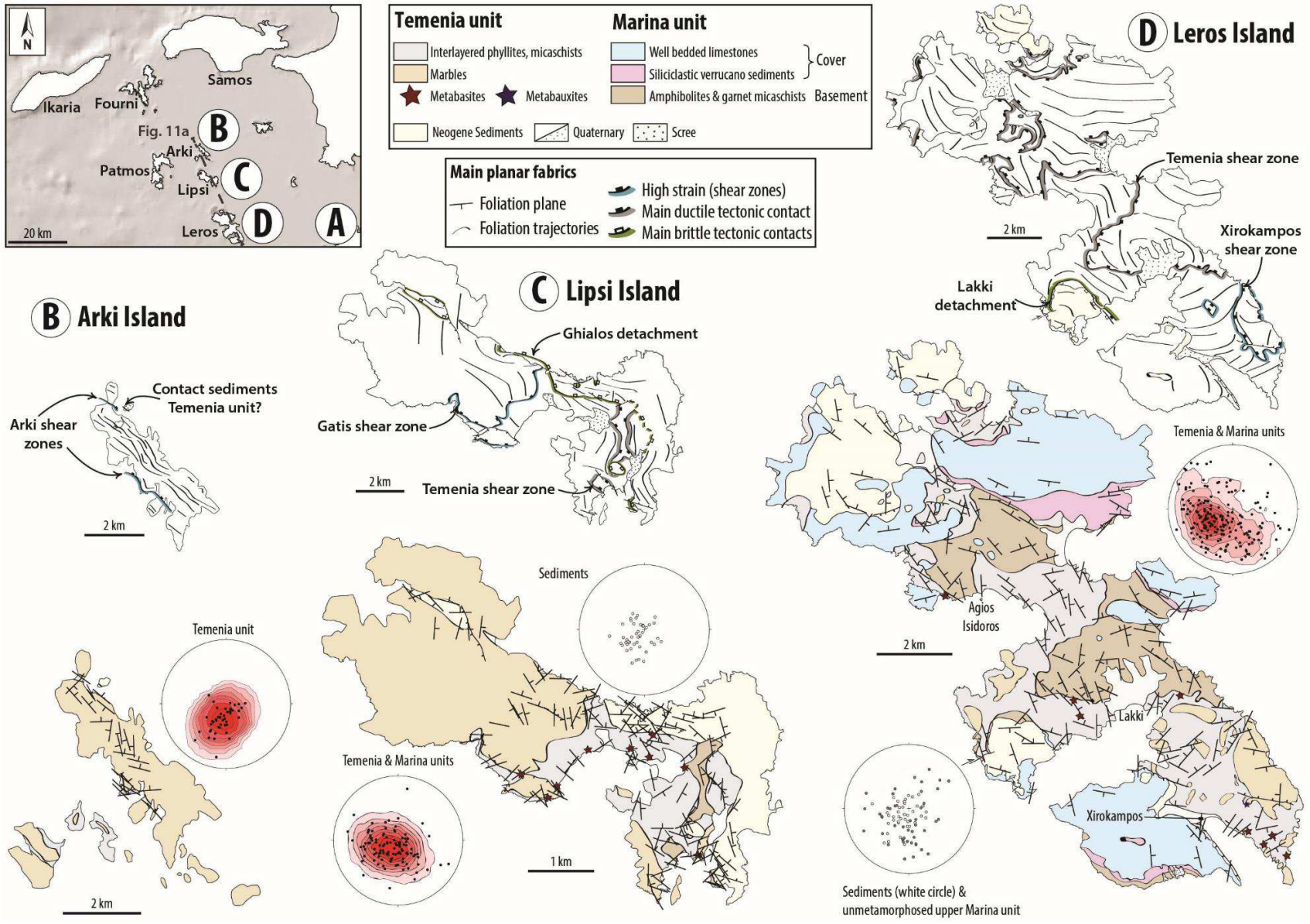
N
Samos
Ikaria
Fourni
Fig. 11a
B
Arki
Patmos
C
Lipsi
D
A
Leros
20 km
Temenia unit
Marina unit
Interlayered phyllites, micaschists
Marbles
Metabasites
Metabauxites
Well bedded limestones
Siliciclastic verrucano sediments
Amphibolites & garnet micaschists
Cover
Basement
Neogene Sediments
Quaternary
Scree
Main planar fabrics
Foliation plane
Foliation trajectories
High strain (shear zones)
Main ductile tectonic contact
Main brittle tectonic contacts
B Arki Island
Contact sediments
Temenia unit?
Arki shear
zones
2 km
Temenia unit
2 km
C Lipsi Island
Ghialos detachment
Gatis shear zone
2 km
Temenia shear zone
Sediments
Temenia & Marina units
1 km
D Leros Island
Temenia shear zone
2 km
Xirokampos
shear zone
Lakki
detachment
Temenia & Marina units
Agios
Isidoros
2 km
Lakki
Xirokampos
Sediments (white circle) &
unmetamorphosed upper Marina unit

Figure IV.4: Geological and foliation maps of Dodecanese islands. (a) Location of the study area. See Figure IV.1 for location. (b), (c) and (d) represent maps of Arki, Lipsi and Leors islands, respectively. Lithologic outlines are from new field observations and from a compilation of existing maps [Desio, 1931; Katagas, 1980; Franz and Okrusch, 1992; Franz et al., 2005]. Poles of foliation and bedding in all units are presented in Schmidt's lower hemisphere equal-area projection. Foliation trajectories and traces of the main shear zones are also reported on simplified geological maps.

IV.3. New field observations

We carried out several field surveys in the eastern Aegean region, including field mapping in order to complement the existing IGME geological maps or to realize new geological maps (e.g. Fourni Island). Results are shown in Figures IV.3 and IV.4, and include maps of finite strain markers, foliation trajectories, kinematic indicators and field measurements on stereographic plots. Geological mapping was complemented by a detailed study of metamorphic and structural features of all islands. Large-scale analysis of the distribution of metamorphic markers thus leads to roughly constrained P-T conditions during deformation events. In the following, we present first a general description of the lithological units and tectonic contacts, then new metamorphic data and finally structural information about Fourni, Samos, Leros, Lipsi and Arki.

IV.3.1. Fourni and Thymaena Islands

We present in Figure IV.3b the first geological map of Fourni and Thymaena islands. The geology of the two islands is characterized by a metamorphic sequence comprising three main units (Fig. IV.3b). (i) The Korakas unit crops out in the eastern part of the island and mainly consists of dolomitic marbles with local schists on top. (ii) The overlying Chrisomilia unit, is mainly made of metabasites with minor occurrences of marbles in the upper part. The lower part of this unit is exposed in southeastern Fourni, and consists in thin marble layers. (iii) The uppermost Fourni unit outcrops in central and eastern parts of the island. It includes mainly schists, marbles, quartzites and minor occurrences of metabasites. Finally, above these tectono-metamorphic units, a non-metamorphic nappe (i.e. the Thymaena unit) is observed [Papanikolaou, 1980].

We distinguish three main contacts between these units: (i) Thymaena Detachment between Thymaena and Fourni units, cropping out only on Thymaena Island and possibly in the central part of Fourni (Fig. IV.3b), (ii) Plagia thrust separating Fourni unit from Chrisomilia unit, and (iii) Chrisomilia thrust cropping out in the north of Fourni Island and separating Chrisomilia unit from Korakas unit (Fig. IV.3b).

IV.3.2. Dodecanese islands

We propose here new maps of Leros, Arki and Lipsi Islands (Fig. IV.4). The geology of Leros is detailed in Roche *et al*. [2018a]. These islands are occupied by the Marina unit resting on top of Temenia unit. On Arki, only a thick metamorphic succession of Temenia unit crops out while both Lipsi and Leros are also characterized by a thick sequence of Marina unit. However, relationships between the two units appear clearer in Leros than Lipsi. Indeed, brittle deformation is more-developed in Lipsi overprinting ductile deformation, cross-cutting for instance, the main tectonic contact between these two units (i.e. Temenia shear zone [Roche *et al*., 2018a]). Furthermore, a thin Neogene to recent sedimentary cover is also present on Leros and Lipsi (Figs. IV.4c and IV.4d).

Deformation is preferentially localized along the main tectonic contacts, although second-order ductile to ductile-brittle shear zones are also evidenced, especially along lithological contacts. We thus distinguish four shear zones affecting the Temenia unit in all islands: the Temenia shear zone in the central part of Leros and its equivalent in Lipsi, Gatis, Xirokampos and Arki ductile shear zones (Fig. IV.4).

IV.4. Metamorphism

IV.4.1. Samos

Unlike Fourni and the Dodecanese, Samos has been extensively studied for its metamorphic parageneses (Fig. IV.5a) [Okrusch *et al*., 1984; Chen, 1995]. Ampelos nappe and Vourliotes nappe have thus recorded HP-LT conditions well expressed in metabasite boudins. There, glaucophane, epidote ± chloritoid and white mica are common and well preserved (Figs. IV.5a and IV.5b). Depending on the areas, epidote-chlorite-albite assemblages are more present, showing retrogression to greenschist-facies conditions (Fig. IV.5c).

Our study provides additional data for the distribution of HP-LT rocks on Samos (Fig. IV.5a). Although Okrusch *et al*. [1984] described the paragenesis carpholite-kyanite in a pebble collected on Psili Amos beach (Fig. IV.5a), we were not able to recognize any *in-situ* Fe-Mg-carpholite occurrence in the field. In old metabauxites mines along the eastern coast of Samos, we observe the chloritoid + diaspore assemblage and the diaspore + quartz association (Figs. IV.5d and IV.5e). Such an association has only been found in Sulawesi (New Caledonia), Amorgos (Cyclades) and Vanoise (Western Alps) [Theye *et al*., 1997]. It leads to P-T conditions along a HP-LT gradient, with minimum pressure of 13 kbar and maximum temperatures of 430 °C, i.e. about 100 °C colder than previously published P-T

estimates (Fig. IV.5a) [Ring *et al*., 1999b]. Such cold HP-LT conditions are compatible with the Fe-Mg-carpholite reported by Okrusch *et al*. [1985], but are not common in the Cyclades.

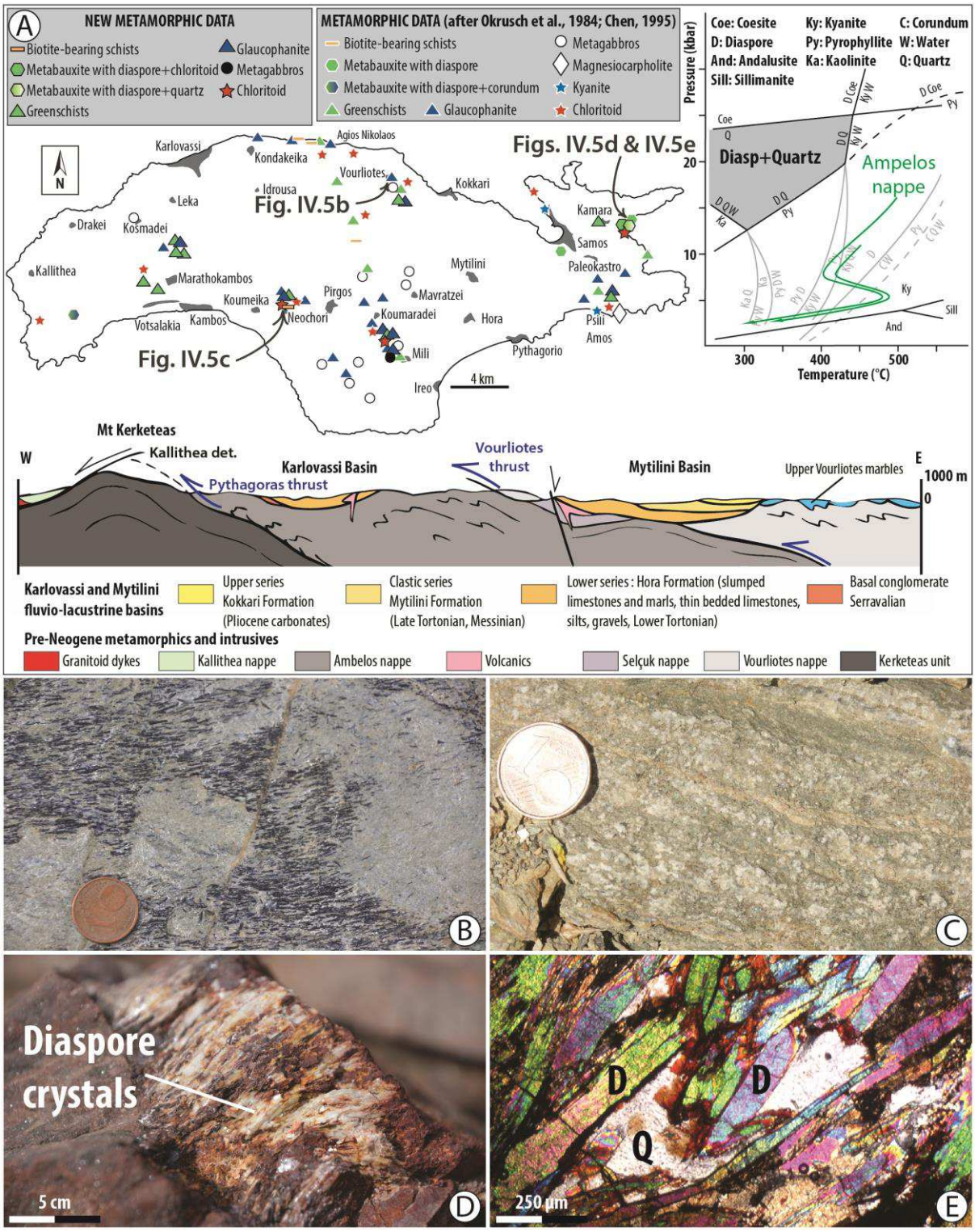

Figure IV.5: Metamorphic observations on Samos. (a) Map of metamorphic index minerals using new field data and data from other studies [Okrusch et al., 1984; Chen, 1995]. E-W synthetic cross-section showing relationships between the different units. Also indicated is the P-T grid showing the stability field of the paragenesis diaspore-quartz [Theye et al., 1997] in a window comprised between 13 – 24 kbar and 250 – 430 °C. We also reported the P-T paths published by Ring et al. [1999b]. (b) Blueschist rocks belonging to Vourliotes nappe showing glaucophane, epidote and white micas paragenesis. (c) Heavily retrogressed metabasites of Ampelos nappe in greenschist-facies conditions with albite - chlorite - epidote - white micas paragenesis. (d) Close up view of metabauxite containing diaspore - quartz - chloritoid and phyllosilicate assemblages in Kamara region. (e) Thin section of metabauxite showing diaspore (D) and quartz (Q) assemblages.

IV.4.2. Fourni and Thymaena islands

We report here preliminary results on metamorphic conditions recorded on Fourni Island (Fig. IV.6). Observed metamorphic parageneses from metabasites in the Chrisomilia unit mainly consist in porphyroblasts of albite - quartz - white mica - chlorite - kyanite, indicating a greenschist-facies metamorphic event (Fig. IV.6a). Locally, some chloritoid pods are also observed in quartzitic levels (Fig. IV.6b) and may suggest a former higher-pressure event. The Fourni unit seems to have also recorded greenschist-facies event. Foliation within schist layers is marked by quartz - white mica - chlorite with locally stretched albite surrounded by chlorite pressure shadows (Fig. IV.6c). It is noteworthy that both units (i.e. Chrisomilia and Fourni units) seem to have recorded lower peak-metamorphic conditions than the nearby Cyclades and Samos islands.

IV.4.3. Dodecanese islands

The metamorphic record was investigated throughout Leros, Arki and Lipsi by studing parageneses from metabasites belonging to Temenia unit (Fig. IV.6d). Near the lighthouse of Arki harbor (Fig. IV.6e), an outcrop shows several bands of blueschists displaying porphyroblastic blue amphibole, interlayered with micaschists, quartz-micaschists and marbles. In other parts of the island, microscopic observations have revealed blue amphiboles (Fig. IV.6g). Greenschist-facies intercalations are also observed and chloritoids mark a stretching lineation around N60°E (Fig. IV.6h). On Lipsi Island, metamorphic assemblages present in metabasites show only chlorite - phengite - epidote - quartz ± albite ± hematite ± rutile ± sphene. The absence of blue amphiboles in the metabasites of Lipsi does not allow ascribing these rocks to the blueschists-facies although lithologies are very similar in all islands. Pressure conditions recorded on Leros are however rather low and it is possible that the same unit on Lipsi was not far from the blueschists-facies conditions on the same HP-LT gradient. The whole Temenia unit would then have been affected by an HP-LT alpine event followed by a retrogression stage in greenschist-facies conditions where chlorite - albite - winchite - epidote - phengite are generally observed.

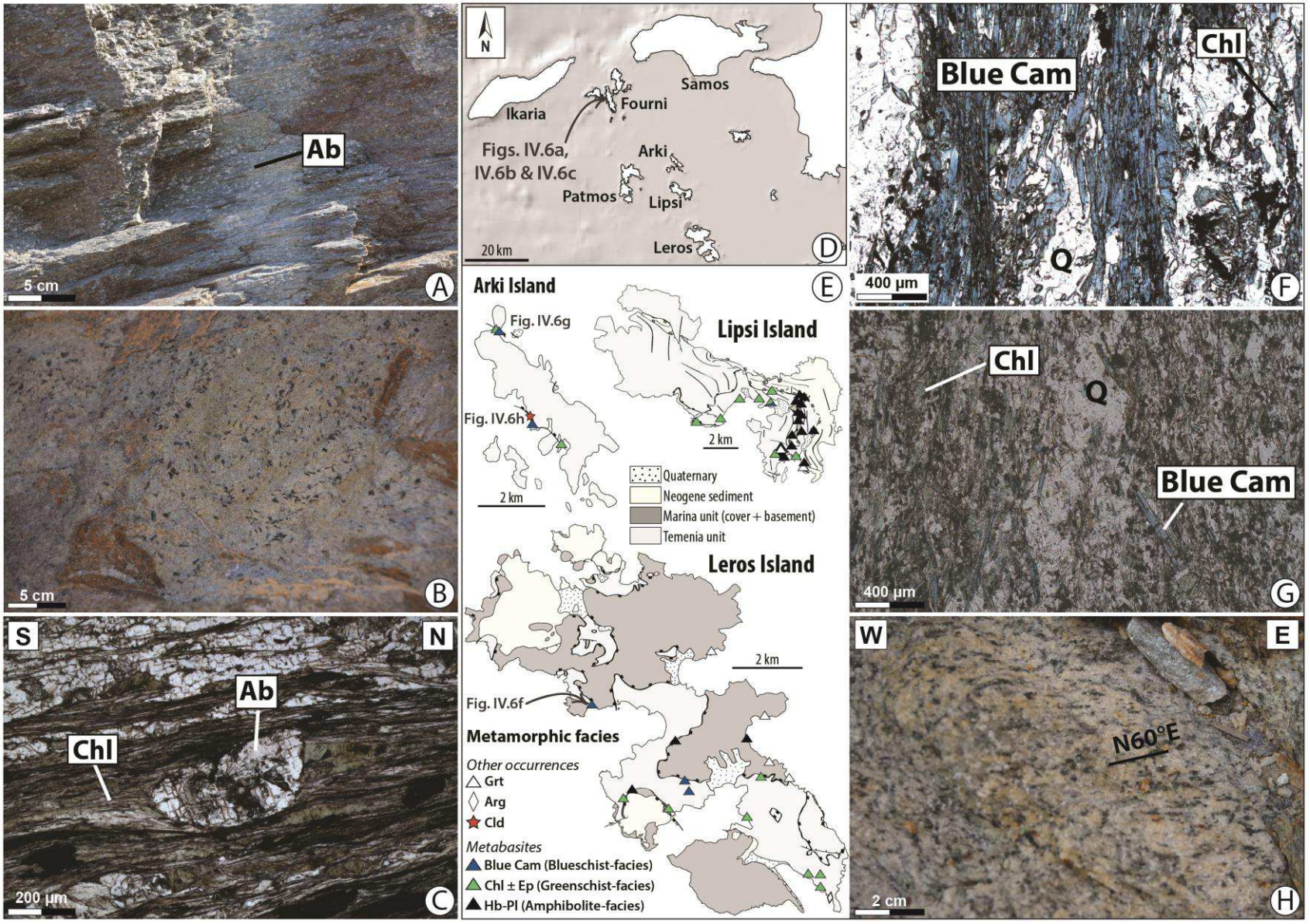
Ab
5 cm
A
5 cm
B
S
N
Ab
Chl
200 µm
C
N
Samos
Fourni
Ikaria
Figs. IV.6a,
IV.6b & IV.6c
Arki
Patmos
Lipsi
Leros
20 km
D
E
Arki Island
Fig. IV.6g
Fig. IV.6h
2 km
Lipsi Island
2 km
Quaternary
Neogene sediment
Marina unit (cover + basement)
Temenia unit
Leros Island
2 km
Fig. IV.6f
Metamorphic facies
Other occurrences
Grt
Arg
Cld
Metabasites
Blue Cam (Blueschist-facies)
Chl ± Ep (Greenschist-facies)
Hb-Pl (Amphibolite-facies)
Blue Cam
Chl
Q
400 µm
F
Chl
Q
Blue Cam
400 µm
G
W
E
N60°E
2 cm
H

Figure IV.6: Metamorphic record on Fourni and on the Dodecanese islands. (a) and (b) Close-up view of albite (Ab) and chloritoid (Cld) pods in the Chrisomilia unit of Fourni Island. (c) Pressure shadow filled by chlorite (Chl) around albite (Ab) showing a greenschist-facies deformation in the Fourni unit. See Figure IV.3b for the location. (d) Location of all studied islands. (e) Metamorphic maps record on Dodecanese islands. (f) and (g) thin sections showing blue-amphiboles (Blue Cam) preserved in the main foliation on Leros and Arki, respectively. (h) Elongation of chloritoid-mica aggregates on Arki Island. See Figure IV.6e for the location.

IV.5. Ductile shearing

IV.5.1. Samos

Our observations on Samos confirm the main conclusions of Ring *et al*. [1999b] for the main trends of stretching lineation. Depending on the locality, the schists of the Ampelos and Vourliotes units are strongly deformed, and stretching lineations are associated with blueschist- to greenschist-facies assemblages (Fig. IV.7a). In both units, it is marked by various types of indicators such as elongated phyllosilicates aggregates (e.g. chlorites and with micas), stretched glaucophane and epidote in metabasites. Both Ampelos and Vourliotes nappes have recorded a common approximately east-west to northeast-southwest stretching, at least during the blueschist-facies metamorphism, even if the central part of the island rather shows a N-S direction of stretching. Conversely, the stretching lineation in the southwestern part of Samos or near Kumaradei, shows a NE-SW to N-S trend direction defined by elongated chlorite and micas aggregates indicating P-T conditions of the greenschist-facies (Fig. IV.7a).

The best examples of shear sense observed in the field are located near the Pythagoras Thrust (Fig. IV.7a). There, blueschist parageneses are associated with E-W or WNW-ESE stretching lineations and top-to-the-W-WNW shear bands (Fig. IV.7b). These observations suggest that the fabric formed together with the Pythagoras Thrust (probably Eocene) has been preserved here and not severely reworked by the subsequent extension, except for the recent normal fault controlling the topography. This localized shearing along this thrust confirms that it is the major tectonic contact in the island as proposed by Ring *et al*. [1999b]. Some N-S stretching lineations and rather clear top-to-the-N shear sense are associated with greenschist-facies parageneses (Fig. IV.7c). However, these criteria are very local and do not allow any definite conclusion. If these observations were confirmed, it would mean that the kinematic direction during the HP-LT event and the retrogression were almost perpendicular to each other, at least locally, in contrast to the interpretation of Ring *et al*. [1999b] that suggest a continuum of ENE-WSW-directed transport during exhumation.

Furthermore, although the contact between the Kallithea nappe and the Kerketeas unit does not crop out continuously, it is characterized in the field by a thin dark-grey marble ultramylonites (approximately 10 centimeters high) at the top of dolomites (Fig. IV.7d). This thin layer carries a NE-trending stretching lineation with locally some normal-sense shear bands spaced a few centimeters apart,

and sigmoidal foliation indicating top-to-the-NE shearing (Fig. IV.7e). This ductile deformation is then overprinted by brittle deformation as suggested by the presence of ultracataclasites and brittle low-angle faults. Locally, centimetric antithetic high-angle normal fault also affected the penetrative foliation. Below this contact, the dolomite is not affected by this deformation showing a strongly localized deformation along this low-angle contact.

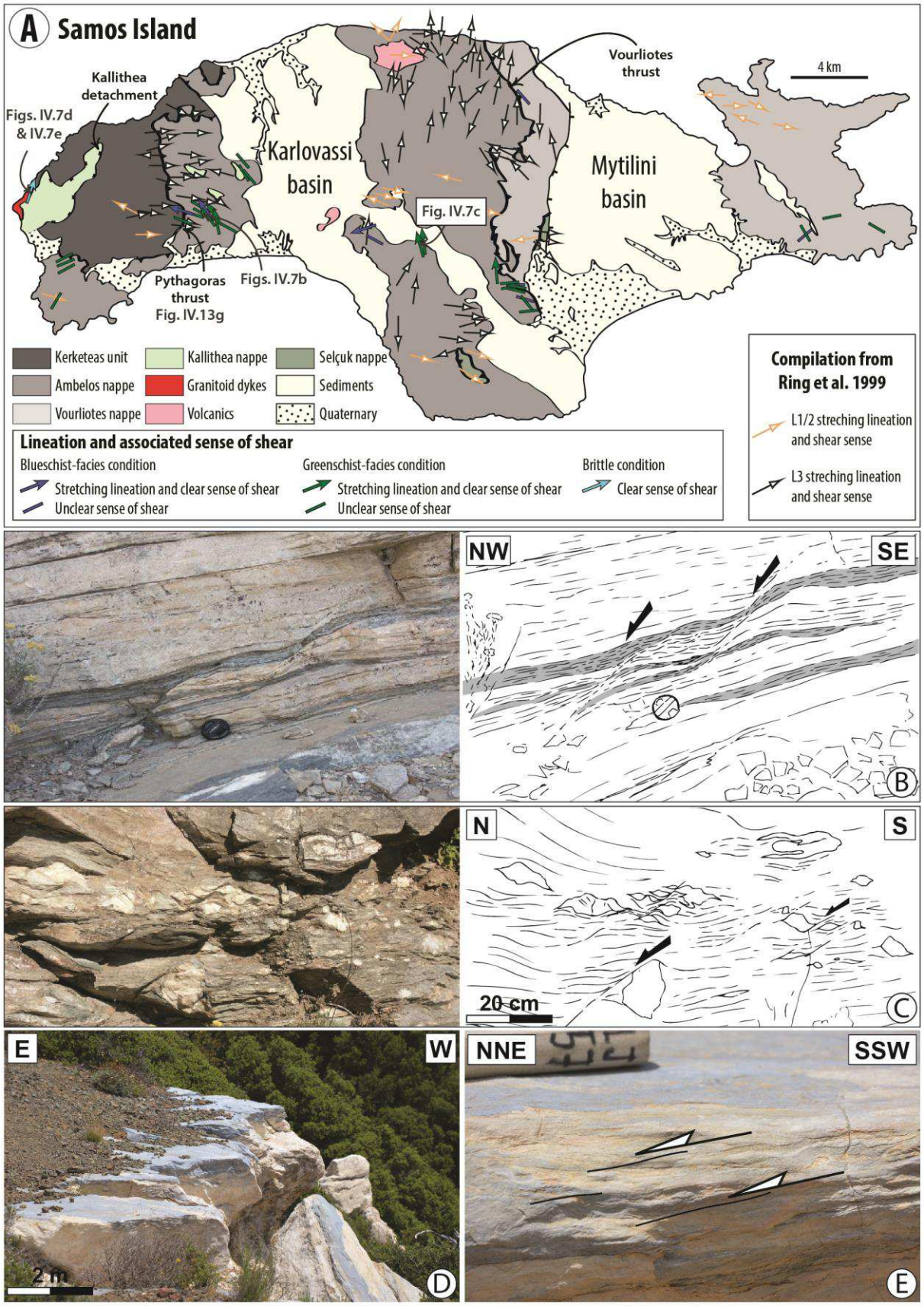
A Samos Island
Kallithea detachment
Figs. IV.7d & IV.7e
Karlovassi basin
Vourliotes thrust
Mytilini basin
4 km
Fig. IV.7c
Pythagoras thrust Fig. IV.13g
Figs. IV.7b
Kerketeas unit
Ambelos nappe
Vourliotes nappe
Kallithea nappe
Granitoid dykes
Volcanics
Selçuk nappe
Sediments
Quaternary
Compilation from Ring et al. 1999
L1/2 streching lineation and shear sense
L3 streching lineation and shear sense
Lineation and associated sense of shear
Blueschist-facies condition
Stretching lineation and clear sense of shear
Unclear sense of shear
Greenschist-facies condition
Stretching lineation and clear sense of shear
Unclear sense of shear
Brittle condition
Clear sense of shear
NW
SE
B
N
S
20 cm
C
E
W
2 m
D
NNE
SSW
E

Figure IV.7: Kinematic of deformation in Samos. (a) Simplified geological map of Samos with lineations and associated sense of shear [Ring et al., 1999; this study]. Also indicated the position of the pictures of Figures IV.7 and IV.13. (b) Field example of top-to-the-NW kinematic indicators shown by shear bands in the vicinity of the Pythagoras thrust in the metapelites and marbles of Ampelos nappe. (c) Outcrop showing top-to-the-N kinematic indicators related to the greenschist-facies retrogression close to Pirgos. (d) Field picture showing the main tectonic contact between Kallithea Nappe and Kerketeas unit. (e) Shear bands within ultramylonites indicating a top-to-the-NNE sense of shear.

IV.5.2. Fourni and Thymaena islands

On Fourni Island, foliation trajectories are given in Figure IV.3b. The main foliation strikes E-W with variable dips towards north or south in the central and western parts of the island. In the south, the foliation in both Fourni and Chrisomilia units turns with an average strike around N45°E, whereas it appears more variable in the north, and particularly within Chrisomilia unit. In addition, the foliation is locally deflected in the vicinity of late steep faults associated with strike-slip kinematic indicators. The original lithological contacts are generally transposed into the main penetrative foliation, as shown by isoclinal folds locally observed within dolomitic marble layers (Fig. IV.8a). A later folding event is also observed in the landscape with the main foliation that is affected by a series of large-scale open folds with E-W axes (Fig. IV.3b). In addition, kink structures are well developed in both Fourni and Chrisomilia units, showing a N50°E strike (Fig. IV.8b).

Stretching lineation is mainly underlined by stretched calcite in marbles layers and by elongated aggregates of albite and white micas in metapelites and metabasites. Its orientation is centered on a value of N150°E with a dominant southwestward plunge in the lower structural level, whereas the orientation of stretching is around N0°E to N10°E in the upper levels (Fourni unit, Fig. IV.8c). Lineation and foliation are, however, bent by the main brittle faults, especially strike-slip faults, resulting in a slight scattering of the stretching direction. For instance, in the eastern part of the island, the orientation of stretching lineation is around N90°E with a dominant eastward plunge (Fig. IV.8c) whereas it trends NW-SE in other areas.

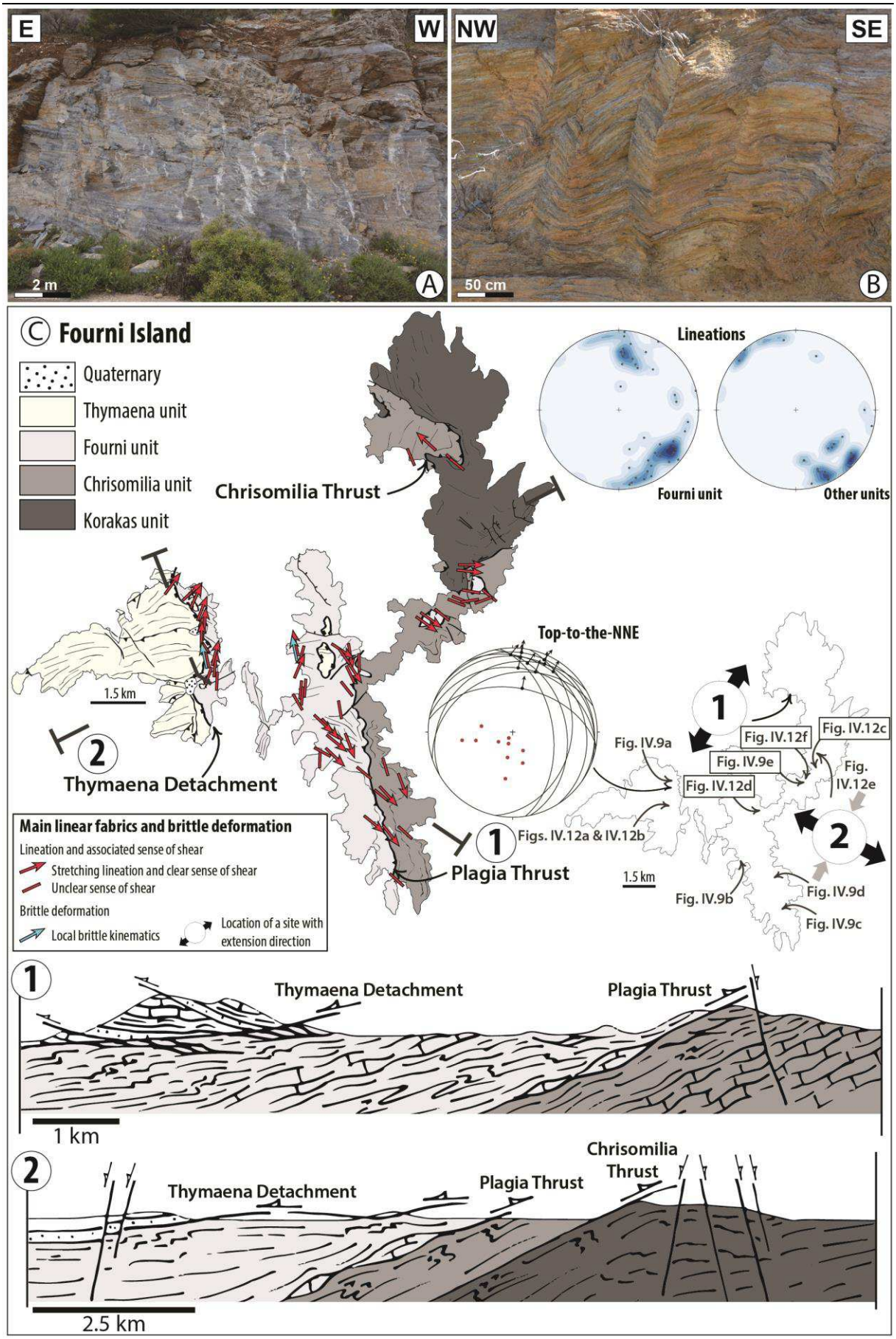
E
W
2 m
A
NW
SE
50 cm
B
© Fourni Island
Quaternary
Thymaena unit
Fourni unit
Chrisomilia unit
Korakas unit
Chrisomilia Thrust
Lineations
Fourni unit
Other units
Top-to-the-NNE
1.5 km
2
Thymaena Detachment
1
Plagia Thrust
Figs. IV.12a & IV.12b
Fig. IV.9a
Fig. IV.12f
Fig. IV.12c
Fig. IV.9e
Fig. IV.12e
Fig. IV.12d
Fig. IV.9b
Fig. IV.9d
Fig. IV.9c
Main linear fabrics and brittle deformation
Lineation and associated sense of shear
Stretching lineation and clear sense of shear
Unclear sense of shear
Brittle deformation
Local brittle kinematics
Location of a site with extension direction
1 km
2.5 km

Figure IV.8: Structure markers on Fourni Island. (a) Intrafolial folds in dolomitic marble layers showing a main flat-lying penetrative foliation in Fourni unit. (b) Kink structures in Chrisomilia unit. (c) A first tectonic map of Fourni and cross-sections, integrating our field observations and those of Papanikolaou [1980] on Thymaena. Stretching lineation and shear criteria are presented in Schmidt's lower hemisphere equal-area projection in different units. Also indicated the position of the pictures of Figures IV.9 and IV.12 and the results of fault-slip data inversion presenting in Figure IV.13h.

Fourni unit is affected by two shearing events, top-to-the-SE and top-to-the-NNE with common kinematic indicators often unambiguous at all scales (Fig. IV.9). As shown in Figure IV.8c, top-to-the-NNE pervasive shearing deformation affected the upper part of this unit, below the Thymaena Detachment, whereas top-to-the-SE kinematic indicators are well preserved in deeper structural levels. In the top of this unit, top-to-the-NNE shear bands are particularly abundant in metapelites and calcschists (Fig. IV.9a and see stereographic projection in Fig. IV.8c). Depending on areas, their spacing ranges from a few millimeters in the weakest lithologies in the vicinity of the main contacts (e.g. close to the Thymeana Detachment) to decimeters in more competent levels. Locally, the angle between shear bands and the main foliation varies, from high-angle in the upper levels of Fourni unit, suggesting an increasingly brittle behavior, to 20 – 35° at the base of this unit. Non-coaxial deformation is also accommodated by sheared quartz veins (Fig. IV.9a) and asymmetric boudinage of competent levels (e.g. marbles, metabasites) into a weaker, generally metapelitic matrix. Controversy, top-to-the-SE kinematic indicators are well preserved in deeper structural levels of this unit with common kinematic criteria including quartz- and white mica-bearing pressure shadows on pyrites (Fig. IV.9b), shear bands and asymmetric quartz veins. In addition, top-to-the-SE more localized brittle ductile deformation is locally observed (Fig. IV.9c). Chrisomilia unit is only affected by top-to-the-SE ductile deformation. For instance, metric shear bands affecting foliation are abundant (Figs. IV.9d and IV.9e). The relative timing of these two episodes of shearing appears clearly in the field. In the whole island of Fourni, below the Thymaena Detachment, shallow north-dipping or steeply-dipping shear bands deform the main regional foliation associated with ductile top-to-the-SE shearing, showing that the-top-to-the-N shearing event overprints the-top-to-the-SE deformation.

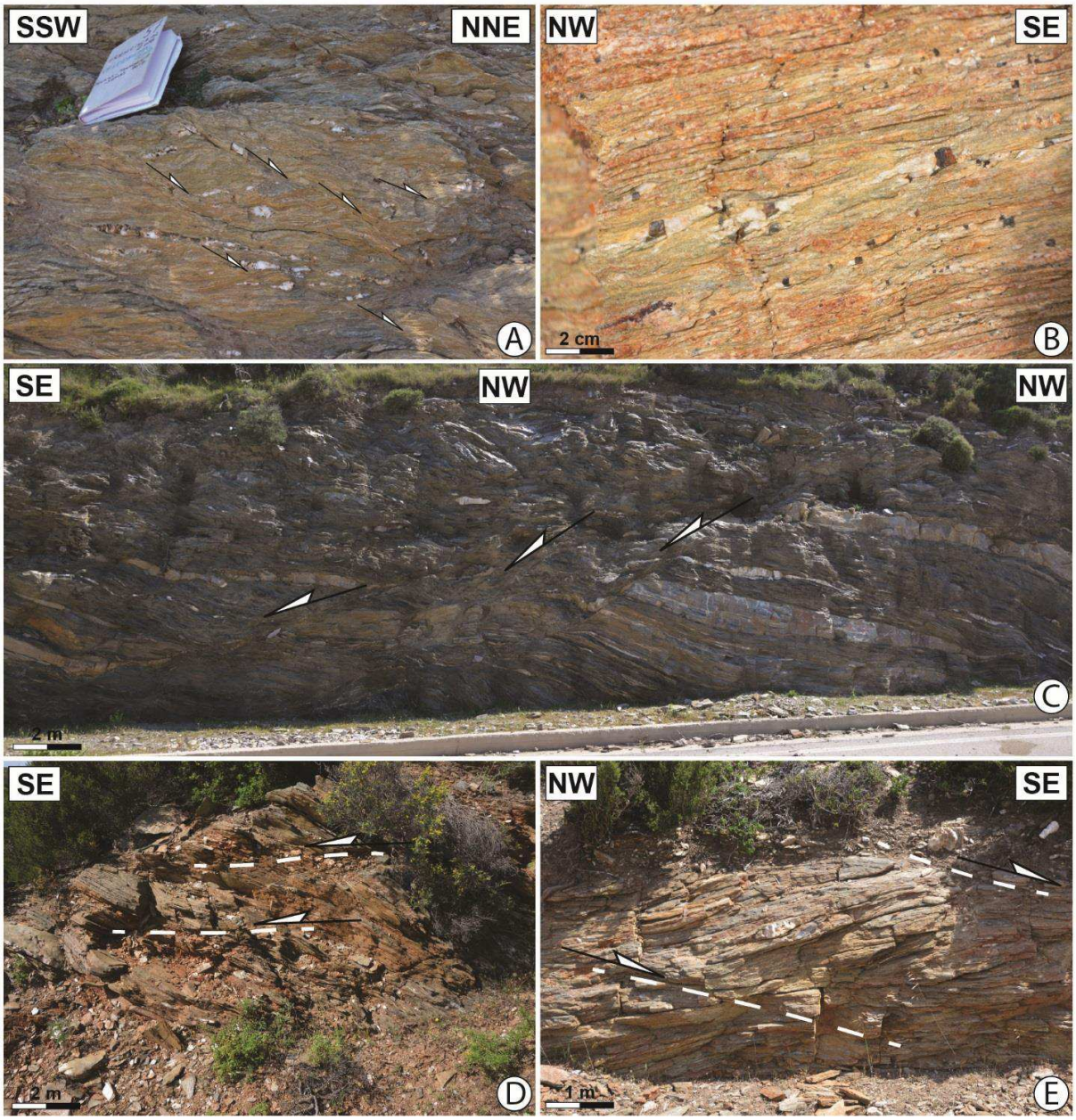

Figure IV.9: Kinematic of deformation on Fourni. (a) Close-up view of top-to-the-NE shear bands in Thymeana Island. (b) Pressure shadows on pyrites in Fourni unit showing a top-to-the-SE shearing. (c) Low to medium-angle normal faults indicating a top-to-the-SE shearing in Fourni unit close to the contact with Chrisomilia unit. (d) Metric shear bands showing a top-to-the-SE sense of shear in Chrisomilia unit. (e) Shear bands and asymmetric quartz veins indicating the same shearing direction in the same unit. The position of the pictures are indicated in Figure IV.8.

IV.5.3. Dodecanese

In the Temenia unit of Dodecanese islands, foliation trajectories and lineations are given in Figures IV.4 and IV.10. The main foliation strikes N90°E to N135°E with variable dips between 0 and 90°. It is affected by a series of large-scale upright open folds with N45°E plunging axes in the deepest part of Temenia unit (see foliation data on Leros, Figs. IV.4d and IV.11a). There, antiforms are filled

with metabasites (Fig. IV.4d). Foliation in Marina unit is also characterized by a N90°E to N135°E strike, and is gently to steeply dipping. Furthermore, the main foliation tends to increase in intensity toward the Marina/Temenia contact in both units, while the strike and dip of this foliation do not change significantly across it. There, folded foliation develops a new NE crenulation-vergent axial plane of crenulation cleavage with folds axes almost parallel to the main stretching lineation (Fig. IV.11b). These large-scale strain gradients are further complicated by local strain localization over a limited number of ductile shear zones developed along lithological contacts. For instance, a mylonitic foliation is well developed at the contact between marbles and schists in Arki (Fig. IV.11c). Intense shearing is also defined by mesoscopic folds in schists and black marble layers (Fig. IV.11d). Depending on localities, isoclinal folds with axes perpendicular to stretching lineation (Fig. IV.11d) and opens folds associated with crenulation lineations (trending NE-SW, Fig. IV.11b) are developed. Both folding events are probably contemporaneous with the partly mylonitic foliation localized above (i.e. in the upper structural levels located close to the main contact). These events are thus apparently related to layer-normal thinning during shear deformation.

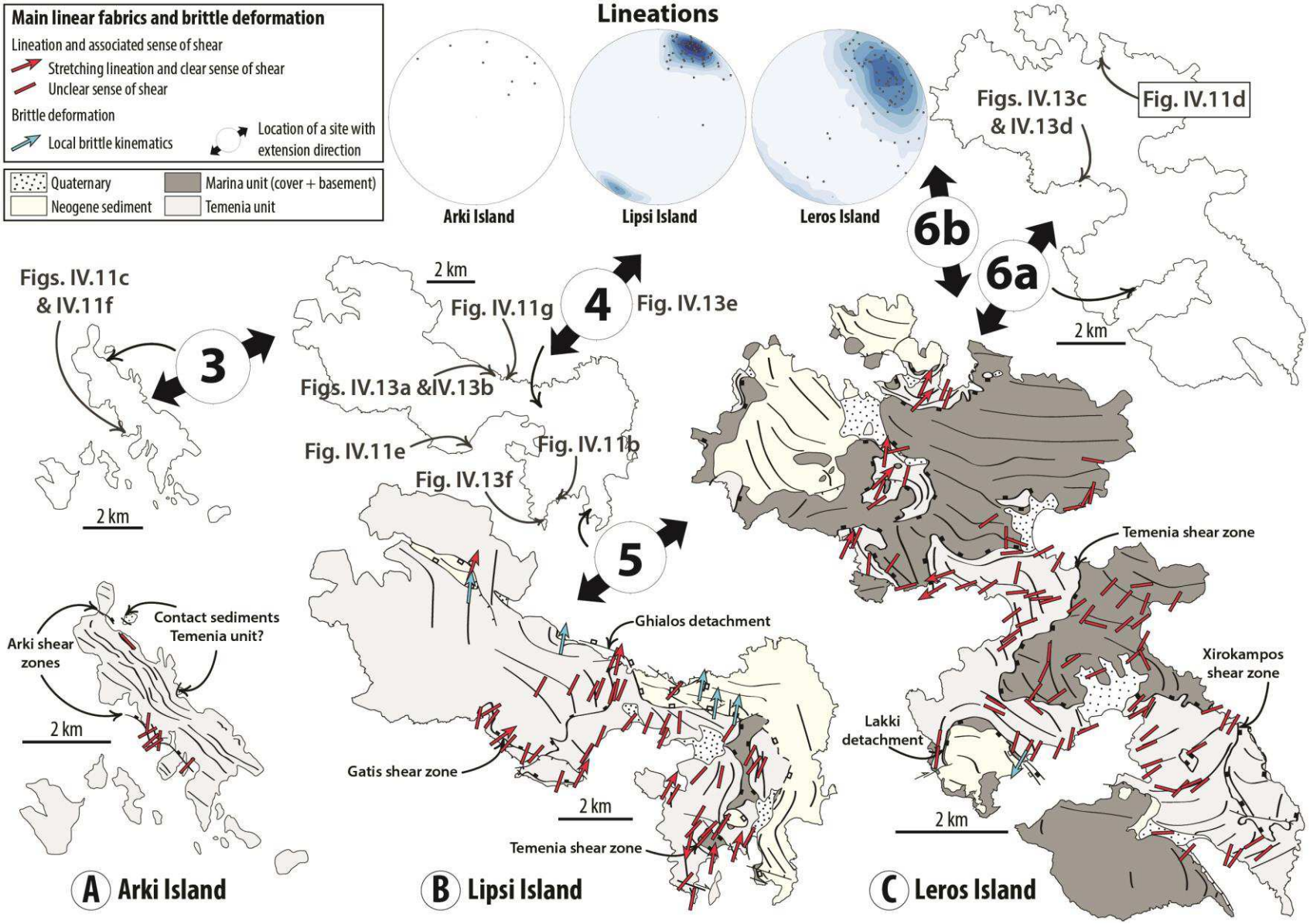
Main linear fabrics and brittle deformation
Lineation and associated sense of shear
Stretching lineation and clear sense of shear
Unclear sense of shear
Brittle deformation
Local brittle kinematics
Location of a site with extension direction
Quaternary
Neogene sediment
Marina unit (cover + basement)
Temenia unit
Lineations
Arki Island
Lipsi Island
Leros Island
Figs. IV.13c & IV.13d
Fig. IV.11d
6b
6a
2 km
Figs. IV.11c & IV.11f
3
Fig. IV.11g
4
Fig. IV.13e
Figs. IV.13a &IV.13b
Fig. IV.11e
Fig. IV.11b
Fig. IV.13f
5
Temenia shear zone
Ghialos detachment
Xirokampos shear zone
Lakki detachment
Gatis shear zone
Contact sediments Temenia unit?
Arki shear zones
A Arki Island
B Lipsi Island
C Leros Island

Figure IV.10: Geological and stretching lineation maps of Arki, Lipsi and Leros islands. Stretching lineation in all units are presented in Schmidt's lower hemisphere equal-area projection. Also indicated the main senses of shear and the position of the pictures of Figures IV.11 and IV.13. In addition, the results of the fault slip data inversion are showed as inset for each island, for more details see Figure IV.13h.

Stretching lineation is marked by various types of indicators, depending upon lithology, deformation and P-T conditions. Lineation is outlined by stretched quartz and elongated phyllosilicates aggregates such as chlorites and white micas in metapelites, epidote and rare blue amphiboles in metabasites and chloritoids in quartzite levels (e.g. Fig. IV.6). On Arki, the direction of stretching appears more scattered than on Lipsi, with an average trend around N-S (Fig. IV.10). On Lispsi, the orientation of stretching lineation is centered on a value of N45°E with a dominant northeastward plunge, whereas on Leros it shows a large dispersion between N0° and N90°E with an average around NE-SW and a variable plunge depending on the area (Fig. IV.10).

At first glance, the whole Temenia unit is affected by a pervasive top-to-the-NE ductile shearing attested by numerous kinematic indicators in the three islands (Figs. IV.10 and IV.11, see also Roche *et al*. [2018a] for Leros field pictures). Shear bands are well developed at all scales (Figs. IV.11e and IV.11f) with notably (i) large-scale asymmetric boudinage in alternating lithologies and (ii) centimetric-scale top-to-the-NE kinematic indicators well preserved in metaconglomerate levels (Fig. IV.11g). At the scale of the outcrop, the rarity of HP-LT rocks occurrences in the field makes difficult any discussion about the kinematics of deformation active during the HP event. Conversely, greenschist-facies parageneses appear conspicuously associated with top-to-the-NE shearing deformation. Indeed, the regional foliation is made of greenschist-facies minerals such as epidote while chlorite concentrates in pressure shadows or in folded layers in both metapelites and metabasites.

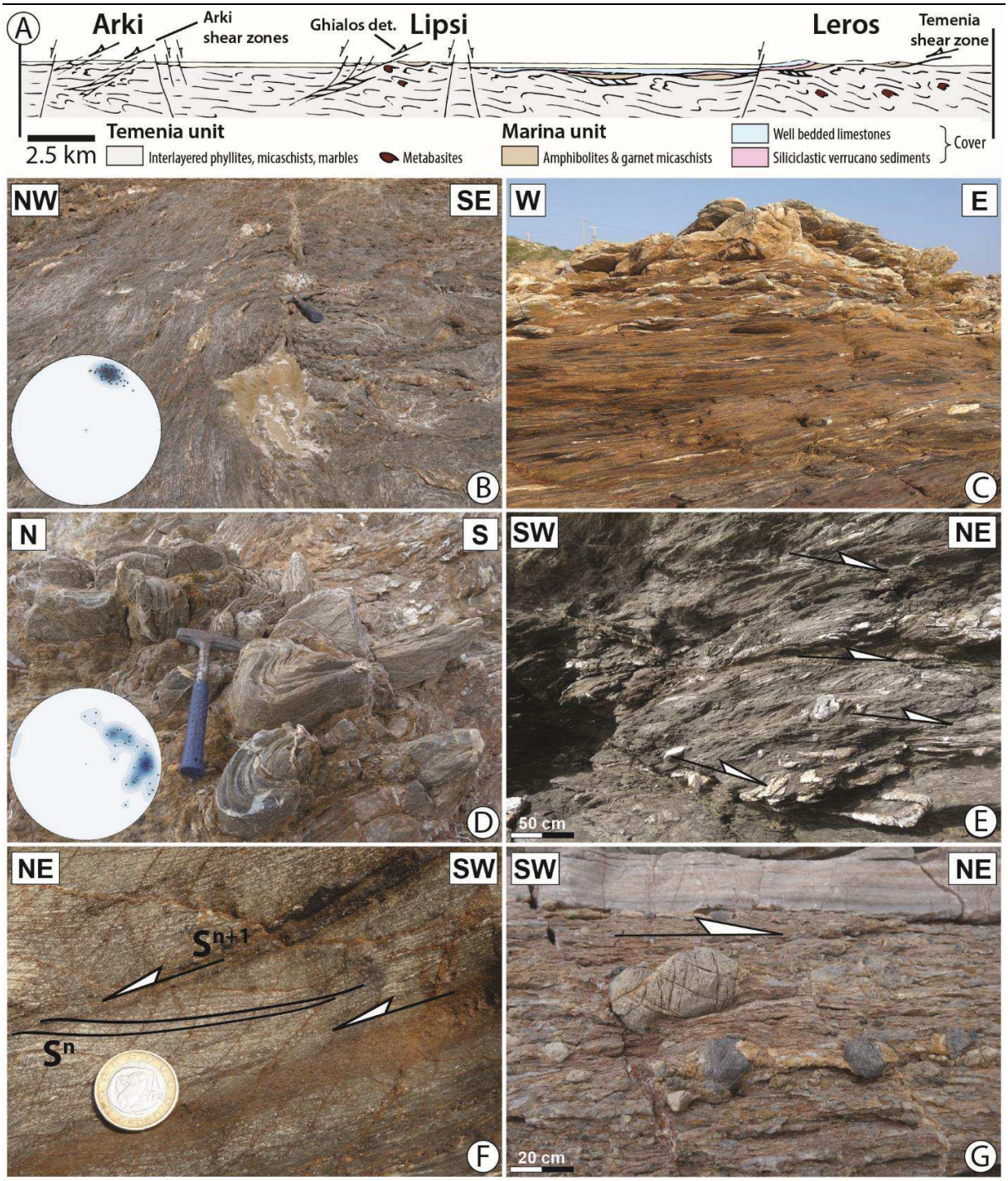

Figure IV.11: Structure markers and kinematics of deformation in the Dodecanese islands. (a) Synthetic cross-section showing relationships between the different units through the Dodecaenese islands. (b) Transposition of the steeply dipping foliation into the flat-lying penetrative foliation close to Temenia shear zone on Lipsi. Note that fold axes are roughly parallel to the stretching lineation. (c) Flat-lying penetrative foliation in schist layers, south of Arki. (d) Mesoscopic isoclinal folds with NE to SE trending fold axes in Temenia unit on Leros. (e) Centimetric-scale top-to-the-NE shear bands on Lipsi. (f) Shear bands within mylonites indicating a top-to-the-NNE sense of shear on Arki. (g) Metaconglomerate levels showing a top-to-the-NE sense of shear on Lipsi. See Figure IV.10 for the location.

IV.6. Brittle deformation

We briefly present here a few examples of brittle deformation, and fault slip analyses to improve the general view of the brittle kinematics since the Miocene (Figs. IV.12 and IV.13). Major high-angle normal faults are also present on the studied islands (for complementary informations see detailed study of Ring *et al*. [2017]).

On Fourni, the main contact between Fourni unit and the upper non-metamorphic Thymaena unit is marked by breccia and cataclasites (Fig. IV.12a) over a thickness of approximately 20 meters. Yellowish foliated cataclasites associated with fluid circulations are folded asymetricaly, and locally show sigmoidal foliation compatible with the top-to-the-NNE shearing (Fig. IV.12b). Below this contact, top-to-the-NNE deformation gradually decreases, while the-top-to-the-SE deformation is totally erased. In addition, in the vicinity of strike-slip faults, top-to-the-E brittle deformation is also recorded between the Fourni and the Chrisomilia unit on probable older faults (Fig. IV.12c). A new set of major SE-NW to E-W striking faults with a strike-slip component offset the contacts between the main units (e.g. Chrisomilia and Korakas units, Fig. IV.8c; Chrisomilia and Fourni units, Fig. IV.12d). Shallow-dipping striae along the main fault planes (Fig. IV.12e) and on smaller-scale faults in the breccia in the north are consistent with a NW-SE extension (see stereogram on Fig. IV.8c). This set of faults is crosscut by steeply N-S striking high-angle normal faults (Fig. IV.8c). According to Ring *et al*. [2017], this set of faults represents the youngest increment, related to the late Miocene to recent extension. These faults can also be oriented SE (e.g. Amorgos and Astipalea islands) to WNW-ESE (e.g. eastern Crete).

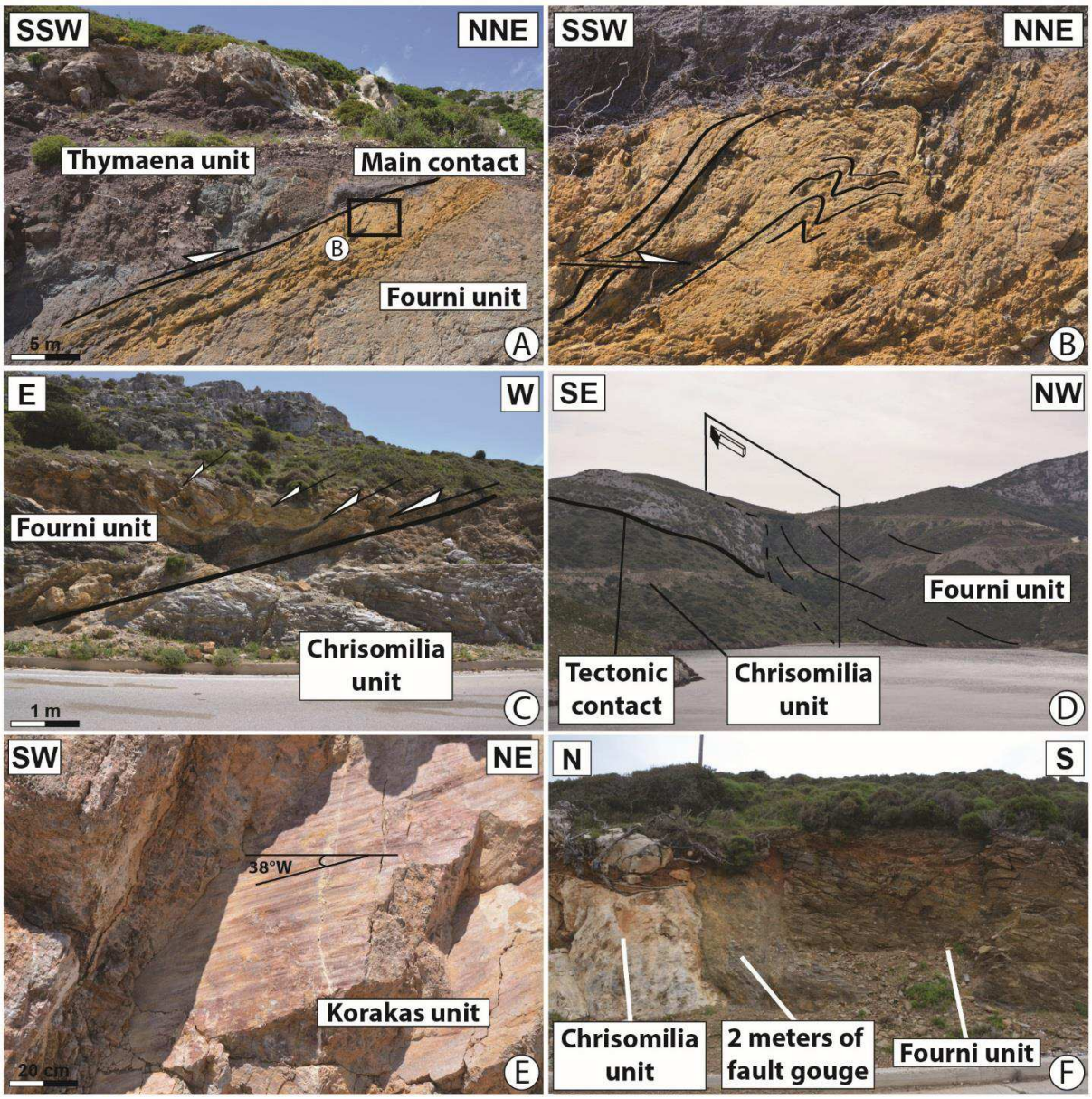

Figure IV.12: Brittle structures on Fourni and Thymaena islands. (a) Large-scale view of the main contact between Fourni unit and the non-metamorphic nappe (i.e. Thymaena unit). (b) Close-up view of the foliated and folded cataclasites from the core of the Thymaena Detachment. (c) Brittle contact between both Chrisomilia and Fourni units showing a top to-the-E deformation. (d) Large-scale view of a dextral strike-slip fault on Fourni. Note that foliation in the basement is strongly affected by this fault. (e) Fault plane and associated striae of major E-W striking strike-slip fault on Fourni that resulted from NE-SW shortening. Note that stereographic projection of striated fault planes corresponds to the number #2 in Figure IV.13h. (f) High-angle normal fault with a probable strike-slip component controlling the relationships between both Chrisomilia and Fourni units. See Figure IV.8c for location.

Similar kinematics of extension are recorded in all Dodecanese islands (Fig. IV.13). Deformation appears more or less localized depending on the area. For instance, Neogene sediments are often in fault contact with the metamorphic rock on Lipsi Island. There, the contact is characterized by a low-angle normal fault parallel to the regional foliation (Fig. IV.13a). Locally, striae along the main fault plane are compatible with the same NE-SW direction of extension (Fig. IV.13b). This major contact in Lipsi may

therefore be interpreted as a low-angle detachment, which we named the Ghialos Detachment. Similar brittle deformation is recorded on Leros, however, with opposite sense of shear. At the scale of the landscape large to small low-angle normal faults dipping 20 – 30° may also control the deposition of Neogene sediments (the Lakki detachment, see Roche *et al*. [2018a]). Here, brittle indicators are compatible with a NE-SW to N-S extension (see stereographic projections on Figs. IV.10 and IV.13h, #6a and #6b). Furthermore, in the area of Agios Isidoros (Fig. IV.4d), the main contact (i.e. Temenia shear zone) appears also ductile-brittle. There, the ductile deformation within Temenia is intense as attested by large amount of low-angle shear zones spaced a few meters. Top-to-the-WSW shear bands become more brittle approaching the base of Marina unit (Figs. IV.13c and IV.13d). The coexistence of opposite kinematic indicators is thus ascribed to the coaxial component of deformation, as also illustrated by large-scale boudinage on Leros [Roche *et al*., 2018a]. In addition, some of these major contacts are locally crosscut by a set of NW-SE striking high-angle normal faults. For instance, in the central part of Lipsi, although the tectonic contact between Neogene sediments and Temenia unit is well exposed (strikes N80°E dipping gently toward the north), it is transected by this set of faults displaying a strike-slip component (Fig. IV.13e). Displacement on faults ranges typically between few meters to decameters. The stress tensor analysis shows a subvertical orientation for the maximum principal stress axis (σ1) whereas the minimum principal stress axis (σ3) is horizontal striking approximately NE-SW (see stereographic plot #4 in Fig. IV.13g). The same sort of faults is also recorded in the southern part of Lipsi where a thick damage zone affects marbles and schists of Temenia unit (Figs. IV.11b and IV.13e). There, foliation strikes N-S and dips deeply toward the north (~ 60°), and turns close to the fault, suggesting a dextral component (Fig. IV.13e).

Furthermore, another set of N-S-oriented high-angle normal faults is recorded on Samos (Fig. IV.13h). There, the present-day topography suggests that the Pythagoras thrust was partly reactivated by a N-S striking fault at least in the southern part. According to Ring *et al*. [1999b], Pythagoras shear zone was top-E directed, and reworked by initial graben formation at about 14 – 13 Ma.

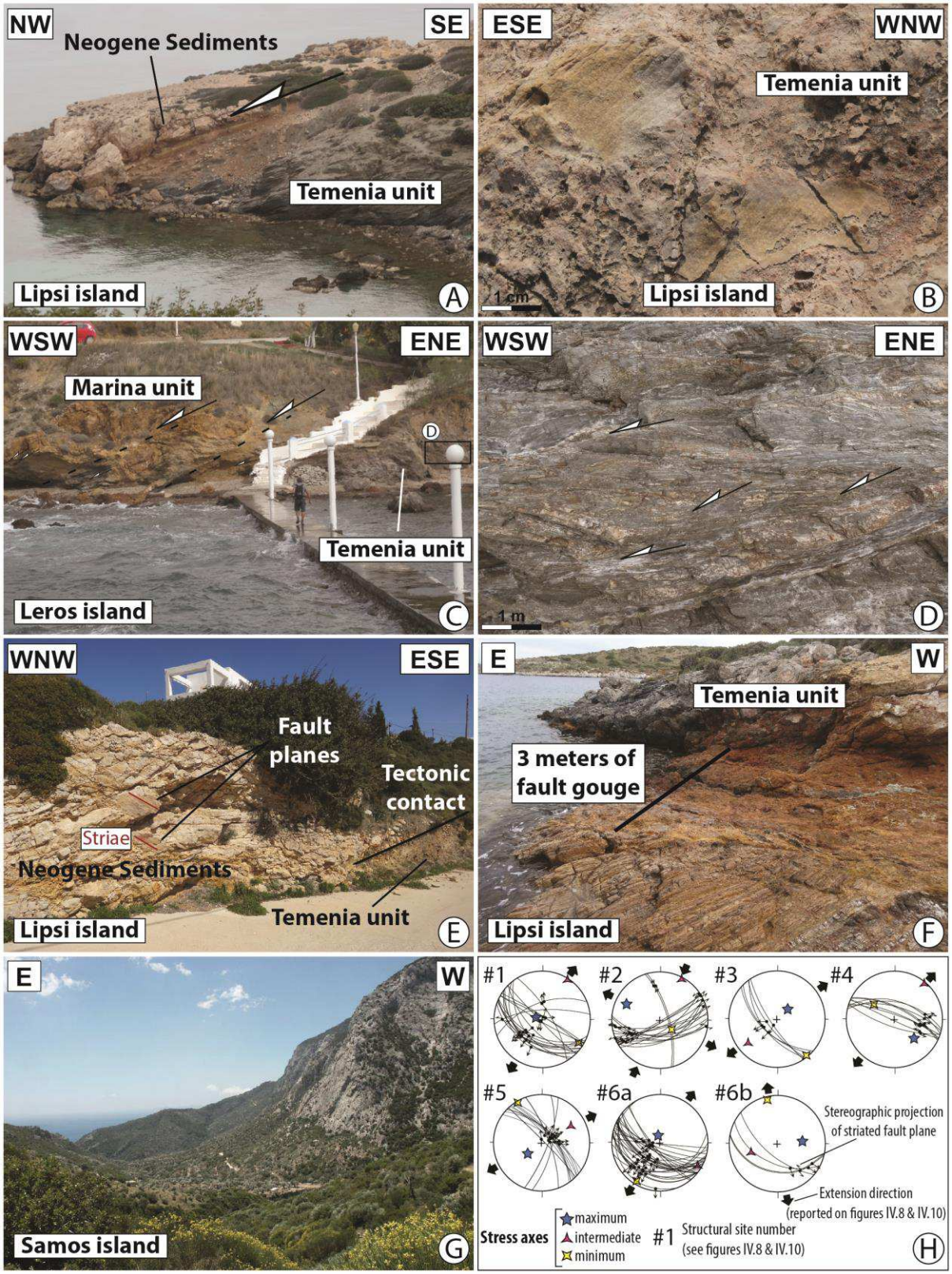

Figure IV.13: Brittle structures on Dodecanese islands and Samos Island. (a) Landscape view of the Ghialos Detachment located in the central part of Lipsi. (b) Close-up view of this detachment showing striae along the main fault plane. (c) Landscape view of Temenia unit, just few meters before the tectonic contact with Marina unit near Agios Isidoros on Leros. Note the presence of low-angle ductile to brittle normal faults. (d) Metric-scale top-to-the-W shear bands observed in the same place. (e) The Ghialos detachment is crosscut by a late high-angle normal fault. Note that stereographic projection of striated fault planes corresponds to the number #4 in Figure

IV.13h. (f) Outcrop view of high-angle fault with a strike-slip component on Lipsi. (g) Large-scale view in the vicinity of Pythagoras thrust zone in Samos. This contact is reworked by a high-angle normal fault. Outcrop shows hanging wall displacements toward the east. (h) Detailed results of the fault slip data inversion plotted in Schmidt's lower hemisphere equal-area projection, using the Win-Tensor software [Delvaux & Sperner, 2003].

IV.7. Discussion

IV.7.1. Correlations between Western Anatolia and the Aegean region

The location of the eastern Aegean islands and the Dodecanese at the transition between the Aegean and western Anatolian regions allows discussing the correlations between these two domains based on our new field observations. But, although the complex evolution before the Eocene is not in the scope of the present paper, it might have had some consequences in differentiating two domains with two different lithospheres. Therefore, some general comparisons have to be recalled about (i) the ophiolite emplacement and (ii) the nature of the continental basement:

i) Papanikolaou [2009; 2013] showed that the timing of tectonic emplacement of the ophiolites in the Hellenides, and their subduction history, shows three major periods of obduction and microcollision: a first during the Late Triassic - Liassic with the closure of the Lesvos-Circum Rhodope oceanic basin (H_6), a second during the late Jurassic - early Cretaceous with the closure of the Axios/Vardar oceanic basin (H_4) and the third during late Cretaceous - Eocene with the closure of the Pindos - Cyclades basin (H_2).

ii) A crucial point is the correlation of the Variscan basement below the Southern Cyclades (Paros, Naxos, Ios) with the "Menderes core" nappes in Turkey. Indeed, the limited outcropping surfaces of basement rocks in the Cyclades and the Hellenides suggest that most of the basement has subducted [Jolivet *et al*., 2004b]. Conversely, the widely outcropping continental basement in the Menderes Massif suggests that the crustal wedge is made of basement units to a large extent. Although this continental basement has a similar structural position as the Variscan basement seen in Ios or Naxos [e.g. Henjes-Kunst & Kreuzer, 1982; Andriessen *et al*., 1987], it is mostly of Panafrican age and no trace of a Panafrican event has been detected in the Aegean domain [e.g. Bonneau & Kienast, 1982; Candan *et al*., 2011]. However, occurrence of Triassic intrusions and the presence of CBU on top of this basement in both regions [Jolivet *et al*., 2004b] suggest a common evolution since the Triassic. In addition, according to Dürr *et al*. [1978], the sedimentary formations of the Marina unit resemble the Lycian Nappes in SW. In this framework, a solution is to see the presence of the large amount of basement on Leros and Kalymnos as a lateral equivalent of Lycian Nappes (without HP-LT evidences), but with a preserved Paleozoic basement that would have overthrust the Menderes Massif and its cover, a basement that is so far unknown in western Turkey. The various basements have recorded different P-T evolutions. Whereas the Cyclades basement was clearly involved in the Hellenic orogenic wedge,

associated with an HP-LT Alpine metamorphic event, this event is less important in the Dodecanese islands (300 – 370 °C at 1 – 3 kbar [Franz & Okrush, 1992]), and not recognized within the basement of the Menderes Massif.

IV.7.1.1. Fourni, Samos, western Anatolia and the Cyclades

The nappe stack of Fourni and Samos offers possible correlations with the nearby Menderes Massif and the Lycian Nappes. From top to bottom, the Kallithea nappe can be correlated with the upper Cycladic Nappe and its Pelagonian basement when looking west, and with the Lycian ophiolite or Lycian ophiolitic mélange that root in the Izmir-Ankara suture zone, when looking east in western Turkey (Fig. IV.14). The presence of a late Cretaceous HT-LP metamorphism associated with an ophiolite on several Cycladic islands shows that the Vardar Ocean ophiolite was once distributed over a large part of the Aegean domain. In addition, the non-metamorphic Thymaena unit on Fourni [Papanikolaou, 1980] and Kefala unit on Ikaria, may also belong to this upper Cycladic Nappe/Pelagonian domain (Fig. IV.14).

On these two islands, the underlying Fourni unit of Fourni Island and Aghios Kirikos unit on Ikaria present similar lithostratigraphic successions and an apparent lack of a significant HP-LT imprint [Papanikolaou, 1978], excluding correlations with the CBU. Indeed, Aghios Kirikos unit is made of marbles and metapelites intercalations, and RSCM results displayed lower temperature ranging between 450 and 390 °C [Beaudoin *et al.*, 2015]. These two units could thus be lateral equivalents of the Menderes cover nappes, having escape deep burial and stacked together with the Cycladic Blueschists nappes in a late stage of accretion of the orogenic wedge.

In the eastern part of Samos Island, the preservation of HP-LT parageneses in Vourliotes nappe with the paragenesis diaspore + quartz suggests that this unit was equilibrated along a very low-temperature and high-pressure gradient, similar to the gradient observed on Amorgos, in the cover of the Menderes Massif, or in the Ören unit, three areas where Fe-Mg carpholite has been observed [Minoux *et al.*, 1981; Rimmelé *et al.*, 2003b; Jolivet *et al.*, 2004b]. However, this cold HP unit overlies on Samos the Upper Cycladic Blueschist Nappe, therefore the correlation in this area is difficult. It could be an equivalent of the Lower Cycladic Blueschist Nappe overthrusted in a late stage of formation of the accretionary wedge on top of the Upper Cycladic Nappe. An alternative solution is that this unit is an equivalent of the Afyon and Ören units.

The underlying Ampelos nappe and Selçuk nappe on Samos are similar to the metasediments and ophiolitic mélange of the CBU of the Dilek Peninsula, resting on top of the Menderes Massif [Candan *et al.*, 1997; Oberhizansli *et al.*, 1998; Ring *et al.*, 1999a]. It may therefore be correlated with the Upper Cycladic Blueschist Nappe that crops out mainly on Syros, Sifnos and Tinos. Even though

Chrisomilia unit of Fourni shows a strong retrogression in greenschist-facies conditions, it can be either correlated with the Ampelos nappe because of the significant amount of metabasite or it would be a part of the Upper Cycladic Blueschist Nappe or with the Lower Cycladic Blueschist Nappe that crops out in more external zones of the CBU (e.g. Folegandros, Leros…).

Finally, a thick marble sequence is recognized in both the lowermost Kerketeas (Samos) and Korakas (Fourni) units. We can correlated these units with the basal unit of the CBU (Almyropotamos unit, equivalent of the Olympus unit), thus with the Gavrovo-Tripolitza nappe.

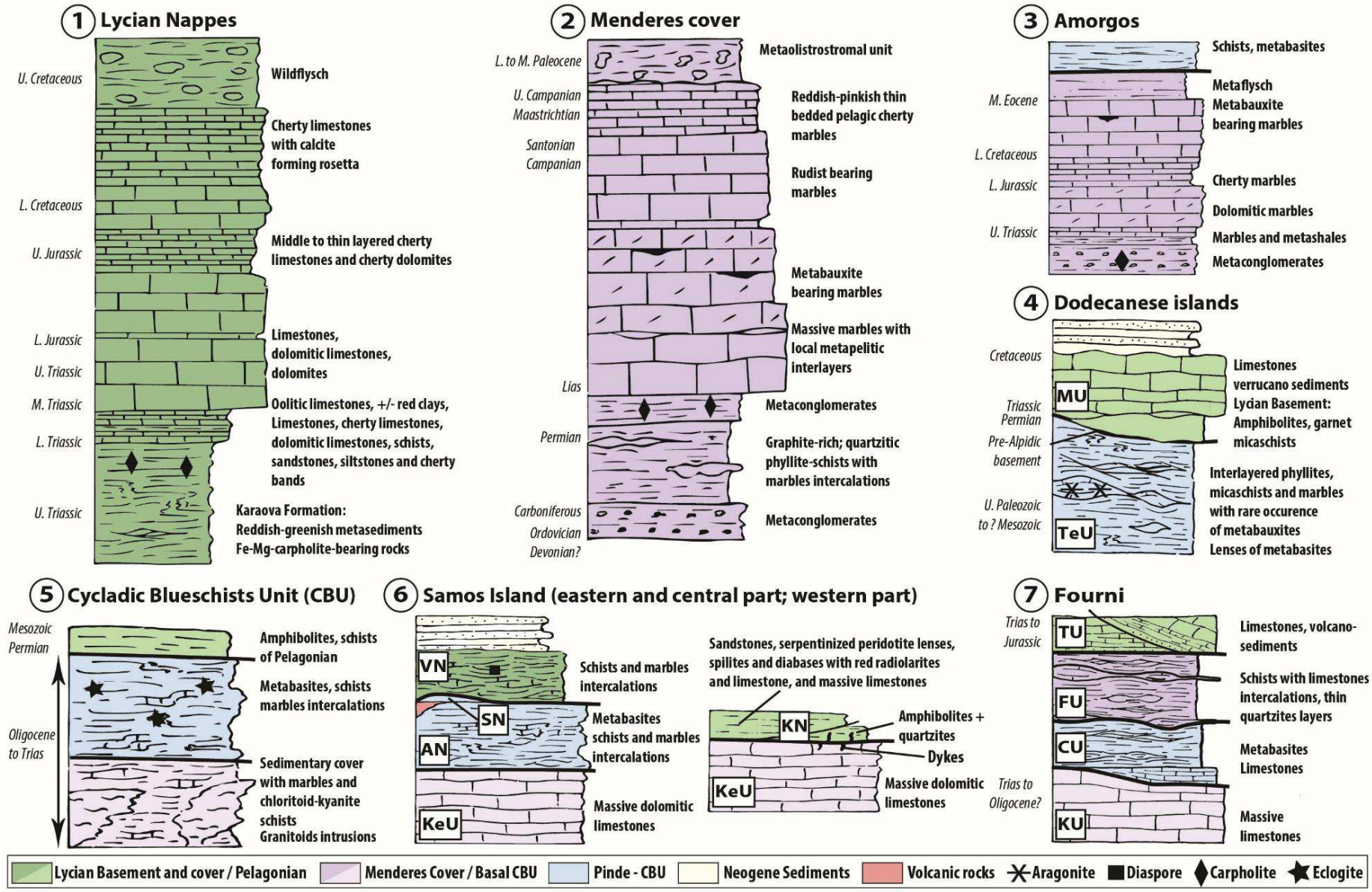
1 Lycian Nappes
U. Cretaceous
Wildflysch
Cherty limestones with calcite forming rosetta
L. Cretaceous
U. Jurassic
Middle to thin layered cherty limestones and cherty dolomites
L. Jurassic
U. Triassic
Limestones, dolomitic limestones, dolomites
M. Triassic
L. Triassic
Oolitic limestones, +/- red clays, Limestones, cherty limestones, dolomitic limestones, schists, sandstones, siltstones and cherty bands
U. Triassic
Karaova Formation: Reddish-greenish metasediments Fe-Mg-carpholite-bearing rocks
2 Menderes cover
L. to M. Paleocene
Metaolistrostromal unit
U. Campanian Maastrichtian
Reddish-pinkish thin bedded pelagic cherty marbles
Santonian Campanian
Rudist bearing marbles
Metabauxite bearing marbles
Massive marbles with local metapelitic interlayers
Lias
Metaconglomerates
Permian
Graphite-rich; quartzitic phyllite-schists with marbles intercalations
Carboniferous Ordovician Devonian?
Metaconglomerates
3 Amorgos
Schists, metabasites
M. Eocene
Metaflysch Metabauxite bearing marbles
L. Cretaceous
L. Jurassic
Cherty marbles
Dolomitic marbles
U. Triassic
Marbles and metashales
Metaconglomerates
4 Dodecanese islands
Cretaceous
Limestones verrucano sediments Lycian Basement: Amphibolites, garnet micaschists
MU
Triassic Permian
Pre-Alpidic basement
Interlayered phyllites, micaschists and marbles with rare occurence of metabauxites Lenses of metabasites
U. Paleozoic to ? Mesozoic
TeU
5 Cycladic Blueschists Unit (CBU)
Mesozoic Permian
Amphibolites, schists of Pelagonian
Metabasites, schists marbles intercalations
Oligocene to Trias
Sedimentary cover with marbles and chloritoid-kyanite schists Granitoids intrusions
6 Samos Island (eastern and central part; western part)
VN
Schists and marbles intercalations
SN
Metabasites schists and marbles intercalations
AN
Massive dolomitic limestones
KeU
Sandstones, serpentinized peridotite lenses, spilites and diabases with red radiolarites and limestone, and massive limestones
KN
Amphibolites + quartzites
Dykes
KeU
Massive dolomitic limestones
7 Fourni
Trias to Jurassic
TU
Limestones, volcano-sediments
FU
Schists with limestones intercalations, thin quartzites layers
CU
Metabasites Limestones
Trias to Oligocene?
KU
Massive limestones
Lycian Basement and cover / Pelagonian
Menderes Cover / Basal CBU
Pinde - CBU
Neogene Sediments
Volcanic rocks
Aragonite
Diaspore
Carpholite
Eclogite

Figure IV.14: Synthetic tectono-stratigraphic sequences of the eastern Mediterranean region showing the main correlation between all units. Data are modified from: 1 – 2: Rimmelé et al. [2003a; 2003b]; 3: Chatzaras et al. [2011]; 4: Roche et al. [2018a] and this study; 5: Jolivet et al. [2004]; 6: Ring et al. [1999a]; this study. Note that the first tectono-stratigraphic sequences of Samos Island corresponds to the central and eastern part of the island, and the second one to the eastern part; 7: This study. Abbreviations: MU (Marina unit), TeU (Temenia unit); VN (Vourliotes nappe); SN (Selçuk Nappe); AN (Ampelos nappe); KeU (Kerketas unit); KN (Kallithea nappe); TU (Thymaena unit); FU (Fourni unit); CU (Chrisomilia unit); KU (Korakas unit).

IV.7.1.2. Dodecanese, Menderes cover and Amorgos Island

The ubiquitous presence of blueschist-facies parageneses in Temenia unit in the two islands of Leros and Arki consolidates the hypothesis of Franz *et al*. [2005] suggesting that the whole Temenia unit was affected by an HP-LT alpine event. The preservation of aragonite, the absence of garnet and RSCM results however, show that Temenia unit has recorded lower peak-metamorphic conditions than the nearby Cyclades islands. In this framework, Temenia unit could be either an equivalent of (i) the metamorphic Ören unit where HP-LT parageneses with Fe-Mg carpholite have been reported [Rimmelé *et al*., 2003a], thus the lower part of the Lycian Nappes, or an equivalent of (ii) the Lower Cycladic Blueschist Nappe or (iii) of the Menderes cover (i.e. Kurudere-Nebiler unit). According to Roche *et al*. [2018a], Temenia unit may be correlated with the Lower Cycladic Blueschist Nappe in terms of lithogies, although a correlation with the Menderes cannot be excluded (Fig. IV.14).

No consensus exists on the belonging of the HP-LT sequences of the Kurudere-Nebiler units (south Menderes). This unit has indeed recorded peak conditions of ~ 450 °C and 10 – 12 kbar while the Upper Cycladic Blueschist Nappe were buried deeper depths of about 550 °C and 19.5 kbar (Fig. IV.2). In Pourteau *et al*. [2010; 2013], the Kurudere unit is correlated with the CBU as a whole but the lithologies and P-T conditions are not equivalent to the typical occurrence of the CBU that should show a large amount of metabasites and well-preserved eclogites (Fig. IV.15). It seems more reasonable to correlate the cover of the Menderes Massif as an equivalent of the Lower Cycladic Blueschist Nappe (Fig. IV.15).

Furthermore, Amorgos exposes a sequence of HP-LT rocks that have undergone two different blueschist-facies metamorphism. A first event is estimated at < 13 kbar and 500 – 600 °C [Rosembaum *et al*., 2007] and may correspond to the eclogite-blueschits-facies observed in the Upper Cycladic Blueschist Nappe. The second event is associated with Fe-Mg-carpholite and saliotite found in metabauxites and is estimated at 8 – 12 kbar and 300 – 350 °C (Fig. IV.12) [Theye *et al*., 1997]. This unit consists on thick Mesozoic marble sequence capped by an early Tertiary metaflysch, and may be correlated with the cover of the Menderes Massif (Fig. IV.15).

This discussion emphasizes the difficulty of correlating the different nappes of the Hellenides once they have been dispersed by the Oligo-Miocene Aegean extension. Two main criteria can be used

for such correlations. (1) One can correlate units with similar stratigraphic successions, and thus pre-orogenic paleogeographic domains, but these domains may have very large areal extents and be involved in different parts of the same belt if large overthrusts are oblique on the main paleogeographic domains. (2) One may alternatively correlate units with approximately similar stratigraphic succession and similar P-T-time evolution or, rather, similar peak pressure-temperature conditions. In this case, the emphasis is put on the position of these units within the subduction channel or accretionary wedge, thus on a syn-orogenic situation. The complexity of the situation in the Eastern Aegean region is also due to a lack of metamorphic age constraints on a number of these islands. Further works should focus on enlarging the radiochronological data set there.

To summarize, the Aegean-Anatolian orogenic wedge is made of continental basement units (Menderes Massif, Cycladic basement) and units essentially made of metasediments or metabasites (the CBU, Kurudere-Nebiler unit, Ören unit). According to this study and the literature [Papanikolaou & Demirtasli, 1987], the following lateral correlations can be made: 1) The Late Triassic-Early Jurassic event known as the Cimmerides orogeny occurs only in the eastern Aegean islands of Lesvos and Chios and possibly also in the Circum Rhodope belt. 2) The late Jurassic - early Cretaceous event is widespread in the so-called internal Hellenides of Brunn [1960] in continental Greece with sparse outcrops in the Aegean: Evia, Skyros, Northern Sporades, Chios and upper non-metamorphic nappe in the Cyclades (Paros, Naxos) and Ikaria, Thymaena, Kallithea in the western part of Samos and in Crete (Asteroussia nappe) (Fig. IV.1). This event is not detected to the east in the Pontides, where it might be covered by the unconformities of the Late Jurassic and Upper Cretaceous that are observed sometimes above the older Liassic unconformity of the Cimmerides. 3) The Eocene event can be followed through the Aegean from the Hellenides (Olympus tectonic window and the Pindos ophiolites to Othris, Argolis, Cyclades, Crete and Dodecanese) to the Anatolides-Taurides (e.g. Tavşanlı Zones, Afyon and Ören units, the Kurudere-Nebiler units).

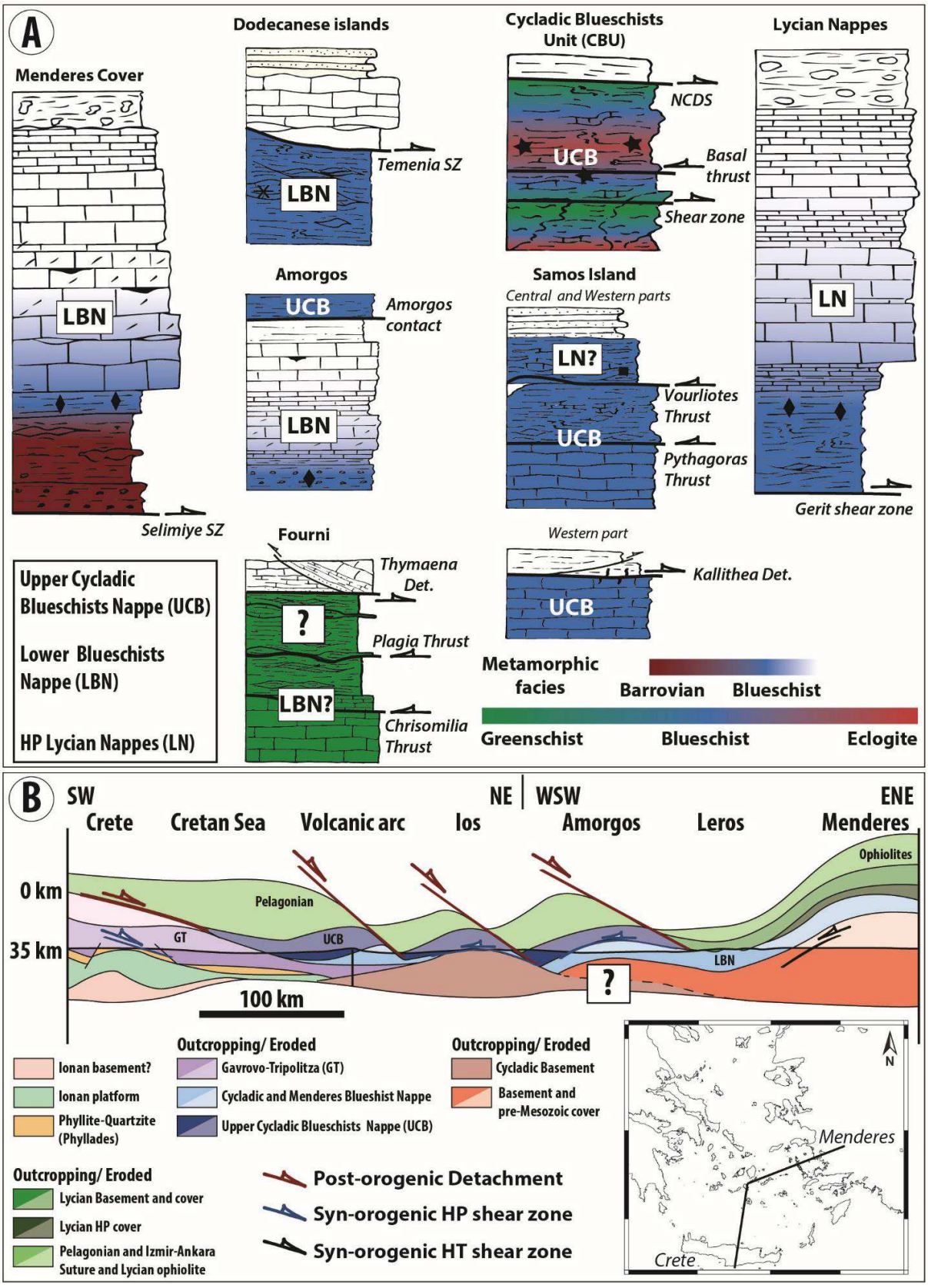

Figure IV.15: Possible correlations based on metamorphic markers in the eastern Mediterranean region. (a) Synthetic metamorphic stratigraphic sequences of the eastern Mediterranean region. (b) Simplified cross-section showing the main relations between tectono-metamorphic units modified from Jolivet et al. [2004]. Black line corresponds to the position of the cross-section.

Although all these units have followed different P-T evolutions, a similar structural position is recognized through the entire region. From bottom to top (Fig. IV.15b), one then finds (i) the colder units such as the Menderes and its cover before the MMM overprint, the Lower Cycladic Blueschist Nappe (Amorgos, Folegandros, the Lower unit of Milos, the western Cyclades, a part of the Dodecanese islands, and probably Fourni units), merged in the Lower Blueschist Nappe (LBN), (ii) the eclogitic rocks observed mainly in the central part of the Cyclades, in Samos and on Dilek peninsula (i.e. the Upper Cycladic Blueschist Nappe), and (iii) the Lycian units and Vourliotes nappe in Samos (?) that were buried and exhumed earlier (Figs. IV.14 and IV.15). This overall vertical succession can be locally modified suggesting late out of sequence thrusting.

IV.7.2. Tectonic evolution of the Aegean-Anatolia region

Figure IV.16 is a map of kinematic indicators covering the Aegean Sea and the Menderes Massif, based on previous works [Jolivet *et al*., 2013 and references therein] and enriched with our new observations made in the eastern Aegean islands, the Dodecanese and the Menderes Massif. It is worthwhile to note that the main shearing directions and the main sense of shear are not significantly affected by Miocene to recent paleomagnetic rotations, especially in the central and eastern regions, even if the south-western part of Turkey have recorded an anticlockwise rotation [Walcott & White, 1998].

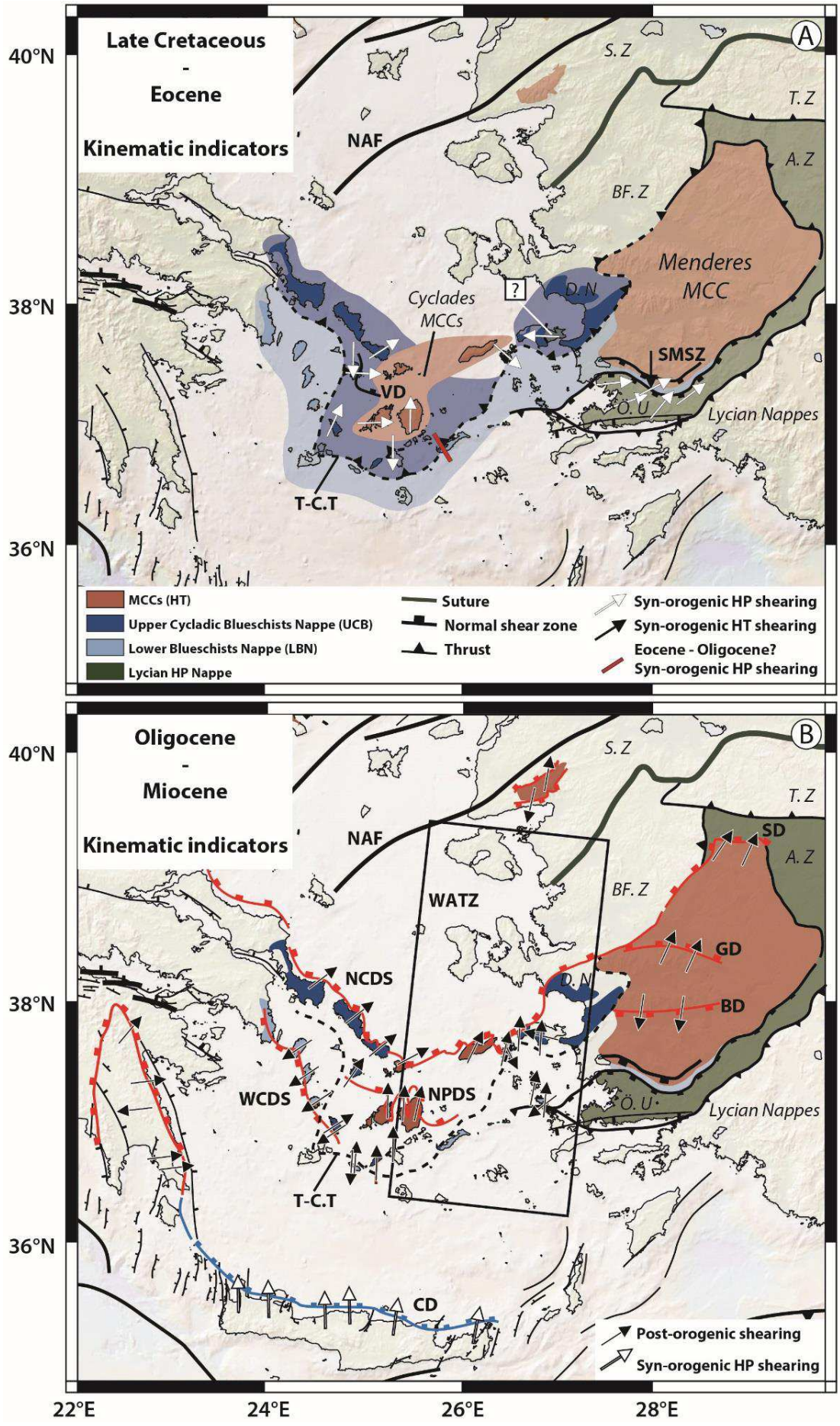
Late Cretaceous
-
Eocene
Kinematic indicators
A
S. Z
T. Z
A. Z
BF. Z
NAF
Menderes
MCC
Cyclades
MCCs
?
D. N
SMSZ
VD
T-C.T
Ö. U
Lycian Nappes
40°N
38°N
36°N
MCCs (HT)
Upper Cycladic Blueschists Nappe (UCB)
Lower Blueschists Nappe (LBN)
Lycian HP Nappe
Suture
Normal shear zone
Thrust
Syn-orogenic HP shearing
Syn-orogenic HT shearing
Eocene - Oligocene?
Syn-orogenic HP shearing
Oligocene
-
Miocene
Kinematic indicators
B
S. Z
T. Z
A. Z
BF. Z
NAF
WATZ
SD
GD
BD
NCDS
WCDS
NPDS
D. N
Ö. U
Lycian Nappes
T-C.T
CD
Post-orogenic shearing
Syn-orogenic HP shearing
22°E
24°E
26°E
28°E

Figure IV.16: Tectonic map of the eastern Mediterranean region showing the main tectonic structures and associated kinematic indicators (a) in Cretaceous - Eocene time and in (b) Oligocene - Miocene time. Data are from this study, and from earlier studies in the Cyclades [e.g. Jolivet et al., 2013 and references therein] and the Menderes Massif and its periphery [e.g. Hetzel et al. 1995a; 1995b and references therein].

IV.7.2.1. Kinematic of deformation from the Cretaceous to the Oligocene

a. Prograde deformation

The first stage of deformation corresponds to the stacking of units by thrusting, probably during prograde evolution or at pressure peak. Most kinematic indicators related to this episode of nappe stacking have been erased during subsequent exhumation and further extension, but a limited number of outcrops evidencing this kinematics in the Cyclades and in the Olympos-Ossa region are however preserved. For instance, on Syros, Philippon *et al*. [2011] suggest that the sense of shear was toward the south during this first episode (Fig. IV.16a). Syn-orogenic top-to-the-SW shear sense criteria have also been preserved in the Olympos-Ossa region [Schermer *et al*., 1990; Ricou *et al*., 1998; Jolivet *et al*., 2004b]. In addition, our study shows that top-to-the-SE kinematic indicators associated with thrusts are also well preserved on Fourni Island in the lower part of Fourni unit (Figs. IV.8 and IV.16a). Althoug no clear P-T conditions are established on Fourni, we suggest that these kinematic indicators are related to this compressional event, and thus recorded during the prograde phase.

The overall architecture of the Menderes Massif and Lycian Nappes also calls for a top-to-the-S emplacement of nappes. The Lycian Nappes, including the lowermost Ören metamorphic unit, root within the Izmir-Ankara suture zone along the northern margin of the Menderes [Rimmelé *et al*., 2003a; 2005, Pourteau *et al*., 2013]. Large-scale top-to-the-south shear zones are described within the Menderes Massif (i.e. South Menderes Shear Zone (SMSZ); Fig. IV.16a), between the basement and the cover [e.g. Bozkurt & Park, 1994; Hetzel *et al*., 1995a; 1995b; Hetzel & Reischmann, 1996] and their significance, whether they are thrusts or detachments or both, is debated.

b. Syn-orogenic deformation

Even if the Miocene extension history of Samos is quite complex as demonstrated the presence of N-S lineations under greenschist-facies conditions in the central part of the island (Fig. IV.8a), a continuum from ductile (blueschist- to greenschist-facies) to brittle deformation is preserved across the contact between the Kerketeas and the Ampelos units with a top-to-the-W-NW shearing (Fig. IV.16a). This deformation emphasizes the idea that the Pythagoras shear zone has accommodated a part of the

exhumation of the CBU during the HP-LT metamorphic event. Similar structures are also observed in the Aegean domain and in the southern Turkey.

For instance in the Aegean domain, a top-to-the-E shearing deformation along the Vari Detachment (outcrops in Syros) allows the exhumation of the entire CBU sequence within the subduction channel (Fig. IV.16a) [e.g. Jolivet *et al*., 2003; 2010; Ring & Layer, 2007; Huet *et al*., 2009; Laurent *et al*., 2016]. A top-to-the-S thrusting in Ios Island is also coeval with the extensional shear zone of Vari (Fig. IV.16a) [Huet *et al*., 2009]. According to this study, an extrusion structure is proposed to explain exhumation of the CBU. However, recent studies [e.g. Grasemann *et al*., 2018; Roche *et al*., 2018a] show the existence of a Lower Cycladic Blueschist Nappe outcropping at the southern part of Ios (Fig. IV.16a), as a consequence this basal thrust cannot explain the entire exhumation of CBU. In the HP-LT Lycian Nappes, different P-T conditions within the Lycian Nappes indicate the existence of many shear zones accommodating the exhumation of a large wedge. Top-to-the-east shear senses are recorded within the entire sequence, and deformation appears more localized close to the contact between the Lycian and Menderes Massif [Rimmele *et al*., 2005].

This short discussion emphasizes the 3-D complexity of the wedge, where HP-LT syn-orogenic exhumation shearing may be approximately E-W in some places (i.e. parallel to the trench; e.g. Syros, Samos, Ören unit) whereas it is for instance N-S in other areas (e.g. Ios Island) (Fig. IV.16a). In any case, the accretionary complex is particularly wide and may be defined by three main metamorphic units: the Lower Blueschist Nappe (LBN), (ii) the Upper Cycladic Blueschist Nappe, and (iii) the HP-LT Lycian Nappes (including the Vourliotes nappe of Samos?) (Fig. IV.16a).

IV.7.2.2. An overall NNE-SSW gradient of extension during Oligo-Miocene to Present

The overall picture of the extensional kinematics of the Aegean Sea and western Anatolia shows that the direction and sense of displacement along the main detachments during slab retreat is consistent over the entire eastern and central Aegean Sea (Fig. IV.16b). This area presents a pervasive network of large-scale to small-scale ductile-brittle shear zones in all metamorphic units and ductile and brittle criteria show an overall consistent top-to-the-NNE kinematics with localized top-to-the-SW kinematics probably due to coaxial deformation. In most cases, contacts such as the Ghialos Detachment, the Lakki Detachment and the Thymaena Detachment were thus active during both ductile and brittle conditions (e.g. Figs. IV.8c, IV.10, IV.12 and IV.13). These features observed in the eastern Aegean Sea complete the description of extensional shearing direction and sense over the entire back-arc region. The top-NNE kinematic indicators are thus distributed over a wide region, from the Central Aegean (Paros-Naxos) to the Dodecanese and Eastern Aegean islands. Further west (western Cyclades) and east (Menderes Massif), one instead observes a partly symmetrical deformation, characterized by several detachment

systems exhibiting opposing kinematics (e.g. the WCDS and NCDS in the Cyclades, the Büyük Menderes and the Gediz detachments, Fig. IV.16b). However, the bivergent pattern in the Menderes Massif is mostly due to the most recent part of extension, from ~ 20 Ma to the present. Before this event, the main detachment exhuming the Menderes Massif was active in the north (Simav Detachment) with a top-to-the-N kinematics, exhuming partially molten crust (Fig. IV.16b). The top-NNE kinematics of the eastern and central Aegean is associated with HT-LP metamorphic overprint (with local anatexy) in Ikaria, Mykonos and Naxos from ~ 20 Ma to the Late Miocene, and with the emplacement of the Aegean granitoids. To summarize, the top-to-the-NNE asymmetrical extension encompassed a larger domain in the Oligocene than seen in the more recent evolution. According to many studies [Jolivet & Brun, 2010; Jolivet *et al*., 2013; Gessner *et al*., 2013; Gessner *et al*., 2017], this NNE extension is mainly driven by slab retreat and slab tearing. We therefore challenge the hypothesis of Ring *et al*. [2017] suggesting the existence of a diffuse Aegean-Anatolia plate boundary that would have started to form in the early Miocene at the western edge of the northern Menderes Massif. It is indeed a diffuse shear zone but not a plate boundary as the deformation west of it is certainly not rigid. Nonethelsess, it is noteworthy that different fission track age patterns have been recorded in both regions (i.e. Cyclades and Menderes Massif) (see the complitaion of Ring *et al*. [2017]), suggesting a difference of exhumation and erosion rates. In addition, we suggest that the asymmetrical pattern of the central and eastern Aegean Sea is due to a more active asthenospheric flow than below the Menderes.

Furthermore, according to Ring *et al*. [1999b], NNE extension was interrupted by a short-lived phase of E-W shortening between 9 and 8.6 Ma. This compressional event, which may also be associated with some strike-slip component [Papanikolaou, 1979], is ascertained in Samos by the presence a several reverse faults that affect both the margins of the Miocene basin and the basin itself. Folds formed in the Miocene deposits before the deposition of the Mytilini formation are also compatible with his event. This Miocene compressional event has also been recognized on Mykonos during the late stages of cooling of the intrusion some 9 Ma ago [Menant *et al*., 2013]. Ascertained compressional structures are otherwise not frequent in the Aegean but those observed in Samos and Mykonos need to be explained. Following Menant *et al*. [2013], we suggest that the extrusion of Anatolia may be responsible for this regional compressional event in the central Aegean, before strike-slip deformation localized on the edge of the Aegean domain when the NAF reached the north Aegean Sea in the Late Miocene [Armijo *et al*., 1999; Koukouvelas & Aydin, 2002]. Armijo *et al*. [2003] proposed that propagation of the NAF and its satellites would produce a compressional stress regime, just south of the western tip of the faults, while an extensional regime would be active north of the fault. The short compressional event could be then due to the propagation of such a strike-slip system, just north of Samos. However, this would make the NAF propagate earlier than usually postulated (~ 5 Ma) as the age of the compression is estimated between 9 and 8.6 Ma [Ring *et al*., 1999b]. It is thus important to obtain more data to precise this point.

Finally, late brittle deformation is compatible with a N-S to NNE-SSW extension over large areas. For instance, in the Menderes massif, E-W striking high-angle normal faults control the structure of Neogene basins. These set of faults, seismically active, started to operate around ~ 5 Ma ago [Ring *et al*., 2003], and are co-directional with the extension direction of earlier low-angle normal faults. In addition, inversion of GPS data that estimates the present-day strain field [Pérouse *et al*., 2012; Aktug *et al*., 2009], and fault mechanism from the earthquake on Lesbos (data from the USGS Earthquake Hazards Program) showing a normal component, are both consistent with a N-S extension.

IV.7.3. Slab tearing: which consequences in the overriding plate?

Before discussing tectonic and thermal consequences of slab tearing, we need to clarify the timing of the tear formation below western Turkey. Govers and Fichtner [2016] suggested that the slab tear started to forms around 35 Ma following the arrival of the Central Anatolian Crystalline Complex (CACC) in the accretionary complex. However, as discussed by Jolivet *et al*. [2015], the main evidence of a differential rotation between the western branch of the Hellenides-Taurides and the eastern branch is shown by paleomagnetic measurements [e.g. Morris & Anderson, 1996; Van Hinsbergen *et al*., 2010], which also corresponds to the exhumation of high-temperature metamorphic domes below top-NE detachments in the central and eastern Aegean Sea and emplacement of the Aegean granitoids. Indeed, local counterclockwise rotations have been recorded in the central Menderes Massif and Naxos Island [Morris & Anderson, 1996; Avigad *et al*., 1998; Van Hinsbergen, 2010; Van Hinsbergen *et al*., 2010] suggesting a fast rotation in the Hellenides between 15 and 8 Ma [Van Hinsbergen & Schmid, 2012]. This pediod of fast differential rotation has thus been interpreted by Jolivet *et al*. [2015] as the age of the main slab-tearing event, thus much later than postulated by Govers and Fichtner [2016]. Slab tearing could have started earlier though, but at a slower pace.

Within the transition zone from the Menderes massif to the Cyclades, we showed that the direction of extension is consistently NNE-SSW with no major change in trend, and the sense of shear is predominantly top-to-the-N (Fig. IV.16b). Most of the observed deformation relates to low-angle normal faults and ductile shear zones, without any clear large-scale strike-slip fault systems that could have been expected above a slab tear. As expected, the tear in the slab is a rather wide feature, and confirms the ideas put forward by Gessner *et al*. [2013] and Jolivet *et al*. [2015] of a wide zone of gradient of extension accommodating the left-lateral displacement imposed by the faster retreat south of the Aegean Sea than of the Menderes Massif. Most of the related deformation in the crust is accommodated by low-angle shear zones and faults and not by large strike-slip faults, which is compatible with the idea that the deformation in this region is largely controlled by the flow of asthenospheric mantle underneath [Jolivet *et al*., 2015; Menant *et al*., 2016a]. Using seismic anisotropy data, Endrun *et al*. [2013] confirms

also this hypothesis, suggesting a strong coupling between SW-NE mantle fabrics and the frozen-in fabric in the lower crust.

However, brittle deformation mainly recorded in Miocene basins shows a more complex evolution (e.g. E-W compression in the Miocene, see above). It highlights a possible decoupling between the upper and lower crust, at some period, which could be temporary control by stresses transmitted through the lithosphere during the propagation of the NAF. But the overall geometry and kinematics revealed by this study suggests that asthenospheric flow is the main driver. The thermal effects induced by slab dynamics (i.e. mantle flows and shear heating) appear clearly since the Miocene and are essential in the eastern Agean domain [e.g. Roche *et al*., 2018b]. Slab dynamics controls the bulk of heat souce at the base of the crust and therefore explains (i) the development of crustal thermal domes (i.e. MCCs) through time, (ii) the retrogression in greenschist-facies or amphibolite-facies conditions in the Aegean domain, (ii) the current localization of geothermal resources in the Menderes massif [Roche *et al*., 2018c].

IV.8. Conclusion

Based on a field study in the eastern part of the Aegean Sea (Eastern Aegean islands and Dodecanese) that have been little studied so far, we (1) produce new geological maps and describe the tectonic evolution of several islands and (2) clarify the correlations and differences between the Aegean Sea and the Menderes Massif in terms of lithological and tectonic units and in terms of metamorphic evolution. We correlate the cover of the Menderes Massif where HP-LT parageneses have been described with the Lower Cycladic Blueschist Nappe, and the higher-temperature and higher-pressure rocks found on Samos and on Dilek Peninsula, with the Upper Cycladic Blueschist Nappe. We (3) further show that, in the transition zone between the Aegean domain and the Menderes massif, extension related to slab retreat and tearing keeps a constant NNE-SSW direction accommodating the difference in finite extension rates, with a simple ductile crustal flow of shallow-dipping shear zones that probably reflects the underneath flowing asthenospheric mantle. Neither localized first-order strike-slip fault nor significant rotation of blocks about a vertical axis, at least in the middle-lower crust are observed, but upper crustal deformation may be partly decoupled and may have recorded lithospheric scale changes of stress regime.

IV.9. Acknowledgements

This work has received funding from the Labex Voltaire homed at Orléans University and BRGM, from the European Research Council (ERC) under the seventh Framework Programme of the European Union (ERC Advanced Grant, grant agreement No 290864, RHEOLITH), and from the Institut Universitaire de France.

IV.10. References

Akkök, R. (1983). Structural and metamorphic evolution of the northern part of the Menderes massif: new data from the Derbent area and their implication for the tectonics of the massif. The Journal of Geology, 91(3), 342-350.

Aktug, B., Nocquet, J. M., Cingöz, A., Parsons, B., Erkan, Y., England, P., ... & Tekgül, A. (2009). Deformation of western Turkey from a combination of permanent and campaign GPS data: Limits to block-like behavior. Journal of Geophysical Research: Solid Earth, 114(B10).

Altherr, R., Kreuzer, H., Wendt, I., Lenz, H., Wagner, G. A., Keller, J., ... & Hohndorf, A. (1982). A late Oligocene/early Miocene high temperature belt in the Attic-Cycladic crystalline complex (SE Pelagonian, Greece). Geologisches Jahrbuch E, 23, 97-164.

Altherr, R., Schliestedt, M., Okrusch, M., Seidel, E., Kreuzer, H., Harre, W., ... & Wagner, G. A. (1979). Geochronology of high-pressure rocks on Sifnos (Cyclades, Greece). Contributions to Mineralogy and Petrology, 70(3), 245-255.

Andriessen, P. A. M., Banga, G., & Hebeda, E. H. (1987). Isotopic age study of pre-Alpine rocks in the basal units on Naxos, Sikinos and Ios, Greek Cyclades. Geologie en Mijnbouw, 66(3), e14.

Angelier, J., Lybéris, N., Le Pichon, X., Barrier, E., & Huchon, P. (1982). The tectonic development of the Hellenic arc and the Sea of Crete: a synthesis. Tectonophysics, 86(1-3), 159165167-163196.

Aral, İ. (1989). Geology of the Menderes Massif and the Lycian Nappes south of Denizli, western Taurides.

Armijo, R., Flerit, F., King, G., & Meyer, B. (2003). Linear elastic fracture mechanics explains the past and present evolution of the Aegean. Earth Planet Sci Lett 217:85–95. doi:10.1016/S0012-821X(03)00590-9

Armijo, R., Lyon-Caen, H., & Papanastassiou, D. (1992). East-west extension and Holocene normal-fault scarps in the Hellenic arc. Geology, 20(6), 491-494.

Armijo, R., Meyer, B., Hubert, A., & Barka, A. (1999). Westward propagation of the North Anatolian fault into the northern Aegean: Timing and kinematics. Geology, 27(3), 267-270.

Armijo, R., Meyer, B. G. C. P., King, G. C. P., Rigo, A., & Papanastassiou, D. (1996). Quaternary evolution of the Corinth Rift and its implications for the Late Cenozoic evolution of the Aegean. Geophysical Journal International, 126(1), 11-53.

Ashley, K. T., Caddick, M. J., Steele-MacInnis, M. J., Bodnar, R. J., & Dragovic, B. (2014). Geothermobarometric history of subduction recorded by quartz inclusions in garnet. Geochemistry, Geophysics, Geosystems, 15(2), 350-360.

Aubouin, J. (1959). Contribution à l'étude géologique de la Grèce septentrionale: les confins de l'Epire et de la Thessalie; Place des Hellénides parmi les édifices structuraux de la Méditerranée orientale. Laboratoire de géologie de l'Université.

Augier, R., Jolivet, L., Gadenne, L., Lahfid, A., & Driussi, O. (2015). Exhumation kinematics of the Cycladic Blueschists unit and back-arc extension, insight from the Southern Cyclades (Sikinos and Folegandros Islands, Greece). Tectonics, 34(1), 152-185.

Avigad, D. (1998). High-pressure metamorphism and cooling on SE Naxos (Cyclades, Greece). European Journal of Mineralogy, 10(6), 1309-1319.

Avigad, D., & Garfunkel, Z. (1989). Low-angle faults above and below a blueschist belt—Tinos Island, Cyclades, Greece. Terra Nova, 1(2), 182-187.

Avigad, D., & Garfunkel, Z. (1991). Uplift and exhumation of high-pressure metamorphic terrains: the example of the Cycladic blueschist belt (Aegean Sea). Tectonophysics, 188(3), 357-372.

Avigad, D., Baer, G., & Heimann, A. (1998). Block rotations and continental extension in the central Aegean Sea: Palaeomagnetic and structural evidence from Tinos and Mykonos (Cyclades, Greece), Earth Planet.

Sci. Lett., 157, 23–40, doi:10.1016/S0012-821X(98)00024-7.

Avigad, D., Ziv, A., & Garfunkel, Z. (2001). Ductile and brittle shortening, extension-parallel folds and maintenance of crustal thickness in the central Aegean (Cyclades, Greece). Tectonics, 20(2), 277-287.

Barka, A. A. (1992). The north Anatolian fault zone. In Annales tectonicae (Vol. 6, No. Suppl, pp. 164-195).

Bassias, Y., & Triboulet, C. (1994). Tectono-metamorphic evolution of blueschist formations in the Peloponnesus (Parnon and Taygetos Massifs, Greece): a model of nappe stacking during Tertiary orogenesis. The Journal of Geology, 102(6), 697-708.

Beaudoin, A., Augier, R., Laurent, V., Jolivet, L., Lahfid, A., Bosse, V., ... & Menant, A. (2015). The ikaria high-temperature metamorphic core complex (Cyclades, Greece): geometry, kinematics and thermal structure. Journal of Geodynamics, 92, 18-41.

Bernoulli, D., De Graciansky, P. C., & Monod, O. (1974). The extension of the Lycian Nappes (SW Turkey) into the southeastern Aegean Islands. Eclogae Geologicae Helvetiae, 67(1), 39-90.

Bijwaard, H., Spakman, W., & Engdahl, E. R. (1998). Closing the gap between regional and global travel time tomography. Journal of Geophysical Research: Solid Earth, 103(B12), 30055-30078.

Biryol, C., Beck, S. L., Zandt, G., & Özacar, A. A. (2011). Segmented African lithosphere beneath the Anatolian region inferred from teleseismic P-wave tomography. Geophysical Journal International, 184(3), 1037-1057.

Bonneau, M. (1972). La nappe métamorphique de l'Astéroussia, lambeau d'affinités pélagoniennes charrié jusque sur la zone de Tripolitza de la Crête moyenne (Grece). CR Acad Sci Sér D, 275, 2303-2306.

Bonneau, M. (1982). Evolution geodynamique de l9arc egeen depuis le Jurassique superieur jusqu9au Miocene. Bulletin de la Societé géologique de France, 7(2), 229-242.

Bonneau, M. (1984). Correlation of the Hellenide nappes in the south-east Aegean and their tectonic reconstruction. Geological Society, London, Special Publications, 17(1), 517-527.

Bonneau, M., & Kienast, J. R. (1982). Subduction, collision et schistes bleus; l9exemple de l9Egee (Grece). Bulletin de la Société geologique de France, 7(4), 785-791.

Bousquet, R., Goffé, B., Henry, P., Le Pichon, X., & Chopin, C. (1997). Kinematic, thermal and petrological model of the Central Alps: Lepontine metamorphism in the upper crust and eclogitisation of the lower crust. Tectonophysics, 273(1), 105-127.

Bozkurt, E. (2001). Neotectonics of Turkey–a synthesis. Geodinamica acta, 14(1-3), 3-30.

Bozkurt, E. (2004). Granitoid rocks of the southern Menderes Massif (southwestern Turkey): field evidence for Tertiary magmatism in an extensional shear zone. International Journal of Earth Sciences, 93(1), 52-71.

Bozkurt, E. (2007). Extensional v. contractional origin for the southern Menderes shear zone, SW Turkey: tectonic and metamorphic implications. Geological Magazine, 144(1), 191-210.

Bozkurt, E., & Park, L. R. (1994). Southern Menderes Massif: an incipient metamorphic core complex in western Anatolia, Turkey. Journal of the Geological Society, 151(2), 213-216.

Bozkurt, E., & Park, R. G. (1999). The structure of the Palaeozoic schists in the southern Menderes Massif, western Turkey: a new approach to the origin of the main Menderes metamorphism and its relation to the Lycian Nappes. Geodinamica Acta, 12(1), 25-42.

Bozkurt, E., & Satir, M. (2000). The southern Menderes Massif (western Turkey): geochronology and exhumation history. Geological Journal, 35(3-4), 285-296.

Bozkurt, E., & Oberhänsli, R. (2001). Menderes Massif (Western Turkey): structural, metamorphic and magmatic evolution-a synthesis. International Journal of Earth Sciences, 89(4), 679-708.

Bröcker, M., & Franz, L. (1998). Rb–Sr isotope studies on Tinos Island (Cyclades, Greece): additional time constraints for metamorphism, extent of infiltration-controlled overprinting and deformational activity. Geological Magazine, 135(3), 369-382.

Bröcker, M., Kreuzer, H., Matthews, A., & Okrusch, M. (1993). 40Ar/39Ar and oxygen isotope studies of polymetamorphism from Tinos Island, Cycladic blueschist belt, Greece. Journal of metamorphic Geology, 11(2), 223-240.

Bröcker, M., Bieling, D., Hacker, B., & Gans, P. (2004). High-Si phengite records the time of greenschist facies overprinting: implications for models suggesting mega-detachments in the Aegean Sea. Journal of Metamorphic Geology, 22(5), 427-442.

Bröcker, M., Baldwin, S., & Arkudas, R. (2013). The geological significance of 40Ar/39Ar and Rb–Sr white mica ages from Syros and Sifnos, Greece: a record of continuous (re) crystallization during exhumation?. Journal of Metamorphic Geology, 31(6), 629-646.

Brunn, J. H. (1956). Contribution À L'étude Géologique Du Pinde Septentrional Et D'une Partie de la Macédoine Occidentale.With a Map, Annales Geologiques des Pays Helleniques, 7, 1-358.

Brunn, J. H., Argyriadis, I., Ricou, L. E., Poisson, A., Marcoux, J., & De Graciansky, P. C. (1976). Eléments majeurs de liaison entre Taurides et Hellénides. Bulletin de la Société géologique de France, 7(2), 481-497.

Brunn, J. H., de Graciansky, P. C., Gutnic, M., Juteau, T., Lefevre, R., Marcoux, J., ... & Poisson, A. (1970). Structures majeures et corrélations stratigraphiques dans les Taurides occidentales. Bulletin de la Societe geologique de France, 7(3), 515-556.

Candan, O., Dora, O., Oberhänsli, R., Oelsner, F., & Dürr, S. T. (1997). Blueschist relics in the Mesozoic cover series of the Menderes Massif and correlations with Samos Island, Cyclades.

Candan, O., Dora, O., Oberhänsli, R., Çetinkaplan, M., Partzsch, J., Warkus, F., & Dürr, S. (2001). Pan-African high-pressure metamorphism in the Precambrian basement of the Menderes Massif, western Anatolia, Turkey. International Journal of Earth Sciences, 89(4), 793-811.

Candan, O., Cetinkaplan, M., Oberhansli, R., & Rimmele, G. (2002). Fe–Mg carpholite-pyrophyllite-chloritoid bearing Triassic metapelites from Afyon Zone Turkey: first evidence for Alpine Low-Grade high-P/low-T metamorphism. In Ist international symposium of Istanbul Technical University the faculty of mines on Earth sciences and engineering.

Candan, O., Çetinkaplan, M., Oberhänsli, R., Rimmelé, G., & Akal, C. (2005). Alpine high-P/low-T metamorphism of the Afyon Zone and implications for the metamorphic evolution of Western Anatolia, Turkey. Lithos, 84(1), 102-124.

Candan, O., Koralay, O. E., Akal, C., Kaya, O., Oberhänsli, R., Dora, O. Ö., ... & Chen, F. (2011). Supra-Pan-African unconformity between core and cover series of the Menderes Massif/Turkey and its geological implications. Precambrian Research, 184(1), 1-23.

Candan, O., Koralay, O. E., Topuz, G., Oberhänsli, R., Fritz, H., Collins, A. S., & Chen, F. (2016). Late Neoproterozoic gabbro emplacement followed by early Cambrian eclogite-facies metamorphism in the Menderes Massif (W. Turkey): Implications on the final assembly of Gondwana. Gondwana Research, 34, 158-173.

Catlos, E. J., & Çemen, I. (2005). Monazite ages and the evolution of the Menderes Massif, western Turkey. International Journal of Earth Sciences, 94(2), 204-217.

Celet, P., & Ferriere, J. (1978). Les Hellénides internes: le Pélagonien. Eclogae Geol Helv, 71(3), 467-495.

Cenki-Tok, B., Expert, M., Işık, V., Candan, O., Monié, P., & Bruguier, O. (2016). Complete Alpine reworking of the northern Menderes Massif, western Turkey. International Journal of Earth Sciences, 105(5), 1507-1524.

Çetinkaplan, M. (2002). Tertiary high pressure/low temperature metamorphism in the Mesozoic cover series of the Menderes Massif and correlation with the Cycladic Crystalline Complex. Unpublished PhD thesis, Universitesi Izmir.

Chatzaras, V., Xypolias, P., & Doutsos, T. (2006). Exhumation of high-pressure rocks under continuous compression: a working hypothesis for the southern Hellenides (central Crete, Greece). Geological Magazine, 143(6), 859-876.

Chatzaras, V., Xypolias, P., Kokkalas, S., & Koukouvelas, I. (2011). Oligocene–Miocene thrusting in central Aegean: insights from the Cycladic island of Amorgos. Geological Journal, 46(6), 619-636.

Chen, G. (1995). Evolution of the high-and medium-pressure metamorphic rocks on the island of Samos, Greece (Doctoral dissertation).

Chen, G., Okrusch, M., & Sauerschell, W. (1995). Polymetamorphic evolution of high-pressure rocks on Samos, Greece. In: Piskin, O., Ergun, M., Savascin, M.Y., Tarcan, G. (Eds.), International Earth Sciences Colloquium on the Aegean Region, Proceedings, Izmir, Turkey, pp. 359–365.

Collins, A. S., & Robertson, A. H. (2003). Kinematic evidence for Late Mesozoic–Miocene emplacement of the Lycian Allochthon over the western Anatolide belt, SW Turkey. Geological Journal, 38(3-4), 295-310.

Creutzburg, N. (1977). General Geological Map of Greece: Crete Island, 1: 200 000. Institute of Geology and Mining Research.

De Boorder, H., Spakman, W., White, S. H., & Wortel, M. J. R. (1998). Late Cenozoic mineralization, orogenic collapse and slab detachment in the European Alpine Belt. Earth and Planetary Science Letters, 164(3), 569-575.

Delph, J. R., Biryol, C. B., Beck, S. L., Zandt, G., & Ward, K. M. (2015). Shear wave velocity structure of the Anatolian Plate: anomalously slow crust in southwestern Turkey. Geophysical Journal International, 202(1), 261-276.

Delvaux, D., & Sperner, B. (2003). New aspects of tectonic stress inversion with reference to the TENSOR program. Geological Society, London, Special Publications, 212(1), 75-100.

Desio, A. (1931). Le isole italiane dell'Egeo (studi geologici egeografico-fisici). – Mem descritt. Carta geol. Italia 24: 1–347.

Dewey, J. F., Shackleton, R. M., Chengfa, C., & Yiyin, S. (1988). The tectonic evolution of the Tibetan Plateau. Philosophical Transactions of the Royal Society of London A: Mathematical, Physical and Engineering Sciences, 327(1594), 379-413.

Dilek, Y., & Altunkaynak, Ş. (2009). Geochemical and temporal evolution of Cenozoic magmatism in western Turkey: mantle response to collision, slab break-off, and lithospheric tearing in an orogenic belt. Geological Society, London, Special Publications, 311(1), 213-233.

Dora, O. Ö., Candan, O., Kaya, O., Koralay, E., & Dürr, S. (2001). Revision of" Leptite-gneisses" in the Menderes Massif: a supracrustal metasedimentary origin. International Journal of Earth Sciences, 89(4), 836-851.

Dragovic, B., Samanta, L. M., Baxter, E. F., & Selverstone, J. (2012). Using garnet to constrain the duration and rate of water-releasing metamorphic reactions during subduction: an example from Sifnos, Greece. Chemical Geology, 314, 9-22.

Dragovic, B., Baxter, E. F., & Caddick, M. J. (2015). Pulsed dehydration and garnet growth during subduction revealed by zoned garnet geochronology and thermodynamic modeling, Sifnos, Greece. Earth and Planetary Science Letters, 413, 111-122.

Dubois, R., Bignot, G. (1979). Présence d'un ''hardground'' nummulitique au sommet de la série crétacée d'Almyropotamos (Eubée méridionale, Grèce). C R Acad Sci Paris 289:993–995

Duchêne, S., Aïssa, R., Vanderhaeghe, O. (2006). Pressure-temperaturetime evolution of metamorphic rocks from Naxos (Cyclades, Greece): constraints from thermobarometry and Rb/Sr dating. Geodin Acta 19:299–319. doi:10.3166/ga.19.301-321

Dürr, S. H. (1975). Über alter und geotektonische Stellung des Menderes-Kristallins, SW-Anatolien und seine Aequivalente in der mittleren Aegaeis. na.

Dürr, S., Altherr, R., Keller, J., Okrusch, M., & Seidel, E. (1978). The median Aegean crystalline belt: stratigraphy, structure, metamorphism, magmatism. Alps, Apennines, Hellenides, 38, 455-476.

Endrun, B., Lebedev, S., Meier, T., Tirel, C., & Friederich, W. (2011). Complex layered deformation within the Aegean crust and mantle revealed by seismic anisotropy. Nature Geoscience, 4(3), 203.

Erdoğan, B., & Güngör, T. (2004). The problem of the core-cover boundary of the Menderes Massif and an emplacement mechanism for regionally extensive gneissic granites, western Anatolia (Turkey). Turkish Journal of Earth Sciences, 13(1), 15-36.

Ersoy, E. Y., & Palmer, M. R. (2013). Eocene-Quaternary magmatic activity in the Aegean: implications for mantle metasomatism and magma genesis in an evolving orogeny. Lithos, 180, 5-24.

Faccenna, C., Jolivet, L., Piromallo, C., & Morelli, A. (2003). Subduction and the depth of convection in the Mediterranean mantle. Journal of Geophysical Research: Solid Earth, 108(B2).

Faccenna, C., Bellier, O., Martinod, J., Piromallo, C., & Regard, V. (2006). Slab detachment beneath eastern Anatolia: A possible cause for the formation of the North Anatolian fault. Earth and Planetary Science Letters, 242(1), 85-97.

Feenstra, A. (1985). Metamorphism of bauxites on Naxos, Greece (Doctoral dissertation, Instituut voor Aardwetenschappen RUU).

Flerit, F., Armijo, R., King, G., & Meyer, B. (2004). The mechanical interaction between the propagating North Anatolian Fault and the back-arc extension in the Aegean. Earth and Planetary Science Letters, 224(3), 347-362.

Franz, L., & Okrusch, M. (1992). Aragonite-bearing blueschists on Arki island, Dodecanese, Greece. European journal of mineralogy, 4(3), 527-537.

Franz, L., Okrusch, M., Seidel, E., & Kreuzer, H. (2005). Polymetamorphic evolution of pre-Alpidic basement relics in the external Hellenides, Greece. Neues Jahrbuch für Mineralogie-Abhandlungen: Journal of Mineralogy and Geochemistry, 181(2), 147-172.

Gautier, P., & Brun, J. P. (1994). Crustal-scale geometry and kinematics of late-orogenic extension in the central Aegean (Cyclades and Ewia Island). Tectonophysics, 238(1-4), 399-424.

Gessner, K., Ring, U., Lackmann, W., Passchier, C. W., & Gungor, T. (1998). Structure and crystal thickening of the Menderes massif, southwest Turkey, and consequences for large-scale correlations between Greece and Turkey. Δελτίον της Ελληνικής Γεωλογικής Εταιρίας, 32(1), 145-152.

Gessner, K., Ring, U., Johnson, C., Hetzel, R., Passchier, C. W., & Güngör, T. (2001a). An active bivergent rolling-hinge detachment system: Central Menderes metamorphic core complex in western Turkey. Geology, 29(7), 611-614.

Gessner, K., Gallardo, L. A., & Markwitz, V. (2011). West Anatolian Transfer Zone: 3D Model of Southwest Turkey Reveals Role of Slab Edge in Continental Extension. In AGU Fall Meeting Abstracts.

Gessner, K., Piazolo, S., Güngör, T., Ring, U., Kröner, A., & Passchier, C. W. (2001b). Tectonic significance of deformation patterns in granitoid rocks of the Menderes nappes, Anatolide belt, southwest Turkey. International Journal of Earth Sciences, 89(4), 766-780.

Gessner, K., Gallardo, L. A., Markwitz, V., Ring, U., & Thomson, S. N. (2013). What caused the denudation of the Menderes Massif: Review of crustal evolution, lithosphere structure, and dynamic topography in southwest Turkey. Gondwana Research, 24(1), 243-274.

Gessner, K., Markwitz, V., & Güngör, T. (2017). Crustal fluid flow in hot continental extension: tectonic framework of geothermal areas and mineral deposits in western Anatolia. Geological Society, London, Special Publications, 453, SP453-7.

Godriaux, Y. (1962). L'Olympe, une fenêtre tectonique dans les Hellénides internes, CR Acad. Sc. Paris, 255, 1761-1763.

Godfriaux, Y. (1965). Etude géologique de la région de l'Olympe. thèse d'Etat thesis, Université de Lille, 280 pp.

Godfriaux Y, Pichon JF (1980) Sur l'importance des événements tectoniques et métamorphiques d'âge tertiaire en Thessalie septentrionale (L'Olympe, Ossa et Flamburon). Annales géol Soc Nord 99:367–376.

Godfriaux, I., & Ricou, L. E. (1991). Direction et sens de transport associes au cherriage synmetamorphe sur l'Olympe= Διεύθυνση και έννοια κίνησης της συμμεταμορφικής επώθησης πάνω στον Όλυμπο. Δελτίον της Ελληνικής Γεωλογικής Εταιρίας, 25(1), 207-229.

Göncüoğlu, M. C., Dirik, K., & Kozlu, H. (1997). General characteristics of pre-Alpine and Alpine Terranes in Turkey: Explanatory notes to the terrane map of Turkey. In Annales Geologique de Pays Hellenique (Vol. 37, pp. 515-536).

Govers, R., & Wortel, M. J. R. (2005). Lithosphere tearing at STEP faults: response to edges of subduction zones. Earth and Planetary Science Letters, 236(1), 505-523.

Govers, R., & Fichtner, A. (2016). Signature of slab fragmentation beneath Anatolia from full-waveform tomography. Earth and Planetary Science Letters, 450, 10-19.

Grasemann, B., Schneider, D. A., Stöckli, D. F., & Iglseder, C., 2012, Miocene bivergent crustal extension in the Aegean: Evidence from the western Cyclades (Greece): Lithosphere, v. 4, no. 1, p. 23-39.

Grasemann, B., Huet, B., Schneider, D., Rice, H., Lemonnier, N., & Tschegg, C. (2018). Evidence for large-scale imbrication during Eocene syn-orogenic exhumation of the Hellenic subduction channel (Cyclades, Greece). In EGU General Assembly Conference Abstracts (Vol. 19, p. 2937).

Greiling, R. (1982). The metamorphic and structural evolution of the Phyllite-Quartzite nappe of western Crete. Journal of Structural Geology, 4(3), 291-297.

Groppo, C., Forster, M., Lister, G., & Compagnoni, R. (2009). Glaucophane schists and associated rocks from Sifnos (Cyclades, Greece): New constraints on the P–T evolution from oxidized systems. Lithos, 109(3), 254-273.

Hall, R., Audley-Charles, M. G., & Carter, D. J. (1984). The significance of Crete for the evolution of the Eastern Mediterranean. Geological Society, London, Special Publications, 17(1), 499-516. Jansen, J.B.H., Geological map of Naxos (1/50 000), Nation. Inst. Geol. Mining Res., Athens, 1973.

Hayward, A. B. (1984). Miocene clastic sedimentation related to the emplacement of the Lycian Nappes and the Antalya Complex, SW Turkey. Geological Society, London, Special Publications, 17(1), 287-300.

Henjes-Kunst, F., & Kreuzer, H. (1982). Isotopic dating of pre-alpidic rocks from the island of Ios (Cyclades, Greece). Contributions to Mineralogy and Petrology, 80(3), 245-253.

Hetzel, R., & Reischmann, T. (1996). Intrusion age of Pan-African augen gneisses in the southern Menderes Massif and the age of cooling after Alpine ductile extensional deformation. Geological Magazine, 133(5), 565-572.

Hetzel, R., Passchier, C. W., Ring, U., & Dora, Ö. O. (1995a). Bivergent extension in orogenic belts: the Menderes massif (southwestern Turkey). Geology, 23(5), 455-458.

Hetzel, R., Ring, U., Akal, C., & Troesch, M. (1995b). Miocene NNE-directed extensional unroofing in the Menderes Massif, southwestern Turkey. Journal of the Geological Society, 152(4), 639-654.

Huet, B., Labrousse, L., & Jolivet, L. (2009). Thrust or detachment? Exhumation processes in the Aegean: Insight from a field study on Ios (Cyclades, Greece). Tectonics, 28(3).

Işik, V., & Tekeli, O. (2001). Late orogenic crustal extension in the northern Menderes massif (western Turkey): evidence for metamorphic core complex formation." International Journal of Earth Sciences 89.4 (2001): 757-765.

Jacobshagen, V., Dürr, S., Kockel, F., Kopp, K. O., Kowalczyk, G., Berckhemer, H., & Büttner, D. (1978). Structure and geodynamic evolution of the Aegean region. Alps, Apennines, Hellenides, 537-564.

Jansen, J. B. H. (1977). Metamorphism on Naxos, Greece (Doctoral dissertation, Utrecht).

Jolivet, L. (2001). A comparison of geodetic and finite strain pattern in the Aegean, geodynamic implications. Earth and Planetary Science Letters, 187(1), 95-104.

Jolivet, L., & Faccenna, C. (2000). Mediterranean extension and the Africa-Eurasia collision. Tectonics, 19(6), 1095-1106.

Jolivet, L., & Brun, J. P. (2010). Cenozoic geodynamic evolution of the Aegean. International Journal of Earth Sciences, 99(1), 109-138.

Jolivet, L., Goffé, B., Monié, P., Truffert-Luxey, C., Patriat, M., & Bonneau, M. (1996). Miocene detachment in Crete and exhumation P-T-t paths of high-pressure metamorphic rocks. Tectonics, 15(6), 1129-1153.

Jolivet, L., Faccenna, C., Goffé, B., Burov, E., & Agard, P. (2003). Subduction tectonics and exhumation of high-pressure metamorphic rocks in the Mediterranean orogens. American Journal of Science, 303(5), 353-409.

Jolivet, L., Famin, V., Mehl, C., Parra, T., Aubourg, C., Hébert, R., & Philippot, P. (2004a). Progressive strain localisation, boudinage and extensional metamorphic complexes, the Aegean Sea Case, in Whitney DL, Teyssier C. and Siddoway CS, Gneiss domes in orogeny: Boulder, Colorado. Geological Society of America Special Paper, 380, 185-210.

Jolivet, L., Rimmelé, G., Oberhänsli, R., Goffé, B., & Candan, O. (2004b). Correlation of syn-orogenic tectonic and metamorphic events in the Cyclades, the Lycian nappes and the Menderes massif. Geodynamic implications. Bulletin de la Société Géologique de France, 175(3), 217-238.

Jolivet, L., Faccenna, C., & Piromallo, C. (2009). From mantle to crust: Stretching the Mediterranean. Earth and Planetary Science Letters, 285(1-2), 198-209.

Jolivet, L., Lecomte, E., Huet, B., Denèle, Y., Lacombe, O., Labrousse, L., ... & Mehl, C. (2010). The north cycladic detachment system. Earth and Planetary Science Letters, 289(1), 87-104.

Jolivet, L., Faccenna, C., Huet, B., Labrousse, L., Le Pourhiet, L., Lacombe, O., ... & Philippon, M. (2013). Aegean tectonics: Strain localisation, slab tearing and trench retreat. Tectonophysics, 597, 1-33.

Jolivet, L., Faccenna, C., Agard, P., Frizon de Lamotte, D., Menant, A., Sternai, P., & Guillocheau, F. (2015a). Neo-Tethys geodynamics and mantle convection: from extension to compression in Africa and a conceptual model for obduction. Canadian journal of earth sciences, 53(11), 1190-1204.

Jolivet, L., Menant, A., Sternai, P., Rabillard, A., Arbaret, L., Augier, R., ... & Labrousse, L. (2015b). The geological signature of a slab tear below the Aegean. Tectonophysics, 659, 166-182.

Karabulut, H., Paul, A., Afacan Ergün, T., Hatzfeld, D., Childs, D. M., & Aktar, M. (2013). Long-wavelength undulations of the seismic Moho beneath the strongly stretched Western Anatolia. Geophysical Journal International, 194(1), 450-464.

Katagas, C. G. (1980). Metamorphic zones and physical conditions of metamorphism in Leros Island, Greece. Contributions to Mineralogy and Petrology, 73(4), 389-402.

Katagas, C., & Sapountzis, E. (1977). Petrochemistry of low and medium grade mafic metamorphic rocks from Leros island, Greece. Mineralogy and Petrology, 24(1), 39-55.

Katzir, Y., Matthews, A., Garfunkel, Z., Schliestedt, M., & Avigad, D. (1996). The tectono-metamorphic evolution of a dismembered ophiolite (Tinos, Cyclades, Greece). Geological Magazine, 133(3), 237-254.

Kaymakci, N., Özçelik, Y., White, S. H., & Van Dijk, P. M. (2009). Tectono-stratigraphy of the Çankırı Basin: late Cretaceous to early Miocene evolution of the Neotethyan suture zone in Turkey. Geological Society, London, Special Publications, 311(1), 67-106.

Keiter, M., Piepjohn, K., Ballhaus, C., Lagos, M., & Bode, M. (2004). Structural development of high-pressure metamorphic rocks on Syros island (Cyclades, Greece). Journal of Structural Geology, 26(8), 1433-1445.

Koralay, O. E., Candan, O., Chen, F., Akal, C., Oberhänsli, R., Satır, M., & Dora, O. Ö. (2012). Pan-African magmatism in the Menderes Massif: geochronological data from leucocratic tourmaline orthogneisses in western Turkey. International Journal of Earth Sciences, 101(8), 2055-2081.

Koukouvelas, I. K., & Aydin, A. (2002). Fault structure and related basins of the North Aegean Sea and its surroundings. Tectonics, 21(5).

Krahl, J., Kauffmann, G., Kozur, H., Richter, D., Förster, O., & Heinritzi, F. (1983). Neue Daten zur biostratigraphie und zur tektonischen lagerung der Phyllit-Gruppe und der Trypali-Gruppe auf der Insel Kreta (Griechenland). Geologische Rundschau, 72(3), 1147-1166.

Kumerics, C., Ring, U., Brichau, S., Glodny, J., & Monié, P. (2005). The extensional Messaria shear zone and associated brittle detachment faults, Aegean Sea, Greece. Journal of the Geological Society, 162(4), 701-721.

Lallemant, S., Truffert, C., Jolivet, L., Henry, P., Chamot-Rooke, N., & De Voogd, B. (1994). Spatial transition from compression to extension in the Western Mediterranean Ridge accretionary complex. Tectonophysics, 234(1-2), 33-52.

Laurent, V., Jolivet, L., Roche, V., Augier, R., Scaillet, S., & Cardello, G. L. (2016). Strain localization in a fossilized subduction channel: Insights from the Cycladic Blueschist Unit (Syros, Greece). Tectonophysics, 672, 150-169.

Laurent, V., Huet, B., Labrousse, L., Jolivet, L., Monie, P., & Augier, R. (2017). Extraneous argon in high-pressure metamorphic rocks: Distribution, origin and transport in the Cycladic Blueschist Unit (Greece). Lithos, 272, 315-335.

Laurent, V., Lanari, P., Naïr, I., Augier, R., Lahfid, A., & Jolivet, L. (2018). Exhumation of eclogites and blueschists (Cyclades, Greece): P-T evolution constrained by thermobarometry and thermodynamic modelling. Journal of Metamorphic Geology.

Le Pichon, X., & Angelier, J. (1979). The Hellenic arc and trench system: a key to the neotectonic evolution of the eastern Mediterranean area. Tectonophysics, 60(1), 1-42.

Le Pichon, X., Angelier, J. (1981a). The Aegean Sea. Philos Trans R Soc Lond 300:357–372. doi:10.1098/rsta.1981.0069.

Le Pichon, X., & Angelier, J. (1981b). The Hellenic arc and trench system: a key to the neotectonic evolution of the eastern Mediterranean sea. Philos Trans R Soc Lond 300:357–372. doi:10.1098/rsta. 1981.0069.

Le Pichon, X., Angelier, J., Osmaston, M. F., & Stegena, L. (1981). The Aegean Sea. Philosophical Transactions of the Royal Society of London A: Mathematical, Physical and Engineering Sciences, 300(1454), 357-372.

Le Pichon, X., Chamot-Rooke, N., Lallemant, S., Noomen, R., & Veis, G. (1995). Geodetic determination of the kinematics of central Greece with respect to Europe: Implications for eastern Mediterranean tectonics. Journal of Geophysical Research: Solid Earth, 100(B7), 12675-12690.

Li, C., Van der Hilst, R. D., Meltzer, A. S., & Engdahl, E. R. (2008). Subduction of the Indian lithosphere beneath the Tibetan Plateau and Burma. Earth and Planetary Science Letters, 274(1), 157-168.

Lips, A. L., Cassard, D., Sözbilir, H., Yilmaz, H., & Wijbrans, J. R. (2001). Multistage exhumation of the Menderes massif, western Anatolia (Turkey). International Journal of Earth Sciences, 89(4), 781-792.

Lister, G. S., Banga, G., & Feenstra, A. (1984). Metamorphic core complexes of Cordilleran type in the Cyclades, Aegean Sea, Greece. Geology, 12(4), 221-225.

Makris, J. (1978). The crust and upper mantle of the Aegean region from deep seismic soundings. Tectonophysics, 46(3-4), 269-284.

McClusky, S., Balassanian, S., Barka, A., Demir, C., Ergintav, S., Georgiev, I., ... & Kastens, K. (2000). Global Positioning System constraints on plate kinematics and dynamics in the eastern Mediterranean and Caucasus. Journal of Geophysical Research: Solid Earth, 105(B3), 5695-5719.

McKenzie, D. (1972). Active tectonics of the Mediterranean region. Geophysical Journal International, 30(2), 109-185.

Menant, A., Jolivet, L., Augier, R., & Skarpelis, N. (2013). The North Cycladic Detachment System and associated mineralization, Mykonos, Greece: Insights on the evolution of the Aegean domain. Tectonics, 32(3), 433-452.

Menant, A., Jolivet, L., & Vrielynck, B. (2016a). Kinematic reconstructions and magmatic evolution illuminating crustal and mantle dynamics of the eastern Mediterranean region since the late Cretaceous. Tectonophysics, 675, 103-140.

Menant, A., Sternai, P., Jolivet, L., Guillou-Frottier, L., & Gerya, T. (2016b). 3D numerical modeling of mantle flow, crustal dynamics and magma genesis associated with slab roll-back and tearing: The eastern Mediterranean case. Earth and Planetary Science Letters, 442, 93-107.

Menant, A., Jolivet, L., Tuduri, J., Loiselet, C., Bertrand, G., & Guillou-Frottier, L. (2018). 3D subduction dynamics: A first-order parameter of the transition from copper-to gold-rich deposits in the eastern Mediterranean region. Ore Geology Reviews, 94, 118-135.

Mercier, J. L., Sorel, D., Vergely, P., & Simeakis, K. (1989). Extensional tectonic regimes in the Aegean basins during the Cenozoic. Basin research, 2(1), 49-71.

Mezger, K., & Okrusch, M. (1985). Metamorphism of the variegated sequence at Kallithea, Samos, Greece. Mineralogy and Petrology, 34(1), 67-82.

Minoux, L., Bonneau, M., & Kienast, J. R. (1980). L'île d'Amorgos, une fenêtre des zones externes au coeur de l'Egée (Grèce), métamorphisée dans le faciès schistes bleus. Comptes Rendu de l'Academie des Sciences de Paris, 291, 745-8.

Morris, A., & Anderson, M. (1996). First palaeomagnetic results from the Cycladic Massif, Greece, and their implications for Miocene extension directions and tectonic models in the Aegean, Earth Planet. Sci. Lett.

142, 397–408, doi:10.1016/0012-821X(96)00114-8.

Mposkos, E. (1978). Diasporit-und Smirgelvorkommen der Insel Samos (Griechenland). In Fourth International Congress for the Study of Bauxites (Vol. 2, pp. 614-631).

Mposkos, E., & Perdikatsis, V. (1984). Petrology of glaucophane metagabbros and related rocks from Samos, Aegean-island (Greece).

Oberhanslı, R., Candan, O., Dora, O., & Durr, S. (1997). Eclogites within the Menderes Crystalline Complex, Western Turkey, Anatolia. Lithos, 41, 135-150.

Oberhänsli, R., Goffe, B., Jolivet, L., & Vidal, O. (1998). High-pressure–low-temperature metamorphism and deformation in the Bündnerschiefer of the Engadine window: implications for the regional evolution of the eastern Central Alps. Journal of Metamorphic Geology, 16(5), 657-674.

Oberhänsli, R., Partzsch, J., Candan, O., & Cetinkaplan, M. (2001). First occurrence of Fe-Mg-carpholite documenting a high-pressure metamorphism in metasediments of the Lycian Nappes, SW Turkey. International Journal of Earth Sciences, 89(4), 867-873.

Oberhänsli, R., Candan, O., Bousquet, R., Rimmele, G., Okay, A., & Goff, J. (2010). Alpine high pressure evolution of the eastern Bitlis complex, SE Turkey. Geological Society, London, Special Publications, 340(1), 461-483.

Oberhizansli, R., Monie, P., Candan, O., & Warkus, F. C. (1998). The age of blueschist metamorphism in the Mesozoic cover series of the Menderes Massif.

Okay, A. I. (1986). High-pressure/low-temperature metamorphic rocks of Turkey. In Blueschists and eclogites (Vol. 164, pp. 333-348). Geological Society of America Memoir 164.

Okay, A.I. (1989). Geology of the Menderes Massif and the Lycian Nappes South of Denizli, Western Taurides. Mineral Res Expl Bull 109:37–51

Okay, A. I., & Kelley, S. P. (1994). Tectonic setting, petrology and geochronology of jadeite+ glaucophane and chloritoid+ glaucophane schists from north-west Turkey. Journal of Metamorphic Geology, 12(4), 455-466.

Okay, A. I., & Tüysüz, O. (1999). Tethyan sutures of northern Turkey. Geological Society, London, Special Publications, 156(1), 475-515.

Okay, A. I., Satir, M., Maluski, H., Siyako, M., Monie, P., Metzger, R., & Akyüz, S. (1996). Paleo-and Neo-Tethyan events in northwestern Turkey: geologic and geochronologic constraints. World and Regional Geology, 1(8), 420-441.

Okrusch, M., Richter, P., & Katsikatsos, G. (1984). High-pressure rocks of Samos, Greece. Geological Society, London, Special Publications, 17(1), 529-536.

Papanikolaou, D. (1977a). On the structural geology and tectonics of Paros Island (Aegean Sea). In Annales géologiques des Pays helléniques (Vol. 28, pp. 450-463).

Papanikolaou, D. (1977b). Contribution to the geology of Ikaria island, Aegean Sea.ANNALES Geologiques des Pays Helleniques, 29/1, 1-28.

Papanikolaou, D. (1978). Contribution to the geology of Aegean Sea: the island of Andros. Annales geologiques des Pays Helleniques, 29/2, 477-553.

Papanikolaou, D. (1979). Unites tectoniques et phases de deformation dans l'ile de Samos, Mer Egee, Grece. Bulletin de la Société géologique de France, 7(6), 745-752.

Papanikolaou, D. (1980). Thrust sheets of the island of Thymaena-indication of northward displacements in the aegean during miocene. Comptes endus hebdomadaires des seances de l academie des sciences serie d, 290(4), 307-310.

Papanikolaou, D. J. (1987). Tectonic evolution of the Cycladic blueschist belt (Aegean Sea, Greece). In Chemical transport in metasomatic processes (pp. 429-450). Springer Netherlands.

Papanikolaou, D. (1989). Are the medial crystalline massifsof the eastern Mediterranean drifted Godwanian fragments? Special Publications Geological Society of Greece, 1, 63-90.

Papanikolaou, D. (1997). The tectonostratigraphic terranes of the Hellenides. Annales Geologiques des Pays Helleniques, 37, 495-514.

Papanikolaou, D. (2009). Timing of tectonic emplacement of the ophiolites and terrane paleogeography in the Hellenides. Lithos, 108, 262-280.

Papanikolaou, D. (2013). Tectonostratigraphic models of the alpine terranes and subduction history of the Hellenides. Tectonophysics, 595-596, 1-24.

Papanikolaou, D. & Demirtasli, E. (1987). Geological correlations between the alpine segments of the Hellenides-Balkanides and Taurides-Pontides.In: Flugel H.W., Sassi, F.P. & Grecula, P. editors, Pre-Variscan and Variscan events in the alpine Mediterranean mountain belts, Mineralia Slovaca, Monography, Bratislava, 387-396.

Papanikolaou, D. & Vassilakis, E. (2010). Thrust faults and extensional detachment faults in Cretan tectono-stratigraphy: implications for Middle Miocene extension. Tectonophysics, 488, 233-247.

Parra, T., Vidal, O., & Jolivet, L. (2002). Relation between the intensity of deformation and retrogression in blueschist metapelites of Tinos Island (Greece) evidenced by chlorite–mica local equilibria. Lithos, 63(1), 41-66.

Patzak, M., Okrusch, M., & Kreuzer, H. (1994). The Akrotiri Unit on the island of Tinos, Cyclades, Greece: Witness to a lost terrane of Late Cretaceous age.(With 18 figures and 8 tables in the text). Neues Jahrbuch fur Geologie und Palaontologie-Abhandlungen, 194(2), 211-252.

Perouse, E., Chamot-Rooke, N., Rabaute, A., Briole, P., Jouanne, F., Georgiev, I., & Dimitrov, D. (2012). Bridging onshore and offshore present-day kinematics of central and eastern Mediterranean: implications for crustal dynamics and mantle flow. Geochemistry, Geophysics, Geosystems, 13(9).

Philippon, M., Brun, J. P., & Gueydan, F. (2011). Tectonics of the Syros blueschists (Cyclades, Greece): From subduction to Aegean extension. Tectonics, 30(4).

Piromallo, C., & Morelli, A. (2003). P wave tomography of the mantle under the Alpine-Mediterranean area. Journal of Geophysical Research: Solid Earth, 108(B2).

Pourteau, A., Candan, O., & Oberhänsli, R. (2010). High-pressure metasediments in central Turkey: Constraints on the Neotethyan closure history. Tectonics, 29(5).

Pourteau, A., Sudo, M., Candan, O., Lanari, P., Vidal, O., & Oberhänsli, R. (2013). Neotethys closure history of Anatolia: insights from 40Ar–39Ar geochronology and P–T estimation in high-pressure metasedimentary rocks. Journal of Metamorphic Geology, 31(6), 585-606.

Pourteau, A., Bousquet, R., Vidal, O., Plunder, A., Duesterhoeft, E., Candan, O., & Oberhänsli, R. (2014). Multistage growth of Fe–Mg–carpholite and Fe–Mg–chloritoid, from field evidence to thermodynamic modelling. Contributions to Mineralogy and Petrology, 168(6), 1090.

Pourteau, A., Oberhänsli, R., Candan, O., Barrier, E., & Vrielynck, B. (2016). Neotethyan closure history of western Anatolia: a geodynamic discussion. International Journal of Earth Sciences, 105(1), 203-224.

Régnier, J. L., Ring, U., Passchier, C. W., Gessner, K., & Güngör, T. (2003). Contrasting metamorphic evolution of metasedimentary rocks from the Cine and Selimiye nappes in the Anatolide belt, western Turkey. Journal of Metamorphic Geology, 21(7), 699-721.

Régnier, J. L., Mezger, J. E., & Passchier, C. W. (2007). Metamorphism of Precambrian–Palaeozoic schists of the Menderes core series and contact relationships with Proterozoic orthogneisses of the western Çine Massif, Anatolide belt, western Turkey. Geological Magazine, 144(1), 67-104.

Reilinger, R., McClusky, S., Vernant, P., Lawrence, S., Ergintav, S., Cakmak, R., ... & Nadariya, M. (2006). GPS constraints on continental deformation in the Africa-Arabia-Eurasia continental collision zone and implications for the dynamics of plate interactions. Journal of Geophysical Research: Solid Earth, 111(B5).

Reilinger, R., McClusky, S., Paradissis, D., Ergintav, S., & Vernant, P. (2010). Geodetic constraints on the tectonic evolution of the Aegean region and strain accumulation along the Hellenic subduction zone. Tectonophysics, 488(1), 22-30.

Reinecke, T., Altherr, R., Hartung, B., Hatzipanagiotou, K., Kreuzer, H., Harre, W., ... & Böger, H. (1982). Remnants of a Late Cretaceous high temperature belt on the island of Anafi (Cyclades, Greece). N. Jb. Miner. Abh, 145(2), 157-182.

Ricou, L. E., Burg, J. P., Godfriaux, I., & Ivanov, Z. (1998). Rhodope and Vardar: the metamorphic and the olistostromic paired belts related to the Cretaceous subduction under Europe. Geodinamica Acta, 11(6), 285-309.

Rigo, A., Lyon-Caen, H., Armijo, R., Deschamps, A., Hatzfeld, D., Makropoulos, K., ... & Kassaras, I. (1996). A microseismic study in the western part of the Gulf of Corinth (Greece): Implications for large-scale normal faulting mechanisms. Geophysical Journal International, 126(3), 663-688.

Rimmelé, G., Jolivet, L., Oberhänsli, R., & Goffé, B. (2003a). Deformation history of the high-pressure Lycian Nappes and implications for tectonic evolution of SW Turkey. Tectonics, 22(2).

Rimmelé, G., Oberhänsli, R., Goffé, B., Jolivet, L., Candan, O., & Çetinkaplan, M. (2003b). First evidence of high-pressure metamorphism in the "Cover Series" of the southern Menderes Massif. Tectonic and metamorphic implications for the evolution of SW Turkey. Lithos, 71(1), 19-46.

Rimmele, G., Parra, T., Goffe, B., Oberhaensli, R., Jolivet, L., & Candan, O. (2005). Exhumation paths of high-pressure–low-temperature metamorphic rocks from the Lycian Nappes and the Menderes Massif (SW Turkey): a multi-equilibrium approach. Journal of Petrology, 46(3), 641-669.

Rimmelé, G., Oberhänsli, R., Candan, O., Goffé, B., & Jolivet, L. (2006). The wide distribution of HP-LT rocks in the Lycian Belt (Western Turkey): implications for accretionary wedge geometry. Geological Society, London, Special Publications, 260(1), 447-466.

Ring, U., & Reischmann, T. (2002). The weak and superfast Cretan detachment, Greece: exhumation at subduction rates in extruding wedges. Journal of the Geological Society, 159(3), 225-228.

Ring, U., & Layer, P. W. (2003). High-pressure metamorphism in the Aegean, eastern Mediterranean: Underplating and exhumation from the Late Cretaceous until the Miocene to Recent above the retreating Hellenic subduction zone. Tectonics, 22(3).

Ring, U., Gessner, K., Güngör, T., & Passchier, C. W. (1999a). The Menderes Massif of western Turkey and the Cycladic Massif in the Aegean—do they really correlate?. Journal of the Geological Society, 156(1), 3-6.

Ring, U., Laws, S., & Bernet, M. (1999b). Structural analysis of a complex nappe sequence and lateorogenic basins from the Aegean island of Samos, Greece, J. Struct. Geol., 21, 1575-1601.

Ring, U., Layer, P. W., & Reischmann, T. (2001). Miocene high-pressure metamorphism in the Cyclades and Crete, Aegean Sea, Greece: Evidence for large-magnitude displacement on the Cretan detachment. Geology, 29(5), 395-398.

Ring, U., Will, T., Glodny, J., Kumerics, C., Gessner, K., Thomson, S., ... & Drüppel, K. (2007). Early exhumation of high-pressure rocks in extrusion wedges: Cycladic blueschist unit in the eastern Aegean, Greece, and Turkey. Tectonics, 26(2).

Ring, U., Thomson, S. N., & Rosenbaum, G. (2009). Timing of the Amorgos detachment system and implications for detachment faulting in the southern Aegean Sea, Greece. Geological Society, London, Special Publications, 321(1), 169-178.

Ring, U., Glodny, J., Will, T., & Thomson, S. (2010). The Hellenic subduction system: high-pressure metamorphism, exhumation, normal faulting, and large-scale extension. Annual Review of Earth and Planetary Sciences, 38, 45-76.

Ring, U., Gessner, K., & Thomson, S. N. (2017). South Menderes Monocline: Low-temperature thermochronology constrains role of crustal extension in structural evolution of southwest Turkey. Tectonophysics, 712, 455-463.

Robertson, A. H. F., Clift, P. D., Degnan, P. J., & Jones, G. (1991). Palaeogeographic and palaeotectonic evolution of the Eastern Mediterranean Neotethys. Palaeogeography, Palaeoclimatology, Palaeoecology, 87(1-4), 289-343.

Robertson, A. H. F., Dixon, J. E., Brown, S., Collins, A., Morris, A., Pickett, E., ... & Ustaömer, T. (1996). Alternative tectonic models for the Late Palaeozoic-Early Tertiary development of Tethys in the Eastern Mediterranean region. Geological Society, London, Special Publications, 105(1), 239-263.

Roche, V., Laurent, V., Cardello, G. L., Jolivet, L., & Scaillet, S. (2016). Anatomy of the Cycladic Blueschist Unit on Sifnos Island (Cyclades, Greece). Journal of Geodynamics, 97, 62-87.

Roche, V., Conand, C., Jolivet, J., & Augier, R. (2018a). Tectonic evolution of Leros Island (Dodecanese, Greece) and correlations between the Aegean Domain and the Menderes Massif. Geological Society, London. 10.1144/jgs2018-028.

Roche, V., Sternai, P., Guillou-Frottier, L., Menant, A., Jolivet, L., Bouchot, V. & Gerya T. (2018b). Emplacement of metamorphic core complexes and associated geothermal systems controlled by slab dynamics. Earth and Planetary Science Letters.

Roche, V., Bouchot, V., Beccaletto, L., Jolivet, L., Guillou-Frottier, L., Bozkurt, E., Oguz, K., Tuduri, J., and B., Tokay. (2018c). Structural, lithological and geodynamic controls on geothermal activity in the Menderes geothermal Province (Western Anatolia, Turkey). IJES.

Roche, V., Jolivet., L., Scaillet, S., Duval, F., Tuduri, J., … & Di Carlo, I. (in prep.). Tectonic and thermal evolution of a Metamorphic Core Complex: the Menderes Massif (Western Turkey).

Rosenbaum, G., Ring, U., & Kühn, A. (2007). Tectono-metamorphic evolution of high-pressure rocks from the island of Amorgos (Central Aegean, Greece). Journal of the Geological Society, 164(2), 425-438.

Royden, L. H. (1993). Evolution of retreating subduction boundaries formed during continental collision. Tectonics, 12(3), 629-638.

Salaün, G., Pedersen, H. A., Paul, A., Farra, V., Karabulut, H., Hatzfeld, D., ... & SIMBAAD Team. (2012). High-resolution surface wave tomography beneath the Aegean-Anatolia region: constraints on upper-mantle structure. Geophysical Journal International, 190(1), 406-420.

Sanchez-Gomez, M., Avigad, D., & Heimann, A. (2002). Geochronology of clasts in allochthonous Miocene sedimentary sequences on Mykonos and Paros Islands: implications for back-arc extension in the Aegean Sea. Journal of the Geological Society, 159(1), 45-60.

Satir, M., & Friedrichsen, H. (1986). The origin and evolution of the Menderes Massif, W-Turkey: a rubidium/strontium and oxygen isotope study. Geologische Rundschau, 75(3), 703-714.

Scheffler, F., Oberhänsli, R., Pourteau, A., Candan, O., & Di Lucia, M. (2014). The Rosetta Marbles from Fesleen, Ören Unit, SW Anatolia. International Journal of Earth Sciences: Geologische Rundschau, 103(2), 485.

Scheffler, F., Oberhänsli, R., Pourteau, A., Immenhauser, A., & Candan, O. (2016). Sedimentologic to metamorphic processes recorded in the high-pressure/low-temperature Mesozoic Rosetta Marble of Anatolia. International Journal of Earth Sciences, 105(1), 225-246.

Schermer, E. R. (1990). Mechanisms of blueschist creation and preservation in an A-type subduction zone, Mount Olympos region, Greece. Geology, 18(11), 1130-1133.

Schermer, E. R. (1993). Geometry and kinematics of continental basement deformation during the Alpine orogeny, Mt. Olympos region, Greece. Journal of Structural Geology, 15(3-5), 571-591.

Schermer, E. R., Lux, D. R., & Burchfiel B. C. (1990). Temperature-time history of subducted continental crust, Mount Olympos region, Greece. Tectonics, 9, (5), 1165-1195.

Schmidt, A., Pourteau, A., Candan, O., & Oberhänsli, R. (2015). Lu–Hf geochronology on cm-sized garnets using microsampling: New constraints on garnet growth rates and duration of metamorphism during continental collision (Menderes Massif, Turkey). Earth and Planetary Science Letters, 432, 24-35.

Schneider, D. A., Senkowski, C., Vogel, H., Grasemann, B., Iglseder, C., & Schmitt, A. K. (2011). Eocene tectonometamorphism on Serifos (western Cyclades) deduced from zircon depth-profiling geochronology and mica thermochronology. Lithos, 125(1), 151-172.

Schuiling, R. D. (1962). On petrology, age and structure of the Menderes migmatite complex (SW-Turkey). Bulletin of the Mineral Research and Exploration Institute of Turkey, 58, 71-84.

Seidel, E. (1978). Zur petrologie der phyllit-quarzit-serie Kretas. na.

Seidel, E., Kreuzer, H., & Harre, W. (1982). A late Oligocene/early Miocene high pressure belt in the external Hellenides. Geologisches Jahrbuch E, 23, 165-206.

Seidel, M., Seidel, E., & Stöckhert, B. (2007). Tectono-sedimentary evolution of lower to middle Miocene half-graben basins related to an extensional detachment fault (western Crete, Greece). Terra Nova, 19(1), 39-47.

Şengör, A.M.C. (1984). The Cimmeride orogenic concept and the rectonics of Eurasia. Geol. Soc. Amer. Sp. Papaers, 195, 74p.

Şengör, A. M. C., & Yilmaz, Y. (1981). Tethyan evolution of Turkey: a plate tectonic approach. Tectonophysics, 75(3-4), 181193203-190199241.

Şengör, A. M. C., Satir, M., & Akkök, R. (1984). Timing of tectonic events in the Menderes Massif, western Turkey: Implications for tectonic evolution and evidence for Pan-African basement in Turkey. Tectonics, 3(7), 693-707.

Seyítoğlu, G., & Scott, B. C. (1996). The cause of NS extensional tectonics in western Turkey: tectonic escape vs back-arc spreading vs orogenic collapse. Journal of Geodynamics, 22(1-2), 145-153.

Seyitoğlu, G., Scott, B. C., & Rundle, C. C. (1992). Timing of Cenozoic extensional tectonics in west Turkey. Journal of the Geological Society, 149(4), 533-538.

Shaked, Y., Avigad, D., & Garfunkel, Z. (2000). Alpine high-pressure metamorphism at the Almyropotamos window (southern Evia, Greece). Geological Magazine, 137(4), 367-380.

Sözbilir, H. (2002). Geometry and origin of folding in the Neogene sediments of the Gediz Graben, western Anatolia, Turkey. Geodinamica Acta, 15(5-6), 277-288.

Spakman, W., & Wortel, R. (2004). A tomographic view on western Mediterranean geodynamics. The TRANSMED Atlas, The Mediterranean Region from Crust to Mantle, 31-52.

Spakman, W., Wortel, M. J. R., & Vlaar, N. J. (1988). The Hellenic subduction zone: a tomographic image and its geodynamic implications. Geophysical research letters, 15(1), 60-63.

Stampfli, G. M., Vavassis, I., De Bono, A., Rosselet, F., Matti, B., & Bellini, M. (2003). Remnants of the Paleotethys oceanic suture-zone in the western Tethyan area. Stratigraphic and structural evolution on the Late Carboniferous to Triassic continental and marine successions in Tuscany (Italy): regional reports and general correlation. Bolletino della Società Geologica Italiana, Volume speciale, 2, 1-24.

Stavropoulos, A., Gerolymatos, I., & Institute of geology and mineral exploration (Grèce),. (1999). Geological map of Greece. Athens: Institute of Geology and Mineral Exploration.

Sternai, P., Jolivet, L., Menant, A., & Gerya, T. (2014). Driving the upper plate surface deformation by slab rollback and mantle flow. Earth and Planetary Science Letters, 405, 110-118.

Theodoropoulos, D. (1979). Geological Map of Greece 1: 50000, Samos Island. NIGMR, Athens.

Theye, T., & Seidel, E. (1991). Petrology of low-grade high-pressure metapelites from the External Hellenides (Crete, Peloponnese) A case study with attention to sodic minerals. European Journal of Mineralogy, 343-366.

Theye, T., & Seidel, E. (1993). Uplift-related retrogression history of aragonite marbles in western Crete (Greece). Contributions to Mineralogy and Petrology, 114(3), 349-356.

Theye, T., Seidel, E., & Vidal, O. (1992). Carpholite, sudoite, and chloritoid in low-grade high-pressure metapelites from Crete and the Peloponnese, Greece. European Journal of Mineralogy, 4(3), 487-507.

Theye, T., Chopin, C., Grevel, K. D., & Ockenga, E. (1997). The assemblage diaspore+ quartz in metamorphic rocks: a petrological, experimental and thermodynamic study. Journal of Metamorphic Geology, 15(1), 17-28.

Thiebault, F. (1982). L'evolution geodynamique des Hellenides externs en Peloponnese meridionale.Publ. Soc. Geol. Nord, 6, 574p.

Thomson, S. N., Stöckhert, B., & Brix, M. R. (1998). Thermochronology of the high-pressure metamorphic rocks of Crete, Greece: implications for the speed of tectonic processes. Geology, 26(3), 259-262.

Tirel, C., Brun, J. P., & Burov, E. (2004). Thermomechanical modeling of extensional gneiss domes. Geological Society of America Special Papers, 380, 67-78.

Torsvik, T. H., & Cocks, L. R. M. (2009). The Lower Palaeozoic palaeogeographical evolution of the northeastern and eastern peri-Gondwanan margin from Turkey to New Zealand. Geological Society, London, Special Publications, 325(1), 3-21.

Trotet, F., Vidal, O., & Jolivet, L. (2001). Exhumation of Syros and Sifnos metamorphic rocks (Cyclades, Greece). New constraints on the PT paths. European Journal of Mineralogy, 13(5), 901-902.

Urai, J. L., Schuiling, R. D., & Jansen, J. B. H. (1990). Alpine deformation on Naxos (Greece). Geological Society, London, Special Publications, 54(1), 509-522.

Van Hinsbergen, D. J. (2010). A key extensional metamorphic complex reviewed and restored: the Menderes Massif of western Turkey. Earth-Science Reviews, 102(1), 60-76.

Van Hinsbergen, D. J. J., & Schmid, S. M. (2012). Map view restoration of Aegean–West Anatolian accretion and extension since the Eocene. Tectonics 31, TC5005.

Van Hinsbergen, D. J. J., Hafkenscheid, E., Spakman, W., Meulenkamp, J. E., & Wortel, R. (2005). Nappe stacking resulting from subduction of oceanic and continental lithosphere below Greece. Geology, 33(4), 325-328.

Van Hinsbergen, D. V., Van der Meer, D. G., Zachariasse, W. J., & Meulenkamp, J. E. (2006). Deformation of western Greece during Neogene clockwise rotation and collision with Apulia. International Journal of Earth Sciences, 95(3), 463.

Van Hinsbergen, D. J., Dekkers, M. J., Bozkurt, E., & Koopman, M. (2010). Exhumation with a twist: paleomagnetic constraints on the evolution of the Menderes metamorphic core complex, western Turkey. Tectonics, 29(3).

Vanderhaeghe, O. (2004). Structural development of the Naxos migmatite dome. Geological Society of America Special Papers, 380, 211-227.

Vigner, A. (2002). Images sismiques par réflexions verticale et grand-angle de la croûte en contexte extensif: les Cyclades et le Fossé Nord-Egéen (Doctoral dissertation, Institut de Physique du Globe (Paris)).

Walcott, C. R., & White, S. H. (1998). Constraints on the kinematics of post-orogenic extension imposed by stretching lineations in the Aegean region. Tectonophysics, 298(1), 155-175.

Weidmann, M., Solounias, N., Drake, R. E., & Curtis, G. H. (1984). Neogene stratigraphy of the eastern basin, Samos Island, Greece. Geobios, 17(4), 477-490.

Whitney, D. L., & Bozkurt, E. (2002). Metamorphic history of the southern Menderes massif, western Turkey. Geological Society of America Bulletin, 114(7), 829-838.

Whitney, D. L., Teyssier, C., Kruckenberg, S. C., Morgan, V. L., & Iredale, L. J. (2008). High-pressure–low-temperature metamorphism of metasedimentary rocks, southern Menderes Massif, western Turkey. Lithos, 101(3), 218-232.

Will, T., Okrusch, M., SchmaÈdicke, E., & Chen, G. (1998). Phase relations in the greenschist-blueschist-amphibolite-eclogite facies in the system Na 2 O-CaO-FeO-MgO-Al 2 O 3-SiO 2-H 2 O (NCFMASH), with application to metamorphic rocks from Samos, Greece. Contributions to Mineralogy and Petrology, 132(1), 85-102.

Wijbrans, J.R., Schliestedt, M., York, D., 1990. Single grain argon laser probe dating of phengites from the blueschist to greenschist transition on Sifnos (Cyclades, Greece). Contr. Mineral. and Petrol. 104, 582–593. doi:10.1007/BF00306666

Wortel, M. J. R., & Spakman, W. (2000). Subduction and slab detachment in the Mediterranean-Carpathian region. Science, 290(5498), 1910-1917.

Zachariasse, W. J., van Hinsbergen, D. J., & Fortuin, A. R. (2011). Formation and fragmentation of a late Miocene supradetachment basin in central Crete: implications for exhumation mechanisms of high-pressure rocks in the Aegean forearc. Basin Research, 23(6), 678-701.

CHAPITRE V : Evolution structurale et thermique du Massif du Menderes du Crétacé à l'actuelle (Turquie)

Après avoir abordé dans les *chapitres III et IV*, la cinématique et l'évolution des roches qui se localisent à l'aplomb de cette déchirure entre le Massif du Menderes et les Cyclades, l'évolution tectono-métamorphique et par conséquent thermique du Massif du Menderes sera présentée dans ce chapitre. Il est important de noter que l'état thermique actuel est matérialisé par la présence de nombreuses sources thermales et d'activité fumerolienne. Or, cet état thermique résulte de l'évolution de la dynamique du slab hellénique. En ce sens, si l'on veut comprendre les anomalies thermiques actuelles, il faut nécessairement comprendre dans un premier temps l'histoire évolutive de la zone de subduction et plus particulièrement celle du Massif du Menderes ou les transferts de chaleur liée à la dynamique de subduction évoluent spatialement et temporellement.

Bien que le Massif du Menderes soit considéré comme un MCC, exhumé lors de l'extension post-orogénique à l'Oligo-Miocène, aucun consensus dans la littérature n'est encore réellement établi sur son évolution. En effet, deux principaux points sont encore sujets à controverses et donc fréquemment débattus : la structure générale du Massif du Menderes et la présence d'une unité de Haute-Pression dans la partie sud de ce dernier. Bien que de nombreuses études de terrain sur la cinématique de la déformation ont été menées, leurs interprétations diffèrent d'une étude à l'autre [*e.g.* Ring *et al.*, 1999 ; Gessner *et al.*, 2001a ; 2001c ; Okay, 2001 ; Bozkurt & Park, 1994 ; Lips *et al.*, 2001], faute de données radiochronométriques dans l'ensemble du massif. En effet, le massif du Menderes a subi une évolution polymétamorphique complexe marquée par deux épisodes de haute-température. Alors que le premier correspond à un métamorphisme barrovien associé à l'épaississement crustal lors de la collision alpine, le second est corrélé à l'extension post-orogénique qui se traduit par un amincissement crustal dans un domaine arrière-arc. La zone de cisaillement de Selimiye offre un exemple parfait de ces controverses. Selon différentes études, elle est interprétée comme (i) une zone de cisaillement alpine top-sud qui de développe lors de l'enfouissement des sédiments dans le prisme orogénique [Gessner *et al.*, 2001a; Gessner *et al.*, 2013], (ii) une zone de cisaillement extensive top-sud à la fin de l'épisode alpin [Bozkurt & Park, 1994 ; Whitney & Bozkurt, 2002 ; Bozkurt, 2007], (iii) un pli plurikilométrique de la couverture causé par le raccourcissement alpin (Fig. V.1a) [Okay, 2001 ; Erdogan & Gûngör, 2004]. Par ailleurs, la cinétique de la phase compressive est également sujette à discussion. Alors que certains auteurs expliquent l'épaississement crustal par la formation de nappes, où les unités se juxtaposent par succession de chevauchements à vergence sud (Fig. V.1b) [Ring *et al.*, 1999 ; Gessner *et al.*, 2001a], d'autres supposent l'existence de rétro-chevauchement à cinématique top nord pour expliquer l'épisode d'épaississement crustal [Bozkurt & Park, 1994 ; Hetzel *et al.*, 1998 ; Bozkurt, 2001]. Ces controverses majeures témoignent donc de la complexité entre les structures héritées (associées à l'épisode alpin compressif) et les structures extensives permettant l'exhumation du massif à l'Oligo-Miocène [*e.g.* Hetzel *et al.*, 1995a ; 1995b ; Gessner *et al.*, 2001c ; Bozkurt, 2001 ; Bozkurt *et al.*, 2011].

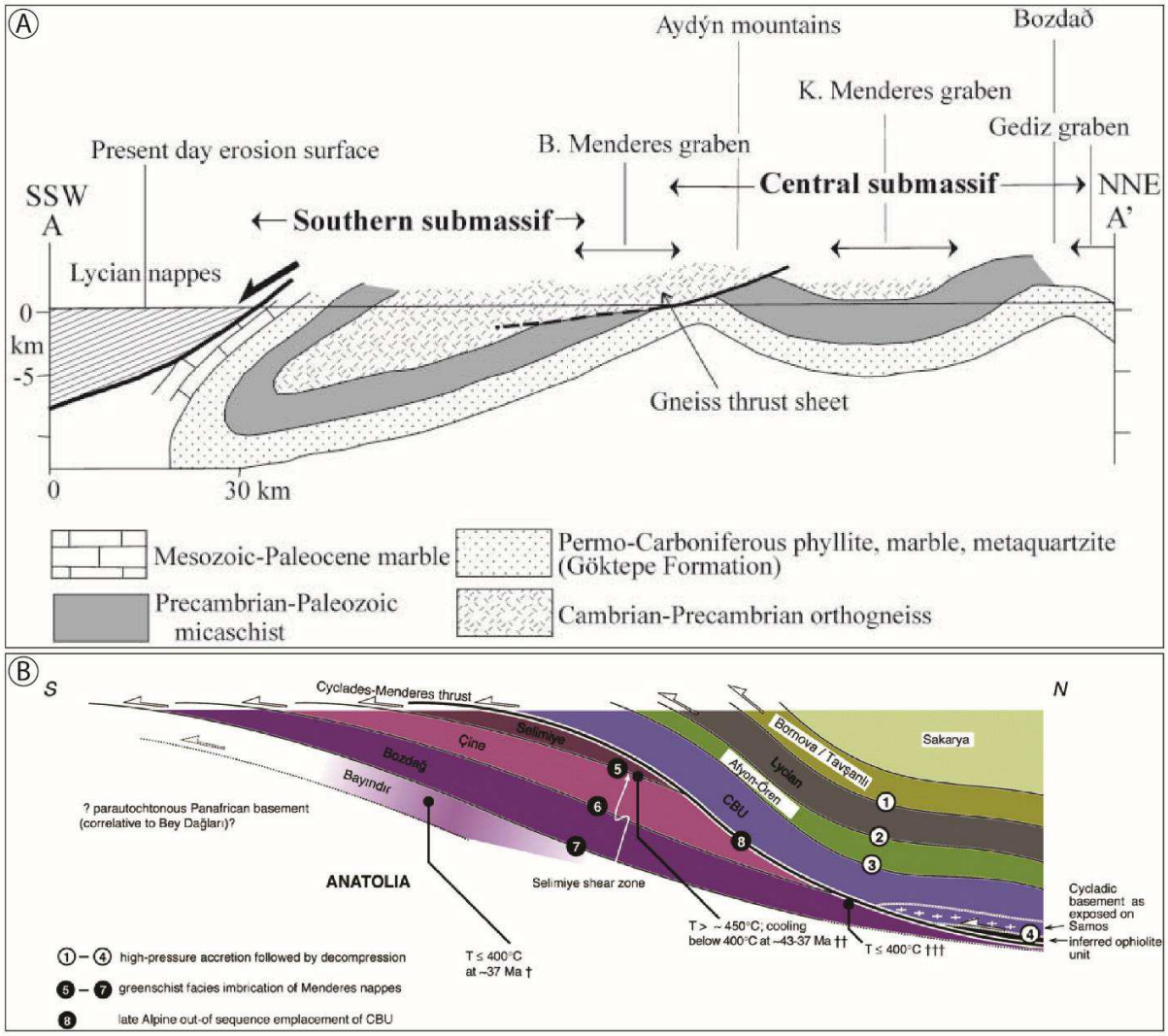

Figure V.1: différents modèles expliquant la formation de la partie sud du MCC. (a) Modèle proposé par Okay [2001] et (b) modèle proposé par Gessner et al. [2013].

A l'échelle régionale, un autre problème majeur concerne la présence de la magnésio-carpholite au sud du Menderes (dans la couverture mésozoïque du Menderes (?)), impliquant des conditions métamorphiques de HP-BT (Fig. V.2). Rimmelé *et al.* [2003] ont estimé les conditions métamorphiques de ces roches entre 10 – 12 kbar pour une température de ~ 440 °C. Ainsi, cette découverte a conduit les auteurs à reconsidérer les corrélations entre cette région et le reste du massif du Menderes. Ils proposent donc qu'une partie du Massif du Menderes (socle et couverture) a dans un premier temps enregistré un métamorphisme de HP à l'Eocène, qui dans un second temps a été surimposé par un métamorphisme de HT (*i.e.* barrovien) pendant la phase alpine. A contrario, la plupart des études assimilent ces séries, composées de méta-conglomérats et de marbres, à l'unité des Schistes Bleus Cycladiques (SBC) [*e.g.* Ring *et al.*, 1999 ; Gessner *et al.*, 2013 ; Pourteau *et al.*, 2016]. Bien que des similitudes aient été montrées par ces auteurs entre cette unité et celle des SBC, aucune corrélation claire n'a été établie. Cette interprétation implique donc que le Massif du Menderes n'a jamais subi des conditions métamorphiques de HP à l'Eocène comme le propose Rimmelé *et al.* [2003].

Afin d'apporter de nouvelles contraintes sur cette évolution, une étude de terrain régionale a été menée, des âges ^{40}Ar-^{39}Ar sur micas et U-Pb sur monazites, ainsi que des températures RSCM ont été mesurés. Tous ces résultats sont présentés à la suite sous la forme d'un article.

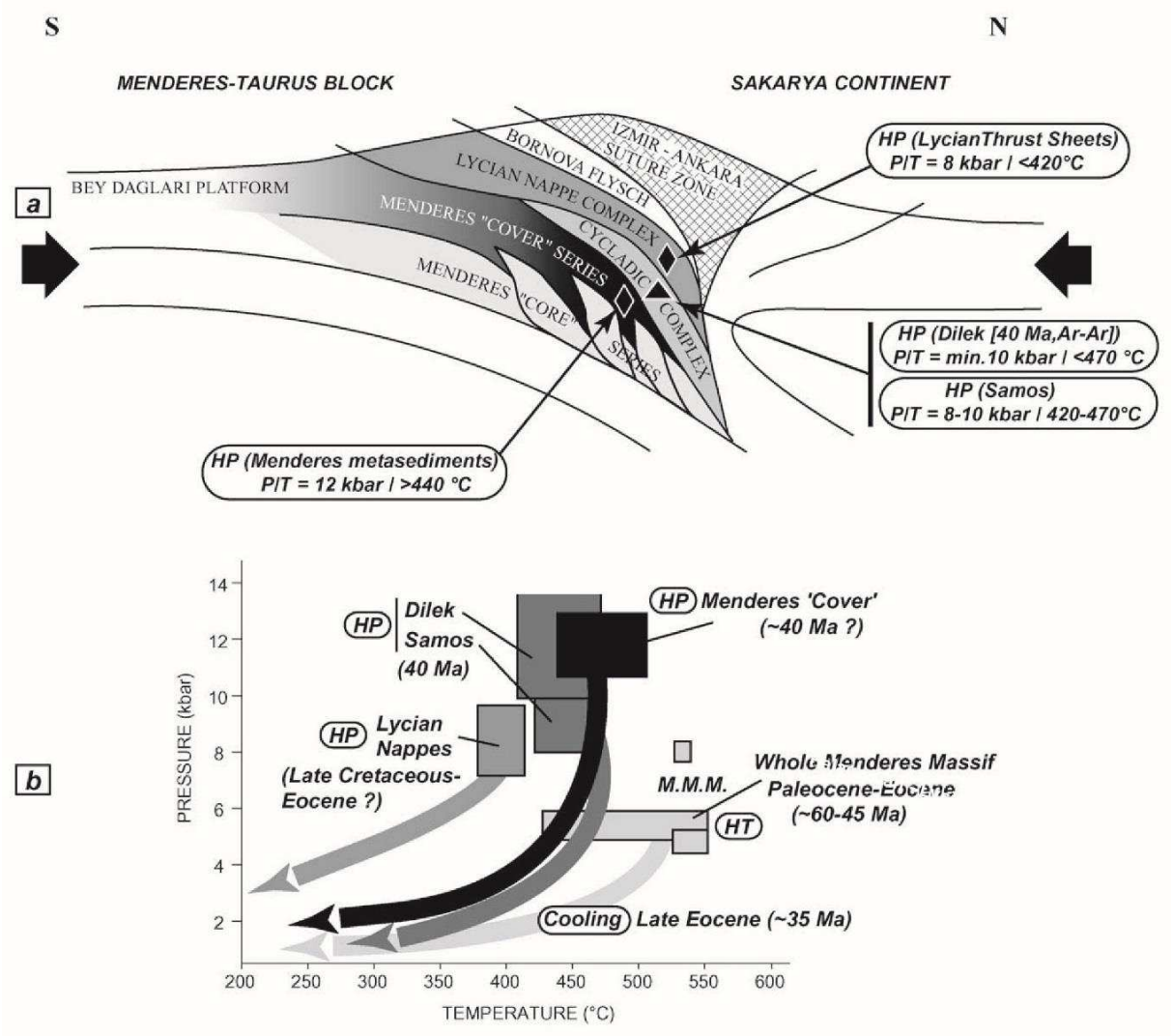

Figure V.2: les différentes unités métamorphiques observées dans la région du Menderes. (a) représentation schématique montrant les principales positions des unités de HP-BT d'après Rimmelé et al. [2003]. (b) conditions P-T-t des unités au pic métamorphique et lors de leurs remontées vers la surface.

Principaux résultats :

Les résultats préliminaires (*i.e.* RSCM et radiométriques) montrent qu'un métamorphisme HT-LP associé à une nouvelle fabrique dans la partie centrale du Massif du Menderes (CMM) se développe au Miocène lors de l'extension post-orogénique. Cette extension est accommodée par différentes zones de cisaillement, dont certaines déjà connu par la communauté (*e.g.* le détachement de Gediz et du Büyük Menderes Miocène). Cette étude révèle l'existence d'une nouvelle zone de cisaillement à cinématique

S. Nommée BSZ (Bozdag Shear Zone), cette zone de cisaillement est précoce par rapport au Gediz détachement.

Par ailleurs, les âges ^{40}Ar-^{39}Ar (> 50 Ma) *in situ* réalisés sur les paragenèses de HP-BT dans le sud du Massif (proche de Selimiye) suggèrent que cette partie du Massif a enregistré des conditions HP-BT avant la surimpression barrovienne à l'Eocène (MMM, Main Menderes Metamoprhism), qui a en partie remis à zéro le géochronomètre argon (âge ~ 40 Ma sur l'ensemble de la pastille et en *step heating*). Ce dernier qui affecte en grande partie le Massif du Menderes, est principalement exhumé par le biais de la zone de cisaillement syn-orogénique, appelée Selimiye Menderes Shear Zone (SMSZ). Un modèle géodynamique à l'échelle lithosphérique est ensuite discuté. Ce dernier tente d'expliquer les relations entre les différentes unités métamorphiques et ainsi de montrer l'évolution thermique du massif qui se résume en trois étapes : (i) un métamorphisme HP-BT pré-Eocène qui affecte la couverture nord du Menderes ; (ii) le métamorphisme barrovien MMM et (iii) un métamorphisme HT-BP associée à l'extension post-orogénique et la mise en place du dôme.

En résumé, les anomalies thermiques régionales résultent de l'évolution de la zone de subduction égéenne en profondeur. Ces anomalies sont probablement associées aux processus géodynamiques (*i.e.* retrait et déchirure), qui contrôlent la structure et la géométrie de grande échelle. Afin d'apporter des contraintes thermiques et physiques à ces processus, une approche numérique a été utilisée et elle fera l'objet du dernier chapitre.

Tectonic and thermal evolution of a Metamorphic Core Complex: the Menderes Massif (Western Turkey)

Vincent ROCHE[1, 2, 3*], Stéphane SCAILLET[1, 2, 3], Laurent JOLIVET[4], Florian DUVAL[1, 2, 3], Johann TUDURI[3, 1, 2], Morgan BEZARD[1, 2, 3], Erdin BOZKURT[5, 6], Bülent TOKAY[5], Abdel LAHFID[3, 1, 2], Jérémie MELLETON[3, 1, 2], Philippe LACH[3, 1, 2], Ida DI CARLO[1, 2, 3]

[1] *Université d'Orléans, ISTO, UMR 7327, 45071, Orléans, France*

[2] *CNRS/INSU, ISTO, UMR 7327, 45071 Orléans, France*

[3] *BRGM, ISTO, UMR 7327, BP 36009, 45060 Orléans, France*

[4] *Sorbonne Universités, UPMC Univ Paris 06, CNRS, Institut des Sciences de la Terre de Paris (iSTeP), 4 place Jussieu 75005 Paris, France*

[5] *Middle East Technical University, Department of Geological Engineering, Üniversiteler Mahallesi, Dumlupınar Bulvarı No: 1, 06800 Ankara, Turkey*

[6] *Center for Global Tectonics & State Key Laboratory of Geological Processes and Mineral Resources, China University of Geosciences, Wuhan, 388 Lumo Road, Hongshan District, Wuhan 430074, Hubei Province, China*

(Cet article fera l'objet d'une soumission dans les prochaines semaines à Tectonics)

Abstract

The Menderes Massif is a wide Metamorphic Core Complex (MCC), which has recorded different P/T conditions from ~ 60 Ma to the Present above the Hellenic subduction zone. It is thus a good candidate to better understand relationships between slab dynamics and associated thermal anomalies. Using high-resolution laser ^{40}Ar-^{39}Ar dating of mica and U-Pb dating of monazite, RSCM T_{max} data combined with a detailed regional-scale kinematic-structural data, this study presents new constraints on the Eocene-Miocene thermal evolution. A first HT-LP metamorphism event associated with nappe stacking started in Eocene times and lasted until Oligocene times, affecting the entire MCC. This crustal thickening was mainly exhumed along a syn-orogenic extensional shear zone (Selimiye shear zone) in Eocene time, outcropping in the southern part of the massif. The presence of HP-LT rocks within the Menderes cover in the same area suggests that the northern part has undergone HP-LT conditions before the Eocene Barrovian metamorphism overprint, which is confirmed by our new ^{40}Ar-^{39}Ar ages. Furthermore, a second HT-LP metamorphism event developed mainly during the Miocene in the northern and central parts. Exhumation of the MCC started around ~ 30 Ma resulting from slab dynamics (*i.e.* tearing and slab retreat). It was first accommodated by the Simav and the Büyük Menderes detachments, and then by the Alaşehir detachment and the Bozdağ shear zone.

V.1. Introduction

Understanding the origin of continental lithospheric- and crustal-scale thermal anomalies in back-arc context requires studying the long-term thermo-tectonic evolution of subduction zone encompassing the full range of parameters driving the circulation of fluids at different scales. During subduction, collision and subsequent post-orogenic extension, changes of the thermal regime are observed in exhumed units which record the evolution of crustal and lithospheric thermicity. In the internal zones of Mediterranean belts, tectonic units exhumed during subduction often preserve high-pressure and low-temperature (HP-LT) assemblages dating from early nappe stacking episodes [Jolivet *et al.*, 2003; Brun & Faccenna, 2008; Labrousse *et al.*, 2016]. On the contrary, in post- orogenic collapse of the thickened crust, Metamorphic Core Complexes (MCC) expose a high-temperature core formed by the flow of a weakened, partially molten lower crust [*e.g.* Buck, 1991; Brun & Van den Driessche, 1994; Block & Royden, 2010; Rey *et al.*, 2009], thus implying high-temperature and low-pressure (HT-LP) metamorphism. As a result, the thermal evolution of such assemblages depends of many parameters such as the proximity of the cold subducting slab, the velocity of subduction/exhumation of crustal units, whether or not continental basement is involved in the wedge (radioactive heat production), the depth of the lithosphere-asthenosphere boundary, the intensity of shear heating and mantle flows associated with slab dynamics [e.g. Jolivet *et al*., 2003; Gerya *et al*., 2002; Agard *et al*., 2009; Roche *et al*., 2018a].

Considered as one of the world's largest MCC, the Menderes Massif has recorded a succession of tectonic stages with different P/T gradients from ~ 60 Ma to the Present above the Hellenic subduction zone. It is thus a good candidate to better understand relationships between slab dynamics and associated thermal anomalies. Although evidences of HP-LT metamorphism in the southern part of the Menderes Massif are still discussed [*e.g.* Ring *et al.*, 1999; Rimmelé *et al.,* 2003; Whitney *et al.,* 2008; Pourteau *et al.*, 2016], this massif has recorded two successive HT-LP overprints. The first one (Eocene) is associated with the Alpine orogeny, corresponding to crustal thickening and nappe stacking due to the imbrication of crustal units belonging to the Anatolide-Taurides above the Hellenic subduction zone [*e.g.* Satır & Frieddrichsen, 1986; Bozkurt & Satır, 2000; Gessner *et al*., 2001a; Okay, 2001; Schmidt *et al.*, 2015; Cenki Tok *et al.*, 2016]. A second one (Oligo-Miocene) is related to post-orogenic back-arc extension during the formation of the Aegean Sea [Catlos & Cemen, 2005; Cenki Tok *et al.*, 2016], mainly accommodated by low-angle normal fault systems. The geodynamic interpretation of these successive stages is debated [*e.g.* Bozkurt & Park, 1994; Ring *et al.*, 1999; Okay, 2001; Gessner *et al.*, 2001c; Whitney *et al.* 2008; Iredale *et al.*, 2013], especially regarding the kinematic significance (compressional or extensional) and timing of major shear zones.

This study investigates the thermal evolution of the Menderes massif by means of extensive RSCM (Raman Spectroscopy on Carbonaceous Materials) analyses coupled with high-resolution laser ^{40}Ar-^{39}Ar dating of white mica and biotite and U-Pb dating of monazite. Our data are combined with

detailed regional-scale kinematic-structural data to place constraints on the Eocene-Miocene thermal evolution of the Menderes MCC (MMCC) and the timing of deformation localization in connection with the evolving thermal structure of the complex. Our multi-disciplinary kinematic, paleothermal, and thermochronological approach is integrated into a lithospheric-scale geodynamic model exploring the interactions between the crust and mantle to explain the thermal anomaly associated with the MMCC formation.

V.2. Geological setting

Western Anatolia has recorded a succession of tectonic events associated with the dynamics of the African slab during the subduction of the Vardar Ocean, the collision of Apulia and the subduction of the Eastern Mediterranean. After the closure of the Vardar Ocean located to the north of the Aegean domain in the late Cretaceous-Paleocene, the convergence between Apulian and European plates led to the formation of a crustal south-verging orogenic wedge (Hellenides and Taurides) [*e.g.* Bonneau & Kienast, 1982; Dercourt *et al.,* 1986; Jolivet & Brun, 2010]. It consists of a stack of continental and oceanic crustal slices where both HP-LT and HT-LP conditions are recorded. Recently, Roche *et al.* [2018b] described a similar structural position through the entire region, including the Dodecanese and eastern Aegean islands that had received less attention so far. They found from top to bottom, (i) the Lycian units which were exhumed in the Late Cretaceous, (ii) the high-pressure and low-temperature units (HP-LT units of the Upper Cycladic Blueschist Nappe), and finally (iii) the colder HP-LT units of the Lower Blueschist Nappe including the Menderes and its cover before the Barrovian Main Menderes Metamorphism (MMM [Şengör *et al.*, 1984]) overprint, and the Lower Cycladic Blueschist Nappe (*e.g.* Amorgos, a part of the Dodecanese and Fourni islands). These correlations complete the superposition of two nappes in the Cycladic Blueschists proposed by Grasemann *et al*. [2017] and Roche *et al*. [2018b]. Since the Oligo-Miocene, the kinematics in this region has been mainly controlled by the southward retreat [*e.g.* Le Pichon *et al.*, 1981; Jolivet & Faccenna, 2000; Jolivet & Brun, 2010] and the tearing of the African slab under the Menderes Massif (Fig. V.3) [*e.g.* De Boorder *et al.*, 1998; Piromallo & Morelli, 2003; Dilek & Altunkaynak, 2009; Ersoy *et al.*, 2010; Jolivet *et al.*, 2015; Govers & Fichtner, 2016]. Slab dynamics is thus responsible for back-arc extension [*e.g.* Malinverno & Ryan, 1986; Jolivet & Faccenna, 2000; Jolivet & Brun, 2010; Ring *et al.,* 2010; Roche *et al.*, 2018a], where low-angle normal faults accommodate MCC exhumation such as the Menderes Massif, the Naxos, Mykonos and Ikaria domes [*e.g.* Lister *et al.*, 1984; Gautier & Brun, 1994; Gessner *et al.*, 2001c; Vanderhaeghe & Whitney, 2004 ; Lecomte *et al.*, 2010; Denèle *et al.*, 2011 ; Beaudoin *et al.* 2015].

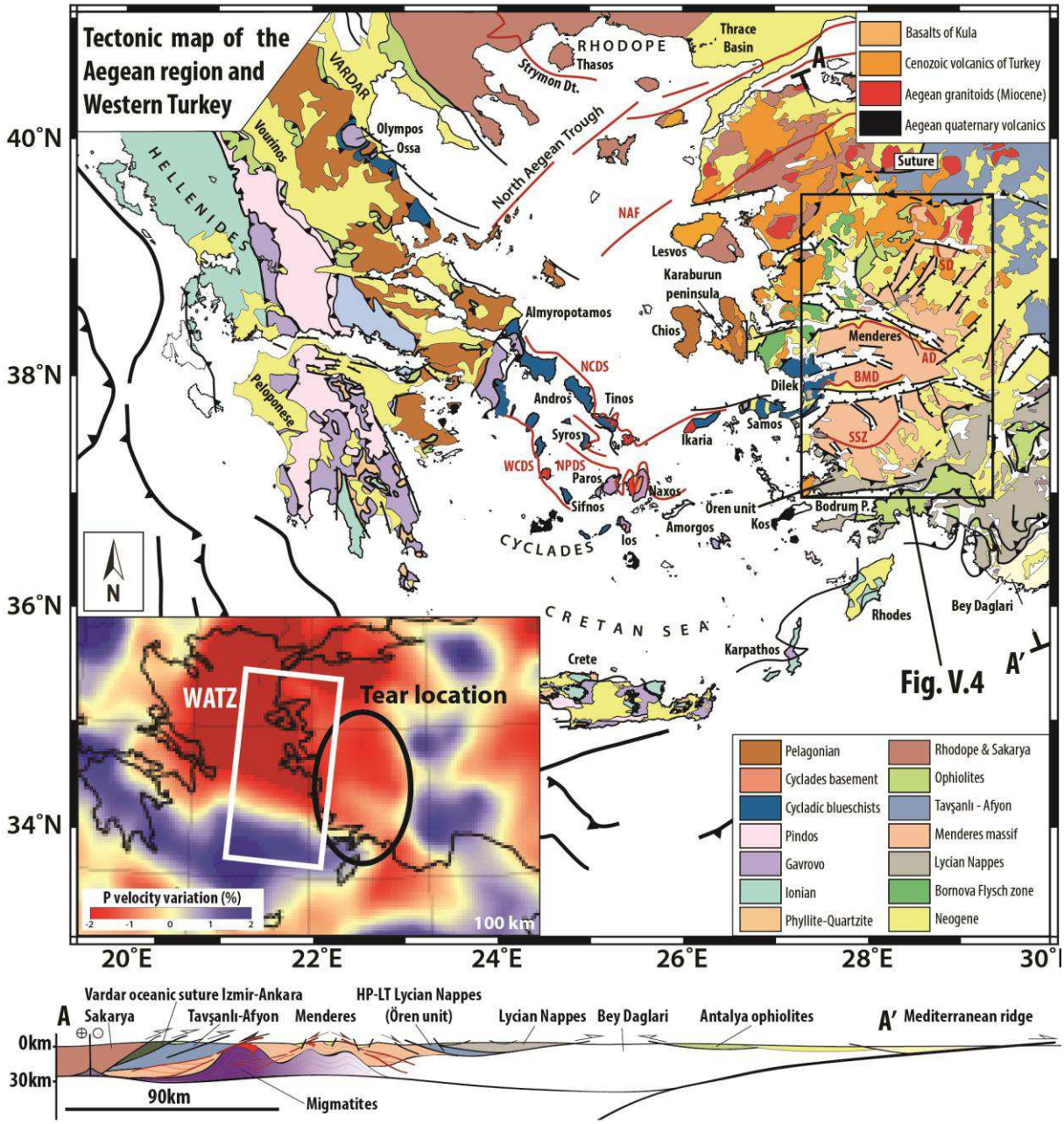

Figure V.3: Main tectonic units of Western Anatolia. Contours are taken from Jolivet et al. [2004] and Pourteau et al. [2016]. Also indicated are the main tectonic features and the tomographic model of Piromallo and Morelli [2003] showing the position of the slab tear at c. 100 km. Abbreviations: BMD (Büyük Menderes detachment); AD (Alaşehir detachment); NAF (North Anatolian Fault); SD (Simav detachment); SSZ (Selimiye shear zone); WATZ (West Anatolia Transfer Zone). Figure V.4 is indicated by black rectangle.

V.2.1. The Lycian Nappes and the Cycladic Blueschist Unit (CBU)

The Lycian Nappes extend over a large area, from the Bey Dagları platform in the southeast to the Izmir-Ankara suture zone, north of the Menderes Massif (Fig. V.3) [Güngör & Erdogan, 2001; Rimmelé *et al.*, 2006]. From base to top, this unit is made of HP-LT metasediments, overlain by an un-metamorphosed tectonic unit, then covered by a mélange unit, and finally an ophiolitic sequence

[Rimmelé *et al.*, 2004]. According to Pourteau *et al.* [2013; 2016], the HP-LT rocks of the Lycian Nappes (*i.e.* Ören unit) can be correlated with the Tavşanlı-Afyon unit cropping out to the north and northeast of the Menderes (Fig. V.3). The HP-LT parageneses of Ören Unit are characterized by the presence of Fe-Mg-carpholite [Oberhänsli *et al.*, 2001; Rimmelé *et al.*, 2004; 2006]. The regional peak of metamorphism is estimated at 10 – 12 kbar and 400 °C Rimmelé *et al.* [2004] and dated around 62 – 59 Ma (^{40}Ar-^{39}Ar on white micas [Pourteau *et al.*, 2013]). The exhumation of Ören Unit was mainly accommodated by different shear-zones such as the "Akçakaya Shear Zone" and the "Gerit Shear Zone" [Rimmelé *et al.* 2004; 2006] with top-to-the-NE or -E kinematic indicators [Rimmelé *et al.*, 2004; 2006]. This unit structurally overlies the CBU and the MMCC in ascending order (Fig. V.3). In addition, the southward emplacement of the Lycian Nappes onto the MMCC is constrained between Upper Cretaceous and Late Miocene [*e.g.* Hayward, 1984; Van Hinsbergen, 2010].

The CBU crops out mainly in the Cyclades, but also in Western Anatolia (Fig. V.3) where it overlies the Menderes Massif [Schuiling, 1962; Ring *et al.* 2001; Whitney & Bozkurt, 2002; Candan *et al.*, 2011]. There, the CBU is mainly composed of series of metabasites with marbles and metapelites intercalations. According to Ring *et al.* [2007], this unit experienced similar HP-LT metamorphism as the Cyclades (*e.g.* Syros, Sifnos, Samos), with a synchronous metamorphic evolution with an Eocene peak of pressure (~ 54 – 44 Ma using Lu-Hf and Sm-Nd on garnets [Lagos *et al.*, 2007; Dragovic *et al.*, 2015]).

V.2.2. The Menderes MCC (MMCC)

V.2.2.1. Lithology of the MMCC

The Menderes Massif consists of a composite basement-cover assemblage recording a complex metamorphic and structural evolution from the early Paleozoic to the Tertiary (Fig. V.4) [*e.g.* Ring *et al.*, 1999; Lips *et al.*, 2001; Bozkurt & Oberhänsli, 2001]. Two main tectono-metamorphic units are classically distinguished with a basal unit mostly made of augen gneiss interleaved with (poly-metamorphic) metasediments, metagranites, metagabbros and HT gneisses (including migmatite) [Schuiling, 1962], and a metasedimentary succession of micaschists, garnet bearing-schists, gneisses interleaved with marble, with minor metaconglomerates levels and quartzites [Dürr, 1975].

According to many studies, the augen gneisses of the basement are Precambrian in age [*e.g.* Schuiling, 1962; Satir & Frieddrichsen, 1986; Reischmann *et al.*, 1991], and may therefore represent a Pan-African basement as suggest by Şengör *et al.* [1984]. The granitic precursors of this basement mostly date back to Early Cambrian times (521 – 572 Ma [*e.g.* Hetzel & Reischmann 1996; Loos & Reischmann 1999]). However, others studies challenged this interpretation of these Neoproterozoic

dates, suggesting a Tertiary protolith ages [Bozkurt *et al.*, 1995; Bozkurt & Park, 2001]. According to these studies, most age data are from granitoids that may (i) contain inherited minerals and/or (ii) have been remobilized during later events (*e.g.* Alpine event). The metasedimentary succession corresponds to the cover series, and may be divided into two sub-units, a Paleozoic schist sequence covered by a Mesozoic-Cenozoic marble unit [Dürr, 1975] ending with typical deformed reddish Cretaceous marbles and fossiliferous limestone and sandstone assemblages of Paleocene-Eocene age [Özer *et al.*, 2001]. All this sequence is well exposed in different areas such as in the Büyük Menderes graben, and in the southern part of the Selimiye area (Fig. V.4).

Furthermore, the tectonic relationships between the core (*i.e.* the basal unit) and the cover series are still debated [*e.g.* Erdogan, 1992]. Some authors interpret the succession as a nappe stack [*e.g.* Partzch *et al.*, 1998; Ring *et al.*, 1999; Gessner *et al.,* 2001a], whereas others as a genuine basement-cover association [*e.g.* Bozkurt & Oberhänsli 2001; Okay, 2001]. In most places, the basal unit overlays the cover unit (*e.g.* near Zeytinköy area, Fig. V.4), but locally some of the gneissic rocks and associated granitoids intrude the overlying cover (*e.g.* near Selimiye [Bozkurt *et al.*, 1995; Bozkurt & Park, 2001]).

V.2.2.2. Structure and metamorphism of the MMCC: the main controversies

The MMCC can be divided in three sub-massifs, which are separated by tectonically active E-W trending graben systems (*e.g.* Seyitoglu & Scott, 1991; Yilmaz *et al.*, 2000; Bozkurt & Sözbilir, 2004). From north to south, (i) the Gördes Massif (North Menderes Massif, NMM,), separated from the Ödemis Massif by the Alaşehir graben; (ii) the Ödemis Massif in the center (Central Menderes Massif, CMM) is separated from the Çine Massif (South Menderes Massif, SMM) south of the Büyük Menderes graben (Fig. V.4) [Bozkurt & Oberhänsli, 2001]. Close to the northern part of Gördes Massif, the Simav detachment can be observed and the Alaşehir detachment is positioned between the Gördes Massif and the Ödemis Massif (Fig. V.4). Kinematics of deformation associated with both detachments shows a consistent top-to-the-NNE sense of shear [*e.g.* Hetzel *et al.*, 1995a; 1995b; Işık & Tekeli, 2001; Gessner *et al.,* 2001c]. Conversely, located between the Ödemis Massif and the Çine Massif, the Büyük Menderes detachment presents top-to-the-S kinematic indicators [*e.g.* Emre & Sözbilir, 1997; Gessner *et al.,* 2001c; Ring *et al.,* 2003]. Within this general framework, although a consensus exists about the Oligo-Miocene NNE-SSW directed post-orogenic extension, the exact situation is still problematic and the age of metamorphism and kinematic indicators are still controversial:

(i) the two-stage exhumation process is controversial, whether symmetrical [Ring *et al.,* 2003] or asymmetrical [Seyitoglu *et al.,* 2004]);

(ii) the multi-staged activity of the detachments remains matters of debate (*i.e.* low-angle normal faults [*e.g.* Hetzel *et al.,* 1995a; 1995b; Emre & Sozbilir, 1997; Sozbilir, 2001; Oner & Dilek, 2011] vs. high-angle normal faults that gradually became low-angle with time [*e.g.* Gessner *et al.,* 2001b; Bozkurt, 2001; Seyitoğlu *et al.,* 2002; Purvis & Robertson, 2005; Çiftçi & Bozkurt, 2009; 2010; Demircioğlu *et al.,* 2010; Seyitoğlu *et al.,* 2014]);

(iii) the metamorphism associated with the Miocene post-orogenic extension is still poorly studied.

Furthermore, one of the main problems concerns the imprint of the Alpine metamorphism dated from the Eocene to Oligocene (*e.g.* 43 and 37 Ma, $^{40}Ar/^{39}Ar$ on white micas [Hetzel & Reischman, 1996]; ~ 42.6 – 34.8 Ma, Lu-Hf ages on garnet [Schmidt *et al.,* 2015]; 42.3 ± 9.1 Ma, U-Pb on allanite [Cenki-Tok *et al.*, 2016]). Some studies propose that the entire Menderes Massif was affected by a HT-LP Barrovian conditions (*i.e.* MMM) and thus by a strong reworking during the Eocene [*e.g.* Bozkurt *et al.*, 1993; Catlos & Cemen, 2005; Lips *et al.*, 2001; Cenki-Tok *et al.*, 2016], while others suggest instead that the imprint of the Alpine metamorphism was minor, only expressed as local greenschist-facies parageneses [*e.g.* Gessner *et al.*, 2001a]. These two points of view have direct consequences on the age of kinematic indicators. In addition, Gessner *et al.* [2001a] showed that the core of the Menderes is also affected by a first amphibolite-facies metamorphism at *c*. 550 Ma (magmatic zircon ^{207}Pb-^{206}Pb) with a ductile top-to-the-NE shearing. As a result, north-directed fabrics may be relics of earlier deformation events [Gessner *et al.*, 2001a; 2001c; 2004], and the Menderes nappe stack was entirely assembled by south-directed shearing. However, other authors interpreted these fabrics as witnesses of the Alpine nappe stacking [*e.g.* Bozkurt & Park, 1994; Hetzel *et al.*, 1995a; Hetzel *et al.*, 1998; Lips *et al.*, 2001; Bozkurt, 2007]. For instance, in the CMM, Lips *et al.* [2001] have reported a 36 ± 2 Ma ^{40}Ar-^{39}Ar age derived from white mica in the cover unit in the Büyük Menderes area that they ascribe to a (i) regional northward-directed tectonic transport (initiated during the Eocene-Oligocene) or a (ii) regional cooling postdating deformation. This problem is also well exposed in the SMM, through the Selimiye south-dipping shear zone near Kurudere (Fig. V.4). There, the age of the older fabric (*i.e.* top-to-the-N) and the nature (compressional vs. extensional) of the contact are controversial [Bozkurt & Park, 1994; Hetzel & Reischmann, 1996; Gessner *et al.*, 2001a; 2004; Régnier *et al.*, 2003; 2007; Bozkurt, 2007; Iredale *et al.,* 2013].

Another matter of debate is the evidence of a HP-LT metamorphic event in the southern part of the MMCC, close to Kurudere. There, Rimmelé *et al.* [2003] found the paragenesis kyanite+magnesio-carpholite, implying P-T conditions around 12 – 14 kbar and 470 – 500 °C in a metaconglomerate attributed to the Late Triassic at the base of the Mesozoic sequence ending with reddish Cretaceous marbles and considered as the normal sedimentary cover of the Paleozoic basement cropping out just north of it. Rimmelé *et al.* [2003] concluded that this finding implies that the whole Menderes Massif

has recorded a first HP-LT metamorphism event before the MMM overprint. Several more recent studies have challenged this conclusion by attributing the Kurudere metamorphic rocks to the CBU rather than to the Menderes Massif [*e.g.* Ring *et al.*, 2007; Régnier *et al.*, 2007; Pourteau *et al.*, 2013]. This point is critical in defining the conditions of burial and the origin of the Menderes nappe stack (*i.e.* by subduction during formation of the Hellenides and Taurides).

V.3. Structural analysis of the Menderes MCC from new field data

To complement recent data indicating a complete Eocene Alpine reworking of the basement and the cover in the NMM and post-orogenic Oligo-Miocene exhumation [Cenki-Tok *et al.*, 2016], we undertook a detailed study of the CCM and SMM (Fig. V.4). The new structural observations were collected along a N-S section running from the Alaşehir detachment to the contact with the Lycian Nappes in the south, where the timing and tectonic significance of deformation and metamorphism remain unclear.

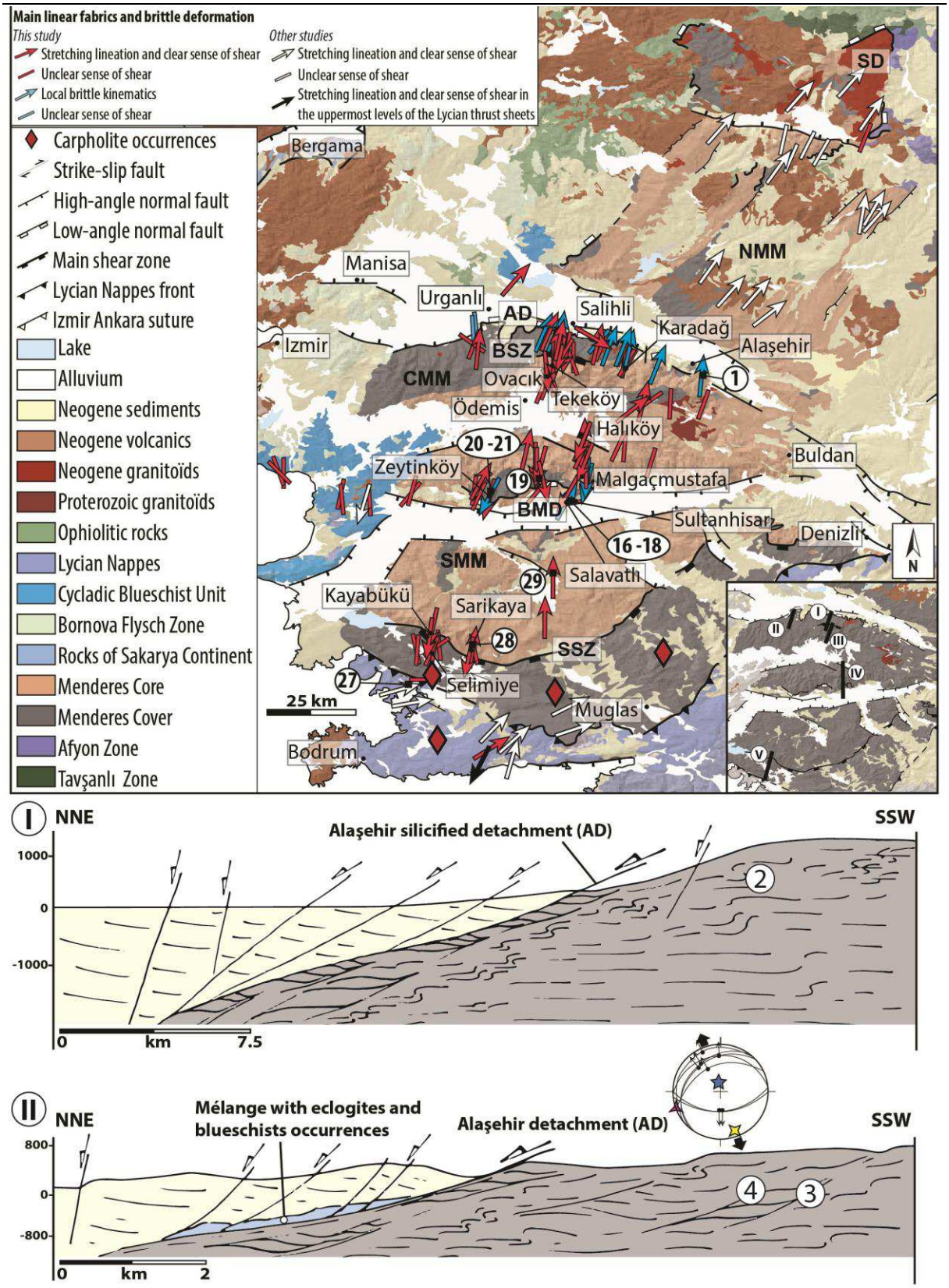
Main linear fabrics and brittle deformation
This study
Stretching lineation and clear sense of shear
Unclear sense of shear
Local brittle kinematics
Unclear sense of shear
Other studies
Stretching lineation and clear sense of shear
Unclear sense of shear
Stretching lineation and clear sense of shear in the uppermost levels of the Lycian thrust sheets
Carpholite occurrences
Strike-slip fault
High-angle normal fault
Low-angle normal fault
Main shear zone
Lycian Nappes front
Izmir Ankara suture
Lake
Alluvium
Neogene sediments
Neogene volcanics
Neogene granitoïds
Proterozoic granitoïds
Ophiolitic rocks
Lycian Nappes
Cycladic Blueschist Unit
Bornova Flysch Zone
Rocks of Sakarya Continent
Menderes Core
Menderes Cover
Afyon Zone
Tavşanlı Zone
Bergama
Manisa
Izmir
Urganlı
AD
BSZ
CMM
Salihli
Karadağ
Alaşehir
NMM
SD
Ovacık
Tekeköy
Ödemis
Halıköy
Buldan
20 -21
19
Zeytinköy
Malgaçmustafa
BMD
Sultanhisar
Denizli
16 -18
SMM
29
Salavatlı
Kayabükü
Sarikaya
28
SSZ
27
Selimiye
Muglas
25 km
Bodrum
N
I
II
III
IV
V
I NNE
SSW
Alaşehir silicified detachment (AD)
1000
0
-1000
2
0 km 7.5
II NNE
Mélange with eclogites and blueschists occurrences
Alaşehir detachment (AD)
SSW
800
0
-800
4
3
0 km 2

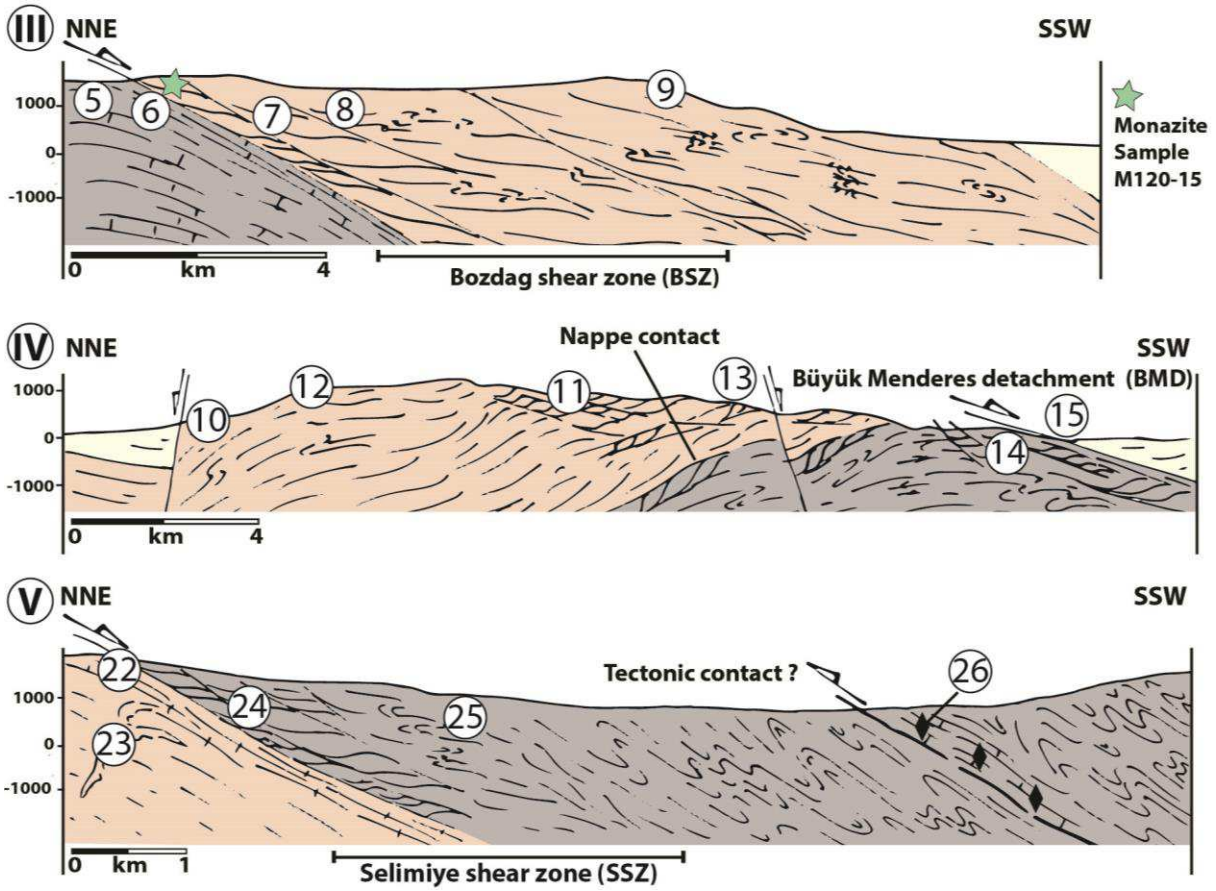

Figure V.4: Main tectono-metamorphic units of the Menderes Massif area. Contours are taken from different studies [e.g. Gessner et al., 2013; Rimmelé et al., 2006; Bozkurt et al., 2011 and references therein]. Stretching lineations and associated shear sense are from this study and from the studies of Ring and Layer [2003], Rimmelé et al. [2006] and Cenki-Tok et al. [2016]. Simplified cross-sections are indicated by black dashed and capital numbers in the map located in the bottom right part of the Figure. Also indicated are the main tectonic features. Abbreviations: AD (Alaşehir detachment); BMD (Büyük Menderes detachment); BSZ (Bozdağ shear zone); CMM (Central Menders Massif); NMM (North Menderes Massif); SD (Simav detachment); SMM (Southern Menderes Massif); SSZ (Selimiye shear zone). Numbers indicate different locations of field pictures: 1 (Fig. V.5a); 2 (Fig. V.5b); 3 & 4 (Figs. V.5c and V.5d); 5 (Fig. V.5e); 6 (Fig. V.5f); 7 (Fig. V.5g); 8 (Fig. V.5h); 9 (Fig. V.6a); 10 (Fig. V.6b); 11 (Fig. V.6d); 12 (Fig. V.6c); 13 (Fig. V.6e); 14 (Fig. V.6f); 15 (Fig. V.6g); 16, 17 & 18 (Figs. V.7a, V.7b and V.7c); 19 & 20 (Figs. V.7d and V.7e). 21 (Fig. V.7f); 22 (Fig. V.8a); 23 (Fig. V.8b); 24 (Fig. V.8c); 25 (Fig. V.8d); 26 (Fig. V.8e); 27 (Fig. V.8f); 28 (Fig. V.8g) and 29 (Fig. V.8h).

V.3.1. Alaşehir detachment: Salihli, Alaşehir and Urganlı areas

The Alaşehir detachment displays a continuum of deformation from ductile to brittle conditions particularly well exposed in the metamorphic cover series near Salihli (Fig. V.4) [*e.g.* Hetzel *et al.*, 1995a; 1995b; Lips *et al.*, 2001; Gessner *et al.*, 2001b; Sözbilir, 2001; Seyitoglu *et al.*, 2002; Işık *et al.*, 2003; Bozkurt & Sözbilir, 2004; Hetzel *et al.*, 2013]. This activity was accompanied by syn-tectonic granodiorite intrusions located in the footwall of the detachment [*e.g.* Glodny & Hetzel, 2006]. According to Rossetti *et al.* [2017], the Salihli granodiorite was emplaced at shallow crustal levels under upper greenschist-to-amphibolite facies metamorphic conditions (530 – 580 °C and P < 2 GPa).

Our data confirm that a thick ductile shear zone is present below the brittle part of the Alaşehir detachment in Salihli area (Fig. V.5a). A clear deformation gradient with top-to-the-NNE shear sense indicators (dense array of centimetric shear bands, asymmetric boudinage and folds, Fig. V.5b) is observed towards the main fault plane. South of Urganlı (Fig. V.4), the fault plane of the Alaşehir detachment strikes E-W and dips gently toward the north, with a ~ NNW-SSE motion (Fig. V.4, cross-section II). Brittle kinematic indicators are distinct from Salihli and Alaşehir areas, and associated with a ~ 50 cm-thick silicified cataclasite zone. Close to the contact, the foliation is characterized by a variable strike and moderate dip values. It carries two stretching lineations, one N20°E trending and another trending NW-SE (Fig. V.4). Most ductile kinematic indicators are consistent with a top-to-the-NNE shearing. Similar to Salihli area, a pervasive network of meso-scale to small-scale shear bands in metapelites deforms the main foliation in ductile then brittle conditions (Fig. V.5c). Locally, flanking structures defined by rotated quartz veins (Fig. V.5d), and asymmetric veins filled with quartz and albite indicate the same sense of shearing. Furthermore, eclogite and blueschist relics are locally found above the detachment (Fig. V.4).

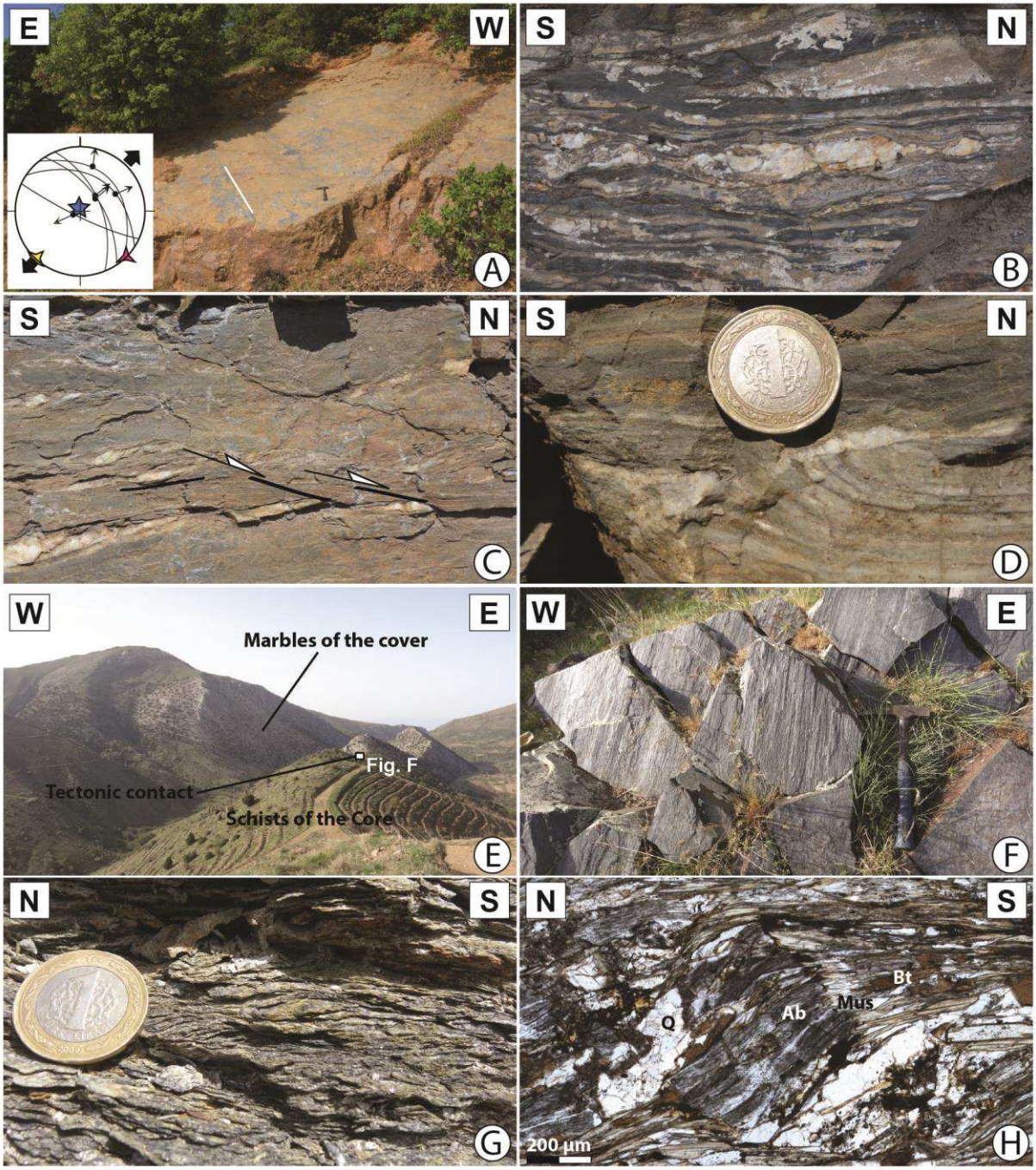

Figure V.5: Kinematic of deformation in the Salihli, Alaşehir, Urganlı and Bozdağ - Birgi areas. (a) Thick cataclasites associated with the Alaşehir detachment. Note that slickenlines are well-defined along the main fault plane. Result of the fault slip data inversion show a NE-SW extension. (b) Asymmetric quartz vein boudinage and folds overturn towards the north, showing a top-to-the-N sense of shear. (c) Centimetric shear bands which deformed the main foliation indicating the same direction of shearing. (d) Quartz vein cutting through the main foliation, and sheared towards the north forming a flanking structure. (e) Large-scale view of the contact between the core and the cover series near Bozdağ. The background corresponds to marbles levels that define an antiform structure. (f) Close-up view of a quartzite rich in organic matter displaying N-S stretching direction indicated by elongated clusters of white micas. (g) Shear bands spaced a few centimeters apart showing an intense top-to-the-S ductile deformation. (h) Biotite and muscovite pressure shadow around a porphyroblast albite showing a top-to-the-S shearing in thin section. See Figure V.4 for location.

V.3.2. The Bozdağ - Birgi areas

According to Hetzel *et al.* [1998], Bozdağ schists are distinguished from the cover series by (i) the absence of intercalated marble and quartzite levels and (ii) the occurrence of amphibolites. The contact between these two main units is well exposed north of Tekeköy (Fig. V.4) where the cover series form a large-scale anticline (Fig. V.5e). Foliation in the southern flank is E-W trending and dips ~ 45° toward the south. The edge of the cover (mylonitized graphitic-quartzite) displays clusters of white micas stretching N160°E (Figs. V.4 and V.5f). The northern flank of the dome-structure dips gently toward the north (Fig. V.5e).

Structurally above the cover series, the Bozdağ schist contain Qtz + Bt + Ky + St ± Mu and Chl, with locally porphyroblast of Ab and Grt (see Whitney & Evans [2010] for mineral abbreviations). This unit also contains amphibolite lenses with Hbl + Pl + Grt and Qtz [Dora *et al.*, 1990]. Foliation is consistent with that of the cover (E-W striking, dip ~ 45° toward the south) and carries a N22°E trending stretching lineation defined by elongated chlorite and biotite (Fig. V.4). Kinematic indicators are very common with top-to-the-S pervasive shearing deformation affecting the deeper structural levels of this unit (Fig. V.5g). For instance, synkinematic biotite or chlorite within shear bands and wrapping albite porphyroblasts are well exposed (Fig. V.5f). Top-to-the-S non-coaxial deformation is also indicated by asymmetric boudinage of competent levels (*e.g.* amphibolite lenses) into a weaker, generally metapelitic, matrix, and by asymmetric sheared quartz veins. The presence of straight quartz and graphite inclusions within albite porphyroblasts and garnets is ascribed to a first deformation stage by Hetzel *et al.* [1998], showing a top-to-the-N sense of shear.

South of Ovacık (Fig. V.4), the upper part of the basement consists of Q + Kfs + Bt + Grt ± Pl ± Sil pelitic gneiss [Hetzel *et al.*, 1998]. Deformed pegmatites also locally occur within paragneiss levels. Foliation strikes E-W to NE-SW with variable dip toward the S-SE (Fig. V.4). The orientation of stretching lineation, mainly defined by elongated biotite and quartz, is around N150°E to N170°E (Fig. V.4). Deformation appears more coaxial with both top-to-the-N and top-to-the-S criteria scantly exposed throughout this area (Fig. V.6a), with unclear field relationship.

V.3.3. Halıköy - Sultanhisar and Salavatlı areas

Southern of Halıkoÿ (Fig. V.4), Bt ± Mu + Q + Chl mica-schists are dominant with common intercalations of graphite-schists of variable thickness [Akçay *et al.*, 2006]. Foliation strikes E-W to SE-NW and dips toward the north with a N10 – 20°E trending stretching lineation defined by elongated aggregates of white mica (Fig. V.4). Kinematic indicators are still ambiguous, indicating top-to-the-NE (Fig. V.6b) or top-to-the-SE deformation. Further south, NE-SW to E-W foliation dips more gently

towards southeast or north, but the stretching lineation constantly trends N20°E (Fig. V.4). The foliation in the paragneiss is defined by Bt + Mu + Q ± Grt, and kinematic indicators show top-to-the-S sense of shear (Fig. V.6c). Asymmetric boudinage of competent levels is also consistent with a top-to-the-S shearing (Fig. V.6d). Deformation frequently appears more localized than in Bozdağ area, and brittle faults with thin fault gouges reactivate and/or cross cut low-angle ductile shear zones (Fig. V.6c). In both cases, kinematics of ductile and brittle deformation are consistent. Nonetheless, it is noteworthy that deeper structural levels of the basal unit are also deformed by low-angle shear zones, which dips towards the north (Fig. V.6e). There, foliation dips ~ 50° towards the northwest, stretching lineation trends N22°E and kinematic indicators show a top-to-the-S shearing (Fig. V.6e). In the northern part of Malgaçmustafa (Fig. V.4), the contact between the cover of the MMCC is not directly exposed probably due to the presence of a set of high-angle normal faults. However, there is a clear change in lithologies, with quartzite, schist and marble intercalations. The strike of foliation is still E-W, but the dip changes toward the south. The foliation is parallel to the Büyük Menderes detachment. A later meter-scale folding event is also observed with large-scale open folds with E-W trending axes. Shearing deformation is mostly accommodated by localized shear bands and quartz veins evolving toward cataclasites (Figs. V.6f and V.6g), suggesting conditions close to the brittle-ductile transition.

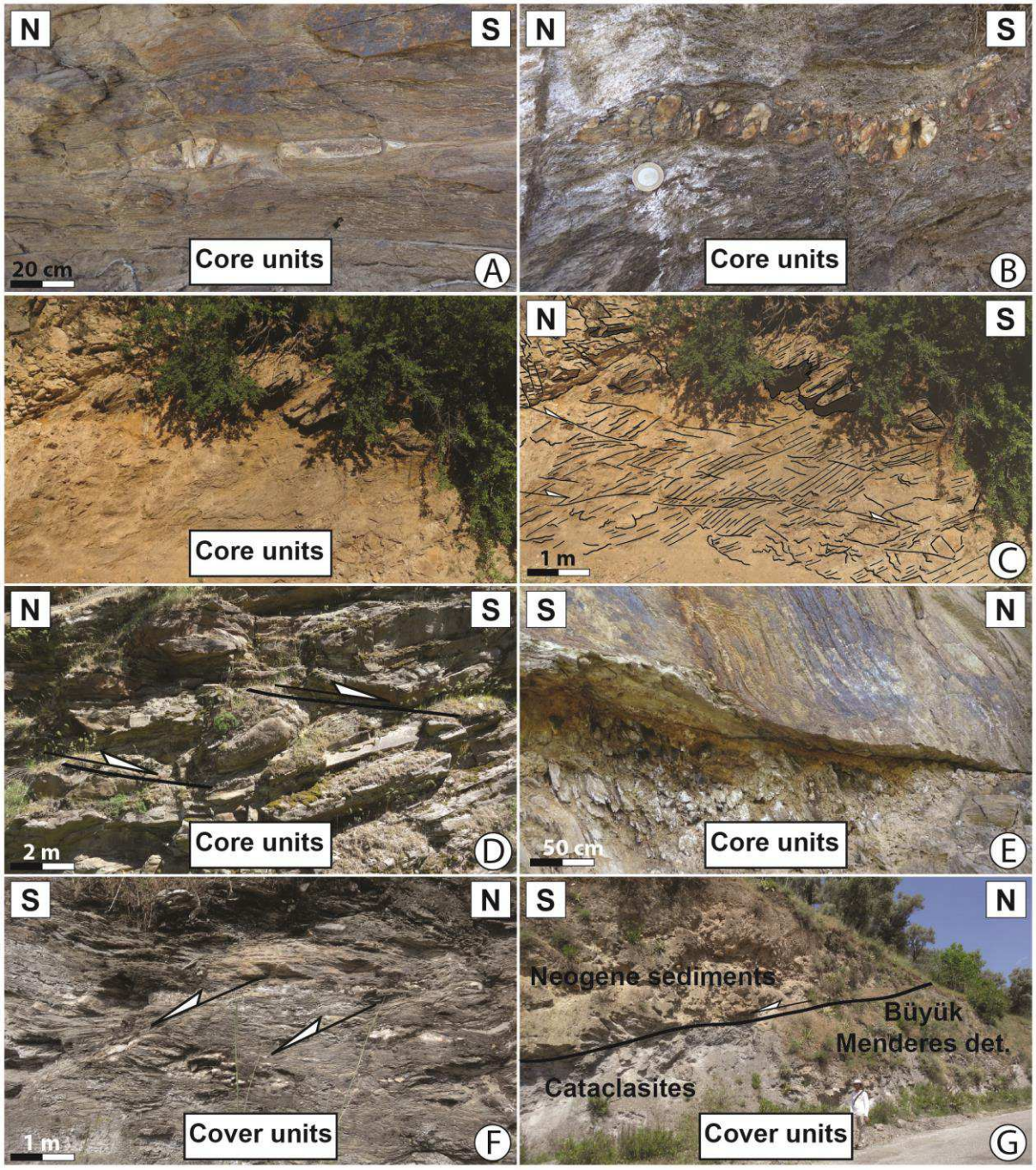

Figure V.6: Kinematic of deformation in the Halıköy - Sultanhisar and Salavatlı areas. (a) Symmetric quartz vein boudinage in the paragneiss units. (b) Sheared quartz vein in schists showing top-to-the-N deformation. (c) Ductile and "brittle" shear bands showing top-S shearing. (d) Asymmetric boudinage of a competent level indicating top-to-the-S shearing. (e) Close-up view of shear bands showing the same sense of shear. (f) Centimetric to metric shear bands in schist levels showing an overall top-to-the-S sense of shear. (g) Low-angle contact between Neogene sediments and metamorphic basement. Note that the basement is strongly affected by brittle deformation. See Figure V.4 for location.

North of Salavatlı (Fig. V.4), the foliation in the cover strikes NW-SE with moderate dip values toward the east, and stretching lineation is N30°E, marked by white micas. Although two sense of shear are present, most shear bands and asymmetric marbles pebbles are compatible with a top-to-the-SW shearing (Fig. V.7a). The Büyük Menderes detachment is not exposed due to a set of major normal to

strike-slip faults that control the first-order distribution of lithologies of the two main units (augen gneiss and schist-marble sequences, Figs. V.7b and V.7c). There, augen gneiss unit displays a strong brittle deformation and lies on top on the Menderes cover. The first set of faults strikes NW-SE and dips toward the SW and the NE (Fig. V.7b) whereas the second ones cut across the previous one, displaying a N-S to N30°E trend with a steeper dip toward the east (Fig. V.7c) (see more details in Roche *et al.* [2018c]).

Similar features was observed in the Menderes cover. For instance, foliation in low-grade schist strikes W-E with moderate dip values toward the north near Zeytinköy (Fig. V.4). Stretching lineation is N16°E marked by white micas. There, a network of shear bands deforms the main foliation from ductile to brittle indicating a top-to-the-S shearing. Folds are also overturn toward the southwest (Fig. V.7e), thus compatible with this shearing event. The same kinematic of deformation is recorded in the cover series located west of Salavatlı (*e.g.* dense array of centimetric shear bands (Fig. V.7f) and asymmetric quartz vein boudinage).

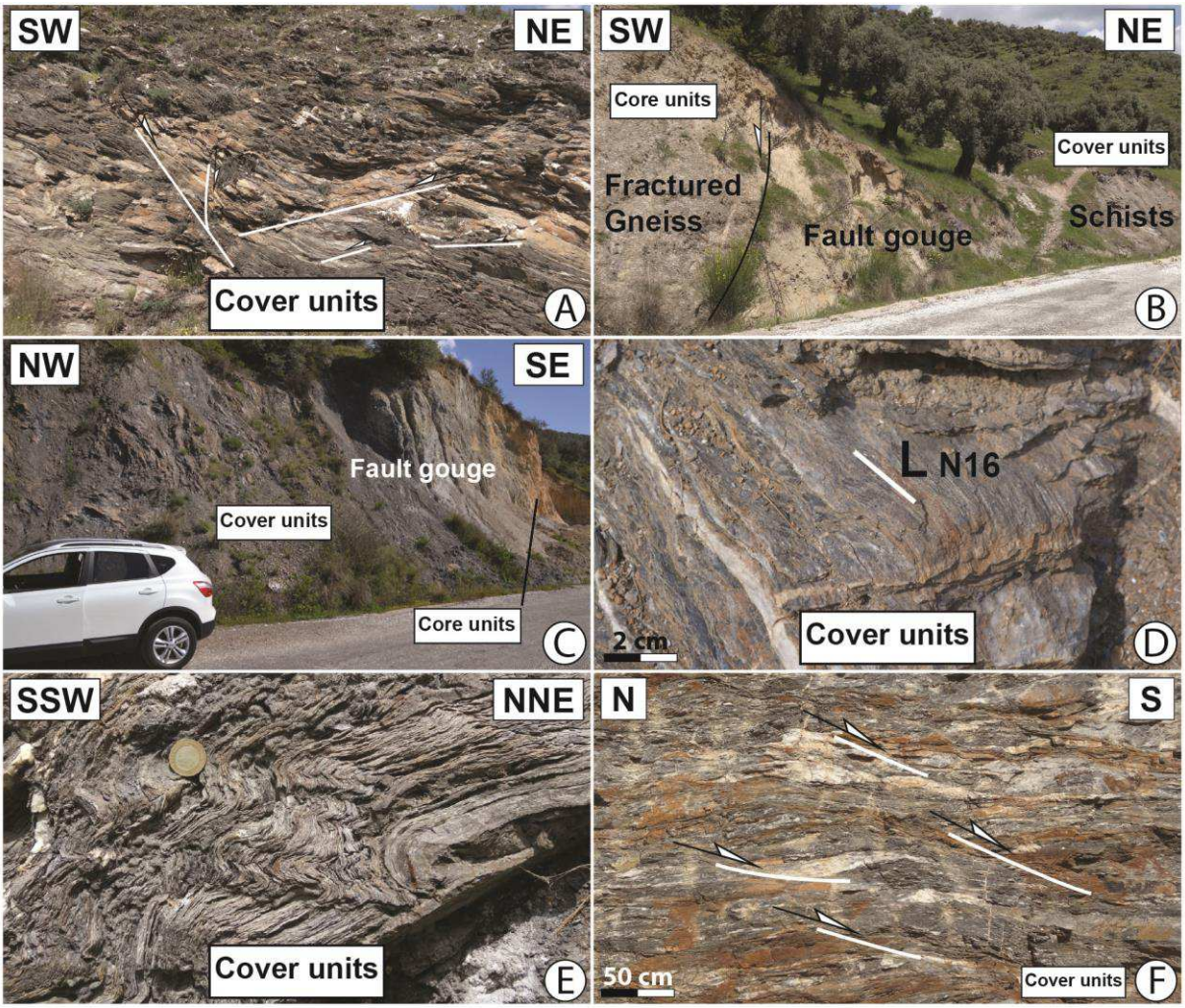

Figure V.7: Kinematic of deformation in the Büyük Menderes graben. (a) Metric to centimetric low-angle normal faults deforming the main foliation in the cover series with a top-SW shearing. Note also the presence of brittle kinematic indicators indicating opposite shearing. (b) NW-SE trending normal fault between gneiss (basement unit) and schists (cover unit). (c) N20°E trending high-angle transfer fault separating the basement and the cover units. (d) Stretching lineations underline by white micas in schists. (e) Folds overturn in the SSW direction. A local crenulation cleavage is developed within the hinge of these folds. (f) Close-up view of centimetric low-angle normal faults indicating a top-to-the-S sense of shear. See Figure V.4 for location.

V.3.4. SMM area: from Kurudere to Çine

In the Selimiye area (Fig. V.4), a well-developed foliation can be observed across the whole metasedimentary cover as well as within a part of the underlying gneiss core (Fig. V.8a). From bottom to top, the metasedimentary rocks consist mainly in (i) lower fine-grained biotite and muscovite schists; (ii) garnet-bearing rocks within the biotite-muscovite schist and calc-schists and (iii) marbles with phyllite intercalations [Whitney *et al.*, 2008]. Foliation strikes E-W strike and dips gently toward the SW (Fig. V.4). The stretching lineation is consistent through the entire cover sequence, and it is mainly defined by stretched minerals such as quartz, plagioclase, hornblende and chloritoid, plus mica/chlorite aggregates. The lineation is N15°E (± 15°) and plunges toward the south. The main contact between the core of the Menderes Massif and its cover is well exposed near Kayabükü (Fig. V.4) where it appears as a thick mylonitic zone that affects both units (Fig. V.8a). Late undeformed dykes cut across the gneiss foliation and are locally sheared toward the south (Fig. V.8b). Just above this contact, the sedimentary cover shows top-to-the-S shearing markers increasing in abundance close to the contact, and disappearing toward the south. Consistent top-to-the-S ductile shearing is revealed by (i) micro- to macroscopic shear-bands (Fig. V.8c), (ii) pressure shadows surrounding garnets (Fig. V.8d) and (iii) asymmetric boudinage. The cover of the Menderes crops out above this main shear zone north of Kurudere. It consists of Late Triassic metaconglomerates with magnesiocarpholite-kyanite assemblages (Fig. V.8e) [Rimmelé *et al.*, 2003] overlain by Mesozoic marbles. There, the foliation strikes approximately E-W and dips toward the south. N-S-trending lineation is marked by the stretching of white mica and kyanite (Fig. V.8e). According to Whitney *et al.* [2008] the associated kinematics is top-to-the-N.

Top-to-the-N deformation is also recorded throughout the entire area within the core of the Massif and its cover as observed predominantly in thin section close to the main contact, and far from it. According to Bozkurt and Park [1999] asymmetric pressure shadows around porphyroblasts, curved quartz inclusion trails in garnet and albite (Fig. V.8d), and asymmetry of intrafolial folds are evidence of a previous top-to-the-N deformation. In addition, the uppermost part of the Menderes sedimentary cover is also strongly folded (Fig. V.8f). These folds with E-W axes are often overturned toward the north, keeping a top-to-the-N sense of shear. Similar to Selimiye area, top-to-the-S shear-bands cut older top-to-the-N shear bands associated with quartz veins boudinage in the granite near Sarikaya (Figs. V.4

and V.8g). Similar kinematic was also observed near Çine (Fig. V.4). There, orthogneisses (augen gneisses), migmatites, gneisses and pegmatites, belonging to the MMCC core display a N-S-trending lineation marked by elongated biotite and muscovite aggregates with metric-to centimetric shear bands indicating a top-to-the-N deformation (*e.g.* mica-rich shear bands wrapping around feldspar augen, Fig. V.8h). Locally, the basement is intensely deformed with the development of a penetrative foliation, but the origin of this deformation is still unclear.

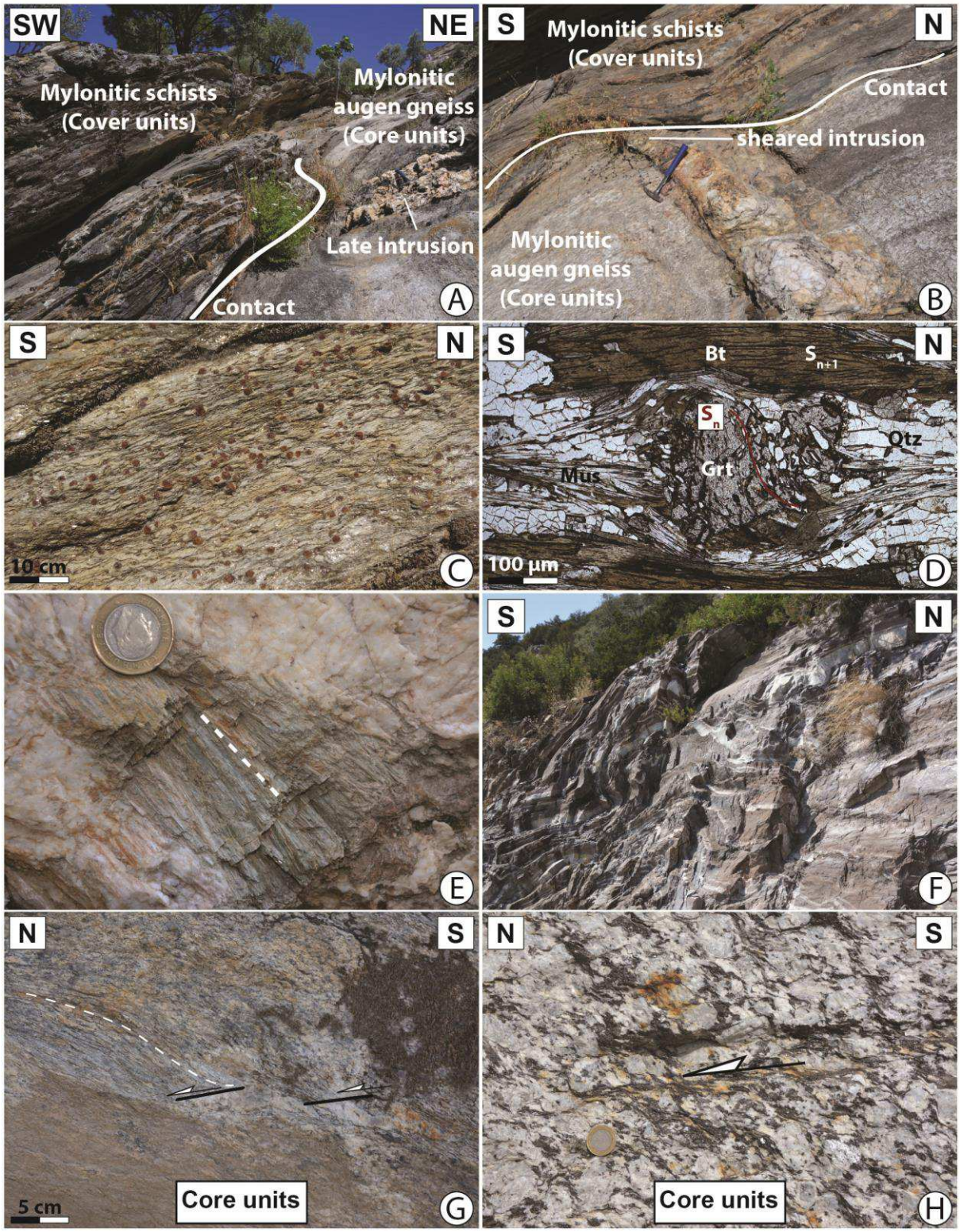

Figure V.8: Kinematic of deformation in the Selimiye area and in the SMM. (a) Intrusive and then mylonitized contact between the Core and the Cover, implying a strong reworking of the basement. (b) Dyke crosscutting the main penetrative foliation. (c) Shear bands in garnet-bearing rocks showing a top-to-the-S sense of shear. (d) Biotite and muscovite pressure shadow around garnet indicating a top-to-south shearing in thin section. Note that an early fabric is preserved in garnet inclusion. (e) Carpholite bearing rocks near Kurudere. (f) Metric folds in the red marbles of the Menderes cover with ~ N120°E fold axes. (g) Asymmetric quartz veins in a granite and associated shear bands. (h) Centimetric shear bands decorated with biotite and muscovite around feldspars in the Augen gneiss unit. See Figure V.4 for location.

V.4. Quantitative T and age constraints

^{40}Ar-^{39}Ar and U-Pb dating as well as peak-temperature conditions were quantitatively explored (see *Appendix V.8.1.* for analytical details). Mica (biotite and/or muscovite) ^{40}Ar-^{39}Ar dating was conducted on 15 rock samples along selected cross-sections to provide a regional coverage (Tables V.1 and V.2). U-Pb monazite ages were also obtained on two samples from the CMM (Table V.2). The maximum temperature (T_{max}) was estimated using Raman Spectroscopy of Carbonaceous Material (RSCM) (Table V.3). Analytical techniques used herein are briefly presented in *Appendix V.8.1.3.* and described at length elsewhere [*e.g.* Beyssac *et al.*, 2002; Lahfid *et al.*, 2010]. Carbonaceous material (CM)-rich metasedimentary rocks were collected across the entire massif to provide a complete transect of T_{max} across the Menderes MCC (Table V.3).

V.4.1. ^{40}Ar-^{39}Ar dating in the CMM and SMM

Six main rock types were analyzed by the step heating method applied to single grains or minute mica-rich aggregates using a continuous CO_2-laser source. (i) A metaconglomerate level with carpholite-bearing paragenesis in Kurudere Unit (samples M89a-15; M89b-15). (ii) A coarse-grained orthogneisses with feldspar porphyroclasts (sample M85-15). (iii) Fine-grained paragneisses with feldspar ± garnets (M143-15; M145-15; M146-15). (iv) Muscovite-rich schist layers within quartzite (M48-15; M148-15; M57-16; M79-16). (v) Biotite-muscovite schists with or without garnets (M47-16; M67-16; M69-16). (vi) Biotite-muscovite schists with albite (M115-15; M140-15). In addition, *in-situ* dating was performed with the UV laser probe on three polished rock disks selected from key locations and/or displaying diagnostic microstructures (metapelites M69-16, M89-15, and M115-15). Location of these samples are given in the *Appendix V.8.2.* in the Figure V.19 and some results are presented in Figure V.9a. Results are also presented in the form of tables (*e.g.* Tables V.1 and V.2; *Appendix V.8.2.*, Tables V.5, V.6, V.7, V.8 and V.9).

	Location				Sample information		Step Heating				
Samples	*Lat*	*Long*	*Localities*	*Area*	*Structural position*	*Lithologies*	*Runs*	*Mineral*	*Weight (µg)*	*Number of grain*	*TGA (Ma)(1σ)*
M148-15	37.9702	28.1704	Haliköy-Malgaçemir	CMM	Footwall of the Büyük Menderes detachment	Quartzite + white mica	N148-MS2	Ms	0.380	12	25.1 ± 0.3
M146-15	37.9797	28.1711	Haliköy-Malgaçemir	CMM	Footwall of the Büyük Menderes detachment	Paragneiss	N145-MS2	Bt	0.216	8	23.6 ± 0.1
							N147-MS2	Ms	0.276	5	26.5 ± 0.3
M115-15	38.3484	28.0878	Bozdağ	CMM	Hanging-wall of the Bozdağ shear zone	Micaschist	N143-MS2	Ms	0.186	2	19.3 ± 0.1
							N144-MS2	Bt	0.310	9	19.2 ± 0.1
M145-15	37.9874	28.1738	Haliköy-Malgaçemir	CMM	Footwall of the Büyük Menderes detachment	Para-gneiss	N149-MS2	Bt	0.184	3	25.1 ± 0.2
							N146-MS2	Ms	0.306	2	22.4 ± 0.3
M67-16	37.4571	27.6679	Kandad-Konak	SMM	Selimiye shear zone	Garnet Schist	N162-MS2	Ms	0.336	1	32.8 ± 0.3
							N154-MS2	Bt	0.280	3	18.3 ± 0.1
M57-16	37.8965	27.8505	Zeytinköy	CMM	Footwall of the Büyük Menderes detachment	Micaschist	N156-MS2	Ms	0.208	1	18 ± 3
M140-15	38.0772	28.1602	Haliköy-Malgaçemir	CMM	Footwall of the Büyük Menderes detachment	Micaschist	N157-MS2	Ms	0.260	1	20.2 ± 0.3
							N153-MS2	Bt	0.176	2	21.9 ± 0.1
M85-15	37.5228	28.0359	Umur	SMM	Menderes Basement (Cine nappe)	Orthogneiss	N150-MS2	Bt	0.350	3	222.2 ± 0.9
							N160-MS2	Ms	0.050	2	89.5 ± 0.4
M47-16	38.2101	28.5599	Uluderbent	CMM	Hanging-wall of the Alaşehir detachment	Micaschist	N70-MS3	Bt	0.020	1	24.4 ± 0.2
							N69-MS3	Ms	0.032	1	24.8 ± 0.2
M143-15	38.0352	28.1590	Haliköy-Malgaçemir	CMM	Footwall of the Büyük Menderes detachment	Micaschist ± garnet	N158-MS2	Ms	0.270	4	23.7 ± 0.2
M48-15	37.9004	28.1066	Sultanhisar	CMM	Footwall of the Büyük Menderes detachment	Schist	N161-MS2	Ms	0.280	1	19.1 ± 0.3
M127-15	38.2986	28.0509	Ovacik	CMM	Hanging-wall of the Bozdağ shear zone	Micaschist	N163/N165-MS2	Ms	0.100	2	-
M79-16	37.4020	27.6697	Haciahmetler	SMM	Mezosoic Cover	Para-gneiss	N155-MS2	Ms	0.170	10	38.4 ± 0.2
M89a-15	37.4000	27.6100	Kurudere	SMM	Mezosoic Cover	Metaconglomerate ± carpholite	N166.MS2	Ms	0.104	1	37.3 ± 0.3
M89b-15							N167.MS2	Ms	0.076	1	37.1 ± 0.4

Table V.1: ^{40}Ar-^{39}Ar step heating from the Menderes Metamorphic Core Complex (Western Turkey).

All chemical analyses of white micas and biotite were conducted with an automated Camebax electron microprobe in Orléans and Grenoble. Operating conditions were 15 kV accelerating voltage, 6.062 nA sample current and 10 set counting time. Natural minerals were used as standards. As shown in Figures V.9b and V.9c, large variations in white micas and biotites composition are observed according to the mineral paragenesis (intersample variations marked by $X_{(Mg)}$ = Mg/(Mg + Fe)) and (2) of the extent of the [(Mg,Fe)Si-Al_2] celadonitic substitution for the white micas and [(Mg,Fe)Si-Ti] (intrasample variations). Intersample variations are controlled by the whole rock chemistry, muscovite from sample M57-16 represents the most Mg-rich mica schist with $X_{(Mg)}$ mean values around 0.75. Other samples display intermediate $X_{(Mg)}$ values between 0.70 and 0.30 (Fig. V.9b). A large spread of the $X_{(Mg)}$ ranging from 0.10 to 0.55 is also observed within muscovite from sample M79-16 that consists on muscovite-rich layer within quartzite (Fig. V.9b). It is noteworthy that the celadonitic substitution explains the main chemical variation within each sample. The highest contents of Si are recorded in the biotite-muscovite schists (M47-16). This sample shows a large spread of the Si apfu values ranging from 3.65 to 3.10 (Fig. V.9b). Other samples range between 3.5 and 3.0 apfu (Fig. V.9b). Samples M47-16 and M57-16 are the most Mg-rich biotite schist with $X_{(Mg)}$ values between 0.70 to 0.60 (Fig. V.9c) whereas the $X_{(Mg)}$ of other samples range from 0.50 to 0.40. The highest contents of Si and Ti are recorded in the biotite-muscovite schists (M67-16; M47-16) (Fig. V.9c). With a few measurements only, it can be noted a strong variation of Si apfu within the augen gneiss (M85-15) and the quartzite (M57-16) in spite of the low amount of data (Fig. V.9c).

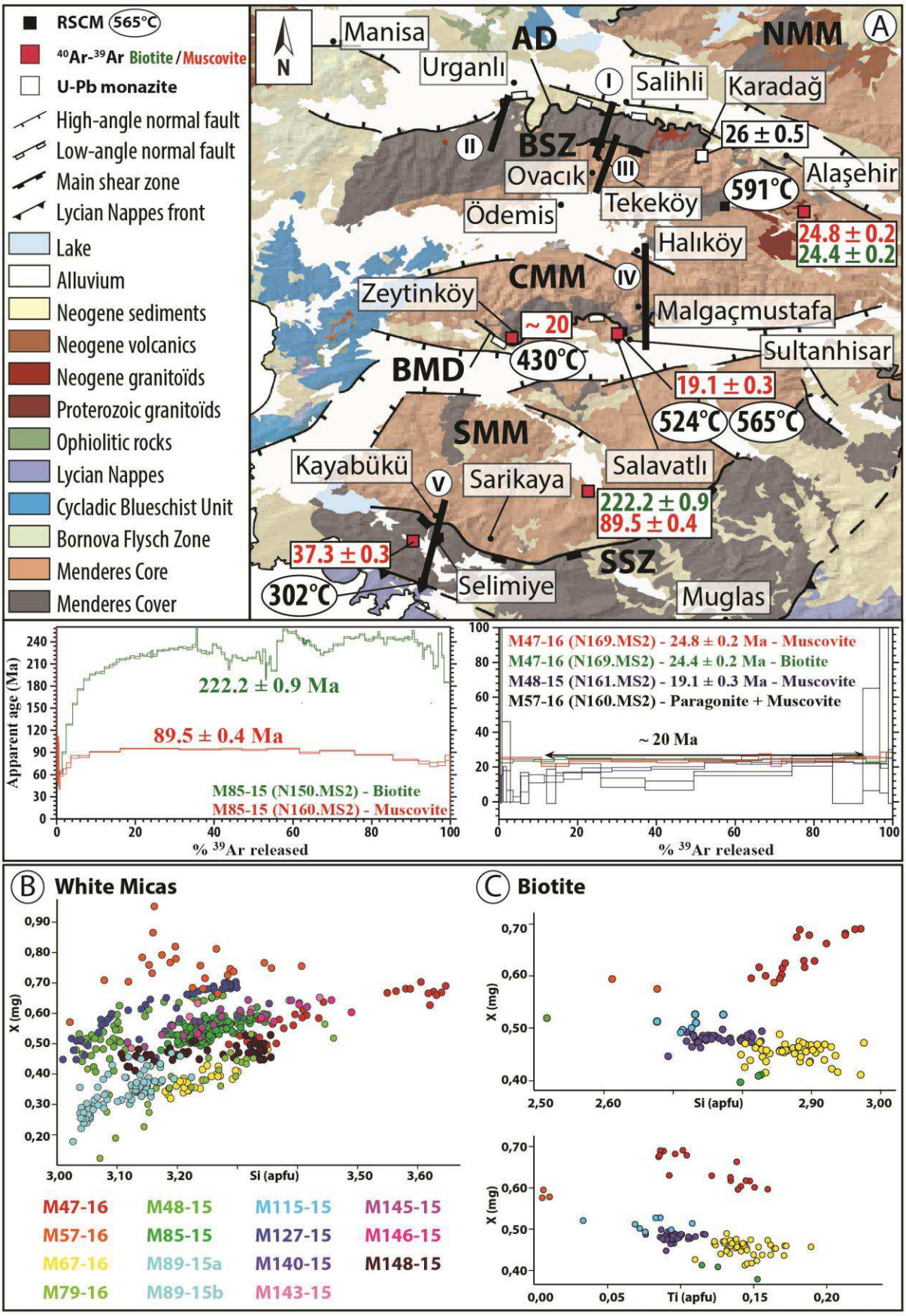
RSCM 565°C
40Ar-39Ar Biotite / Muscovite
U-Pb monazite
High-angle normal fault
Low-angle normal fault
Main shear zone
Lycian Nappes front
Lake
Alluvium
Neogene sediments
Neogene volcanics
Neogene granitoïds
Proterozoic granitoïds
Ophiolitic rocks
Lycian Nappes
Cycladic Blueschist Unit
Bornova Flysch Zone
Menderes Core
Menderes Cover
N
Manisa
Urganlı
AD
NMM
A
Salihli
Karadağ
I
II
BSZ
III
Ovacık
26 ± 0.5
Alaşehir
591°C
Tekeköy
Ödemis
Halıköy
24.8 ± 0.2
24.4 ± 0.2
CMM
IV
Zeytinköy
~ 20
Malgaçmustafa
Sultanhisar
430°C
BMD
19.1 ± 0.3
524°C
565°C
SMM
Kayabükü
V
Sarikaya
Salavatlı
222.2 ± 0.9
89.5 ± 0.4
37.3 ± 0.3
SSZ
302°C
Selimiye
Muglas
Apparent age (Ma)
222.2 ± 0.9 Ma
89.5 ± 0.4 Ma
M85-15 (N150.MS2) - Biotite
M85-15 (N160.MS2) - Muscovite
% 39Ar released
M47-16 (N169.MS2) - 24.8 ± 0.2 Ma - Muscovite
M47-16 (N169.MS2) - 24.4 ± 0.2 Ma - Biotite
M48-15 (N161.MS2) - 19.1 ± 0.3 Ma - Muscovite
M57-16 (N160.MS2) - Paragonite + Muscovite
~ 20 Ma
% 39Ar released
B White Micas
X (mg)
Si (apfu)
M47-16
M48-15
M115-15
M145-15
M57-16
M85-15
M127-15
M146-15
M67-16
M89-15a
M140-15
M148-15
M79-16
M89-15b
M143-15
C Biotite
X (mg)
Si (apfu)
X (mg)
Ti (apfu)

Figure V.9: Geochronological ages with mica composition and RSCM temperature results in CMM and SMM. (a) Simplified geological map of the Menderes Massif showing the distribution of RSCM temperatures and ^{40}Ar-^{39}Ar ages and monazites ages. Red, black and whites squares indicate ^{40}Ar-^{39}Ar ages, Raman temperatures, and monazites, respectively. Also indicated is diagrams showing ^{40}Ar-^{39}Ar step-heating bulk sample age spectra of micas. (b) $X_{(mg)}$-Si diagram showing the main variations in white mica composition in all samples. (c) $X_{(mg)}$-Si and $X_{(mg)}$-Ti diagrams showing the main variations in biotite composition in all samples. Note that some analyses are given in Appendix V.8.3., Tables V.12, V.13, V.14.

V.4.1.1. CMM area

Samples M48-15 and M57-16 are located in the Büyük Menderes area (*Appendix V.8.2.*, Fig. V.19a). Foliation is mainly defined by recrystallized quartz. However, these quartzite levels are locally interbedded with thin levels of fine-grained micas and chlorite. Both samples are rich in organic matter. Both ^{40}Ar-^{39}Ar release spectra were obtained by incrementally heating two muscovite grains (0.280 µg and 0.208 µg), and each sample defines plateau-like segments over 90% (Fig. V.9a) and ~ 85% (Fig. V.9a) of the total ^{39}Ar release, with calculated weighted mean ages of 19.1 ± 0.3 Ma (1σ) and ~ 20 Ma, respectively (Fig. V.9a). Sample M47-16 is a mica-schist from which we separated two clusters of micas (0.032 µg of muscovite) and (0.02 µg of biotite). The corresponding age spectra for muscovite and biotite show integrated ages of 24.8 ± 0.2 Ma (1σ) and 24.4 ± 0.2 Ma (1σ), respectively (Fig. V.9a).

	Location				Sample information		*In Situ*		
							$^{40}Ar/^{39}Ar$		U-Pb
Samples	*Lat*	*Long*	*Localities*	*Area*	*Structural position*	*Lithologies*	*Runs*	*TGA (Ma)(1σ)*	*TGA (Ma)(2σ)*
M69-16	37.4520	27.6642	Selimiye	SMM	Selimiye shear zone	Garnet Schist	N73-MS1	45.9 ± 0.5	nb
M89a-15	37.4000	27.6100	Kurudere	SMM	Mezosoic Cover	Metaconglomerate ± carpholite	N74-MS1	39.1 ± 0.2	nb
M115-15	38.3484	28.0878	Bozdağ	CMM	Hanging-wall of the Bozdağ shear zone	Micaschist	N72-MS1	19,4 ± 0,2	nb
M24-16	38.3546	28.3158	Karadağ	CMM	Hanging-wall of the Alaşehir detachment	Micaschist	-	nb	26.0 ± 0.5
M120-15	38.3604	28.0892	Bozdağ	CMM	Hanging-wall of the Bozdağ shear zone	Micaschist	-	nb	21.5 ± 0.5

Table V.2: ^{40}Ar-^{39}Ar and U-Pb in situ data from the Menderes Metamorphic Core Complex (Western Turkey).

V.4.1.2. The Bozdağ - Birgi areas

Sample M115-15 is defined by biotite-muscovite schists with porphyroblasts of albite, displaying two main fabrics. The first one is only defined by the presence of albite with straight organic matter inclusion trails (S_n) (Fig. V.5h), and the second one is developed during a greenschist-facies deformation with biotite, muscovite and chlorite growing in the shear bands and in pressure shadows around albite porphyroblasts (Fig. V.5h). It shows a penetrative deformation associated with Bozdağ shear zone. A cluster of white micas and biotites directly extracted from the hand specimen and weighing about 0.186 and 0.31 µg, respectively was analyzed by step heating. The corresponding age spectra show a total gas

age of 19.3 ± 0.1 Ma (1σ) for white micas and 19.2 ± 0.1 Ma (1σ) for biotite (Figs. V.10a and V.10b). At first glance, *in situ* results are consistent with the step heating ages (Figs. V.10c and *Appendix V.8.2.*, Table V.5). In details, results show mostly an age distribution range from 16.34 to 20.92 Ma with a mean value of 19.09 Ma for all micas. Note that two biotites located in the main foliation, yield an age of 26.36 ± 3.02 Ma (1σ) (#69, see *Appendix V.8.2.*, Table V.5) and 12.93 ± 0.98 Ma (1σ) (#6, see *Appendix V.8.2.*, Table V.5). Sample M127-15 is defined by a large amount of quartz with minor muscovite, biotite and garnets from which we separated a small population of white micas (0.1 µg). Muscovites yield a plateau age of ~ 18 Ma related to 60 % of ^{39}Ar released (Fig. V.10a and V.10b).

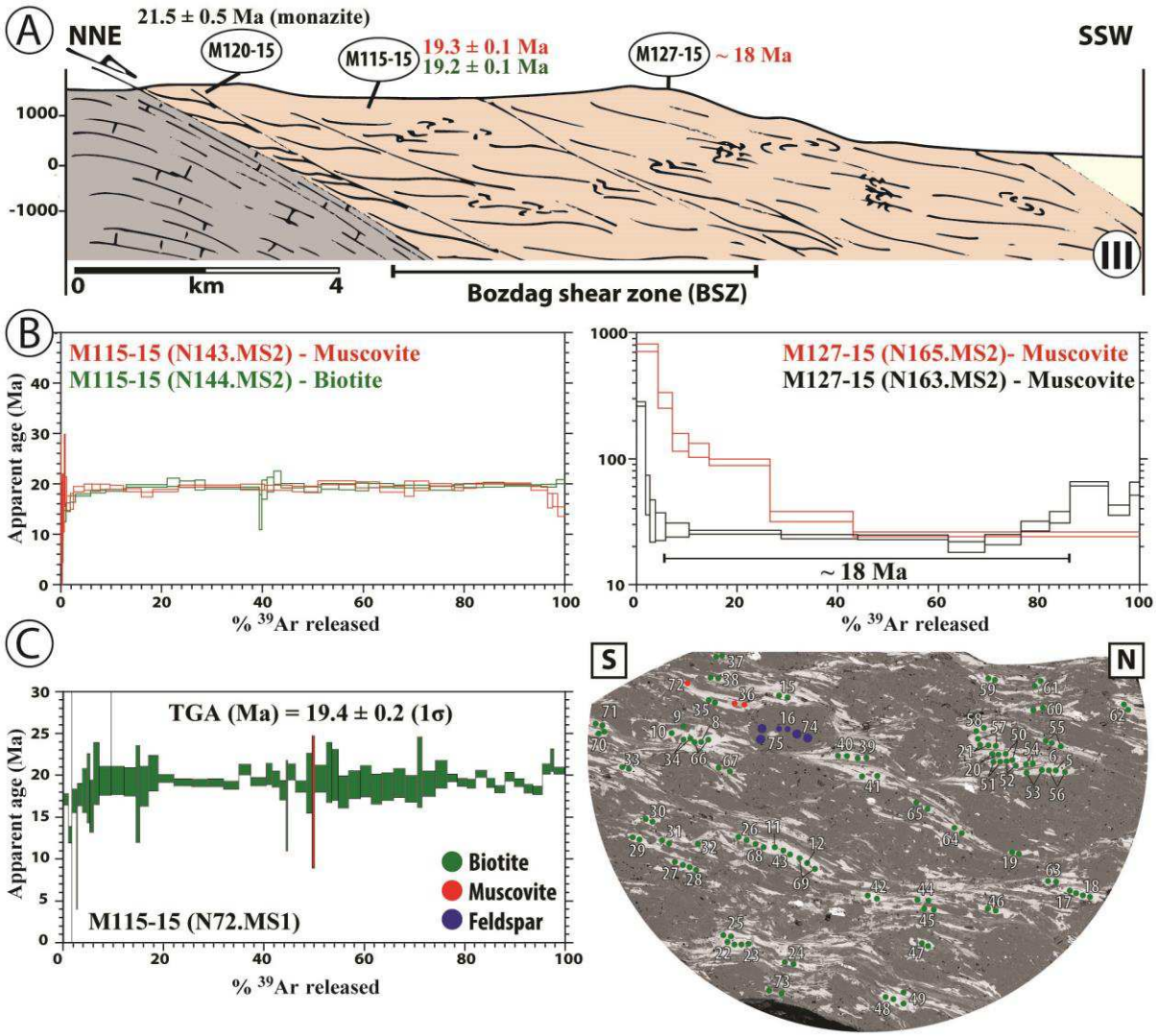

Figure V.10: Main ^{40}Ar-^{39}Ar results in the northern part of CMM. (a) Simplified cross-section of the area with integrated ^{40}Ar-^{39}Ar ages. (b) and (c) Diagrams showing ^{40}Ar-^{39}Ar step-heating bulk sample age spectra of micas and in situ analyses of biotite garnets-bearing rock, respectively. In situ results are indicated in Appendix V.8.2., Table V.5. Note the homogenous ages on the left diagram in between the foliation and the shear bands in the disk.

V.4.1.3. Halıköy - Sultanhisar areas

The fine-grained paragneiss is well-exposed in the CMM, and particularly in the central part of the massif. There, foliation is mainly defined by quartz and mica aggregates. In some cases, crenulation cleavage is also developed in muscovite rich-levels (*e.g.* Sample M145-15). Sample M140-15 seems to be less deformed than the previous ones displaying two generations of biotite. The late generation marks the foliation and the earlier one is perpendicular to it. Albite porphyroblasts are also observed in thin section, and seems to be associated with the first biotite generation. Chlorite and muscovite also mark the main foliation. One white mica and a small population of biotites directly extracted from the hand specimen (0.26 and 0.176 µg, respectively) were also analyzed. The corresponding age spectrum shows a total gas age for muscovite of 20.2 ± 0.3 Ma (1σ) and 21.9 ± 0.1 Ma (1σ) for biotite (Figs. V.11a and V.11b; *Appendix V.8.2.*, Table V.8). Samples M143-15 and M145-15 consist of fine-grained paragneisses with feldspar, micas ± garnets. A small population of muscovite (0.27 µg) directly extracted from the hand specimen M143-15 were analyzed. 23 heating steps were extracted given a concordant ^{40}Ar-^{39}Ar spectrum of 23.7 ± 0.2 Ma (Fig. V.11). We separated a small population of micas from sample M145-15 (0.184 µg of biotite and 0.306 µg of muscovite), from which 19 and 22 heating steps were extracted to give a concordant ^{40}Ar-^{39}Ar spectrum of 24.1± 0.2 Ma (biotite) and 22.4 ± 0.3 Ma (muscovite) (*e.g. Appendix V.8.2.*, Table V.9), respectively (Fig. V.11). Sample M146-15 is similar to the previous one, and we separated a small population of white micas (0.276 µg) and biotites (0.216 µg). The corresponding age spectrum shows apparent ages climbing to 70 Ma for muscovite (Fig. V.11). The total gas age for muscovite and biotite is 26.5 ± 0.3 Ma (1σ) and 23.6 ± 0.1 Ma (1σ), respectively (Fig. V.11). Sample M148-15 belongs to the quartzite group and it is rich in organic matter. This sample consists on fine-grained micas, recrystallized quartz and chlorite from which we separated a small population of white micas (0.38 µg) from which 21 heating steps were extracted to give a concordant ^{40}Ar-^{39}Ar spectrum of 25.1 ± 0.3 Ma (1σ) (Fig. V.11).

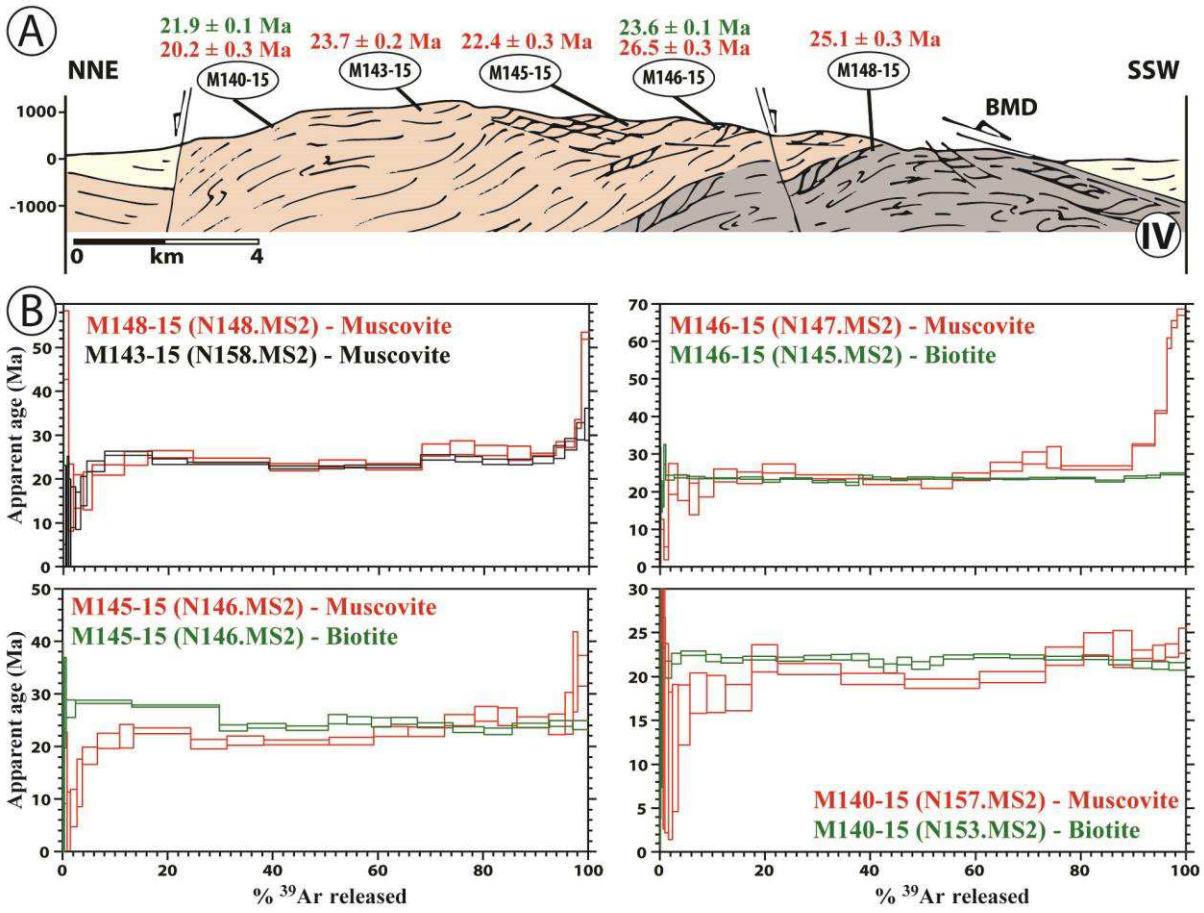

Figure V.11: Main ^{40}Ar-^{39}Ar results in the southern part of CMM. (a) Simplified cross-section of the area with integrated ^{40}Ar-^{39}Ar ages. (b) Diagrams showing ^{40}Ar-^{39}Ar step-heating bulk sample age spectra of micas.

V.4.1.4. SMM area: from Çine to Kurudere

The coarse-grained orthogneisses are characterized by the abundance of large augen of crystallized feldspars (Fig. V.8h). Depending on localities, these feldspars are totally transposed in a mylonitic foliation parallel to the main foliation, with strong grain-size reduction in shear zone. Sample M85-15 represents an intermediate stage of this deformation displaying a large amount of elongated biotite and muscovite within the shear bands and around the feldspars. A cluster of white micas and biotites directly extracted from the hand specimen and weighing about 0.05 and 0.35 µg, respectively, were analyzed by step heating. The corresponding age spectrum for biotite (Fig. V.9a) shows apparent ages climbing to ~ 250 Ma. The total gas age for muscovite and biotite are 89.5 ± 0.4 Ma (1σ) and 222.2 ± 0.9 Ma (1σ), respectively (Fig. V.9a).

Samples M67-16 and M69-16 consist in biotite-muscovite schists ± garnets. Foliation is defined by biotite, muscovite and quartz. Locally, biotite oblique on the main foliation is also observed (*e.g.* Sample M67-16). The presence of garnets with quartz inclusion trails in sample M69-16 indicates a first deformation event, whereas the main fabric corresponds to a later event associated with biotite and

muscovite crystallization. A cluster of white micas (0.336 µg) and a small population of biotites (0.28 µg) were directly extracted from sample M67-16. The total gas ages for muscovite and biotite are 32.8 ± 0.3 Ma (1σ) and 18.3 ± 0.1 Ma (1σ), respectively (Figs. V.12a and V.12b). Sample 79-16 belongs to the quartzite group, and foliation is mainly defined by quartz, white micas and chlorite. We separated a small population of white micas (0.17 µg) from which 20 heating steps were extracted to give a concordant ^{40}Ar-^{39}Ar spectrum at 38.4 ± 0.2 Ma (Figs. V.12a and V.12b). Sample M69-16 was analyzed using the *in situ* method. Results are consistent within the foliation and shear bands, showing an average of 45.9 ± 0.5 Ma (1σ) (Fig. V.12c*; Appendix V.8.2.*, Table V.6). In addition, two biotites yield an older age of 67.04 ± 4.29 Ma (1σ) (#64, see *Appendix V.8.2.*, Table V.6) and 74.37 ± 4.54 Ma (1σ) (#63, see *Appendix V.8.2.*, Table V.6) (Fig. V.12c).

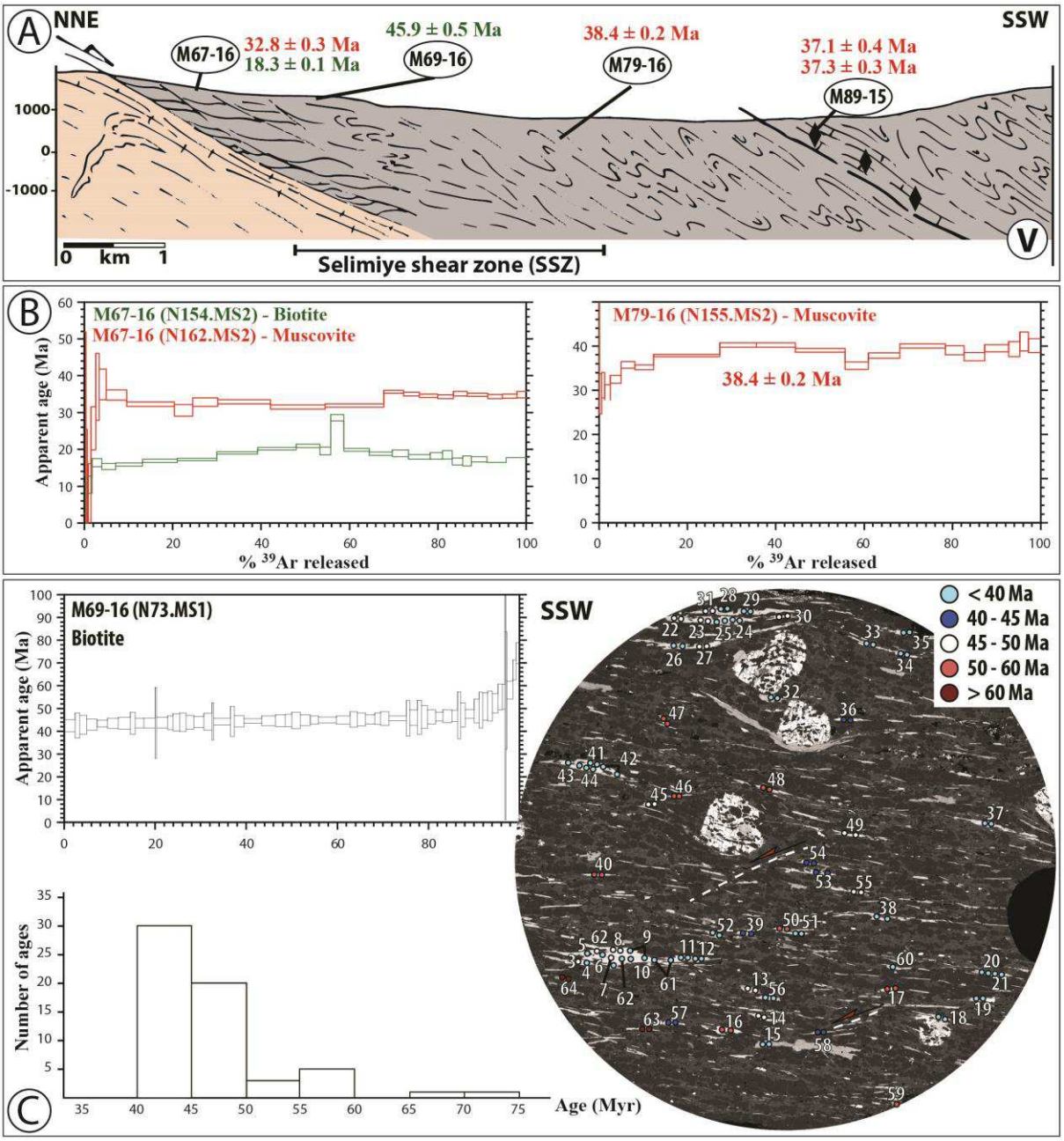

Figure V.12: Main ^{40}Ar-^{39}Ar results in the SMM. (a) Simplified cross-section of the area with ^{40}Ar-^{39}Ar ages. (b) ^{40}Ar-^{39}Ar step-heating bulk sample age spectra of micas in the southern SMM. Integrated ages are given with 1σ. (c) In situ analyses of biotite garnets-bearing rocks. Note the difference between these ages and the intrasample variation of the sample M67-16. In situ results are indicated in Appendix V.8.2., Table V.6.

Foliation in the Kurudere metaconglomerate is marked by the high-pressure association Qtz + Car + Ky ± Ms + Chl (Sample M89-15a) (Fig. V.13a). Locally, HP-LT rocks are strongly retrograded under greenschist-facies conditions (Sample M89-15b), involving breakdown of carpholite into kyanite and chlorite. In addition, white micas in thin sections also have a rounded shape in quartz-rich levels (Fig. V.13b). Both methods (*i.e. in situ* and step heating) show a total gas age for muscovite of 37 – 39 Ma (1σ) (Figs. V.12a and V.13b). Note that the corresponding age spectrum for muscovite on the little

disk shows apparent ages ranging from 36 – 57 Ma (Fig. V.13b) and reaching locally 76.57 ± 8.88 Ma (1σ) (#91, *Appendix V.8.2.*, Table V.7).

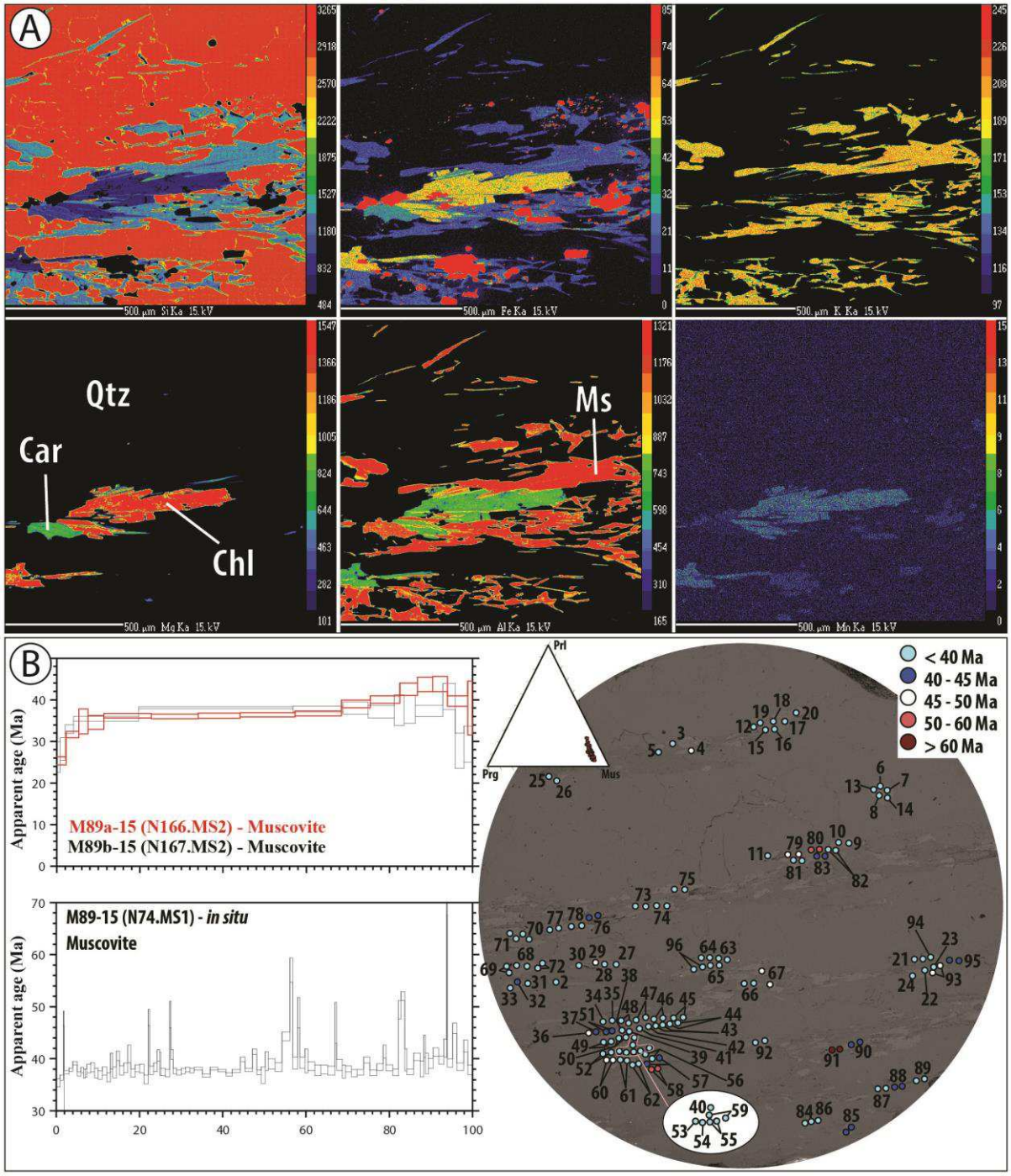

Figure V.13: Main ^{40}Ar-^{39}Ar results in carpholite bearing rocks near Kurudere. (a) Carpholite bearing-rocks and associated chemical mapping with EPMA on Si, Fe, K, Mg, Al and Mn. Note that carpholite is locally preserved in the foliation. (b) ^{40}Ar-^{39}Ar step-heating bulk sample age spectra of micas and in situ analyses of the muscovite in the carpholite-bearing rocks. In situ results are indicated in Appendix V.8.2., Table V.7.

V.4.2. U-Pb dating in the CMM

Sample M120-15 is located in the CMM close to Tekeköy (Fig. V.4) and shows a strong deformation. There, foliation cross cuts locally porphyroblast of albite and garnet. It is marked by the association quartz + micas (Fig. V.14a). Elongated subhedral monazites grains are present only in the foliation associated with the white micas (Figs. V.14a and V.14b). It is important to note the minor occurrence of chlorite in the thin section, suggesting a low fluid circulation during the shear zone activity. Sample M24-16 is located in the hanging-wall of the Alaşehir detachment located in the north of Karadağ zone (Fig. V.9 and *Appendix V.8.2.*, Fig. V.19). It is characterized by the abundance of micas, quartz and feldspars (Fig. V.14c). Similar to the previous one, monazites are associated with mica crystallization that defines the main foliation together with iron oxides. Although monazite grains are elongated, deformation in this sample is less important. In addition, monazite is also rich in inclusions, and locally affected by deformation. No evidence of zonation was observed by SEM imaging (Fig. V.14d). Operating conditions were 15 kV accelerating voltage, and 40 nA sample current. Natural minerals were used as standards.

Results of the two samples are shown in Figure V.14, Table V.2 and in *Appendix V.8.2.* (Tables V.10 and V.11). Although the variability in error ellipses in Figure V.14 is a direct consequence of limited amount of ^{235}U and ^{207}Pb in these monazites, the ages are consistent with ^{238}U-^{206}Pb geochronometer. Monazite grains measured in situ in thin sections from a schist (M120-15) from Bozdağ shear zone yield a concordia age of 21.5 ± 0.5 Ma (MSWD = 2.5; n = 14; Fig. V.14d). These monazites grains are small (< 20 µm) and mainly included in white micas (Fig. V.14b). Monazite grains analyzed in situ in thin sections from schist (M24-16) yield a concordia age of 26.5 ± 0.5 Ma (MSWD = 9.1; n = 25; Fig. V.14f). These monazites have an intermediate size ranging from 10 to 50 µm, and occur mainly within micas (Figs. V.14c and V.14d). In addition, results of two samples are consistent with the Th-Pb diagram (Fig. V.14g).

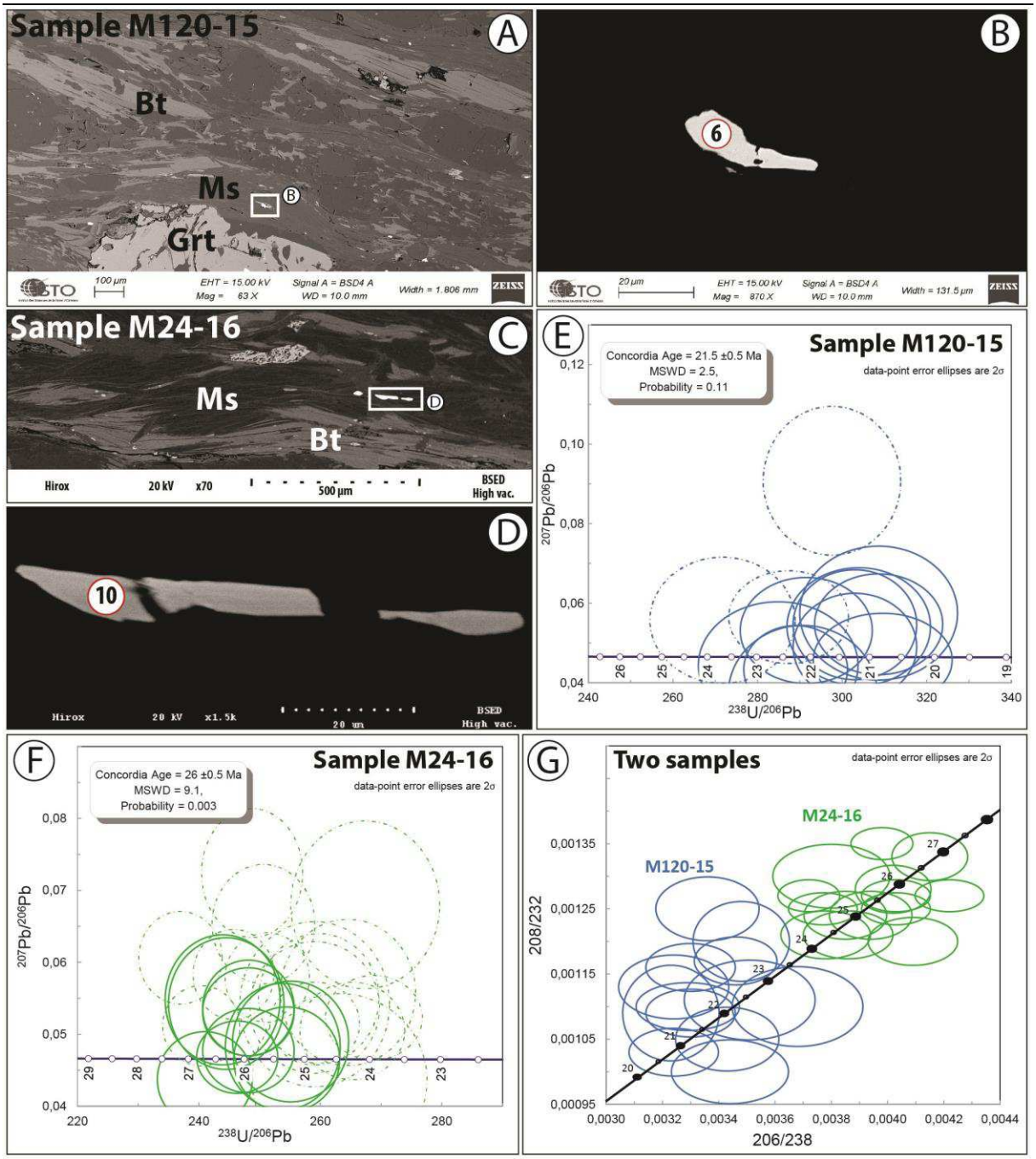

Figure V.14: Tera-Wasserburg and Th-Pb plots of monazite. (a) Sample M120-15 showing elongated monazite included in the main foliation marked by muscovite. (b) Close-up view of monazite analyzed. The number corresponds to the analyze 6, see Appendix V.8.2., Table V.11. (c) Sample M24-16 showing elongated monazite included in muscovite, which defined the main foliation. (d) Close-up view of monazite analyzed and corresponding number of this analyze (see Appendix V.8.2., Table V.10). (e) and (f) Concordia diagram for monazite grains from schist samples M120-15 and M24-16. (g) Th-Pb diagram showing results of two samples. All analyses shown at 2σ error ellipses. Sample locations are indicated in Figures V.9a and V.19.

V.4.3. RSCM T_{max} results

The data set consists of 36 CM-bearing samples collected in metasedimentary layers regularly distributed within both the cover and the basement (*i.e.* core) of the Menderes Massif; 12 samples are located in the Selimiye area and others in the CMM and SMM (*Appendix V.8.2.*, Fig. V.19). RSCM temperatures are reported in Figure V.9. A sufficient number of spectra were routinely recorded for each sample to bring out (and smooth out) the within-sample structural heterogeneity of CM. Internal dispersion of RSCM T_{max} presents generally unimodal distributions and the error ranges from 11 to 47 °C (Table V.3). This high dispersion is possibly due to the presence of an inherited component of CM [Beyssac *et al.*, 2002].

	Location				Sample information		Strututral Data					RSCM			
							Foliation		Lineation				Tmax		
Samples	Lat	Long	Localities	Area	Structural position	Lithologies	DipDir	Dip	Direction	Plunge	Shear Sense	n	Mean	SD	Sigma 1
E-703-17	37.4551	27.6646	Kandad-Konak	SMM	Selimiye shear zone	Semipelitic Schist	206	35	32	196	Top-to-the-S	20	587.45	25.02	5.59
E-707-17	37.4488	27.6654	Kandad-Konak	SMM	Selimiye shear zone	Bt-Ms-Qtz Schist	-	-	-	-	-	20	569.81	23.47	5.25
E-710-17	37.4451	27.6650	Kandad-Konak	SMM	Selimiye shear zone	Quartz Schist	-	-	-	-	-	20	569.92	47.82	10.69
E-711-17	37.4445	27.6649	Kandad-Konak	SMM	Selimiye shear zone	Garnet Schist	203	27	24	196	Top-to-the-S	18	581.29	29.52	6.96
E-716-17	37.4412	27.6618	Kandad-Konak	SMM	Selimiye shear zone	Garnet Schist	202	39	35	194	Top-to-the-S	18	562.87	24.73	5.83
E-718-17	37.4407	27.6614	Kandad-Konak	SMM	Selimiye shear zone	Qtz-Bt-Ms Schist	198	48	45	192	Top-to-the-S	20	569.93	35.64	7.97
E-721-17	37.4404	27.6613	Kandad-Konak	SMM	Selimiye shear zone	Mica-qtz Schist ± garnet	202	49	46	192	Top-to-the-S	20	583.31	24.10	5.39
E-722-17	37.4402	27.6613	Kandad-Konak	SMM	Selimiye shear zone	Mica-qtz Schist ± garnet	180	34	30	187	Top-to-the-S	21	551.17	47.88	10.45
E-723-17	37.4400	27.6612	Kandad-Konak	SMM	Selimiye shear zone	Garnet Schist	188	40	36	200	Top-to-the-S	20	559.74	20.48	4.58
E-724-17	37.4395	27.6609	Kandad-Konak	SMM	Selimiye shear zone	Garnet Schist	198	47	43	204	Top-to-the-S	19	565.10	25.45	5.84
E-726-17	37.4391	27.6604	Kandad-Konak	SMM	Selimiye shear zone	Fine-grained Garnet Schist	155	57	48	185	Top-to-the-S	19	583.75	46.93	10.77
E-727-17	37.4392	27.6594	Kandad-Konak	SMM	Selimiye shear zone	Quartz Schist	212	46	13	205	Top-to-the-S	21	566.88	24.06	5.25
M75-16	37.4130	27.6863	Kilavuz	SMM	Hanging-wall of the Selimiye shear zone	Schist	-	-			Top-to-the-S	28	564.79	29.50	5.58
M74-16	37.3031	27.6280	Avşar	SMM	Lycian Nappes	Flysch	-	-	130	-	-	22	301.95	35.45	7.56
M49-16	38.2192	28.3831	Igdeli	CMM	Hanging-wall of the Alaşehir detachment	Schist	-	-	55	-	Top-to-the-N	20	591.11	30.28	6.77
M40-Sb-16	38.3824	28.3295	Çikrikçi	CMM	CBU?	Blue-schist	-	-	-	-	-	19	521.00	26.81	6.15
M57-16	37.8965	27.8505	North Aydin	CMM	Footwall of the Büyük Menderes detachment	Schist	328	28	30	-	Top-to-the-S	20	430.00	9.62	2.15
M58-15	38.3815	28.0787	North Bozdağ	CMM	Footwall of the Alaşehir detachment	Micaschist	228	72	20		-	16	580.00	22.36	5.59
M59-15	38.3905	28.0782	North Bozdağ	CMM	Footwall of the Alaşehir detachment	Micaschist	110	47	-	-	-	18	565.00	13.06	3.08
M61-15	38.4327	28.0910	Allahdiyen	CMM	Footwall of the Alaşehir detachment	Schist	331	12	25	-	Top-to-the-N	16	530.00	22.18	5.54
M108-15	38.4145	28.0861	Allahdiyen	CMM	Footwall of the Alaşehir detachment	Schist	65	28	20	-	Top-to-the-N	14	560.00	16.31	4.36
M110-15	38.3993	28.0808	Allahdiyen	CMM	Footwall of the Alaşehir detachment	Schist	304	24	-	-	-	13	491.00	21.21	5.88
M115-15	38.3484	28.0878	Bozdağ	CMM	Hanging-wall of the Bozdağ shear zone	Micaschist	177	37	10	-	Top-to-the-S	17	576.00	27.00	6.55
M118-15	38.3545	28.0891	Bozdağ	CMM	Hanging-wall of the Bozdağ shear zone	Micaschist	220	27	30	-	Top-to-the-S	15	545.00	20.80	5.37
M120-15	38.3604	28.0892	Bozdağ	CMM	Hanging-wall of the Bozdağ shear zone	Micaschist	-	-	14	-	Top-to-the-S	16	597.00	27.58	6.89
M122-15	38.3616	28.1275	Bozdağ	CMM	Hanging-wall of the Bozdağ shear zone	Schist	176	58	2	-	-	16	590.00	16.29	4.07
M123-15	38.3624	28.1275	Bozdağ	CMM	Hanging-wall of the Bozdağ shear zone	Quartzite	196	48	5	-	-	16	607.00	20.25	5.06
M135-15	38.0879	28.1673	Haliköy	CMM	Footwall of the Büyük Menderes detachment	Schist	18	24	10	-	Top-to-the-N	5	572.00	11.66	5.21
M138-15	38.0815	28.1640	Haliköy	CMM	Footwall of the Büyük Menderes detachment	Metasediment	30	33	12	-	-	15	577.00	25.40	6.56
M140-15	38.0772	28.1602	Haliköy-Malgaçemir	CMM	Footwall of the Büyük Menderes detachment	Schist	43	12	10	-	Top-to-the-S	16	573.00	16.77	4.19
M142-15	38.0641	28.1648	Haliköy-Malgaçemir	CMM	Footwall of the Büyük Menderes detachment	Schist	-	-	20	-	Top-to-the-S	13	583.00	18.93	5.25
M143-15	38.0352	28.1590	Haliköy-Malgaçemir	CMM	Footwall of the Büyük Menderes detachment	Schist ± garnet	354	8	18	-	Top-to-the-S	16	562.00	31.44	7.86
M145-15	37.9874	28.1738	Haliköy-Malgaçemir	CMM	Footwall of the Büyük Menderes detachment	Para-gneiss	332	53	22	-	Top-to-the-S	11	544.00	18.33	5.53
M146-15	37.9797	28.1711	Haliköy-Malgaçemir	CMM	Footwall of the Büyük Menderes detachment	Para-gneiss	-	-	20	-	Top-to-the-S	14	524.00	22.52	6.02
M48-15	37.9004	28.1066	Sultanhisar	CMM	Footwall of the Büyük Menderes detachment	Schist	50	56	35	-	-	18	524.00	14.21	3.35
M49-15	37.9019	28.1048	Sultanhisar	CMM	Footwall of the Büyük Menderes detachment	Schist	74	12	30	-	Top-to-the-S & top-N	15	565.00	29.29	7.56

Table V.3: Results of Raman spectra performed on samples from the Menderes Metamorphic Core Complex (Western Turkey), including the number of spectra, the maximum temperature experienced by the rock, the standard deviation (SD) and the error range (1σ). See location of the samples and results in Figures V.19, V.9a and V.15.

RSCM temperatures within the Menderes Massif embrace a wide range of temperatures from 430 to 607 °C and drastically contrast with the Lycian Nappes unit (Figs. V.9a and V.15): marbles belonging to Ören Unit display a temperature of 302 ± 30 °C (Fig. V.9a). The highest temperature, 607 °C, was obtained from the basal part of the cover near Bozdağ (Fig. V.15). Conversely, samples from the Menderes cover display lower temperatures ranging from 430 to 524 °C in the Büyük Menderes area, near Zeytinköy and Sultanhisar (Fig. V.9a) where the cover lies structurally underneath the core series. Samples from Selimiye unit record variable temperatures as in the northern part of the massif (*i.e.* in the Alaşehir area) between 551 and 587 °C (Fig. V.15). Although metamorphic parageneses show a contrast between core and cover (*i.e.* disappearance of garnets [Whitney & Bozkurt, 2002]), no major gap of T_{max} is observed across the contact and samples taken from the basement in the CMM show the same distribution of T_{max} ranging from 524 to 597 °C (Fig. V.15). Finally, a slightly lower temperature of 521 ± 26 °C was obtained in the hanging wall of the Alaşehir detachment in a blueschist sample (Fig. V.15). To summarize, RSCM T_{max} distribution in the Menderes cover displays strong regional variation whereas temperatures of the core are more uniform.

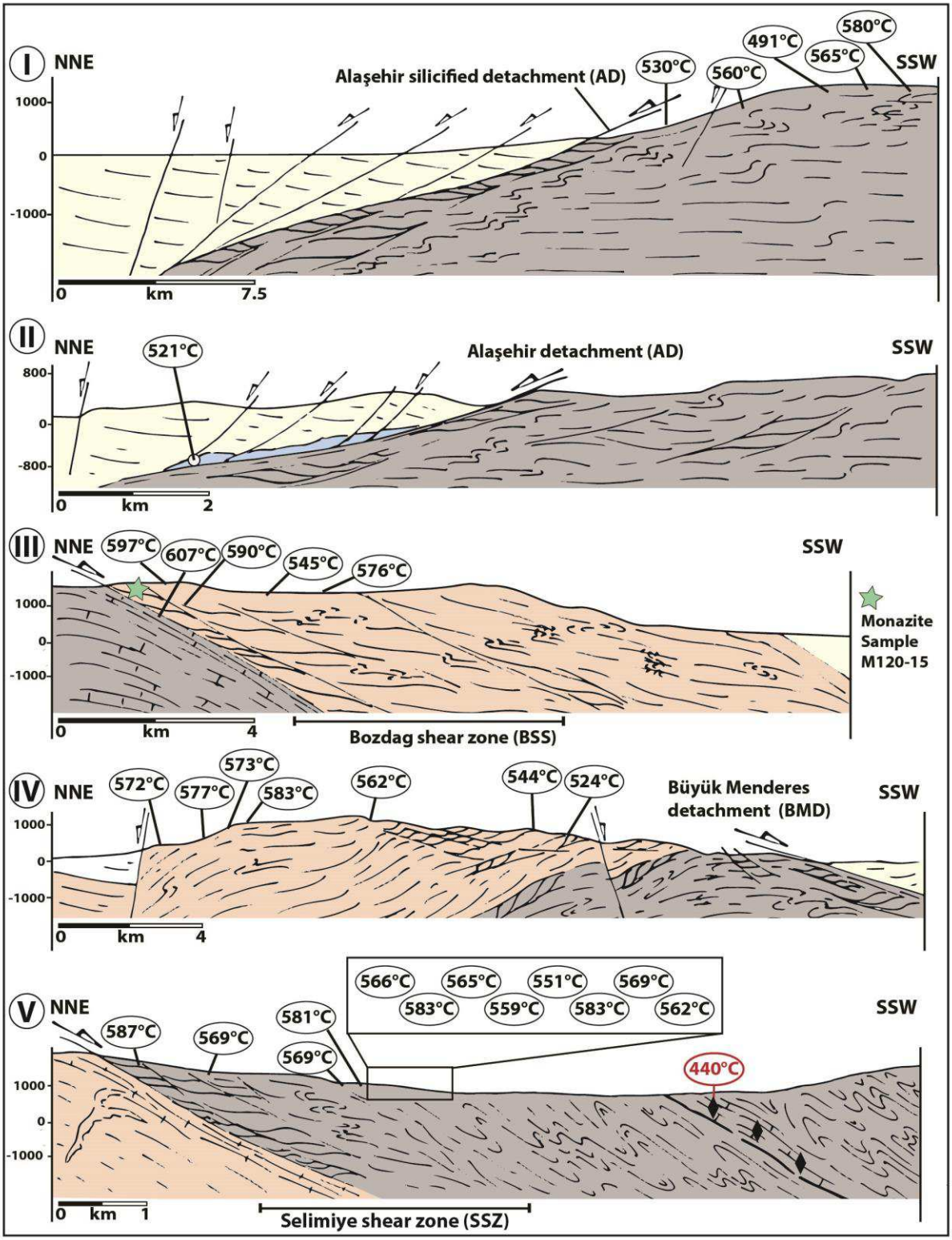

Figure V.15: Simplified cross-sections showing the distribution of RSCM temperature results. Note that red temperature in the fifth cross-section corresponds to P-T estimation from Rimmelé et al. [2003].

V.5. Discussion

V.5.1. Tectonic contacts in the CMM and SMM

Our structural study confirms the existence of a major structural contact between the core and the cover in the CMM, and sheds light on the relationships between these two units in the SMM.

In the CMM near Bozdağ, all macroscopic kinematic indicators indicate top-to-the-S shearing with a strong localization of strain within quartzite levels belonging to the cover (Figs. V.4 and V.5f). This top-to-the-S deformation is attested by the high concentration of shear bands (Fig. V.5g), and localized within a 4 km-thick shear zone. Although a first top-to-the-N shearing is also preserved in some localities [Hetzel *et al.*, 1998], it is clear that top-to-the-S criteria overprint these previous structures. The distribution of monazites ages and ^{40}Ar-^{39}Ar ages in this area is consistent, yielding ^{40}Ar-^{39}Ar ages of ca. 21.5 Ma and ~ 20 Ma, respectively (Fig. V.16a). This shear zone can be thus interpreted as a top-to-the-S exhumation shear zone, acting mainly during the Miocene, whereas top-to-the-N shearing may be related to the Alpine nappe stacking event. Furthermore, we highlighted that deformation near Malgaçmustafa appears quite different (Fig. V.9). Indeed, the dip change of low-angle normal faults in the deeper structural levels (*i.e.* north vs. south; Figs. V.6c, V.6d and V.6e) may suggest (i) two events of shearing or (ii) the existence of major high-angle normal faults that progressively titled these structures. However, no field evidences of high-angle normal faults have been observed. In addition, our ^{40}Ar-^{39}Ar step heating results in this area (Fig. V.11a) show apparent ages climbing to 60 Ma (Fig. V.11b). Similar to the previous hypothesis, we suggest that north dipping shear bands may be associated with nappe stacking (*i.e.* Alpine fabrics), whereas the second ones correspond to the activity of the Büyük Menderes detachment. Although these two main events of shearing present some similarities in terms of kinematics and metamorphic conditions, the timing of these deformation events seems to be different.

In the southern part of the Menderes cover near Selimiye, top-to-the-S deformation is localized within a 5 km-thick shear zone (Figs. V.4 and V.8c). There, all macroscopic kinematic indicators show a consistent top-to-the-S sense of shear with a strong localization of strain near the main contact (Fig. V.8a). The initial intrusive contact between the Menderes core and its cover was reworked by this localized top-S shearing event. Field evidence also confirms that top-to-the-S shearing fabrics crosscuts earlier top-to-the-N shear criteria. Although, our ^{40}Ar-^{39}Ar dates are broadly consistent with the study of Hetzel and Reischmann [1996] (43 – 37 Ma in the SSZ), they highlight a strong variation ranging from 47 to 18 Ma (Fig. V.16a). Hence, a more detailed study is required to constrain (i) the duration of the thermal even within the SMM, (ii) the degree of resetting due to reworking of previous structures, (iii) the diachronous exhumation within the shear zone. At first glance, the SSZ then gives an age around 50 – 35 Ma for the Barrovian-type metamorphism (Fig. V.16a), and associated top-S shearing, close to

the previous estimations of Schmidt *et al.* [2015] in the western part of Selimiye area. We therefore conclude that this shear zone (i) started to exhume during the Eocene Barrovian MMM, acting as a thrust transporting the HP-LT Mesozoic cover and part of its basement toward the south (see *section V.5.3.1*), and (ii) was still active during the Miocene (*e.g.* 18.3 Ma ^{40}Ar-^{39}Ar age on biotite, Fig. V.16a).

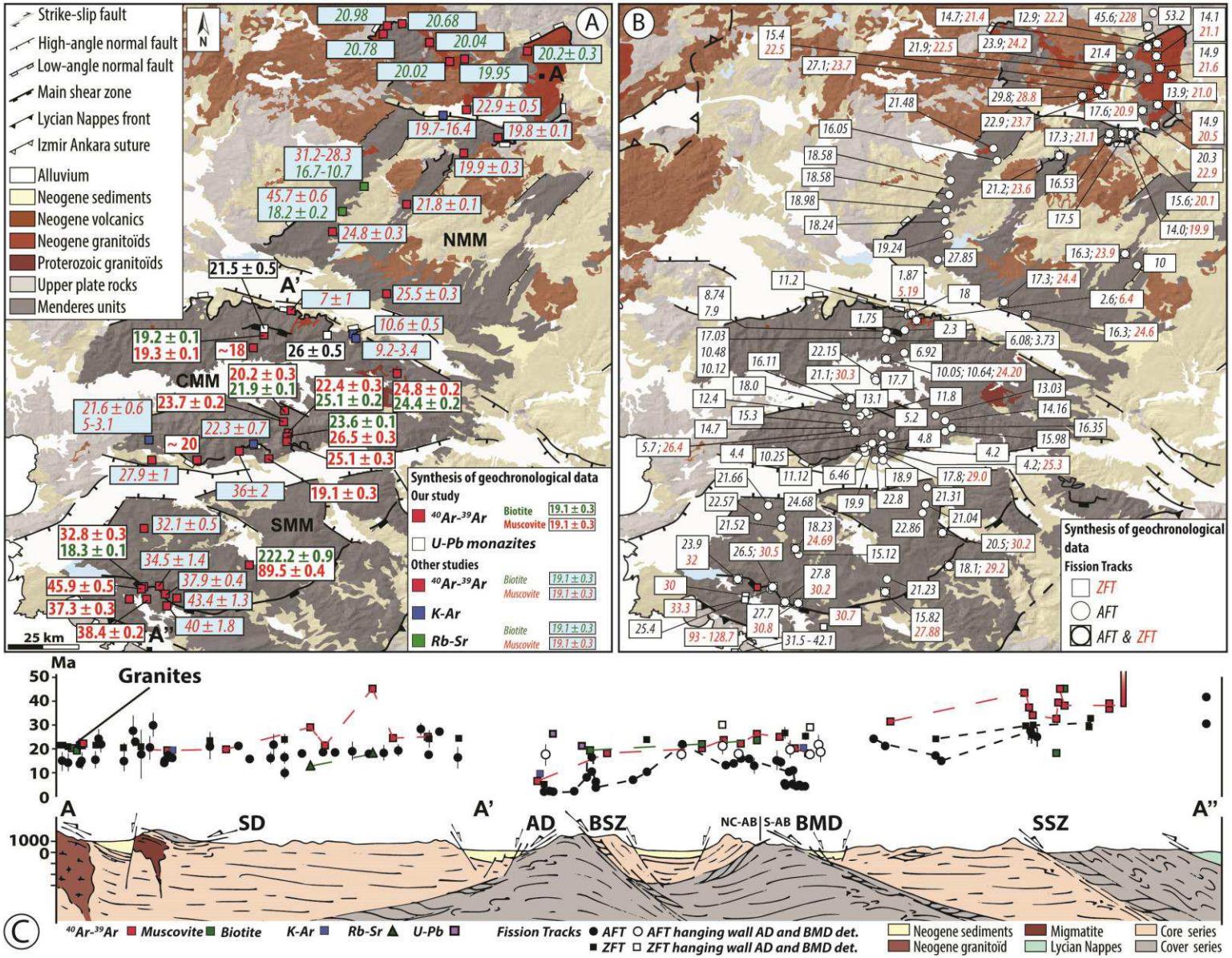
Strike-slip fault
High-angle normal fault
Low-angle normal fault
Main shear zone
Lycian Nappes front
Izmir Ankara suture
Alluvium
Neogene sediments
Neogene volcanics
Neogene granitoïds
Proterozoic granitoïds
Upper plate rocks
Menderes units
N
A
A'
A''
NMM
CMM
SMM
25 km
Synthesis of geochronological data
Our study
40Ar-39Ar Biotite Muscovite
U-Pb monazites
Other studies
40Ar-39Ar Biotite Muscovite
K-Ar
Rb-Sr Biotite Muscovite
B
Synthesis of geochronological data
Fission Tracks
ZFT
AFT
AFT & ZFT
C
Ma
Granites
SD
AD
BSZ
NC-AB
S-AB
BMD
SSZ
40Ar-39Ar Muscovite Biotite
K-Ar
Rb-Sr
U-Pb
Fission Tracks AFT
AFT hanging wall AD and BMD det.
ZFT
ZFT hanging wall AD and BMD det.
Neogene sediments
Neogene granitoïd
Migmatite
Lycian Nappes
Core series
Cover series

Figure V.16: Synthesis of geochronological ages in the entire MMCC. (a) Simplified geological map of the Menderes Massif showing the distribution of ^{40}Ar-^{39}Ar ages, K-Ar, Rb-Sr ages and monazite ages. Red and white squares indicate sample localities of our data. All ages are from our study and from Lips et al. [2001], Işık et al. [2004], Erkul [2010], Bozkurt et al. [2011], Hetzel et al. [2013], Cenki-Tok et al. [2016]. (b) Same geological map showing the distribution of AFT and ZFT from Gessner et al. [2001c], [2013], Ring and Layer [2003], Thomson and Ring [2006], Buscher et al. [2013], Hetzel et al. [2013], Ring et al. [2017], Wölfler et al. [2017]. (c) Simplified cross-section through the Menderes Massif showing cooling ages in relation to position along this section. The position of this section was located in the Figure V.16a. All data are presented in the Appendix V.8.4., Tables V.15, V.16 and V.17. Note that NC-AB and S-AB abbreviations correspond to the northern and central part of Aydın block and southern Aydın block, respectively. Abbreviations: AD (Alaşehir detachment); BSZ (Bozdağ shear zone); BMD (Büyük Menderes detachment); SD (Simav detachment) and SSZ (Selimiye shear zone).

V.5.2. Distribution of T_{max} (RSCM)

The Menderes area has recorded successive episodes of metamorphism since the Cretaceous. Although interpreting the significance of T_{max} in a poly-metamorphic history of a large and complex structure where the peak of temperature might have been reached at different moments at different places may prove difficult, the presence of Miocene monazites in the CMM allows discussing several hypotheses.

Monazite in sample M120-15 has probably crystallized close to peak metamorphism at ca. 21.5 Ma (Fig. V.16a). The quasi-absence of chlorite in the paragenesis suggests that monazite is not associated with late pervasive fluid circulation. RSCM results show that CM reached locally ~ 600 °C (Fig. V.15), we therefore propose that this T_{max} is associated with the Miocene extension. According to Cenki-Tok *et al.* [2016], a larger part of the cover and the basement in the CMM seems to be affected by the main extensional event. Nonetheless, RSCM results from Zeytinköy area in the CMM indicate a cold T_{max} for the sedimentary cover (Fig. V.9a). This implies that the Eocene Barrovian-type metamorphism and the Miocene HT-LP extensional event did not have an effect everywhere in the Menderes Massif. This cold temperature in this area may suggest (i) a tectonic contact within the cover units and/or (ii) a strong gradient within the cover series. Accordingly, thermal inversion signaling the overthrusting of the basement above the cover in this area implies no significant thermal re-equilibration. Although HP-LT parageneses were not found in this pre-Mesozoic cover, the cover and the basement units within the entire Menderes Massif have thus recorded different tectono-metamorphic evolutions.

Furthermore, in the Selimiye area (Fig. V.9a), Whitney & Bozkurt [2002] show an overall temperature gradient within the metamorphic Paleozoic cover from 550 °C for the structurally deepest rocks near the contact with the orthogneiss, to 430 °C for the southernmost rocks. The RSCM analysis shows a more complex situation with no clear T_{max} gradient across the main shear zone (Fig. V.15). According to their study, a single thermal event accompanied the main foliation and top-to-the-N fabrics during the Alpine orogeny. However, our ^{40}Ar-^{39}Ar ages and the results of Schmidt *et al.* [2015] showing an increase of temperature during the Barrovian MMM, suggest that the SSZ has been mainly active

during top-to-the-S thrusting and/or exhumation in the Eocene. We therefore suggest that T_{max} in the Selimiye shear zone (SSZ), which can be correlated to the Barrovian-type metamorphic event, was recorded in the same period, keeping in mind that the presence of an inherited component of CM in the entire shear zone could be an alternative explanation. According to Gessner *et al.* [2001b], the top-to-the-N deformation is associated with amphibolite-facies. In this case, T_{max} may be correlated with this pre-Alpine metamorphism event. Interpretation of RSCM results is thus currently ambiguous in this area.

Finally, RSCM analysis in the Lycian Nappes in the upper part of the metamorphic Ören unit yields a maximum temperature around 300 °C (± 30 °C) (Fig. V.9a). Using the metamorphic paragenesis with Fe-Mg carpholite, P-T estimates give higher values between 350 and 450 °C for a pressure around 12 Kbar depending upon the area [Rimmelé *et al.,* 2005]. In both cases, low temperature imply that the Lycian Nappes mostly escaped from the Barrovian-type metamorphism seen in the Menderes Massif and preserved the record of a cold subduction gradient in the Late Cretaceous. The difference between the T_{max} estimated by the two methods could be explained by a regional heterogeneity within the unit.

V.5.3. Metamorphism and deformation across the Menderes Massif

V.5.3.1. HP-LT metamorphism

The geodynamic significance of the HP-LT metamorphism recorded in the Triassic metaconglomerate of Kurudere unit depends whether it was initially attached to the Menderes basement as a sedimentary cover or not. Most recent studies suggest the existence of a tectonic contact between the HP-LT Kurudere unit and the underlying HT-LP Selimiye unit [*e.g.* Ring *et al.*, 1999; Whitney *et al.*, 2008; Pourteau *et al.,* 2016]. According to different studies [Rimmelé *et al.*, 2004; Whitney *et al.*, 2008], P-T estimates within the HP-LT parageneses yield peak temperature around 470 – 570 °C at a pressure of 10 – 12 kbar. The most likely shear zone below Kurudere unit is the top-S SSZ where Eocene ages have been retrieved (*e.g.* Fig. V.12). Our geochronological investigations in this area (*i.e.* Kurudere) suggest that the HP-LT metamorphism event (~ 60 Ma ^{40}Ar-^{39}Ar on muscovite) predates the HT-LP Barrovian-type metamorphism and the HP-LT event in the Cycladic Blueschist Unit (~ 50 Ma). The Eocene (37 Ma) ^{40}Ar-^{39}Ar ages obtained with both *in-situ* and step-heating methods on samples M89a-15 and M89-15b likely correspond to resetting of the Ar isotopic system due to the HT-LP Barrovian-type metamorphism and the replacement of phengite by muscovite (Fig. V.13b). If Kurudere Unit has been transported (Figs. V.17a and V.17b), it thus occurred before or during the Eocene HT-LP overprint. There is no evidence for HP-LT conditions in the southern Menderes Palaeozoic lower cover schists. This can be due to (i) a relatively short timing of this HP event, (ii) a deep burial difference

and/or (iii) an initial difference in the protolith, with less water-rich materials in the schists than in the Mesozoic cover preventing the formation of Fe-Mg-carpholite bearing parageneses. Alternatively, this may reflect complete overprinting of earlier HP-LT parageneses by the later Barrovian-type metamorphic event. No evidence of a major contact between schists and HP-LT metaconglomerates has been reported. In addition, the HP-LT rocks of Kurudere unit, located in the upper structural levels, are locally affected by the HT-LP overprint though they escaped the late-top-to-the-S deformation of SSZ. Following Rimmelé *et al.* [2003], we suggest that the entire cover of the SMM experienced HP-LT metamorphism during the late Cretaceous, and that most of the HP-LT parageneses in deeper units were obliterated by the Eocene MMM overprint. But, in order to take into account the top-S shearing accommodated by the SSZ, the Kurudere carpholite-bearing unit should be initially placed north of its present position at a distance that cannot be precisely constrained (Fig. V.17a).

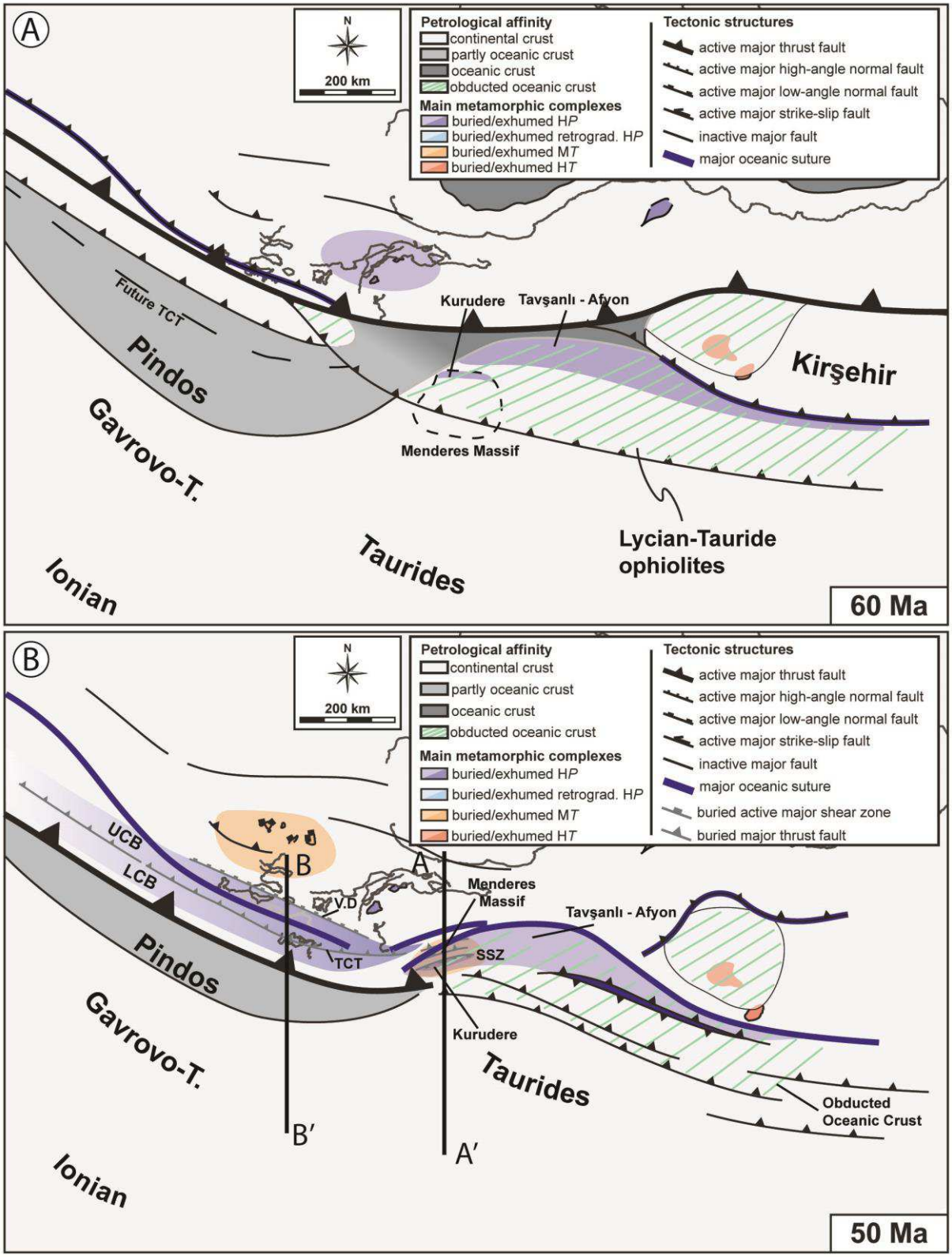
A
N
200 km
Petrological affinity
continental crust
partly oceanic crust
oceanic crust
obducted oceanic crust
Main metamorphic complexes
buried/exhumed HP
buried/exhumed retrograd. HP
buried/exhumed MT
buried/exhumed HT
Tectonic structures
active major thrust fault
active major high-angle normal fault
active major low-angle normal fault
active major strike-slip fault
inactive major fault
major oceanic suture
Future TCT
Pindos
Gavrovo-T.
Ionian
Kurudere
Tavşanlı - Afyon
Kirşehir
Menderes Massif
Taurides
Lycian-Tauride
ophiolites
60 Ma
B
N
200 km
Petrological affinity
continental crust
partly oceanic crust
oceanic crust
obducted oceanic crust
Main metamorphic complexes
buried/exhumed HP
buried/exhumed retrograd. HP
buried/exhumed MT
buried/exhumed HT
Tectonic structures
active major thrust fault
active major high-angle normal fault
active major low-angle normal fault
active major strike-slip fault
inactive major fault
major oceanic suture
buried active major shear zone
buried major thrust fault
UCB
LCB
Pindos
Gavrovo-T.
Ionian
B
B′
A
A′
V.D
TCT
Menderes
Massif
SSZ
Tavşanlı - Afyon
Kurudere
Taurides
Obducted
Oceanic Crust
50 Ma

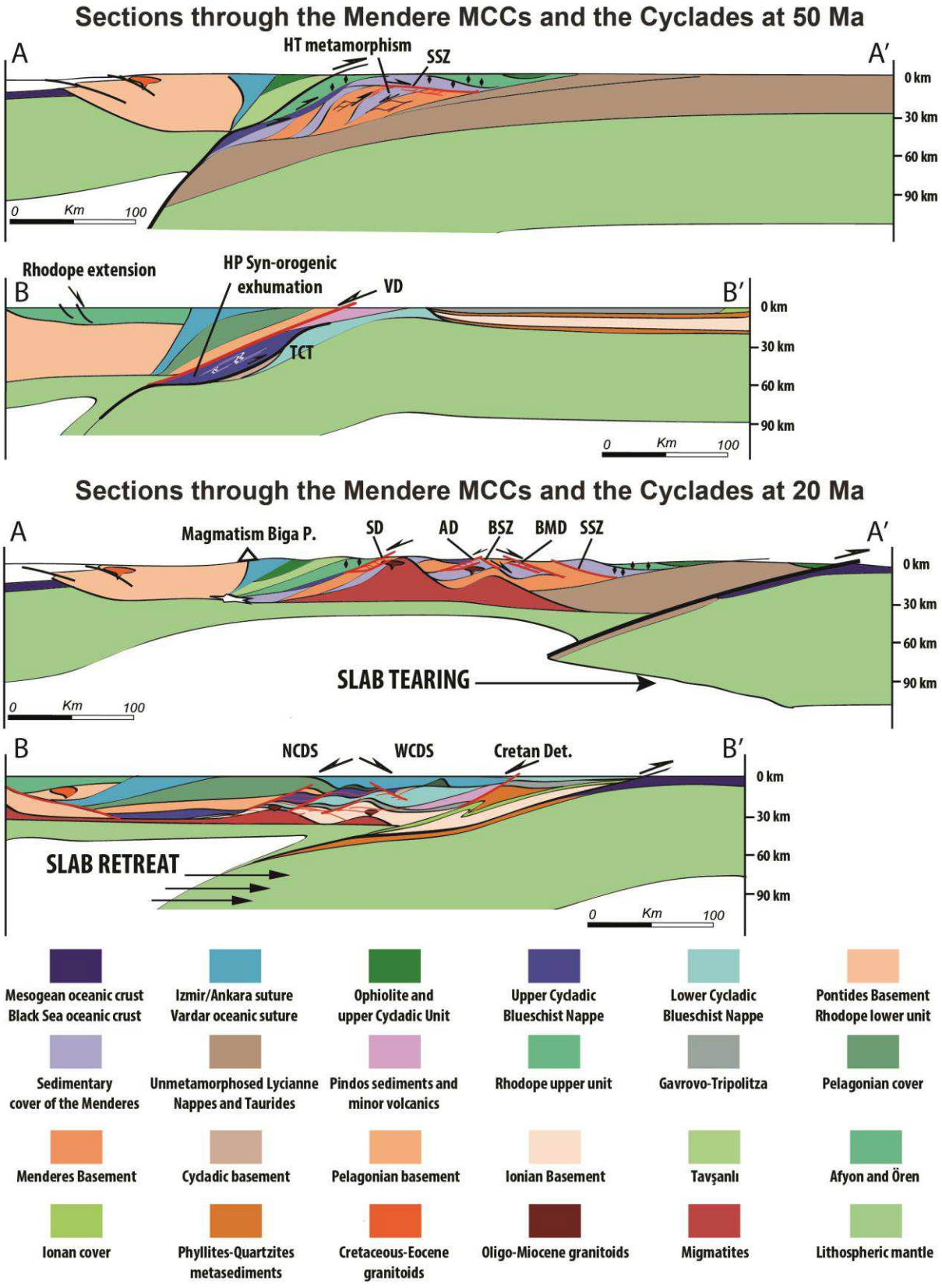
Sections through the Mendere MCCs and the Cyclades at 50 Ma
A
HT metamorphism
SSZ
A'
0 km
30 km
60 km
90 km
0 Km 100
Rhodope extension
HP Syn-orogenic exhumation
VD
B
B'
TCT
0 km
30 km
60 km
90 km
0 Km 100
Sections through the Mendere MCCs and the Cyclades at 20 Ma
A
Magmatism Biga P.
SD
AD
BSZ
BMD
SSZ
A'
0 km
30 km
60 km
90 km
SLAB TEARING
0 Km 100
B
NCDS
WCDS
Cretan Det.
B'
0 km
30 km
60 km
90 km
SLAB RETREAT
0 Km 100
Mesogean oceanic crust Black Sea oceanic crust
Izmir/Ankara suture Vardar oceanic suture
Ophiolite and upper Cycladic Unit
Upper Cycladic Blueschist Nappe
Lower Cycladic Blueschist Nappe
Pontides Basement Rhodope lower unit
Sedimentary cover of the Menderes
Unmetamorphosed Lycianne Nappes and Taurides
Pindos sediments and minor volcanics
Rhodope upper unit
Gavrovo-Tripolitza
Pelagonian cover
Menderes Basement
Cycladic basement
Pelagonian basement
Ionian Basement
Tavşanlı
Afyon and Ören
Ionan cover
Phyllites-Quartzites metasediments
Cretaceous-Eocene granitoids
Oligo-Miocene granitoids
Migmatites
Lithospheric mantle

Figure V.17: Geodynamic evolution of the study area. (a) and (b) Paleotectonic maps modified from the kinematic reconstruction of Menant et al. [2016], using our new geochronological data. Abbreviations: UCB (Upper Cycladic Blueschists Nappe); LCB (Lower Cycladic Blueschists Nappe); SSZ (Selimiye shear zone) and TCT (Trans-Cycladic Thrust from Grasemann et al. [2017]). (c) Simplified cross-sections of the study area and the Aegean domain in the Eocene- and Miocene-time. The position of this section was located in the Figure V.17b. Abbreviations: AD (Alaşehir detachment); BSZ (Bozdağ shear zone); BMD (Büyük Menderes detachment); NCDS (North Cycladic detachment system); SD (Simav detachment); SSZ (Selimiye shear zone); VD (Vari detachment) and WCDS (West Cycladic detachment system).

V.5.3.2. HT-LP Metamorphism and deformation before and during the Alpine orogeny

Top-to-the-N kinematic indicators are widespread throughout the whole CMM and SMM, implying a wider distribution of deformation, without localized strain along heterogeneities, as compared to the top-to-the-S deformation (Fig. V.4). Similar conclusions were reached by previous studies [*e.g.* Hetzel *et al.*, 1998; Lips *et al.*, 2001; Bozkurt, 2004; Whitney *et al.*, 2008; Iredale *et al.*, 2013], though there is no consensus on the age of this deformation (see *section V.1.2.2*). However, the pre-Alpine ^{40}Ar-^{39}Ar biotite age of sample M85-15 (~ 240 Ma) and muscovite (89.5 Ma) in the basement allows us to reconsider the main exhumation phase in the SMM. This result shows that the Alpine overprint only partly affected the SMM with the preservation of pre-alpine fabrics (and their primary ^{40}Ar-^{39}Ar age) through the thermal effect associated with the Alpine Barrovian-type metamorphism. The biotite age may be associated with inherited magmatic fabrics whereas the apparent Upper Cretaceous age for muscovite has no clear geological significance. However, partial biotite and muscovite resetting places constraints on the duration of the thermal pulse locally associated with nappe stacking during the Alpine orogeny (~ 50 Ma, Fig. V.9a). These ages thus suggest that the top-to-the-N fabric may be associated with Pre-Alpine ages in some localities. In that sense, we are more in the line of Gessner *et al.* [2001b], suggesting that top-to-the-N fabric in the SSZ may be related to a pre-Alpine deformation event. Then, top-to-the-S deformation cross cuts the previous fabrics in the southern part of the SMM in Eocene time. These fabrics were totally overprinted in such places (*e.g.* Th-Pb ages of 47.1 ± 6.3 44.7 ± 6.1 and 42.8 ± 3.6 Ma on monazites in the matrix [Catlos & Cemen, 2005]) during the Alpine orogeny. According to Régnier *et al.* [2007], the mylonites in the contact between the core and cover series in the northern SMM indicate top-to-the-N shearing. If this deformation event is contemporaneous with the top-to-the-S deformation recorded in the SSZ, the collapse model of Iredale *et al.* [2013] could be considered.

V.5.3.3. HT-LP Metamorphism and deformation during the Oligo-Miocene in the CMM

At first glance, the regional pattern of ^{40}Ar-^{39}Ar muscovite and biotite ages in the CMM is consistently ranging from 19 to 26 Ma with, however, there is some differences between the north and the south (Figs. V.16a and V.16c). In addition, older ages may be locally preserved (*e.g.* 36 Ma ^{40}Ar-^{39}Ar age on white mica in the cover of CMM [Lips *et al*., 2001]).

Biotite and muscovite near Ovacık yield a ^{40}Ar-^{39}Ar age of ca. 20 Ma, and RSCM results show that CM reached locally ~ 600 °C (Fig. V.15). Considering that peak temperature was recorded around 21.5 Ma (*i.e.* monazite crystallization) (Fig. V.16a), and assuming a nominal closure temperature of ca. 300 °C for ^{40}Ar-^{39}Ar in biotite, a Miocene cooling rate of ca. 200 °C/Myr is inferred for the Alaşehir and Bozdağ shear zones. Whereas the deformation associated with Bozdağ shear zone in only ductile, Alaşehir detachment is still active under brittle conditions until 7 Ma [Lips *et al*., 2001]. Depending on the areas, kinematics of brittle motion are either compatible with NE-SW (*e.g.* Salihli, Alaşehir) or with NW-SE extension (*e.g.* Urganlı). In addition, Figure V.18a reveals two phases of footwall exhumation histories. The first is defined by the oldest ^{40}Ar-^{39}Ar ages from the southern part of the Bozdağ shear zone, which range between 18 and 19.3 Ma (Figs. V.16a and V.18a). Using a geothermal gradient of 50 °C/km (even though a higher gradient may be recorded due to local fluid circulation and/or slab dynamics), exhumation rate increases through time from 0.4 km/Myr for the early Miocene to the latest Miocene to 0.55 km/Myr in the Pliocene. The second one corresponds to rapid exhumation rate of 1.17 km/Myr for the latest Miocene to Pliocene from the northern part of the CMM (Fig. V.18a), mainly caused by slip on the Alaşehir detachment. This idea was also supported by K-Ar data ranging between 4 and 3 Ma from fault gouge in the same area [Hetzel *et al*., 2013].

In the Büyük Menderes graben, the regional pattern of ^{40}Ar-^{39}Ar muscovite and biotite ages yields an older age than for Alaşehir graben (Figs. V.16a and V.16c). We therefore suggest that cooling in the footwall of Büyük Menderes detachment started before cooling in the footwall of Alaşehir detachment (Figs. V.18a and V.18b). Thermochronological data are consistent with this interpretation (Fig. V.18b) In addition, in the Halıköy - Sultanhisar areas, the oldest muscovite ages are of 26.5 Ma. Younging toward the edges of the southern part of the CMM is moreover observed (*i.e.* 20.2 Ma in the north and 19.1 Ma in the south) (Figs. V.16a and V.16c). The absence of tectonic contact close to Halıköy may suggest a complex thermal equilibration recorded during exhumation. Conversely, in the southern part of the CMM, this difference may be related to the activity of Büyük Menderes detachment and/or reworking structures related to exhumation, implying partial mineral resetting. According to Wölfler *et al*. [2017], this activity has recorded two phases enhancing footwall cooling and exhumation (Fig. V.18b).

Furthermore, monazite in feldspar-bearing rocks located in the hanging-wall of the Alaşehir detachment yields an U-Pb age of 26.5 ± 0.5 Ma. This age is consistent with our ^{40}Ar-^{39}Ar results yielding an older age in the eastern part of the CMM (*i.e.* muscovite and biotite ages ~ 24.8 and 24.4 Ma, respectively; Figs. V.16b and V.16c) than in the northern part of the CMM (*e.g.* near Salavatlı, Ovacık; Figs. V.16a and V.16c), and with the metamorphic event dated at 25.5 Ma in a metaconglomerate level belonging to the Mesozoic cover sequence near Kula (Fig. V.16a) [Cenki-Tok *et al.*, 2016]. We therefore suggest that extension in the NMM started earlier compared to the northern CMM, probably during the end of Oligocene as suggested by previous studies [*e.g.* Jolivet *et al.*, 2013; Gessner *et al.*, 2013]. This result is also consistent with Apatite Fission Tracks (AFT) and Zircon Fission Tracks (ZFT) that highlight different cooling stages for the Menderes Massif (Fig. 15). A first event was recorded in the NMM and the SMM and the upper part of the Çine unit in the hanging wall of the Alaşehir and the Büyük Menderes detachments (Figs. V.16b, V.16c, V.18c and V.18d). It started in the Late Oligocene and ended in the Early to Middle Miocene (19 – 33 Ma for zircon fission-track ages, and an average age of 21 – 22 Ma for apatite fission-track) (Figs. V.18c and V.18d) [*e.g.* Gessner *et al.*, 2001c; Ring & Layer, 2003]. The second event is mainly developed in the CMM and associated with the activity of three main shear zones. Cooling started during the end of the Miocene and ended in the Pliocene-Pleistocene in the footwall of Alaşehir and Büyük Menderes detachments (Figs. V.16 and V.18) [*e.g.* Gessner *et al.*, 2001c; Wölfler *et al.*, 2017].

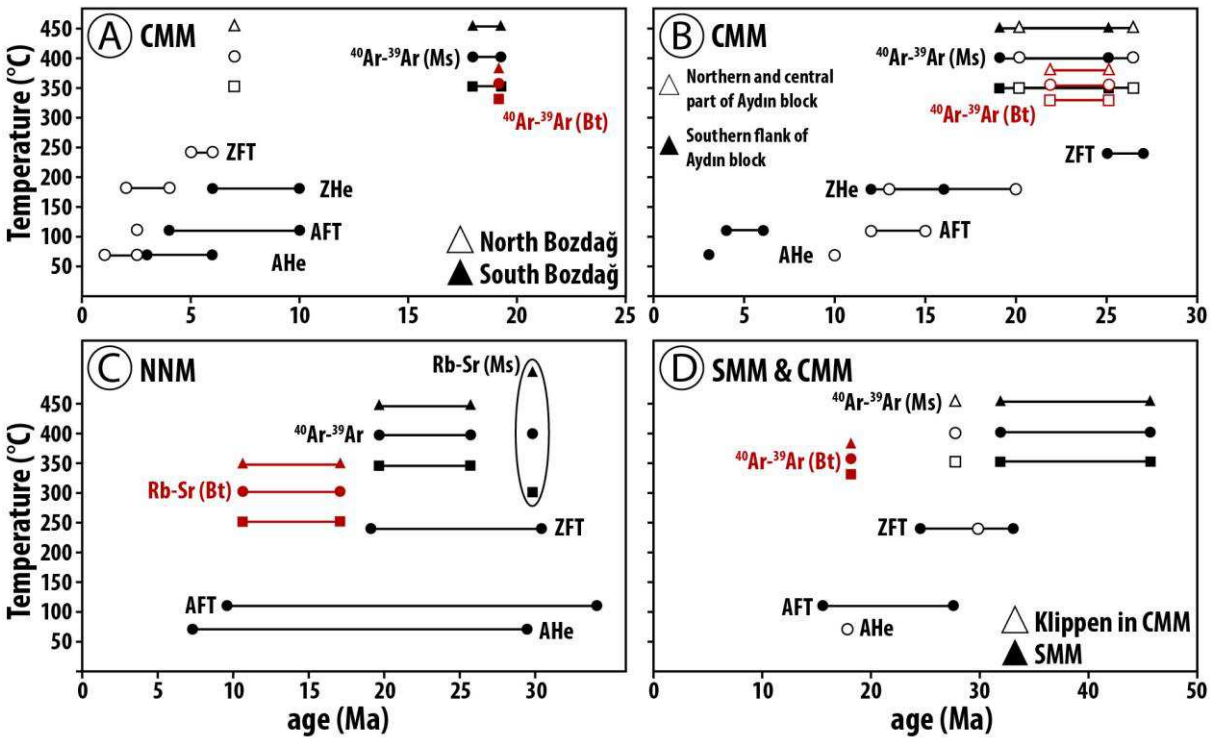

Figure V.18: Exhumation paths calculated from the cooling ages of different mineral from this study, Bozkurt et al. [2011], Wölfler et al. [2017] and references therein. (a) and (b) Samples are collected from the CMM, excluding the 36 ± 2 Ma ^{40}Ar-^{39}Ar age from Lips et al. [2001], which corresponds to the Alpine thermal event. (c) Samples are collected from the NNM, excluding the 45.7 ± 0.6 Ma Rb-Sr age from Bozkur et al. [2011], which also corresponds to the Alpine thermal event. (d) Samples are collected from the CMM and the SMM. Note that red and white colors correspond to the biotite and muscovite, respectively. Triangle, circle and square correspond to the temperatures interval: the argon closure temperature of muscovite and biotite is 400 ± 50 °C and 380 – 330 °C [e.g. McDougall & Harrison, 1999], respectively; the Rb-Sr closure temperature of muscovite and biotite is 500 ± 50 °C and 300 ± 50 °C [e.g. Jäger et al., 1967], respectively. Abbreviations: ZFT (zircon fission-track), closure temperature ~ 240 °C [e.g. Hurford, 1986]; ZHE (zircon (U-Th)/He), closure temperature ~180 °C [e.g. Reiners et al., 2004]; AFT (apatite fission-track), closure temperature ~110 °C [Gleadow & Duddy, 1981; Wagner & van den Haute, 1992] and AHe (apatite (U-Th)/He),closure temperature ~70 °C [e.g. Ehlers & Farley, 2003].

V.5.4. A possible evolution of the Menderes Massif

Based on our results, we suggest that the metamorphic history of the Menderes Massif and its cover results from a continuum of subduction toward the north. By modifying the reconstructions of Menant *et al.* [2016] and using here the correlations between tectonic units from the Cyclades to the Menderes Massif recently proposed by Roche *et al.* [2018b] (Fig. V.17), the MMCC evolution can be summarized as follows:

(i) The HP-LT record along the N-S section across the Menderes Massif shows the succession of several episodes: 80 Ma in the oceanic Tavşanlı Zone (*e.g.* Rb-Sr ages [Sherlock *et al.*, 1999]), 70 – 65 Ma in the Lycian Nappes (*i.e.* Ören unit) (*e.g.* ^{40}Ar-^{39}Ar ages [Ring & Layer, 2003; Pourteau *et al.*, 2013]) and 60 Ma in the Menderes cover, thus a younger ages from top to bottom when

descending in the nappe stack. Top-to-the-NE deformation started in HP-LT conditions in Afyon/Ören units and then in the Menderes Massif before 60 Ma. These cold parageneses marked by the presence of carpholite are not affected by high-temperature metamorphism, suggesting a syn-orogenic exhumation within the cold subduction channel. Conversely, the polymetamorphic basement (*i.e.* core series) has not recorded this HP-LT event for different reasons (see above).

(ii) In Eocene time until ~ 30 Ma, the accumulation of crustal units in the accretionary wedge led to an increase of internal heating of the nappe stack because of the radioactive content of basement rocks [*e.g.* Bousquet *et al.*, 1997; Jolivet *et al.*, 2004]. The Barrovian-type MMM was then recorded in the basement while the more superficial cover recorded only mildly this reheating [Whitney & Bozkurt, 2002], thus explaining the preservation of HP-LT parageneses. Depending on the areas, pre-alpine fabrics in the core series (*i.e.* Çine nappe) are totally overprinted by the Alpine orogeny fabrics (*e.g.* ^{40}Ar-^{39}Ar ages from the studies of Bozkurt *et al*. [2011] and Lips *et al*. [2001]), whereas in places cold temperatures within the cover are preserved (Fig. V.9a), suggesting an absence of such metamorphism. Thus, the Menderes Massif is composed of different tectono-metamorphic elements. In addition, during stacking, the cover unit was partly decoupled from the basement through a top-to-the-S shear zone (*i.e.* SSZ) that contributed to the syn-orogenic exhumation of the core between Eocene and Oligocene (Fig. V.17). Contemporaneous with the Barrovian-type MMM, HP-LT metamorphism is recorded in the central part of the Cyclades (*e.g.* Syros and Sifnos) and on Samos. This tectono-metamorphic unit (the Upper Cycladic Blueschists Nappe, UCB) overlies the Menderes Massif, and was probably buried and exhumed in Eocene time (Fig. V.17). We therefore suggest that a part of HP-LT rocks of the UCB was taken in the Menderes nappe stack in the Eocene, between the Menderes and Lycian sequences [Okay, 2001; Gessner *et al.*, 2013; Pourteau *et al.*, 2013; 2016], probably due to the obliquity of subduction in this region (Fig. V.17).

(iii) In the Oligo-Miocene, extension induced by slab dynamics (*i.e.* slab rollback and tearing) starts in the Menderes Massif. T_{max} and ^{40}Ar-^{39}Ar results bring new constraints on the duration and on the intensity of HT-LT metamorphism related to the emplacement of the thermal dome. The regional pattern of ^{40}Ar-^{39}Ar muscovite and biotite ages in the CMM suggests a rapid cooling that took place through the argon closure temperature interval. Data suggest also a duration of ~ 7 Ma of the thermal event with a peak temperature reaching locally ~ 600 °C. In the entire MMCC, exhumation was mainly accommodated by localized shear zones and also supported by migmatites (in the NMM) and synkinematic granitoïd intrusions (*i.e.* Salihli and Simav granodiorites in the CMM and the NMM, respectively). Our geochronology compilation shows that deformation and exhumation is first localized within the Simav and the Büyük Menderes detachments, and then migrates southward to the northern part of the CMM with the Alaşehir detachment and the Bozdağ shear zone (Figs. V.16 and V.18). Hence, the deformation regime during coeval extension appears more coaxial with a predominant top-N and top-S shearing below the Simav detachment in the north and the Büyük Menderes detachment in the CMM, respectively. Nonetheless, the exhumation rates between these two major structures are quite

different (Figs. V.16 and V.18) and seems to be more important in the NMM in the Miocene. In that sense, the NMM underwent accelerated uplift and faster exhumation in the Miocene than the CMM (Fig. V.18c). Finally, deformation migrates toward the north of CMM with the Alaşehir detachment and Bozdağ shear zone, and it still active in the entire CMM. Hence, the MMCC recorded a diachronous uplift and cooling history [Baran *et al*., 2017].

V.6. Conclusion

The tectonic and thermal evolution of the MMCC since the Cretaceous is complex. Although top-to-the-N kinematic indicators in the CMM and SMM may correspond to a pre-Alpine event in some areas, there is a complete overprinting of these fabrics in such places during the Alpine orogeny and then during the Miocene post-orogenic extension. The first HT-LP metamorphism event associated with nappe stacking started in Eocene times and lasted until Oligocene times, affecting mainly the CMM and the SMM. This crustal thickening is also coeval with the formation and exhumation of the Cycladic Blueschists in the nearby Aegean Sea, and it was mainly exhumed along a syn-orogenic extensional shear zone (*i.e.* SSZ) in the SMM. The presence of HP-LT rocks within the Menderes cover suggests that the northern part (or the entire massif ?) has undergone HP-LT conditions before the Eocene Barrovian metamorphism overprint. In the CMM, HT-LP metamorphism and associated deformation fabrics developed mainly during Miocene. Extension is thus localized into different shear zones such as the Bozdağ shear zone (ductile deformation), the Alaşehir and the Büyük Menderes detachments (ductile-brittle deformation) accommodating exhumation of the MMCC over 10 Ma as a consequence of slab tearing and retreat. Exhumation was supported by HT-LP metamorphism in the NMM and CMM, suggesting that a large-scale thermal anomaly encompasses the Menderes Massif, the eastern and central Aegean Sea.

V.7. Acknowledgements

This work has received funding from the Labex Voltaire (ANR-10-LABX-100-01) homed at Orléans University and BRGM, from the European Research Council (ERC) under the seventh Framework Programme of the European Union (ERC Advanced Grant, grant agreement No 290864, RHEOLITH), and from the Institut Universitaire de France. The authors are grateful to S. Janiec and J.G. Badin (ISTO) for the preparation of thin sections.

V.8. Appendix

V.8.1. Analytical methods

V.8.1.1. ^{40}Ar-^{39}Ar Geochronology

^{40}Ar-^{39}Ar dating experiments were conducted on single grains and small-sized populations (weighing < 200 µg) extracted by gently crushing the samples previously cut in small pieces with a diamond saw to avoid any surface alteration. Samples were first inspected for freshness in thin section and carefully checked after crushing to avoid any sign of alteration possibly associated to microfractures. Loose grains were ultrasonically bathed in deionized water and rinsed until no suspension was released, then dried in a vented oven at 50 °C and handpicked under a high-magnification binocular. Selected single grains were further inspected in polarized light under a microscope to check for inclusions, defects, and/or µm-scale alteration. Those that were sufficiently thin (and transparent, white micas) appeared fresh and homogeneous. Small clusters of cohesive micas too small to be analyzed individually (< 10 µg, < 200 µm) were optically inspected under the binocular to avoid specimens with even marginal/cryptic alteration. Many contained small (< 10 µm) inclusions of dark prismatic crystals of oxide. The final separates (clusters) and single grains were further etched in a light (< 5 %) HNO_3 solution during 10-20 sec to remove any residual alteration, and ultrasonically rinsed in deionized water for 1 min. The sample were individually wrapped in small disk-shapped Al packets (5 mm across, 0.5 mm thick) and stacked as a monoaxial irradiation pile with a monitor level (packet) every 5 samples. The stack was loaded into a thin-walled (< 0.1 mm) Al tube about 2 cm long with two Al plugs securing both ends.

Double polished rock sections were prepared from 10 mm OD circular cores drilled perpendicular to the XZ plane of fabric-dominated samples (micaschists). These were further polished to produce 2.0 to 1.5 mm thick disks that were imaged by SEM and analyzed with the EMP to provide µ-geochemical control on the phases and µ-structures exposed on the face analyzed with the Ar/Ar UV laser-probe. The disk were re-polished to 1 µm finish for removing the carbon coating, then ultrasonically rinsed in deionized water to remove any residual/adhering particle left by the polishing. No gluing substrate was used to secure or harden the disks to avoid contamination by organic compounds. The disks were individually wrapped in domestic Al-foils and stacked as a monoaxial irradiation pile with a monitor disk level made up of 99 % pure Al (10 mm diam., 1.5 mm thick) sandwiched between every sample level. Each monitor disk holds 7 centrally and radially arrayed standard positions to provide lateral J-gradient control across every disk (and depth control by interpolating between every coaxially aligned hole positions along the can axis). The samples + standards stack is contained into a thin-walled (< 0.1 mm) 10 mm ID Al tube about 4 cm long with two Al plugs closing both ends.

The single grains + rock sections were irradiated together for 5 h along with the neutron flux standard sanidine FCs (28.305 ± 0.036 Ma [Renne *et al.*, 2010]) in the dedicated Cd-lined CLICIT neutron flux facility housed at TRIGA-Corvallis (OR, USA). Upon receipt of the cans back from irradiation, the samples were unwrapped and loaded in the ultra-low-blank extraction lines equipping the three high-resolution Helix SFT mass-spectrometers (Thermo Scientific®) operated by the Ar/Ar laboratory at ISTO. These are outfitted to commutable CO_2 (10.6 µm) or deep-UV (213 nm) laser-based extraction systems for single-grain (or cluster) stepheating experiments and spatially controlled in situ dating. Each extraction line features two dedicated viewports for the corresponding wavelength, and a home-built manifold assembly for automated processing and purification of the evolved gases (-127 °C cold trap plus 2 hot GP50 SAES® getters) using pneumatically actuated all-metal Swagelok transfer valves and tubing. 6 min static cold blanks are systematicaly measured before every gas admission. Isotopic abundances were determined in pulse-counting mode by peak-switching on the SEM detector operated at 750 mass resolution between m/e = 35, 36, 37, 38, 39, 40 (SEM and cup) and regressed back to inlet time using in-house software for the magnet operation and data acquisition. The data were regressed and corrected for instrumental parameters (blank, mass discrimination, SEM dead-time, post irradiation decay, atmospheric contamination, J-gradient monitoring) following Scaillet [2000] and Scaillet *et al.* [2008]. Typical blanks (in fA) were: $2.810*10^{-2}$ (m/e = 36), $2.961*10^{-2}$ (m/e = 37), $7.340*10^{-3}$ (m/e = 38), $3.659*10^{-2}$ (m/e = 39), $4.200*10^{-1}$ (m/e = 40). Isotopic interference corrections were applied using average production ratios for CLICIT as published in the literature. Mass-discrimination and dead-time correction factors were systematically monitored overnight using a fully automated air-calibration system featuring a 6-l tank filled with purified atmospheric argon and connected to the mass-spectrometer through the laser extraction system via two pneumatically-actuated air pipettes of approximately 0.1 and 1.0 cc. Intensity of the calibrating air signals was systematically varied over the full dynamic range of the ion counting system (0 to 200 fA) by blending different combinations of 0.1 and 1.0 cc-pipetted air aliquots to check for any pressure dependence and/or nonlinear ion yields.

V.8.1.2. U-Pb method

In this study, monazites dating were performed at the GEMOC laboratory in Orsay (university of Paris Sud). Analyses were supervised by Philippe Lach, in collaboration with Guillaume Delpech, Fréderic Haurine and Gaël Monvoisin. 40 µm thick sections were analyzed using an ICP-MS Element XR configured to H cone, coupled to a laser Cetac Excite 193nm with short duration of the pulse. Samples were located in volum HelEx II® ablation chamber and ablated material are transported by He flux and mixed to Ar before entering the plasma. Analytical conditions are described in the Table V.4.

Laser	
Type	CETAC Excite
Wavelength	193nm
Laser frequency	2Hz
Fluence	3.5J.cm^{-2}
Ablation spot size	5 µm
ICP-MS	
Model	Element XR
Type	Magnet
ICP RF Power	953W
Cooling gaz (Ar)	16 l.min^{-1}
Carrier gaz (He)	0.77 l.min^{-1}
Auxiliary gaz (Ar)	0.7 l.min^{-1}
Acquisition parameters	
Measured isotopes	^{202}Hg, ^{204}Pb, ^{206}Pb, ^{207}Pb, ^{208}Pb, ^{232}Th, ^{238}U
Settling time	300ms(202), 16ms(235), 1ms (reste)
background	20s
Acquisition time	40s (80 pulses)

Table V.4: Monazite analyses conditions.

Analyzes are standardized with respect to the monazite of Madmon [Schulz *et al.*, 2007 dated at 515 Ma], and quality control was performed via two standards: the Trebilcock (272 ± 2 Ma [Tomascak *et al.*, 1996]) and Namaqualand (1033 Ma [Knoper *et al.*, 2000]). Data reduction was carried out with Glitter® software and no common lead correction was applied. The results are generated using the ISOPLOT/EX (v.4.15) by Ludwig [2003] at 95% of confidence by taking errors at 2σ.

The concordance was calculated according to the following equation:

$$\text{Conc} = (\text{Age } ^{206}\text{Pb}/^{238}\text{U}) \text{ X100/ } (\text{Age } ^{207}\text{Pb}/^{235}\text{U}) \quad (1)$$

The correlation factor Rho was calculated according to the simplified equation of Schmitz and Shoene [2007]:

$$\rho_{R75\text{-}R68} = (\sigma_{68}/R_{68})/ (\sigma_{75}/R_{75}) \quad (2)$$

R75 = ^{207}Pb/^{235}U; R68 = ^{206}Pb/^{238}U; σ= variation of the isotopic ratio.

V.8.1.3. RSCM (Raman Spectroscopy on Caronaceous Materials)

Raman Spectroscopy on Carbonaceous Materials (RSCM) is a geothermometer used for estimate the maximum temperature conditions reached during regional metamorphism and contact metamorphism [*e.g.* Beyssac *et al.,* 2002; Lahfid *et al.,* 2010; Delchini *et al.*, 2016]. Because graphitization is known as an irreversible reaction, the organization of Carbonaceous Materials (CM) will not be affected during a metamorphic retrogression event. This method is based on the quantification (R2 ratio) of the degree of organization. In this study we essentially used RSCM calibration proposed by Beyssac *et al.* [2002] on sample of high metamorphism grade except one sample for which we apply the Lahafid *et al.* [2010] Raman parameter RA1. According to Beyssac *et al.* [2002], there is a linear correlation between the peak temperature and the R2 ratio [T (°C) = − 445 R2 + 641], and temperature may be estimated in a range of 330 – 640 °C. Lahfid *et al.* [2010] applied this method in low-grade rocks. Despite a complex spectrum (*i.e.* several defects bands), they show a good correlation between temperature and advanced diagenesis ranging from 200 – 330 °C. We therefore applied these both methods to estimate temperatures of the Menderes Massif. Analyses were obtained using the Renishaw InVia Reflex system (BRGM-ISTO, Orléans), and were conducted on thin sections prepared on CM-rich metasediments (metapelites and marbles) cut in the structural X-Z plane. Spectra were then treated using the software Peakfit following the procedure described by Beyssac *et al.* [2002] and Lahfid *et al.* [2010].

V.8.2. Sample distribution and results of ^{40}Ar-^{39}Ar and U-Pb ages

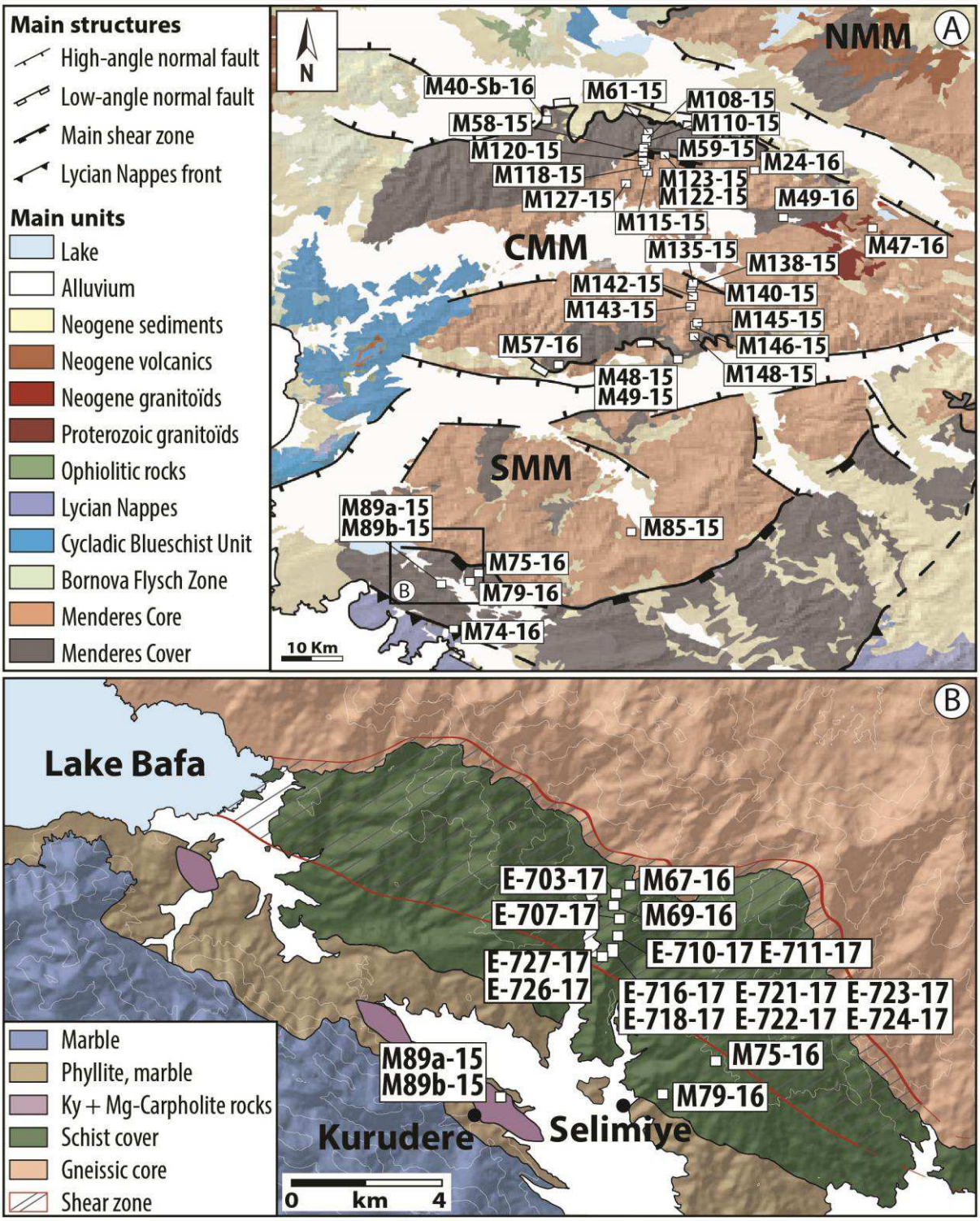

Figure V.19: Sample location. (a) CMM and SMM simplified geological showing the distribution of sampling and (b) zoom in the southern part of the Menderes Massif on the Selimiye area. Map is modified from Whitney et al. [2008].

N72.MS1 (Section 11.82)																				
Spot #	$^{39}Ar_K$	$^{36}Ar_{atm}/^{39}Ar_K$			$^{37}Ar_{Ca}/^{39}Ar_K$			$^{38}Ar_{Cl}/^{39}Ar_K$			$^{40}Ar^*$	$^{40}Ar^*/^{39}Ar_K$			Age (Ma)		
	(V)	(± 1s)			(± 1s)			(± 1s)				(± 1s)			(± 1s)		
# 1	1.41E-06	2.86E+00	±	1.86E-01	1.60E+00	±	4.87E-01	-2.44E-02	±	2.34E-02	5.12	45.57	±	19.02	105.70	±	42.85
# 3	2.75E-07	1.04E+00	±	2.51E-01	1.78E+00	±	3.73E+00	8.88E-02	±	4.64E-02	-0.07	-0.21	±	27.04	-0.49	±	64.63
# 4	1.25E-06	2.44E-01	±	2.04E-02	8.80E-02	±	7.03E-01	7.45E-04	±	1.42E-02	-1.53	-1.09	±	7.23	-2.60	±	17.29
# 5	2.72E-05	1.03E-02	±	4.31E-04	4.11E-02	±	3.25E-02	-9.72E-04	±	7.39E-04	70.24	7.22	±	0.30	17.16	±	0.70
# 6	2.01E-05	2.54E-02	±	7.41E-04	8.55E-02	±	5.25E-02	1.98E-03	±	1.07E-03	42.02	5.43	±	0.41	12.93	±	0.98
# 7	1.27E-07	2.80E+00	±	1.12E+00	-3.45E+00	±	2.04E+01	-8.89E-05	±	3.59E-01	-12.68	-93.15	±	139.60	-237.50	±	380.40
# 8	2.88E-05	8.68E-03	±	9.01E-04	3.08E-02	±	8.96E-02	-2.87E-03	±	1.77E-03	73.56	7.14	±	0.59	16.97	±	1.41
# 9	5.79E-06	2.84E-02	±	4.89E-03	2.42E-01	±	4.47E-01	-3.40E-04	±	8.02E-03	35.83	4.68	±	3.00	11.14	±	7.12
# 10	3.12E-05	5.75E-03	±	9.40E-04	-5.48E-03	±	8.30E-02	2.57E-03	±	1.65E-03	81.43	7.45	±	0.56	17.71	±	1.34
# 11	2.60E-05	9.75E-03	±	2.10E-03	1.14E-04	±	4.50E-02	-1.07E-03	±	1.22E-03	72.67	7.66	±	1.12	18.20	±	2.66
# 12	1.66E-05	1.36E-02	±	3.28E-03	8.69E-02	±	7.66E-02	3.26E-03	±	1.81E-03	65.91	7.77	±	1.76	18.47	±	4.17
# 13	2.20E-05	9.61E-03	±	2.46E-03	3.49E-02	±	5.74E-02	2.88E-03	±	1.40E-03	70.75	6.87	±	1.33	16.34	±	3.14
# 14	3.38E-05	6.63E-03	±	3.33E-03	1.71E+00	±	3.82E-01	-1.35E-03	±	1.46E-03	81.29	8.51	±	1.57	20.23	±	3.72
# 15	7.31E-05	3.59E-03	±	1.54E-03	3.57E-01	±	1.49E-01	-9.18E-04	±	7.26E-04	88.47	8.15	±	0.73	19.36	±	1.72
# 16	7.75E-07	4.79E-01	±	1.51E-01	-6.08E+00	±	1.19E+01	-3.90E-02	±	4.49E-02	68.98	314.50	±	73.53	628.20	±	124.00
# 17	7.51E-05	2.34E-03	±	1.50E-03	-1.55E-01	±	1.21E-01	-8.94E-04	±	6.60E-04	92.20	8.16	±	0.71	19.40	±	1.67
# 18	7.31E-05	2.53E-03	±	1.55E-03	-1.31E-01	±	1.24E-01	-7.10E-04	±	5.99E-04	91.54	8.09	±	0.73	19.23	±	1.73
# 19	2.17E-05	1.03E-02	±	5.23E-03	-1.86E-01	±	4.16E-01	-1.86E-03	±	1.75E-03	71.18	7.48	±	2.46	17.79	±	5.81
# 20	5.27E-05	4.51E-03	±	2.14E-03	-2.50E-02	±	1.71E-01	-2.25E-03	±	8.10E-04	85.51	7.87	±	1.01	18.70	±	2.39
# 21	5.86E-05	1.07E-03	±	1.93E-03	-5.85E-02	±	1.53E-01	-1.65E-03	±	6.79E-04	96.44	8.53	±	0.91	20.27	±	2.15
# 22	9.33E-05	3.14E-03	±	5.16E-04	1.05E-02	±	2.08E-02	1.37E-04	±	4.62E-04	89.91	8.28	±	0.21	19.66	±	0.49
# 23	1.07E-04	1.69E-03	±	4.35E-04	3.24E-03	±	1.78E-02	-8.49E-04	±	3.77E-04	94.19	8.07	±	0.18	19.19	±	0.42
# 24	9.69E-05	7.36E-04	±	5.00E-04	-3.79E-03	±	1.99E-02	-4.01E-04	±	3.69E-04	97.37	8.04	±	0.20	19.10	±	0.47
# 25	9.27E-05	1.97E-03	±	5.29E-04	3.58E-03	±	2.26E-02	-5.98E-04	±	4.63E-04	93.25	8.06	±	0.21	19.15	±	0.49
# 26	9.38E-05	1.47E-03	±	5.11E-04	1.56E-02	±	2.14E-02	-1.49E-03	±	4.16E-04	94.80	7.93	±	0.20	18.85	±	0.48
# 27	7.12E-05	2.74E-03	±	6.67E-04	1.97E-02	±	2.77E-02	1.77E-04	±	4.88E-04	91.51	8.71	±	0.27	20.70	±	0.63
# 28	9.16E-05	2.59E-03	±	5.26E-04	1.13E-03	±	2.16E-02	-6.30E-04	±	5.04E-04	91.37	8.11	±	0.21	19.26	±	0.49
# 29	3.48E-05	-2.86E-03	±	1.35E-03	-8.11E-02	±	5.49E-02	-3.17E-03	±	1.12E-03	111.00	8.50	±	0.54	20.20	±	1.27
# 30	4.68E-05	5.07E-03	±	1.03E-03	-1.15E-02	±	4.62E-02	-1.32E-03	±	7.45E-04	84.59	8.23	±	0.41	19.55	±	0.96
# 31	3.81E-05	3.76E-03	±	1.23E-03	-5.02E-02	±	5.19E-02	-2.69E-03	±	9.02E-04	87.37	7.67	±	0.49	18.24	±	1.16
# 32	8.22E-06	8.12E-03	±	5.79E-03	-1.38E-01	±	2.50E-01	-6.94E-03	±	3.51E-03	74.16	6.89	±	2.29	16.38	±	5.41
# 33	4.60E-05	1.00E-03	±	1.04E-03	-2.94E-02	±	4.16E-02	-5.01E-05	±	9.43E-04	96.68	8.60	±	0.41	20.44	±	0.97
# 34	6.73E-05	3.80E-03	±	7.14E-04	8.98E-03	±	3.02E-02	-1.10E-03	±	6.63E-04	87.49	7.86	±	0.28	18.68	±	0.67
# 35	3.29E-05	2.69E-03	±	3.62E-03	-6.08E-03	±	4.77E-02	2.09E-03	±	1.44E-03	90.98	8.03	±	1.52	19.08	±	3.59
# 36	1.50E-05	8.64E-03	±	7.97E-03	-1.00E-01	±	1.01E-01	8.95E-04	±	3.25E-03	73.50	7.08	±	3.34	16.84	±	7.90
# 37	7.20E-05	2.40E-03	±	1.66E-03	-1.04E-02	±	2.11E-02	1.31E-03	±	7.43E-04	92.08	8.25	±	0.69	19.61	±	1.64
# 38	3.30E-05	9.17E-03	±	3.61E-03	1.61E-02	±	4.87E-02	1.51E-03	±	1.46E-03	75.97	8.57	±	1.51	20.36	±	3.57
# 39	3.88E-05	2.62E-03	±	3.07E-03	1.28E-02	±	3.88E-02	3.67E-04	±	1.27E-03	91.61	8.44	±	1.29	20.06	±	3.05
# 40	6.14E-05	2.49E-03	±	1.94E-03	-1.22E-02	±	2.44E-02	-4.53E-04	±	8.72E-04	91.16	7.59	±	0.81	18.04	±	1.93
# 41	7.05E-05	4.70E-03	±	1.69E-03	1.82E-02	±	2.13E-02	-4.09E-04	±	7.51E-04	85.13	7.96	±	0.71	18.91	±	1.68
# 42	6.25E-05	4.42E-03	±	1.91E-03	4.67E-03	±	2.36E-02	-8.73E-05	±	7.36E-04	86.15	8.13	±	0.80	19.32	±	1.89
# 43	6.53E-05	4.05E-03	±	1.83E-03	-4.28E-04	±	2.53E-02	-2.44E-04	±	9.45E-04	86.61	7.73	±	0.77	18.38	±	1.81
# 44	7.18E-05	1.28E-04	±	1.66E-03	1.89E-02	±	2.24E-02	-1.99E-04	±	7.48E-04	99.52	7.87	±	0.70	18.69	±	1.65
# 45	6.85E-05	-5.76E-04	±	1.73E-03	2.25E-02	±	2.56E-02	-2.17E-03	±	9.20E-04	102.20	8.04	±	0.73	19.10	±	1.72
# 46	7.37E-05	6.25E-04	±	1.61E-03	3.21E-03	±	2.05E-02	-1.30E-03	±	6.96E-04	97.68	7.76	±	0.68	18.44	±	1.60
# 47	2.79E-05	1.23E-02	±	4.27E-03	7.36E-02	±	5.60E-02	-2.11E-03	±	1.73E-03	70.27	8.58	±	1.79	20.39	±	4.23
# 48	7.81E-05	2.54E-03	±	1.53E-03	2.85E-02	±	2.10E-02	-8.05E-04	±	7.66E-04	91.43	8.00	±	0.64	19.01	±	1.51
# 49	7.22E-05	4.21E-03	±	1.65E-03	3.01E-02	±	2.15E-02	-1.23E-03	±	6.99E-04	87.22	8.48	±	0.69	20.15	±	1.63
# 50	6.15E-05	2.99E-03	±	5.91E-04	3.29E-02	±	2.50E-02	3.30E-04	±	5.91E-04	90.25	8.18	±	0.26	19.43	±	0.61
# 51	5.70E-05	7.18E-04	±	6.16E-04	2.61E-02	±	2.91E-02	-1.12E-03	±	5.50E-04	97.45	8.11	±	0.28	19.28	±	0.66
# 52	5.16E-05	2.86E-03	±	6.82E-04	2.50E-02	±	3.09E-02	2.93E-04	±	9.37E-04	90.55	8.09	±	0.31	19.23	±	0.73
# 53	6.69E-05	1.24E-03	±	5.29E-04	1.80E-03	±	2.27E-02	6.09E-04	±	6.77E-04	95.87	8.53	±	0.24	20.27	±	0.56
# 54	4.77E-05	1.51E-03	±	7.35E-04	1.17E-02	±	3.27E-02	-2.29E-03	±	7.90E-04	94.73	8.01	±	0.33	19.04	±	0.78
# 55	6.10E-05	1.68E-02	±	5.94E-04	-6.69E-04	±	2.66E-02	7.12E-04	±	5.39E-04	60.78	7.68	±	0.26	18.25	±	0.62
# 56	5.72E-05	3.52E-03	±	7.28E-04	-2.48E-02	±	2.58E-02	-5.60E-04	±	7.68E-04	88.85	8.30	±	0.30	19.72	±	0.71
# 57	5.72E-05	4.12E-03	±	6.17E-04	-8.17E-03	±	2.58E-02	-4.63E-04	±	6.05E-04	86.84	8.04	±	0.28	19.11	±	0.65
# 58	5.06E-05	3.96E-03	±	6.94E-04	5.95E-03	±	3.08E-02	-4.34E-04	±	8.05E-04	86.94	7.80	±	0.31	18.54	±	0.73
# 59	5.95E-05	2.17E-03	±	5.94E-04	1.03E-03	±	2.53E-02	-1.60E-04	±	6.12E-04	92.34	7.75	±	0.27	18.42	±	0.63
# 60	4.80E-05	1.24E-03	±	8.08E-04	-1.47E-02	±	3.14E-02	1.31E-03	±	8.08E-04	96.02	8.81	±	0.34	20.92	±	0.81
# 61	2.01E-05	-5.28E-04	±	1.75E-03	-1.75E-02	±	7.69E-02	2.88E-04	±	1.75E-03	101.80	8.70	±	0.78	20.67	±	1.85
# 62	6.99E-05	-9.85E-05	±	5.18E-04	-3.47E-02	±	2.20E-02	-3.72E-04	±	5.61E-04	100.40	8.15	±	0.23	19.37	±	0.54
# 63	5.43E-05	2.72E-03	±	1.84E-03	-5.45E-03	±	3.04E-02	-8.24E-05	±	7.57E-04	90.84	7.98	±	0.78	18.96	±	1.85
# 64	3.20E-05	-4.21E-04	±	3.10E-03	1.77E-02	±	4.70E-02	-2.65E-03	±	1.29E-03	101.60	7.89	±	1.33	18.75	±	3.13
# 65	4.12E-05	-5.54E-04	±	2.41E-03	-1.27E-02	±	3.31E-02	2.51E-04	±	1.07E-03	102.00	8.39	±	1.03	19.93	±	2.44
# 66	5.92E-05	-2.15E-03	±	1.68E-03	-9.58E-03	±	2.45E-02	-8.32E-04	±	8.04E-04	108.60	8.06	±	0.72	19.16	±	1.70
# 67	3.10E-05	2.71E-03	±	3.23E-03	8.88E-02	±	4.66E-02	3.18E-05	±	1.28E-03	91.47	8.59	±	1.38	20.41	±	3.25
# 68	5.22E-05	2.89E-03	±	1.91E-03	-1.46E-02	±	2.74E-02	-1.04E-03	±	9.11E-04	90.66	8.29	±	0.82	19.70	±	1.93
# 69	3.32E-05	-9.06E-06	±	3.00E-03	-1.19E-02	±	4.14E-02	-1.12E-03	±	1.23E-03	100.00	11.11	±	1.28	26.36	±	3.02
# 70	5.08E-05	-4.21E-04	±	1.96E-03	2.15E-02	±	2.99E-02	-3.83E-04	±	1.01E-03	101.60	8.07	±	0.84	19.19	±	1.98
# 71	6.04E-05	-8.85E-04	±	1.64E-03	1.39E-02	±	2.30E-02	-5.07E-04	±	6.95E-04	103.30	8.27	±	0.70	19.66	±	1.66
# 72	1.47E-06	-4.58E-02	±	6.77E-02	1.90E+00	±	9.60E-01	-2.07E-03	±	2.64E-02	3795.00	13.90	±	28.92	32.91	±	67.84
# 73	9.68E-06	1.02E-02	±	1.04E-02	4.13E-01	±	1.74E-01	-5.40E-04	±	4.15E-03	79.24	11.48	±	4.41	27.22	±	10.38
# 74	1.12E-07	-3.17E-01	±	9.01E-01	4.29E+01	±	2.00E+01	1.91E-01	±	3.51E-01	118.70	595.50	±	432.50	1049.00	±	577.80
# 75	1.64E-07	-6.60E-01	±	6.37E-01	4.20E+01	±	1.41E+01	7.66E-01	±	3.14E-01	164.60	497.30	±	291.20	912.80	±	419.40

Table V.5: ^{40}Ar-^{39}Ar in situ result of sample M115-15. Note that each lines represent each punctual analyses.

N73.MS1 (Section 11.86)																				
Spot #	$^{39}Ar_K$	$^{36}Ar_{atm}/^{39}Ar_K$			$^{37}Ar_{Ca}/^{39}Ar_K$			$^{38}Ar_{Cl}/^{39}Ar_K$			$^{40}Ar^*$	$^{40}Ar^*/^{39}Ar_K$			Age (Ma)		
	(V)	(± 1s)			(± 1s)			(± 1s)				(± 1s)			(± 1s)		
# 3	3.87E-05	7.63E-03	±	2.05E-03	4.19E-02	±	2.32E-02	2.45E-03	±	1.45E-03	89.94	20.15	±	0.84	47.71	±	1.96
# 4	2.91E-05	2.06E-03	±	2.70E-03	4.67E-02	±	2.82E-02	1.35E-03	±	1.20E-03	96.88	18.91	±	1.11	44.81	±	2.59
# 5	3.65E-05	7.27E-03	±	2.17E-03	3.13E-02	±	2.62E-02	-1.13E-03	±	1.18E-03	89.55	18.41	±	0.88	43.64	±	2.07
# 6	2.48E-05	7.69E-03	±	3.16E-03	-2.33E-02	±	3.34E-02	3.38E-04	±	1.32E-03	89.06	18.49	±	1.30	43.82	±	3.03
# 7	3.91E-05	6.43E-03	±	2.02E-03	3.15E-03	±	2.27E-02	1.86E-03	±	1.09E-03	90.96	19.12	±	0.83	45.29	±	1.94
# 8	7.47E-05	9.52E-03	±	1.06E-03	8.33E-03	±	1.05E-02	3.84E-04	±	6.55E-04	87.27	19.29	±	0.43	45.7	±	1.01
# 9	7.73E-05	4.91E-03	±	1.02E-03	1.08E-02	±	1.33E-02	5.54E-05	±	5.56E-04	92.83	18.79	±	0.42	44.53	±	0.99
# 10	7.79E-05	4.29E-03	±	1.34E-03	-2.72E-02	±	1.75E-02	5.73E-04	±	6.16E-04	93.74	18.99	±	0.57	44.99	±	1.35
# 11	7.27E-05	2.58E-03	±	1.43E-03	-3.54E-02	±	1.90E-02	-1.03E-05	±	5.76E-04	96.09	18.72	±	0.61	44.36	±	1.44
# 12	4.37E-05	1.27E-02	±	2.37E-03	9.21E-03	±	2.97E-02	-1.40E-04	±	9.67E-04	83.50	18.93	±	1.02	44.86	±	2.39
# 13	3.10E-05	1.25E-03	±	3.33E-03	2.88E-02	±	5.45E-02	9.25E-05	±	1.18E-03	98.11	19.09	±	1.43	45.24	±	3.35
# 14	5.78E-05	3.82E-03	±	1.80E-03	2.19E-02	±	2.78E-02	-5.09E-04	±	1.04E-03	94.38	18.99	±	0.78	45.01	±	1.83
# 15	7.76E-07	3.37E-02	±	1.34E-01	2.09E+00	±	1.93E+00	-1.85E-02	±	4.55E-02	93.46	142.4	±	58.43	312.9	±	117.90
# 16	2.65E-05	8.34E-03	±	3.96E-03	1.47E-01	±	5.08E-02	1.91E-03	±	1.48E-03	90.90	24.62	±	1.69	58.11	±	3.93
# 17	1.84E-05	4.24E-03	±	5.59E-03	1.14E-01	±	7.46E-02	7.82E-04	±	2.03E-03	94.91	23.32	±	2.42	55.11	±	5.63
# 18	4.32E-05	5.74E-03	±	2.40E-03	1.17E-03	±	3.52E-02	1.92E-03	±	8.79E-04	91.64	18.61	±	1.03	44.11	±	2.42
# 19	4.80E-05	3.92E-03	±	2.15E-03	2.01E-02	±	3.24E-02	3.62E-05	±	8.44E-04	94.09	18.45	±	0.93	43.72	±	2.17
# 20	4.18E-05	4.01E-03	±	2.46E-03	1.68E-02	±	2.94E-02	4.74E-04	±	1.18E-03	94.06	18.76	±	1.06	44.45	±	2.49
# 21	4.72E-05	6.26E-03	±	2.20E-03	-1.56E-02	±	2.57E-02	-7.43E-05	±	8.78E-04	90.90	18.48	±	0.95	43.8	±	2.21
# 22	3.79E-05	5.90E-03	±	2.74E-03	-4.11E-02	±	3.54E-02	-9.67E-04	±	1.13E-03	91.89	19.72	±	1.18	46.71	±	2.76
# 23	3.58E-05	6.17E-03	±	2.92E-03	2.84E-02	±	3.48E-02	1.51E-04	±	1.28E-03	91.29	19.11	±	1.25	45.27	±	2.92
# 24	4.74E-05	4.78E-03	±	2.19E-03	3.01E-02	±	2.94E-02	9.24E-04	±	9.67E-04	92.86	18.38	±	0.94	43.57	±	2.20
# 25	4.06E-05	-1.04E-03	±	2.55E-03	8.62E-02	±	3.96E-02	3.93E-03	±	1.14E-03	101.60	18.9	±	1.10	44.79	±	2.57
# 26	4.43E-05	5.43E-03	±	2.56E-03	-3.15E-02	±	4.85E-02	2.60E-04	±	9.91E-04	91.87	18.12	±	1.05	42.97	±	2.46
# 27	3.61E-05	9.35E-04	±	3.13E-03	-2.08E-02	±	5.92E-02	1.94E-03	±	1.23E-03	98.59	19.27	±	1.28	45.65	±	2.99
# 28	6.93E-06	6.54E-03	±	1.63E-02	1.18E+00	±	3.07E-01	3.97E-03	±	5.00E-03	90.52	18.45	±	6.65	43.74	±	15.56
# 29	3.46E-05	1.29E-03	±	3.28E-03	1.35E-02	±	6.17E-02	1.22E-04	±	1.15E-03	97.98	18.59	±	1.34	44.06	±	3.13
# 30	2.07E-05	5.38E-03	±	5.49E-03	-8.64E-02	±	1.02E-01	1.77E-03	±	1.99E-03	92.62	19.96	±	2.24	47.25	±	5.24
# 31	3.26E-05	4.32E-03	±	3.47E-03	6.57E-03	±	6.45E-02	-8.14E-04	±	1.17E-03	93.84	19.46	±	1.42	46.1	±	3.33
# 32	8.69E-07	4.56E-01	±	1.36E-01	7.39E-01	±	2.37E+00	-1.42E-03	±	4.53E-02	-5.77	-7.361	±	53.24	-17.75	±	129.00
# 33	1.96E-05	4.74E-03	±	5.77E-03	-3.88E-02	±	1.06E-01	-7.95E-04	±	2.05E-03	92.77	17.97	±	2.35	42.61	±	5.52
# 34	1.66E-05	8.49E-03	±	6.86E-03	-3.85E-02	±	1.30E-01	-8.20E-04	±	2.16E-03	88.20	18.74	±	2.79	44.41	±	6.54
# 35	2.26E-05	2.90E-03	±	5.00E-03	1.29E-02	±	9.40E-02	-1.73E-03	±	1.79E-03	95.55	18.4	±	2.04	43.62	±	4.78
# 36	2.06E-05	4.67E-03	±	5.50E-03	3.28E-02	±	9.67E-02	1.09E-04	±	2.09E-03	93.76	20.71	±	2.24	49.01	±	5.23
# 37	2.81E-05	5.40E-03	±	4.04E-03	5.33E-02	±	7.48E-02	3.95E-04	±	1.31E-03	92.09	18.56	±	1.65	43.99	±	3.86
# 38	2.69E-05	7.62E-03	±	4.22E-03	4.76E-02	±	8.45E-02	6.14E-04	±	1.62E-03	89.18	18.56	±	1.73	44.00	±	4.04
# 39	3.56E-05	1.44E-03	±	3.18E-03	7.34E-02	±	5.79E-02	8.12E-04	±	1.17E-03	97.88	19.61	±	1.31	46.46	±	3.05
# 40	2.57E-05	5.08E-03	±	4.42E-03	3.57E-02	±	8.14E-02	9.70E-04	±	1.74E-03	93.65	22.14	±	1.80	52.35	±	4.20
# 41	5.98E-05	6.90E-03	±	2.10E-03	4.52E-02	±	3.25E-02	-4.37E-04	±	1.00E-03	90.24	18.85	±	0.91	44.67	±	2.14
# 42	5.01E-05	1.13E-02	±	2.52E-03	5.30E-02	±	3.87E-02	8.70E-04	±	1.07E-03	84.68	18.38	±	1.09	43.58	±	2.55
# 43	4.58E-05	6.48E-03	±	2.75E-03	3.45E-02	±	5.27E-02	6.85E-04	±	1.19E-03	90.36	17.95	±	1.19	42.55	±	2.78
# 44	3.37E-05	1.47E-02	±	3.76E-03	3.06E-02	±	5.55E-02	-1.35E-03	±	1.22E-03	81.08	18.66	±	1.62	44.23	±	3.79
# 45	2.56E-05	4.41E-03	±	4.92E-03	5.06E-02	±	8.21E-02	-1.18E-03	±	1.64E-03	93.75	19.56	±	2.12	46.32	±	4.96
# 46	2.31E-06	2.89E-02	±	5.44E-02	-5.71E-01	±	8.15E-01	-3.20E-03	±	1.80E-02	73.50	23.64	±	23.50	55.84	±	54.65
# 47	1.94E-05	1.05E-02	±	6.49E-03	1.55E-01	±	1.03E-01	2.34E-03	±	2.36E-03	87.43	21.6	±	2.80	51.1	±	6.54
# 48	4.91E-06	1.99E-02	±	2.58E-02	5.00E-01	±	4.02E-01	5.66E-03	±	8.33E-03	80.66	24.51	±	11.08	57.87	±	25.74
# 49	1.62E-05	-5.90E-03	±	7.71E-03	-3.10E-03	±	1.22E-01	2.11E-03	±	2.62E-03	109.90	19.31	±	3.34	45.74	±	7.81
# 50	2.10E-05	8.92E-03	±	6.00E-03	3.28E-02	±	9.65E-02	2.29E-03	±	2.14E-03	89.09	21.52	±	2.59	50.91	±	6.04
# 51	3.05E-05	1.60E-03	±	4.12E-03	-5.36E-02	±	6.47E-02	-8.93E-04	±	1.51E-03	97.46	18.11	±	1.78	42.94	±	4.17
# 52	3.55E-05	5.46E-03	±	3.57E-03	-5.39E-02	±	5.44E-02	6.68E-04	±	1.23E-03	92.15	18.91	±	1.54	44.81	±	3.60
# 53	1.61E-05	1.53E-02	±	7.87E-03	8.19E-02	±	1.27E-01	1.50E-03	±	2.87E-03	82.21	20.86	±	3.39	49.38	±	7.92
# 54	1.22E-05	9.71E-03	±	1.03E-02	-1.18E-01	±	1.64E-01	6.16E-04	±	3.52E-03	87.39	19.89	±	4.44	47.09	±	10.38
# 55	1.71E-05	3.65E-03	±	7.39E-03	1.30E-02	±	1.15E-01	1.75E-03	±	2.57E-03	94.77	19.52	±	3.18	46.23	±	7.44
# 56	3.60E-05	8.03E-03	±	1.97E-03	-9.28E-03	±	4.22E-02	-6.59E-04	±	1.14E-03	88.88	18.98	±	0.75	44.97	±	1.75
# 57	3.22E-05	2.33E-03	±	2.18E-03	-9.30E-02	±	4.48E-02	5.21E-04	±	9.65E-04	96.62	19.67	±	0.83	46.58	±	1.94
# 58	2.52E-05	3.43E-03	±	2.79E-03	2.88E-02	±	5.46E-02	-3.00E-04	±	1.05E-03	95.12	19.75	±	1.07	46.78	±	2.51
# 59	1.14E-05	4.87E-03	±	6.15E-03	2.34E-02	±	1.38E-01	3.99E-03	±	2.44E-03	94.20	23.37	±	2.35	55.21	±	5.47
# 60	7.65E-06	4.06E-03	±	9.19E-03	1.13E-01	±	1.79E-01	2.78E-03	±	3.34E-03	93.98	18.72	±	3.49	44.35	±	8.16
# 61	4.52E-05	4.76E-03	±	1.55E-03	1.16E-01	±	3.17E-02	1.78E-03	±	7.92E-04	92.87	18.33	±	0.59	43.44	±	1.39
# 62	2.54E-05	6.80E-03	±	2.77E-03	6.65E-02	±	5.77E-02	6.35E-04	±	1.18E-03	90.55	19.25	±	1.06	45.6	±	2.49
# 63	1.37E-05	1.38E-03	±	5.11E-03	-6.60E-03	±	1.12E-01	5.13E-03	±	2.13E-03	98.73	31.65	±	1.97	74.37	±	4.54
# 64	1.48E-05	5.12E-02	±	4.92E-03	7.49E-02	±	1.17E-01	3.99E-04	±	2.00E-03	65.31	28.47	±	1.86	67.04	±	4.29

Table V.6: ^{40}Ar-^{39}Ar in situ result of sample M69-16. Note that each lines represent each punctual analyses.

N74.MS1 (Section 11.77)																				
Spot #	$^{39}Ar_K$	$^{36}Ar_{atm}/^{39}Ar_K$			$^{37}Ar_{Ca}/^{39}Ar_K$			$^{38}Ar_{Cl}/^{39}Ar_K$			$^{40}Ar^*$	$^{40}Ar^*/^{39}Ar_K$			Age (Ma)		
	(V)	(± 1s)			(± 1s)			(± 1s)				(± 1s)			(± 1s)		
# 1	-2.03E-07	5.60E+00	±	4.12E+00	-1.45E+00	±	7.52E+00	6.71E-01	±	1.27E+00	15.42	301.50	±	1114.00	604.40	±	1898.00
# 2	5.16E-05	6.49E-03	±	7.56E-04	-2.67E-03	±	2.54E-02	-1.57E-03	±	6.84E-04	88.68	15.01	±	0.33	35.40	±	0.76
# 3	4.54E-05	5.53E-03	±	5.78E-04	-1.02E-02	±	3.06E-02	-5.03E-04	±	1.14E-03	90.44	15.45	±	0.21	36.42	±	0.48
# 4	1.43E-05	8.33E-03	±	1.70E-03	-5.67E-02	±	1.01E-01	1.18E-03	±	1.30E-03	89.21	20.36	±	0.60	47.83	±	1.39
# 5	1.99E-06	6.75E-02	±	1.26E-02	-1.17E+00	±	6.85E-01	2.64E-02	±	7.78E-03	42.55	14.77	±	4.16	34.84	±	9.71
# 6	6.73E-05	1.73E-03	±	3.46E-04	-4.30E-02	±	2.13E-02	8.46E-05	±	6.57E-04	96.88	15.89	±	0.13	37.45	±	0.30
# 7	5.85E-05	9.79E-04	±	4.40E-04	-2.53E-02	±	2.38E-02	-3.52E-04	±	6.47E-04	98.24	16.11	±	0.17	37.96	±	0.39
# 8	6.27E-05	1.05E-03	±	4.02E-04	-4.90E-02	±	2.19E-02	-8.45E-04	±	4.67E-04	98.18	16.65	±	0.14	39.21	±	0.33
# 9	5.44E-05	1.64E-03	±	4.61E-04	-4.26E-02	±	2.52E-02	-7.63E-05	±	5.06E-04	97.00	15.73	±	0.18	37.07	±	0.41
# 10	3.84E-05	2.18E-03	±	6.83E-04	-2.92E-02	±	3.70E-02	-1.38E-03	±	7.88E-04	96.14	16.07	±	0.24	37.85	±	0.57
# 11	2.15E-05	4.99E-03	±	1.08E-03	-3.47E-02	±	6.47E-02	-2.09E-04	±	9.79E-04	91.46	15.78	±	0.39	37.18	±	0.91
# 12	2.43E-05	4.88E-03	±	1.00E-03	5.37E-03	±	5.62E-02	-7.42E-04	±	8.49E-04	91.65	15.82	±	0.35	37.27	±	0.81
# 13	5.72E-05	2.54E-03	±	9.30E-04	1.24E-02	±	2.18E-02	-1.65E-03	±	5.22E-04	95.57	16.20	±	0.37	38.16	±	0.86
# 14	5.56E-05	2.44E-03	±	9.58E-04	-8.31E-03	±	2.41E-02	-3.71E-04	±	6.08E-04	95.77	16.30	±	0.38	38.40	±	0.89
# 15	5.15E-05	2.31E-03	±	1.03E-03	-1.73E-02	±	2.44E-02	-9.91E-04	±	6.40E-04	95.87	15.85	±	0.41	37.35	±	0.97
# 16	6.40E-05	1.49E-03	±	8.33E-04	4.04E-03	±	1.91E-02	-7.35E-04	±	6.28E-04	97.27	15.67	±	0.34	36.92	±	0.79
# 17	6.29E-05	1.36E-03	±	8.38E-04	-8.08E-03	±	2.06E-02	1.25E-04	±	5.38E-04	97.55	16.01	±	0.33	37.72	±	0.78
# 18	5.91E-05	2.84E-03	±	9.11E-04	-4.93E-03	±	2.29E-02	-1.66E-05	±	6.36E-04	94.86	15.45	±	0.36	36.41	±	0.84
# 19	3.24E-05	4.36E-03	±	1.63E-03	-2.39E-02	±	3.90E-02	-1.90E-04	±	9.08E-04	92.89	16.82	±	0.65	39.62	±	1.51
# 20	4.68E-05	3.46E-03	±	1.13E-03	-3.93E-03	±	2.90E-02	1.00E-03	±	1.01E-03	93.96	15.91	±	0.45	37.49	±	1.05
# 21	5.33E-05	1.90E-03	±	9.95E-04	-2.49E-02	±	2.29E-02	-1.68E-03	±	7.82E-04	96.86	17.25	±	0.40	40.62	±	0.92
# 22	5.87E-05	7.22E-04	±	9.03E-04	-1.81E-02	±	2.10E-02	-1.25E-04	±	6.79E-04	98.69	16.04	±	0.37	37.79	±	0.86
# 23	5.56E-05	6.97E-04	±	9.64E-04	1.65E-02	±	2.47E-02	-8.85E-04	±	6.65E-04	98.75	16.25	±	0.38	38.29	±	0.89
# 24	4.49E-05	7.75E-04	±	1.19E-03	-1.04E-02	±	2.69E-02	1.72E-03	±	8.94E-04	98.7	17.42	±	0.72	41.02	±	1.68
# 25	6.50E-05	2.70E-03	±	8.31E-04	1.92E-02	±	1.95E-02	-4.44E-04	±	6.52E-04	95.2	15.83	±	0.33	37.30	±	0.76
# 26	6.56E-05	1.14E-03	±	8.04E-04	9.62E-03	±	1.98E-02	-1.79E-04	±	4.52E-04	97.96	16.22	±	0.32	38.20	±	0.74
# 27	5.84E-05	8.16E-04	±	9.16E-04	-5.79E-03	±	2.15E-02	-2.87E-04	±	5.80E-04	98.53	16.19	±	0.36	38.15	±	0.84
# 28	5.93E-05	1.40E-03	±	9.03E-04	-2.82E-02	±	2.13E-02	2.20E-03	±	8.57E-04	97.36	15.28	±	0.36	36.03	±	0.83
# 29	2.71E-05	9.47E-03	±	2.20E-03	1.44E-01	±	3.78E-02	-1.95E-03	±	1.03E-03	87.95	20.42	±	0.68	47.97	±	1.57
# 30	5.40E-05	1.91E-03	±	1.11E-03	-3.42E-03	±	1.80E-02	-1.12E-03	±	6.77E-04	96.6	16.02	±	0.35	37.76	±	0.81
# 31	5.50E-05	1.73E-03	±	1.09E-03	-3.72E-02	±	1.63E-02	-4.69E-04	±	5.86E-04	96.95	16.30	±	0.33	38.40	±	0.78
# 32	3.80E-05	1.40E-03	±	1.56E-03	6.51E-03	±	2.79E-02	1.71E-03	±	8.87E-04	97.66	17.28	±	0.48	40.69	±	1.13
# 33	1.94E-05	3.60E-03	±	3.11E-03	2.14E-02	±	4.59E-02	7.96E-04	±	1.42E-03	93.99	16.61	±	0.95	39.13	±	2.21
# 34	6.25E-05	2.82E-03	±	9.61E-04	1.34E-02	±	1.65E-02	-5.10E-04	±	6.23E-04	95.03	15.93	±	0.30	37.53	±	0.70
# 35	6.32E-05	1.34E-03	±	9.81E-04	-7.63E-03	±	1.37E-02	1.01E-04	±	6.98E-04	97.57	15.84	±	0.30	37.33	±	0.70
# 36	1.64E-05	1.12E-02	±	3.67E-03	-1.29E-01	±	6.82E-02	1.88E-03	±	1.93E-03	86.18	20.66	±	1.11	48.53	±	2.58
# 37	3.09E-05	6.61E-03	±	1.13E-03	4.74E-03	±	4.07E-02	-2.33E-03	±	1.29E-03	89.89	17.36	±	0.41	40.87	±	0.95
# 38	5.60E-05	2.45E-03	±	6.24E-04	-8.44E-03	±	2.08E-02	-1.22E-03	±	8.13E-04	95.68	16.02	±	0.23	37.74	±	0.55
# 39	6.30E-05	3.22E-03	±	5.76E-04	-7.80E-03	±	1.95E-02	1.83E-04	±	6.68E-04	94.35	15.88	±	0.21	37.41	±	0.48
# 40	6.39E-05	2.55E-03	±	5.81E-04	-2.27E-02	±	2.03E-02	-9.43E-04	±	7.34E-04	95.49	15.99	±	0.22	37.68	±	0.51
# 41	6.20E-05	1.67E-03	±	5.77E-04	-1.76E-02	±	1.94E-02	-1.13E-04	±	7.53E-04	97.03	16.10	±	0.20	37.94	±	0.48
# 42	5.95E-05	1.11E-03	±	5.82E-04	-4.90E-03	±	2.07E-02	-9.88E-04	±	6.52E-04	98.00	16.05	±	0.21	37.81	±	0.50
# 43	1.24E-04	8.64E-04	±	2.90E-04	-7.29E-04	±	9.49E-03	-3.60E-04	±	3.98E-04	98.45	16.20	±	0.11	38.17	±	0.25
# 44	1.12E-04	1.98E-03	±	3.23E-04	-9.14E-03	±	1.17E-02	-9.43E-04	±	4.51E-04	96.39	15.62	±	0.12	36.81	±	0.27
# 45	1.16E-04	1.54E-03	±	3.07E-04	1.68E-03	±	1.03E-02	-1.23E-04	±	4.00E-04	97.26	16.19	±	0.12	38.14	±	0.28
# 46	1.13E-04	1.27E-03	±	3.15E-04	-5.44E-03	±	1.04E-02	-3.35E-04	±	4.89E-04	97.7	16.02	±	0.12	37.74	±	0.27
# 47	9.65E-05	1.37E-03	±	3.59E-04	1.37E-03	±	1.23E-02	-1.10E-03	±	4.23E-04	97.5	15.71	±	0.13	37.01	±	0.31
# 48	1.14E-04	1.21E-03	±	3.15E-04	-7.54E-03	±	1.04E-02	-9.36E-04	±	4.32E-04	97.82	16.00	±	0.12	37.71	±	0.27
# 49	6.78E-05	9.46E-04	±	5.59E-04	6.98E-04	±	1.91E-02	-1.11E-03	±	6.24E-04	98.38	16.95	±	0.20	39.92	±	0.46
# 50	1.10E-04	1.72E-03	±	3.29E-04	1.07E-03	±	1.19E-02	-3.20E-04	±	4.48E-04	96.94	16.07	±	0.13	37.86	±	0.30
# 51	6.20E-05	1.92E-03	±	5.81E-04	1.55E-02	±	2.01E-02	-1.85E-04	±	8.07E-04	96.88	17.58	±	0.22	41.38	±	0.50
# 52	6.59E-05	9.14E-04	±	5.56E-04	8.48E-03	±	1.94E-02	1.51E-03	±	6.91E-04	98.33	15.89	±	0.20	37.44	±	0.48
# 53	5.46E-05	3.63E-03	±	1.70E-03	-3.12E-02	±	2.21E-02	2.81E-04	±	9.15E-04	93.6	15.67	±	0.69	36.93	±	1.61
# 54	4.90E-05	3.17E-03	±	1.91E-03	-1.10E-02	±	2.57E-02	-1.35E-04	±	8.75E-04	94.72	16.80	±	0.78	39.58	±	1.82
# 55	9.45E-05	3.87E-03	±	1.00E-03	8.27E-05	±	1.28E-02	-1.64E-04	±	5.29E-04	93.54	16.56	±	0.40	39.02	±	0.94
# 56	1.07E-04	1.66E-03	±	8.72E-04	-1.74E-03	±	1.17E-02	-1.42E-03	±	4.78E-04	97.08	16.33	±	0.36	38.46	±	0.83
# 57	1.10E-04	2.30E-03	±	8.55E-04	-2.06E-03	±	1.14E-02	-2.89E-04	±	5.78E-04	96.52	18.86	±	0.35	44.35	±	0.82
# 58	3.81E-05	5.05E-03	±	2.44E-03	3.12E-02	±	3.41E-02	-1.56E-05	±	1.10E-03	94.23	24.35	±	1.00	57.06	±	2.31
# 59	7.52E-05	3.70E-03	±	1.25E-03	1.27E-02	±	1.91E-02	2.36E-04	±	6.46E-04	93.84	16.66	±	0.51	39.25	±	1.20
# 60	3.02E-05	3.81E-02	±	3.12E-03	-5.40E-02	±	4.24E-02	7.72E-04	±	1.30E-03	64.89	20.82	±	1.26	48.91	±	2.92
# 61	7.91E-05	2.41E-03	±	1.17E-03	1.14E-02	±	1.58E-02	5.21E-04	±	5.13E-04	95.9	16.68	±	0.48	39.29	±	1.12
# 62	3.81E-05	3.49E-03	±	2.44E-03	-6.25E-02	±	3.24E-02	-1.26E-03	±	1.15E-03	94.21	16.80	±	0.99	39.56	±	2.31
# 63	1.07E-04	1.97E-03	±	8.74E-04	7.50E-04	±	1.25E-02	-5.34E-04	±	5.36E-04	96.57	16.39	±	0.36	38.61	±	0.83
# 64	8.49E-05	1.78E-03	±	1.10E-03	-1.59E-03	±	1.46E-02	1.73E-04	±	5.86E-04	96.82	16.04	±	0.45	37.80	±	1.04
# 65	1.04E-04	9.93E-04	±	8.99E-04	-1.04E-02	±	1.17E-02	4.84E-04	±	4.71E-04	98.21	16.12	±	0.37	37.97	±	0.86
# 66	1.01E-04	1.81E-03	±	9.20E-04	9.59E-03	±	1.27E-02	-9.43E-04	±	4.08E-04	96.78	16.03	±	0.38	37.76	±	0.88
# 67	2.23E-05	2.39E-02	±	4.19E-03	1.09E-02	±	5.65E-02	1.54E-04	±	1.69E-03	73.91	19.99	±	1.70	46.98	±	3.94
# 68	8.68E-05	2.43E-03	±	1.07E-03	-2.83E-02	±	1.47E-02	-4.53E-05	±	5.78E-04	95.83	16.49	±	0.44	38.85	±	1.02
# 69	4.20E-05	4.02E-03	±	1.29E-03	-2.63E-02	±	2.35E-02	9.89E-04	±	9.31E-04	93.07	15.94	±	0.55	37.56	±	1.28
# 70	9.12E-05	5.50E-04	±	5.82E-04	4.74E-03	±	1.39E-02	1.20E-03	±	6.33E-04	99.01	16.17	±	0.26	38.09	±	0.60
# 71	7.63E-05	1.68E-03	±	7.04E-04	-4.17E-03	±	1.47E-02	8.45E-04	±	6.90E-04	96.97	15.83	±	0.30	37.30	±	0.71
# 72	9.98E-05	1.45E-03	±	5.45E-04	2.48E-03	±	1.09E-02	-1.07E-03	±	5.27E-04	97.38	15.90	±	0.24	37.46	±	0.56
# 73	9.03E-05	2.97E-03	±	5.97E-04	1.20E-02	±	1.23E-02	4.65E-05	±	4.76E-04	95.05	16.89	±	0.26	39.76	±	0.61
# 74	1.05E-04	2.26E-03	±	5.07E-04	-5.05E-04	±	9.90E-03	-6.83E-04	±	5.59E-04	95.95	15.84	±	0.23	37.33	±	0.53
# 75	8.84E-05	3.83E-03	±	6.07E-04	-1.98E-02	±	1.34E-02	-2.47E-04	±	5.10E-04	93.52	16.33	±	0.27	38.47	±	0.62
# 76	4.52E-05	2.70E-03	±	1.19E-03	-2.77E-02	±	2.52E-02	-9.68E-04	±	1.00E-03	95.67	17.62	±	0.53	41.48	±	1.23
# 77	9.31E-05	2.23E-03	±	5.73E-04	-1.22E-02	±	1.15E-02	-6.72E-04	±	6.04E-04	96.11	16.27	±	0.25	38.33	±	0.58
# 78	8.29E-05	2.81E-03	±	6.47E-04	-1.43E-02	±	1.36E-02	-1.29E-03	±	5.57E-04	95.04	15.88	±	0.28	37.43	±	0.66
# 79	3.13E-05	4.74E-03	±	1.71E-03	-4.65E-02	±	3.61E-02	-9.00E-04	±	1.26E-03	93.76	21.07	±	0.75	49.47	±	1.74
# 80	6.45E-05	2.35E-03	±	8.64E-04	-1.07E-02	±	1.75E-02	-8.32E-04	±	6.86E-04	96.96	22.18	±	0.37	52.06	±	0.86
# 81	2.70E-05	9.39E-02	±	2.47E-03	3.72E-03	±	4.40E-02	-1.93E-03	±	1.48E-03	37.87	16.91	±	0.93	39.82	±	2.16
# 82	1.02E-04	1.90E-03	±	5.25E-04	-9.22E-03	±	1.05E-02	-2.91E-05	±	5.92E-04	96.6	15.94	±	0.23	37.55	±	0.53

# 83	9.49E-05	2.07E-03	±	6.85E-04	8.74E-03	±	1.63E-02	-7.30E-04	±	5.85E-04	96.56	17.17	±	0.30	40.43	±	0.69
# 84	4.98E-05	2.11E-01	±	1.99E-03	-1.33E-02	±	3.01E-02	-1.88E-03	±	1.09E-03	20.6	16.18	±	0.64	38.11	±	1.50
# 85	3.00E-05	5.47E-03	±	2.18E-03	-1.14E-01	±	5.26E-02	-1.58E-03	±	1.17E-03	91.77	18.03	±	0.92	42.43	±	2.15
# 86	3.34E-05	3.03E-03	±	1.97E-03	-6.82E-02	±	4.76E-02	-5.74E-04	±	1.16E-03	94.88	16.60	±	0.83	39.11	±	1.94
# 87	6.92E-05	3.78E-03	±	9.60E-04	7.44E-03	±	2.56E-02	-1.30E-03	±	5.62E-04	93.71	16.61	±	0.41	39.13	±	0.95
# 88	8.31E-05	3.09E-03	±	7.90E-04	3.57E-04	±	1.88E-02	-8.28E-04	±	5.64E-04	95.05	17.55	±	0.34	41.32	±	0.78
# 89	7.99E-05	4.67E-03	±	8.15E-04	1.52E-02	±	2.05E-02	3.05E-04	±	5.38E-04	92.45	16.90	±	0.35	39.80	±	0.81
# 90	3.81E-05	7.86E-03	±	1.72E-03	-1.39E-02	±	4.37E-02	-2.54E-03	±	1.13E-03	88.51	17.90	±	0.73	42.12	±	1.69
# 91	7.15E-06	3.45E-02	±	9.18E-03	-4.44E-03	±	2.17E-01	-7.03E-03	±	4.58E-03	76.31	32.85	±	3.89	76.57	±	8.88
# 92	7.88E-05	1.23E-03	±	8.20E-04	-1.53E-02	±	2.00E-02	-8.45E-04	±	5.65E-04	97.87	16.65	±	0.36	39.21	±	0.83
# 93	6.47E-05	3.93E-03	±	1.01E-03	-8.99E-03	±	2.42E-02	-2.90E-04	±	8.94E-04	94.38	19.51	±	0.43	45.86	±	1.00
# 94	9.62E-05	3.36E-03	±	6.77E-04	-2.80E-02	±	1.60E-02	-5.56E-04	±	4.87E-04	94.28	16.34	±	0.29	38.49	±	0.67
# 95	5.85E-05	4.12E-03	±	1.14E-03	-4.56E-02	±	2.69E-02	-1.55E-03	±	5.90E-04	93.68	18.04	±	0.48	42.45	±	1.12
# 96	7.41E-05	3.27E-03	±	8.85E-04	1.40E-03	±	2.23E-02	3.13E-04	±	5.79E-04	94.34	16.09	±	0.38	37.92	±	0.90

Table V.7: ^{40}Ar-^{39}Ar in situ result of sample M89-15. Note that each lines represent each punctual analyses.

N153.MS2																	
Step #	$^{39}Ar_K$ (V)	$^{36}Ar_{atm}/^{39}Ar_K$ (± 1s)			$^{37}Ar_{Ca}/^{39}Ar_K$ (± 1s)			$^{38}Ar_{Cl}/^{39}Ar_K$ (± 1s)			$^{40}Ar^*$	$^{40}Ar^*/^{39}Ar_K$ (± 1s)			Age (Ma) (± 1s)		
# 1	1.402E-06	2.475E-01	±	3.453E-02	-2.381E+00	±	2.079E+00	-1.516E-02	±	2.858E-02	-12.13	-7.91	±	8.03	-19.52	±	19.93
# 2	1.351E-06	8.761E-02	±	2.838E-02	-2.874E+00	±	2.884E+00	-2.593E-02	±	3.056E-02	-11.01	-2.57	±	8.07	-6.13	±	19.29
# 3	1.355E-06	5.928E-02	±	2.626E-02	3.243E+00	±	2.813E+00	6.233E-02	±	3.004E-02	34.52	9.23	±	7.67	21.87	±	18.05
# 4	7.912E-07	1.503E-01	±	5.351E-02	-2.757E+00	±	3.613E+00	6.824E-02	±	5.673E-02	-143.10	-26.14	±	14.81	-63.39	±	36.56
# 5	1.940E-06	6.907E-01	±	5.945E-02	-1.108E+00	±	1.591E+00	-2.963E-03	±	2.148E-02	0.31	0.64	±	5.99	1.52	±	14.27
# 6	2.677E-06	2.830E-02	±	1.463E-02	-2.965E-01	±	1.328E+00	-2.930E-02	±	1.493E-02	47.04	7.43	±	4.33	17.61	±	10.23
# 7	1.568E-05	2.143E-02	±	2.536E-03	2.474E-01	±	2.171E-01	8.421E-03	±	2.750E-03	62.52	10.56	±	0.75	24.99	±	1.77
# 8	2.887E-05	1.034E-02	±	1.340E-03	2.276E-01	±	1.396E-01	1.788E-03	±	1.418E-03	74.19	8.78	±	0.41	20.80	±	0.96
# 9	4.268E-05	4.725E-03	±	8.660E-04	1.642E-02	±	7.486E-02	-2.755E-04	±	1.156E-03	86.96	9.31	±	0.26	22.06	±	0.62
# 10	1.129E-04	1.774E-03	±	3.240E-04	1.924E-02	±	3.161E-02	-6.254E-05	±	5.585E-04	94.81	9.58	±	0.11	22.68	±	0.25
# 11	7.098E-05	1.494E-03	±	5.517E-04	1.748E-01	±	5.463E-02	1.121E-03	±	7.102E-04	95.49	9.34	±	0.17	22.12	±	0.40
# 12	9.852E-05	2.405E-03	±	4.113E-04	2.510E-02	±	3.734E-02	1.142E-03	±	4.897E-04	92.85	9.23	±	0.13	21.86	±	0.30
# 13	1.518E-04	1.127E-03	±	2.629E-04	7.295E-02	±	2.734E-02	7.012E-05	±	3.541E-04	96.56	9.35	±	0.08	22.14	±	0.20
# 14	1.284E-04	1.182E-03	±	2.928E-04	1.252E-02	±	2.528E-02	-3.992E-04	±	4.223E-04	96.38	9.29	±	0.09	21.99	±	0.22
# 15	1.246E-04	1.167E-03	±	2.976E-04	-6.989E-03	±	2.839E-02	3.168E-04	±	4.850E-04	96.45	9.37	±	0.09	22.19	±	0.22
# 16	9.267E-05	1.764E-03	±	3.840E-04	2.206E-02	±	3.633E-02	-5.894E-04	±	5.621E-04	94.73	9.38	±	0.12	22.22	±	0.29
# 17	8.081E-05	1.547E-03	±	5.237E-04	5.621E-02	±	3.863E-02	1.989E-04	±	6.730E-04	95.36	9.40	±	0.16	22.26	±	0.38
# 18	6.793E-05	3.062E-03	±	6.302E-04	-6.444E-02	±	4.322E-02	1.168E-03	±	6.922E-04	90.95	9.10	±	0.19	21.55	±	0.45
# 19	6.038E-05	4.161E-03	±	6.965E-04	1.729E-02	±	5.702E-02	1.986E-03	±	7.645E-04	87.80	8.85	±	0.21	20.96	±	0.50
# 20	6.656E-05	3.072E-03	±	5.710E-04	-9.159E-02	±	4.867E-02	2.108E-03	±	8.441E-04	91.02	9.20	±	0.17	21.79	±	0.41
# 21	8.346E-05	4.961E-03	±	6.177E-04	-2.161E-02	±	5.117E-02	7.767E-04	±	7.923E-04	85.97	8.98	±	0.19	21.28	±	0.44
# 22	6.126E-05	4.425E-03	±	5.059E-04	1.876E-02	±	6.777E-02	1.489E-03	±	1.352E-03	87.55	9.20	±	0.21	21.78	±	0.48
# 23	1.401E-04	3.567E-03	±	1.960E-04	3.285E-02	±	3.149E-02	1.397E-05	±	5.581E-04	89.91	9.39	±	0.09	22.24	±	0.22
# 24	1.655E-04	3.193E-03	±	1.704E-04	9.348E-03	±	2.406E-02	-2.948E-04	±	5.337E-04	90.91	9.44	±	0.08	22.36	±	0.20
# 25	1.554E-04	3.023E-03	±	1.716E-04	1.496E-02	±	2.875E-02	-4.575E-04	±	6.229E-04	91.32	9.40	±	0.08	22.27	±	0.19
# 26	1.759E-04	3.405E-03	±	1.785E-04	1.434E-02	±	2.565E-02	-2.248E-06	±	4.812E-04	90.27	9.34	±	0.08	22.12	±	0.18
# 27	1.203E-04	4.969E-03	±	2.268E-04	2.878E-02	±	3.531E-02	2.867E-04	±	6.109E-04	86.47	9.38	±	0.10	22.22	±	0.24
# 28	1.100E-04	6.533E-03	±	2.617E-04	1.495E-02	±	3.559E-02	6.003E-04	±	6.746E-04	82.56	9.14	±	0.12	21.65	±	0.27
# 29	8.887E-05	1.027E-02	±	4.704E-04	3.088E-02	±	4.483E-02	2.970E-04	±	8.569E-04	74.82	9.02	±	0.17	21.37	±	0.40
# 30	7.747E-05	1.278E-02	±	4.622E-04	4.589E-02	±	5.292E-02	1.642E-03	±	9.422E-04	70.40	8.98	±	0.18	21.28	±	0.42
# 31	7.935E-05	1.535E-02	±	4.880E-04	-8.199E-02	±	5.495E-02	1.348E-03	±	9.698E-04	66.36	8.95	±	0.18	21.19	±	0.42
Total	2.410E-03	5.021E-03	±	8.596E-05	1.845E-02	±	8.663E-03	4.372E-04	±	1.421E-04	86.17	9.24	±	0.03	21.89	±	0.12

Table V.8: ^{40}Ar-^{39}Ar step heating result of sample M140-15. Each lines represent each step heating. The apparent age is located at the end of lines. Note that the last line corresponds to the total fusion of the sample.

N146.MS2																			
Step #	**$^{39}Ar_K$**	**$^{36}Ar_{atm}/^{39}Ar_K$**			**$^{37}Ar_{Ca}/^{39}Ar_K$**			**$^{38}Ar_{Cl}/^{39}Ar_K$**			**$^{40}Ar^*$**	**$^{40}Ar^*/^{39}Ar_K$**			**Age (Ma)**		
	(V)	**(± 1s)**			**(± 1s)**			**(± 1s)**				**(± 1s)**			**(± 1s)**		
# 1	7.279E-07	-6.760E-02	±	3.209E-01	-2.562E+00	±	3.309E+00	4.942E-02	±	1.169E-01	195.50	40.90	±	99.07	94.85	±	223.80
# 2	4.637E-06	1.671E-02	±	4.959E-02	4.223E-02	±	4.048E-01	1.199E-02	±	1.601E-02	57.84	6.77	±	14.73	16.06	±	34.76
# 3	2.382E-05	2.630E-02	±	9.743E-03	1.721E-03	±	6.814E-02	2.499E-03	±	3.581E-03	46.48	6.75	±	2.89	16.00	±	6.82
# 4	2.078E-05	2.447E-02	±	1.111E-02	-5.930E-02	±	4.400E-02	4.453E-03	±	3.872E-03	17.19	1.50	±	3.29	3.57	±	7.82
# 5	4.540E-05	1.871E-02	±	5.090E-03	5.513E-02	±	3.830E-02	6.277E-03	±	1.916E-03	38.73	3.49	±	1.51	8.30	±	3.58
# 6	3.558E-05	1.482E-02	±	6.482E-03	1.593E-01	±	4.728E-02	6.903E-03	±	2.134E-03	55.77	5.52	±	1.93	13.10	±	4.55
# 7	1.005E-04	9.342E-03	±	2.308E-03	3.620E-02	±	1.715E-02	8.864E-04	±	8.955E-04	73.63	7.71	±	0.69	18.26	±	1.62
# 8	1.464E-04	3.786E-03	±	2.072E-03	-1.700E-02	±	2.476E-02	4.743E-04	±	8.390E-04	88.85	8.92	±	0.61	21.11	±	1.45
# 9	9.390E-05	3.768E-03	±	3.232E-03	-7.444E-02	±	3.832E-02	-3.626E-04	±	1.245E-03	89.29	9.29	±	0.96	21.98	±	2.25
# 10	3.799E-04	2.795E-03	±	7.982E-04	5.844E-04	±	9.778E-03	1.916E-04	±	3.700E-04	92.16	9.71	±	0.24	22.97	±	0.56
# 11	2.386E-04	5.170E-03	±	1.272E-03	6.510E-03	±	1.496E-02	1.256E-04	±	5.898E-04	85.00	8.65	±	0.38	20.49	±	0.89
# 12	2.468E-04	4.427E-03	±	1.232E-03	-1.257E-02	±	1.417E-02	3.994E-04	±	5.442E-04	87.23	8.93	±	0.37	21.14	±	0.86
# 13	4.331E-04	5.171E-03	±	7.071E-04	4.439E-03	±	8.529E-03	4.366E-05	±	3.913E-04	85.19	8.79	±	0.21	20.81	±	0.49
# 14	2.960E-04	4.431E-03	±	1.027E-03	1.043E-02	±	1.247E-02	-2.681E-04	±	4.263E-04	87.16	8.89	±	0.30	21.03	±	0.72
# 15	2.263E-04	2.104E-03	±	1.345E-03	1.820E-02	±	1.744E-02	4.858E-05	±	5.526E-04	93.96	9.67	±	0.40	22.88	±	0.94
# 16	2.447E-04	2.281E-03	±	1.248E-03	8.898E-03	±	1.566E-02	2.791E-04	±	5.723E-04	93.48	9.66	±	0.37	22.85	±	0.87
# 17	2.011E-04	-4.626E-04	±	1.519E-03	-7.800E-03	±	1.782E-02	5.046E-05	±	6.556E-04	101.30	10.58	±	0.45	25.01	±	1.06
# 18	1.520E-04	-1.015E-03	±	2.007E-03	-2.253E-02	±	2.371E-02	-7.251E-04	±	8.129E-04	102.80	11.09	±	0.60	26.21	±	1.40
# 19	1.267E-04	-1.008E-03	±	2.415E-03	1.273E-02	±	2.973E-02	-1.274E-03	±	9.966E-04	102.80	10.87	±	0.72	25.69	±	1.69
# 20	2.107E-04	4.612E-04	±	1.442E-03	2.203E-02	±	1.659E-02	6.078E-04	±	5.973E-04	98.71	10.41	±	0.43	24.63	±	1.01
# 21	1.101E-04	2.879E-03	±	2.753E-03	3.409E-02	±	3.663E-02	-3.918E-04	±	1.110E-03	92.33	10.24	±	0.82	24.22	±	1.92
# 22	5.329E-05	1.060E-02	±	5.726E-03	7.603E-02	±	6.672E-02	-5.618E-04	±	2.408E-03	78.05	11.14	±	1.70	26.32	±	3.99
# 23	2.775E-05	2.023E-02	±	1.098E-02	5.596E-02	±	1.396E-01	2.832E-03	±	4.201E-03	70.83	14.52	±	3.27	34.23	±	7.63
# 24	7.183E-05	1.039E-02	±	4.222E-03	1.261E-01	±	5.885E-02	2.886E-05	±	1.629E-03	82.62	14.60	±	1.26	34.43	±	2.94
Total	3.491E-03	4.088E-03	±	3.998E-04	8.343E-03	±	4.583E-03	2.845E-04	±	1.662E-04	88.69	9.47	±	0.12	22.41	±	0.30

Table V.9: ^{40}Ar-^{39}Ar step heating result of sample M145-15. Each lines represent each step heating. The apparent age is located at the end of lines. Note that the last line corresponds to the total fusion of the sample.

Samples	Isotopic ratios		Ages (Ma)		Isotopic ratios		Ages (Ma)		Isotopic ratios		Ages (Ma)		Isotopic ratios		Ages (Ma)						
	$^{207}Pb/^{206}Pb$	σ (%)	$^{207}Pb/^{206}Pb$	σ	$^{207}Pb/^{235}U$	σ (%)	$^{207}Pb/^{235}U$	σ	$^{206}Pb/^{238}U$	σ (%)	$^{206}Pb/^{238}U$	σ	$^{208}Pb/^{232}Th$	σ (%)	$^{208}Pb/^{232}Th$	σ	Rho	conc	U	Th	Pb
M24-16-1	4.77E-02	4.79E-03	84.5	222.97	2.59E-02	2.59E-03	26	2.57	4.03E-03	1.00E-04	25.9	0.61	1.25E-03	2.00E-05	25.2	0.45	0.25	100	5610	33146	274
M24-16-2	5.31E-02	5.00E-03	333.3	199.86	2.99E-02	2.80E-03	29.9	2.76	4.03E-03	1.00E-04	25.9	0.62	1.27E-03	2.00E-05	25.7	0.44	0.26	87	5618	38625	274
M24-16-3	4.36E-02	9.83E-03	0.1	347.53	2.19E-02	4.89E-03	22	4.86	3.80E-03	1.70E-04	24.5	1.09	1.30E-03	4.00E-05	26.4	0.76	0.20	111	6054	51865	279
M24-16-4	5.79E-02	5.08E-03	524.5	181.95	3.31E-02	2.90E-03	33.1	2.85	3.98E-03	9.00E-05	25.6	0.61	1.35E-03	2.00E-05	27.2	0.47	0.26	77	6278	37869	303
M24-16-5	5.43E-02	7.48E-03	381.8	283.35	2.97E-02	4.06E-03	29.8	4	4.09E-03	1.30E-04	26.3	0.86	1.20E-03	3.00E-05	24.3	0.61	0.23	88	6868	44657	340
M24-16-6	5.83E-02	5.12E-03	540.9	181.81	3.27E-02	2.87E-03	32.7	2.82	4.07E-03	9.00E-05	26.2	0.6	1.28E-03	2.00E-05	25.9	0.45	0.25	80	6067	33836	299
M24-16-7	4.68E-02	4.11E-03	39.2	197.8	2.66E-02	2.33E-03	26.6	2.31	4.06E-03	9.00E-05	26.1	0.59	1.28E-03	2.00E-05	25.9	0.45	0.25	98	6709	34339	330
M24-16-8	5.15E-02	4.72E-03	262.4	196.94	2.73E-02	2.49E-03	27.3	2.46	3.86E-03	9.00E-05	24.8	0.59	1.35E-03	3.00E-05	27.3	0.51	0.26	91	6476	30145	303
M24-16-9	5.12E-02	4.55E-03	248.7	192.39	3.03E-02	2.70E-03	30.3	2.66	4.16E-03	9.00E-05	26.8	0.6	1.20E-03	2.00E-05	24.3	0.43	0.24	88	6274	32306	316
M24-16-10	5.37E-02	5.43E-03	356.4	213.64	3.00E-02	3.02E-03	30	2.97	4.03E-03	1.00E-04	25.9	0.66	1.27E-03	3.00E-05	25.7	0.51	0.25	86	4605	24651	224
M24-16-11	4.65E-02	5.97E-03	22.3	282.43	2.54E-02	3.25E-03	25.5	3.22	3.93E-03	1.10E-04	25.3	0.68	1.28E-03	2.00E-05	25.9	0.48	0.22	99	4065	29412	193
M24-16-12	6.80E-02	9.53E-03	868.4	266.06	3.71E-02	5.13E-03	37	5.02	3.74E-03	1.40E-04	24.1	0.9	1.23E-03	4.00E-05	24.9	0.73	0.27	65	4294	24586	194
M24-16-13	5.48E-02	7.39E-03	403.3	276.79	3.08E-02	4.11E-03	30.8	4.05	4.10E-03	1.30E-04	26.4	0.85	1.26E-03	4.00E-05	25.5	0.79	0.24	86	4980	18544	247
M24-16-14	4.90E-02	6.86E-03	147.2	298.71	2.67E-02	3.72E-03	26.8	3.68	3.92E-03	1.20E-04	25.2	0.78	1.43E-03	4.00E-05	28.8	0.83	0.22	94	5750	19760	272
M24-16-15	6.53E-02	6.77E-03	784.6	203.49	3.72E-02	3.82E-03	37.1	3.74	3.99E-03	1.10E-04	25.7	0.74	1.23E-03	3.00E-05	24.9	0.55	0.27	69	5657	33626	273
M24-16-16	5.05E-02	5.53E-03	216.7	235.45	2.69E-02	2.94E-03	27	2.91	3.77E-03	1.00E-04	24.3	0.65	1.25E-03	2.00E-05	25.3	0.49	0.24	90	4199	26451	191
M24-16-17	7.24E-02	7.32E-03	997.4	192.8	3.93E-02	3.94E-03	39.2	3.85	4.02E-03	1.10E-04	25.8	0.73	1.28E-03	3.00E-05	25.9	0.57	0.27	66	4426	24354	214
M24-16-18	4.37E-02	5.42E-03	0.1	154.32	2.65E-02	3.28E-03	26.6	3.24	4.15E-03	1.10E-04	26.7	0.71	1.33E-03	3.00E-05	26.9	0.53	0.21	100	5121	31212	256
M24-16-19	6.06E-02	5.26E-03	626.2	176.81	3.70E-02	3.21E-03	36.9	3.14	4.22E-03	1.00E-04	27.1	0.67	1.27E-03	2.00E-05	25.7	0.49	0.27	73	5515	30839	281
M24-16-20	4.83E-02	7.19E-03	112.4	318.01	2.47E-02	3.65E-03	24.7	3.61	3.94E-03	1.20E-04	25.4	0.8	1.24E-03	3.00E-05	25.1	0.58	0.21	103	6268	41136	298
M24-16-21	5.37E-02	7.47E-03	359.6	286.64	3.00E-02	4.14E-03	30	4.08	3.86E-03	1.30E-04	24.8	0.84	1.21E-03	3.00E-05	24.4	0.66	0.24	83	3694	20506	171
M24-16-22	5.50E-02	7.36E-03	411.4	274.4	2.98E-02	3.96E-03	29.8	3.9	3.85E-03	1.20E-04	24.8	0.77	1.24E-03	3.00E-05	25	0.62	0.23	83	3381	18006	157
M24-16-23	5.58E-02	8.31E-03	444	301.16	3.02E-02	4.46E-03	30.2	4.4	3.78E-03	1.30E-04	24.3	0.81	1.21E-03	3.00E-05	24.4	0.62	0.23	80	3745	22158	170
M24-16-24	5.42E-02	9.38E-03	377.8	348.79	2.89E-02	4.96E-03	29	4.89	3.86E-03	1.50E-04	24.8	0.97	1.63E-03	5.20E-04	33	10.47	0.23	86	2245	207	104
M24-16-25	5.23E-02	4.79E-03	299.1	195.88	2.77E-02	2.54E-03	27.7	2.51	3.72E-03	9.00E-05	24	0.57	1.27E-03	2.00E-05	25.6	0.46	0.26	87	6569	33675	295

Table V.10: U-Pb age dating results from the sample M24-16. Note that errors are given at 1σ.

Samples	Isotopic ratios		Ages (Ma)		Isotopic ratios		Ages (Ma)		Isotopic ratios		Ages (Ma)		Isotopic ratios		Ages (Ma)						
	$^{207}Pb/^{206}Pb$	σ (%)	$^{207}Pb/^{206}Pb$	σ	$^{207}Pb/^{235}U$	σ (%)	$^{207}Pb/^{235}U$	σ	$^{206}Pb/^{238}U$	σ (%)	$^{206}Pb/^{238}U$	σ	$^{208}Pb/^{232}Th$	σ (%)	$^{208}Pb/^{232}Th$	σ	Rho	conc	U	Th	Pb
M120-15-1	4.34E-02	9.00E-03	0.1	300.74	2.16E-02	4.46E-03	21.7	4.43	3.46E-03	1.20E-04	22.3	0.74	1.17E-03	3.00E-05	23.6	0.57	0.17	103	2638	16928	110
M120-15-2	5.46E-02	1.13E-02	395.5	407.05	2.60E-02	5.32E-03	26	5.27	3.30E-03	1.30E-04	21.2	0.86	1.09E-03	3.00E-05	22	0.59	0.19	82	2602	19979	103
M120-15-3	4.91E-02	1.10E-02	150.8	454.26	2.22E-02	4.93E-03	22.3	4.9	3.30E-03	1.30E-04	21.3	0.86	1.16E-03	3.00E-05	23.5	0.62	0.18	96	2411	19010	96
M120-15-4	5.32E-02	1.09E-02	335.1	407.81	2.56E-02	5.19E-03	25.6	5.14	3.43E-03	1.50E-04	22.1	0.95	1.05E-03	4.00E-05	21.2	0.72	0.22	86	2388	14658	99
M120-15-5	4.44E-02	1.31E-02	0.1	508.04	2.18E-02	6.36E-03	21.9	6.32	3.51E-03	1.90E-04	22.6	1.23	1.11E-03	5.00E-05	22.5	1	0.19	103	2362	12745	100
M120-15-6	5.75E-02	1.38E-02	511.3	453.91	2.76E-02	6.52E-03	27.6	6.44	3.24E-03	1.60E-04	20.9	1.06	1.13E-03	4.00E-05	22.8	0.84	0.21	76	2793	17407	109
M120-15-7	4.57E-02	9.62E-03	0.1	425.3	2.01E-02	4.18E-03	20.2	4.16	3.23E-03	1.40E-04	20.8	0.91	1.09E-03	6.00E-05	22	1.12	0.21	103	4045	9906	157
M120-15-8	5.65E-02	9.53E-03	470.8	336.14	2.93E-02	4.89E-03	29.3	4.83	3.48E-03	1.40E-04	22.4	0.89	1.20E-03	5.00E-05	24.3	0.95	0.24	76	2511	8379	105
M120-15-10	5.47E-02	1.04E-02	400.1	376.07	2.44E-02	4.58E-03	24.5	4.54	3.24E-03	1.30E-04	20.9	0.82	1.03E-03	3.00E-05	20.8	0.62	0.21	85	2404	14207	94
M120-15-11	9.08E-02	1.53E-02	1442	290.79	4.36E-02	7.22E-03	43.4	7.02	3.36E-03	1.50E-04	21.6	0.99	1.25E-03	4.00E-05	25.2	0.83	0.27	50	1341	8086	54
M120-15-12	3.73E-02	1.40E-02	0.1	253.73	1.69E-02	6.29E-03	17	6.28	3.44E-03	1.70E-04	22.1	1.06	1.00E-03	4.00E-05	20.2	0.82	0.13	130	2766	15551	114
M120-15-13	5.41E-02	1.21E-02	374.9	438.02	2.43E-02	5.40E-03	24.4	5.36	3.29E-03	1.50E-04	21.2	0.94	1.10E-03	3.00E-05	22.2	0.65	0.21	87	2155	16592	85
M120-15-14	5.57E-02	1.29E-02	440.3	447.84	3.15E-02	7.23E-03	31.4	7.12	3.68E-03	1.90E-04	23.7	1.19	1.10E-03	5.00E-05	22.2	0.92	0.22	75	1931	10913	85

Table V.11: U-Pb age dating results from the sample M120-15. Note that errors are given at 1σ.

V.8.3. Representative microprobe analyses

SiO2	TiO2	Al2O3	FeO	MnO	MgO	CaO	Na2O	K2O	Cr2O3	Total
46.5245	0.8041	36.7125	1.3971	0.0063	0.814	0.0003	0.9118	9.2851	0.1253	96.581
49.393	0.7153	32.5958	1.7847	0	1.9697	0.0074	0.6473	9.5688	0.0873	96.7693
50.5604	0.6198	31.1348	1.7625	0.0302	2.3883	0.0013	0.5002	9.4462	0.0359	96.4796
50.9532	0.6436	31.2724	1.9149	0.0303	2.5149	0	0.5476	9.2541	0.043	97.174
50.4935	0.6024	31.106	1.954	0.0037	2.5172	0	0.5912	9.5172	0.0371	96.8223
50.4316	0.6071	30.9188	2.1341	0.0445	2.6118	0	0.5337	9.4031	0.0301	96.7148
50.3572	0.6254	31.4122	1.7831	0	2.3525	0.0001	0.4848	9.5166	0.0187	96.5506
50.1935	0.6479	32.007	1.8484	0.0107	2.1553	0.0009	0.4902	9.5079	0.0673	96.9291
48.7883	0.6384	32.8699	2.0783	0.0246	1.9059	0.0026	0.5387	9.4056	0.039	96.2913
49.1424	0.847	37.5112	1.4631	0.0059	0.8712	0	0.4592	5.4646	0.1301	95.8947
46.0222	0.8937	36.6237	1.3167	0	0.7906	0.0096	0.679	9.8971	0.0167	96.2493
50.6121	0.5795	31.5385	1.8529	0	2.2831	0.0109	0.5091	9.4356	0.0122	96.8339
50.0045	0.6384	31.3267	1.9346	0.001	2.3044	0	0.5404	9.4457	0.0458	96.2415
50.3226	0.6368	30.9606	1.9715	0.0169	2.5074	0	0.5785	9.465	0.0253	96.4846
50.2353	0.614	31.0935	1.9817	0.0047	2.5044	0.001	0.5666	9.3894	0.0129	96.4035
50.4429	0.6286	31.407	1.9191	0.0392	2.3633	0	0.566	9.4927	0.0288	96.8876
50.2452	0.6463	31.2903	1.8383	0.0015	2.4147	0	0.6226	9.4899	0.0188	96.5676
49.5624	0.6409	32.2059	1.8403	0.0067	2.1309	0	0.6072	9.6477	0.0322	96.6742
49.2259	0.6567	32.6331	1.8204	0	2.0008	0	0.6608	9.5308	0.0392	96.5677
49.8844	0.6556	32.1388	1.8464	0.0062	2.1879	0.0443	0.5855	9.4446	0.064	96.8577
50.1398	0.609	31.8845	1.8123	0.0225	2.2834	0	0.551	9.5869	0.0351	96.9245
50.4342	0.6314	31.2453	1.8997	0	2.3988	0	0.551	9.3875	0.0417	96.5896
50.4406	0.6213	31.4551	1.8069	0.0146	2.337	0	0.5472	9.4945	0.0493	96.7665
50.308	0.6269	31.4522	1.826	0.0128	2.353	0.0009	0.5225	9.4213	0.0872	96.6108
48.3833	0.662	34.2652	1.5028	0.0141	1.5514	0.0155	0.4847	9.8228	0.0407	96.7425
47.7245	0.777	33.7083	1.608	0.0119	1.5369	0.008	0.7917	9.6833	0.0791	95.9287
49.8852	0.669	31.8136	1.6633	0.0324	2.0417	0	0.5861	9.7291	0.0531	96.4735
49.0036	0.5497	32.2461	1.749	0.0008	1.9412	0	0.68	9.7506	0.0507	95.9717
46.9128	0.7345	35.115	1.5116	0.0032	1.2108	0.0019	0.8999	9.6066	0.0693	96.0656
49.5936	0.6448	32.083	1.5604	0.0296	1.901	0.0012	0.6475	9.615	0.0472	96.1233
47.3919	0.6653	34.5255	1.5454	0.0282	1.3822	0	0.8755	9.6076	0.0595	96.0811
46.748	0.6824	35.1157	1.3278	0	1.1122	0	0.9609	9.5167	0.0603	95.524
48.4587	0.7322	33.1083	1.7081	0	1.7887	0	0.6906	9.7463	0.0445	96.2774
46.6431	0.7165	35.4526	1.419	0.0239	1.1162	0	0.932	9.6458	0.0269	95.976
46.1272	0.7849	36.6421	1.1554	0.0301	0.6902	0	0.8539	9.8152	0.0568	96.1558
50.0981	0.6108	30.3556	2.12	0.0005	2.5725	0	0.5728	9.5509	0.0306	95.9118
50.0428	0.601	31.3901	1.8204	0.0308	2.206	0	0.533	9.7544	0.058	96.4365
46.72	0.7445	35.2851	1.4522	0	1.0695	0	0.9346	9.6499	0.0202	95.876
46.7017	0.7457	35.604	1.524	0	0.9927	0.0058	0.931	9.7828	0.0124	96.3001
46.7524	0.7699	35.2799	1.6602	0.0093	1.1946	0	0.9508	9.6923	0	96.3094
47.7772	0.7852	33.8945	1.7146	0.0049	1.5336	0	0.8394	9.6794	0.0235	96.2523
50.1149	0.6131	31.4161	1.7303	0	2.1291	0.0036	0.5169	9.7588	0.0187	96.3015
46.9476	0.6938	35.3737	1.4609	0	1.1297	0	0.9181	9.6473	0.0134	96.1845
46.5382	0.6899	36.6007	1.3233	0.0377	0.6563	0	1.0311	9.5857	0.0372	96.5001
46.124	0.7242	36.7942	1.2623	0	0.6493	0	1.0742	9.6146	0.0341	96.2769
46.1412	0.7952	36.5799	1.3968	0	0.6355	0	1.01	9.6574	0.0402	96.2562
46.1564	0.6649	37.5178	1.3382	0.0229	0.6201	0.0029	1.0198	9.3932	0.0159	96.7521
46.4782	0.5921	36.8498	1.2995	0.0203	0.7792	0.0025	0.9492	9.4817	0.0091	96.4616

Table V.12: Sample M127-15 (muscovite).

SiO2	TiO2	Al2O3	FeO	MnO	MgO	CaO	Na2O	K2O	F	Total
45.356	0.141	33.922	2.184	0.095	0.467	0	0.634	9.872	0	92.67
45.84	0.169	34.464	2.369	0	0.487	0.005	0.579	9.189	0.186	93.288
46.105	0	33.214	2.264	0.025	0.639	0	0.673	9.81	0	92.729
45.981	0.189	33.66	2.382	0	0.685	0	0.575	9.799	0.217	93.487
45.998	0.046	33.187	2.331	0	0.741	0	0.551	9.894	0.325	93.073
46.54	0.138	33.019	2.227	0.022	0.922	0	0.54	9.354	0.108	92.871
46.182	0.084	33.78	2.556	0.083	0.796	0	0.577	9.965	0	94.021
46.809	0.074	33.679	2.299	0.034	0.629	0	0.67	9.951	0.218	94.363
46.637	0.079	33.744	2.041	0.049	0.741	0	0.676	9.718	0.327	94.013
47.296	0.046	33.8	2.191	0	0.728	0.011	0.654	9.534	0.054	94.312
47.168	0	32.994	2.236	0	0.783	0	0.562	9.673	0.139	93.555
48.977	0	34.491	2.219	0.104	0.83	0	0.375	7.278	0	94.276
46.932	0.013	34.228	2.479	0.003	0.766	0	0.561	9.138	0.139	94.259
46.245	0.02	33.868	2.079	0	0.671	0	0.803	9.422	0.187	93.295
46.118	0.215	34.153	2.396	0.127	0.608	0	0.699	9.28	0.232	93.827
46.249	0.093	33.606	2.242	0.064	0.661	0	0.66	10.012	0.235	93.823
45.558	0.166	34.286	1.904	0	0.488	0	0.766	9.793	0.108	93.069
45.849	0.073	34.348	1.785	0	0.46	0.007	0.713	9.465	0.099	92.799
46.226	0	33.933	2.223	0	0.653	0	0.692	10.043	0.278	94.048
46.218	0	33.716	2.405	0.032	0.763	0	0.71	9.613	0.185	93.641
45.446	0	33.794	1.936	0	0.619	0	0.776	9.584	0.246	92.4
45.925	0.031	33.615	2.531	0.063	0.771	0	0.586	9.625	0.093	93.239
47.276	0.086	34.462	2.338	0	0.774	0.029	0.586	9.012	0	94.564
46.939	0.092	33.656	2.357	0	0.685	0	0.656	10.094	0.185	94.664
45.83	0.009	33.514	2.535	0.054	0.604	0	0.623	10.064	0	93.232
46.033	0.092	33.82	2.161	0	0.684	0	0.609	9.888	0.324	93.61
46.442	0.134	33.965	2.108	0	0.598	0	0.625	9.486	0.37	93.728
46.726	0.058	33.561	2.316	0	0.782	0.023	0.696	9.149	0.323	93.635
47.094	0.139	34.47	2.05	0.003	0.686	0	0.711	9.389	0.191	94.732
46.686	0.021	33.907	1.81	0	0.756	0	0.657	9.585	0.198	93.62
46.371	0	34.353	1.736	0.026	0.651	0	0.548	9.554	0.466	93.705
46.451	0.111	34.323	2.031	0	0.673	0	0.693	9.432	0.233	93.947
45.932	0.051	34.075	2.312	0.026	0.636	0	0.655	9.858	0.231	93.778
46.558	0.088	33.908	2.431	0	0.66	0	0.719	9.668	0.284	94.317
46.761	0.121	32.992	2.342	0.067	0.825	0	0.606	9.63	0.161	93.506
47.366	0.043	33.286	1.756	0.103	0.924	0.016	0.557	9.689	0.975	94.715
46.253	0	33.554	1.967	0	0.823	0.02	0.565	9.872	0.161	93.214
47.13	0.099	33.286	2.291	0.016	0.992	0.014	0.601	9.729	0.507	94.665
47.429	0.183	32.925	1.872	0	0.893	0	0.542	9.436	0.396	93.677

Table V.13: Sample M89b-15 (muscovite).

SiO2	TiO2	Al2O3	FeO	MnO	MgO	CaO	Na2O	K2O	F	Total
35.721	1.638	18.624	19.05	0.107	10.659	0.005	0.05	9.409	0.461	95.724
36.07	1.511	18.358	18.457	0	11.548	0	0.04	8.9	0.077	94.961
36.03	1.34	19.288	19.178	0.18	10.544	0	0.091	9.439	0.192	96.282
36.339	1.276	19.33	18.759	0.109	10.639	0	0.091	9.57	0.269	96.383
32.684	0.576	20.288	20.536	0.036	12.511	0	0.077	7.462	0.371	94.542
35.179	1.886	18.496	18.958	0.025	11.242	0	0.075	9.342	0.44	95.643
36.533	1.224	19.434	18.722	0.051	11.013	0	0.108	8.709	0.687	96.481
37.11	1.476	18.454	18.095	0.212	11.443	0	0.105	8.939	0.617	96.452

Table V.14: Sample M115-15 (biotite).

V.8.4. Geochronological data

Studies	Location			Lithology & Structural position	Ages in the Menderes Massif (Western Turkey)			
	Lat	*Long*	*Area*		*Method*	*Mineral*	*Ages (Ma)*	*Error (±)*
Hetzel & Reischmann, 1996	37.4241	27.7398	SMM	Weakly deformed augen-gneiss / Footwall of SSZ	^{40}Ar-^{39}Ar	Muscovite	37.90	0.40
"	37.4094	27.7799	SMM	Weakly deformed augen-gneiss / Footwall of SSZ	^{40}Ar-^{39}Ar	Muscovite	43.40	1.30
"	37.4509	27.7201	SMM	Deformed mica-schist / Hanging-wallof the SSZ	^{40}Ar-^{39}Ar	Muscovite	34.50	1.40
"	37.3767	27.7419	SMM	Muscovite-schist / Hanging-wallof the SSZ	^{40}Ar-^{39}Ar	Muscovite	40.00	1.80
Cenki-Tok et al., 2016	38.9934	28.8007	NMM	Mica-schist / Footwall of the SD	^{40}Ar-^{39}Ar	Muscovite	19.90	0.30
"	39.0439	28.9211	NMM	Migmatite	^{40}Ar-^{39}Ar	Biotite	19.80	0.10
"	38.8102	28.6000	NMM	Mica-schist (ultramylonite)	^{40}Ar-^{39}Ar	Muscovite	21.80	0.20
"	38.4894	28.5260	NMM	Metaconglomerate / base of the Mesozoic section	^{40}Ar-^{39}Ar	Muscovite	25.50	0.30
Erkul, 2010	39.4504	28.5288	NMM	Granites (texture equigranular)	^{40}Ar-^{39}Ar	Biotite	20.98	-
"	39.4199	28.5148	NMM	Granites (texture equigranular)	^{40}Ar-^{39}Ar	Biotite	20.78	-
"	39.4566	28.5817	NMM	Granites (texture equigranular)	^{40}Ar-^{39}Ar	Biotite	20.68	-
"	39.3860	28.6810	NMM	Granites (texture porphyritic)	^{40}Ar-^{39}Ar	Biotite	20.04	-
"	39.3177	28.7516	NMM	Granites (texture protomylonitic)	^{40}Ar-^{39}Ar	Biotite	20.02	-
"	39.3306	28.8031	NMM	Granites (texture porphyritic)	^{40}Ar-^{39}Ar	Biotite	19.95	-
Ring et al., 2003	38.7106	28.3303	NMM	-	^{40}Ar-^{39}Ar	Muscovite	24.80	0.30
"	37.6541	27.6617	SMM	-	^{40}Ar-^{39}Ar	Muscovite	32.10	0.50
"	37.8982	27.6911	CMM	-	^{40}Ar-^{39}Ar	Muscovite	27.90	1.00
Lips et al., 2001	37.9000	28.0100	CMM	Mica-schist / Footwall of the BMD	^{40}Ar-^{39}Ar	White Mica	36.00	2.00
"	38.4600	28.1900	CMM	Cataclasites in the footwall of the AD	^{40}Ar-^{39}Ar	White Mica	7.00	1.00
Isik et al., 2004	-	-	NMM	Mylonitized high-grade gneiss / Footwall of the SD	^{40}Ar-^{39}Ar	Muscovite	22.86	0.47
"	-	-	NMM	Egrgöz granitoid	^{40}Ar-^{39}Ar	Biotite	20.19	0.28
Hetzel et al., 2013	37.9631	27.6780	CMM	Dark grey fault gouge / BMD	K-Ar	White Mica	3.10	0.10
"	37.9631	27.6780	CMM	Dark grey fault gouge / BMD	K-Ar	White Mica	3.60	0.20
"	37.9631	27.6780	CMM	Dark grey fault gouge / BMD	K-Ar	White Mica	5.00	0.20
"	37.9631	27.6780	CMM	Yellow cataclasites / BMD	K-Ar	White Mica	21.60	0.60
"	37.9483	28.0524	CMM	Brownish to grey fault gouge / BMD	K-Ar	White Mica	22.30	0.70
"	38.3368	28.4112	CMM	Light brown gouge-fault core / AD	K-Ar	White Mica	10.60	0.30
"	38.3451	28.4063	CMM	Grey gouge-fault core / AD	K-Ar	White Mica	9.20	0.30
"	38.3451	28.4063	CMM	Grey gouge-splay fault / Footwall of the AD	K-Ar	White Mica	3.70	0.20
"	38.3451	28.4063	CMM	Grey gouge-splay fault / Footwall of the AD	K-Ar	White Mica	3.40	0.10
"	38.3451	28.4064	CMM	Grey gouge-splay fault / Footwall of the AD	K-Ar	White Mica	4.00	0.20
"	39.1251	28.7262	CMM	Yellow cataclasites in hanging wall / Simav graben-southern boundary fault	K-Ar	White Mica	18.80	0.40
"	39.1251	28.7262	CMM	Grey fault gouge / Simav graben-southern boundary fault	K-Ar	White Mica	16.40	0.60
"	39.1251	28.7262	CMM	Grey fault gouge / Simav graben-southern boundary fault	K-Ar	White Mica	17.20	0.40
"	39.1251	28.7262	CMM	Grey fault gouge / Simav graben-southern boundary fault	K-Ar	White Mica	18.60	0.40
"	39.1251	28.7262	CMM	Grey fault gouge / Simav graben-southern boundary fault	K-Ar	White Mica	19.70	0.40
Bozkurt et al., 2011	38.8720	28.4519	NMM	Low-grade mylonites/foliated cataclasites / Uppermost part of the SD	Rb-Sr	Muscovite	31.20	1.80
"	38.8720	28.4519	NMM	Low-grade mylonites/foliated cataclasites / Uppermost part of the SD	Rb-Sr	Biotite Brown	13.10	3.60
"	38.8720	28.4519	NMM	Low-grade mylonites/foliated cataclasites / Uppermost part of the SD	Rb-Sr	Biotite Green	10.70	0.20
"	38.8720	28.4519	NMM	Low-grade mylonites/foliated cataclasites / Middle part of the SD	Rb-Sr	Muscovite coarse	30.00	0.10
"	38.8720	28.4519	NMM	Low-grade mylonites/foliated cataclasites / Middle part of the SD	Rb-Sr	Muscovite fine	28.30	1.60
"	38.8720	28.4519	NMM	Low-grade mylonites/foliated cataclasites / Middle part of the SD	Rb-Sr	Whole rock-muscovite coarse-muscovite fine	29.50	1.40
"	38.8720	28.4519	NMM	Low-grade mylonites/foliated cataclasites / Middle part of the SD	Rb-Sr	Biotite fine (brown)	14.50	0.40
"	38.8720	28.4519	NMM	Low-grade mylonites/foliated cataclasites / Middle part of the SD	Rb-Sr	Biotite coarse (brown)	13.60	0.40
"	38.8720	28.4519	NMM	Low-grade mylonites/foliated cataclasites / Middle part of the SD	Rb-Sr	Whole rock-biotite coarse-biotite fine	14.00	9.50
"	38.8720	28.4519	NMM	Low-grade mylonites/foliated cataclasites / Middle part of the SD	Rb-Sr	Biotite green (±brown)	12.20	0.40

"	38.8720	28.4519	NMM	Low-grade mylonites/foliated cataclasites / Lowest part of the SD	Rb-Sr	Muscovite	28.50	0.80
"	38.8720	28.4519	NMM	Low-grade mylonites/foliated cataclasites / Lowest part of the SD	Rb-Sr	Muscovite	28.60	0.80
"	38.8720	28.4519	NMM	Low-grade mylonites/foliated cataclasites / Lowest part of the SD	Rb-Sr	Biotite Brown	15.10	0.60
"	38.8720	28.4519	NMM	Low-grade mylonites/foliated cataclasites / Lowest part of the SD	Rb-Sr	Biotite Brown	16.70	0.60
"	38.7811	28.3705	NMM	Orthogneiss (blastomylonitic texture)	Rb-Sr	Muscovite	45.70	0.60
"	38.7811	28.3705	NMM	Orthogneiss (blastomylonitic texture)	Rb-Sr	Biotite	18.20	0.20

Table V.15: Compilation of ^{40}Ar-^{39}Ar, K-Ar and Rb-Sr data.

Authors	Location			Lithology & Structural position	Method	Age (Ma)	Error (±)
	Lat	*Long*	*Area*				
Ring et al., 2003	-	-	CMM	High grade metamorphic rocks	ZFT	24.20	1.12
"	-	-	SMM	High grade metamorphic rocks	ZFT	27.88	1.52
"	-	-	SMM	High grade metamorphic rocks	ZFT	24.69	0.90
"	-	-	CMM	High grade metamorphic rocks	ZFT	5.19	0.28
Thomson & Ring, 2006	39.0342	28.7678	NMM	Quartzite - Çine unit	ZFT	23.60	2.20
"	39.0842	28.9325	NMM	Mica-schist - Çine unit	ZFT	21.10	1.50
"	39.0844	28.9672	NMM	Mica-schist - Çine unit	ZFT	20.10	1.40
"	39.0897	28.9617	NMM	Leucogranite - Çine unit	ZFT	19.90	1.70
"	39.1325	29.0269	NMM	Schist - Çine unit	ZFT	20.90	1.80
"	39.1606	29.0878	NMM	Granite	ZFT	20.50	1.50
"	39.2708	29.1475	NMM	Granite	ZFT	21.00	1.50
"	39.2964	29.0836	NMM	Granite	ZFT	21.60	1.50
"	39.3436	29.0750	NMM	Granite	ZFT	21.10	1.50
"	39.2681	29.0480	NMM	Granite	ZFT	22.50	1.60
"	39.4606	29.0086	NMM	Flysch - Izmir / Ankara Flysch	ZFT	228.00	23.00
"	39.3953	29.0397	NMM	Granite	ZFT	22.20	1.50
"	39.3881	29.0269	NMM	Granite	ZFT	21.40	1.50
"	39.2872	28.9744	NMM	Mylonite - Çine unit?	ZFT	22.50	1.50
"	39.3072	28.9514	NMM	Granite	ZFT	24.20	1.70
"	39.2244	28.8808	NMM	Granite	ZFT	23.70	1.90
"	39.2139	28.8972	NMM	Granite boudin - Çine unit	ZFT	23.70	1.90
"	39.1986	28.8083	NMM	Granite	ZFT	28.80	2.00
"	39.0900	29.0444	NMM	Granite	ZFT	22.90	1.60
"	38.7139	28.9256	NMM	Augen-gneiss - Çine unit	ZFT	23.90	1.90
"	38.4458	28.5319	NMM	Mica-schist - Çine unit	ZFT	24.40	3.00
"	38.3964	28.6422	NMM	Granite Triassic	ZFT	24.60	2.30
Buscher et al., 2013	38.4005	28.2236	CMM	Mylonitic granodiorite / Footwall of the AD	ZFT	6.40	0.90
Ring et al., 2017	37.6411	28.3139	SMM	Augen-gneiss - Çine unit	ZFT	30.20	2.40
"	37.3919	27.8003	SMM	Augen-gneiss - Çine unit	ZFT	30.80	3.40
"	37.4533	27.7168	SMM	Augen-gneiss - Çine unit	ZFT	30.50	3.40
"	37.5169	28.3506	SMM	Quartzite - Selimiye unit	ZFT	29.20	4.90
"	37.3779	27.7944	SMM	Quartzite - Selimiye unit	ZFT	30.80	2.80
"	37.3935	27.7511	SMM	Quartzite - Selimiye unit	ZFT	30.20	2.70
"	37.4766	27.5848	SMM	Quartzite - Selimiye unit	ZFT	32.00	4.70
"	37.3032	27.9006	SMM	Quartzite conglomerate - cover SMM?	ZFT	30.70	2.90
"	37.4007	27.6179	SMM	Quartzite conglomerate - cover SMM?	ZFT	33.30	3.50
"	37.4130	27.6206	SMM	Quartzite conglomerate - cover SMM?	ZFT	30.10	1.70
"	37.2145	27.5812	Ören	Meta-arkose - Ören unit	ZFT	128.70	12.80
"	37.2145	27.5812	Ören	Meta-arkose - Ören unit	ZFT	113.60	9.50
"	37.2153	27.5822	Ören	Meta-arkose - Ören unit	ZFT	127.40	14.50
"	37.2405	27.5813	Ören	Meta-arkose - Ören unit	ZFT	93.00	5.80
"	37.2110	27.5815	Ören	Meta-arkose - Ören unit	ZFT	95.90	10.40
"	37.2135	27.5750	Ören	Meta-arkose - Ören unit	ZFT	116.30	12.90
Wölfler et al., 2017	38.1207	27.9806	CMM	Augen-gneiss - Çine nappe	ZFT	30.30	2.10
"	37.9227	28.0861	CMM	Augen-gneiss - Çine nappe / Hanging wall of BMD	ZFT	29.00	1.90
"	37.9241	28.0864	CMM	Mica-schist - Cover unit / Footwall of BMD	ZFT	25.30	1.70
"	37.9721	27.9892	CMM	Mica-schist - Cover unit / Footwall of BMD	ZFT	26.40	2.60

Table V.16: Compilation of Zircon fission-track (ZFT) data.

Authors	Location			Lithology & Structural position	Method	Age (Ma)	Error (±)
	Lat	*Long*	*Area*				
Ring et al., 2003	-	-	CMM	High grade metamorphic rocks	AFT	22.15	3.26
"	-	-	CMM	High grade metamorphic rocks	AFT	10.05	0.57
"	-	-	CMM	High grade metamorphic rocks	AFT	10.64	0.64
"	-	-	CMM	High grade metamorphic rocks	AFT	6.92	0.56
"	-	-	CMM	High grade metamorphic rocks	AFT	17.03	1.08
"	-	-	CMM	High grade metamorphic rocks	AFT	10.48	1.40
"	-	-	CMM	High grade metamorphic rocks	AFT	7.90	1.75
"	-	-	CMM	High grade metamorphic rocks	AFT	3.73	0.61
"	-	-	CMM	High grade metamorphic rocks	AFT	6.08	0.83
"	-	-	CMM	High grade metamorphic rocks	AFT	8.74	2.67
"	-	-	CMM	High grade metamorphic rocks	AFT	1.75	0.62
"	-	-	CMM	High grade metamorphic rocks	AFT	10.12	0.55
"	-	-	CMM	High grade metamorphic rocks	AFT	16.11	1.74
"	-	-	CMM	High grade metamorphic rocks	AFT	10.25	0.89
"	-	-	CMM	High grade metamorphic rocks	AFT	11.12	0.64
"	-	-	CMM	High grade metamorphic rocks	AFT	6.46	0.49
"	-	-	CMM	High grade metamorphic rocks	AFT	15.98	1.05
"	-	-	CMM	High grade metamorphic rocks	AFT	16.35	3.42
"	-	-	CMM	High grade metamorphic rocks	AFT	14.16	2.73
"	-	-	CMM	High grade metamorphic rocks	AFT	13.03	0.60
"	-	-	NMM	High grade metamorphic rocks	AFT	16.53	0.72
"	-	-	NMM	High grade metamorphic rocks	AFT	21.48	2.17
"	-	-	NMM	High grade metamorphic rocks	AFT	16.05	1.08
"	-	-	NMM	High grade metamorphic rocks	AFT	18.58	0.85
"	-	-	NMM	High grade metamorphic rocks	AFT	18.58	0.62
"	-	-	NMM	High grade metamorphic rocks	AFT	18.98	1.81
"	-	-	NMM	High grade metamorphic rocks	AFT	18.24	1.61
"	-	-	NMM	High grade metamorphic rocks	AFT	19.24	1.17
"	-	-	NMM	High grade metamorphic rocks	AFT	27.85	1.22
"	-	-	CMM	High grade metamorphic rocks	AFT	22.57	1.10
"	-	-	SMM	High grade metamorphic rocks	AFT	21.66	1.16
"	-	-	SMM	High grade metamorphic rocks	AFT	22.86	1.63
"	-	-	SMM	High grade metamorphic rocks	AFT	21.04	2.19
"	-	-	SMM	High grade metamorphic rocks	AFT	21.31	1.80
"	-	-	SMM	High grade metamorphic rocks	AFT	24.68	2.19
"	-	-	SMM	High grade metamorphic rocks	AFT	21.52	1.98
"	-	-	SMM	High grade metamorphic rocks	AFT	18.23	0.96
"	-	-	SMM	High grade metamorphic rocks	AFT	15.12	1.09
"	-	-	SMM	High grade metamorphic rocks	AFT	19.06	1.11
"	-	-	SMM	High grade metamorphic rocks	AFT	18.20	1.15
"	-	-	SMM	High grade metamorphic rocks	AFT	18.23	0.96
"	-	-	SMM	High grade metamorphic rocks	AFT	15.82	1.25
"	-	-	SMM	High grade metamorphic rocks	AFT	21.23	1.80
Thomson & Ring, 2006	39.0342	28.7678	NMM	Quartzite - Çine unit	AFT	21.20	5.50
"	39.0825	28.9558	NMM	Leucogranite - Çine unit	AFT	17.50	2.60
"	39.0842	28.9325	NMM	Mica-schist - Çine unit	AFT	17.30	2.00
"	39.0844	28.9672	NMM	Mica-schist - Çine unit	AFT	15.60	2.50
"	39.0897	28.9617	NMM	Leucogranite - Çine unit	AFT	14.00	1.80
"	39.1325	29.0269	NMM	Schist - Çine unit	AFT	17.60	9.90
"	39.1606	29.0878	NMM	Granite	AFT	14.90	4.10
"	39.2708	29.1475	NMM	Granite	AFT	13.90	4.20
"	39.2964	29.0836	NMM	Granite	AFT	14.90	3.30
"	39.3436	29.0750	NMM	Granite	AFT	14.10	3.30
"	39.2681	29.0480	NMM	Granite	AFT	15.40	3.50
"	39.5039	29.0250	NMM	Flysch - Izmir / Ankara Flysch	AFT	53.20	20.90
"	39.4606	29.0086	NMM	Flysch - Izmir / Ankara Flysch)	AFT	45.60	6.10
"	39.3953	29.0397	NMM	Granite	AFT	12.90	3.30
"	39.3881	29.0269	NMM	Granite	AFT	14.70	3.70
"	39.2872	28.9744	NMM	Mylonite - Çine unit?	AFT	21.90	3.40
"	39.3600	28.9680	NMM	Pegmatite (Triassic granite?)	AFT	21.40	2.70
"	39.3072	28.9514	NMM	Granite	AFT	23.90	4.00
"	39.2244	28.8808	NMM	Granite	AFT	27.10	6.20
"	39.2139	28.8972	NMM	Granite boudin - Çine unit	AFT	22.90	3.00
"	39.1986	28.8083	NMM	Granite	AFT	29.80	4.50
"	39.0900	29.0444	NMM	Granite	AFT	20.30	4.60
"	38.7139	28.9256	NMM	Augen-gneiss - Çine unit	AFT	16.30	2.40
"	39.6697	29.0197	NMM	Leucogranite - Çine unit?	AFT	10.00	2.40
"	38.4458	28.5319	NMM	Mica-schist - Çine unit	AFT	17.30	4.80
"	38.3964	28.6422	NMM	Granite Triassic	AFT	16.30	5.10
Buscher et al., 2013	38.4191	28.2151	CMM	Augen gneiss - Çine unit / klippe in hanging wall of the AD	AFT	18.00	4.90
"	38.4005	28.2236	CMM	Mylonitic granodiorite / Footwall of the AD	AFT	2.60	1.30
"	38.4210	28.1964	CMM	Augen gneiss - Çine unit / klippe in hanging wall of the AD	AFT	11.2	3.3
"	38.3667	28.1803	CMM	Mylonitic granodiorite / Footwall of the AD	AFT	2.3	1.7
Gessner et al., 2013	37.6411	28.3139	SMM	Çine unit	AFT	20.5	2.7
"	37.5168	28.3503	SMM	Çine unit	AFT	18.1	10.5
"	37.3885	27.8002	SMM	Çine unit	AFT	27.7	10.1
"	37.4422	27.7040	SMM	Selimiye unit	AFT	25.4	8.3
"	37.4518	27.7173	SMM	Çine unit	AFT	26.5	7.4
"	37.3893	27.7507	SMM	Selimiye unit	AFT	27.8	7.00
"	37.4725	27.5842	SMM	Selimiye unit	AFT	23.9	5.6
"	37.2145	27.5842	Ören	Ören unit	AFT	31.5	5.8
"	37.2153	27.5822	Ören	Ören unit	AFT	42.1	7.2
"	37.2110	27.5815	Ören	Ören unit	AFT	36.7	7.4

Ring et al., 2017	37.6411	28.3139	SMM	Augen-gneiss - Çine unit	AFT	20.5	2.7
″	37.3919	27.8003	SMM	Augen-gneiss - Çine unit	AFT	27.7	10.1
″	37.4533	27.7168	SMM	Augen-gneiss - Çine unit	AFT	26.5	7.4
″	37.5169	28.3506	SMM	Quartzite - Selimiye unit	AFT	18.1	10.5
″	37.4481	27.7067	SMM	Mica-schist - Selimiye unit	AFT	25.4	8.3
″	37.3935	27.7511	SMM	Quartzite - Selimiye unit	AFT	27.8	7.00
″	37.4766	27.5848	SMM	Quartzite - Selimiye unit	AFT	23.9	5.6
″	37.2145	27.5812	Ören	Meta-arkose / Ören unit	AFT	31.5	5.8
″	37.2153	27.5822	Ören	Meta-arkose / Ören unit	AFT	42.1	7.2
″	37.2110	27.5815	Ören	Meta-arkose / Ören unit	AFT	36.7	7.4
Wölfler et al., 2017	38.1841	28.0610	CMM	Augen-gneiss - Çine unit	AFT	17.7	2.8
″	38.0392	28.0265	CMM	Paragneiss - Bozdağ unit / Footwall of BMD	AFT	11.8	3.4
″	38.0438	28.0186	CMM	Paragneiss - Bozdağ unit / Footwall of BMD	AFT	13.1	3.6
″	38.0361	28.0066	CMM	Paragneiss - Bozdağ unit / Footwall of BMD	AFT	12.4	1.4
″	38.0814	27.9482	CMM	Augen-gneiss - Çine unit	AFT	18.00	3.1
″	38.1207	27.9806	CMM	Augen-gneiss - Çine unit	AFT	21.1	3.8
″	37.9553	28.0443	CMM	Augen-gneiss - Çine unit / Hanging wall of BMD	AFT	19.9	4.00
″	37.9227	28.0861	CMM	Augen-gneiss - Çine unit / Hanging wall of BMD	AFT	17.8	3.1
″	37.9241	28.0864	CMM	Mica-schist - Cover unit / Footwall of BMD	AFT	4.2	1.3
″	37.9310	28.0876	CMM	Mica-schist - Cover unit / Footwall of BMD	AFT	4.2	2.1
″	37.9387	28.0884	CMM	Mica-schist - Cover unit / Footwall of BMD	AFT	4.8	1.4
″	37.9537	28.1034	CMM	Mica-schist - Cover unit / Footwall of BMD	AFT	5.2	2.00
″	37.9721	27.9892	CMM	Mica-schist - Cover unit / Footwall of BMD	AFT	5.7	0.9
″	37.9803	27.9663	CMM	Mica-schist - Cover unit / Footwall of BMD	AFT	14.7	2.4
″	37.9892	27.9641	CMM	Mica-schist - Cover unit / Footwall of BMD	AFT	15.3	4.4
″	37.8846	28.0630	CMM	Augen-gneiss - Çine unit / Hanging wall of BMD	AFT	18.9	4.2
″	37.8862	28.0476	CMM	Augen-gneiss - Çine unit / Hanging wall of BMD	AFT	22.8	5.8
″	37.9682	28.0899	CMM	Mica-schist - Cover / Footwall of BMD	AFT	4.4	1.1

Table V.17: Compilation of Apatite fission-track (AFT) data.

V.9. References

Akçay, M., Özkan, H. M., Moon, C. J., & Spiro, B. (2006). Geology, mineralogy and geochemistry of the gold-bearing stibnite and cinnabar deposits in the Emirli and Halıköy areas (Ödemiş, İzmir, West Turkey). Ore Geology Reviews, 29(1), 19-51.

Agard, P., Yamato, P., Jolivet, L., & Burov, E. (2009). Exhumation of oceanic blueschists and eclogites in subduction zones: timing and mechanisms. Earth-Science Reviews, 92(1-2), 53-79.

Baran, Z. O., Dilek, Y., & Stockli, D. (2017). Diachronous uplift and cooling history of the Menderes core complex, western Anatolia (Turkey), based on new Zircon (U-Th)/He ages. Tectonophysics, 694, 181-196.

Beaudoin, A., Augier, R., Laurent, V., Jolivet, L., Lahfid, A., Bosse, V., ... & Menant, A. (2015). The ikaria high-temperature metamorphic core complex (Cyclades, Greece): geometry, kinematics and thermal structure. Journal of Geodynamics, 92, 18-41.

Beyssac, O., Goffé, B., Chopin, C., & Rouzaud, J. N. (2002). Raman spectra of carbonaceous material in metasediments: a new geothermometer. Journal of metamorphic Geology, 20(9), 859-871.

Block, L., & Royden, L.H. (2010). Core complex geometries and regional scale flow in the lower crust. Tectonics 9, 557–567. http://dx.doi.org/10.1029/TC009i004p00557.

Bonneau, M. & Kienast, J.R. (1982). Subduction, collision et schistes bleus: exemple de l'Egée, Grèce. Bull. Soc. géol. France, 7: 785-791.

Bousquet, R., Goffé, B., Henry, P., Le Pichon, X., & Chopin, C. (1997). Kinematic, thermal and petrological model of the Central Alps: Lepontine metamorphism in the upper crust and eclogitisation of the lower crust. Tectonophysics, 273(1), 105-127.

Bozkurt, E. (2001). Late Alpine evolution of the central Menderes Massif, western Turkey. International Journal of Earth Sciences, 89(4), 728-744.

Bozkurt, E. (2004). Granitoid rocks of the southern Menderes Massif (southwestern Turkey): field evidence for Tertiary magmatism in an extensional shear zone. International Journal of Earth Sciences, 93(1), 52-71.

Bozkurt, E. (2007). Extensional v. contractional origin for the southern Menderes shear zone, SW Turkey: tectonic and metamorphic implications. Geological Magazine, 144(1), 191-210.

Bozkurt, E., & Park, L. R. (1994). Southern Menderes Massif: an incipient metamorphic core complex in western Anatolia, Turkey. Journal of the Geological Society, 151(2), 213-216.

Bozkurt, E., & Park, R. G. (1999). The structure of the Palaeozoic schists in the southern Menderes Massif, western Turkey: a new approach to the origin of the main Menderes metamorphism and its relation to the Lycian Nappes. Geodinamica Acta, 12(1), 25-42.

Bozkurt, E., & Satir, M. (2000). The southern Menderes Massif (western Turkey): geochronology and exhumation history. Geological Journal, 35(3-4), 285-296.

Bozkurt, E., & Oberhänsli, R. (2001). Menderes Massif (Western Turkey): structural, metamorphic and magmatic evolution-a synthesis. International Journal of Earth Sciences, 89(4), 679-708.

Bozkurt, E., & Park, R. G. (2001). Discussion on the evolution of the Southern Menderes Massif in SW Turkey as revealed by zircon dating. J. Geol. Soc. Lond. 158:393–395.

Bozkurt, E., & Sözbilir, H. (2004). Tectonic evolution of the Gediz Graben: field evidence for an episodic, two-stage extension in western Turkey. Geol. Mag. 141, 63–79.

Bozkurt, E., Park, R. G., & Winchester, J. A. (1993). Evidence against the core/cover interpretation of the southern sector of the Menderes Massif, west Turkey. Terra Nova 5:445–451.

Bozkurt, E., Winchester, J. A., & Park, R. G. (1995). Geochemistry and tectonic significance of augen gneisses from the southern Menderes Massif (West Turkey). Geological Magazine, 132(3), 287–301.

Bozkurt, E., Satır, M., & Buğdaycıoğlu, Ç. (2011). Surprisingly young Rb/Sr ages from the Simav extensional detachment fault zone, northern Menderes Massif, Turkey. Journal of geodynamics, 52(5), 406-431.

Brun, J. P., & van den Driessche, J. (1994). Extensional gneiss domes and detachment fault systems; structure and kinematics. Bulletin de la Société Géologique de France, 165(6), 519-530.

Brun, J. P., & Faccenna, C. (2008). Exhumation of high-pressure rocks driven by slab rollback. Earth and Planetary Science Letters, 272(1-2), 1-7.

Buck, W. R. (1991). Modes of continental lithospheric extension. Journal of Geophysical Research: Solid Earth, 96(B12), 20161-20178.

Buscher, J. T., Hampel, A., Hetzel, R., Dunkl, I., Glotzbach, C., Struffert, A., ... & Rätz, M. (2013). Quantifying rates of detachment faulting and erosion in the central Menderes Massif (western Turkey) by thermochronology and cosmogenic 10Be. Journal of the Geological Society, 170(4), 669-683.

Candan, O., Koralay, O. E., Akal, C., Kaya, O., Oberhänsli, R., Dora, O. Ö., ... & Chen, F. (2011). Supra-Pan-African unconformity between core and cover series of the Menderes Massif/Turkey and its geological implications. Precambrian Research, 184(1), 1-23.

Catlos, E. J., & Çemen, I. (2005). Monazite ages and the evolution of the Menderes Massif, western Turkey. International Journal of Earth Sciences, 94(2), 204-217.

Cenki-Tok, B., Expert, M., Işık, V., Candan, O., Monié, P., & Bruguier, O. (2016). Complete Alpine reworking of the northern Menderes Massif, western Turkey. International Journal of Earth Sciences, 105(5), 1507-1524.

Çiftçi, N. B., & Bozkurt, E. (2009). Evolution of the Miocene sedimentary fill of the Gediz Graben, SW Turkey. Sedimentary Geology, 216(3-4), 49-79.

Çiftçi, N. B., & Bozkurt, E. (2010). Structural evolution of the Alaşehir Graben, SW Turkey: temporal and spatial variation of the graben basin. Basin Research, 22(6), 846-873.

De Boorder, H., Spakman, W., White, S. & Wortel, M.J. (1998). Late Cenozoic mineralization, orogenic collapse and slab detachment in the European Alpine Belt. Earth and Planetary Science Letters, 164, 569–575, https://doi.org/10.1016/S0012-821X(98)00247-7

Delchini, S., Lahfid, A., Plunder, A., & Michard, A. (2016). Applicability of the RSCM geothermometry approach in a complex tectono-metamorphic context: The Jebilet massif case study (Variscan Belt, Morocco). Lithos, 256, 1-12.

Denèle, Y., Lecomte, E., Jolivet, L., Lacombe, O., Labrousse, L., Huet, B., & Le Pourhiet, L. (2011). Granite intrusion in a metamorphic core complex: the example of the Mykonos laccolith (Cyclades, Greece). Tectonophysics, 501(1-4), 52-70.

Demircioğlu, D., Ecevitoğlu, B., & Seyitoğlu, G. (2010). Evidence of a rolling hinge mechanism in the seismic records of the hydrocarbon-bearing Alaşehir graben, western Turkey. Petroleum Geoscience, 16(2), 155-160.

Dercourt, J., Zonenshain, L.P., Ricou, L.E., Kuzmin, V.G., Le Pichon, X., Knipper, A.L., Grandjacquet, C., Sbortshikov, I.M., Geyssant, J., Lepvrier, C., Pechersky, D.H., Boulin, J., Sibuet, J.C., Savostin, L.A., Sorokhtin, O., Westphal, M., Bazhenov, M.L., Lauer, J.P. & Biju-Duval, B. (1986). Geological evolution of the Tethys belt from the Atlantic to the Pamir since the Lias. Tectonophysics, 123: 241-315.

Dilek, Y., & Altunkaynak, Ş. (2009). Geochemical and temporal evolution of Cenozoic magmatism in western Turkey: mantle response to collision, slab break-off, and lithospheric tearing in an orogenic belt. Geol. Soc. Lond. Spec. Publ. 311, 213–233.

Dora, O. Ö., Kun, N., & Candan, O. (1990). Metamorphic history and geotectonic evolution of the Menderes Massif. Proc Int Earth Sci Congr Aegean Regions, 2, 102-115.

Dragovic, B., Baxter, E. F., & Caddick, M. J. (2015). Pulsed dehydration and garnet growth during subduction revealed by zoned garnet geochronology and thermodynamic modeling, Sifnos, Greece. Earth and Planetary Science Letters, 413, 111-122.

Dürr, S. H. (1975). Über alter und geotektonische Stellung des Menderes-Kristallins, SW-Anatolien und seine Aequivalente in der mittleren Aegaeis. na.

Ehlers, T. A., & Farley, K. A. (2003). Apatite (U–Th)/He thermochronometry: methods and applications to problems in tectonic and surface processes. Earth and Planetary Science Letters, 206(1-2), 1-14.

Emre, T., & Sözbilir, H. (1997). Field evidence for metamorphic core complex, detachment faulting and accommodation faults in the Gediz and Büyük Menderes grabens, western Anatolia, in: International Earth Sciences Colloquium on the Aegean Region, Izmir-Güllük, Turkey. pp. 73–93.

Erdogan, B. (1992). Problem of core-mantle boundary of Menderes Massif. In Proceedings of the International Symposium on Eastern Mediterranean Geology, Adana. Geosound (Vol. 20, pp. 314-315).

Erdoğan, B., & Güngör, T. (2004). The problem of the core-cover boundary of the Menderes Massif and an emplacement mechanism for regionally extensive gneissic granites, western Anatolia (Turkey). Turkish Journal of Earth Sciences, 13(1), 15-36.

Erkül, F. (2010). Tectonic significance of synextensional ductile shear zones within the Early Miocene Alaçamdağ granites, northwestern Turkey. Geological Magazine, 147(4), 611-637.

Ersoy, E.Y., Helvacı, C., & Palmer, M.R. (2010). Mantle source characteristics and melting models for the earlymiddle Miocene mafic volcanism in Western Anatolia: implications for enrichment processes of mantle lithosphere and origin of K-rich volcanism in postcollisional settings. Journal of Volcanology and Geothermal Research, 198, 112–128.

Gautier, P., & Brun, J. P. (1994). Ductile crust exhumation and extensional detachments in the central Aegean (Cyclades and Evvia Islands). Geodinamica Acta, 7(2), 57-85.

Gerya, T. V., Stöckhert, B., & Perchuk, A. L. (2002). Exhumation of high-pressure metamorphic rocks in a subduction channel: A numerical simulation. Tectonics, 21(6), 6-1.

Gessner, K., Ring, U., Passchier, C. W., & Güngör, T. (2001a). How to resist subduction: evidence for large-scale out-of-sequence thrusting during Eocene collision in western Turkey. Journal of the Geological Society, 158(5), 769-784.

Gessner, K., Piazolo, S., Güngör, T., Ring, U., Kröner, A., & Passchier, C. W. (2001b). Tectonic significance of deformation patterns in granitoid rocks of the Menderes nappes, Anatolide belt, southwest Turkey. International Journal of Earth Sciences, 89(4), 766-780.

Gessner, K., Ring, U., Johnson, C., Hetzel, R., Passchier, C. W., & Güngör, T. (2001c). An active bivergent rolling-hinge detachment system: Central Menderes metamorphic core complex in western Turkey. Geology, 29(7), 611-614.

Gessner, K., Collins, A. S., Ring, U., & Güngör, T. (2004). Structural and thermal history of poly-orogenic basement: U–Pb geochronology of granitoid rocks in the southern Menderes Massif, Western Turkey. Journal of the Geological Society, 161(1), 93-101.

Gessner, K., Gallardo, L. A., Markwitz, V., Ring, U., & Thomson, S. N. (2013). What caused the denudation of the Menderes Massif: Review of crustal evolution, lithosphere structure, and dynamic topography in southwest Turkey. Gondwana Research, 24(1), 243-274.

Gleadow, A. J. W., & Duddy, I. R. (1981). A natural long-term track annealing experiment for apatite. Nuclear Tracks, 5(1-2), 169-174.

Glodny, J., & Hetzel, R. (2007). Precise U–Pb ages of syn-extensional Miocene intrusions in the central Menderes Massif, western Turkey. Geological Magazine, 144(2), 235-246.

Govers, R. & Fichtner, A. (2016). Signature of slab fragmentation beneath Anatolia from full-waveform tomography. Earth and Planetary Science Letters 450 10–19; http://dx.doi.org/10.1016/j.epsl.2016.06.014.

Grasemann, B., Huet, B., Schneider, D. A., Rice, A. H. N., Lemonnier, N., & Tschegg, C. (2017). Miocene postorogenic extension of the Eocene synorogenic imbricated Hellenic subduction channel: New constraints from Milos (Cyclades, Greece). GSA Bulletin.

Güngör, T. & Erdogan, B. (2001). Emplacement age and direction of the Lycian Nappes in the Söke–Selçuk region, western Turkey. International Journal of Earth Sciences, 89(4), 874–882.

Hayward, A. B. (1984). Miocene clastic sedimentation related to the emplacement of the Lycian Nappes and the Antalya Complex, SW Turkey. Geological Society, London, Special Publications, 17(1), 287-300.

Hetzel, R., & Reischmann, T. (1996). Intrusion age of Pan-African augen gneisses in the southern Menderes massif and the age of cooling after Alpine ductile extensional deformation. Geol Mag 133: 565–572

Hetzel, R., Passchier, C. W., Ring, U., & Dora, Ö. O. (1995a). Bivergent extension in orogenic belts: the Menderes massif (southwestern Turkey). Geology, 23(5), 455-458.

Hetzel, R., Ring, U., Akal, C., & Troesch, M. (1995b). Miocene NNE-directed extensional unroofing in the Menderes Massif, southwestern Turkey. Journal of the Geological Society, 152(4), 639-654.

Hetzel, R., Romer, R. L., Candan, O., & Passchier, C. W. (1998). Geology of the Bozdağ area, central Menderes massif, SW Turkey: Pan-African basement and Alpine deformation. International Journal of Earth Sciences: Geologische Rundschau, 87(3), 394.

Hetzel, R., Zwingmann, H., Mulch, A., Gessner, K., Akal, C., Hampel, A., ... & Wedin, F. (2013). Spatiotemporal evolution of brittle normal faulting and fluid infiltration in detachment fault systems: A case study from the Menderes Massif, western Turkey. Tectonics, 32(3), 364-376.

Hurford, A. J. (1986). Cooling and uplift patterns in the Lepontine Alps South Central Switzerland and an age of vertical movement on the Insubric fault line. Contributions to mineralogy and petrology, 92(4), 413-427.

Iredale, L. J., Teyssier, C., & Whitney, D. L. (2013). Cenozoic pure-shear collapse of the southern Menderes Massif, Turkey. Geological Society, London, Special Publications, 372(1), 323-342.

Işık, V., & Tekeli, O. (2001). Late orogenic crustal extension in the northern Menderes Massif (western Turkey): evidence for metamorphic core complex. International Journal of Earth Sciences 89, 757–765.

Işık, V., Seyitoğlu, G., & Çemen, I. (2003). Ductile-brittle transition along the Alaşehir detachment fault and its structural relationship with the Simav detachment fault, Menderes massif, western Turkey. Tectonophysics 374, 1–18.

Işık, V., Tekeli, O., & Seyitoglu, G. (2004). The 40Ar/39Ar age of extensional ductile deformation and granitoid intrusion in the northern Menderes core complex: implications for the initiation of extensional tectonics in western Turkey. Journal of Asian Earth Sciences, 23(4), 555-566.

Jager, E., Niggli, E., & Wenk, E. (1967). Rb-Sr Altersbestimmungen an Glimmern der Zentralalpen. Kummerly & Frey.

Jolivet, L., & Faccenna, C. (2000). Mediterranean extension and the Africa-Eurasia collision. Tectonics, 19(6), 1095-1106.

Jolivet, L. & Brun, J.P. (2010). Cenozoic geodynamic evolution of the Aegean. International Journal of Earth Sciences, 99(1), pp.109-138.

Jolivet, L., Faccenna, C., Goffé, B., Burov, E., & Agard, P. (2003). Subduction tectonics and exhumation of high-pressure metamorphic rocks in the Mediterranean orogens. American Journal of Science, 303(5), 353-409.

Jolivet, L., Rimmelé, G., Oberhänsli, R., Goffé, B., & Candan, O. (2004). Correlation of syn-orogenic tectonic and metamorphic events in the Cyclades, the Lycian nappes and the Menderes massif. Geodynamic implications. Bulletin de la Société Géologique de France, 175(3), 217-238.

Jolivet, L., Faccenna, C., Huet, B., Labrousse, L., Le Pourhiet, L., Lacombe, O., ... & Philippon, M. (2013). Aegean tectonics: Strain localisation, slab tearing and trench retreat. Tectonophysics, 597, 1-33.

Jolivet, L., Menant, A., Sternai, P., Rabillard, A., Arbaret, L., Augier, R., ... & Labrousse, L. (2015). The geological signature of a slab tear below the Aegean. Tectonophysics, 659, 166-182.

Knoper, M., Armstrong, R. A., Andreoli, M. A. G., & Ashwal, L. D. (2000). The Steenkampskraal monazite vein: a subhorizontal stretching shear zone indicating extensional collapse of Namaqualand at 1033 Ma?. Journal of African Earth Sciences, 31(1), 38-38.

Labrousse, L., Huet, B., Le Pourhiet, L., Jolivet, L., & Burov, E. (2016). Rheological implications of extensional detachments: Mediterranean and numerical insights. Earth-Science Reviews, 161, 233-258.

Lagos, M., Scherer, E. E., Tomaschek, F., Münker, C., Keiter, M., Berndt, J., & Ballhaus, C. (2007). High precision Lu–Hf geochronology of Eocene eclogite-facies rocks from Syros, Cyclades, Greece. Chemical Geology, 243(1), 16-35.

Lahfid, A., Beyssac, O., Deville, E., Negro, F., Chopin, C. & Goffé, B. (2010). Evolution of the Raman spectrum of carbonaceous material in low-grade metasediments of the Glarus Alps (Switzerland). Terra Nova, 22(5), pp.354-360.

Lecomte, E., Jolivet, L., Lacombe, O., Denèle, Y., Labrousse, L., & Le Pourhiet, L. (2010). Geometry and kinematics of Mykonos detachment, Cyclades, Greece: Evidence for slip at shallow dip. Tectonics, 29(5).

Le Pichon, X., Angelier, J., Osmaston, M. F., & Stegena, L. (1981). The Aegean Sea. Philosophical Transactions of the Royal Society of London A: Mathematical, Physical and Engineering Sciences, 300(1454), 357-372.

Lips, A. L., Cassard, D., Sözbilir, H., Yilmaz, H., & Wijbrans, J. R. (2001). Multistage exhumation of the Menderes massif, western Anatolia (Turkey). International Journal of Earth Sciences, 89(4), 781-792.

Lister, G. S., Banga, G., & Feenstra, A. (1984). Metamorphic core complexes of Cordilleran type in the Cyclades, Aegean Sea, Greece. Geology, 12(4), 221-225.

Loos, S., & Reischmann, T. (1999). The evolution of the southern Menderes Massif in SW Turkey as revealed by zircon dating. Journal of the Geological Society, 156(5), 1021-1030.

Ludwig, K. R. (2003). Using Isoplot/Ex, Version 3. A Geochronological Toolkit for Microsoft Excel. Berkeley Geochronology Ctr. Spec., Pub, 4.

Malinverno, A., & Ryan, W.B.F. (1986). Extension in the Tyrrhenian Sea and shortening in the Apennines as result of arc migration driven by sinking of the lithosphere. Tectonics 5, 227–245. doi:10.1029/TC005i002p00227

McDougall, I., & Harrison, T. M. (1999). Geochronology and Thermochronology by the 40Ar/39Ar Method. Oxford University Press on Demand.

Menant, A., Jolivet, L., & Vrielynck, B. (2016). Kinematic reconstructions and magmatic evolution illuminating crustal and mantle dynamics of the eastern Mediterranean region since the late Cretaceous. Tectonophysics, 675, 103-140.

Oberhänsli, R., Partzsch, J., Candan, O., & Cetinkaplan, M. (2001). First occurrence of Fe-Mg-carpholite documenting a high-pressure metamorphism in metasediments of the Lycian Nappes, SW Turkey. International Journal of Earth Sciences, 89(4), 867-873.

Okay, A. I. (2001). Stratigraphic and metamorphic inversions in the central Menderes Massif: a new structural model. International Journal of Earth Sciences, 89(4), 709-727.

Oner, Z., & Dilek, Y. (2011). Supradetachment basin evolution during continental extension: The Aegean province of western Anatolia, Turkey. Bulletin, 123(11-12), 2115-2141.

Özer, S., Sözbilir, H., Özkar, İ., Toker, V., & Sari, B. (2001). Stratigraphy of Upper Cretaceous-Palaeogene sequences in the southern and eastern Menderes Massif (western Turkey). International Journal of Earth Sciences, 89(4), 852-866.

Partzsch, J. H., Oberhänsli, R., Candan, O., & Warkus, F. C. (1998). The evolution of the central Menderes Massif, west Turkey: a complex nappe pile recording 1.0 Ga of geological history. In Seventh Symposium Tektonik-Strukturgeologie-Kristallingeologie, Freiberg (pp. 166-168).

Piromallo, C., & Morelli, A. (2003). P wave tomography of the mantle under the Alpine-Mediterranean area. Journal of Geophysical Research: Solid Earth, 108(B2). https://doi.org/10.1029/2002JB001757

Pourteau, A., Sudo, M., Candan, O., Lanari, P., Vidal, O., & Oberhänsli, R. (2013). Neotethys closure history of Anatolia: insights from 40Ar–39Ar geochronology and P–T estimation in high-pressure metasedimentary rocks. Journal of Metamorphic Geology, 31(6), 585-606.

Pourteau, A., Oberhänsli, R., Candan, O., Barrier, E., & Vrielynck, B. (2016). Neotethyan closure history of western Anatolia: a geodynamic discussion. International Journal of Earth Sciences, 105(1), 203-224.

Purvis, M., & Robertson, A. (2005). Sedimentation of the Neogene–Recent Alaşehir (Gediz) continental graben system used to test alternative tectonic models for western (Aegean) Turkey. Sedimentary Geology, 173(1-4), 373-408.

Renne, P.R., Mundil, R., Balco, G., Min, K., & Ludwig, K. R. (2010). Joint determination of ^{40}K decay constants and $^{40}Ar^*/^{40}K$ for the Fish Canyon sanidine standard, and improved accuracy for $^{40}Ar/^{39}Ar$ geochronology. Geochim. Cosmochim. Acta 74, 5349–5367.

Régnier, J. L., Ring, U., Passchier, C. W., Gessner, K., & Güngör, T. (2003). Contrasting metamorphic evolution of metasedimentary rocks from the Cine and Selimiye nappes in the Anatolide belt, western Turkey. Journal of Metamorphic Geology, 21(7), 699-721.

Régnier, J. L., Mezger, J. E., & Passchier, C. W. (2007). Metamorphism of Precambrian–Palaeozoic schists of the Menderes core series and contact relationships with Proterozoic orthogneisses of the western Çine Massif, Anatolide belt, western Turkey. Geological Magazine, 144(1), 67-104.

Reiners, P. W., Spell, T. L., Nicolescu, S., & Zanetti, K. A. (2004). Zircon (U-Th)/He thermochronometry: He diffusion and comparisons with 40Ar/39Ar dating. Geochimica et cosmochimica acta, 68(8), 1857-1887.

Reischmann, T., Kröner, A., Todt, W., Dür, S., & Sengör, AMC. (1991). Episodes of crustal growth in the Menderes Lassif, W Turkey, inferred from zircon dating. Terra Abstr 3:34.

Rey, P. F., Teyssier, C., & Whitney, D. L. (2009). The role of partial melting and extensional strain rates in the development of metamorphic core complexes. Tectonophysics, 477(3), 135-144.

Rimmelé, G., Oberhänsli, R., Goffé, B., Jolivet, L., Candan, O., & Çetinkaplan, M. (2003). First evidence of high-pressure metamorphism in the "Cover Series" of the southern Menderes Massif. Tectonic and metamorphic implications for the evolution of SW Turkey. Lithos, 71(1), 19-46.

Rimmelé, G., Parra, T., Goffe, B., Oberhaensli, R., Jolivet, L., & Candan, O. (2004). Exhumation paths of high-pressure–low-temperature metamorphic rocks from the Lycian Nappes and the Menderes Massif (SW Turkey): a multi-equilibrium approach. Journal of Petrology, 46(3), 641-669.

Rimmelé, G., Parra, T., Goffe, B., Oberhaensli, R., Jolivet, L., & Candan, O. (2005). Exhumation paths of high-pressure–low-temperature metamorphic rocks from the Lycian Nappes and the Menderes Massif (SW Turkey): a multi-equilibrium approach. Journal of Petrology, 46(3), 641-669.

Rimmelé, G., Oberhänsli, R., Candan, O., Goffé, B., & Jolivet, L. (2006). The wide distribution of HP-LT rocks in the Lycian Belt (Western Turkey): implications for accretionary wedge geometry. Geological Society, London, Special Publications, 260(1), 447-466.

Ring, U., & Layer, P. W. (2003). High-pressure metamorphism in the Aegean, eastern Mediterranean: Underplating and exhumation from the Late Cretaceous until the Miocene to Recent above the retreating Hellenic subduction zone. Tectonics, 22(3).

Ring, U., Gessner, K., Güngör, T., & Passchier, C. W. (1999). The Menderes Massif of western Turkey and the Cycladic Massif in the Aegean—do they really correlate?. Journal of the Geological Society, 156(1), 3-6.

Ring, U., Willner, A. P., & Lackmann, W. (2001). Stacking of nappes with different pressure-temperature paths: An example from the Menderes nappes of western Turkey. American Journal of Science, 301(10), 912-944.

Ring, U. W. E., Johnson, C., Hetzel, R., & Gessner, K. (2003). Tectonic denudation of a Late Cretaceous–Tertiary collisional belt: regionally symmetric cooling patterns and their relation to extensional faults in the Anatolide belt of western Turkey. Geological Magazine, 140(4), 421-441.

Ring, U., Will, T., Glodny, J., Kumerics, C., Gessner, K., Thomson, S., ... & Drüppel, K. (2007). Early exhumation of high-pressure rocks in extrusion wedges: Cycladic blueschist unit in the eastern Aegean, Greece, and Turkey. Tectonics, 26(2).

Ring, U., Glodny, J., Will, T., & Thomson, S. (2010). The Hellenic subduction system: high-pressure metamorphism, exhumation, normal faulting, and large-scale extension. Annual Review of Earth and Planetary Sciences, 38, 45-76.

Ring, U., Gessner, K., & Thomson, S. N. (2017). South Menderes Monocline: Low-temperature thermochronology constrains role of crustal extension in structural evolution of southwest Turkey. Tectonophysics, 712, 455-463.

Roche, V., Sternai, P., Guillou-Frottier, L., Menant, A., Jolivet, L., Bouchot, V., Gerya, T. (2018a). Emplacement of metamorphic core complexes and associated geothermal systems controlled by slab dynamics. Earth and Planetary Science Letters, 498, 322-333.

Roche, V., Jolivet, L., Papanikolaou, D., Bozkurt, E., Menant, A., & Rimmelé, G. (2018b). Slab fragmentation beneath the Aegean/Anatolia transition zone: insights from the tectonic and metamorphic evolution of the Eastern Aegean region. Tectonophysics.

Roche, V., Bouchot, V., Beccaletto, L., Jolivet, L., Guillou-Frottier, L., Bozkurt, E., Oguz, K., Tuduri, J. & Tokay, B. (2018c). Structural, lithological and geodynamic controls on geothermal activity in the Menderes geothermal Province (Western Anatolia, Turkey). IJES.

Rossetti, F., Asti, R., Faccenna, C., Gerdes, A., Lucci, F., & Theye, T. (2017). Magmatism and crustal extension: Constraining activation of the ductile shearing along the Alaşehir detachment, Menderes Massif (western Turkey). Lithos, 282, 145-162.

Satir, M., & Friedrichsen, H. (1986). The origin and evolution of the Menderes Massif, W-Turkey: a rubidium/strontium and oxygen isotope study. Geologische Rundschau, 75(3), 703-714.

Scaillet, S. (2000). Numerical error analysis in $^{40}Ar/^{39}Ar$ dating. Chem. Geol. 162, 269–298.

Scaillet, S., Vita-Scaillet, G., & Guignol, H. (2008). Oldest human footprints dated by $^{40}Ar/^{39}Ar$. Earth. Planet. Sci. Lett. 275: 320-325.

Schmidt, A., Pourteau, A., Candan, O., & Oberhänsli, R. (2015). Lu–Hf geochronology on cm-sized garnets using microsampling: New constraints on garnet growth rates and duration of metamorphism during continental collision (Menderes Massif, Turkey). Earth and Planetary Science Letters, 432, 24-35.

Schmitz, M. D., & Schoene, B. (2007). Derivation of isotope ratios, errors, and error correlations for U-Pb geochronology using 205Pb-235U-(233U)-spiked isotope dilution thermal ionization mass spectrometric data. Geochemistry, Geophysics, Geosystems, 8(8).

Schuiling, R. D. (1962). On petrology, age and structure of the Menderes migmatite complex (SW-Turkey). Bulletin of the Mineral Research and Exploration Institute of Turkey, 58, 71-84.

Schulz, B., Brätz, H., Bombach, K., & Krenn, E. (2007). In situ Th–Pb dating of monazite by 266 nm laser ablation and ICP-MS with a single collector, and its control by EMP analysis. Z angew Geol, 35, 377-392.

Seyitoğlu, G., & Scott, B. (1991). Late Cenozoic crustal extension and basin formation in west Turkey. Geological Magazine, 128(2), 155-166.

Seyitoglu, G., Tekeli, O., Çemen, I., Sen, S., Isik, V., 2002. The role of the flexural rotation/rolling hinge model in the tectonic evolution of the Alasehir graben, western Turkey. Geol. Mag. 139, 15–26.

Seyitoğlu, G., Işık, V., Cemen, I., 2004. Complete Tertiary exhumation history of the Menderes massif, western Turkey: an alternative working hypothesis. Terra Nova, 16(6), 358-364.

Seyitoğlu, G., Işik, V., Esat, K., 2014. A 3D model for the formation of turtleback surfaces: the Horzum Turtleback of western Turkey as a case study. Turkish Journal of Earth Sciences, 23(5), 479-494.

Sengör, A. M. C., Satir, M., & Akkök, R. (1984). Timing of tectonic events in the Menderes Massif, western Turkey: Implications for tectonic evolution and evidence for Pan-African basement in Turkey. Tectonics, 3(7), 693-707.

Sherlock, S., Kelley, S., Inger, S., Harris, N., & Okay, A. (1999). 40 Ar-39 Ar and Rb-Sr geochronology of high-pressure metamorphism and exhumation history of the Tavsanli Zone, NW Turkey. Contributions to Mineralogy and Petrology, 137(1-2), 46-58.

Sözbilir, H. (2001). Extensional tectonics and the geometry of related macroscopic structures: field evidence from the Gediz detachment, western Turkey. Turkish Journal of Earth Sciences, 10(2), 51-67.

Thomson, S. N., & Ring, U. (2006). Thermochronologic evaluation of postcollision extension in the Anatolide orogen, western Turkey. Tectonics, 25(3).

Tomascak, P. B., Krogstad, E. J., & Walker, R. J. (1996). U-Pb monazite geochronology of granitic rocks from Maine: implications for late Paleozoic tectonics in the northern Appalachians. The Journal of Geology, 104(2), 185-195.

Vanderhaeghe, O., & Whitney, D. L. (2004). Structural development of the Naxos migmatite dome. Special Papers-Geological Society Of America, 211-228.

Van Hinsbergen, D. J. (2010). A key extensional metamorphic complex reviewed and restored: the Menderes Massif of western Turkey. Earth-Science Reviews, 102(1), 60-76.

Wagner, M., Altherr, R., & Van Den Haute, P. (1992). Apatite fission-track analysis of Kenyan basement rocks: constraints on the thermotectonic evolution of the Kenya dome. A reconnaissance study. Tectonophysics, 204(1-2), 93-110.

Whitney, D. L., & Bozkurt, E. (2002). Metamorphic history of the southern Menderes massif, western Turkey. Geological Society of America Bulletin, 114(7), 829-838.

Whitney, D. L., & Evans, B. W. (2010). Abbreviations for names of rock-forming minerals. American mineralogist, 95(1), 185-187.

Whitney, D. L., Teyssier, C., Kruckenberg, S. C., Morgan, V. L., & Iredale, L. J. (2008). High-pressure–low-temperature metamorphism of metasedimentary rocks, southern Menderes Massif, western Turkey. Lithos, 101(3), 218-232.

Wölfler, A., Glotzbach, C., Heineke, C., Nilius, N. P., Hetzel, R., Hampel, A., ... & Christl, M. (2017). Late Cenozoic cooling history of the central Menderes Massif: Timing of the Büyük Menderes detachment and the relative contribution of normal faulting and erosion to rock exhumation. Tectonophysics, 717, 585-598.

Yilmaz, Y., Genç, Ş. C., Gürer, F., Bozcu, M., Yilmaz, K., Karacik, Z., ... & Elmas, A. (2000). When did the western Anatolian grabens begin to develop?. Geological Society, London, Special Publications, 173(1), 353-384.

CHAPITRE VI : Rôle de la subduction dans la localisation des dômes métamorphiques et des champs géothermaux

L'objectif majeur de ce chapitre, est de fournir des contraintes thermiques et physiques aux modèles conceptuels proposés dans les premiers chapitres. Pour ce faire, une approche numérique multi-échelle a été utilisée par l'intermédiaire du code I3ELVIS [Gerya, 2010] et du logiciel Comsol Multiphysics™.

Comme une grande majorité des codes numériques actuels modélisant des processus à l'échelle lithosphérique, le code I3ELVIS a l'avantage d'utiliser des rhéologies viscoplastiques non-newtoniennes et réalistes [Ranalli, 1995] en couplant les équations de continuité, de quantité de mouvement et d'énergie. En ce sens, les fluides peuvent se déformer ductilement (*i.e.* par fluage-dislocation) et plastiquement lorsqu'un certain seuil de contraintes (*i.e.* seuil de plasticité) est atteint. Ces fluides de compositions différentes représentent donc différentes lithologies (*e.g.* croûte continentale, manteau…). Ils sont également définis par une densité spécifique, qui est fonction de la pression et de la température. Couplée à l'équation de la chaleur, les effets thermiques dans le modèle sont pris en compte et ont donc une influence directe sur la rhéologie et la densité des types de roches. Ainsi, dans la continuité des travaux de Sternai *et al.* [2014] et de Menant *et al*. [2016], l'évolution dynamique de la zone subduction est-Méditerranéenne depuis l'Oligocène a été modélisée afin d'étudier les relations 3D entre les flux mantelliques, la déformation crustale et les anomalies thermiques associées. Il est important de noter que l'aspect thermique n'a pas été discuté dans ces études. Plus en détail, le setup de base de Sternai *et al*. [2014] a été modifié par l'intermédiaire de Taras Gerya afin d'extraire du modèle la variable *shear heating*. Les modèles numériques ont par conséquent été relancés sur la plateforme Brutus et Euler de l'ETH Zurich.

Afin d'apporter des contraintes sur la circulation des fluides dans la croûte, le logiciel Comsol Multiphysics™ a également été utilisé. A partir d'un ensemble d'interfaces physique, ce logiciel permet de résoudre l'équation de la chaleur pour des propriétés physiques inhomogènes ou dépendantes de la température, et/ou pour des conditions limites particulières. Il permet également à l'utilisateur de configurer intégralement des simulations physiques et par conséquent d'implémenter des équations concernant la dépendance en température pour la densité et la dépendance en profondeur pour la perméabilité. Ainsi, chaque équation et chaque paramètre peuvent être contrôlés par l'utilisateur. Ce logiciel présente donc un aspect pratique mais également une très bonne résolution comparé au modèle 3D (*e.g.* 32000 triangles dont la taille est inférieure à 20 mètres dans le détachement, voir l'annexe du papier).

Principaux résultats :

Les principaux résultats 3D montrent que les flux mantelliques (*i.e.* les composantes poloïdales et toroïdales du champ de vitesse) et le *shear heating* induit par la dynamique du slab (*i.e.* retrait et déchirure) ont un effet significatif sur les températures du Moho sur un intervalle de temps de plusieurs

millions d'années. Cette dynamique contrôle la mise en place d'instabilités thermomécaniques en base de croûte. Dans le détail, ce « boudinage thermique » observé à différentes échelles (lithosphérique et crustale), favorise et amplifie la formation de contrastes rhéologiques, qui a leur tour permettent une localisation de la déformation. Cette localisation conduit à la formation de détachements crustaux. Ces structures accommodent ensuite l'exhumation des MCCs. Ainsi, il est clair que la dynamique du slab (*i.e.* retrait et déchirure) contrôle la distribution spatiale et temporelle des anomalies thermiques en grande profondeur. Ces dernières favorisent le fluage de la croûte et par conséquent la formation des dômes de HT.

Les résultats 2D montrent que les fluides profonds circulent dans la croûte et remontent par l'intermédiaire des détachements perméables. Le gradient topographique influence également la circulation des fluides surfaciques. Alors qu'une anomalie thermique négative se développe au toit du détachement, une anomalie positive apparait dans le mur de ce dernier. De ce fait, les réservoirs sont localisés sous le détachement, principalement alimenté par les eaux météoriques qui se sont réchauffées en profondeur. En résumé, les détachements contrôlent la mise en place des champs géothermaux de haute énergie.

Les résultats de ces modèles numériques sont comparables aux systèmes naturels observés dans le domaine de la méditerranée (*e.g.* la province du Menderes, Larderello en Italie) et dans l'ouest des États-Unis (*e.g.* la province du Basin & Range) et soulignent l'importance de la dynamique de subduction dans la genèse de ces systèmes. Bien qu'il n'existe aucun consensus sur une classification mondiale des systèmes géothermaux (*chapitre I, I.1.3*), une typologie dynamique de la subduction qui prenne en compte l'évolution spatio-temporelle des anomalies thermiques serait plus judicieuse afin d'améliorer l'exploration géothermale (voir discussion).

Emplacement of metamorphic core complexes and associated geothermal systems controlled by slab dynamics

Vincent ROCHE[1, 2, 3], Pietro STERNAI[4], Laurent GUILLOU-FROTTIER[3, 1, 2], Armel MENANT[5], Laurent JOLIVET[6], Vincent BOUCHOT[3, 1, 2] and Taras GERYA[7]

[1] *Université d'Orléans, ISTO, UMR 7327, 45071, Orléans, France*

[2] *CNRS/INSU, ISTO, UMR 7327, 45071 Orléans, France*

[3] *BRGM, ISTO, UMR 7327, BP 36009, 45060 Orléans, France*

[4] *Department of Earth Sciences, University of Geneva, Switzerland*

[5] *Institut de Physique du Globe de Paris, Sorbonne Paris Cité, Univ. Paris Diderot, CNRS, 75005 Paris, France*

[6] *Sorbonne Universités, UPMC Univ Paris 06, CNRS, Institut des Sciences de la Terre de Paris (iSTeP), 4 place Jussieu 75005 Paris, France*

[7] *Institute of Geophysics – Swiss Federal Institute of Technology (ETH), Zürich, Switzerland*

(Cet article a été publié au journal EPSL)

Abstract

Slab rollback results in the development of low-angle normal faults (detachments) and metamorphic core complexes (MCCs) in back-arc domains. Although mechanical consequences of slab dynamics on lithospheric and crustal behaviors have already been studied, thermal effects have not been investigated yet. This study shows that slab rollback produces lithospheric-scale thermal perturbations intrinsically associated with emplacement of amagmatic high-enthalpy geothermal systems. Using a multi-scale numerical modeling approach, with lithospheric-scale 3-D thermo-mechanical models of subduction, and 2-D models of fluid flow at the scale of detachments, we demonstrate that subduction-induced extensional tectonics controls the genesis and distribution of crustal-scale thermal domes from the base of the crust, and the location of high-energy geothermal systems. We find that when slab tearing occurs, Moho temperatures can temporarily increase by up to 250 °C due to significant shear heating in the flowing upper mantle. Associated thermal anomalies (with characteristic width and spacing of tens and hundreds of km, for crustal and lithospheric scales, respectively) then migrate systematically toward the retreating trench. These thermal domes weaken the crust, localize deformation and enhance the development of crustal-scale detachments. These thermo-mechanical instabilities mimic genesis of high-temperature MCCs with migmatitic cores in the back-arc domain, such as those of the Menderes (western Anatolia, Turkey) and Larderello (southern Tuscany) provinces in the Mediterranean realm, and those in the Basin and Range (western United States), where detachments control the bulk of the heat transport. At the scale of MCCs, the bulk fluid flow pattern is controlled by topography-driven flow while buoyancy-driven flow dominates within the permeable detachments, focusing reservoir location of high-energy geothermal systems at shallow depth beneath the detachments.

VI.1. Introduction

The development of geothermal power plants has been increasing since the 1970s, building upon more than 100 years of history in geothermal energy extraction. Currently, the installed global capacity is estimated at 12.6 GWe (Gigawatt electrical), and forecasts for 2050 point to a worldwide capacity of 140 GWe, approximately 8.3% of total world electricity production [Bertani, 2016]. Many of the high enthalpy geothermal resources (HEGRs) that make such an ambitious goal possible are located in the vicinity of subduction zones and volcanic arcs, where both magmatic and tectonic processes operate (Fig. VI.1). Others are located in "amagmatic" provinces such as the Menderes Massif in Western Turkey and the Basin and Range in the Western United States. Particularly noteworthy for this study is that while geothermal systems associated with magmatism have been studied in detail [*e.g.* Cumming, 2009] those located in "amagmatic" provinces have received less attention [Moeck *et al.*, 2014].

Recent to present (*i.e.* Pliocene-Quaternary) magmatism in the upper crust across the Menderes Massif and the Basin and Range is rare [Blackwell *et al.*, 2009; Faulds *et al.*, 2010] compared to that of the Larderello geothermal field [Santilano *et al.*, 2015] (Fig. VI.1). Open discussions on the possible role of hidden magmatic intrusions on these geothermal systems remains debated. Even if present, however, magmatic intrusions alone cannot explain the extent of these geothermal provinces (several thousand of km² each), and therefore cannot account for high concentration of HEGRs. We thus seek for other sources of heat (deeper and larger-scale) possibly associated with deep, large-scale geodynamic processes involved by the nearby subduction systems.

Slab rollback induces lithospheric extension in the overriding plate where low-angle normal faults (detachments) control both the exhumation of metamorphic core complexes (MCCs) and the magma ascent and/or fluid circulation [*e.g.* Reynolds & Lister, 1987; Huet *et al.*, 2011]. Because detachments may correspond to permeable structures deeply rooted down to the brittle-ductile transition [Famin *et al.*, 2004; Mezri *et al.*, 2015], active extensional domains in back-arc regions could represent favorable settings for HEGRs. The possible sources of heat responsible for regional high temperature-low pressure (HT-LP) metamorphic overprint recorded in these MCCs include (i) heating associated with thermal diffusion of excess heat generated by nappe stacking (increased radiogenic crustal heat [*e.g.* Bousquet *et al.*, 1997]), (ii) shear-heating in the mantle [*e.g.* Schubert & Yuen, 1978], or (iii) advection of hot asthenosphere to shallow depths during slab retreat [Wannamaker *et al.*, 2008; Jolivet *et al.*, 2015]. However, no unifying mechanism responsible for both the generation of MCCs and emplacement of high-enthalpy geothermal systems in the same regions has yet been recognized. This is however a crucial question since HEGRs represent a major economic interest in terms of exploration for carbon-free energy resources.

Here, we first document the self-consistent formation of crustal domes in the back-arc domain as a result of thermo-mechanical instabilities in 3-D numerical simulations of ocean-continent subduction dynamics. These models provide crucial thermal constraints for the mantle and crust, and show the importance of shear heating and fast mantle flow on the overall heat budget. Subduction-induced thermal signature in the overriding crust obtained from these experiments is then used as basal thermal boundary condition in 2-D numerical models dedicated to the understanding of fluid flow in the upper crust in presence of detachments that accommodate the formation of these domes. Results show that deep upper crustal hot fluids are drained upward by the permeable detachment. It is therefore consistent with geological observations from MCCs and associated geothermal fields in the Mediterranean realm (Anatolia and Tuscany) and in the western United States.

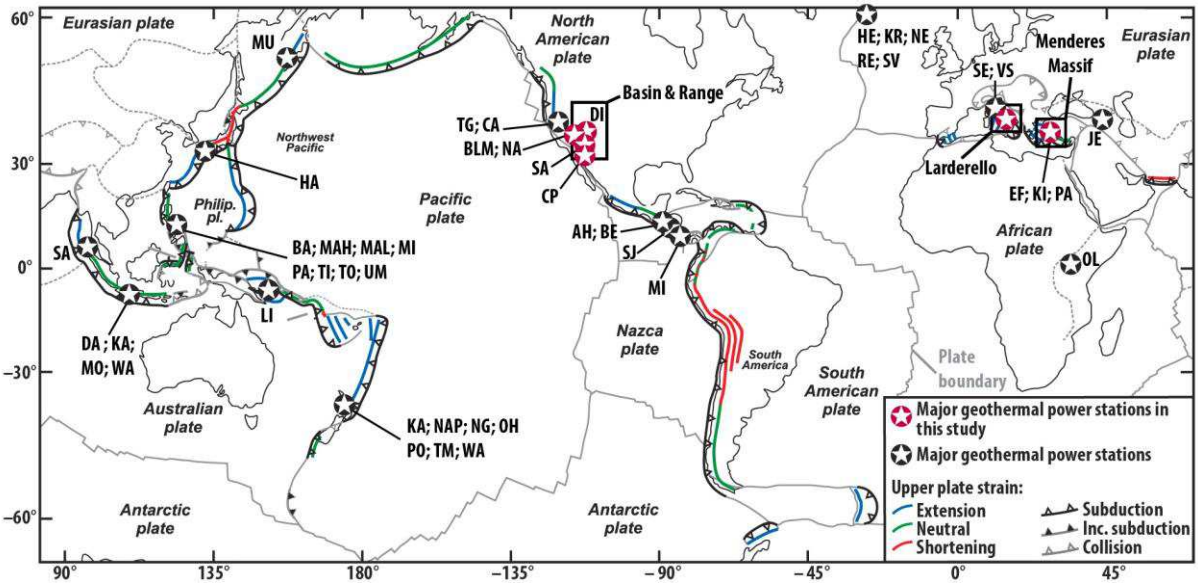

Figure VI.1: The major subduction zones on Earth (modified from Schellart et al. [2007]). Black stars show the locations of major geothermal power stations that are larger than 50 MWe that are currently operational or under construction. Red stars are reserved for highlighting those within the study areas mentioned in this study. Geothermal stations: JE, Jermaghbyur (Armenia); Mi, Miravalles (Costa Rica); AH, Ahuachapán, BE, Berlín (El Salvador); HE, Hellisheidi, KR, Krafla, NE, Nesjavellir, RE, Reykjanes, SV, Svartsengi (Iceland); DA, Darajat, KA, Kamojang, MO, Mount Salak, SA, Sarulla, WA, Wayang Windu (Indonesia) ; LA, Larderello, SE, Serrazzano, VS, Valle Secolo (Italy) ; HA, Hatchobaru (Japan); OL, Olkaria (Kenya); CP, Cerro Prieto (Mexico); KA, Kawerau, NAP, Nga Awa Purua, NG, Ngatamariki, OH, Ohaaki, PO, Poihipi, TM, Te Mihi, WA, Wairakei (New Zealand); SJ, San Jacinto Tizate (Nicaragua); LI, Linhir (Papua New Guinea); BA, Bacman I, MAH, Mahanagdong, MAL, Malitbog, MI, Mindanao I-II, PA, Palinpinon I-II, TI, Tiwi A-B-C, TO, Tongonan 1, UM, Upper Mahiao (Philippines); MU, Mutnovskaya, Russia; EF, Efeler, KI, Kızıldere, PA, Pamukören (Turkey); BLM, CA, Calistoga, DV, Dixie Valley, NA, Navy, SA, Salton Sea, TG, The Geysers (United States).

VI.2. Geodynamic and geothermal settings of the Menderes Massif

During the Cenozoic, the eastern Mediterranean region (Figs. VI.2a and 2b) has undergone a two-step tectono-metamorphic evolution. In the late Cretaceous-Eocene, the convergence of Africa and Eurasia first led to the closure of the Izmir-Ankara Ocean. At this time, the accretion of subducting continental and oceanic tectonic units [*e.g.* Jolivet & Brun, 2010] led to the formation of a south-verging crustal-scale orogenic wedge. Since the Oligo-Miocene, collapse of the Hellenides-Taurides belt in this region is mainly controlled by the southward retreat of the African slab, further accelerated in the middle Miocene by a major slab tearing event evidenced by tomographic models below western Turkey (Fig. VI.2c) [*e.g.* Piromallo & Morelli, 2003]. Extension in the overriding plate has thus led to the exhumation of different MCCs such as the Cyclades in the Aegean Sea and the Menderes Massif in western Anatolia, accommodated by crustal-scale low-angle normal faults such as the Simav, Alaşehir and Büyük Menderes detachments [Hetzel *et al.*, 1995; Bozkurt *et al.*, 2011] (Figs. VI.2 and 2c). Current, plate kinematics in this region are characterized by more localized extension, mainly controlled by the westward motion of Anatolia [Reilinger *et al.*, 2006] and by N-S extension accommodated by steep normal faults in the Gediz and Büyük Menderes Grabens, both consequences of slab dynamics [*e.g.* Gessner *et al.*, 2013; Sternai *et al.*, 2014; Jolivet *et al.,* 2015].

The Menderes Massif is also recognized as an active geothermal area (See *Appendix VI.8.1.*, Fig. VI.11a). This region is characterized by long wavelength east-west variations of surface heat flow density with values locally exceeding 90 mW m^{-2} [Erkan, 2015]. At depth, it seems that a similar east-west long wavelength thermal anomaly is also present, as suggested by the Curie-point isotherm map of Aydin *et al.* [2005]. According to these authors, the depth of the 580 °C isotherm would be lower than 10 km in western Anatolia (See *Appendix VI.8.1.*, Fig. VI.11b). It turns out that most of the geothermal systems in Turkey are located in the Menderes Massif (Fig. VI.2b) where recent magmatism is almost absent. Here, geothermal fields are characterized by medium- to high-enthalpy, with reservoir temperature values ranging from 120 to 287 °C [*e.g.* Baba *et al.*, 2015]. Most are used for district heating systems (*e.g.* Balçova and Salihli), whereas a few are exploited for electricity production (*e.g.* Germencik, Salavatlı; Kızıldere; Alaşehir). Some authors have suggested that most of the geothermal activity can be considered as amagmatic in origin [Faulds *et al.*, 2010; Gessner *et al.*, 2017]. However, Ozdemir *et al.* [2017] considered a probable magmatic intrusion in the crust to explain the heat source. Since there is presently no evidence for the existence of such plutons, some authors suggest a deeper and larger heat source triggered by large-scale tectonic processes such as subduction [Kaya, 2015; Gessner *et al.*, 2017]. In that sense, Kaya [2015] invoked a possible lithospheric thinning as the origin of the anomalously high heat flow. This example show that large-scale processes related to lithosphere dynamics could be involved in the genesis of geothermal systems. We thus need to employ a multi-scale

approach (lithospheric- and crustal-scales), to improve the characterization of heat transfer possesses from the mantle to the geothermal system.

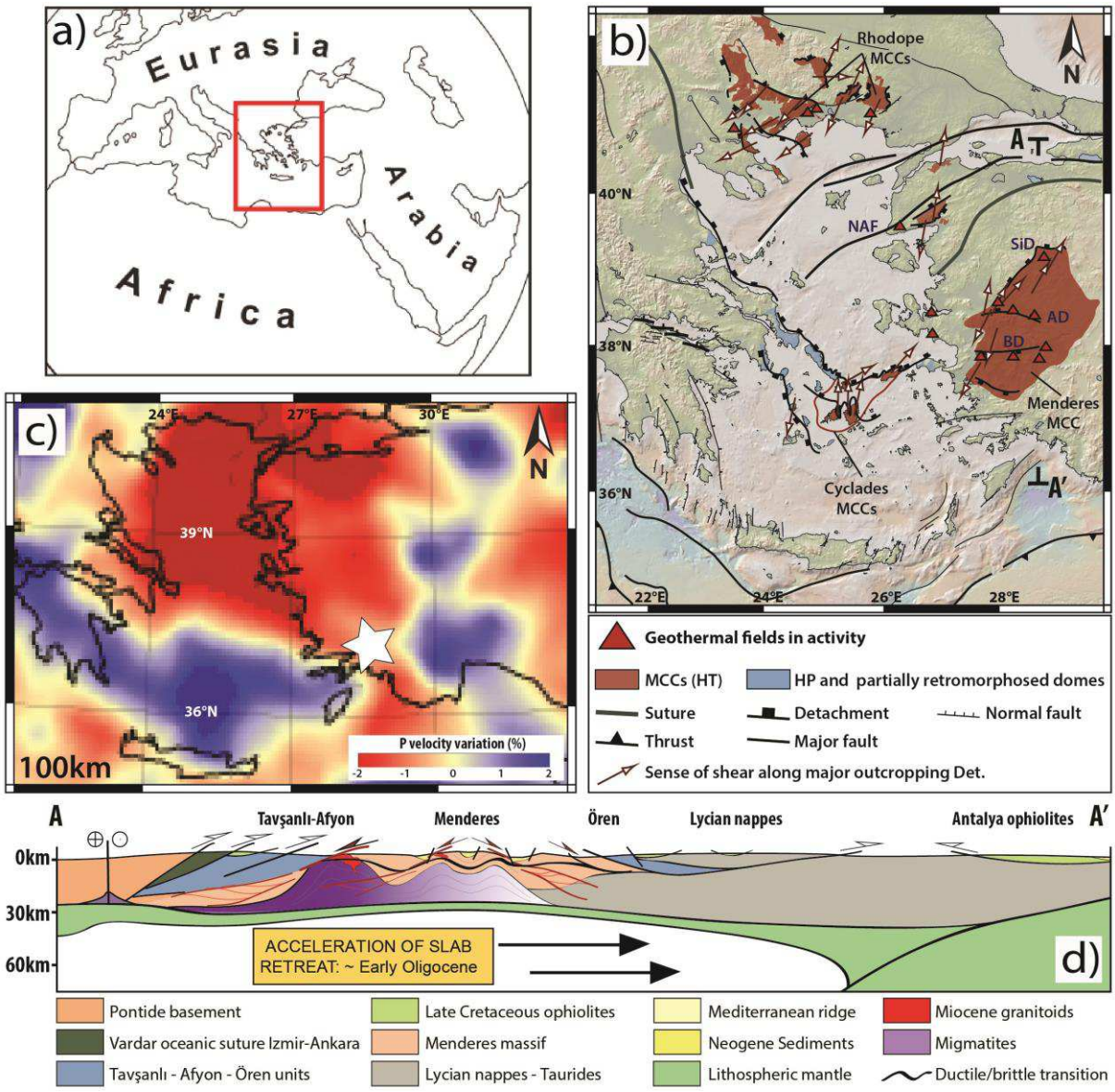

Figure VI.2: (a) Global map with red box showing the location on the study area. (b) Simplified tectonic maps showing the main metamorphic core complexes and associated detachments faults in the Aegean region (modified from Jolivet et al. [2015]). SiD: Simav Detachment, AD: Alaşehir Detachment, BD: Büyük Menderes Detachment, NAF: North Anatolian Fault. (c) Tomographic models from Piromallo and Morelli [2003] showing the Vp anomalies at the 100 km depth. White star shows the location of a slab tear below the Menderes Massif. (d) Simplified cross-sections highlighting slab retreat and formation of crustal detachments.

VI.3. 3-D thermal evolution of subduction

In a previous study dedicated to the analysis of surface deformation in the Aegean-Anatolian domain, Sternai *et al.* [2014] found that mantle flow due to slab rollback and tearing can drag the upper plate from below, and explain upper plate extension and the formation of the North Anatolian Fault.

Their results emphasize the active role of mantle flow in driving the surface strain and horizontal crustal velocities. However, the associated thermal processes were not described by these authors. Because heat transport is inherently coupled with deformation, mantle shearing may provide a strong heat source. We thus must consider it, especially if we want to describe in detail the thermal features associated with 3-D subduction dynamics when slab rollback and tearing occur. Indeed, while radioactive heat production is considered as the main heat source in the continental crust, shear heating has been suggested to be important in the mantle [Shubert & Yuen, 1978] and thus probably also in arc and back-arc settings where fast slab dynamics may be associated with intense asthenospheric flow. Here, we perform similar numerical simulations than Sternai *et al.* [2014], but improve the analysis by investigating the effects of shear heating. We describe the numerical results from a thermal point of view, by focusing on the localization of crustal thermal anomalies.

VI.3.1. Model set-up

The numerical simulations were performed with the code "I3ELVIS" [Gerya, 2010] that solves the momentum, continuity and energy equations based on a staggered finite difference scheme combined with a marker-in-cell technique. Realistic and non-Newtonian visco-plastic rheologies are used in the model, and implies temperature- and pressure-dependent viscosities (see *Appendix VI.8.2.1.*). The model setup is shown in Figure VI.3 The model domain measures 2000 x 328 x 1000 km in the x, y and z dimensions, respectively and is resolved by 501 x 165 x 197 grid points resulting in a resolution of 4, 2 and 5 km in the x, y and z dimensions, respectively. It includes three continental plates (C1, C2 and C3), allowing reproduction of similar tectonic events that affected the Tethys convergent domains (subduction, collision, slab tearing, trench retreat [Sternai *et al.,* 2014]). These three continental plates are defined by a crust of 35 km, 50 km and 45 km thick (Fig. VI.3). In addition to the trench-parallel weak fracture zone allowing for subduction initiation, the model includes a trench perpendicular weak fracture zone within the oceanic domain, which allows for slab tearing (Fig. VI.3).

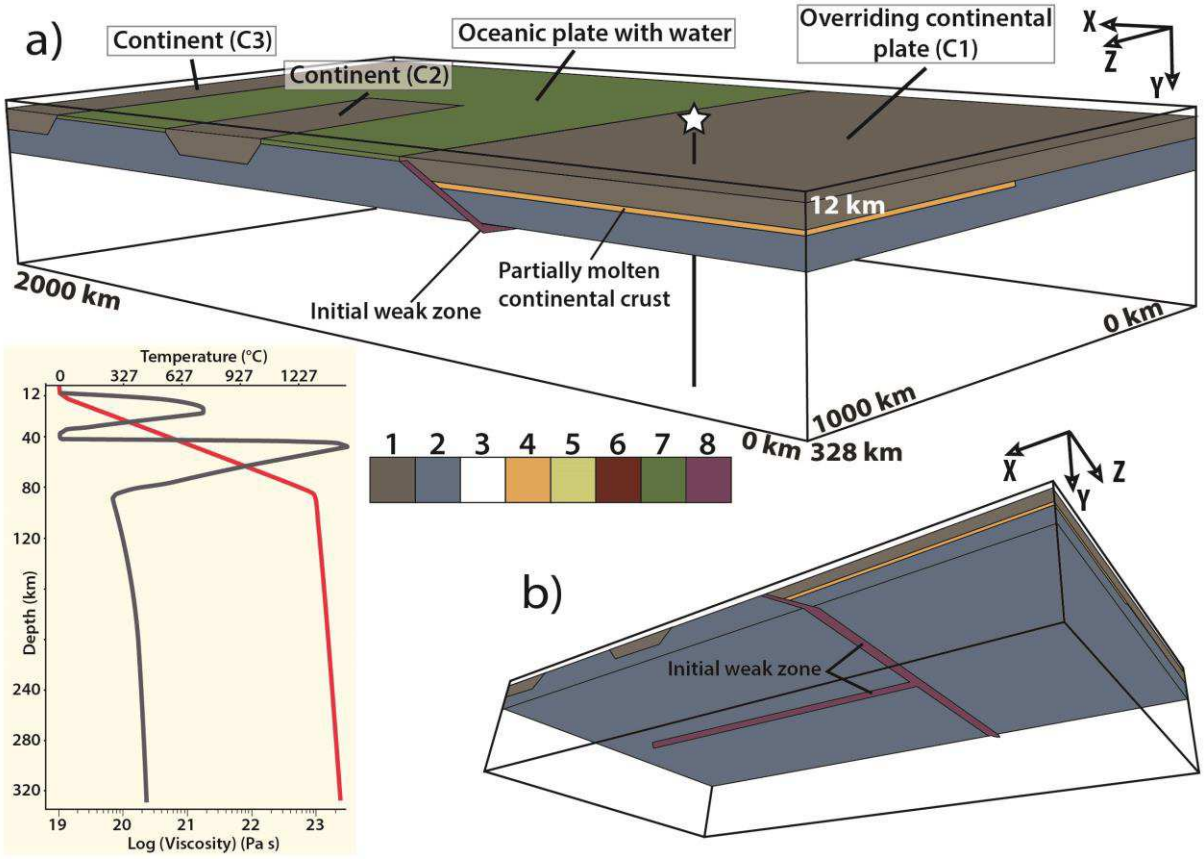

Figure VI.3: Numerical setup. (a) 3D initial model setup where the top layer ("sticky air", y<~12 km") and the water are cut off for clarity. Colours showing different rock types: 1-continental crust 2-lithospheric mantle; 3-asthenospheric mantle; 4-partially molten continental crust; 5-hydrated crust; 6-partially molten mantle; 7-oceanic crust; 8-hydrated/serpentinized mantle (initially imposed "weak fracture zone"). Initial vertical profiles of viscosity (grey) and temperature (red), taken at the location shown by the white star. (b) Location of the "weak zones" (i.e. hydrated/serpentinized mantle) into the lithosphere to trigger subduction (z-parallel) and to allow slab tearing (x-parallel) in the initial model.

The initial thermal structure of C1, C2 and C3 is laterally uniform with 0 °C at the surface and 1300 °C at 90, 140 and 150 km depth, respectively. The initial thermal structure of the oceanic lithosphere corresponds to the cooling age of 120 Ma [*e.g.* Turcotte & Schubert, 2002]. The initial temperature gradient in the asthenospheric mantle is ~ 0.5 °C km^{-1} (adiabatic). Boundary conditions involve free slip on the z = 0 and z = 1000 km sides of the model domain, while uniform and constant x-parallel velocities equal to ~ 1.8 cm yr^{-1} (convergence) are imposed at the x = 2000 km boundary, and the x = 0 km is fixed. Global mass conservation is ensured by material outflow through the permeable lower boundary (y = 328 km). Surface processes are also implemented using a highly simplified gross-scale erosion-sedimentation law. The parametric study on various boundary conditions and parameters is presented in Sternai *et al.* [2014].

Heat production by viscous or plastic shearing (H_s), consisting of the dissipation of the mechanical energy during irreversible non-elastic deformation, is controlled by the deviatoric stresses σ'_{ij} and strain rates $\dot{\varepsilon}'_{ij}$, as follow [Gerya, 2010]:

$$H_s = \sigma'_{ij}\,\dot{\varepsilon}'_{ij} \quad (1)$$

The possibility to investigate H_s in our numerical simulations is a major advance with respect to the previous models presented in Sternai *et al.* [2014]. In order to test the possibility that slab tearing would enhance mantle shear heating, two series of numerical models, with and without slab tearing, have been performed, all other settings being equal (*i.e.* same boundary conditions, material properties, see more information in *Appendix VI.8.2.*).

VI.3.2. Results

Before focusing on thermal effects associated with slab dynamics, we briefly present the model evolution. The overall sequence of events is robust and includes first an early subduction of the oceanic domain between C1 and C2 with localized extensional deformation in the back-arc domain. During this first subduction event, a toroidal mantle flow occurs below C1, as induced by the down-going slab. This event also controls crustal flow (essentially decoupled from the mantle) and surface deformation. Afterward, continental collision between C1 and C2 occurs, locally increasing slab dip and thus favoring slab tearing. Later subduction of the oceanic domain between C1 and C3 induces widespread extensional deformation in the back-arc domain. This last event is highly conditioned by the previous horizontal to sub-horizontal return flow of hot asthenosphere, which warms up the incipiently subducting lithosphere close to the slab tear, enhancing here a non-cylindrical (*i.e.* not parallel to the initial upper plate margin) slab rollback. Rheological stratification of the upper plate in the back-arc domain is characterized at this stage by a thin rigid lithospheric mantle (~ 10 km). Deformation is localized in the overriding plate with strike-slip deformation propagating toward the subducting plate [Sternai *et al.*, 2014].

VI.3.2.1. Thermo-mechanical instabilities

The early subduction event is characterized by the development of several positive thermal anomalies (*i.e.* anomalously high temperatures) (i) at the base of the crust with wavelengths around 200 km, and (ii) in the overriding lower crust, within a partially molten low-viscosity layer, with wavelengths around 30 km (Figs. VI.4a and VI.4b). The thermal instabilities in the low-viscosity crust generate dome-like structures cored by partially molten low-viscosity material (orange color in Figures VI.4a and VI.4b). These domes are elongated parallel to the subduction trench and separated by 200 – 300 km (Fig. VI.4a). With time, new thermal domes appear toward the trench, controlled by the flow of low viscosity material in response to both slab rollback and tearing (Fig. VI.4b). The strain rate distribution shows that mature crustal domes preferentially localize deformation, rather than incipient crustal domes closer to the trench (Fig. VI.4c). In addition, deformation localizes around the edges of these domes,

showing the importance of lateral crustal strength contrasts on strain localization. At 14.8 Myr, two domes have disappeared but the thickness of the partially molten layer at the base of the crust has tripled (from ~ 4 km to 15 km thick, Fig. VI.4b). Meanwhile, the horizontal component of flow velocity in the partially molten layer has decreased (from ~ 5 to ~ 1 cm yr^{-1}, Fig. VI.4c). On the opposite, above the slab tear, the deformation is localized and horizontal component of crustal and mantle velocities have increased up to ~ 6 and ~ 9 cm yr^{-1}, respectively. The shear heating and the advective mantle heat flow components near the fast velocity zones are enhanced accordingly, as detailed below.

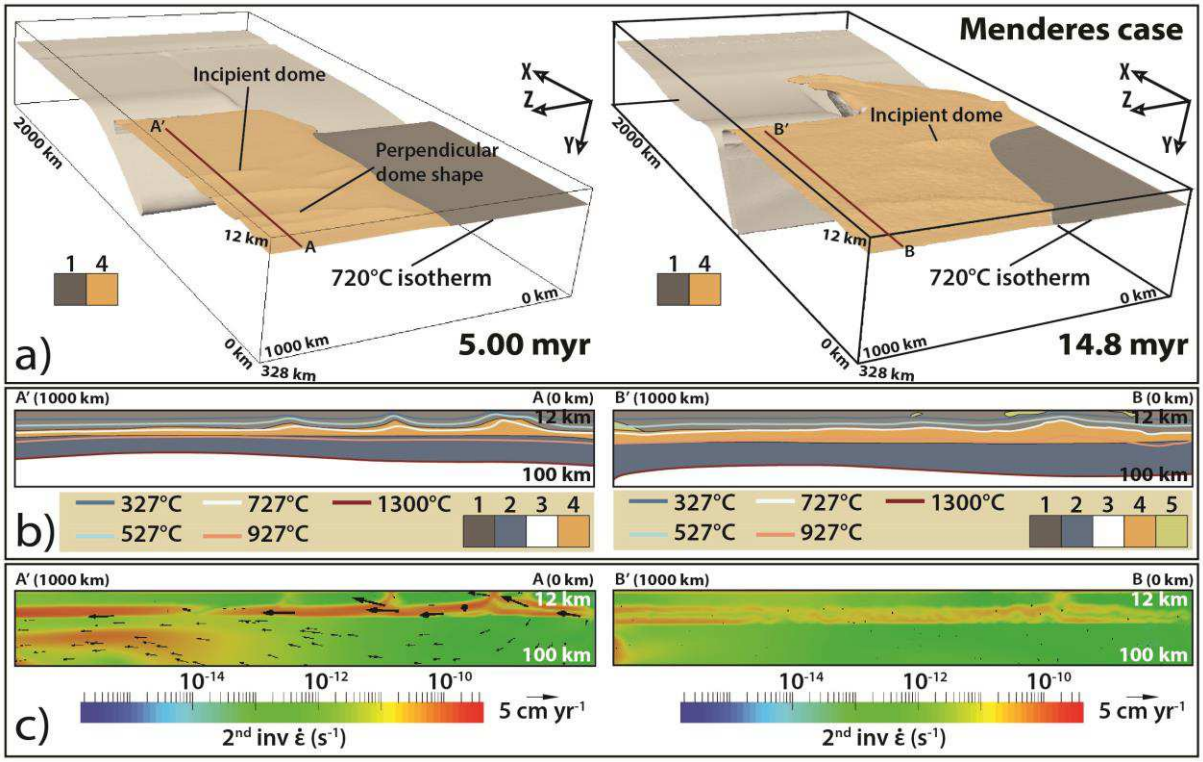

Figure IV.4: Thermo-mechanical evolution of the model. (a) The 720 °C isotherm at 5 myr and at 14.8 myr, respectively. Colors showing different rock types: 1, 4 indicate upper and lower crust, respectively, see also Figure VI.3. (b) Vertical cross-sections showing different rock types and isotherms. Colors showing different rock types: 1-2-3-4 as defined in Figure VI.3. (c) Vertical cross-sections showing the second invariant of the strain rate tensor and velocity vectors.

VI.3.2.2. Slab dynamics and shear heating

The contribution of shear heating to heat production in our reference model (with slab tearing between C2 and the oceanic domain) is compared to similar simulations without slab tearing (Fig. VI.5; see also *Appendix VI.8.1.*, Fig. VI.12). The frictional heat produced in back-arc domain locally reaches values of ~ 5.0 µW m^{-3} regardless of slab tearing (Fig. VI.5). However, when slab tearing occurs, a larger-scale thermal perturbation appears and develops below and at the base of the crust (~ 400 x 200 km at 12.4 Myr; see Fig. VI.5b). Anomalies associated with shear heating are thus distributed over a larger domain in the case of tearing because of a more widespread mantle flow around the tear, and

appear more localized and parallel to the subduction trench without tearing (Fig. VI.5a, see right panels). In addition, our results show that the amount of heat produced by shearing leads to an increase of mantle heat flow (Q_m) at the base of the crust, and particularly above the tear. In particular, for average shear heating of ~ 2.0 μW m^{-3} and mantle thickness of 30 km (Fig. VI.5c, profile 1), the contribution to the heat flow nearby the subduction front is of ~ 60 mW m^{-2} at 12.4 Myr. Conversely, far from the subduction front, shear heating is insignificant (< 1.0 nW m^{-3}, see Fig. VI.5c, profile 4), implying no contribution of this mechanism to heat production by this mechanism (Fig. VI.5d, profile 1).

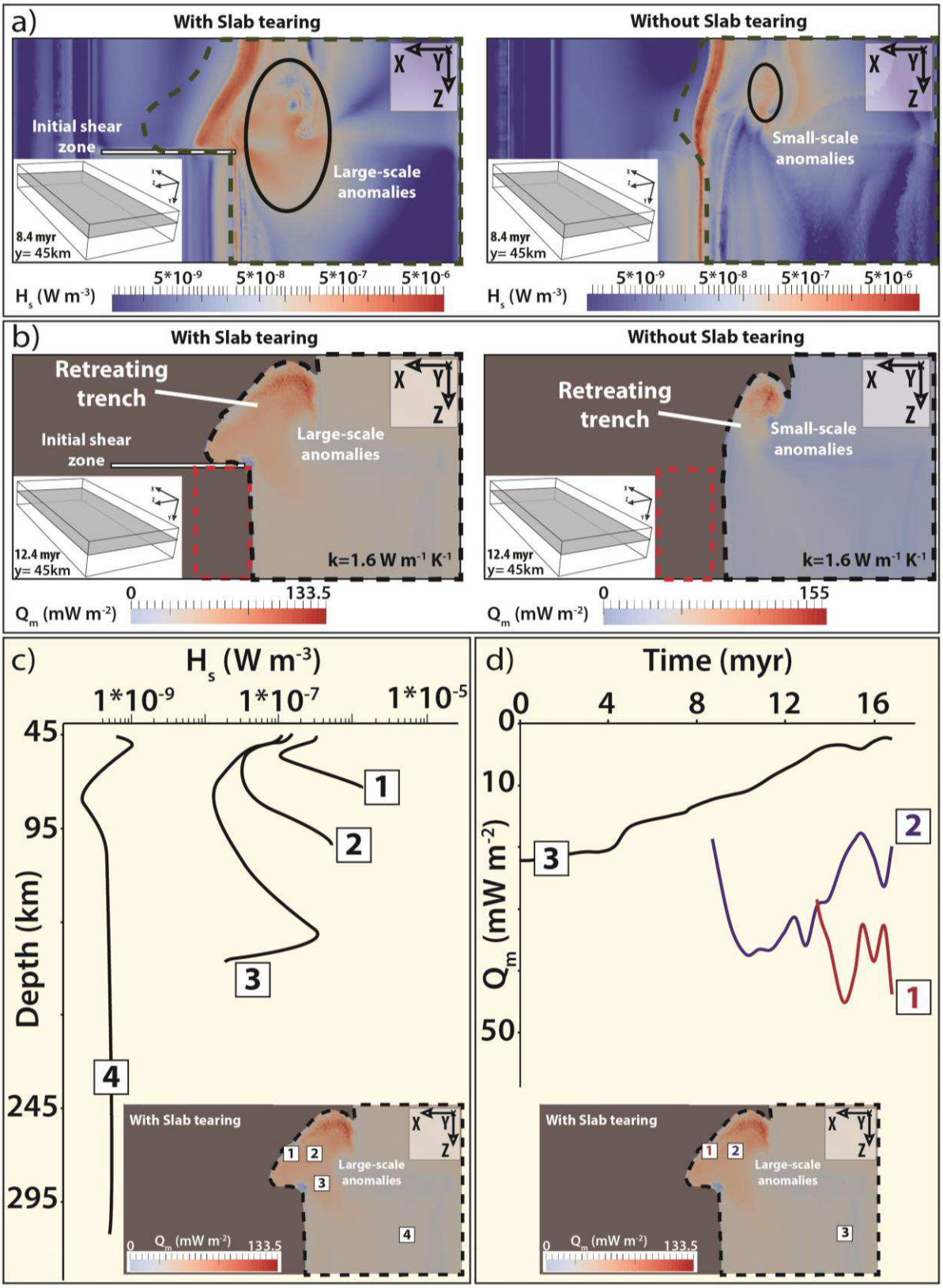
a)
With Slab tearing
Without Slab tearing
Initial shear zone
Large-scale anomalies
Small-scale anomalies
8.4 myr
y= 45km
H_s (W m^{-3})
5*10^{-9} 5*10^{-8} 5*10^{-7} 5*10^{-6}
b)
Retreating trench
Initial shear zone
Large-scale anomalies
Small-scale anomalies
12.4 myr
y= 45km
k=1.6 W m^{-1} K^{-1}
Q_m (mW m^{-2})
0 133.5
0 155
c)
H_s (W m^{-3})
1*10^{-9} 1*10^{-7} 1*10^{-5}
Depth (km)
45 95 245 295
1 2 3 4
With Slab tearing
Large-scale anomalies
d)
Time (myr)
0 4 8 12 16
Q_m (mW m^{-2})
0 10 50
1 2 3

Figure VI.5: Mantle heat source with and without tearing at the mantle-crust transition. (a) Plan view of shear heating (H_s) at the mantle-crust transition at 8.4 Myr. Dashed line on both panels shows the plan view of the overriding plate C1. (b) Plan view of mantle heat flow (Q_m) at the mantle-crust transition at 12.4 Myr. Black and red dashed lines on both panels show the plan view of the overriding mantle, and of the overriding C2, respectively. (c) Vertical depth-shear heating (H_s) profiles in the mantle below the stretched overriding plate at t_0 + 14.8 myr, taken at the location shown by the white squares. (d) Evolution of mantle heat flow (Q_m) at the mantle-crust transition. The values are taken at the location shown by the white squares.

Shear heating in the mantle during slab retreat and tearing plays a key role in increasing temperatures at the base of the back-arc crust, where mantle heat flow values are around 100 mW m^{-2} and reach locally up to 130 mW m^{-2} above the slab tear at 12.4 Myr (Fig. VI.5b, see left panels). We found that 46 % of the heat flow at the base of the crust is due to mantle shear heating, the remaining part being due to the advection of hot material. In the absence of slab tearing, the average of mantle heat flow at similar times is around 80 mW m^{-2}, reaching locally up to 155 mW m^{-2} but over a much smaller area, (Fig. VI.5b, right). We therefore suggest that advection of hot asthenosphere to shallow depths during slab retreat and tearing plays an important role in increasing temperatures at the base of the crust (Fig. VI.6). Furthermore, mantle heat flow values may reach steady-state after ~ 4 Myr (values around 40 – 50 mW m^{-2}, Fig. VI.5d).

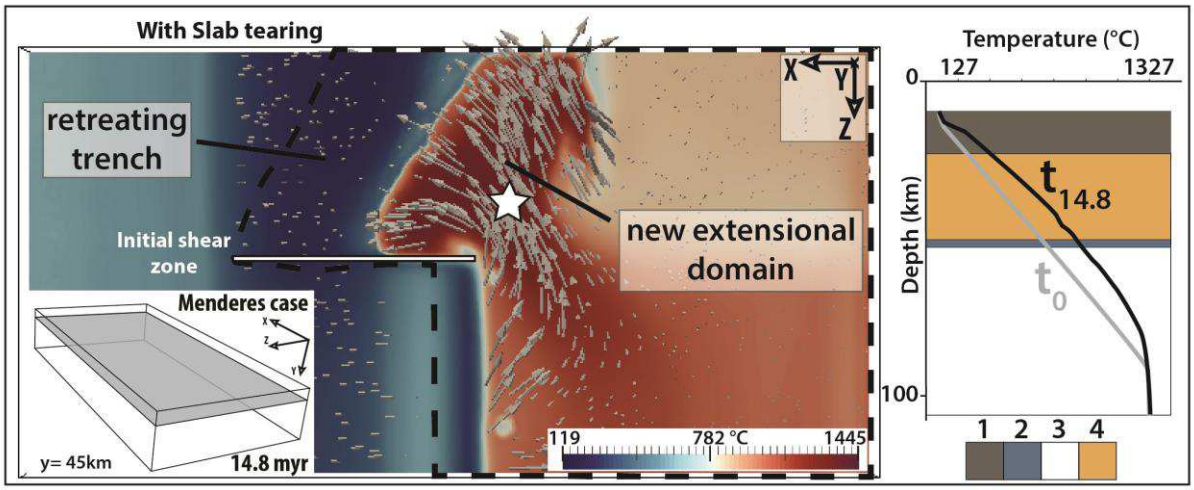

Figure VI.6: Plan view of temperature anomaly at the mantle-crust transition (~ 45 km depth) in the case of slab tearing. Grey arrows represent the velocity vectors in the asthenosphere. Black dashed line on the left panel shows the plan view of the overriding plate C1. Right panel: vertical temperature profiles at t_0 and t_0 + 14.8 myr, taken at the location shown by the white star. Colors showing different rock types: 1-2-3-4, as defined in Fig. VI.3.

To summarize, slab tearing facilitates the rollback of the subducting plate and extension within the upper plate. Consequently, slab tearing and its associated mantle flow contributes to the increase in heat flux at the base of the crust by (i) enhancing mantle shear heating and (ii) controlling the return flow of hot asthenosphere (*e.g.* toroidal and poloidal mantle flow components). Both mechanisms together appear to be able to increase the Moho temperature by up to 250 °C (Fig. VI.6). Therefore, slab

tearing may (i) affect the heat source responsible for regional HT-LP metamorphic rocks in MCCs and (ii) explain regional high-temperature anomalies across amagmatic geothermal systems in post-subduction settings.

VI.4. From subcrustal thermal anomalies to geothermal systems: 2-D model of fluid circulation

Results of the 3-D model show that at 12.4 Myr, mantle heat flow can reach anomalously high values exceeding 130 mW m^{-2} (Fig. VI.5b). At 10 km depth above the tearing, temperature values vary between 450 and 500 °C, and are thus similar to estimated temperatures from aeromagnetic data at the same depth in the Menderes Massif (~ 580 °C) [Aydin *et al.*, 2005]. Using these results, we defined a 2-D fluid flow model in a porous media to analyse the thermal consequences of anomalously high basal heat flow on fluid circulation in the upper crust. The advantage of this model is a good spatial resolution (see *Appendix VI.8.2.2.*), representative permeability, and realistic rock and fluid properties.

The model measures 120 x 10 km and is designed to represent a SSW-NNE cross-section of the Menderes massif. We choose the basal heat flow in order to (1) account for previous 3-D numerical results where mantle heat flow could reach values up to 130 mW m^{-2} (Fig. VI.5b), and (2) reproduce temperatures above 500 °C at 10 km depth, as suggested by Curie-point depths in western Anatolia. The objective of this model is to understand the effects of high basal heat flux on the fluid flow circulation pattern, in particular around permeable detachments. In the following, we describe the main characteristics of the model setup and present the main results.

VI.4.1. Model setup

Coupling between Darcy's law, heat transfer equation and mass conservation is performed using the Comsol Multiphysics™ software (finite element method). Details about the numerical procedure (benchmark experiments, model setup, fluid and rock properties) are given in *Appendix VI.8.2.2*. A cross-section of the model is shown in Figure VI.7, where two detachment faults (with an angle varying from 10 to 20°) represent the Büyük Menderes and the Alaşehir Menderes detachments (Fig. VI.2b). Figure VI.7a illustrates the mesh refinement in permeable zones (close to the surface and within the detachments). A convective flux condition was imposed at the top of the detachments, in order to allow the emergence of hot fluids at the surface. In addition, we use temperature-dependent density and viscosity laws for fluids (see *Appendix VI.8.2.2.*). No magmatic source is present in the model, and the chosen basal heat flow value at a depth of 10 km corresponds to 120 mW m^{-2} (Fig. VI.7b). This value is therefore consistent with both criteria (*i.e.* mantle heat flow from our 3-D model and Curie-point depths

estimations). A constant pressure of 10^5 Pa is imposed at the surface allowing fluid influx while no flow is allowed across the others boundaries of the box (Fig. VI.7b). At time t = 0, thermal regime is purely conductive (see white isotherms in Figure VI.7c). Then, permeability values are switched on (color code of Figure VI.7c) and the transient evolution of temperature and velocity fields are recorded during 5 Myr. Permeability in the basement (k_b) decreases exponentially with depth [Manning & Ingebritsen, 1999] (see Fig. VI.7c and *Appendix VI.8.2.2.*) while detachment permeability is assumed constant (k_D). Because permeability remains poorly constrained, we decided to test a wide range of realistic permeabilities for the basement (*i.e.* from 10^{-17} to 10^{-14} m²) and the detachment fault with same range of values (Fig. VI.7b).

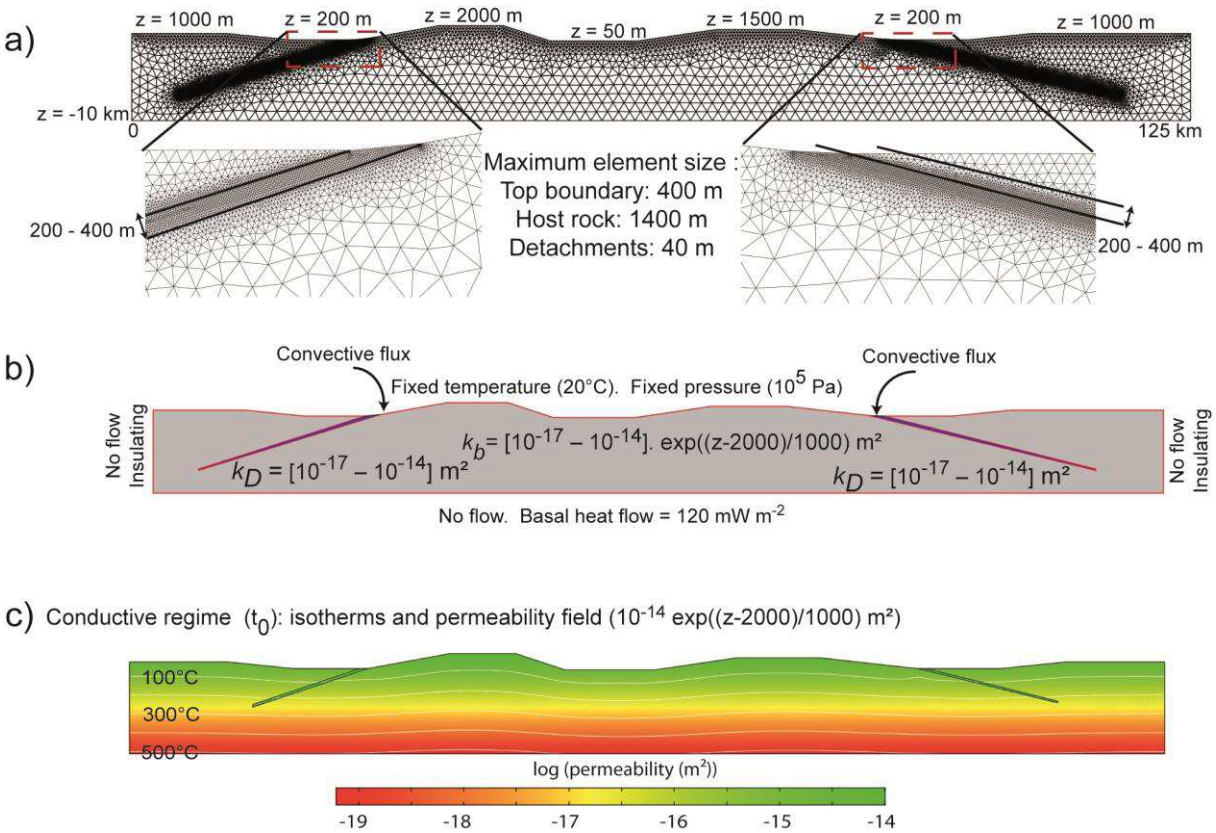

Figure VI.7: (a) Geometry and mesh used for 2-D models of fluid circulation in the upper crust of the Menderes area, where MCCs and detachments are reproduced. This cross-section would correspond, from left to right, to a N-S cross-section, from Salihli to Salavatlı geothermal areas. Mesh is refined at the top surface and within detachments, where permeability is the highest. (b) Boundary conditions and range of values for permeability (note the depth-dependence of the host rock permeability). (c) Steady-state conductive regime, where isotherms in white are separated by 100 °C. Colors refer to permeability values affected at time t > 0 (see text) for the case detailed in Figure VI.9.

VI.4.2. Results

VI.4.2.1. Role of basement and detachment permeabilities

Figure VI.8 illustrates steady-state temperature fields for different combinations of both basement and detachment permeability. In Figure VI.8a, results show the major role of k_b to distort significantly the isotherms, even if k_D is high (10^{-14} m²). In the top case of Figure VI.8a, isotherms remain flat and no thermal reservoir forms beneath the detachments. Alternatively, in the bottom case, with realistic higher permeability values, shows a general fluid circulation pattern characterized by: (i) surface meteoric fluids that flow from topographic highs to the top of the detachment fault and other topographic lows, inducing a negative thermal anomaly in the hanging walls of detachments; (ii) at depth, hot fluids are drained upward by the permeable detachments allowing for isotherms to rise along the fault zones (see uplifted isotherms in bottom case of Figure VI.8a). A positive thermal anomaly is due to hot fluids rising up toward the top of the detachment while a negative thermal anomaly induced by topography-driven flow grows in the hanging walls of detachments, leading to the formation of hot fluid reservoirs beneath the detachments (near the surface). To synthetize, at the scale of the whole massif, thermal undulations mimicking dome-like structures are localized beneath topographic lows in the case of a high basement permeability (Fig. VI.8a, bottom case).

When k_D is varied (Fig. VI.8b), it turns out that thermal reservoirs establish at shallow depth when both k_D and maximum k_b values are important (10^{-14} m², bottom right case in Figure VI.8b). In the case where k_D is low (10^{-17} m², top case in Figure VI.8b) two thermal reservoirs appear only with a high maximum k_b value, suggesting that topography-driven flow is dominant. However, temperatures at shallow depth and fluid velocity values within the detachment are much lower than in the high k_D case (bottom right case in Figure VI.8b). Crustal-scale permeable faults and their induced high topography thus control the spatial distribution of upper-crust thermal anomalies at depth, mimicking dome-like structures beneath topographic lows (Fig. VI.8a, bottom case, and Fig. VI.8b, right column).

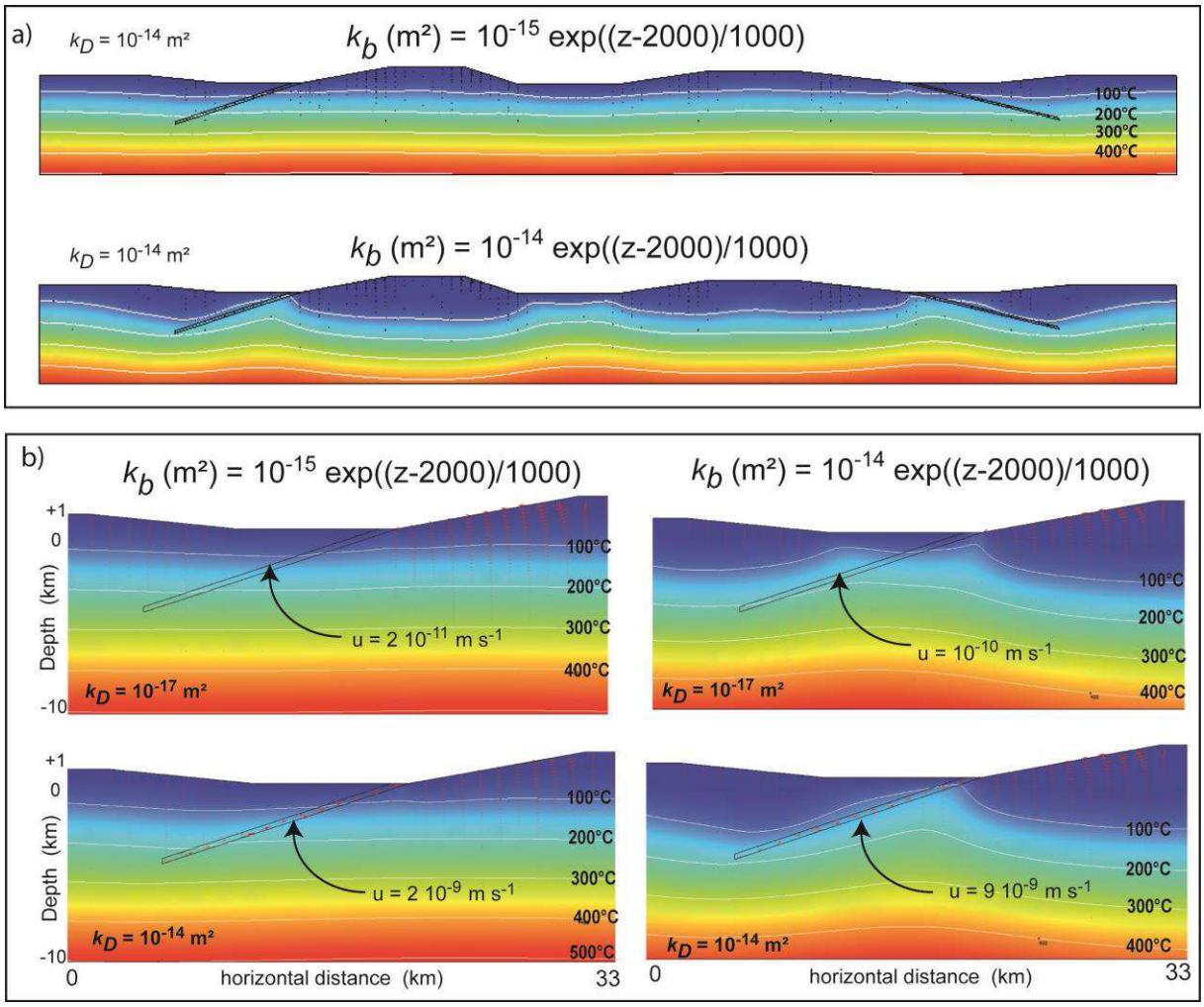

Figure VI.8: Results for thermal perturbations due to fluid circulation in permeable zones for varying basement permeability (k_b) and for varying detachment permeability (k_D). (a) role of the basement permeability for a fixed value of k_D (10^{-14} m²). (b) Zoom on the left detachment, with varying permeabilities (small k_D value in the top row; high k_D value in the bottom row). Left (right) column corresponds to a small (high) basement permeability.

VI.4.2.2. Fluid flow field and temperature profiles

Figure VI.9a illustrates the fluid flow velocity pattern in the case of Figure VI.8a (bottom case). Fluid flow is favored by high-topographic zones and permeable zones such as detachments. Located within detachments, high velocities areas (> 10^{-10} m / s – or 0.32 cm / yr) are recorded down to 5 km deep (red areas). The bottom figure shows a horizontal temperature profile at 1 km depth. It is important to note that temperature anomalies of ~ 140 °C are focused close to the top of the detachments. Figure VI.9b (left column) shows computed vertical temperature profiles at different distances from the two detachments, at a given time (*i.e.* 4 x 10^4 yr). Figure VI.9b (right column) illustrates temperature measurements at the Aydin-Salavatlı geothermal field, Büyük Menderes Graben, within 2 boreholes ~1.5 km apart. Although the comparison of daily-measured thermal profiles with these two sets of vertical temperature profiles is limited, one can observe some similarities with (i) a high-temperature

gradient at the surface, decreasing rapidly with depth, and (ii) some negative values of the temperature gradient. In addition, modeled temperatures are comparable, with emergence temperatures around 60 °C and reservoir temperatures at depth around 180 – 200 °C. Because our density law is simplified (see *Appendix VI.8.2.2.*), and because the vapor phase is not accounted for, the computed profiles show rather smooth curves when compared to measurements. However, the typical convective signatures in temperature profiles are similar.

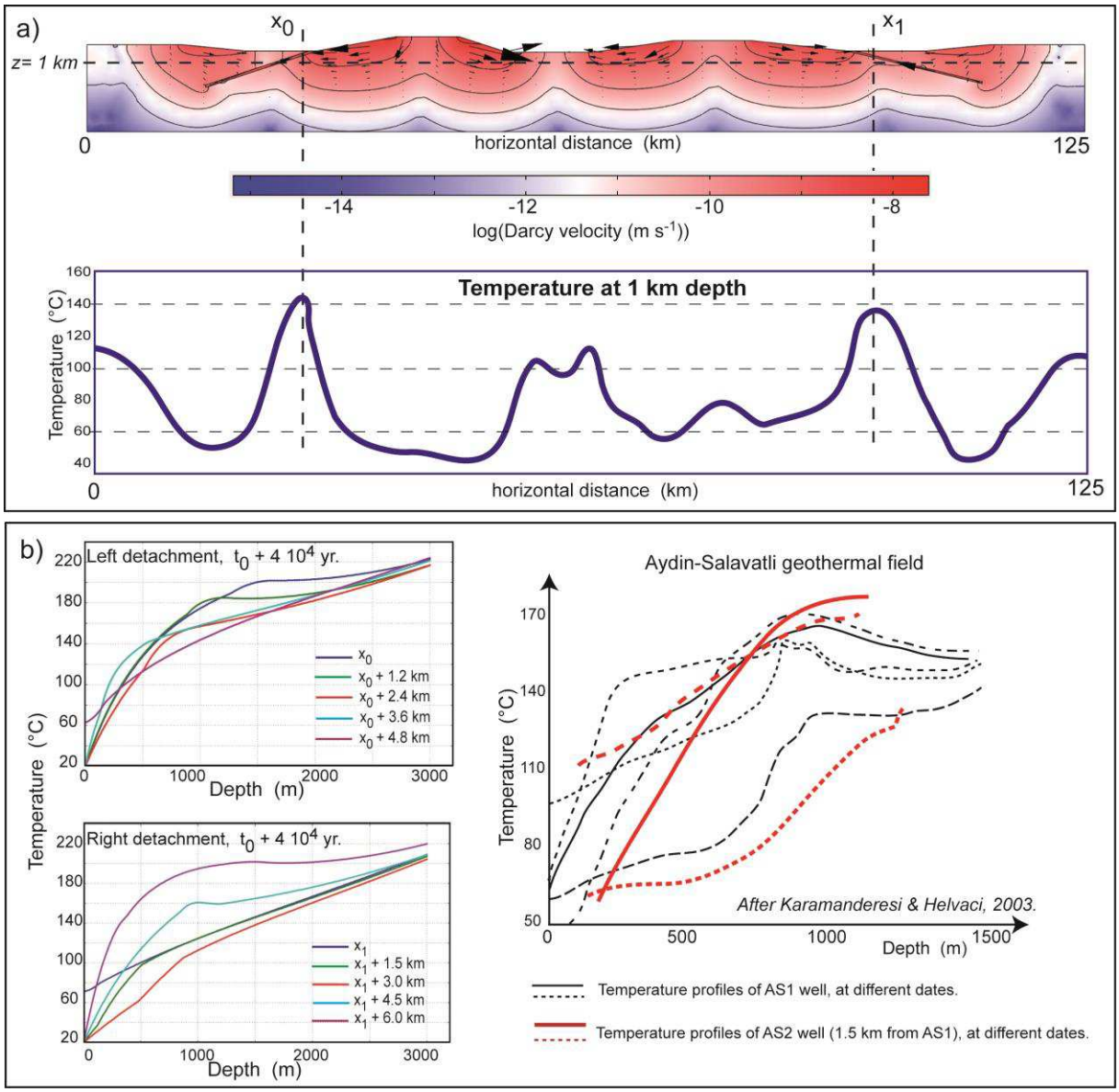

Figure VI.9: Results for the experiment shown in the lower case of Figure VI.8a (and right case of Figure VI.8b). (a) Fluid flow velocity field (colors, isocontours and arrows) and horizontal temperature profile at 1 km depth (dashed line in the fluid flow pattern). Note that the largest temperature perturbations correspond to the top of the detachment locations (x_0 and x_1). (b) Computed vertical temperature profiles at time t_0 + 4 10^4 yr. x0 and x1 are indicated in Figure VI.9a. On the right, measured temperature profiles at the Aydin-Salavatlı geothermal field; black curves (plain and dashed) correspond to different measures in the same AS1 borehole (different dates of measurements) and red lines are measured in the AS2 borehole, 1.5 km from the AS1 borehole [Karamanderesi & Helvaci, 2003].

VI.5. Discussion

VI.5.1. Large-scale thermo-mechanical boudinage, and emplacement of MCC in Western Anatolia

The modeled thermo-mechanical instabilities (Fig. VI.4) are not only analogous to crustal and lithospheric boudinage [Ricard & Froidevaux, 1986], but they add a thermal component to what was generally assumed to be purely mechanical. These instabilities developed in back-arc extension are triggered by both shear heating and hot mantle flows. These mechanisms indeed induce a thermal weakening of the lithosphere, thus controlling the development of boudinage at different scales, and the localization of MCCs in the extensional crust. It is important to note that these domes are also promoted by the low-viscosity crust, which is related to the chosen initial thermal regime in our models. When the slab tear is accounted for, the crust is weak over a wider domain above the tear, increasing its ability to flow [*e.g.* Block & Royden, 1990; Rey *et al.*, 2009] and to form HT domes. In other words, shear heating and mantle flow control the position of positive thermal anomalies in the overriding crust, which, in turn, control the deformation pattern in the lower crust during extension. Such a lithospheric thermal weakening is further enhanced by the accumulation of magmas in the back-arc domain, which is widely promoted by slab rollback and tearing processes [Menant *et al.*, 2016b].

In the Cyclades (Greece), the dominant wavelength of MCCs (several tens of kilometers, similar to the spacing between the different islands) is compatible with that expected for crustal-scale boudinage (Fig. VI.4). At the scale of the whole Aegean domain, long-wavelength variations of Moho depth [Tirel *et al.*, 2004; Karabulut *et al.*, 2013] are more reminiscent of lithospheric-scale boudinage (several hundreds of km; Fig. VI.4). This boudinage of the crust induces migmatite-cored MCCs which were first exhumed in the northern Menderes Massif in the Micoene [Cenki-Tok *et al.*, 2016], and then in the central and eastern Cyclades since the lower Miocene [Jolivet *et al.*, 2015], coevally with a further acceleration of trench retreat related to the Hellenic slab tearing. This is consistent with our model, where dome-like structures, cored by partially molten low-viscosity material, develop first in the back-arc domain, and then migrate toward the trench, in response to both slab rollback and tearing (Figs. VI.4a and VI.4b). In addition, we suggest also that heat excess due to these subduction dynamics controlled the retrogression in the greenschist-facies of high-pressure metamorphic rocks in Cyclades (post-orogenic extension), consistently with acceleration of slab retreat around 35 Ma [Jolivet *et al.*, 2015]. Furthermore, our numerical experiments highlight an increase of Moho temperature during a few Myrs related to asthenosphere upwelling below the back-arc domain (Figs. VI.5d and VI.6). We therefore suggest a similar heating for the mantle-crust boundary in the Anatolian-Aegean domain, which is coherent with the presence of HT metamorphic domes and the formation of syn-extension

granites and migmatites throughout the entire western Anatolian-Aegean domain between 20 Ma and 8 Ma [Jolivet *et al.*, 2015; Menant *et al.*, 2016a].

In the Menderes MCC (located above the slab tear, see Fig. VI.2), strain was first localized in the north, along the Simav Detachment (early Miocene, stage 1 after Gessner *et al.* [2013]) accommodating the exhumation of an asymmetric migmatite-cored MCC [Rey *et al.*, 2009; Cenki-Tok *et al.*, 2016]. Then, strain migrated southward, toward the trench and localized within the central part of the Menderes Massif (Fig. VI.2c). The Alaşehir and Büyük Menderes detachments assisted exhumation of the lower crust during slab tearing (middle-late Miocene, stage 2 after Gessner *et al.* [2013]). This implies that the central part of the Menderes Massif had become weaker than the previously activated Simav area, probably due to the extra source of heat associated with slab tearing. According to Labrousse *et al.* [2016], the evolution of the style of extension from an asymmetric MCC (localized deformation, case of the Simav detachment) to a double-dome symmetric MCC (distributed deformation, case of the Menderes detachments) implies that heat input at the base of the crust is higher than heat dissipation due to stretching. These observations are consistent with the thermal features observed in our model, which emphasize the crucial role of shear heating, as well as poloidal and toroidal components of mantle flow, to heat the lower crust (Figs. VI.5 and VI.6). Both mechanisms are thus responsible for the presence of large-scale thermal anomalies at depth (*i.e.* 580 °C at 10 km depth) and at the surface (*i.e.* heat flow values around 100 mW m^{-2} [Erkan, 2015]). As a consequence, the thermal state of the crust induced by elevated mantle heat flow could control the style of extension (asymmetric versus symmetric MCC).

Furthermore, hot fluids circulating within crustal-scale permeable faults help increasing basal temperatures (around the ductile/brittle transitions) by several tens of °C (Fig. VI.8a), resulting in a positive feedback for the formation of new shear zones and MCCs at depth. In this case, magmatic bodies such as granitoids and migmatites may be developed and localized below the detachment, as it seems to be the case in the Menderes with the Salihli diorite and Simav granites.

The progressive formation of HT domes topped with extensional detachments can thus be summarized as follows: (1) mechanical (boudinage) and thermal instabilities within the stretched lithosphere generate a series of domes, periodically spaced, producing rheological heterogeneities (*i.e.* low-viscosity layers) that are likely to localize extensional shearing deformation on their edges [Jolivet *et al.*, 2004; Le Pourhiet *et al.*, 2003; Huet *et al.*, 2011] and (2) upward flow of deep hot fluids and downward flow of cold surface fluids further increase thermal contrasts across the shear zones, enhancing the localization of deformation.

VI.5.2. Detachments and localization of HEGRs in Western Anatolia

The relationships between the localization of the deformation and thermal domes (Fig. VI.4) are similar to that documented in MCCs, and may be associated with crustal-scale permeable faults, which can provide pathways for meteoric waters to flow into the actively deforming middle crust [*e.g.* Famin *et al.*, 2004; Mulch *et al.*, 2006]. As shown in Figure VI.5, the excess of mantle heat flow is transfered by conduction into the crust, affecting the fluids present in the crustal porosity. These fluids may then undergo deformation-driven flow in ductile shear zones [*e.g.* Oliver, 1996], but also thermally driven (*i.e.* buoyancy-driven) flow through the crust, where high permeability detachments may easily collect and bring up deep hot fluids. Indeed, our 2-D numerical models suggest that an elevated basal temperature (580 °C) at 10 km depth would induce temperatures of 300 – 350 °C at a depth of 6 km and thus a sufficiently high fluid density contrast to permit upward flow along the low-angle fault in the shallower crust. In that case, buoyancy-driven flow is superimposed to topography-driven flow (Fig. VI.8). In other words, the topography-driven flow, which prevails in the regional fluid flow pattern, is dominated by buoyancy-driven flow within highly permeable detachments.

Although the spatiotemporal evolution of permeability within detachments is poorly known, field observations on these geological structures [Famin *et al.*, 2004] suggest that they could represent highly permeable zones of several hundreds of meters thick where fluid flow is facilitated (Fig. VI.10). Moreover, if these channelized fluid flow systems are tectonically active, earthquake faulting may be associated with seismic pumping that enhances fluid migration toward dilation zones [Sibson *et al.*, 1975; Famin *et al.*, 2005]. As a consequence, detachments may be considered as the crustal-scale structural control for the circulation of deep geothermal fluids related to HEGRs [*e.g.* Bellani *et al.*, 2004], driving the long-term crustal-scale history of the geothermal systems (Fig. VI.10). However, it is noteworthy that most of the geothermal systems in the Menderes Massif reside in fault intersection zones, where N-S transfer faults and low-angle normal faults mostly formed dilational jogs that seem to promote the emergence of hot waters and gas vents. Fault interactions would thus allow for fluid rising in the hanging wall from the reservoirs located below the detachment (Fig. VI.8b, right column), and control the location of thermal springs. Further numerical simulations would therefore be required to confirm this hypothesis based on field observations.

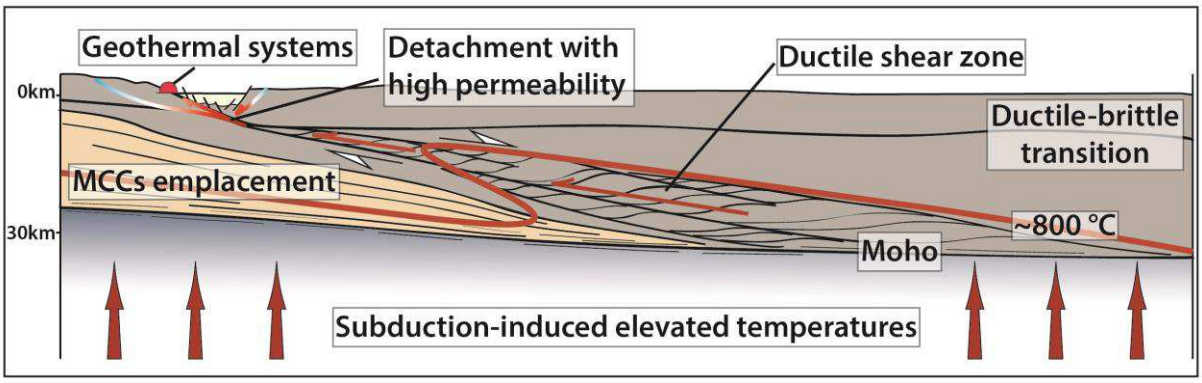

Figure 10: Schematic cross-section showing fluid flow associated with detachment zone in back-arc area. Red arrows indicate fluid circulation in ductile crust and circulation of meteoric fluids in the upper crust are underlined by colored pathways (blue for cold and red for warm).

VI.5.3. Subduction dynamics and localization of HERSs: the Larderello (Tuscany) and the Basin and Range (Western United States) areas

Our 3-D and 2-D model results are relevant to other regions, and thus may explain relationships between subduction dynamics and the location of geothermal provinces; for instance, (i) in the Larderello area (Tuscany) post-orogenic extension is active in back-arc domain; or (ii) in the Basin and Range Province (western United States). In both cases, MCCs are exhumed along low-angle normal faults, and therefore represent a favorable setting for HEGRs. While some of them are considered as "amagmatic" in origin [*e.g.* Bellani *et al.*, 2004; Faulds *et al.*, 2010], some authors believe to a magmatic heat source [*e.g.* Koenig & McNitt, 1983; Santilano *et al.*, 2015]. Through these two main additional examples, we show that the "magmatic" vs. "amagmatic" classification may be ambiguous according to the long-term behavior of these geothermal systems.

In the Northern Tyrrhenian Sea and Tuscany regions, subduction dynamics has also been controlled by slab retreat since the Oligo-Miocene. This region is characterized by a shallow Moho discontinuity (20 – 25 km depth), and a reduced lithosphere thickness due to uprising asthenosphere and the delamination of crustal lithosphere [Gianelli, 2008]. At crustal-scale a series of low-angle normal faults crosscut the old thrusts [*e.g.* Faccenna *et al.*, 1997; Jolivet *et al.*, 1998], and thus cannot be explained by a reactivation of pre-existing inherited discontinuities. Instead, our numerical models suggest that thermo-mechanical boudinage induced by slab rollback triggers the formation of localized shear zones and allows the exhumation of MCCs (*e.g.* Elba Islands, *Appendix VI.8.1.*, Fig. VI.13). These shear zones are still active [Bellani *et al.*, 2004] and may control the ascent of magmatic intrusions, such as beneath the Larderello geothermal field. We therefore suggest that magmatic intrusions in the upper crust result directly from the deep thermal anomaly associated with slab dynamics during extension.

Although subduction dynamics are quite different in the Basin and Range province (*i.e.* first characterized by slab retreat since the Eocene at the northern edge of the Farallon slab [Schellart *et al.*, 2010], and then by an asthenospheric upwelling above the Californian slab window at 30 Ma [Atwater, 1970]), similar remarks also hold for this region. Indeed, our results are consistent with geological observations where the presence of a conductor at 15 – 35 km depth range [Wannamaker *et al.*, 2008] suggests that the central part of the Basin and Range domain has become weaker, probably due to an extra source of heat associated with slab window (*i.e.* magma underplating due to mantle flow and shear heating). In light of our numerical results, we propose that fast-flowing asthenosphere also strongly heats the lithospheric mantle and the lower crust via shear heating and mantle upwelling processes. Lithospheric weakening thus promotes the propagation of major fault zones throughout the crust, leading to the connection between the weaker conductive lower crust and the brittle upper crust (Fig. VI.10). Hot thermal fluids at depth can then ascend within the damage fault zones, which thus control the location of HEGRs at the surface [Faulds *et al.*, 2010]. It is noteworthy that the presence of recent intrusions (*e.g.* Steam Boat, Casa Diablo in the Walker Lane geothermal belt [Koenig & McNitt, 1983]) locally enhances thermally-driven flow, by increasing the temperatures of the geothermal systems but this seems marginal as very few active volcanism is recognized in this region [Faulds *et al.*, 2010].

VI.6. Conclusion

3-D numerical experiments show that the mantle flow and shear heating resulting from slab retreat and tearing have a significant effect on Moho temperatures during 5 – 10 Myrs. Such a mechanism induces lithospheric and crustal thermal boudinage with different wavelengths, which in turn creates thermally-driven rheological contrasts that localize deformation and lead to the formation of crustal-scale permeable detachments. These structures allow for the exhumation of MCCs and for the emplacement of HEGRs comparable to those observed in the Mediterranean realm and in the Western United States. Although there is no consensus on a worldwide classification of geothermal systems, our results highlight the importance of the spatial and temporal scales of subduction dynamics in the control of genesis of geothermal systems.

VI.7. Acknowledgements

This work has been financially supported by the LABEX VOLTAIRE (ANR-10-LABX-100-01) of the University of Orléans and by the French Geological Survey (BRGM). This paper is a contribution of the ERC RHEOLITH Project (ERC advanced grant no. 290864). Pietro Sternai is

grateful to the Swiss NSF Ambizione grant PZ00P2_168113/1. Numerical simulations were performed on the ETH-Zürich clusters BRUTUS and EULER.

VI.8. Appendix

VI.8.1. Supplementary Figures

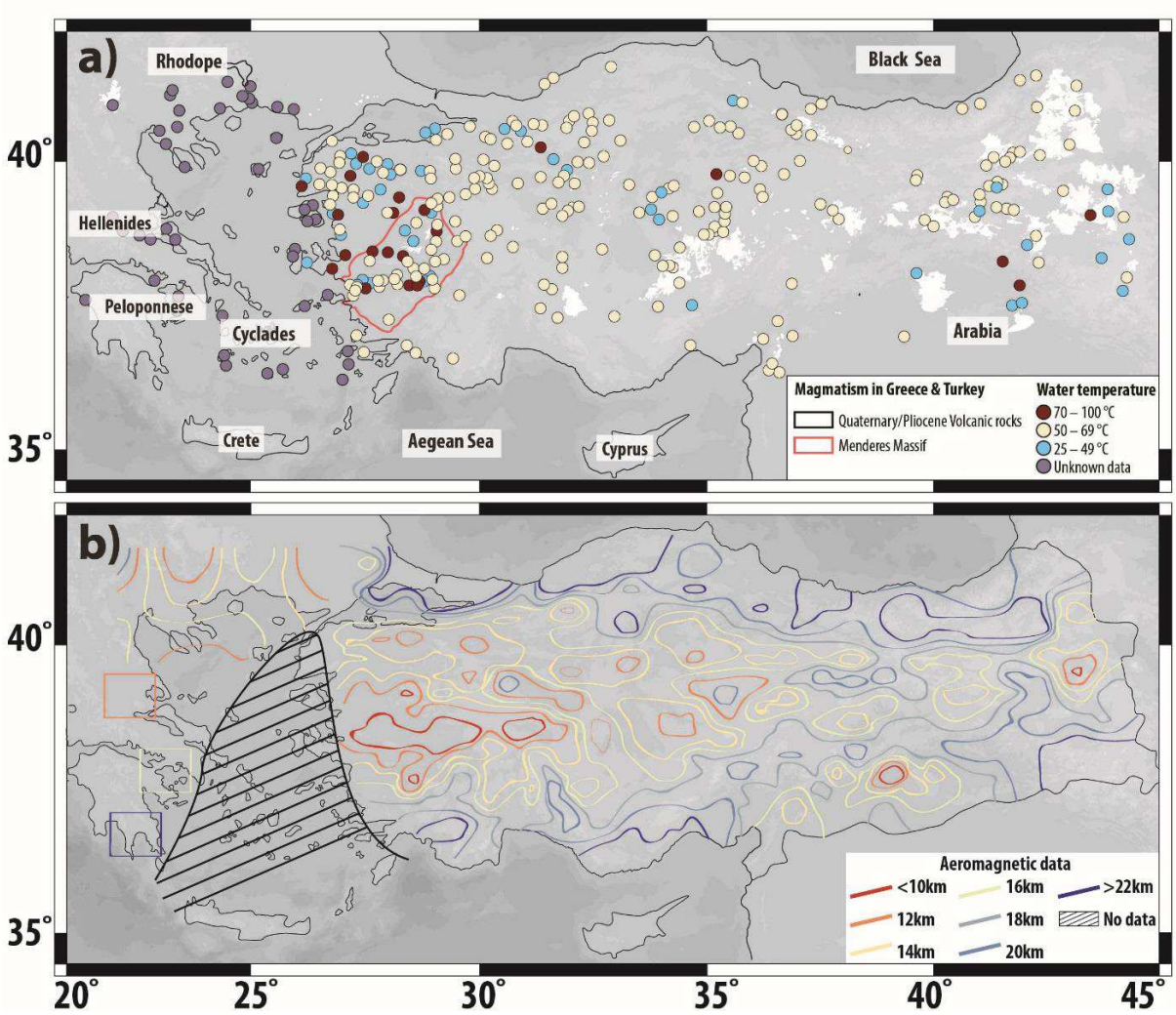

Figure VI.11: Maps of the Aegean-Anatolian region. (a) Geothermal map of eastern Mediterranean region highlighting major thermal occurrences based on a compilation of several data sources [MTA, 2005; Mendrinos et al., 2010; Andritsos et al., 2015], and spatial distribution of Pliocene-Quaternary volcanic rocks (from the geological map of the MTA). (b) Curie-point depth map from Tselentis [1991], Stampolidis and Tsokas [2002] and Aydin et al. [2005].

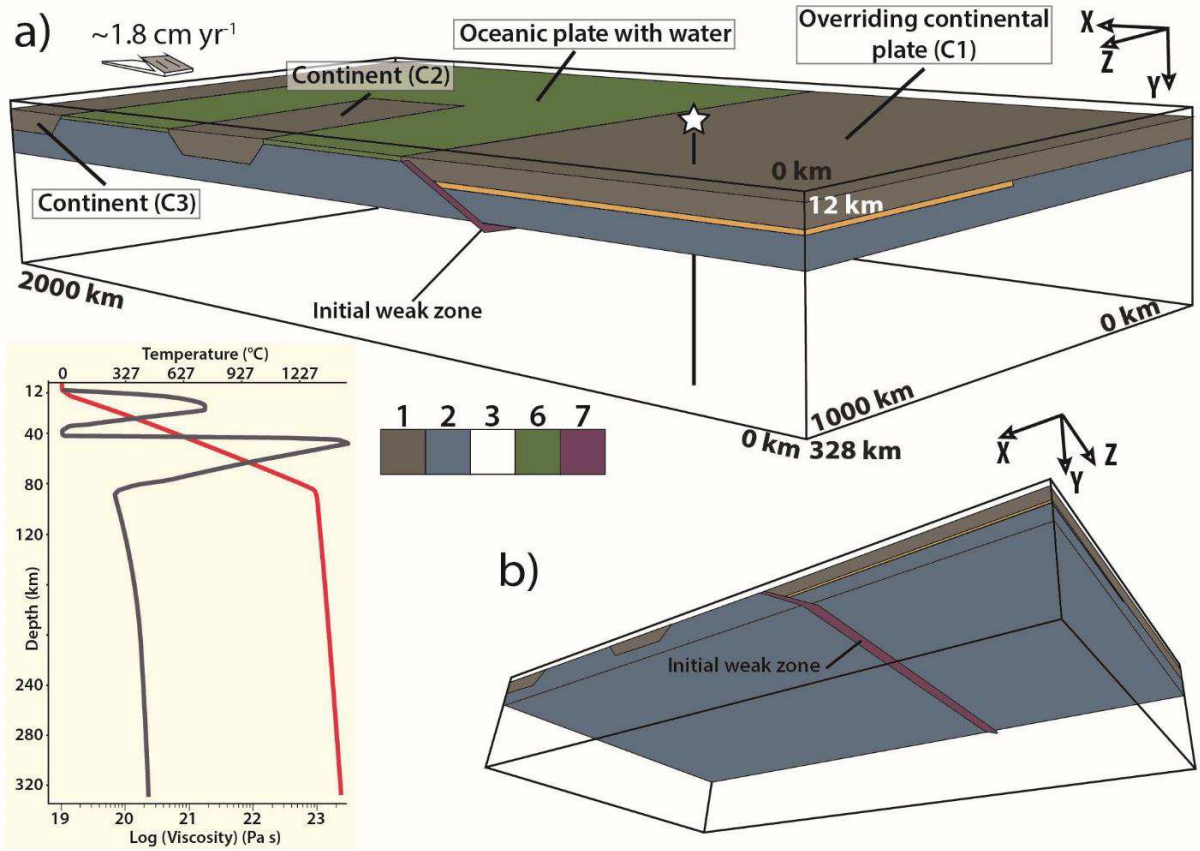

Figure VI.12: Experimental setup without slab tearing. (a) 3D initial model setup where the top layer ("sticky air", y < ~ 12 km") and the water are cut off for clarity. Colours showing different rock types as defined in Fig. 3. Vertical viscosity (grey) and temperature (red) profiles at t_0, taken at the location shown by the white star. (b) Location of the "weak zone" (i.e. hydrated/serpentinized mantle) into the lithosphere to initialise subduction (z-parallel).

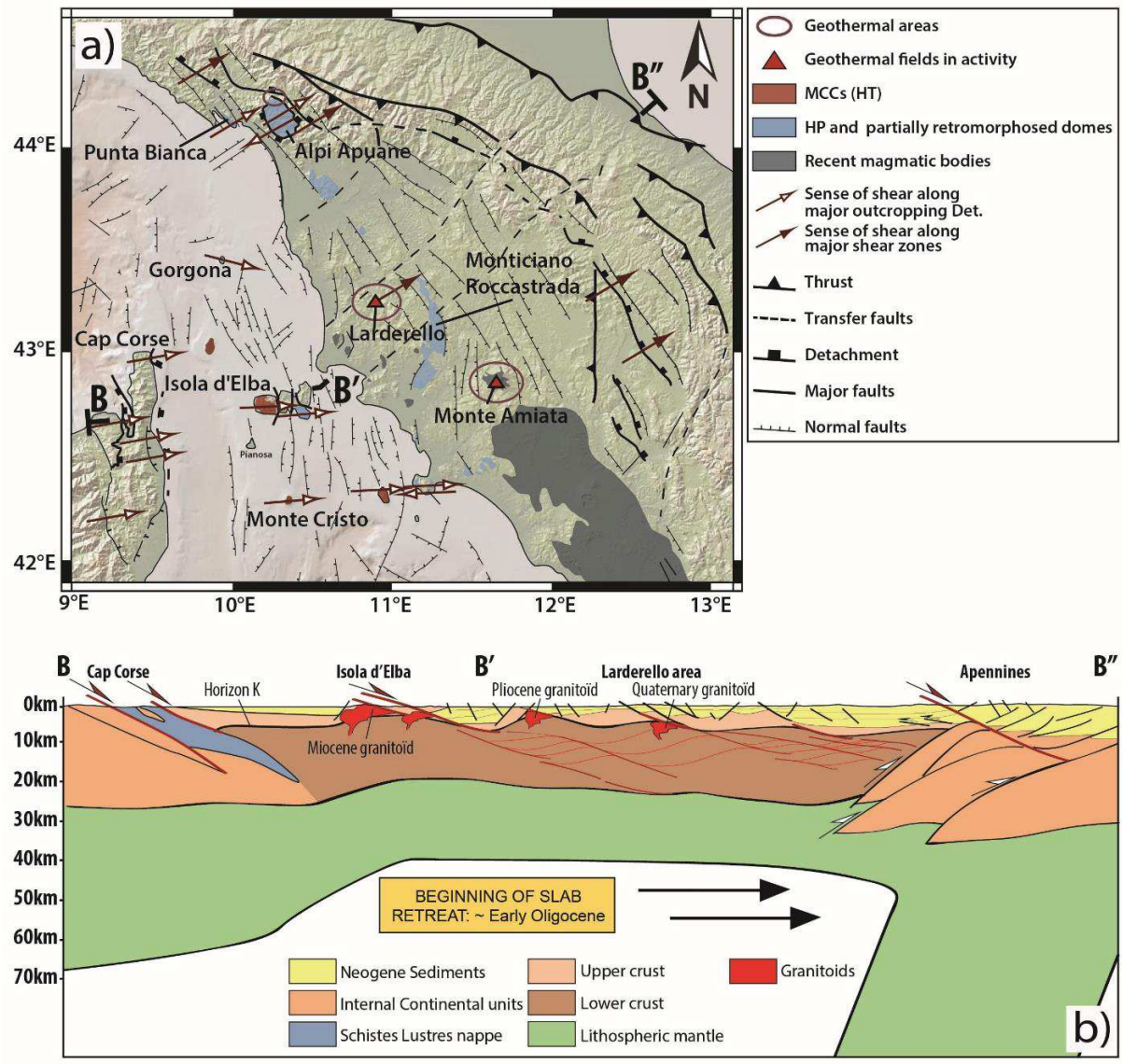

Figure VI.13: Simplified tectonic map showing the main metamorphic core complexes and associated detachments faults. (a) Map of the Northern Tyrrhenian region and Northern Apennines, modified from Jolivet et al. [1998]. (b) Simplified cross-section highlighting slab retreat and formation of crustal detachments.

VI.8.2. Supplementary Materials

VI.8.2.1. 3-D Numerical approach

Continuity and momentum equations

The code I3ELVIS uses a staggered finite difference scheme combined with the marker-in-cell (MIC) technique [Gerya, 2010]. Lagrangian advecting markers are thus combined with an immobile Eulerian grid. The continuity equation describes the conservation of mass during the deformation of a continuous medium (rocks) and its Eulerian formulation is:

$$\frac{\partial \rho}{\partial t} + div(\rho \vec{v}) = 0, \quad (2)$$

where $\frac{\partial}{\partial t}$ is the Eulerian time derivative, ρ is the local density, $\vec{v}$ is the local velocity and div() denotes the divergence operator.

The conservation of momentum is obtained through the solution of the Stokes equation:

$$\frac{\partial \sigma'_{ij}}{\partial x_j} - \frac{\partial P}{\partial x_i} + \rho g_i = 0, \quad (3)$$

where *i* and *j* denote the coordinate indices (*i.e.* x, y, z), σ' is the deviatoric stress tensor, x_i and x_j denote spatial coordinates, g is the i^{th} component of the gravity vector $\vec{g}$ and $\frac{Dv_i}{Dt}$ is the substantive time derivative of the i^{th} component of the velocity vector (*i.e.* acceleration vector).

Heat conservation equation

Heat transport is defined by Fourier's law of heat conduction, which relates the heat flux q to the temperature gradient in space as:

$$q_i = -k \frac{\partial T}{\partial x_i}, \quad (4)$$

where T is temperature and k is the thermal conductivity of the material which depends on pressure (P), T, and composition of the material. In order to predict changes in temperature due to heat transport, the heat conservation equation is solved using the following Lagrangian temperature equation which consider advective and conductive heat transport, as well as internal heat generation:

$$\rho C_p \frac{DT}{Dt} = -\frac{\partial q_i}{\partial xi} + H, \quad (5)$$

where *Cp* is the isobaric heat capacity, $\frac{DT}{Dt}$ is the substantive time derivative of temperature and *H* is the volumetric heat productions. The latter term includes several types of heat generation/consumption processes:

$$H = H_r + H_s + H_a \,, \tag{6}$$

where H_r is the radiogenic heat production, H_s is the shear heating and H_a is the adiabatic heat production. H_s is related to dissipation of the mechanical energy during irreversible non-elastic (*e.g.* viscous) deformation and can be calculated as:

$$H_s = \sigma'_{ij}\dot{\varepsilon}'_{ij} \,, \tag{7}$$

where $\dot{\varepsilon}'$ is the strain rate tensors. H_a corresponds to heat production related to pressure changes. It can be calculated as follows:

$$H_a = T\alpha\frac{DP}{Dt} \,, \tag{8}$$

where $\frac{DP}{Dt}$ is the substantive time derivative of pressure. It is important to note that adiabatic effects can be both positive or negative compared to shear and radioactive heating.

Viscous rheology of rocks

The physical properties of rocks used in our experiments are given in Table VI.1. Among them, the density of solid rocks depends on *P*, *T*, and composition. In our experiments, ρ_{solid} is calculated as follow:

$$\rho_{solid} = \rho_{rsolid}\,[1 + \beta(P - P_r)] * [1 - \alpha(T - T_r)], \tag{9}$$

where ρ_{rsolid} is the standard density of solid rocks at reference pressure P_r (typically 10^5 Pa = 1 bar) and temperature T_r (typically 298.15 °K = 25 °C); α and β are respectively the thermal expansion and compressibility of rock. As density is also modified by phase changes (such as partial melting which is implemented in this code), effective rock density ρ_{eff} is calculated as follow:

$$\rho_{eff} = \rho_{solid}\,(1 - M + M\frac{\rho_{0molten}}{\rho_{0solid}}), \tag{10}$$

where $\rho_{0molten}$ is the standard density of molten rock, and *M* is the volumetric melt fraction in partially molten rock (see below for more information). In addition, non-Newtonian visco-plastic rheologies used in our experiments are implemented by both ductile and brittle/plastic experimentally constrained laws. Effective viscosity for dislocation creep thus depends on the strain rate, pressure and temperature. It is calculated as follow:

$$\eta_{creep} = \dot{\varepsilon}_{II}^{\frac{1-n}{n}} A_D^{\frac{-1}{n}} \exp\left(\frac{E + P\,V}{n\,R\,T}\right), \tag{11}$$

where $\dot{\varepsilon}_{II}$ is the second invariant of the strain rate tensor, R is the gas constant, n is the creep exponent, A is the pre-exponential factor, E is the activation energy) and V is the activation volume. These parameters depend on the applied viscous flow law (*i.e.* wet quartzite, plagioclase (An_{75}), dry olivine and wet olivine flow laws; Table VI.1) [*Ranalli*, 1995]. This ductile behavior is limited with a brittle/plastic one, implemented by using the Drucker-Prager criterion σ_{yield} (*i.e.* plastic strength) [*Ranalli*, 1995] as follow:

$$\eta_{creep} \leq \frac{\sigma_{yield}}{2\dot{\varepsilon}_{II}}, \quad (12)$$

where σ_{yield} is calculated as:

$$\sigma_{yield} = c + p \sin(\varphi), \quad (13)$$

where c is the cohesion of the rock and φ is the effective internal friction angle depending on the fluid and melt contents (see details in Gerya and Meilick [2011]).

Fluid/melt dynamics: example of partial melting

In our experiments, partial melting process is also included. The volumetric melt fraction (M_0) is then calculated for all rocks, excepted hydrated mantle, as follow:

$$M_0 = 0 \text{ at } T < T_{solidus}$$

$$M_0 = \frac{T - T_{solidus}}{T_{liquidus} - T_{solidus}} \text{ at } T_{solidus} < T < T_{liquidus} \quad (14)$$

$$M_0 = 1 \text{ at } T > T_{liquidus}$$

where M_0 is the volumetric fraction of melt with no previous melt extraction, $T_{solidus}$ and $T_{liquidus}$ are, respectively, the solidus and liquidus temperatures depending on the pressure and rock composition (Table V I . 1). For the hydrated mantle, the degree of partial melting also depends on the water content according to the parameterization of Katz *et al.* [2003]. Resulting partially molten rocks can then undergo a succession of melt extraction episodes depending on their melt extraction threshold M_{max} and non-extractable melt fraction M_{min}, both equal to 1%. Only the exceeding volumetric melt fraction (*i.e.* > 1 %) is then extracted from partially molten rocks, thus generating partially molten rock markers. For each extraction episode, the melt fraction M_{ext} recorded in the partially molten rock markers is calculated as follow:

$$M_{ext} = M - M_{min}, \quad (15)$$

where M is the volumetric melt fraction in partially molten rock, accounting for previous melt extraction events. It is calculated as:

$$M = M_0 - \Sigma M_{ext}, \quad (16)$$

where ΣM_{ext} is the total melt fraction from previous extraction episodes. Then, M varies dynamically until remaining solid rock is no longer able to undergo additional partial melting (*i.e.* $\Sigma M_{ext} > M_0$).

Partially molten rock markers resulting from these extraction episodes are then instantaneously transmitted to the surface as free melt is assumed to propagate upward much faster than rocks deform [Hawkesworth, 1997].

Material	k	Hr	ρ_0	C_P	E_a	V_a	α	β	n	η_0	Viscous flow law	sin (Φ_{eff})
	(W m^{-1} K^{-1})	(mW m^{-3})	(kg m^{-3})	(J kg^{-1} K^{-1})	(kg mol^{-1})	(m^3 mol^{-1})	(K^{-1})	(kbar^{-1})		(Pa^n s)		
Sticky-air	20	0	1	100	0	0	0	0	1	$1x10^{19}$	Air	0
Water	20	0	1000	3330	0	0	0	0	1	$1x10^{19}$	Water	0
Sediment	0.64+807/(T+77)	2	2600	1000	154	8	$3x10^{-5}$	$1x10^{-3}$	2.3	$1.97x10^{17}$	Wet Qz.	0.15
Cont. Crsut (C1 & C3)	0.64+807/(T+77)	2	2750	1000	154	8	$3x10^{-5}$	$1x10^{-3}$	2.3	$1.17x10^{17}$	Wet Qz.	0.15
Cont. Crsut (2)	1.18+807/(T+77)	2	2950	1000	238	8	$3x10^{-5}$	$1x10^{-3}$	3.2	$4.8x10^{22}$	Wet Qz.	0.15
Oc. Crust	1.18+474/(T+77)	0.25	3000	1000	238	8	$3x10^{-5}$	$1x10^{-3}$	3.2	$4.8x10^{22}$	Wet Qz.	0.15
Mantle	0.73+1293/(T+77)	0.02	3300	1000	532	8	$3x10^{-5}$	$1x10^{-3}$	3.5	$3.98x10^{16}$	Dry Ol.	0.6
Weak zone	0.73+1293/(T+77)	0.05	3300	1000	47	8	$3x10^{-5}$	$1x10^{-3}$	4	$5x10^{20}$	Wet Ol.	0

Table VI.1: Material properties used in the numerical experiments. k denotes the thermal conductivity, H_r is the radiogenic heat production, ρ_0 is the density, C_p is the specific heat capacity, E_a is the activation energy, V_a is the activation volume, α is the thermal expansion, β is the compressibility coefficient, n is the stress exponent, η_0 is the reference viscosity and Φ_{eff} is the effective internal friction angle. Qz. and Ol. correspond to the abbreviations of Quartzite and Olivine.

VI.8.2.2. 2-D Numerical approach

The numerical model presented in Figures VI.7 and VI.8 has been built on the same basis as those published by Guillou-Frottier *et al.* [2013]. Darcy's law is coupled with the heat equation in a porous medium and with mass conservation. We have used the Comsol Multiphysics™ software, where temperature-dependent properties can be easily implemented. Benchmark experiments have already been performed and published [Garibaldi *et al.*, 2010].

The numerical mesh consisted in more than 32,000 triangles, with a maximum size of 40 m within the detachment. Petrophysical properties are given in Table VI.2. Fluid density law was chosen to fit the experimental data for pure water between 20 and 350 °C:

$$\rho_L(T) = 1002.4 - 0.1905 * T - 0.0025 * T^2 \quad (17)$$

where T is temperature in °C and ρ_L the fluid density in kg m^{-3}. For temperature greater than 350°C, fluid density is assigned a constant value of 630 kg m^{-3}. This choice has no fundamental consequences on the results since at these high temperatures, fluid is located at depth greater than 5 km, where permeability does not allow fluid circulation. For the fluid dynamic viscosity, the law used has been written as:

$$\mu(T) = 2.414\ 10^{-5} \times \exp\left(\frac{570}{T+133}\right) \quad (18)$$

where T is in °C and dynamic viscosity μ is in Pa s.

The initial pressure field increases linearly with depth. The initial temperature field is computed in a conductive regime, such that the surface temperature is 20 °C and the bottom of the box (10 km depth) is close to 500 °C, as it is suggested by Aydin *et al.* [2005]. To reach a temperature around ~ 500 °C at a depth of 10 km, a basal heat flow of 120 mW m^{-2} is imposed during the transient behaviour. At $t > 0$, permeability values (see Table VI.2) are affected to the two units, and transient evolution of temperature and velocity fields are recorded. The chosen permeability law accounts for depth-dependence reaching a low value (~ 10^{-18} m^2) at the brittle-ductile transition, as suggested by Violay *et al*. [2017].

	Basement	**Detachment**
Eq. thermal conductivity(*)	2.8	1.6
Porosity (%)	5	30
Permeability (**) (m^2)	$[10^{-17} – 10^{-14}]\exp((z-2000)/1000)$	$[10^{-17} – 10^{-14}]$
Heat production ($\mu W.m^{-3}$)	1.0	0

Table VI.2: Material properties used in the numerical experiments. (*) the equivalent thermal conductivity accounts for solid matrix and fluid-filled pores. (**) permeability decreases exponentially with depth, except in the detachment.

VI.9. References

Andritsos, N., Dalambakis, P., Arvanitis, A., Papachristou, M., & Fytikas, M. (2015). Geothermal developments in Greece–Country update 2010-2014. In Proceedings World Geothermal Congress 2015 (pp. 19-24).

Atwater, T. (1970). Implications of plate tectonics for the Cenozoic tectonic evolution of western North America. Geological Society of America Bulletin, 81(12), 3513-3536.

Aydın, İ., Karat, H. İ., & Koçak., A. (2005). Curie-point depth map of Turkey. Geophysical Journal International, 162(2), 633-640.

Baba, A., Şimşek, C., Gündüz, O., Elçi, A., & Murathan, A. (2015). Hydrogeochemi-cal properties of geothermal fluid and its effect on the environment in Gediz Graben, western Turkey.

Bellani, S., Brogi, A., Lazzarotto, A., Liotta, D., & Ranalli., G. (2004). Heat flow, deep temperatures and extensional structures in the Larderello Geothermal Field (Italy): constraints on geothermal fluid flow: Journal of Volcanology and Geothermal Research, 132(1), 15-29.

Bertani, R. (2016). Geothermal power generation in the world 2010–2014 update report. Geothermics, 60, 31-43.

Blackwell, D. D., Smith, R. P., Waibel, A., Richards, M. C., & P., Step. (2009). Why Basin and Range systems are hard to find II: Structural model of the producing geothermal system in Dixie Valley, Nevada. Geothermal Resources Council Transactions, 33, 441-446.

Block, L., & Royden, L.H. (1990). Core complex geometries and regional scale flow in the lower crust: Tectonics 9, 557–567.

Bousquet, R., Goffe, B., Henry, P., LePichon, X., & Chopin, C. (1997). Kinematic, thermal and petrological model of the Central Alps: lepontine metamorphism in the upper crust and eclogitisation of the lower crust: Tectonophysics 273, 105–127.

Bozkurt, E., Satır, M., & Buğdaycıoğlu, C. (2011). Surprisingly young Rb/Sr ages from the Simav extensional detachment fault zone, northern Menderes Massif, Turkey. Journal of geodynamics, 52(5), 406-431.

Cenki-Tok, B., Expert, M., Işık, V., Candan, O., Monié, P., & Bruguier, O. (2016). Complete Alpine reworking of the northern Menderes Massif, western Turkey: International Journal of Earth Sciences, 105(5), 1507-1524.

Cumming, W. (2009). Geothermal resource conceptual models using surface exploration data. In Proceedings.

Erkan, K. (2015). Geothermal investigations in western Anatolia using equilibrium temperatures from shallow boreholes. Solid Earth, 6(1), 103.

Faccenna, C., Mattei, M., Funiciello, R. & Jolivet, L. (1997). Styles of back-arc extension in the Central Mediterranean: Terra Nova, 9, 126-130.

Famin, V., Philippot, P., Jolivet, L., & Agard, P. (2004). Evolution of hydrothermal regime along a crustal shear zone, Tinos Island, Greece. Tectonics, 23(5).

Famin, V., Hébert, R., Philippot, P., & Jolivet, L. (2005). Ion probe and fluid inclusion evidence for co-seismic fluid infiltration in a crustal detachment. Contributions to Mineralogy and Petrology, 150(3), 354-367.

Faulds, J., Coolbaugh, M., Bouchot, V., Moek, I., & Oguz, K. (2010). Characterizing structural controls of geothermal reservoirs in the Great Basin, USA, and Western Turkey: Developing successful exploration strategies in extended terranes. In World Geothermal Congress 2010 (pp. 11-p).

Garibaldi, C., Guillou-Frottier, L., Lardeaux, J.M., Bonté, D., Lopez, S., Bouchot, V., & P., Ledru. (2010). Thermal anomalies and geological structures in the Provence basin : implications for hydrothermal circulations at depth. Bulletin de la Société Géologique de France 181, 363-376.

Gerya, T. (2010). Introduction to Numerical Geodynamic Modelling: Cambridge University Press.

Gerya, T. V., & Meilick, F. I. (2011). Geodynamic regimes of subduction under an active margin: effects of rheological weakening by fluids and melts, J. Metamorph. Geol., 29(1), 7–31, doi:10.1111/j.1525-1314.2010.00904.x.

Gessner, K., Gallardo, L. A., Markwitz, V., Ring, U., & Thomson, S. N. (2013). What caused the denudation of the Menderes Massif: Review of crustal evolution, lithosphere structure, and dynamic topography in southwest Turkey: Gondwana Research, 24(1), 243-274.

Gessner, K., Markwitz, V., & Güngör, T. (2017). Crustal fluid flow in hot continental extension: tectonic framework of geothermal areas and mineral deposits in western Anatolia. Geological Society, London, Special Publications, 453, SP453-7.

Gianelli, G. (2008). A comparative analysis of the geothermal fields of Larderello and Mt. Amiata, Italy. Geothermal energy research trends. Nova Science, New York, 59-85.

Guillou-Frottier, L., Carrė, C., Bourgine, B., Bouchot, V., & Genter, A. (2013). Structure of hydrothermal convection in the Upper Rhine Graben as inferred from corrected temperature data and basin-scale numerical models. Journal of Volcanology and Geothermal Research, 256, 29-49.

Hawkesworth, C. J. (1997). U-Th Isotopes in Arc Magmas: Implications for Element Transfer from the Subducted Crust, Science, 276(5312), 551–555, doi:10.1126/science.276.5312.551.

Hetzel, R., Passchier, C. W., Ring, U. & Dora, O. O. (1995). Bivergent extension in orogenic belts: the Menderes massif (southwestern Turkey): Geology, 23, 455-458.

Huet, B., Le Pourhiet, L., Labrousse, L., Burov, E., & Jolivet, L. (2011). Post-orogenic extension and metamorphic core complexes in a heterogeneous crust: the role of crustal layering inherited from collision. Application to the Cyclades (Aegean domain). Geophysical Journal International, 184(2), 611-625.

Jolivet, L., & Brun, J.P. (2010). Cenozoic geodynamic evolution of the Aegean. International Journal of Earth Sciences, 99(1), 109-138.

Jolivet, L., Faccenna, C., Goffé, B., Mattei, M., Rossetti, F., Brunet, C., ... & Parra, T. (1998). Midcrustal shear zones in postorogenic extension: example from the northern Tyrrhenian Sea: Journal of Geophysical Research: Solid Earth, 103(B6), 12123-12160.

Jolivet, L., Famin, V., Mehl, C., Parra, T., Aubourg, C., Hébert, R., & Philippot, P. (2004). Strain localization during crustal-scale boudinage to form extensional metamorphic domes in the Aegean Sea: Geological Society of America Special Papers, 380, 185-210.

Jolivet, L., Menant, A., Sternai, P., Rabillard, A., Arbaret, L., Augier, R., ... & Labrousse, L. (2015). The geological signature of a slab tear below the Aegean: Tectonophysics, 659, 166-182.

Karabulut, H., Paul, A., Ergün, T. A., Hatzfeld, D., Childs, D. M., & Aktar, M. (2013). Long-wavelength undulations of the seismic Moho beneath the strongly stretched Western Anatolia: Geophysical Journal International, 194(1), 450-464.

Karamanderesi, İ. H. (2013). Characteristics of geothermal reservoirs in Turkey. IGA Academy Report, 0102-2013.

Katz, R. F., Spiegelman, M., & Langmuir, C. H. (2003). A new parameterization of hydrous mantle melting. Geochemistry, Geophysics, Geosystems, 4(9).

Kaya, A. (2015). The effects of extensional structures on the heat transport mechanism: An example from the Ortakçı geothermal field (Büyük Menderes Graben, SW Turkey). Journal of African Earth Sciences, 108, 74-88.

Koenig, J. B., & McNitt, J.R. (1983). Controls on the location and intensity of magmatic and non-magmatic geothermal systems in the Basin and Range province: Geothermal Resources Council (No. 13, p. 93). Special Report.

Labrousse, L., Huet, B., Le Pourhiet, L., Jolivet, L., & Burov, E. (2016). Rheological implications of extensional detachments: Mediterranean and numerical insights: Earth-Science Reviews, 161, 233-258.

Le Pourhiet, L., Burov, E., & Moretti, I. (2003). Initial crustal thickness geometry controls on the extension in a back arc domain: Case of the Gulf of Corinth. Tectonics, 22(4).

Manning, C. E., & Ingebritsen, S. E. (1999). Permeability of the continental crust: Implications of geothermal data and metamorphic systems. Reviews of Geophysics, 37(1), 127-150.

Menant, A., L. Jolivet, & Vrielynck, B. (2016a). Kinematic reconstructions and magmatic evolution illuminating crustal and mantle dynamics of the eastern Mediterranean region since the late Cretaceous: Tectonophysics, 675, 103-140; doi:110.1016/j.tecto.2016.1003.1007.

Menant, A., Sternai, P., Jolivet, L., Guillou-Frottier, L., & Gerya, T. (2016b). 3D numerical modeling of mantle flow, crustal dynamics and magma genesis associated with slab roll-back and tearing: The eastern Mediterranean case. Earth and Planetary Science Letters, 442, 93-107.

Mendrinos, D., Choropanitis, I., Polyzou, O., & Karytsas, C. (2010). Exploring for geothermal resources in Greece. Geothermics, 39(1), 124-137.

Mezri, L., Le Pourhiet, L., Wolf, S., & Burov, E. (2015). New parametric implementation of metamorphic reactions limited by water content, impact on exhumation along detachment faults, Lithos, 236-237, 287-298; http://dx.doi.org/210.1016/j.lithos.2015.1008.1021.

Moeck, I. S. (2014). Catalog of geothermal play types based on geologic controls. Renewable and Sustainable Energy Reviews, 37, 867-882.

MTA, Geothermal Energy Projects Reports (1970-2008).

Mulch, A., Teyssier, C., Cosca, M. A., & Vennemann, T. W. (2006). Thermomechanical analysis of strain localization in a ductile detachment zone: Journal of Geophysical Research: Solid Earth, 111(B12).

Oliver, N. H. S. (1996). Review and classification of structural controls on fluid flow during regional metamorphism: Journal of Metamorphic Geology, 14(4), 477-492.

Ozdemir, A., Yasar, E., & Cevik, G. (2017). An importance of the geological investigations in Kavaklıdere geothermal field (Turkey). Geomechanics and Geophysics for Geo-Energy and Geo-Resources, 3(1), 29-49.

Özen, T., Bülbül, A., & Tarcan, G. (2012). Reservoir and hydrogeochemical characteriza-tions of geothermal fields in Salihli, Turkey. J. Asian Earth Sci.60, 1–17.

Piromallo, C., & Morelli, A. (2003). P wave tomography of the mantle under the Alpine-Mediterranean area. Journal of Geophysical Research: Solid Earth, 108(B2).

Ranalli, G. (1995). Rheology of the Earth, Chapman & Hall., London, UK.

Reilinger, R., McClusky, S., Vernant, P., Lawrence, S., Ergintav, S., Cakmak, R., ... & Nadariya, M. (2006). GPS constraints on continental deformation in the Africa-Arabia-Eurasia continental collision zone and implications for the dynamics of plate interactions. Journal of Geophysical Research: Solid Earth, 111(B5).

Rey, P.F., Teyssier, C., & Whitney, D. L. (2009). The Role of Partial Melting and Extensional Strain Rates in the Development of Metamorphic Core Complexes, in Chardon, D., Rey, P., Teyssier, C., and Whitney, D.L., eds., Hot Orogen: Tectonophysics, v. 477, p. 135–144.

Reynolds, S. J., & Lister, G. S. (1987). Structural aspects of fluid-rock interactions in detachment zones: Geology, 15(4), 362-366.

Ricard, Y., & Froidevaux, C. (1986). Stretching instabilities and lithospheric boudinage: Journal of Geophysical Research: Solid Earth, 91(B8), 8314-8324.

Santilano, A., Manzella, A., Gianelli, G., Donato, A., Gola, G., Nardini, I., ... & Botteghi, S. (2015). Convective, intrusive geothermal plays: what about tectonics?. Geothermal Energy Science, 3(1), 51-59.

Schellart, W. P., Freeman, J., Stegman, D. R., Moresi, L., & May, D. (2007). Evolution and diversity of subduction zones controlled by slab width. Nature, 446(7133), 308.

Schellart, W. P., Stegman, D. R., Farrington, R. J., Freeman, J., & Moresi, L. (2010). Cenozoic tectonics of western North America controlled by evolving width of Farallon slab. Science, 329(5989), 316-319.

Schubert, G., & Yuen, D. A. (1978). Shear heating instability in the Earth's upper mantle. Tectonophysics, 50(2-3), 197-205.

Sibson, R. H., Moore, J. M. M., & Rankin, A. H. (1975). Seismic pumping—a hydrothermal fluid transport mechanism: Journal of the Geological Society, 131(6), 653-659.

Stampolidis, A., & Tsokas, G. N. (2002). Curie point depths of Macedonia and Thrace, N. Greece. Pure and Applied Geophysics, 159(11), 2659-2671.

Sternai, P., L. Jolivet, A. Menant, & Gerya, T. (2014). Driving the upper plate surface deformation by slab rollback and mantle flow: Earth Planet. Sci. Lett., 405, 110–118, doi:10.1016/j.epsl.2014.08.023.

Tirel, C., Gueydan, F., Tiberi, C., & Brun, J. P. (2004). Aegean crustal thickness inferred from gravity inversion. Geodynamical implications. Earth and Planetary Science Letters, 228(3), 267-280.

Tselentis, G. A. (1991). An attempt to define Curie point depths in Greece from aeromagnetic and heat flow data. pure and applied geophysics, 136(1), 87-101.

Turcotte, D. L., & Schubert, G. (2002). Geodynamics, Cambridge University Press, Cambridge.

Violay, M., Heap, M. J., Acosta, M., & Madonna, C. (2017). Porosity evolution at the brittle-ductile transition in the continental crust: Implications for deep hydro-geothermal circulation. Scientific reports, 7(1), 7705.

Wannamaker, P. E., Hasterok, D. P., Johnston, J. M., Stodt, J. A., Hall, D. B., Sodergren, T. L., ... & Unsworth, M. J. (2008). Lithospheric dismemberment and magmatic processes of the Great Basin–Colorado Plateau transition, Utah, implied from magnetotellurics. Geochemistry, Geophysics, Geosystems, 9(5).

SYNTHESE - DISCUSSION - PERSPECTIVES & ABRIDGED ENGLISH VERSION

L'objectif de ce travail de thèse était de caractériser la province géothermale de l'Anatolie Occidentale qui fait l'objet d'un paradoxe puisqu'elle est presqu'exempte de toute activité volcanique aujourd'hui. Au cours de ce travail, les relations entre les anomalies thermiques de différentes échelles (*i.e.* lithosphérique et crustale) associées à la dynamique de subduction (*i.e.* retrait et déchirure), et aux systèmes hydrothermaux actifs de HT, ont été discutés. Afin de mieux comprendre l'évolution thermique de la zone de subduction hellénique dans la partie orientale de la Méditerranée, des études sur l'histoire thermique passée et actuelle ont été menées principalement dans le Massif du Menderes qui offre une opportunité unique pour l'étude de ces processus. Après un résumé succinct des principaux axes de ce travail de thèse, une synthèse sur l'évolution géodynamique et thermique du Crétacé à l'actuel de la zone de subduction sera également présentée. Finalement, une typologie simplifiée, regroupant quelques exemples de systèmes géothermaux de haute température HT, associée aux différentes dynamiques de subduction sera proposée.

Ce travail se résume en 5 axes majeurs :

(i) Une étude de terrain montrant le rôle des structures d'échelle crustale (*i.e.* détachements) sur la localisation des champs géothermaux en contexte d'arrière-arc (*cf. chapitre II*). Ces failles permettent aux fluides de circuler dans la croûte depuis la zone de transition fragile-ductile jusqu'à la surface sans nécessairement invoquer la contribution de systèmes magmatiques localisés dans la croûte supérieure.

(ii) Une étude de terrain sur l'une des îles du Dodécanèse qui se localise à l'aplomb de la déchirure du panneau plongeant afin de caractériser la cinématique de la déformation et le degré de métamorphisme associé à cette dernière dans une région peu étudiée par la communauté scientifique (*cf. chapitre III*).

(iii) Une étude de terrain sur l'ensemble de la zone située à l'aplomb de la déchirure afin, d'une part, de mettre en évidence les corrélations entre les unités du Menderes et des Cyclades et, d'autre part, de discuter de l'évolution thermique de la zone de subduction hellénique (*cf. chapitre IV*).

(iv) Une étude sur l'évolution thermique et tectonique du Massif du Menderes afin de voir la distribution spatio-temporelle des anomalies thermiques associées à l'évolution de cette zone de subduction (*cf. chapitre V*).

(v) La réalisation de modèles numériques 3D et 2D afin d'apporter des contraintes physiques sur le régime thermique lié à la dynamique de subduction (*i.e.* retrait et déchirure du panneau plongeant), associés aux systèmes de HT (*cf.* c*hapitre VI*).

VII.1. Évolution de la dynamique de subduction dans la partie orientale de la Méditerranée : conséquences tectoniques et thermiques

La région est-méditerranéenne est marquée par des différences de premier ordre. Par exemple, l'âge de l'obduction en Turquie occidentale est estimé à 85 – 70 Ma [Okay *et al*., 2001], alors qu'il est estimé fin Jurassique (~ 135 Ma) dans les Hellènides [*e.g.* Jolivet *et al*., 2004]. La transition entre ces deux domaines est alors localisée au niveau de la Mer Egée, comme en témoigne l'obduction de l'unité supérieure des Cyclades d'âge Crétacé Supérieur (~ 96 – 65 Ma) sur l'unité du Pinde [Maluski *et al*., 1977 ; Patzak *et al*., 1994 ; Jolivet *et al*., 2004]. Ring *et al*. [1999] soulignent également les disparités entre la nature du socle des Cyclades et celle du Menderes. Même si le socle continental du Menderes a une position structurale similaire (*i.e.* au même niveau dans le prisme orogénique) à celle du socle varisque observé à Ios ou à Naxos (*i.e.* socle des Cyclades) [*e.g.* Henjes-Kunst & Kreuzer, 1982 ; Andriessen *et al*., 1987], leurs âges et leurs distributions spatiales diffèrent. Considéré comme panafricain par Sengör *et al*. [1984b], l'âge du protholithe des augen gneiss, qui affleure dans l'ensemble du Massif du Menderes et qui compose essentiellement le socle de ce dernier, est Précambrien [*e.g.* Schuiling, 1962 ; Sengör *et al*., 1984b ; Satır & Friedrichsen, 1986 ; Reischmann *et al*., 1991]. A contrario, le socle des Cyclades affleure de manière parcellaire sur l'île de Ios et aucune origine panafricaine n'a été détectée dans le domaine Egéen [*e.g.* Bonneau & Kienast, 1982 ; Candan *et al*., 2011]. Selon Jolivet *et al*. [2004], cette différence majeure s'explique par l'enfouissement quasi-intégral du socle cycladique. Ainsi, la chaîne des Hellènides se compose principalement de matériel sédimentaire accrété au Crétacé dont les différentes unités tectono-métamorphiques ont enregistré un métamorphisme de HP-BT à l'Eocène [*e.g.* Altherr *et al*., 1979 ; Wijbrans *et al*., 1990 ; Lagos *et al*., 2007].

Néanmoins, la présence (i) d'intrusions triasiques communes dans les deux régions, ainsi que celle (ii) de l'unité des Schistes Bleus Cycladiques reconnue dans les deux domaines (structuralement au-dessus du Massif du Menderes) [Jolivet *et al*., 2004], suggèrent une évolution commune mais diachronique (*i.e.* la HP-BT débute au Crétacé Supérieur en Turquie) depuis cette période. Principalement contrôlée par la dynamique de subduction, cette évolution se caractérise par une succession de différents épisodes métamorphiques de HP-BT (exhumation syn-orogénique) et de HT-MP (*i.e.* empilement d'écailles de socle et extension post-orogénique) en Turquie et dans le domaine Egéen.

VII.1.1. Crétacé Supérieur à Éocène inférieur : un gradient métamorphique HP-BT sur l'ensemble de la région

Il apparait évident que le socle du Menderes a subi une évolution tectono-métamorphique qui diffère du socle des Cyclades, puisqu'à l'heure actuelle aucune étude ne montre la présence d'un métamorphisme HP-BT d'âge Alpin dans cette région. En ce sens, le socle du Menderes se rapproche du socle du Dodécanèse, ce dernier ayant enregistré une surimpression alpine dans des conditions du faciès des schistes verts (300 – 370 °C à 1 – 3 kbar) [Franz & Okrush, 1992 ; Franz *et al*., 2005]. Néanmoins, la couverture du Menderes (Kurudere) montre des paragenèses de HP similaires en terme de conditions P-T, à celle de la nappe des Schistes Bleus Externes [Grasemann *et al*., 2018]. La présence de (i) magnésio-carpholites [Rimmelé *et al*., 2003 ; Whitney *et al*., 2008] dans cette unité de couverture, mais également de (ii) carpholite dans les métapélites, (iii) d'aragonite dans les marbres et (iv) d' amphibole bleue dans les métabasites dans les unités d'Ören/Afyon [Pourteau *et al*., 2016], suggère une exhumation rapide le long d'un gradient métamorphique de HP-BT. Ce type de gradient est également observé à Amorgos et dans les îles du Dodécanèse, mais il diffère de celui observé dans les Cyclades où la Fe-Mg carpholite est absente et le grenat omniprésent. Ainsi, cette unité localisée structuralement entre le Massif des Menderes et les Nappes Lyciennes (*i.e.* Ören et Afyon) sur la péninsule de Dilek [Rimmelé *et al*., 2006], mais également dans les Cyclades (*i.e.* l'unité éclogitique des Schistes Bleus Cycladiques) [Grasemann *et al*., 2018], a été enfouie à plus grande profondeur, comme en témoigne la présence fréquente d'éclogite, de grenatite et de glaucophanite (Fig. VII.1). Par ailleurs, alors que l'exhumation dans le facies des schistes bleus des roches de HP est enregistrée vers 70 Ma dans Tavşanlı [*e.g.* Sherlock *et al*., 1999] et se termine vers ~60 Ma dans la couverture du Menderes, l'exhumation dans les Cyclades débute vers 50 Ma et se termine vers 30 Ma en Crête [*e.g.* Jolivet & Brun, 2010].

Il est clair que cette dynamique (*e.g.* exhumation syn-orogénique, voir Laurent *et al*. [2016] et Roche *et al*. [2016] en *Annexe B*) ne permet pas d'expliquer les anomalies thermiques actuelles localisées en profondeur et en surface dans cette région. Néanmoins, les conditions aux limites de la zone de subduction Hellénique changent à l'Eocène avec l'entrée en subduction du socle du Menderes. Facilité par la désintégration radioactive dans le socle et par l'épaississement crustal, un premier épisode de HT-BP se développe donc dans le Massif du Menderes.

VII.1.2. Éocène: un paradoxe entre HP-BT et HT-BP

Contemporain du métamorphisme de HP-BT dans l'unité des Schistes Bleus Cycladiques, la région du Menderes est affectée par un métamorphisme régional barrovien (Fig. VII.1). Ce dernier affecte à la fois le socle du Menderes mais également sa couverture paléozoïque et mésozoïque [*e.g.*

Candan *et al*., 2011 ; Koralay *et al*., 2012]. Il est associé à (i) un épaississement crustal induit par l'imbrication de la plate-forme Anatolide-Tauride et par un transport vers le sud des Nappes Lyciennes et de la couverture du Menderes (*i.e.* Kurudere) ; (ii) la présence en quantité importante du socle du Menderes augmentant ainsi la production de chaleur générée par la radioactivité. Selon différentes études géochronologiques (*e.g.* sur micas [Satır & Friedrichsen, 1986 ; Hetzel & Reischman, 1996], sur monazite [Catlos & Çemen, 2005], sur grenats [Schmidt *et al*., 2015], sur allanite [Cenki-Tok *et al*., 2016]), et selon l'étude d'Özer *et al*. [2001] (*i.e.* âge moyen de 60 Ma pour la plus jeune unité de la couverture affectée par le métamorphisme barrovien), le métamorphisme barrovien commence à l'Eocène et se termine à l'Oligocène dans sa partie sud (42 – 35 Ma [Schmidt *et al*., 2015]). Il est important de noter que la variabilité des températures RSCM calculées dans la couverture (*cf. chapitre IV*) souligne la complexité de cette zone de subduction. La présence des T_{max} froides (~ 430 °C, *cf. chapitre V*) dans le cœur du Massif du Menderes suggère que l'évènement thermique alpin n'a pas été enregistré dans cette partie du dôme. En accord avec de nombreuses études [*e.g.* Catlos & Çemen, 2005 ; Schmidt *et al*., 2015 ; Cenki-Tok *et al*., 2016], le métamorphisme barrovien est principalement enregistré dans le Nord et le Sud du Massif (*e.g.* la zone de Selimiye, le socle et la couverture dans le sud de Simav).

Le métamorphisme barrovien du Menderes est donc corrélé à des anomalies thermiques importantes, principalement visibles à l'échelle crustale. Ces anomalies régionales, liées à l'épaississement crustal et par conséquent à une augmentation de la production de chaleur radioactive, affectent en partie les unités du Menderes et modifient donc les valeurs du flux de chaleur. Paradoxalement, aucune activité magmatique n'a été recensée dans le massif à cette période et par conséquent aucune minéralisation en lien avec ce magmatisme n'a été enregistrée (*e.g.* absence de systèmes porphyriques) [*e.g.* Menant *et al*., en révision].

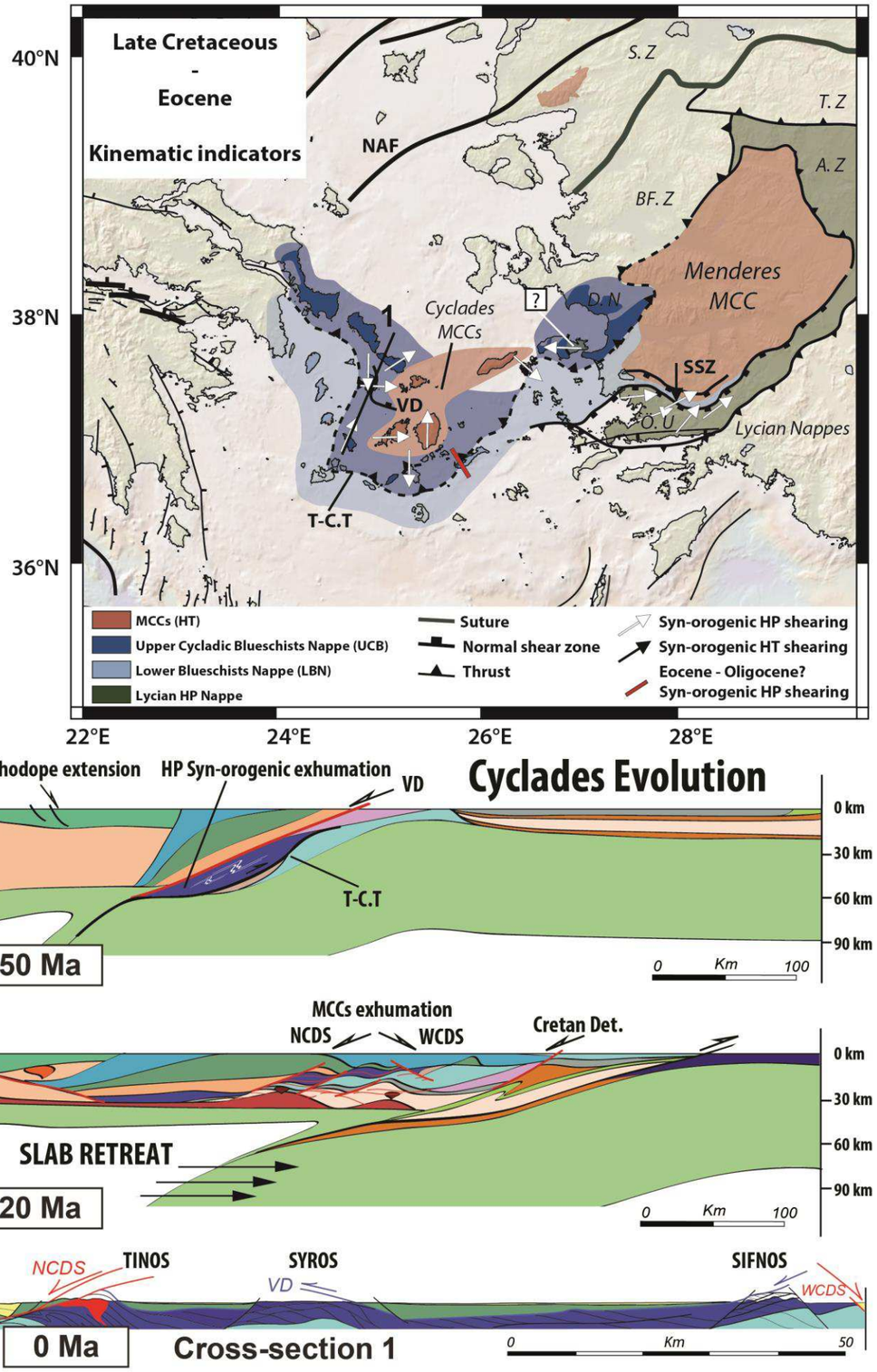
Late Cretaceous
-
Eocene
Kinematic indicators
S. Z
T. Z
A. Z
BF. Z
NAF
Menderes
MCC
Cyclades
MCCs
D. N
?
1
VD
SSZ
Ö. U
Lycian Nappes
T-C.T
40°N
38°N
36°N
MCCs (HT)
Upper Cycladic Blueschists Nappe (UCB)
Lower Blueschists Nappe (LBN)
Lycian HP Nappe
Suture
Normal shear zone
Thrust
Syn-orogenic HP shearing
Syn-orogenic HT shearing
Eocene - Oligocene?
Syn-orogenic HP shearing
22°E
24°E
26°E
28°E
Rhodope extension
HP Syn-orogenic exhumation
VD
T-C.T
Cyclades Evolution
50 Ma
0 km
30 km
60 km
90 km
0
Km
100
MCCs exhumation
NCDS
WCDS
Cretan Det.
SLAB RETREAT
20 Ma
NCDS
TINOS
SYROS
VD
SIFNOS
WCDS
0 Ma
Cross-section 1
0
Km
50

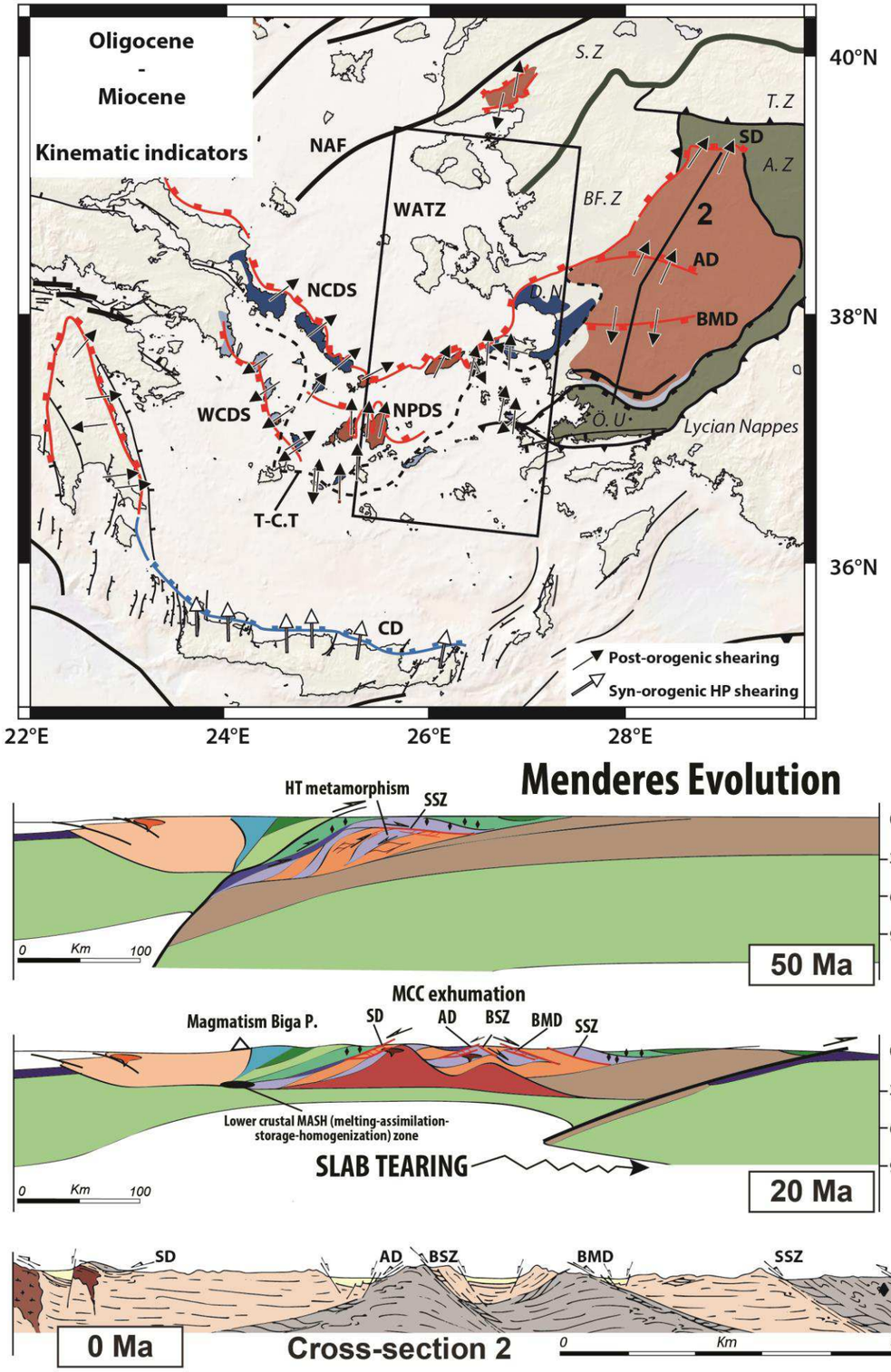
Oligocene
-
Miocene
Kinematic indicators
S. Z
T. Z
A. Z
BF. Z
NAF
WATZ
SD
2
AD
BMD
D. N
NCDS
WCDS
NPDS
Ö. U
Lycian Nappes
T-C.T
CD
40°N
38°N
36°N
Post-orogenic shearing
Syn-orogenic HP shearing
22°E
24°E
26°E
28°E
Menderes Evolution
HT metamorphism
SSZ
50 Ma
0 km
30 km
60 km
90 km
0
Km
100
MCC exhumation
Magmatism Biga P.
SD
AD
BSZ
BMD
SSZ
Lower crustal MASH (melting-assimilation-storage-homogenization) zone
SLAB TEARING
20 Ma
SD
AD
BSZ
BMD
SSZ
0 Ma
Cross-section 2
0
Km
80

Figure VII.1 : synthèse tectono-métamorphique de la région est-méditerranéenne montrant l'évolution depuis 50 Ma jusqu'à l'Actuel. Les abréviations correspondent aux précédentes figures (e.g. Figs. IV.16, V.16 and V.17).

VII.1.3.Oligocène au Miocène : un gradient métamorphique HT-MP sur l'ensemble de la région

A l'Oligocène, l'évolution géodynamique se caractérise par une accélération du retrait du panneau plongeant vers le sud, marqué par la migration rapide de l'arc volcanique, induisant l'effondrement gravitaire de la chaîne des Hellénides et des Anatolides-Taurides et par un amincissement crustal [*e.g.* Bonneau, 1984 ; Jolivet & Faccenna, 2000]. Bien que l'empilement des nappes ait été en partie déstructuré lors de l'effondrement de ces édifices, et lors de l'extension post-orogénique, des études stratigraphiques et des observations de terrain ont permis d'établir des corrélations entre ces unités [*e.g.* Bonneau, 1984 ; Ring *et al*., 1999 ; Jolivet *et al*., 2004]. L'extension induite par cette dynamique (*i.e.* le retrait) est principalement accommodée par des détachements (*e.g.* NCDS, le Détachement de Simav), qui contrôlent la mise en place des MCCs dans la région des Cyclades et en Turquie Occidentale (Fig. VII.1) [*e.g.* Lister *et al*., 1984 ; Jolivet *et al*., 2010 ; 2013]. Il est important de souligner qu'à l'échelle crustale, la cinématique de la déformation est cohérente sur l'ensemble de la région durant cette période. Elle se caractérise par une asymétrie importante marquée par des critères de cisaillement à vergence nord. Contemporain de cette déformation, la rétromorphose dans le facies des schistes verts (associée à une augmentation de la température) des unités de HP-BT des Cyclades est couramment observée (*e.g.* Tinos, Sifnos, voir Roche *et al*. [2016]).

Au début du Miocène, un changement drastique des conditions de la dynamique de subduction modifie l'évolution tectono-métamorphique dans la région. Fondées sur la tomographie sismique, plusieurs études mettent en évidence une absence de panneau plongeant sous l'ouest de la Turquie [*e.g.* Bijwaard *et al*., 1998 ; Biryol *et al*., 2011]. Même si le timing de la déchirure fait débat dans la littérature (*i.e.* Eocène ou Miocène [Jolivet *et al*., 2015 ; Menant *et al*., 2016 ; Govers & Fichtner, 2016]) différents arguments suggèrent que les effets thermiques se développent dès le Miocène. En effet, la présence (i) de migmatites datées à 22.2 ± 0.2 Ma dans le nord du Massif du Menderes [*e.g.* Cenki-Tok *et al*., 2016] et dans les Cyclades (*e.g.* Ikaria, Mykonos, Naxos) [*e.g.* Vanderhaeghe, 2004 ; Denèle *et al*., 2011 ; Beaudoin *et al*., 2015], (ii) de granitoïdes dans l'ensemble de la région (20 à 8 Ma [Jolivet *et al*., 2015]), et (iii) l'accélération rapide du panneau plongeant sous la mer Egée [*e.g.* Jolivet *et al*., 2015 ; Brun *et al*., 2017] sont des témoins essentiels soulignant les conséquences de cette déchirure à cette période. Néanmoins, la direction de l'étirement reste similaire aux paléo-directions enregistrées à l'Oligo-Miocène dans l'ensemble de la région (*cf. chapitre IV*). De ce fait, l'extension est accommodée en Turquie occidentale par trois zones de cisaillement dont les conditions et les cinématiques diffèrent d'un endroit à l'autre : le Gediz-Alaşehir détachement et le Büyük Menderes détachement, tous deux actifs dans des conditions ductile-fragile; et la zone de cisaillement de Bozdag (Fig. VII.1, *cf. chapitre V*). Bien que ces différentes structures extensives d'échelle crustale

enregistrent des sens de cisaillement opposés, elles restent compatibles avec une extension N-S. La déformation dans cette région semble donc plus symétrique comparée à l'Oligo-Miocène et diffère de la partie orientale des Cyclades. Cette différence d'asymétrie pourrait être corrélée à l'activité du flux asthénosphérique (*i.e.* plus importante sous les Cyclades et sous les Dodécanèse) dont la direction d'écoulement s'effectuerait parallèlement à cette zone. Par ailleurs, aucune complication tectonique n'est observée à l'aplomb de la déchirure dans la croûte de la plaque supérieure (*cf. chapitres III et IV*). A part la rotation antihoraire de 20° au Miocène du Massif du Menderes (15 – 5 Ma) [Van Hinsbergen *et al*., 2010], aucune autre rotation majeure n'est en effet enregistrée dans la région. De plus, cette rotation semble être accommodée par les détachements et les failles décrochantes N-S qui dissèquent le massif du Menderes en différents blocs kilométriques (*cf. chapitre II*). Ainsi, nos travaux sur les îles du Dodécanèse et des îles de l'est de l'Egée montrent que la déformation semble plutôt être accommodée par une large zone de cisaillement avec une direction de cisaillement constante en accord avec la dynamique du retrait vers le sud du panneau plongeant sous la Mer Egée (Fig. VI.2) [*e.g.* Gessner *et al*., 2013 ; Jolivet *et al*., 2015].

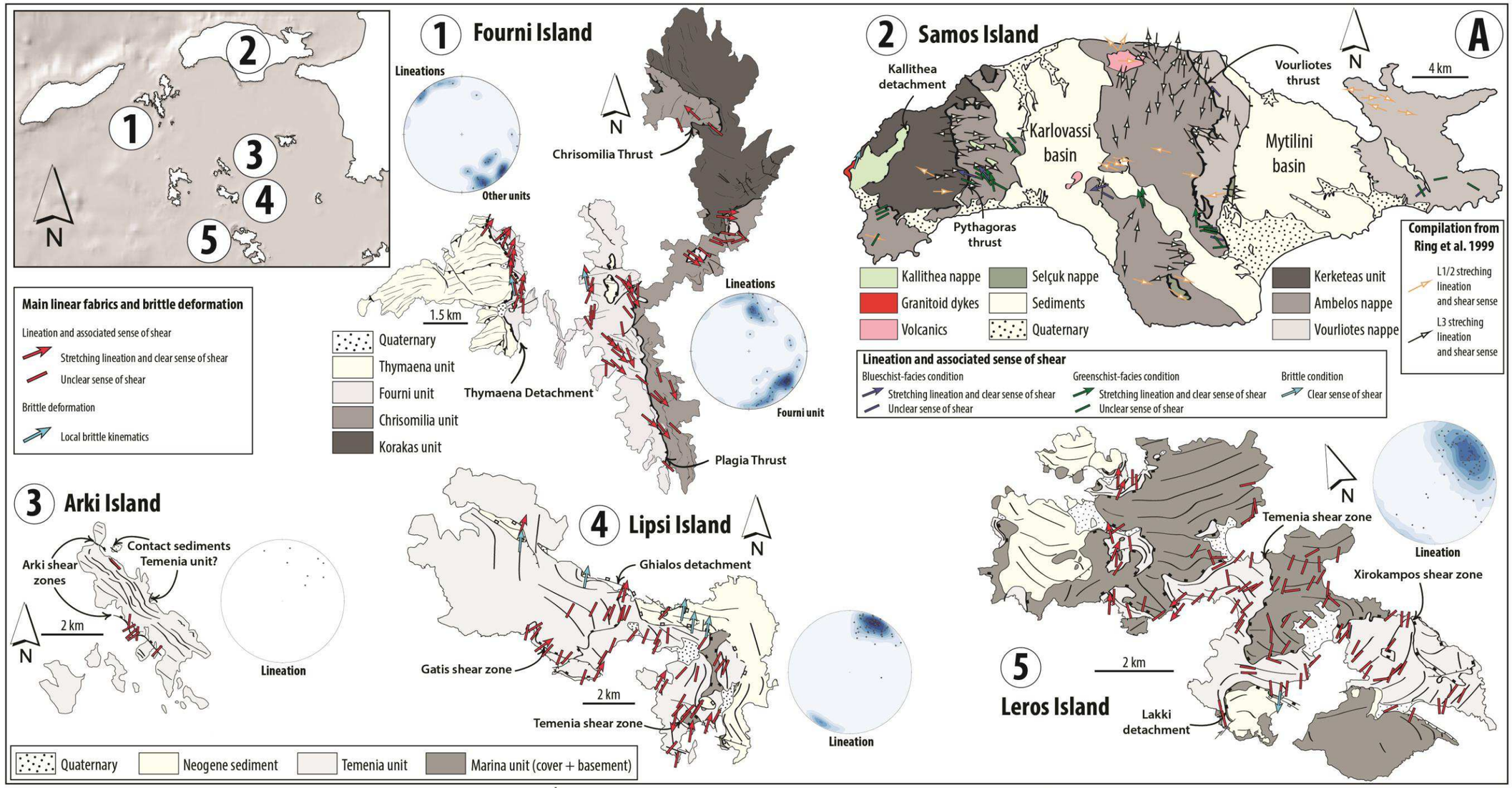
1
2
3
4
5
N
Main linear fabrics and brittle deformation
Lineation and associated sense of shear
Stretching lineation and clear sense of shear
Unclear sense of shear
Brittle deformation
Local brittle kinematics
1 Fourni Island
Lineations
Other units
Chrisomilia Thrust
1.5 km
Thymaena Detachment
Lineations
Fourni unit
Plagia Thrust
Quaternary
Thymaena unit
Fourni unit
Chrisomilia unit
Korakas unit
2 Samos Island
A
Kallithea detachment
Karlovassi basin
Mytilini basin
Vourliotes thrust
4 km
Pythagoras thrust
Kallithea nappe
Granitoid dykes
Volcanics
Selçuk nappe
Sediments
Quaternary
Kerketeas unit
Ambelos nappe
Vourliotes nappe
Compilation from Ring et al. 1999
L1/2 streching lineation and shear sense
L3 streching lineation and shear sense
Lineation and associated sense of shear
Blueschist-facies condition
Stretching lineation and clear sense of shear
Unclear sense of shear
Greenschist-facies condition
Stretching lineation and clear sense of shear
Unclear sense of shear
Brittle condition
Clear sense of shear
3 Arki Island
Contact sediments
Temenia unit?
Arki shear zones
2 km
Lineation
4 Lipsi Island
Ghialos detachment
Gatis shear zone
2 km
Temenia shear zone
Lineation
Temenia shear zone
Xirokampos shear zone
Lineation
5
Leros Island
2 km
Lakki detachment
Quaternary
Neogene sediment
Temenia unit
Marina unit (cover + basement)

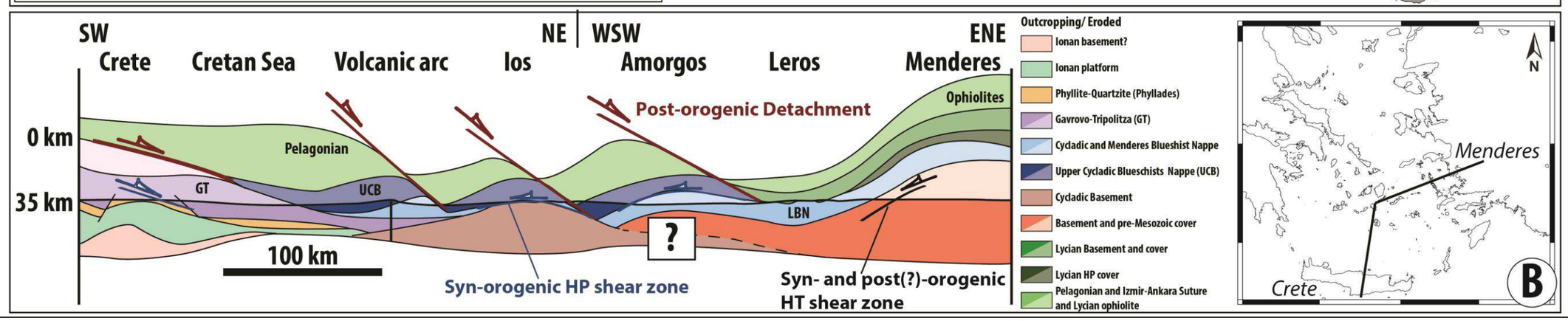
SW
Crete
Cretan Sea
Volcanic arc
NE
WSW
Ios
Amorgos
Leros
ENE
Menderes
0 km
35 km
Pelagonian
GT
UCB
LBN
?
100 km
Post-orogenic Detachment
Ophiolites
Syn-orogenic HP shear zone
Syn- and post(?)-orogenic HT shear zone
Outcropping/ Eroded
Ionan basement?
Ionan platform
Phyllite-Quartzite (Phyllades)
Gavrovo-Tripolitza (GT)
Cycladic and Menderes Blueshist Nappe
Upper Cycladic Blueschists Nappe (UCB)
Cycladic Basement
Basement and pre-Mesozoic cover
Lycian Basement and cover
Lycian HP cover
Pelagonian and Izmir-Ankara Suture and Lycian ophiolite
N
Menderes
Crete
B

Figure VII.2 : synthèse des travaux sur les îles du Dodécanèse et des îles de l'est de l'Egée. (a) différentes cartes tectono-métamorphiques montrant les cinématiques de la déformation. (b) Coupe générale montrant les correspondances entre les unités du Menderes, des Cyclades et du Dodécanèse. Le trait de coupe est indiqué dans le chapitre III, Fig. IV.16.

VII.1.3.1. Conséquences thermiques de cette dynamique

Les données de terrain (*e.g.* migmatites) confirment que la dynamique du slab (*i.e.* retrait et déchirure) entraine une augmentation des températures dans la zone arrière-arc. Cet excès de chaleur se matérialise également par la mise en place de provinces volcaniques au Miocène, caractérisées par de nombreuses occurrences de gîtes minéralisés de type épithermaux neutres et intermédiaires à Au et Au-Ag-Pb-Zn, respectivement, dans le massif du Rhodope et dans la péninsule de Biga au nord-est de la Turquie [*e.g.* Yılmaz *et al*., 2001 ; Marchev *et al*., 2005]. D'après Marchev *et al*. [2005] et Ersoy & Palmer, [2013], la signature de ce magmatisme serait de type arrière-arc avec une composante crustale (dominante) et mantellique (secondaire). Il est important de souligner que le manteau lithosphérique de la plaque supérieure a été métasomatisé lors d'un précédent évènement d'arc, impliquant ainsi une augmentation de sa fertilité. Comme indiqué dans le *chapitre I*, les modèles conceptuels des gîtes de types porphyriques et épithermaux [*e.g.* Hedenquist *et al*., 2000 ; Richards, 2005 ; 2009] sont similaires aux modèles de systèmes géothermaux de HT en lien avec du magmatisme. Ainsi, à cette époque la région est marquée par de nombreux évènements ponctuels correspondant à la mise en place d'intrusions magmatiques dans la croûte supérieure. Ces intrusions génèrent alors la chaleur nécessaire au développement de systèmes de HT, qui fonctionnent sur une durée limitée. Contemporain à ces gisements magmatiques de HT, la partie centrale du Massif du Menderes s'exhume rapidement par le biais de nombreuses zones de cisaillement (*cf. chapitre IV*). Associées à la mise en place du dôme métamorphique, des anomalies thermiques régionales affectent entièrement la partie centrale du massif mais également la partie septentrionale. Ces anomalies atteignent localement des températures supérieures à 600 °C comme en témoignent les T_{max} obtenues par la méthode RSCM et l'âge Miocène des unités métamorphiques de HT-BP du cœur du dôme du Menderes datées en U-Pb sur monazites (~ 22 Ma, *cf. chapitre V*).

Pour résumer, la dynamique de subduction de cette région contrôle la distribution spatiale et temporelle des anomalies thermiques dans cette zone d'arrière-arc. En accord avec les résultats des simulations numériques (Fig. VII.3) (*cf. chapitre VI*), ce régime thermique est principalement induit par (i) le shear heating dans le manteau, par (ii) les composantes poloïdales et toroïdales des flux mantelliques. Dans le cas de la région égéenne, le flux de chaleur est anormalement élevé depuis plusieurs dizaines de millions d'années (*e.g.* ~ 30 Ma).

VII.1.4.Miocène à Actuel : une activité tectonique encore présente

Il est important de noter que la cinématique associée à la déformation fragile dans la région est compatible avec une extension NNE-SSW. Ces observations sont donc cohérentes depuis l'Oligo-Miocène, où un continuum de déformation (ductile jusqu'au fragile) a été enregistré sur l'ensemble du domaine (Figs. VII.1 et VII.2). Selon de nombreuses études [*e.g.* Jolivet & Brun, 2010 ; Jolivet *et al*., 2013 ; Gessner *et al*., 2013 ; Gessner *et al*., 2017], cette extension récente NNE-SSW est principalement contrôlée par le retrait du panneau plongeant et la déchirure du slab. Même si l'effet thermique associé à cette déchirure apparait essentiel (voir *VII.1.3.1* et *VII.4.1.1*), aucune déformation fragile de premier ordre à cinématique décrochante (*i.e.* similaire à l'orientation de la WATZ (Fig. VII.1), Gessner *et al*. [2013]) associée à cette dynamique n'a été enregistrée depuis la fin du Miocène dans la plaque supérieure.

Par ailleurs, un évènement E-W compressif, daté à 9 – 8.6 Ma, est localement observé sur l'île de Samos (*cf. chapitre IV*) [Ring *et al*., 1999]. Il se traduit par (i) un jeu de failles inverses qui affectent principalement les bordures des bassins Miocène mais également par (ii) des plis orientés NW-SE développés dans certaines unités sédimentaires Néogène. Alors que ces auteurs les associent à des structures compressives, les données de terrain acquises lors de différentes missions suggèrent plutôt des géométries similaires à celle des slumps (structures d'effondrement résultant d'un glissement gravitaire). Ainsi, les instabilités gravitaires à l'origine de ces slumps pourraient être associés à une dynamique extensive où l'activité des failles délimiterait les bassins. Cette hypothèse pourrait donc remettre en cause l'âge de l'évènement compressif. Par ailleurs, les structures compressives (*i.e.* failles inverses) décrites sur cette île ne sont pas fréquentes en Mer Egée. Néanmoins, on retrouve sur l'île de Mykonos une transition dans le temps d'une extension NE-SW à une compression WNW-ESE, en passant par un stade décrochant, à la fin de l'histoire du refroidissement du pluton (11,5 ± 0,5 à 8,9 ± 0,4 Ma, U-Th /He sur apatite d'après Brichau *et al*. [2008]) et du jeu du détachement (NCDS) [Menant *et al*., 2013]. Cet épisode compressif bref est également daté aux environs de 9 Ma. La présence de structures similaires est, par ailleurs, décrite dans le graben de Gediz, proche d'Alaşehir (Massif du Menderes). Dans cette région, des axes de plis E-W affectent également les sédiments Miocène. Alors que certaines études associent ces structures à de l'extension [*e.g.* Seyitoglu *et al*., 2000 ; Sözbilir, 2001] d'autres supposent un épisode compressif [Koçyigit *et al*., 1999a ; Bozkurt , 2002]. Bien que l'âge de ces structures soit peu contraint, cette phase enregistrée sur les îles de Samos et de Mykonos et potentiellement dans le Menderes doit être expliquée. L'une des possibilités consisterait à utiliser le mouvement de la faille nord-anatolienne (NAF) et de ses satellites au Miocène supérieur [Armijo *et al*., 1999 ; Koukouvelas & Aydin, 2002 ; Menant *et al*., 2013]. Cette dernière produirait un régime de contrainte compressive à l'extrémité ouest de la faille, ainsi qu'au sud de celle-ci [Armijo *et al*., 2003]. Si l'âge de la compression est compris entre 9 et 8,6 Ma, la NAF se propagerait plus tôt que prévu (âge

estimé ~ 5 Ma). Il est donc important d'obtenir plus de données dans le nord du Massif du Menderes pour préciser ce point.

La fin de l'exhumation est également compatible avec une extension N-S à NNE-SSW dans l'ensemble de la région. Par exemple, des failles à fort pendage orientées E-W, contrôlent la structure des grabens et par conséquent les dépôts néogènes dans le Massif du Menderes. Selon Gessner *et al*. [2001] et Ring *et al*. [2003a], cet ensemble de failles, encore actif de nos jours, commence à fonctionner vers ~ 5 Ma. Des failles de transfert N-S dissèquent également le Massif du Menderes en différents blocs kilométriques. Ainsi, la présence des détachements et de ces différents types de failles favorisent la circulation des fluides dans la croûte supérieure (zone de recharge ou de décharge) et contrôlent la localisation des sources thermales. Paradoxalement, la région égéenne semble moins affectée par cette déformation récente.

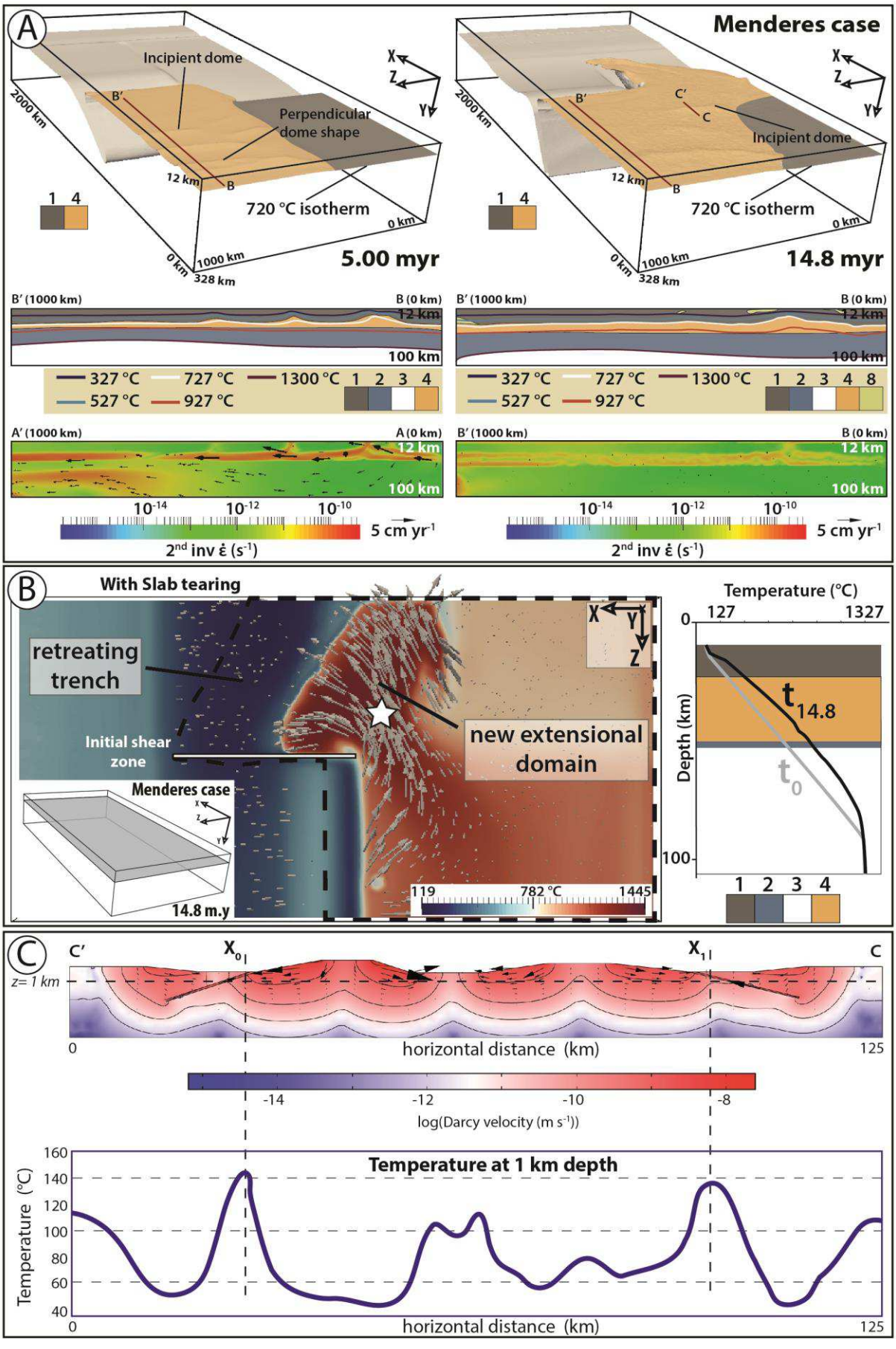
A
Incipient dome
Perpendicular dome shape
720 °C isotherm
5.00 myr
Menderes case
Incipient dome
720 °C isotherm
14.8 myr
B′ (1000 km)
B (0 km)
12 km
100 km
327 °C
727 °C
1300 °C
527 °C
927 °C
A′ (1000 km)
A (0 km)
2nd inv ε̇ (s-1)
5 cm yr-1
B
With Slab tearing
retreating trench
Initial shear zone
new extensional domain
Menderes case
14.8 m.y
Temperature (°C)
Depth (km)
t14.8
t0
C
z= 1 km
horizontal distance (km)
log(Darcy velocity (m s-1))
Temperature at 1 km depth
Temperature (°C)

Figure VII.3 : synthèse des données numériques. (a) Dômes thermiques générés par la dynamique du slab. (b) Anomalie thermique en base de croûte contrôlée par le shear heating et par les flux mantelliques. (c) Circulation des fluides le long des détachements. Noter que la vitesse des fluides est plus importante dans les détachements et que la température à un kilomètre de profondeur est anormalement élevée sous ces derniers. Pour plus d'information se référer au chapitre VI.

VII.1.4.1. Conséquences thermiques de cette dynamique

La dynamique de la subduction et l'évolution tectonique qui en résulte exercent un contrôle de premier ordre sur la localisation des champs de HT actuels. Cette dynamique engendre la formation d'anomalies thermiques régionales qui se localisent à la base de la croûte, puis se propagent dans les niveaux crustaux supérieurs par conduction (Figs. VII.3a et VII.3b). Un des aspects fondamentaux concerne donc l'échelle de temps nécessaire au processus de diffusion associée à la dynamique du slab. Pour ce régime thermique diffusif, l'échelle de temps t_{diff} est définie par l'équation suivante :

$$t_{diff} = L^2 / \kappa$$

où L est la profondeur du Moho en mètre et κ la diffusivité thermique des roches qui s'exprime en $m^2.s^{-1}$. Ainsi, en prenant une profondeur du Moho de ~ 25 km sous le Massif du Menderes [Karabulut *et al*., 2013] et une diffusivité thermique (κ) de 10^{-6} $m^2.s^{-1}$, l'anomalie thermique actuelle observée en surface (matérialisée par la présence de nombreuses sources et d'activités fumeroliennes) pourrait correspondre à l'expression de la déchirure qui a commencé à affecter thermiquement le Moho depuis ~ 20 Ma (Fig. VII.4a). Cette hypothèse semble également confirmée par la présence de températures élevées (~ 580 °C) à de faible profondeur (~ 8 km sous le Menderes) [Aydin *et al*., 2005 ; Bilim *et al*., 2016]. Ces anomalies thermiques régionales impliquent donc une remontée de la transition fragile-ductile (dont les températures atteindraient 400 °C selon Violay et al. [2017]) à de faible profondeurs (4 – 5 km) et suggèrent également l'existence d'une large zone de migmatisation, et/ou de sous plaquage magmatique (potentiellement fertile, *cf. VII.3.1.*) à la base de la croûte sur l'ensemble du MCC du Menderes. En ce sens, la province géothermale du Menderes se rapproche de celle du Basin & Range (*cf. chapitre I.2.1.2.*). Une étude magnétotellurique sur l'ensemble de la zone d'étude permettrait d'apporter de nouvelles contraintes sur la thermicité de la croûte. Par ailleurs, bien que la région des Cyclades offre de nombreuses similitudes avec le Massif du Menderes, le potentiel géothermal reste peu connu en raison des difficultés de prospection dans les domaines marins.

VII.2. Les systèmes hydrothermaux amagmatiques actifs vs. fossiles en contexte d'arrière-arc : vers un modèle conceptuel général

Avant de décrire brièvement les caractéristiques géologiques et hydrologiques des systèmes amagmatiques de HT, il est essentiel de rappeler la différence majeure entre ces systèmes et les systèmes magmatiques. Alors que la durée du système thermique (et de l'anomalie associée) avec source de chaleur profonde s'exprime en surface après plusieurs dizaines de millions d'années (~ 30 Ma dans le cas de notre étude – besoin de diffuser la chaleur compte-tenu de la profondeur de la source) et sur de larges zones (plusieurs centaines de km²), les anomalies thermiques associées aux systèmes magmatiques sont locales et présentes sur une courte période de temps comparé à la dynamique de subduction (*e.g.* bassin arrière-arc couplé à une activité magmatique dans la TVZ en Nouvelle-Zélande, < 2 Ma [Houghton *et al.*, 1995]). Par conséquent, la durée de vie du système amagmatique semble nettement supérieure à celle du système magmatique.

Circulation des fluides : de la croûte inférieure à la surface

La croûte inférieure ductile est assimilable à une couche imperméable, où les pores sont supposés se refermer par fluage des grains, diminuant ainsi la perméabilité mais augmentant la valeur de la pression fluide jusqu'à la pression lithostatique [Kerrich *et al.*, 1984]. Dans un tel contexte, la transition fragile-ductile doit représenter une barrière hydrologique infranchissable à l'infiltration en profondeur de fluides surfaciques. Néanmoins, des études montrent que les fluides météoriques descendent sous cette transition en période sismique [*e.g.* Famin *et al.*, 2004 ; Mezri *et al.*, 2015]. Les fluides surfaciques sont aspirés de manière dynamique par la propagation de la rupture sismique dans le domaine ductile sous la zone sismogénique [*e.g.* Sibson *et al.*, 1975]. La présence du CO_2 et du B en quantité importante et le rapport isotopique élevé de l'hélium dans les fluides hydrothermaux ($^3He/^4He$ ~1 Ra) (*cf. chapitre II*), impliquent des échanges entre les eaux météoriques et les fluides métamorphiques. De ce fait, il existe une connexion entre la partie fragile du détachement et la zone de cisaillement en profondeur localisée dans la croûte inférieure (Fig. VII.4b, *cf. chapitre II*) [*e.g.* Pik & Marty, 2009].

La circulation à l'intérieur du détachement est complexe. Selon l'étude de Famin [2004], en période intersismique, le système est isolé de la surface, suggérant une absence de connexion avec les réservoirs superficiels. La circulation dans la zone faillée est convective et les fluides s'infiltrent jusqu'à la transition fragile-ductile. Cette circulation profonde génère donc des instabilités thermiques dans la croûte supérieure (Fig. VII.3c, *cf. chapitre VI*). Par ailleurs, une partie des hauts reliefs du Menderes correspond au plan du détachement. La forte perméabilité induite par la tectonique dans ces niveaux structuraux et la présence de failles E-W à fort pendage alimentent généralement les réservoirs localisés à faible profondeur aux niveaux des bas topographiques. A contrario, lorsqu'une faille de transfert

recoupe le détachement, les fluides hydrothermaux émergent à la surface. En période sismique, le système est alors connecté à la surface impliquant ainsi une recharge en eaux surfaciques sur l'ensemble du système. Cette perturbation dynamique détruit provisoirement les cellules de convection, et pourrait expliquer la précipitation massive de métaux. Cette dernière est aussi facilitée par le soulèvement local du Massif, qui modifie temporairement les conditions de pression à l'intérieur du réservoir.

La présence de drains crustaux (*i.e.* détachement et faille de transfert) favorisent donc la circulation des fluides et par conséquent contrôlent la localisation des sources thermales mais également des gîtes fossiles (Fig. VII.4c). Ces structures à perméabilité variable, sont encore actives en profondeur (cas de la partie centrale du Menderes). Les détachements sont également sujets au *shear heating* (*e.g.* voir l'étude de Duprat-Oualid *et al*. [2013] sur le rôle du *shear heating* associé à un chevauchement). Similaire aux effets observés dans le manteau (*cf. chapitre VI*), ce processus pourrait induire localement une augmentation de la température du fluide. Alors que les failles à faible pendage représentent des structures de premier ordre (plurikilométrique), les failles de transfert N-S sont considérées comme des zones de décharge de second ordre (kilométriques). Ces structures accommodent la déformation et forment des zones de dilatance qui permettent aux fluides de remonter vers la surface [Person *et al*., 2012].

Caractéristiques du réservoir

Il est important de noter qu'une barrière de perméabilité est déterminante car elle permet le maintien des suppressions de fluide à de faible profondeur et favorise le développement des réservoirs. En effet, le gradient topographique induit par l'exhumation du MCC et la roche couverture bloquent les fluides géothermaux sous le détachement, permettant ainsi une homogénéisation des températures sur plusieurs dizaines voire centaines de mètres (correspondant à l'épaisseur de la shear zone du Détachement de Gediz). Dans le Menderes, cette roche couverture dont l'épaisseur est estimée à 20 – 50 cm, est principalement composée de silice mais peut être également associée à des gouges de faille.

Dans ce type de système, la géométrie du réservoir est contrôlée par l'activité tectonique et la lithologie. En effet, une intense fracturation du socle favorise l'augmentation de la perméabilité permettant ainsi aux fluides de s'accumuler sous la barrière de perméabilité définie par le plan du détachement. En période intersismique, la fracturation enregistre une fossilisation progressive, permettant aux fluides hydrothermaux de circuler dans la partie supérieure de la croûte. Ce phénomène décrit par Fournier [1991], permet de maintenir une pression fluide importante et pourrait expliquer la formation de nouveaux réservoirs. En effet, selon la lithologie de l'encaissant (*e.g.* marbres dans le cas du Menderes), la circulation des fluides hydrothermaux engendre une dissolution de l'encaissant entrainant la formation de nouveaux réservoirs. Par ailleurs, il est important de souligner que les processus de dissolution et de karstification, le gradient de pression dû à la topographie et les contraintes

tectoniques régionales vont également influencer la circulation des fluides et par conséquent la localisation des réservoirs.

VII.2.1. Caractéristiques des systèmes géothermaux amagmatiques actifs de HT

Les températures des réservoirs varient sur l'ensemble du Menderes (*e.g.* 155 °C à 1189 m de profondeur à Caferbey ; 287 °C à 2750 m de profondeur à Alaşehir [Karamanderesi, 1997, Baba *et al*., 2015]) comme l'altération des réservoirs. Cette dernière est parfois définie par une altération de type illite - séricite mais enregistre également une altération de type kaolinite (*e.g.* Germencik, Gevrek *et al*. [1989]). Une fois homogénéisé dans le réservoir, le fluide est caractérisé par une composition bicarbonatée sodique (*e.g.* Salihli, Urganlı, Alaşehir, Salavatlı) (Fig. VII.4c) et parfois chlorurée (*e.g.*Germencik) avec un pH neutre à légèrement acide (5 à 7) en présence de gaz dissous (notamment CO_2 et H_2S). Il présente également de faibles teneurs en sel, sauf dans certains cas comme à Seferihisar (en cas de recharge marine). Selon les conditions P-T du réservoir, l'ébullition peut arriver (*e.g.* platy calcite observée à Salihli, *Annexe C*) et des expressions acides comme les fumerolles se développent de façon très localisées sur des points hauts à l'aplomb du réservoir en cours d'ébullition en relation avec l'émission de gaz H_2S. Selon la nature du fluide et de la roche encaissante, différentes manifestations de surface sont répertoriées comme le témoignent les sources chaudes associées à des dépôts carbonatés (*i.e.* travertin), ou à des dépôts siliceux de type silica sinters (Fig. VII.4c). Les interactions fluides-roches sont donc complexes : elles changent – évoluent en fonction de l'endroit et du temps.

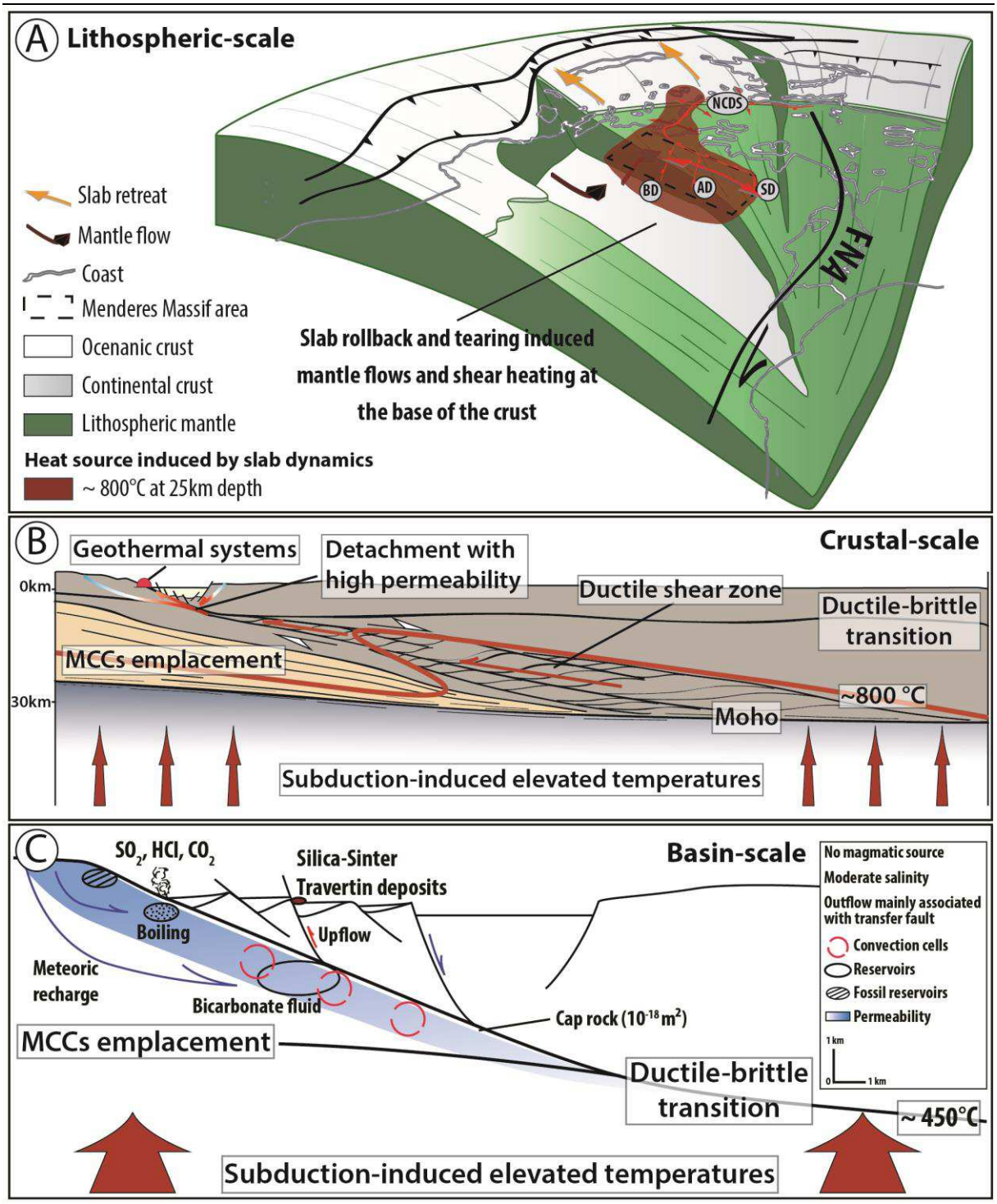

Figure VII.4 : synthèse sur la possible circulation des fluides à différentes échelles. (a) anomalie thermique de grande longueur d'onde associée à la déchirure et au retrait du slab hellénique. (b) modèle conceptuel de la circulation à l'échelle crustale. (c) modèle conceptuel d'un système amagmatique actif.

Implication sur l'exploration

De nombreux paramètres incluant par exemple la perméabilité des zones de cisaillement, le champ de contrainte, le gradient de pression dû à la topographie, la lithologie influencent la géométrie et la localisation des réservoirs en profondeur. Ainsi, l'exploration des systèmes amagmatiques reste complexe et difficile. De ce fait, bien qu'une approche multidisciplinaire soit nécessaire pour cibler les

systèmes géothermaux amagmatiques (*e.g.* géologique, géophysique, géochimique et hydrologique), ce travail basé sur une étude de terrain apporte de nouvelles contraintes pour l'exploration géothermale des systèmes amagmatiques. Une fois la zone ciblée (*e.g.* contexte post-orogénique), les « géothermotectes* » utiles à cette prospection sont :

- les failles crustales à faible pendage et les failles de transfert kilométrique considéré comme des zones de décharge.
- les expressions de surface (*e.g.* les zones d'altération) donnant des informations essentielles sur la qualité du réservoir.
- les zones de bas-relief, où le réservoir est généralement localisé.

VII.2.2.Caractéristiques des systèmes hydrothermaux amagmatiques fossiles de HT

Comme pour les systèmes actifs, la dynamique de subduction exerce un contrôle de premier ordre à l'échelle lithosphérique et crustale sur la localisation des systèmes fossiles. Bien que des études contraignent les mécanismes physico-chimiques à l'origine de ces derniers, notamment dans les domaines d'arcs magmatiques ou dans les zones de collision [*e.g.* Groves *et al*., 1998 ; Sillitoe & Hedenquist, 2003 ; Richards, 2005 ; 2009], il n'existe aucun modèle conceptuel clair sur les systèmes amagmatiques en domaine post-orogénique. Or, le Massif du Menderes offre l'opportunité d'étudier ce type de gisement dont les minéralisations s'apparentent aux gîtes épithermaux de types neutres et intermédiaires (*i.e.* au niveau des caractéristiques texturales, minéralogiques et des fluides). Ce type de minéralisation est principalement présent dans la partie centrale du Massif du Menderes proche de la localité de Salihli, qui pour rappel constitue un champ géothermal actif (*cf. Annexe C*). Dans cette région, le détachement de Gediz affleure sur de grandes distances (kilométriques), présentant de nombreuses évidences de paléo-circulations de fluides hydrothermaux. Différents indices minéralisés riches en métaux précieux Ag, Au associés à As, Hg et Sb ont notamment été observés en altitude où le Détachement de Gediz, à l'affleurement est marquée par une puissante zone silicifiée (~ 15 mètres). On distingue de haut en bas :

i) des cataclasites et des brèches hydrothermales silicifiées ;

ii) des schistes intensément silicifiés parcourus de veines rubanées à remplissage de quartz, adulaires et fantômes de carbonates. Les carbonates remplacés par le quartz présentent une texture en lamelles probablement de type « bladded calcite », qui est typique des domaines d'ébullition en contexte hydrothermal [Dong *et al*., 1995]. Ces veines parallèles au plan de détachement et à la foliation, sont de puissances centimétriques à pluri-décimétriques (max. 40 cm). Elles se caractérisent par des ouvertures en pull-apart (rares) montrant une cinématique normale. Des veines verticales de direction N-S à N020°E sont également observées dont leur puissance est comprise entre 2 cm et 50 cm. Les

veines les plus puissantes semblent s'être mises en place tous les 10–15 mètres. Cette rythmicité n'a toutefois pas pu être démontrée sur l'ensemble du secteur minéralisé en raison de la difficulté d'accès à certains affleurements. Ces veines verticales montrent également un remplissage rubané constitué de quartz, adulaire et carbonate. Certains rubans des veines verticales pourront à l'intersection avec les veines plates (*i.e*. parallèle au détachement), montrer une virgation ;

iii) un réseau de veines anastomosées semblables à un stockwork, sécant sur la schistosité mais jamais verticalisé qui se connecte sur les précédentes générations de veines.

Les résultats préliminaires suggèrent ainsi : (i) un fort contrôle structural du détachement sur la minéralisation, (ii) une minéralisation épizonale dont les textutes et paragenèses sont typiques des systèmes épithermaux neutres, (iii) une mise en place probablement très proche de la surface (< 2 km), (iv) un âge de la minéralisation (âge sur adulaire en attente) probablement post-déformation ductile qui est daté à 7 Ma [Lips *et al*., 2001], suggérant donc l'absence de lien direct avec la mise en place de la granodiorite de Salihli (16 – 17 Ma âge U-Pb [Rossetti *et al*., 2017]), distante de 3 – 4 km.

Ce type de minéralisation pourrait donc être associé à l'exhumation progressive du dôme métamorphique assistée par le fonctionnement du détachement. Cependant, les relations spatiales et temporelles entre gîtes épithermaux et dômes métamorphiques sont très rarement évoquées dans la littérature. On citera quelques exemples de gîtes épithermaux contrôlés, structuralement, par des failles de détachements ou des failles normales listriques tels que le district d'Ada Tepe dans le massif du Rhodope oriental en Bulgarie [Marchev *et al*., 2004] ou le gîte de Lewis-Crofoot dans le Basin & Range au Nevada [Ebert & Rye, 1997]. Dans ces deux cas de figure, la contribution du magmatisme sub-contemporain de la minéralisation est âprement discutée. Sillitoe & Hedenquist [2003] ont par ailleurs précisé que ce type d'occurrences épithermales localisées sur détachement n'étaient généralement pas minéralisées en or et donc sans intérêt économique. Les gîtes épithermaux économiques minéralisées en métaux précieux sont en effet principalement rencontrées dans les domaines d'arcs volcano-plutoniques, insulaires ou continentaux, associés aux zones de subduction ou en domaine d'arrière-arc mais très rarement en contexte de « rifting post-collision » [Sillitoe & Hedenquist, 2003]. La contribution du magmatisme en tant que source de métaux ou de fluides, voire comme moteur thermique, constitue un élément incontournable du modèle génétique [Hedenquist & Lowenstern, 1994].

En revanche, des modèles métallogéniques sur la circulation de fluides crustaux le long de zone de failles majeures d'échelle crustale sont largement décrit dans la littérature. Il s'agit des gîtes d'or qualifiés de mésothermaux associés aux contextes orogéniques ou aux ceintures métamorphiques [Groves *et al*., 1998 ; Groves *et al*., 2003]. Bien que rattachés aux environnements compressifs ou transpressifs, ces modèles de gisements présentent de nombreux exemples amagmatiques, mais restent sans analogue contemporain à notre connaissance. Par analogie avec ce dernier modèle, il est ainsi

possible de proposer que la source de chaleur dans le Massif du Menderes (observée à différents niveaux dans la croûte) favorise la circulation hydrothermale, et par conséquent la mobilisation des différents métaux tels que As-Au dans les domaines profonds et Au-Sb-Hg et Hg-Sb plus en surface. Cette source résulte de la dynamique du slab qui contrôle la mise en place du dôme métamorphique assisté par des failles ductiles puis cassantes d'échelle crustale. Lorsque les fluides hydrothermaux atteignent les environnements de sub-surface, leurs températures relativement basses (< 200 – 250 °C) induisent une très faible solubilité de l'or, impliquant un transport relativement limité [Fontboté *et al*., 2017]. Cependant, entre 150 et 200 °C, les complexes bisulfurés peuvent transporter et donc déposer des quantités significatives de Sb et de Hg dans cette partie superficielle de la croûte [Williams-Jones & Norman, 1997]. Ainsi, l'étude de ces paléo-systèmes hydrothermaux est essentielle, car elle apporte de nouvelles contraintes sur les conditions actuelles du réservoir (*e.g.* P-T, le type d'altération…). Plus généralement, un modèle épisodique (*e.g.* pompage sismique) et/ou en continu semble envisageable sur plusieurs millions d'années.

VII.3. Perspectives

VII.3.1. Evolution de la zone de subduction : localisations des systèmes géothermaux HT

Alors que la majorité des systèmes géothermaux de HT sont localisés dans les zones de subduction, il n'existe pas de réelle classification pour ces systèmes. Or, ce travail de thèse confirme que les anomalies thermiques profondes (*i.e.* mantelliques) sont associées à la dynamique de subduction. Cette dernière est complexe puisqu'elle évolue spatialement et temporellement. De ce fait, qu'ils soient de type magmatique et/ou amagmatique, une typologie « dynamique » des systèmes géothermaux HT est nécessaire pour guider l'exploration géothermale. Par conséquent, une évolution de la zone de subduction (non exhaustive car elle représente une partie des systèmes géothermaux de HT) en fonction des différents systèmes géothermaux de HT est proposée ci-dessous (Fig. VII.5). Il est important de souligner que cette classification en 2D insiste surtout sur le rôle des flux asthénosphériques et du *shear heating* associés au retrait du panneau plongeant. Ces flux marqués par une composante toroïdale importante, facilitent de ce fait le retrait [Kiraly *et al*., 2017].

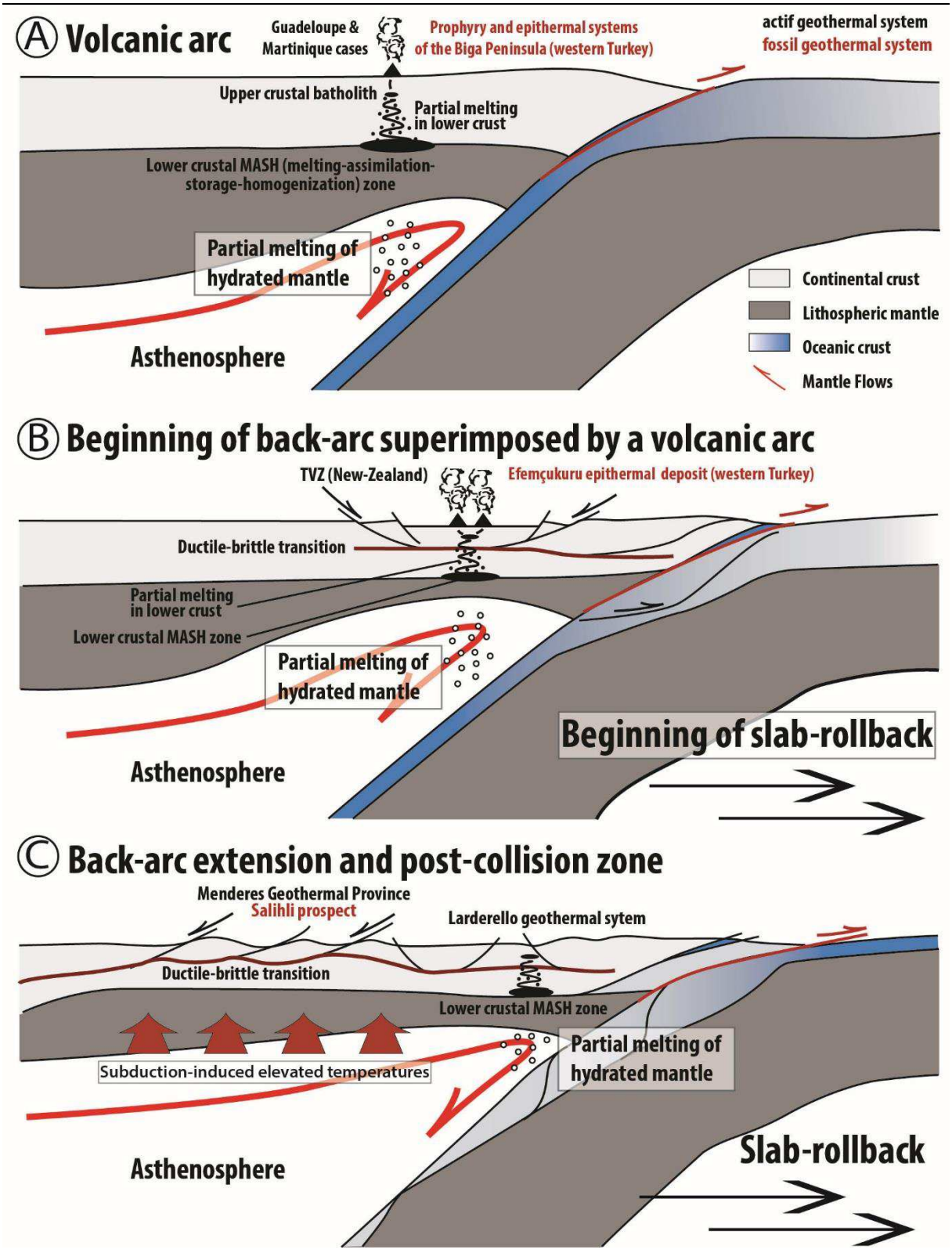

Figure VII.5 : évolution d'une zone de subduction classique présentant différents systèmes HT. (a) Système magmatique de type arc comme la Guadeloupe et la Martinique. (b) Système magmatique de type arc qui se développe dans un domaine d'arrière-arc comme en Nouvelle-Zélande et dans le Massif du Menderes au Miocène. (c) Système amagmatique dans le domaine arrière-arc contrôlé par la dynamique du slab (e.g. la province géothermale du Menderes) et système-post orogénique magmatique (e.g. le site géothermal de Larderello).

Alors que les systèmes magmatiques apparaissent de manière ponctuelle (*i.e.* temporellement et spatialement) à l'échelle de la subduction, les provinces amagmatiques se développent sur plusieurs dizaines de millions d'années (*e.g.* sur des centaines de km²). De ce fait, à l'échelle de la subduction, les systèmes de type « arc » sont généralement précurseurs et l'anomalie thermique en surface est très localisée (*i.e.* maximum de quelques kilomètres) (Fig. VII.5a). A contrario, les anomalies profondes mettent un certain temps à s'exprimer en surface mais semblent affecter les unités sur un large domaine (*e.g.* le Menderes et le Basin & Range). Ainsi, les systèmes magmatiques actifs et fossiles se développent principalement au niveau des arcs volcaniques mais également dans les prémices de l'extension post-orogénique (Figs. VII.5a et b). De plus, il est important de souligner que dans certaines conditions, ces deux types de système sont étroitement liés (*e.g.* le cas de la Nouvelle-Zélande) (Fig. VII.5b). Ainsi, à l'échelle de la subduction les systèmes magmatiques et amagmatiques peuvent se superposer, et les systèmes autrefois actifs deviennent alors fossiles (Fig. VII.5). Néanmoins, dans certains cas de figure, cette distinction est ambiguë et peut par conséquent minimiser voire empêcher la découverte de nouveaux systèmes géothermaux de HT (Fig. VII.5c).

Le champ géothermal de Larderello est un parfait exemple de cette ambiguïté. Dans cette région, la dynamique de subduction est également contrôlée par le retrait du panneau plongeant vers l'est depuis l'Oligo-Miocène. Cette région est par conséquent caractérisée par des flux mantelliques actifs (*i.e.* délamination) qui modifient l'épaisseur de la lithosphère et par conséquent la profondeur du Moho (20 – 25 km de profondeur) [Gianelli, 2008]. À l'échelle crustale une série de failles normales à faible pendage accommodent l'exhumation des MCCs [*e.g.* Faccenna *et al.*, 1997 ; Jolivet *et al.*, 1998]. Comme le magmatisme, ces dômes métamorphiques de HT migrent et rajeunissent d'ouest en est vers la fosse, depuis 30 – 25 Ma jusqu'à l'Actuel [*e.g.* Jolivet *et al.*, 1998]. Néanmoins, des modèles alternatifs montrent une évolution tectonique plus complexe au cours du Miocène-Pléistocène (*i.e.* alternant avec une tectonique extensive et compressive) [*e.g.* Bonini & Sani, 2002]. C'est dans ce contexte géodynamique particulier, que le champ géothermique de Larderello se localise (dans les Apennins, sud de la Toscane). Même s'il est clair que la source de chaleur locale est associée à un intrusif peu profond atteint en forage à 4 km [*e.g.* Gianelli, 2008 ; Santilano *et al.*, 2015], des profils sismiques montrent que des failles normales listriques s'enracinent au niveau de la transition fragile-ductile à 4–5 km de profondeur [Bellani *et al.*, 2004]. Ces auteurs montrent que ces failles contrôlent la circulation des fluides dans la croûte supérieure. Cette région est par ailleurs marquée par une anomalie thermique importante liée à la relaxation thermique du déséquilibre créé par la phase d'épaississement crustal antérieure, mais également à la phase extensive et au retrait du panneau plongeant comme en Egée, qui se caractérise par la présence de détachements à faible pendage vers l'est et d'intrusifs. Dans cet exemple, la classification habituelle de ce champ géothermal dans un contexte magmatique sous-estime l'importance des apports de chaleur plus profonds comme on le voit sur l'exemple du Menderes et cela peut nuire à la découverte de nouveaux systèmes géothermaux.

VII.3.2.Fenêtres mantelliques & zone de transfert : le cas particulier du Basin & Range

Malgré de nombreuses similitudes avec la Province géothermale de l'Anatolie, la province du Basin & Range, se différencie par sa dynamique de subduction (Fig. VII.6). En effet, les flux mantelliques dans cette région sont considérés comme moteurs ; par conséquent ils favorisent le retrait du panneau plongeant. Précisément, à l'Eocène, un changement drastique des conditions de la dynamique de subduction modifie l'évolution tectono-métamophique dans cette région. Cette dynamique correspond à la formation d'une première « fenêtre du slab» qui se développe au point triple lui-même défini par l'intersection entre la plaque Pacifique, la plaque Farallon et la zone de subduction (Fig. VII.6b) [Schellart *et al*., 2010]. D'après cette étude, cette dernière favorise le retrait du panneau plongeant de la plaque Farallon vers l'ouest. Similaire au Massif du Menderes, cette dynamique du slab (contrôlée par les flux mantelliques) est responsable de l'effondrement gravitaire d'une partie de la chaîne des Laramides, et de la mise en place d'une vaste zone extensive comme le témoigne la présence de nombreux MCCs entre les Montagnes Rocheuses et la Sierra Nevada, ainsi que dans le nord des Rocheuses jusqu'au Canada (Fig. VII.6b). Un second événement majeur modifie encore la dynamique régionale : l'apparition d'une nouvelle « fenêtre du slab » qui se localise sous la région californienne vers 30 Ma (Fig. VII.6c) [Atwater, 1970]. En réponse à ce nouveau flux mantellique, une seconde phase d'extension débute vers 30 Ma. Elle est accommodée par des failles à faible pendage qui exhument de nouveaux MCCs au sud du Basin & Range (Fig. VII.6c). Depuis 15 Ma, contrôlé par la dynamique mantellique, le retrait du panneau plongeant s'accélère et l'extension se localise principalement dans la partie centrale du Bassin & Range, à l'aplomb de la fenêtre californienne (Fig. VII.6d) [Schellart *et al*., 2010]. Or, cette même région est marquée par la présence des principaux champs géothermaux amagmatiques de HT (Fig. VII.6f) (*e.g.* 280 °C à une profondeur de 3 km, Dixie Valley [Blackwell *et al*., 2000]). Ainsi, il est probable que la dynamique de subduction associée aux deux fenêtres mantelliques induise (i) des anomalies thermiques importantes dans le domaine post-orogénique et (ii) des structures extensives perméables. Cette dynamique semble donc contrôler la localisation des champs géothermaux dans la province du Basin & Range. Par ailleurs, il est important de noter l'existence de nombreuses zones de transfert (*i.e.* de coulissage) qui accommodent la déformation sur plusieurs dizaines de kilomètres. Ces structures semblent faciliter l'émergence de sources thermales mais également la remontée de magma dans la croûte supérieure (*e.g.* The Geysers ; Salton Trough, Fig. VII.6f).

Des similitudes sont également observées dans la province géothermale du Menderes où des failles crustales décrochantes de second ordre contrôlent la circulation des fluides dans le Massif du Menderes (*cf. chapitre II*). Néanmoins, les failles de premier ordre comme la NAF (North Anatolian Fault) qui est considérée comme une faille d'échelle lithosphérique décrochante, ne présentent aucune

anomalie thermique associée significative. De ce fait, cette faille majeure qui accommode l'extrusion de l'Anatolie vers l'ouest ne semble pas favoriser la circulation des fluides à l'échelle crustale.

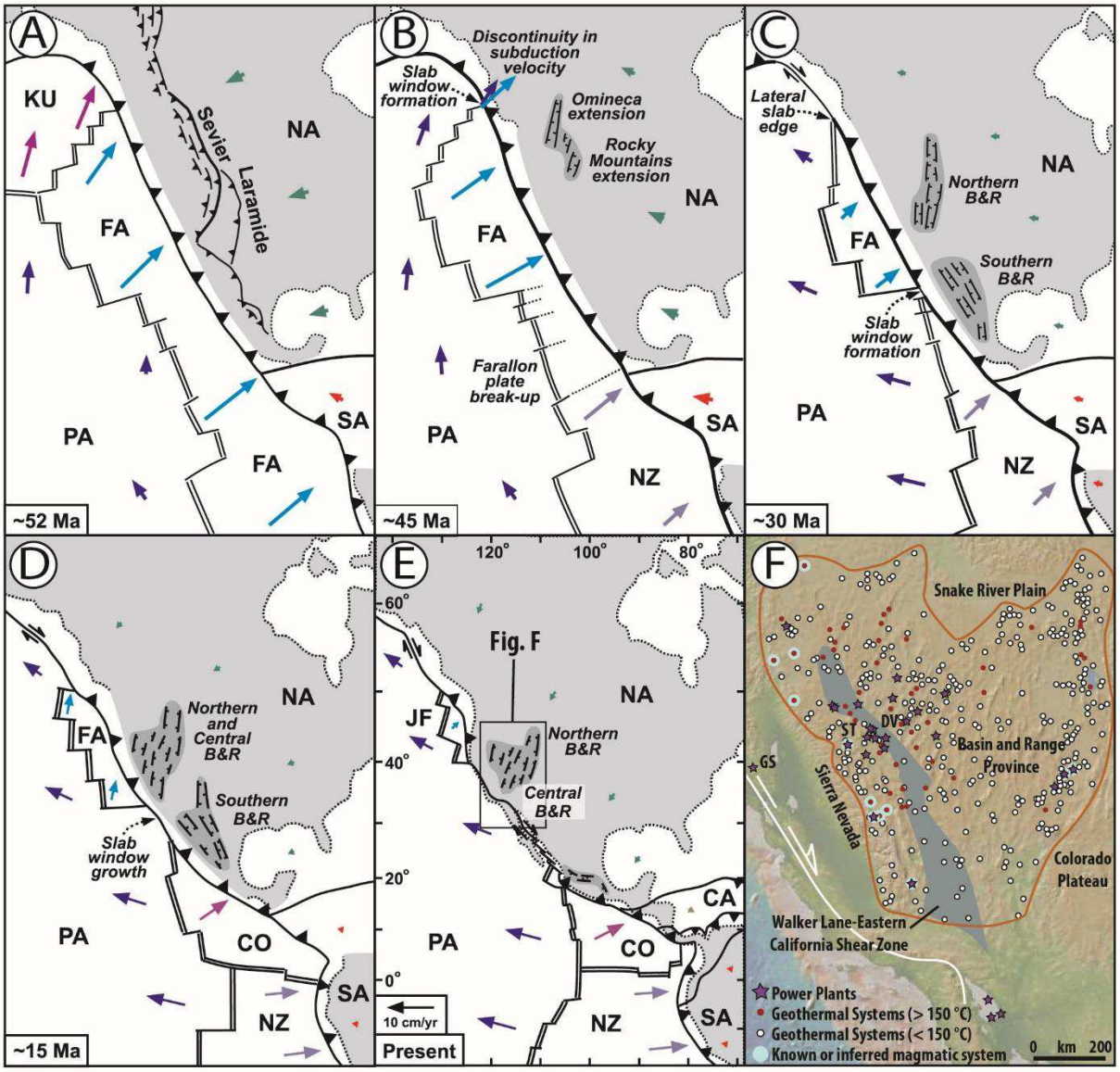

Figure VII.6 : évolution de la plaque Farallon au Cénozoïque, d'après Schellart et al. [2010] : conséquences thermiques. (a) Début Eocène (52 Ma). (b) Milieu Eocène (45 Ma). (c) Oligocène (30 Ma). (d) Milieu Miocène (15 Ma) et (e) l'Actuel (0 Ma). La localisation de la figure VII.6f est également indiquée. Cette figure est modifiée d'après Schellart et al. [2010]. CA : Caribbean ; CO : Cocos ; FA : Farallon ; JF : Juan de Fuca ; KU : Kula ; NA : North America ; NZ : Nazca ; PA : Pacific ; SA : South America. (f) Localisation des champs magmatiques et amagmatiques dans la province du Basin & Range. Les données géothermales sont issues de l'étude de Faulds et al. [2012]. DV : Dixie Valley ; GS : The Geysers ; ST : Salton Trough.

VII.3.3. La dynamique de subduction : un contrôle de premier ordre sur la distribution des systèmes de HT ?

À l'échelle mondiale, il existe une forte corrélation entre la localisation des systèmes de HT et les bordures des slabs. Comme le montre Funiciello *et al*. [2003], Faccenna *et al*. [2004 ; 2005] ou Schellart *et al*. [2007], le roll-back est facilité par les flux mantelliques à proximité des bords latéraux des slabs (Fig. I.14b). Ainsi, les zones de subduction étroites (≤ 1.500 km), témoins de retraits rapides, sont les premiers géothermotectes pour l'exploration géothermale. Dans ces conditions (*e.g.* similaires à la Province Géothermale du Menderes), l'origine de la chaleur sur des systèmes de classe mondiale comme la Nouvelle-Zélande (*e.g.* Kawerau, Nga Awa Purua, Ngatamariki, Ohaaki, Poihipi, Te Mihi, Wairakei), la Nouvelle-Guinée (*e.g.* Linhir), l'Indonésie (*e.g.* Sarulla) pourrait directement être liée aux absences des panneaux plongeants où à la présence d'une déchirure (Fig. VII.7). Les zones comme Scotia et le South Shetland seraient par conséquent fortement favorables aux systèmes de HT (Fig. VII.7a) même si à l'heure actuelle aucune activité humaine n'est encore développée. Par ailleurs, des gîtes fossiles similaires à celui observé dans la province de Salihli (Massif du Menderes) pourraient être également découverts dans ces zones préférentielles.

Même si les résultats préliminaires des modèles numériques 3D suggèrent un transfert rapide de la chaleur en base de croûte, aucune généralité sur le timing de la propagation de ces anomalies ne peut être affirmée. En effet, la grande variabilité des zones de subduction et dynamiques associées implique a fortiori une forte diversité dans la propagation des anomalies thermiques dans la plaque supérieure. Une étude plus détaillée sur la vitesse et la géométrie des slabs pourrait apporter de nouvelles contraintes sur l'évolution thermique de ces zones. Par exemple, Schellart *et al*. [2007] montrent que les vitesses maximales observées en bordures de slab sont comprises entre 6 – 16 $cm.an^{-1}$ confirmant l'observation que les vitesses de retrait des slab étroits sont souvent très élevées, dépassant souvent 10 – 15 $cm.an^{-1}$ [Faccenna *et al*., 2004 ; Nicolosi *et al*., 2006]. Ces valeurs élevées impliquent la présence de flux mantelliques rapides et suggèrent une déformation mantellique importante modifiant probablement la composante du *shear heating*. Dans la continuité des travaux de Lallemand *et al*. [2005] et d'Heuret & Lallemand [2005], une approche (i) bibliographique synthétique principalement basée sur la géométrie du panneau plongeant (*e.g.* l'angle du slab) et sur la localisation de sources thermales, et (ii) numériques (*e.g.* l'angle du slab et vitesse de retrait) apporterait de nouvelles contraintes sur les transferts thermiques à grande échelle dans les zones de subduction.

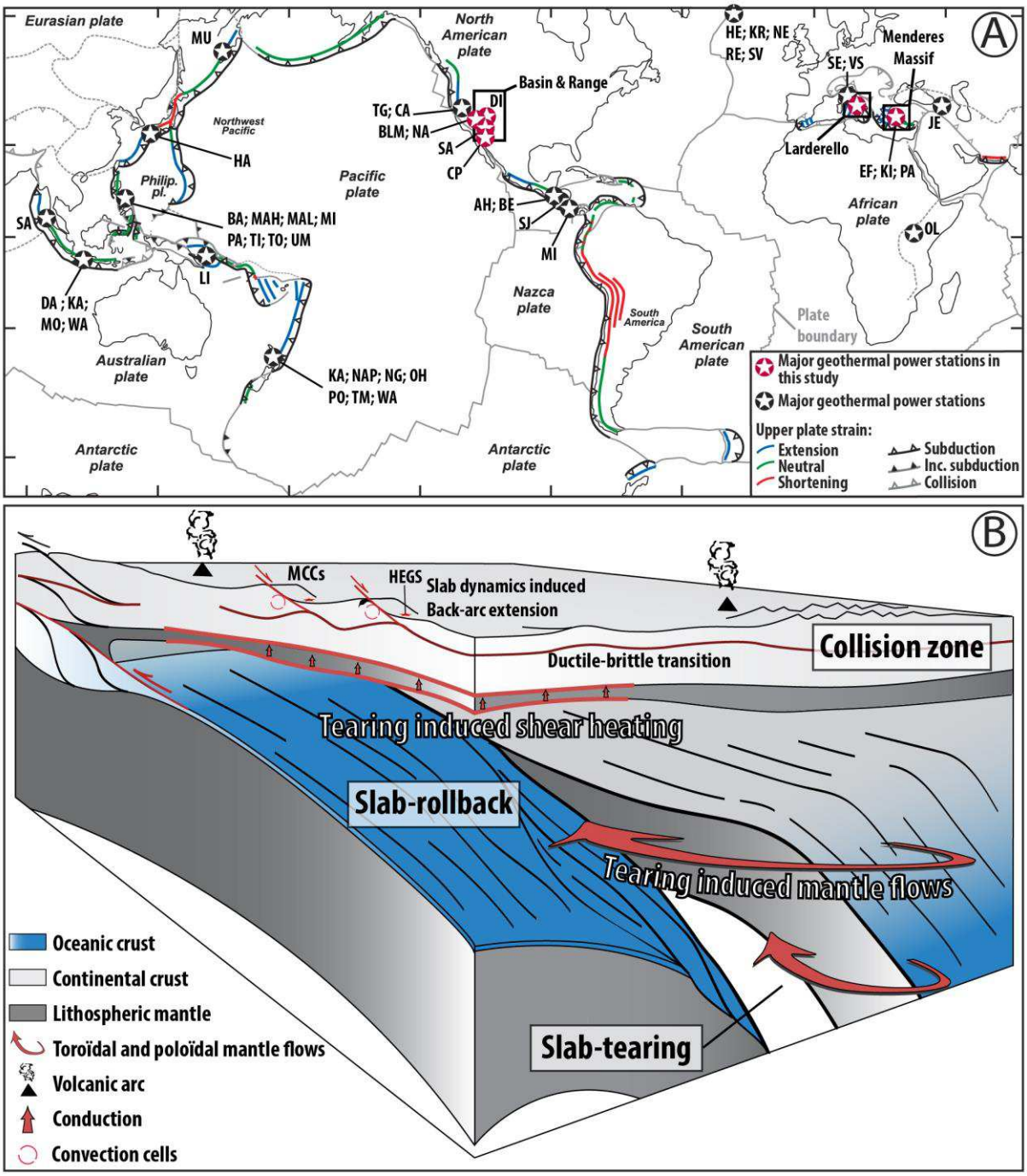

Figure VII.7 : dynamique de subduction et implications sur la localisation des champs géothermaux de HT. (a) carte similaire à la figure I.12 montrant la corrélation entre les principaux champs géothermaux de HT en activité et en construction (étoile rouge et blanche) et les principales zones de subduction dans le monde, modifié d'après Schellart et al. [2007]. BLM, CA, Calistoga, DV, Dixie Valley, NA, Navy, SA, Salton Sea, TG, The Geysers (Etats-Unis) ; SA, Sarulla, (Indonésie) ; KA, Kawerau, NAP, Nga Awa Purua, NG, Ngatamariki, OH, Ohaaki, PO, Poihipi, TM, Te Mihi, WA, Wairakei (Nouvelle-Zélande); LI, Linhir (Nouvelle-Guinée); KI, Kızıldere, (Turquie); Sc (Scotia) ; Sh (South Shetland). (b) Modèle conceptuel montrant une déchirure dans le panneau plongeant et ses conséquences thermiques.

VII.4. Synthesis and Discussion - abridged English version

VII.4.1. The Menderes geothermal Province

VII.4.1.1. Thermal evolution of the Menderes Massif

The thermal evolution of the Menderes area can be summarized in free steps:

i. Cretaceous to Eocene HP-LT parageneses are recorded in the entire Aegean domain. It is thus clear that this past dynamics (*e.g.* syn-orogenic exhumation, see Laurent *et al.* [2016], Roche *et al.* [2016] in *Appendix B*) cannot explain the present-day thermal anomalies related to the geothermal Menderes Province. The kinematics of the Hellenic subduction zone however changed in the Eocene. At that time, the Menderes Massif (*i.e.* its basement) has entered the subduction zone and a first episode of HT-LP metamorphism is recorded (Fig. VII.1). This Barrovian main metamorphism event (MMM) is due to radioactive decay within the thickening basement. The MMM event is therefore correlated with significant thermal anomalies that partly affect Menderes units, changing heat flow in the area at this period. These large-scale thermal anomalies are mainly controlled by heat production within the thick continental crust. However, no magmatic activity was recorded in the massif at this time, coeval with an absence of mineralization (*e.g.* absence of porphyry systems) [*e.g.* Menant *et al.*, 2018]. It should be noted however that the proposition of a first slab tear event in the Eocene by Govers and Fichtner [2016] could also be part of the explanation, although the reconstructions [Menant *et al.*, 2016] do not show a clear tearing event.

ii. From the Oligocene to Miocene, the presence of migmatites and the distribution of granitic intrusions in the back-arc area, coeval with a fast rotation of the Hellenides, confirm that slab rollback and tearing control the spatial distribution of higher temperatures in the crust. This excess of heat in the Miocene is also marked by the emplacement of a mineralized province rich in epithermal deposits, mainly located in the Rhodope Mountains and on the Biga Peninsula in the northeastern part of Turkey [*e.g.* Yılmaz *et al.*, 2001; Marchev *et al.*, 2005]. According to Marchev *et al.* [2005] and Ersoy and Palmer, [2013], back-arc magmatism tends to be mildly (high-K ± Na calcalkaline) to strongly alkaline with crustal (dominant) and mantle (secondary) components. In addition, according to Richards [2005], the source region shares many isotopic and geochemical characteristics with the previous arc event. This period is thus considered as fertile, attested by the emplacement of many porphyry-epithermal deposits such as Mo–Cu Pınarbaşı [Delibaş *et al.*, 2017] and Efemçukuru ore deposits [Oyman *et al.*, 2003]. The region is marked by numerous punctual events associated with the emplacement of magmatic intrusions in the upper crust. The heat associated with these intrusions favors the development of the deep equivalent of HEGS, although their activity are limited in time. Contemporaneous with these geothermal magmatic deposits, the entire MCC of the Menderes Massif is rapidly exhumed by several

shear zones (see *chapter VI*). Associated with this dome exhumation, a regional thermal anomaly affects first the northern part of the Massif and then its entire central part. The presence of miocene monazites and the obtained T_{max} results (see *chapter V*) show that these anomalies have reached temperatures around 600 °C within the crust.

iii. From the Miocene to Present, subduction dynamics and induced crustal deformation controlled the emplacement of active HEGS in the Menderes Massif at different scales. Subduction dynamics controls the spatial and temporal distribution of thermal anomalies in the back-arc domain and, in agreement with our numerical results (Fig. VII.3) (*chapter VI*), the thermal regime in the crust is mainly induced by (i) shear heating in the mantle and by (ii) the poloidal and toroidal components of underlying mantle flow. Both mechanisms are responsible for an increase of Moho temperature. In the case of the Aegean region, we suggest that heat flow is abnormally high during several tens of millions years (*e.g.* ~ 30 Ma). One fundamental aspect thus consists in the time scale of the propagation of thermal anomalies through the crust. Based on heat conduction, the time scale t_{diff} is defined by the following equation:

$$t_{diff} = L^2 / \kappa$$

where L is Moho depth (meter) and κ represents heat conduction ($m^2.s^{-1}$). For instance, considering a Moho depth of ~ 25 km under the Menderes Massif [Karabulut *et al.*, 2013] and taking a thermal diffusivity (κ) of 10^{-6} $m^2.s^{-1}$, the current thermal anomaly observed at the surface (shown by the presence of numerous sources and gaz events) could reflect the thermal expression of a 20 Ma old slab tear at Moho depth. This hypothesis is consistent with the presence of high temperatures (~ 580 °C) at shallow depths (~ 8 km under the Menderes) [Aydin *et al.*, 2005; Bilim *et al.*, 2016]. Consequently, an increase of temperature is observed in the ductile brittle-transition (reaching locally 400 °C, according to Violay *et al.* [2017]) at shallow depths (4 – 5 km), favoring the emplacement of a large zone of migmatization and/or magmatic underplating at the base of the crust. In that sense, the geothermal Province of the Menderes Massif is similar to the Basin & Range province. A magnetotelluric study on the entire Menderes area could bring new constraints on the thermal conditions of the crust. At smaller scale the distribution of heat within the crust is controlled by the circulation of fluids within the upper crust and the brittle-ductile transition (Fig. VII.3c) (*see chapter VI*). Active detachments convey fluids downward and upward and the formation of geothermal reservoirs is finally controlled by these detachments and steeper normal and transfer faults.

VII.4.1.2. Amagmatic fossil vs. active geothermal systems in the Menderes Massif

Before briefly describing the geological and hydrological characteristics of HEGS, it is necessary to recall the major difference between amagmatic and magmatic. While the geothermal system (and the associated thermal anomaly) associated with a deep heat source is expressed at the surface after several tens of millions of years (*e.g.* ~ 30 Ma in the case of our study) and over large areas (several tens of km²), the thermal anomalies associated with magmatic systems are more local and present over a shorter period of time compared to the time constants of subduction dynamics (*e.g.* back-arc basin coupled with magmatic activity in the TVZ in New Zealand, < 2 Ma [Houghton *et al.*, 1995]). As a result, the time life of the amagmatic system will be much greater than for magmatic ones.

Deep fluid circulation

Fluid circulation inside detachments, at depth, is complex. According to Famin *et al.* [2004], during the inter-seismic period, below the brittle-ductile transition, fluids are isolated from the surface, without any connection with superficial reservoirs. Circulation in the fault zone is convective, and meteoric fluids reach locally the ductile-brittle transition (Fig. VII.4b) [*e.g.* Famin *et al.*, 2004; Mezri *et al.*, 2015]. During the co-seismic period, fluids are dynamically pumped downward by propagation of the seismic rupture in the ductile domain [*e.g.* Sibson *et al.*, 1975; Famin *et al.*, 2004]. The presence of CO_2 and B in large quantities, and the high isotopic ratio of helium within hydrothermal fluids (3He / 4He ~ 1 Ra) (*chapter II*), indeed documents exchanges between meteoric and metamorphic waters through connection of the brittle part of the detachment with the deeper ductile shear zone located in the lower crust (*chapter II*, Fig. II.12) [*e.g.* Pik & Marty, 2009]. In addition, this deep circulation favors the emplacement of thermal instabilities in the upper crust (*chapter VI*, numerical model Fig. VI.9). It is important to note that part of the high-topography zone of the Menderes Massif corresponds to the detachment fault plane. The high permeability induced by deformation in these shallow structural levels and the presence of E-W high-angle striking faults usually enhance the emplacement of shallow reservoirs. When a transfer fault intersects the detachment, hydrothermal fluids emerge to the surface. During the seismic period, the system is connected to the surface, favoring a pervasive infiltration of meteoric waters within the whole system. This unstable dynamics temporarily modifies convection cells, and could explain the massive precipitation of metals (*e.g.* Sb; Au…). This precipitation is also enhanced by the exhumation of the massif, which modifies pressure conditions inside the reservoir.

The presence of crustal drains such as detachment and transfer faults enhances crustal fluid circulation, and therefore controls the location of hot springs. These structures with variable permeability, are still active at depth (*e.g.* the central part of the Menderes Massif). In addition, the activity of detachments may induce some shear heating (*e.g.* see the study of Duprat-Oualid *et al.* [2013] on the role of the shear heating associated with thrust activity in collision zones), but its effect on the

surrounding crust strongly depends upon the vigor of fluid circulation, which is poorly controlled. Similar to the effects observed in the mantle (*chapter VI*), this process could locally induce an increase of fluid temperature. While low-angle normal faults represent the first-order structural control for the location of HEGS (multi-kilometer), N-S transfer faults are considered as second-order discharge zones (kilometer). These structures sometimes intersect or root on the detachment, forming areas of dilatancy (*i.e.* jogs) that allow fluids to ascent to the surface [Person *et al.*, 2012].

Reservoir characteristics

The cap rock represents a barrier of permeability and allows fluids circulation at shallow depths, thus enhancing the development of reservoirs. Indeed, cap rock blocks geothermal fluids under the detachment, thus allowing a homogenization of temperature over several tens to few hundreds of meters (corresponding to the thickness of the shear zone of the Gediz Detachment). In the Menderes Massif, this cap rock, whose thickness is estimated around 20 – 50 cm, is mainly composed of silicified material but can also be associated with fault gouge. In these systems, the geometry of the reservoir is therefore mainly controlled by tectonic activity and lithology. Indeed, intense fracturing of the basement favors the increase of permeability, and allows the accumulation of fluids under the detachement permeability barrier. In addition, dissolution and karstification processes, the pressure gradient due to topography and the regional tectonic stress regime also influence the circulation of fluids, and consequently the location of reservoirs.

a. Active geothermal systems

Reservoir temperatures vary throughout the region (*e.g.* 155 °C to 1189 m depth at Caferbey, 287 °C at 2750 m depth at Alaşehir, [Karamanderesi, 1997; Baba *et al.*, 2015]) together with rock alteration in reservoirs. Besides illite-sericite alteration, reservoirs also record a kaolinite alteration (*e.g.* Germencik [Gevrek *et al.*, 1981]). Once homogenized in the reservoir, the fluid is characterized by a sodium bicarbonated composition (*e.g.* Salihli, Urganlı, Alaşehir, Salavatlı) and sometimes chloritized (*e.g.* Germencik) with a neutral to slightly acidic pH (5 to 7) in the presence of dissolved gases (including CO_2 and H_2S). It also has low salinity, except in some cases like in Seferihisar (near sea). Depending on P-T conditions of the reservoir, boiling may occur (*e.g.* platy calcite observed at Salihli) and acidic expressions such as fumaroles are localized directly above the boiling reservoir in relation with the emission of H_2S gases. Depending on the nature of the fluid and the host rock, different surface manifestations can be observed such as hot springs associated with carbonate deposits (*i.e.* travertine), or silica sinters (Fig. VII.4c). Fluid-rock interactions are therefore complex: they change-evolve according to location and time.

Numerous parameters including, for example, permeability of shear zones, stress field, pressure gradient due to the topography effect, and lithology, influence the geometry and the location of reservoirs at depth. Thereby, the exploration of amagmatic systems remains complex and difficult and a multidisciplinary approach is needed to target amagmatic geothermal systems (*e.g.* geological, geophysical, geochemical and hydrological). This work, based on field study, radiochronology and numerical modelling, provides new constraints for geothermal exploration. Useful geothermotects (*) for prospection in regions of large-scale heat flow anomalies are:

- Low-angle crustal normal faults and kilometer-scale transfer faults
- Surface expressions (*e.g.* alteration zones) giving information on P-T conditions of the reservoir
- Low topography areas, where the reservoir is usually localized

(*) structures enhancing the concentration of geothermal deposits

b. Fossil geothermal systems

As for active systems, subduction dynamics exerts a primary control at lithospheric- and crustal-scale on the location of low- to high-sulphidation epithermal deposits. Although many studies constrain the physicochemical mechanisms at the origin of these deposits, especially in the domains of magmatic arcs an in collision zones [*e.g.* Groves *et al.*, 1998; Sillitoe & Hedenquist, 2003; Richards, 2005; 2009], there is no clear relationship between epithermal deposits and metamorphic domes in a post-orogenic domain. In that sense, the link between post-collisional metallogenic evolution (*i.e.* porphyry-epithermal), magmatism and extension remains poorly constrained. Nevertheless, a few examples of epithermal deposits document a structural control by detachment faults or listric normal faults, such as the AdaTepe district in the Eastern Rhodope Mountains in Bulgaria [Marchev *et al.*, 2004], or the Lewis-Crofoot in the Basin & Range in Nevada [Ebert & Rye, 1997]. In both cases, the contribution of sub-contemporary magmatism associated with mineralization is strongly discussed. In addition, Sillitoe and Hedenquist [2003] also indicated that this type of epithermal occurrences located within the detachment was generally not mineralized in gold, and thus without economic interest. The Menderes Massif offers the opportunity to study this type of deposit.

Such epithermal occurences crops out near the locality of Salihli, where both an active and fossil systems coexist (see *Appendix C*). In this region, the Gediz Detachment crops out over large distance (kilometric), presenting numerous evidences of paleo-circulations of hydrothermal fluids. Various mineralized occurrences rich in precious metals (*e.g.* Ag, Au, As, Hg, Sb) have been observed in the high reliefs where the activity of the Gediz Detachment is marked by a thick cataclasite zone (~ 15 meters). From top to bottom, there is:

- Silicified cataclasites and breccias.
- Pervasively silicified schists characterized by quartz banded veins, adularia and carbonate ghosts. Carbonates have been locally replaced by quartz and display a lamellar texture of "bladded calcite". According to Dong *et al.* [1995], this texture indicates boiling event in a hydrothermal context. Parallel to the plane of detachment and foliation, these veins are centimetric to multi-decimetric (max 40 cm), and sometimes characterized by opening systems such as pull-aparts (rare) showing a normal kinematics. Vertical veins striking N-S to N020 ° E are also observed (2 cm to 50 cm). These veins are filled by quartz, adularia and carbonates.
- A network of anastomosed veins similar to a stockwork, parallel to the main schistosity.

Preliminary results therefore suggest that (i) detachment controls mineralization deposits, which may be considered as epizonal (*i.e.* textures and parageneses similar to low-sulphidation epithermal deposits), (ii) the emplacement of the mineralization is close to the surface (<2 km) and (iii) with an age that post-dates the ductile-brittle deformation (dated at 7 Ma [Lips *et al.*, 2001]), suggesting no direct link with the Salihli granodiorite emplacement (16 – 17 Ma age U-Pb [Rossetti *et al.*, 2017]). This type of mineralization may therefore be associated with the exhumation of the metamorphic dome induced by the detachment activity. In that sense, this deposit is similar to gold deposits described as mesothermal shear zone-hosted deposits mainly associated with metamorphic belts [Groves *et al.*, 1998; Groves *et al.*, 2003]. Even if the deformation associated with the emplacement of these deposits is compressional and/or transpressional, these kinds of models present many similarities with amagmatic geothermal systems.

In the Menderes Massif, we propose that the heat source at the base of the crust coupled to the exhumation of the MCC is induced by slab dynamics. Within the crust, the low-angle crustal normal faults control the hydrothermal fluid circulation, and therefore the mobilization of different metals such as As-Au in deep domains and then Au-Sb-Hg and Hg-Sb in shallower domains. Indeed, when hydrothermal fluids reach the sub-surface, their relatively low temperature (< 200 – 250 °C) induces a very low solubility of gold, minimizing gold transport [Fontboté *et al.*, 2017]. In addition, between 150 and 200 °C, disulfide complexes can be transported, and thus precipitate significant amounts of Sb and Hg in the lower part of the crust [Williams-Jones & Norman, 1997].

In summary, these paleo-systems are similar to the amagmatic active HT geothermal systems. Indeed, the deep heat source induces migmatitization and/or accumulation of magma at the base of the crust, allowing the mobilization of gold and other metals. Accordingly, the study of these paleo-systems is essential, because they bring new constraints on the current conditions of the reservoir (*e.g.* P-T, the type of alteration ...) where geothermal resources are located. More generally, an episodic model (*e.g.* seismic pumping) and / or a continuous model seem possible over several million years.

VII.4.2. Subduction dynamics: a first order control on the distribution of high-enthalpy geothermal systems (HEGS)?

While the majority of HEGS are located at the vicinity of subduction zones, there is no real classification for these systems. However, this work confirms that deep thermal anomalies (*i.e.* at Moho depth) are associated with the surrounding subduction dynamics. In that sense, whether geothermal systems are magmatic or not, a dynamic typology of HEGS is necessary to guide geothermal exploration. In the following, we therefore present a simplified evolution of the subduction zone depending on the different HEGS (Fig. VII.5). It is important to emphasize that this 2D classification especially insists on the role of asthenospheric flows and of shear heating, both associated with slab rollback and tearing. At the scale of a subduction zone, magmatic geothermal systems are generally precursors. In these systems, the thermal anomaly at the surface is localized (*i.e.* a few kilometers long maximum) and appears temporarily (Fig. VII.5a). Conversely, deep thermal anomalies take some time to express themselves at the surface (over tens of millions of years) and seem to affect the crust over a large area (*e.g.* over hundreds of km², Menderes and the Basin & Range). Furthermore, it is important to note that under certain conditions, these two types of system are closely related (*e.g.* the case of New-Zealand) (Fig. VII.5b). Thus, at the subduction scale, the magmatic and amagmatic systems can be superimposed on each other, while the associated timescales and wavelengths differ. Nevertheless, in some cases (see below) this distinction is ambiguous, and can therefore minimize or even prevent the discovery of new HEGS.

VII.4.2.1. The complexity of Larderello geothermal system (Italy)

The geothermal field of Larderello is a perfect example of this ambiguity (*i.e.* magmatic or amagmatic?). In this region, subduction dynamics is also controlled by the eastward slab rollback from the Oligo-Miocene to the Present [Faccenna *et al.*, 1997; Jolivet *et al.*, 1998]. This region is therefore characterized by active mantle flows (*i.e.* delamination) that modify the thickness of the lithosphere, and hence, the depth of the Moho (20 – 25 km depth) [Gianelli, 2008]. At crustal-scale, a series of low-angle normal faults accommodate the exhumation of MCCs [*e.g.* Faccenna *et al.*, 1997; Jolivet *et al.*, 1998]. These HT metamorphic domes and associated magmatism (*i.e.* granitic intrusions and volcanism) migrate from west to east close to the trench from 30 – 25 Ma to the Present [*e.g.* Jolivet *et al.*, 1998]. Nevertheless, alternative models show a more complex tectonic evolution from the Miocene to the Pleistocene (*i.e.* alternating extensive and compressive tectonics) [*e.g.* Bonini & Sani, 2002]. The Larderello geothermal field, located in the Apennines (southern Tuscany), is a direct consequence of this particular geodynamical setting. Although it is clear that the local heat source is associated with a shallow intrusive at 4 km depth [*e.g.* Gianelli, 2008; Santilano *et al.*, 2015], seismic profiles show that

normal listric faults root at the ductile-brittle transition at 4 − 5 km depth [Bellani *et al.*, 2004]. According to these authors, these faults control fluids circulation in the upper crust. Furthermore, this region is also marked by a significant thermal anomaly related to the thermal relaxation of a first crustal thickening event, but also to the extensional event induced by slab rollback (as in the Aegean domain, which is characterized by detachments and associated intrusives). In this example, the usual classification of this geothermal field in a magmatic context underestimates the importance of a deeper heat source at the base of the crust. This may prevent the discovery of new HEGS in the Larderello area.

VII.4.2.2. The case of the mantle windows (e.g. the Basin & Range, West America)

Despite many similarities with the geothermal Province of the Menderes Massif, the deep dynamics that controls the heat source in the Basin & Range, is different (Fig. VII.6). According to Schellart *et al.* [2010], mantle flows are the source of slab/trench migration. Precisely, in the Eocene, a drastic change of the conditions of subduction dynamics modified the tectono-metamorphic evolution in this region. Because of different subduction velocities on either side of the Pacific-Farallon-North American triple junction (Fig. VII.6b), a first slab window occurred [Schellart *et al.*, 2010]. According to this study, this mantle window favors the westward rollback of the Farallon plate. Similar to the Menderes case, this slab dynamics (mainly controlled by mantle flows) triggers first the gravitational collapse of part of the Laramides orogen, and is then responsible for extensional deformation distributed over a large area as evidenced by the presence of MCCs, extending from the Rocky Mountains to Sierra Nevada, as well as in the northern Rockies Mountains in the US and Canada [Wernicke, 1992] (Fig. VII.6b). Around 30 Ma, a second major event further modifies the regional tectonic evolution: a new slab window located under California starts to localize (Fig. VII.6c) [Atwater, 1970]. In response to this new mantle flows, a second extensional event occurs during this period. It is accommodated by low-angle normal faults that exhume new MCCs in the southern Basin & Range (Fig. VII.6c). Since 15 Ma, mainly controlled by fast mantle flow, slab rollback is accelerating and extension is mainly located in the central part of the Basin & Range, just above the Californian window (Fig. VII.6d) [Schellart *et al.*, 2010]. As already presented (*cf. I.2.1.2.*), this region is characterized by HEGS (Fig. VII.6f) (*e.g.* 280 ° C at a depth of 3 km, Dixie Valley [Blackwell *et al.*, 2000]). It is likely that subduction dynamics associated with both mantle windows induce significant thermal anomalies in the post-orogenic domain. Similar to the Menderes Massif, extension induces crustal-scale detachments and/or listric faults that accommodate the exhumation of MCCs. These faults represent the main control on the location of geothermal fields in this area. In addition, it is important to note the existence of kilometric transfer faults (dextral or sinistral) that accommodate the deformation over several tens of kilometers. These structures seem to facilitate the emergence of thermal springs but also the ascent of magma in the upper

crust, and thus explain the presence of magmatic geothermal fields such as the Geysers and Salton Trough (Fig. VII.6f).

VII.4.2.3. Subduction dynamics and others HEGS

At first glance, there is a strong correlation between the location of HEGS and the edges of slabs (Fig. VII.7a). According to Funiciello *et al.* [2003], Faccenna *et al.* [2004; 2005] or Schellart *et al.* [2007], slab roll-back is facilitated by mantle flows near the lateral edges of slabs (Fig. I.14b). The narrow subduction zones (≤ 1,500 km) are characterized by fast slab-rollback, and are thus considered as the best place for geothermal exploration (Fig. VII.7b). Under these conditions (*e.g.* similar to the Menderes Geothermal Province), the origin of heat on world-class geothermal systems such as New-Zealand (*e.g.* Kawerau, Nga Awa Purua, Ngatamariki, Ohaaki, Poihipi, Te Mihi, Wairakei) New-Guinea (*e.g.* Linhir), Indonesia (*e.g.* Sarulla) could be directly related to the absence of the slab or a tearing of the slab (Fig. VII.7a). In addition, even if the preliminary results of 3D numerical models suggest a rapid transfer of heat to the base of the crust, no generality on the timing of the propagation of these anomalies can be asserted. Indeed, the large variability of subduction zones and associated dynamics implies a fortiori a high diversity in the propagation of thermal anomalies in the upper plate. For example, Schellart *et al.* [2007] show that the maximum velocities are between 6 – 16 $cm.y^{-1}$ near to the slab borders, often exceeding 10 – 15 $cm.y^{-1}$ [Faccenna *et al.*, 2004; Nicolosi *et al.*, 2006], thus confirming that the fast retreat of narrow slab. These high values therefore suggest the presence of fast mantle flows and probably a significant mantle deformation that favors the shear heating component. In the continuity of the work of Lallemand *et al.* [2005] and Heuret & Lallemand [2005], (i) a synthetic bibliographic approach based mainly on the geometry of the slab (*e.g.* the slab angle) and on the location of HT thermal springs, and (ii) a numerical approach (*e.g.* the dip of the slab and the velocity of the retreat) would bring new constraints on the knowledge of large scale heat transfer around subduction zones.

VII.5. Références

Altherr, R., Schliestedt, M., Okrusch, M., Seidel, E., Kreuzer, H., Harre, W., ... & Wagner, G. A. (1979). Geochronology of high-pressure rocks on Sifnos (Cyclades, Greece). Contributions to Mineralogy and Petrology, 70(3), 245-255.

Andriessen, P. A. M., Banga, G., & Hebeda, E. H. (1987). Isotopic age study of pre-Alpine rocks in the basal units on Naxos, Sikinos and Ios, Greek Cyclades. Geologie en Mijnbouw, 66(3), e14.

Armijo, R., Meyer, B., Hubert, A., & Barka, A. (1999). Westward propagation of the North Anatolian fault into the northern Aegean: Timing and kinematics. Geology, 27(3), 267-270.

Armijo, R., Flerit, F., King, G., & Meyer, B. (2003). Linear elastic fracture mechanics explains the past and present evolution of the Aegean. Earth Planet Sci Lett 217:85–95. doi:10.1016/S0012-821X(03)00590-9

Atwater, T. (1970). Implications of plate tectonics for the Cenozoic tectonic evolution of western North America. Geological Society of America Bulletin, 81(12), 3513-3536.

Aydın, İ., Karat, H. İ., & Koçak, A. (2005). Curie-point depth map of Turkey. Geophysical Journal International, 162(2), 633-640.

Baba, A., Şimşek, C., Gündüz, O., Elçi, A., & Murathan, A. (2015). Hydrogeochemical Properties of Geothermal Fluid and Its Effect on the Environment in Gediz Graben, Western Turkey.

Beaudoin, A., Augier, R., Laurent, V., Jolivet, L., Lahfid, A., Bosse, V., ... & Menant, A. (2015). The ikaria high-temperature metamorphic core complex (Cyclades, Greece): geometry, kinematics and thermal structure. Journal of Geodynamics, 92, 18-41.

Bellani, S., Brogi, A., Lazzarotto, A., Liotta, D., & Ranalli, G. (2004). Heat flow, deep temperatures and extensional structures in the Larderello Geothermal Field (Italy): constraints on geothermal fluid flow: Journal of Volcanology and Geothermal Research, 132(1), 15-29.

Bijwaard, H., Spakman, W., & Engdahl, E. R. (1998). Closing the gap between regional and global travel time tomography. Journal of Geophysical Research: Solid Earth, 103(B12), 30055-30078.

Bilim, F., Akay, T., Aydemir, A., & Kosaroglu, S. (2016). Curie point depth, heat-flow and radiogenic heat production deduced from the spectral analysis of the aeromagnetic data for geothermal investigation on the Menderes Massif and the Aegean Region, western Turkey. Geothermics, 60, 44-57.

Biryol, C., Beck, S. L., Zandt, G., & Özacar, A. A. (2011). Segmented African lithosphere beneath the Anatolian region inferred from teleseismic P-wave tomography. Geophysical Journal International, 184(3), 1037–1057. https://doi.org/10.1111/j.1365-246X.2010.04910.x

Blackwell, D. D., Golan, B., & Benoit, D. (2000). Thermal regime in the Dixie Valley geothermal system. Geothermal Resources Council Transactions, 24, 223-228.

Bonini, M., & Sani, F. (2002). Extension and compression in the Northern Apennines (Italy) hinterland: Evidence from the late Miocene-Pliocene Siena-Radicofani Basin and relations with basement structures. Tectonics, 21(3).

Bonneau, M. (1984). Correlation of the Hellenide nappes in the south-east Aegean and their tectonic reconstruction. Geological Society, London, Special Publications, 17(1), 517–527. https://doi.org/10.1144/GSL.SP.1984.017.01.38

Bonneau, M., & Kienast, J. R. (1982). Subduction, collision et schistes bleus; l'exemple de l'Egee (Grece). Bulletin de La Société Géologique de France, S7–XXIV(4), 785–791. https://doi.org/10.2113/gssgfbull.S7-XXIV.4.785

Bozkurt, E. (2002). Discussion on the extensional folding in the Alaşehir (Gediz) Graben, western Turkey. Journal of the Geological Society, London 159, 105–09.

Brichau, S., Ring, U., Carter, A., Bolhar, R., Monié, P., Stockli, D., & Brunel, M. (2008). Timing, slip rate, displacement and cooling history of the Mykonos detachment footwall, Cyclades, Greece, and implications for the opening of the Aegean Sea basin. Journal of the Geological Society, 165(1), 263-277.

Brun, J. P., Faccenna, C., Gueydan, F., Sokoutis, D., Philippon, M., Kydonakis, K., & Gorini, C. (2017). Effects of slab rollback acceleration on aegean extension. Bulletin of the Geological Society of Greece, 50(1), 5-23.

Candan, O., Koralay, O. E., Akal, C., Kaya, O., Oberhänsli, R., Dora, O. Ö., ... & Chen, F. (2011). Supra-Pan-African unconformity between core and cover series of the Menderes Massif/Turkey and its geological implications. Precambrian Research, 184(1), 1-23.

Catlos E.J., & Cemen, I. (2005). Monazite ages and the evolution of the Menderes Massif, western Turkey. Int J Earth Sci 94:204–217.

Cenki-Tok, B., Expert, M., Işık, V., Candan, O., Monié, P., & Bruguier, O. (2016). Complete Alpine reworking of the northern Menderes Massif, western Turkey. International Journal of Earth Sciences, 105(5), 1507–1524. https://doi.org/10.1007/s00531-015-1271-2

Denele, Y., Lecomte, E., Jolivet, L., Lacombe, O., Labrousse, L., Huet, B., & Le Pourhiet, L. (2011). Granite intrusion in a metamorphic core complex: the example of the Mykonos laccolith (Cyclades, Greece). Tectonophysics, 501(1), 52-70.

Dong, G., Morrison, G., & Jaireth, S. (1995). Quartz textures in epithermal veins, Queensland; classification, origin and implication. Economic Geology, 90(6), 1841-1856.

Duprat-Oualid, S., Yamato, P., & Pitra, P. (2013). Major role of shear heating in intracontinental inverted metamorphism: Inference from a thermo-kinematic parametric study. Tectonophysics, 608, 812-831.

Ebert, S. W., & Rye, R. O. (1997). Secondary precious metal enrichment by steam-heated fluids in the Crofoot-Lewis hot spring gold-silver deposit and relation to paleoclimate. Economic Geology, 92(5), 578-600.

Ersoy, E. Y., & Palmer, M. R. (2013). Eocene-Quaternary magmatic activity in the Aegean: implications for mantle metasomatism and magma genesis in an evolving orogeny. Lithos, 180, 5-24.

Faccenna, C., Mattei, M., Funiciello, R. & Jolivet, L. (1997). Styles of back-arc extension in the Central Mediterranean: Terra Nova, 9, 126-130.

Faccenna, C., Piromallo, C., Crespo-Blanc, A., Jolivet, L., & Rossetti, F. (2004). Lateral slab deformation and the origin of the western Mediterranean arcs. Tectonics, 23(1), n/a-n/a. https://doi.org/10.1029/2002TC001488

Faccenna, C., Civetta, L., D'Antonio, M., Funiciello, F., Margheriti, L., & Piromallo, C. (2005). Constraints on mantle circulation around the deforming Calabrian slab. Geophysical Research Letters, 32(6).

Famin, V. (2004). Fluid circulation in a ductile shear zone (Tinos, Cyclades, Greece): Mechanisms and tectonic implications. PhD Thesis.

Famin, V., Philippot, P., Jolivet, L., & Agard, P. (2004). Evolution of hydrothermal regime along a crustal shear zone, Tinos Island, Greece. Tectonics, 23(5).

Fontboté, L., Kouzmanov, K., Chiaradia, M., & Pokrovski, G. S. (2017). Sulfide minerals in hydrothermal deposits. Elements, 13(2), 97-103.

Foumier, R. O. (1991). The transition from hydrostatic to greater than hydrostatic fluid pressure in presently active continental hydrothermal systems in crystalline rock. Geophysical Research Letters, 18(5), 955-958.

Franz, L., & Okrusch, M. (1992). Aragonite-bearing blueschists on Arki island, Dodecanese, Greece. European Journal of Mineralogy, 4, 527–537.

Franz, L., Okrusch, M., Seidel, E., & Kreuzer, H. (2005). Polymetamorphic evolution of pre-Alpidic basement relics in the external Hellenides, Greece. Neues Jahrbuch Für Mineralogie - Abhandlungen, 181(2), 147–172. https://doi.org/10.1127/0077-7757/2005/0013

Funiciello, F., Faccenna, C., Giardini, D., & Regenauer-Lieb, K. (2003). Dynamics of retreating slabs: 2. Insights from three-dimensional laboratory experiments. Journal of Geophysical Research: Solid Earth, 108(B4).

Gevrek, A. İ., Karamanderesi, İ. H., & Aydın, Ş. N. (1989). Clay mineralogy and hydrothermal alteration studies on Aydın-Germencik geothermal wells. Bildiriler kitabı. Pp:11 -121. IV. Ulusal Kil Sempozyunu, 20-23 Eylül 1989.

Gessner, K., Piazolo, S., Güngör, T., Ring, U., Kröner, A., & Passchier, C. W. (2001). Tectonic significance of deformation patterns in granitoid rocks of the Menderes nappes, anatolide belt, Southwest Turkey. International Journal of Earth Sciences, 89(4), 766–780. https://doi.org/10.1007/s005310000106

Gessner, K., Gallardo, L. A., Markwitz, V., Ring, U., & Thomson, S. N. (2013). What caused the denudation of the Menderes Massif: Review of crustal evolution, lithosphere structure, and dynamic topography in southwest Turkey. Gondwana Research, 24(1), 243–274. https://doi.org/10.1016/j.gr.2013.01.005

Gessner, K., Markwitz, V., & Güngör, T. (2017). Crustal fluid flow in hot continental extension: tectonic framework of geothermal areas and mineral deposits in western Anatolia. Geological Society, London, Special Publications, 453, SP453-7.

Gianelli, G. (2008). A comparative analysis of the geothermal fields of Larderello and Mt. Amiata, Italy. Geothermal energy research trends. Nova Science, New York, 59-85.

Govers, R., & Fichtner, A. (2016). Signature of slab fragmentation beneath Anatolia from full-waveform tomography. Earth and Planetary Science Letters, 450, 10–19. https://doi.org/10.1016/j.epsl.2016.06.014

Grasemann, B., Huet, B., Schneider, D. A., Rice, A. H. N., Lemonnier, N., & Tschegg, C. (2018). Miocene postorogenic extension of the Eocene synorogenic imbricated Hellenic subduction channel: New constraints from Milos (Cyclades, Greece). GSA Bulletin.

Groves, D. I., Goldfarb, R. J., Gebre-Mariam, M., Hagemann, S. G., & Robert, F. (1998). Orogenic gold deposits: a proposed classification in the context of their crustal distribution and relationship to other gold deposit types. Ore geology reviews, 13(1), 7-27.

Groves, D. I., Goldfarb, R. J., Robert, F., & Hart, C. J. (2003). Gold deposits in metamorphic belts: overview of current understanding, outstanding problems, future research, and exploration significance. Economic geology, 98(1), 1-29.

Hedenquist, J. W., & Lowenstern, J. B. (1994). The role of magmas in the formation of hydrothermal ore deposits. Nature, 370(6490), 519-527.

Hedenquist, J. W., Arribas, A., & Gonzalez-Urien, E. (2000). Exploration for epithermal gold deposits. Reviews in Economic Geology, 13(2), 45-77.

Henjes-Kunst, F., & Kreuzer, H. (1982). Isotopic dating of pre-alpidic rocks from the island of Ios (Cyclades, Greece). Contributions to Mineralogy and Petrology, 80(3), 245-253.

Hetzel, R., & Reischmann, T. (1996). Intrusion age of Pan-African augen gneisses in the southern Menderes Massif and the age of cooling after Alpine ductile extensional deformation. Geological Magazine, 133(5), 565-572.

Heuret, A., & Lallemand, S. (2005). Plate motions, slab dynamics and back-arc deformation. Physics of the Earth and Planetary Interiors, 149(1), 31-51.

Jolivet, L., & Faccenna, C. (2000). Mediterranean extension and the Africa-Eurasia collision. Tectonics, 19(6), 1095–1106. https://doi.org/10.1029/2000TC900018

Jolivet, L., & Brun, J. P. (2010). Cenozoic geodynamic evolution of the Aegean. International Journal of Earth Sciences, 99(1), 109–138. https://doi.org/10.1007/s00531-008-0366-4

Jolivet, L., Faccenna, C., Goffé, B., Mattei, M., Rossetti, F., Brunet, C., … Parra, T. (1998). Midcrustal shear zones in postorogenic extension: Example from the northern Tyrrhenian Sea. Journal of Geophysical Research: Solid Earth, 103(B6), 12123–12160. https://doi.org/10.1029/97JB03616

Jolivet, L., Rimmelé, G., Oberhänsli, R., Goffé, B., & Candan, O. (2004). Correlation of syn-orogenic tectonic and metamorphic events in the Cyclades, the Lycian nappes and the Menderes massif. Geodynamic implications. Bulletin de La Societe Geologique de France, 175(3), 217–238. https://doi.org/10.2113/175.3.217

Jolivet, L., Lecomte, E., Huet, B., Denèle, Y., Lacombe, O., Labrousse, L., … Mehl, C. (2010). The North Cycladic Detachment System. Earth and Planetary Science Letters, 289(1–2), 87–104. https://doi.org/10.1016/j.epsl.2009.10.032

Jolivet, L., Faccenna, C., Huet, B., Labrousse, L., Le Pourhiet, L., Lacombe, O., … Driussi, O. (2013). Aegean tectonics: Strain localisation, slab tearing and trench retreat. Tectonophysics, 597–598, 1–33. https://doi.org/10.1016/j.tecto.2012.06.011

Jolivet, L., Menant, A., Sternai, P., Rabillard, A., Arbaret, L., Augier, R., … Le Pourhiet, L. (2015). The geological signature of a slab tear below the Aegean. Tectonophysics, 659, 166–182. https://doi.org/10.1016/j.tecto.2015.08.004

Karabulut, H., Paul, A., Ergün, T. A., Hatzfeld, D., Childs, D. M., & Aktar, M. (2013). Long-wavelength undulations of the seismic Moho beneath the strongly stretched Western Anatolia: Geophysical Journal International, 194(1), 450-464.

Karamanderesi, I. H. (1997). Geology and Hydrothermal Alteration of the Aydın-Salavatlỳ Geothermal Field. West. Anatolia Turk. Revis. Pap. Be Publ. Geothermic.

Kerrich, R., La Tour, T. E., & Willmore, L. (1984). Fluid participation in deep fault zones: evidence from geological, geochemical, and 18O/16O relations. Journal of Geophysical Research: Solid Earth, 89(B6), 4331-4343.

Király, Á., Capitanio, F. A., Funiciello, F., & Faccenna, C. (2017). Subduction induced mantle flow: Length-scales and orientation of the toroidal cell. Earth and Planetary Science Letters, 479, 284-297.

Koçyigit, A., Yusufoglu, H., & Bozkurt, E. (1999). Discussion on evidence from the Gediz Graben for episodic two-stage extension in western Turkey. Journal of the Geological Society, London, 156, 1240-1242.

Koralay, O. E., Candan, O., Chen, F., Akal, C., Oberhänsli, R., Satır, M., & Dora, O. Ö. (2012). Pan-African magmatism in the Menderes Massif: geochronological data from leucocratic tourmaline orthogneisses in western Turkey. International Journal of Earth Sciences, 101(8), 2055-2081.

Koukouvelas, I. K., & Aydin, A. (2002). Fault structure and related basins of the North Aegean Sea and its surroundings. Tectonics, 21(5).

Lagos, M., Scherer, E. E., Tomaschek, F., Münker, C., Keiter, M., Berndt, J., & Ballhaus, C. (2007). High precision Lu–Hf geochronology of Eocene eclogite-facies rocks from Syros, Cyclades, Greece. Chemical Geology, 243(1), 16-35.

Lallemand, S., Heuret, A., & Boutelier, D. (2005). On the relationships between slab dip, back-arc stress, upper plate absolute motion, and crustal nature in subduction zones. Geochemistry, Geophysics, Geosystems, 6(9).

Laurent, V., Jolivet, L., Roche, V., Augier, R., Scaillet, S., & Cardello, G. L. (2016). Strain localization in a fossilized subduction channel: Insights from the Cycladic Blueschist Unit (Syros, Greece). Tectonophysics, 672–673, 150–169.

Lips, A.L., Cassard, D., Sözbilir, H., Yilmaz, H., & Wijbrans, J. R. (2001). Multistage exhumation of the Menderes Massif, western Anatolia (Turkey). Int. J. Earth Sci. 89, 781–792.

Lister, G. S., Banga, G., & Feenstra, A. (1984). Metamorphic core complexes of Cordilleran type in the Cyclades, Aegean Sea, Greece. Geology, 12(4), 221. https://doi.org/10.1130/0091-7613(1984)12<221:MCCOCT>2.0.CO;2

Maluski, H. (1977). Application de la methode> 40Ar-> 39Ar aux mineraux des roches cristallines perturbees par des evenements thermiques et tectoniques en Corse. Bulletin de la Société géologique de France, 7(4), 849-855.

Marchev, P., Raicheva, R., Downes, H., Vaselli, O., Chiaradia, M., & Moritz, R. (2004). Compositional diversity of Eocene–Oligocene basaltic magmatism in the Eastern Rhodopes, SE Bulgaria: implications for genesis and tectonic setting. Tectonophysics, 393(1), 301-328.

Marchev, P., Kaiser-Rohrmeier, M., Heinrich, C., Ovtcharova, M., von Quadt, A., & Raicheva, R. (2005). 2: Hydrothermal ore deposits related to post-orogenic extensional magmatism and core complex formation: The Rhodope Massif of Bulgaria and Greece. Ore Geology Reviews, 27(1), 53-89.

Menant, A., Jolivet, L., Augier, R., & Skarpelis, N. (2013). The North Cycladic Detachment System and associated mineralization, Mykonos, Greece: Insights on the evolution of the Aegean domain. Tectonics, 32(3), 433-452.

Menant, A., Jolivet, L., & Vrielynck, B. (2016). Kinematic reconstructions and magmatic evolution illuminating crustal and mantle dynamics of the eastern Mediterranean region since the late Cretaceous. Tectonophysics, 675, 103–140. https://doi.org/10.1016/j.tecto.2016.03.007

Menant, A., Jolivet, L., Tuduri, J., Loiselet, C., Bertrand, G., & Guillou-Frottier, L. (2018). 3D subduction dynamics, a first-order control of the transition from copper- to 1 gold-rich deposits in the Eastern Mediterranean region. Ore Geology Reviews.

Mezri, L., Le Pourhiet, L., Wolf, S., & Burov, E. (2015). New parametric implementation of metamorphic reactions limited by water content, impact on exhumation along detachment faults. Lithos, 236, 287-298.

Nicolosi, I., Speranza, F., & Chiappini, M. (2006). Ultrafast oceanic spreading of the Marsili Basin, southern Tyrrhenian Sea: Evidence from magnetic anomaly analysis. Geology, 34(9), 717-720.

Okay, A. I., Tansel, İ., & Tueysuez, O. (2001). Obduction, subduction and collision as reflected in the Upper Cretaceous–Lower Eocene sedimentary record of western Turkey. Geological Magazine, 138(2), 117-142.

Özer, S., Sözbilir, H., Özkar, İ., Toker, V., & Sari, B. (2001). Stratigraphy of Upper Cretaceous-Palaeogene sequences in the southern and eastern Menderes Massif (western Turkey). International Journal of Earth Sciences, 89(4), 852-866.

Patzak, M., Okrusch, M., & Kreuzer, H. (1994). The Akrotiri Unit on the island of Tinos, Cyclades, Greece: Witness to a lost terrane of Late Cretaceous age.(With 18 figures and 8 tables in the text). Neues Jahrbuch fur Geologie und Palaontologie-Abhandlungen, 194(2), 211-252.

Person, M., Hofstra, A., Sweetkind, D., Stone, W., Cohen, D., Gable, C. W., & Banerjee, A. (2012). Analytical and numerical models of hydrothermal fluid flow at fault intersections. Geofluids, 12(4), 312-326.

Pik, R., & Marty, B. (2009). Helium isotopic signature of modern and fossil fluids associated with the Corinth rift fault zone (Greece): implication for fault connectivity in the lower crust. Chemical Geology, 266(1), 67-75.

Pourteau, A., Oberhänsli, R., Candan, O., Barrier, E., & Vrielynck, B. (2016). Neotethyan closure history of western Anatolia: a geodynamic discussion. International Journal of Earth Sciences, 105(1), 203-224.

Reischmann, T., Kroner, A., Todt, W., Dtirr, S., & Sengor, AMC. (1991). Episodes of crustal growth in the Menderes Massif, W Turkey, inferred from zircon dating. Terra Abstr 3:34

Richards, J. P. (2005). Cumulative factors in the generation of giant calc-alkaline porphyry Cu deposits, in Super Porphyry Copper & Gold Deposits: A Global Perspective, vol. 1, pp. 7–25, Porter T. M., Adelaide, Australia.

Richards, J. P. (2009). Postsubduction porphyry Cu-Au and epithermal Au deposits: Products of remelting of subduction-modified lithosphere. Geology, 37(3), 247-250.

Rimmelé, G., Jolivet, L., Oberhänsli, R., & Goffé, B. (2003). Deformation history of the high-pressure Lycian Nappes and implications for tectonic evolution of SW Turkey. Tectonics, 22(2), 1–21. https://doi.org/10.1029/2001TC901041

Rimmele, G., Oberhansli, R., Candan, O., Goffe, B., & Jolivet, L. (2006). The wide distribution of HP-LT rocks in the Lycian Belt (Western Turkey): implications for accretionary wedge geometry. Tectonic Development of the Eastern Mediterranean Region, 260(1), 447–466. https://doi.org/10.1144/gsl.sp.2006.260.01.18

Ring, U., Gessner, K., Güngör, T., & Passchier, C. W. (1999). The Menderes Massif of western Turkey and the Cycladic Massif in the Aegean—do they really correlate?. Journal of the Geological Society, 156(1), 3-6.

Ring, U., Johnson, C., Hetzel, R., & Gessner, K. (2003). Tectonic denudation of a Late Cretaceous–Tertiary collisional belt: regionally symmetric cooling patterns and their relation to extensional faults in the Anatolide belt of western Turkey. Geol. Mag. 140, 421–441.

Roche, V., Laurent, V., Cardello, G. L., Jolivet, L., & Scaillet, S. (2016). Anatomy of the Cycladic Blueschist Unit on Sifnos Island (Cyclades, Greece). Journal of Geodynamics, 97, 62–87. https://doi.org/10.1016/j.jog.2016.03.008

Rossetti, F., Asti, R., Faccenna, C., Gerdes, A., Lucci, F., & Theye, T. (2017). Magmatism and crustal extension: Constraining activation of the ductile shearing along the Gediz detachment, Menderes Massif (western Turkey). Lithos, 282, 145-162.

Santilano, A., Manzella, A., Gianelli, G., Donato, A., Gola, G., Nardini, I., ... & Botteghi, S. (2015). Convective, intrusive geothermal plays: what about tectonics?. Geothermal Energy Science, 3(1), 51-59.

Satir, M., & Friedrichsen, H. (1986). The origin and evolution of the Menderes Massif, W-Turkey: a rubidium/strontium and oxygen isotope study. Geologische Rundschau, 75(3), 703-714.

Schellart, W. P., Freeman, J., Stegman, D. R., Moresi, L., & May, D. (2007). Evolution and diversity of subduction zones controlled by slab width. Nature, 446(7133), 308-311.

Schellart, W. P., Stegman, D. R., Farrington, R. J., Freeman, J., & Moresi, L. (2010). Cenozoic tectonics of western North America controlled by evolving width of Farallon slab. Science, 329(5989), 316-319.

Schmidt, A., Pourteau, A., Candan, O., & Oberhänsli, R. (2015). Lu–Hf geochronology on cm-sized garnets using microsampling: New constraints on garnet growth rates and duration of metamorphism during continental collision (Menderes Massif, Turkey). Earth and Planetary Science Letters, 432, 24-35.

Schuiling, R. D. (1962). On petrology, age and structure of the Menderes migmatite complex (SW-Turkey). Bulletin of the Mineral Research and Exploration Institute of Turkey, 58, 71-84.

Sengör, A. M. C., Satir, M., & Akkök, R. (1984). Timing of tectonic events in the Menderes Massif, western Turkey: Implications for tectonic evolution and evidence for Pan-African basement in Turkey. Tectonics, 3(7), 693-707.

Seyitoğlu, G., Cemen, I., & Tekeli, O. (2000). Extensional folding in the Alaşehir (Gediz) graben, western Turkey. Journal of the Geological Society, 157(6), 1097-1100.

Sherlock, S. C., & Arnaud, N. O. (1999). Flat plateau and impossible isochrons: Apparent 40 Ar-39 Ar geochronology in a high-pressure terrain. Geochimica et Cosmochimica Acta, 63(18), 2835-2838.

Sibson, R. H., Moore, J. M. M., & Rankin, A. H. (1975). Seismic pumping a hydrothermal fluid transport mechanism: Journal of the Geological Society, 131(6), 653-659.

Sillitoe, R. H., & Hedenquist, J. W. (2003). Linkages between volcanotectonic settings, ore-fluid compositions, and epithermal precious metal deposits. Special Publication-Society of Economic Geologists, 10, 315-343.

Sözbilir, H., 2001. Extensional tectonics and the geometry of related macroscopic structures: field evidence from the Gediz detachment, western Turkey. Turk. J. Earth Sci. 10, 51–67.

Van Hinsbergen, D. J., Kaymakci, N., Spakman, W., & Torsvik, T. H. (2010). Reconciling the geological history of western Turkey with plate circuits and mantle tomography. Earth and Planetary Science Letters, 297(3), 674-686.

Vanderhaeghe, O. (2004). Structural development of the Naxos migmatite dome. Geological Society of America Special Papers, 380, 211-227.

Violay, M., Heap, M. J., Acosta, M., & Madonna, C. (2017). Porosity evolution at the brittle-ductile transition in the continental crust: Implications for deep hydro-geothermal circulation. Scientific Reports, 7(1), 7705.

Whitney, D. L., Teyssier, C., Kruckenberg, S. C., Morgan, V. L., & Iredale, L. J. (2008). High-pressure–low-temperature metamorphism of metasedimentary rocks, southern Menderes Massif, western Turkey. Lithos, 101(3), 218-232.

Wijbrans, J. R., Schliestedt, M., & York, D. (1990). Single grain argon laser probe dating of phengites from the blueschist to greenschist transition on Sifnos (Cyclades, Greece). Contributions to Mineralogy and Petrology, 104(5), 582-593.

Yılmaz, Y., Genç, Ş.C., Karacık, Z., Altunkaynak, Ş., 2001. Two contrasting magmatic associations of NW Anatolia and their tectonic significance. J. Geodyn. 31, 243–271.

CONCLUSION GENERALE

La région de la méditerranée orientale est une zone complexe caractérisée par différents événements HP-BT et HT-BP depuis le Crétacé. Entre ~ 35 Ma et 20 Ma un changement drastique de la dynamique de subduction affecte l'ensemble des unités tectono-métamorphiques dans la région. Le retrait vers le sud du panneau plongeant Hellénique et la formation d'une déchirure sous l'ouest de la Turquie déclenchent des instabilités thermiques de grandes longueurs d'onde. Cet excès de chaleur est dû (i) aux flux mantelliques liés au retrait et à la déchirure du slab mais également (ii) au shear heating induit par ces déformations supplémentaires rapides dans le manteau. Cette dynamique se traduit dans un premier temps par des événements magmatiques rapides et ponctuels comme le témoigne les nombreuses intrusions magmatiques, mais également par la présence de migmatites d'âge Miocène dans la région du Menderes et des Cyclades. Dans un second temps, sur une période de temps de plusieurs dizaines de millions d'années, ces instabilités affectent thermiquement et mécaniquement la croûte inférieure, qui est par conséquent sujette à (i) une rétromorphose dans les conditions métamorphiques du faciès des schistes verts ou amphibolites, voire à l'anatexie (*e.g.* les Cyclades) mais également à (ii) un boudinage thermo-mécanique induisant la mise en place de dômes métamorphiques (MCCs). Exhumés par l'intermédiaire de failles à faible pendage, nommées détachements, les dômes se développent dans le domaine arrière-arc de cette subduction. Ces failles crustales, caractérisées par une forte perméabilité, permettent aux fluides d'origine surfacique de circuler aisément dans la croûte sur plusieurs millions d'années : elles sont donc considérées comme le premier géothermotecte à l'échelle de la province géothermale.

LISTE DES FIGURES

CHAPITRE I

Figure I.1 : evolution de la capacité mondiale d'électricité géothermique installée (en MWe) et produite (en GWh) depuis 1950 d'après Bertani [2015]. 19

Figure I.2 : carte mondiale indiquant la localisation des champs géothermaux de références selon leurs contextes géodynamiques [Moeck, 2014], quel que soit l'usage (électricité et/ou chaleur). 21

Figure I.3 : classification des systèmes géothermaux selon leurs températures de réservoir et leurs applications respectives d'après le BRGM (Bureau de recherches géologiques et minières) et ADEME (Agence de l'environnement et de la maîtrise de l'énergie). 22

Figure I.4 : similitudes entre les modèles conceptuels actifs et fossiles de systèmes géothermaux magmatiques de HT. 24

Figure I.5 : différents phénomènes géothermaux. 26

Figure I.6 : carte montrant la corrélation entre les principaux champs géothermaux de HT en activité et en construction (étoile blanche et rond rouge) et les principales zones de subduction dans le monde, modifié d'après Schellart *et al*. [2007]. 28

Figure I.7 : modèles conceptuels actifs de systèmes géothermaux magmatiques de HT. 31

Figure I.8 : schémas conceptuels d'une zone de subduction, de collision, de post-collision et d'extension arrière-arc. 34

Figure I.9 : profil MT à travers le Basin & Range d'après Wannamaker *et al*. [2006b]. 37

Figure 1.10 : représentations schématiques de systèmes géothermaux associés à une activité tectonique. 38

Figure I.11 : les circulations au sein d'une zone de cisaillement. Il est important de noter les similitudes entre les deux modèles. 40

Figure I.12 : schéma conceptuel et répartition des zones de subduction à l'échelle mondiale. 44

Figure I.13 : les principales forces à l'œuvre et les modèles géodynamiques associés. 47

Figure I.14 : zones de subduction et flux mantelliques à différentes échelles. 51

Figure I.15 : flux de chaleur orogénique et anomalies thermiques. 53

Figure I.16 : cartes de la Méditerranée orientale. 56

Figure I.17 : cartes paléotectoniques de la Méditerranée orientale extraites du modèle de reconstruction cinématique de Menant *et al*. [2016a], mettant en évidence la distribution spatiale et temporelle des occurrences minéralisées depuis le Crétacé supérieur jusqu'au Miocène. 58

Figure I.18 : cartes de la Méditerranée orientale. 60

CHAPITRE II

Figure II.1 : carte tectonique de la région Méditerranéenne orientale simplifiée montrant les principaux domaines géologiques modifiée d'après le MTA (Mineral Research & Exploration General Directorate) soit l'équivalent du BRGM et d'après Jolivet *et al*. [2013]. 78

Figure II.2 : représentations schématiques de systèmes géothermaux dans le Massif du Menderes associés à une activité volcanique modifié d'après Bülbül et al. [2011] et à une activité tectonique modifié d'après Kaya [2015]. 79

Figure II.3: Tectonic map of eastern Mediterranean region highlighting the main tectono-metamorphic domains and showing location of the study area. Modified from Jolivet *et al*. [2013]. 87

Figure II.4: Plot of δD vs δ18O diagram for different water types. 90

Figure II.5: Isotopic composition of Helium. 92

Figure II.6: Geological and tectonic map of the Alaşehir graben modified from Asti, [2015]. 94

Figure II.7: Kinematic of deformation associated with the Alaşehir detachment in the Salihli area. 96

Figure II.8: Brittle deformation in the Salihli area. 97

Figure II.9: Brittle deformation associated with the Alaşehir detachment in the Alaşehir area. 99

Figure II.10: Brittle deformation in the Alaşehir area. 101

Figure II.11: Brittle deformation in the Salavatlı area. 103

Figure II.12: Stuctures and geothermal activities in the Germencik geothermal field. 104

Figure II.13: Brittle deformation in the Seferihisar area. 106

Figure II.14: Conceptual models at different scales showing the heat source origin and main structural controls on fluid flows in the Menderes Massif. 115

CHAPITRE III

Figure III.1: Upper crustal and upper mantle structures of the Eastern Agean domain and the Western Anatolia. 147

Figure III.2: New geological and tectonic maps of Leros Island modified from Stavropoulos and Gerolymatos [1999]. 149

Figure III.3: Tectonic map of Leros with main cross-sections. 151

Figure III.4: Kinematics of ductile deformation in Temenia Unit. 153

Figure III.5: Large-scale boudinage of the Marina and Temenia units. 154

Figure III.6: Kinematic of brittle deformation in both units. 156

Figure III.7: RSCM distribution and metamorphic record on Leros showing the main metamorphic index minerals. 158

Figure III.8: Metamorphic record on Leros. 160

Figure III.9: P-T grid showing the stability field of the aragonite with T_{max} estimated by the RSCM method. 164

CHAPITRE IV

Figure IV.1: Tectonic map of the eastern Mediterranean region and the location of the study area modified from Jolivet & Brun [2010]. 188

Figure IV.2: Compilation of P-T paths. 192

Figure IV.3: Geological and foliation maps of Samos and Fourni islands. 198

Figure IV.4: Geological and foliation maps of Dodecanese islands. 201

Figure IV.5: Metamorphic observations on Samos. 205

Figure IV.6: Metamorphic record on Fourni and on the Dodecanese islands. 207

Figure IV.7: Kinematic of deformation in Samos. 211

Figure IV.8: Structure markers on Fourni Island. 213

Figure IV.9: Kinematic of deformation on Fourni. 215

Figure IV.10: Geological and stretching lineation maps of Arki, Lipsi and Leros islands. 217

Figure IV.11: Structures markers and kinematics of deformation in the Dodecanese islands. 220

Figure IV.12: Brittle structures on Fourni and Thymaena islands. 222

Figure IV.13: Brittle structures on Dodecanese ans Samos islands. 224

Figure IV.14: Synthetic tectono-stratigraphic sequences of the eastern Mediterranean region. 229

Figure IV.15: Possible correlations based on metamorphic markers. 233

Figure IV.16: Tectonic map of the eastern Mediterranean region showing the main tectonic structures and associated kinematic indicators. 235

CHAPITRE V

Figure V.1: différents modèles expliquant la formation de la partie sud du MCC. 260

Figure V.2: les différentes unités métamorphiques observées dans la région du Menderes. 261

Figure V.3: Main tectonic units of Western Anatolia. 267

Figure V.4: Main tectono-metamorphic units of the Menderes Massif area. 272

Figure V.5: Kinematic of deformation in the Salihli, Alaşehir, Urganlı and Bozdag - Birgi areas. 275

Figure V.6: Kinematic of deformation in the Halıköy - Sultanhisar and Salavatlı areas. 278

Figure V.7: Kinematic of deformation in the Büyük Menderes grabenSelimiye area. 279

Figure V.8: Kinematic of deformation in the Selimiye area and in the SMM. 282

Figure V.9: Geochronological age with mica composition and RSCM temperatures results in the CMM and SMM. 288

Figure V.10: Main ^{40}Ar-^{39}Ar results in the northern part of CMM. 290

Figure V.11: Main ^{40}Ar-^{39}Ar results in the southern part of CMM. 292

Figure V.12: Main ^{40}Ar-^{39}Ar results in the SMM. 294

Figure V.13: Main ^{40}Ar-^{39}Ar results in carpholite bearin rocks near Kurudere. 295

Figure V.14: Tera-Wasserburg and Th–Pb plots of monazite. 297

Figure V.15: Simplified cross-sections showing the distribution of RSCM temperature results. 302

Figure V.16: Synthesis of geochronological ages in the entire MMCC. 305

Figure V.17: Geodynamic evolution of the study area. 310

Figure V.18: Exhumation paths calculated from cooling ages of different mineral. 315

Figure V.19: Sample location. 322

CHAPITRE VI

Figure VI.1: The major subduction zones on Earth (modified from Schellart *et al*. [2007]). 352

Figure VI.2: Simplified tectonic and tomographic maps of the study area. 354

Figure VI.3: Numerical setup. 356

Figure VI.4: Thermo-mechanical evolution of the model. 358

Figure VI.5: Mantle heat source with and without tearing at the mantle-crust transition. 360

Figure VI.6: Plan view of temperature anomaly at the mantle-crust transition (~ 45 km depth) in the case of slab tearing. 361

Figure VI.7: 2-D models of fluid circulation in the upper crust of the Menderes area. 363

Figure VI.8: Results for thermal perturbations due to fluid circulation in permeable zones. 365

Figure VI.9: Results for the experiment shown in the lower case of Figure VI.8a. 366

Figure VI.10: Schematic cross-section showing fluid flow associated with detachment zone in back-arc area. 370

Figure VI.11: Maps of the Aegean-Anatolian region. 373

Figure VI.12: Experimental setup without slab tearing. 374

Figure VI.13: Simplified tectonic map of the northern Tyrrhenian and Apennines areas. 375

CHAPITRE VII

Figure VII.1 : synthèse tectono-métamorphique de la région est-méditerranéenne montrant l'évolution depuis 50 Ma jusqu'à l'Actuel. 391

Figure VII.2 : synthèse des travaux sur les îles du Dodécanèse et des îles de l'est de l'Egée. 395

Figure VII.3 : synthèse des données numériques. 400

Figure VII.4 : synthèse sur la possible circulation des fluides à différentes échelles. 405

Figure VII.5 : évolution d'une zone de subduction classique présentant différents systèmes HT. 410

Figure VII.6 : évolution de la plaque Farallon au Cénozoïque, d'après Schellart *et al*. [2010] : conséquences thermiques. 413

Figure VII.7 : dynamique de subduction et implications sur la localisation des champs géothermaux de HT. 415

LISTE DES TABLES

CHAPITRE II

Table II.1: Catalog of hot springs and geothermal fields associated with the metamorphic core complex formation in the Menderes Massif. 107

Table II.2: Main controls on geothermal fields in the Menderes Massif. 110

CHAPITRE III

Table III.1: RSCM results in all units. 162

Table III.2: Representative blue amphibole chemical analyses from Leros Island. 169

Table III.3: Representative phengite chemical analyses from Leros Island. 170

Table III.4: Representative epidote chemical analyses from Leros Island. 171

Table III.5: Representative chlorite chemical analyses from Leros Island. 172

CHAPITRE V

Table V.1: ^{40}Ar-^{39}Ar step heating results from the Menderes Massif. 285

Table V.2: ^{40}Ar-^{39}Ar and U-Pb *in situ* data from the Menderes Massif. 289

Table V.3: Results of Raman spectra performed on samples from the Menderes Massif. 299

Table V.4: Monazite analyses conditions. 320

Table V.5: ^{40}Ar-^{39}Ar *in situ result* of sample M115-15. 323

Table V.6: ^{40}Ar-^{39}Ar *in situ* result of sample M69-16. 324

Table V.7: ^{40}Ar-^{39}Ar *in situ* result of sample M89-15. 325

Table V.8: 40Ar-39Ar step heating result of sample M140-15. 326

Table V.9: 40Ar-39Ar step heating result of sample M47-16. 327

Table V.10: U-Pb results from the sample M24-16. 329

Table V.11: U-Pb results from the sample M120-15. 329

Table V.12: Sample M127-15 (muscovite). 331

Table V.13: Sample M89b-15 (muscovite). 332

Table V.14: Sample M115-15 (biotite). 332

Table V.15: Compilation of ^{40}Ar-^{39}Ar, K-Ar and Rb-Sr data. 333

Table V.16: Compilation of Zircon fission-track. 334

Table V.17: Compilation of Zircon fission-track. 335

CHAPITRE VI

Table VI.1: Material properties used in the 3D numerical modelling. 379

Table VI.2: Main parameters of 2D numerical modelling. 380

ANNEXES

Lexique (Annexe A)

EJ (Exa Joules) : représente $12{,}6 \times 10^{30}$ Joules.

Epithermal : gîte métallique associé à la circulation de fluides hydrothermaux dans un environnement superficiel (0 – 2 km de profondeur) à faible température (50 – 200 °C). Ce gîte correspond à un système hydrothermal fossile qui constitue généralement l'apex volcanique des systèmes porphyriques (*i.e.* localisés immédiatement au-dessus de la chambre magmatique).

Cap rock : représente une roche couverture (*i.e.* à faible perméabilité) qui favorise le développement de cellules de convection dans un réservoir.

Champ géothermal : représente une expression de surface : *e.g.* les sources thermales, les fumerolles, zone d'altération associées…

Conduction : transfert de chaleur d'un point à un autre sous l'effet d'une différence de température.

Convection : transfert de chaleur induit par un déplacement (vertical et horizontal) d'un fluide accompagné d'un transport de matière.

Détachement : faille à faible pendage qui accommode l'exhumation de roches métamorphiques de haute température (généralement).

Géothermotecte : représente les caractéristiques géologiques, géophysiques ou géochimiques d'un système qui guide l'exploration géothermale à la recherche d'un système similaire.

GWe (Gigawatt-électrique) : unité de puissance qui désigne la capacité de production électrique d'une centrale électrique.

GWh (Gigawattheure) : correspond à la quantité d'électricité fournie en une heure par une puissance de 1 GWe.

Hydrothermalisme : circulation d'un fluide aqueux chaud dont l'origine varie selon l'endroit (*e.g.* météorique, magmatique ou métamorphique). Ce fluide est généralement chargé en substances (*e.g.* métaux et gaz) dissoutes.

MCC : représente un dôme de roches métamorphiques dont le cœur est souvent associé à des migmatites. Ce dôme est exhumé par une faille à faible pendage.

Porphyre : représente ici un gîte métallique associé à un système plutonique dont les minéralisations sont principalement riches en Cu-Mo.

Réservoir : représente un endroit à forte perméabilité où les cellules de convection permettent l'homogénéisation de la température sur plusieurs dizaines voire centaines de mètres de hauteur.

Système géothermal : représente un ensemble d'objets qui définit la géométrie globale du système : expression de surface, réservoir, cap rock, recharge, source de chaleur…

Shear heating : quantité de chaleur produite par « mécanisme de chauffage » dans la croûte ou dans le manteau.

Anatomy of the Cycladic Blueschist Unit on Sifnos Island (Cyclades, Greece) (Annexe B)

Vincent ROCHE[1, 2, 3], Valentin LAURENT[1, 2, 3], Giovanni Luca CARDELLO[1, 2, 3], Laurent JOLIVET[1, 2, 3], Stéphane SCAILLET[1, 2, 3]

[1] Université d'Orléans, ISTO, UMR 7327, 45071, Orléans, France

[2] CNRS/INSU, ISTO, UMR 7327, 45071 Orléans, France

[3]BRGM, ISTO, UMR 7327, BP 36009, 45060 Orléans, France

(Cet article a été publié à Journal of Geodynamics)

Journal of Geodynamics 97 (2016) 62–87

Contents lists available at ScienceDirect

Journal of Geodynamics

journal homepage: http://www.elsevier.com/locate/jog

Anatomy of the Cycladic Blueschist Unit on Sifnos Island (Cyclades, Greece)

Vincent Roche[a,b,c,*], Valentin Laurent[a,b,c], Giovanni Luca Cardello[a,b,c], Laurent Jolivet[a,b,c], Stéphane Scaillet[a,b,c]

[a] Université d'Orléans, ISTO, UMR 7327, 45071 Orléans, France
[b] CNRS/INSU, ISTO, UMR 7327, 45071 Orléans, France
[c] BRGM, ISTO, UMR 7327, BP 36009, 45060 Orléans, France

ARTICLE INFO

Article history:
Received 11 December 2015
Received in revised form 11 March 2016
Accepted 17 March 2016
Available online 24 March 2016

Keywords:
High-pressure and low-temperature metamorphism
Syn-orogenic exhumation
Post-orogenic extension
Strain localization
Sifnos
Aegean domain

ABSTRACT

Since 35 Ma, the kinematics of the Aegean domain has been mainly controlled by the southward retreat of the African slab, inducing back-arc extension. The main structures and associated kinematics are well constrained, but the kinematics of deformation before 35 Ma, coeval with the exhumation of blueschists and eclogites of the Cycladic Blueschist Unit, is still poorly understood. The earlier Eocene syn-orogenic evolution is strongly debated and very different geometrical interpretations and kinematic histories have been proposed in the literature. This study focuses on the high-pressure and low-temperature (HP-LT) parageneses spectacularly exposed and well preserved on Sifnos Island. The new field work provides new structural constraints on the tectonic history of HP-LT units generated in the subduction zone during the Eocene. It further shows how lithological heterogeneities localize strain within an accretionary wedge and how the localisation of strain evolves through time during exhumation. We show, through new geological and metamorphic maps, cross-sections and analyses of kinematic indicators, that Sifnos is characterized by shallow-dipping shear zones reactivating weak zones due to competence contrasts or earlier tectonic contacts. Structures and kinematics associated with these shear zones, show a top-to-the-N to −NE ductile deformation. The lower part of the tectonic pile shows a downward gradient of shearing deformation and is actually a thick top-to-the-NE shear zone, which we name the Apollonia Shear Zone. Through time shearing deformation tends to localize downward, leaving the upper part of the subduction complex preserved from late deformation. The present-day shape and topography of the island is largely controlled by late brittle faults reworking the earlier ductile shear zones. Comparing with the nearby island of Syros, we propose a new tectono-metamorphic evolution of the Cycladic Blueschist Unit, which partly explains the different degrees of retrogression observed on the Cycladic Islands.

1. Introduction

The exposure of high-pressure and low-temperature (HP-LT) metamorphic rocks results from the exhumation of material buried along the plate interface in subduction zones. Part of the exhumation can be achieved during subduction in different ways: 1) by decoupling of crustal units of variable thickness from the subducting lithosphere within the plate interface (Chemenda et al., 1995; Jolivet et al., 2005; Brun and Faccenna, 2008; Agard et al., 2009; Jolivet and Brun, 2010; Ring et al., 2010; Tirel et al., 2013); 2) by circulation of weak material within a thick accretionary complex (corner flow model); 3) in the subduction channel (England and Holland, 1979; Shreve and Cloos, 1986; Platt, 1993; Burov et al., 2001 Gerya et al., 2002). The main difference between the different types of models is the degree of strain localization. The subduction channel concept is highly variable in the literature, from the initial simple double circulation model in the space left between the two plates (England and Holland, 1979; Shreve and Cloos, 1986) to more sophisticated models with several levels of circulation like in Burov et al. (2001). This type of models does not show the details of how tectonic units are finally decoupled from the subducting plate and it only suggests exhumation from large depth in low viscosity material, which implies distributed deformation in the channel. Other models, based on decoupling of crustal units of variable thickness from the subducting lithosphere (Chemenda et al., 1995; Jolivet et al., 2005; Brun and Faccenna, 2008; Agard et al., 2009; Jolivet and Brun, 2010; Ring et al., 2010; Tirel et al., 2013),

* Corresponding author at: Université d'Orléans, ISTO, UMR 7327, 45071 Orléans, France.
E-mail address: v.roche@brgm.fr (V. Roche).

http://dx.doi.org/10.1016/j.jog.2016.03.008

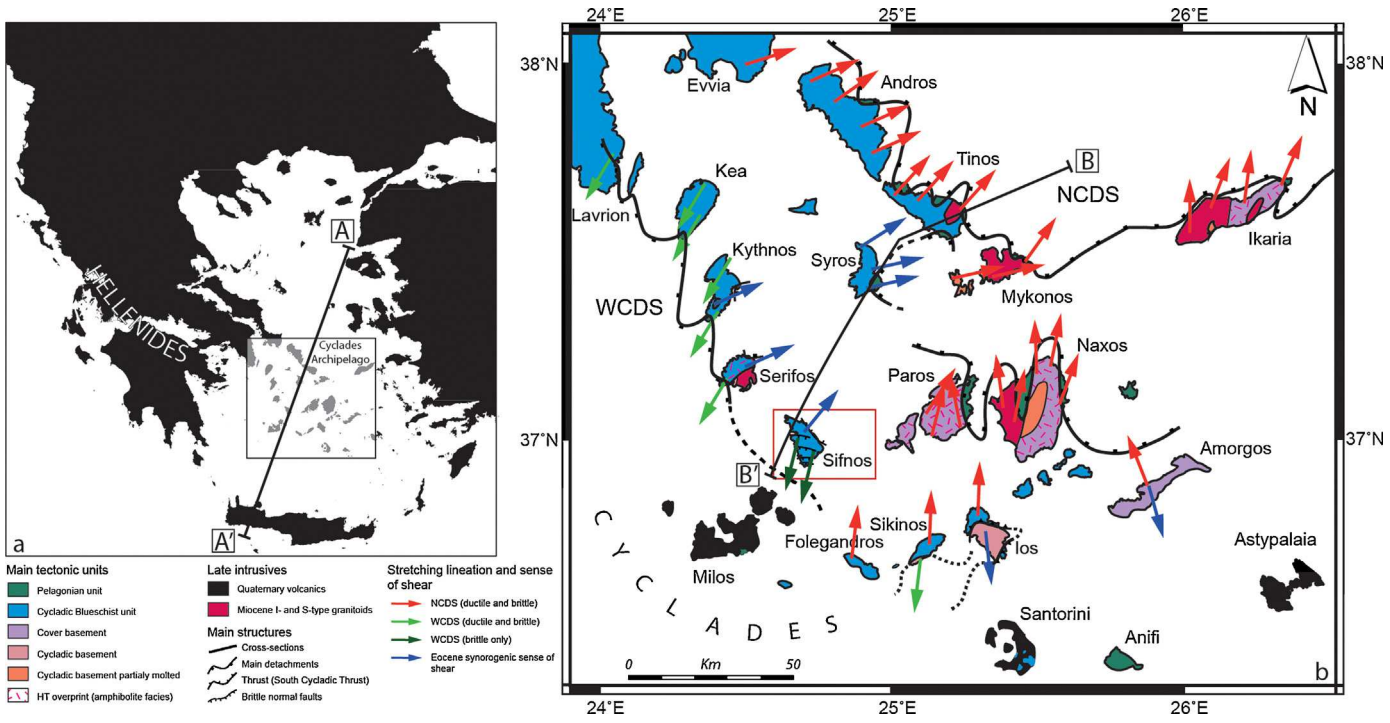

Fig. 1. Tectonic map of the Aegean domain.
Tectonic map of the Aegean domain and schematic geological map of the Cyclades showing the main structures related to both syn-orogenic and post-orogenic episodes, modified after Jolivet and Brun (2010). The original map has been modified incorporating recent works (Kumerics et al., 2005; Rosenbaum et al., 2007; Huet et al., 2009; Grasemann et al., 2012; Augier et al., 2015; Laurent et al., 2015; Beaudoin et al., 2015). Stretching-parallel cross-section through Aegean domain (Fig. 1a) and central Aegean (Fig. 1b) are indicated. Red box: Location of Sifnos.(For interpretation of the references to colour in this figure legend, the reader is referred to the web version of this article.)

also permit the exhumation of high-pressure rocks. However, the piece of crust is extruded upward between a frontal thrust and a normal fault above, which implies a strong localization close to this interface only. These models only differ from the precedent by the degree of localization of deformation. Depending on the size of the exhumed unit, the model is more or less similar to the basic subduction channel model. The extreme localization can be found in the propositions of Chemenda et al. (1995), or Brun and Faccenna (2008) where the exhumed unit is only one, totally rigid, between the frontal thrust and the normal fault. When exhumed units are more numerous and smaller the general picture is quite similar to the subduction channel model. Some of the main problems are thus the degree and the controlling factors of strain localization in subduction complexes. In this paper we show how strain was localized during exhumation through a new field study.

In the Cycladic Archipelago, the exhumation of HP-LT metamorphic rocks was achieved in two stages: the first stage corresponds to the exhumation within the subduction channel during Eocene and the second stage to the exhumation below shallow-dipping detachments in the back-arc region in the Oligocene and Miocene. In the following, we name the first stage 'syn-orogenic exhumation' as opposed to the second stage 'post-orogenic exhumation' for distinguishing exhumation acquired during lithospheric shortening from exhumation acquired during later lithospheric extension (Jolivet et al., 2003; Jolivet and Patriat, 1999; Jolivet et al., 2003,2013; Bonev and Beccaletto, 2007; Forster and Lister, 2009). The syn-orogenic part of exhumation, which is of concern here, is also controlled by kinematic boundary conditions of the subduction channel, with slab retreat probably favouring fast exhumation (Jolivet et al., 1994; Beaumont et al., 1996; Brun and Faccenna, 2008; Tirel et al., 2013). Metamorphic units may thus have different P-T-time histories, starting within the subduction channel in HP-LT conditions and ending within the back-arc region in high-temperature metamorphic core complexes.

Syros and Sifnos islands are located in the central part of the Cyclades Archipelago (Fig. 1a) and show spectacular preservation of blueschists and eclogites parageneses (Fig. 1b; Altherr et al., 1979; Blake et al., 1981; Avigad et al., 1992; Trotet et al., 2001a,b; Rosenbaum et al., 2002; Philippon et al., 2011) that are worldwide known for the study of the geodynamic processes operating at the plate interface. Several petrological studies, P-T estimates and geochronological constraints are available on these two islands (Altherr et al., 1979; Wijbrans et al., 1990; Avigad, 1993; Lister and Raouzaios, 1996; Trotet et al., 2001a; Schmädicke and Will, 2003; Schumacher et al., 2008; Groppo et al., 2009; Dragovic et al., 2012; Bröcker et al., 2013). However, structural studies devoted to the relations between deformation and metamorphism (Trotet et al., 2001b; Rosenbaum et al., 2002; Ring et al., 2003; Keiter et al., 2004, 2011; Bond et al., 2007; Philippon et al., 2011; Ring et al., 2011), are still debated and different geometrical interpretations and kinematic histories have been proposed rendering difficult the choice of a model for the exhumation mechanism.

In this work, we thus revisit the geology of Sifnos, based on new geological maps at the 1:20,000 scale. Our aim is to study the distribution of deformation through evolving P-T conditions to better describe the distribution of strain within the subduction complex and constrain the mechanisms of exhumation of HP-LT units from the subduction zone.

2. Geological setting

The Aegean domain, located in the eastern Mediterranean Sea (Fig. 1a), has undergone a tectonic and metamorphic evolution defined by two main steps. Firstly, from the late Cretaceous to the Eocene, the Africa-Eurasia convergence has led to the formation of the Hellenides-Taurides chain (see location on Fig. 1a) that is composed of a stack of oceanic and continental nappes belonging to Apulia (Aubouin, 1957; Jacobshagen et al., 1978;

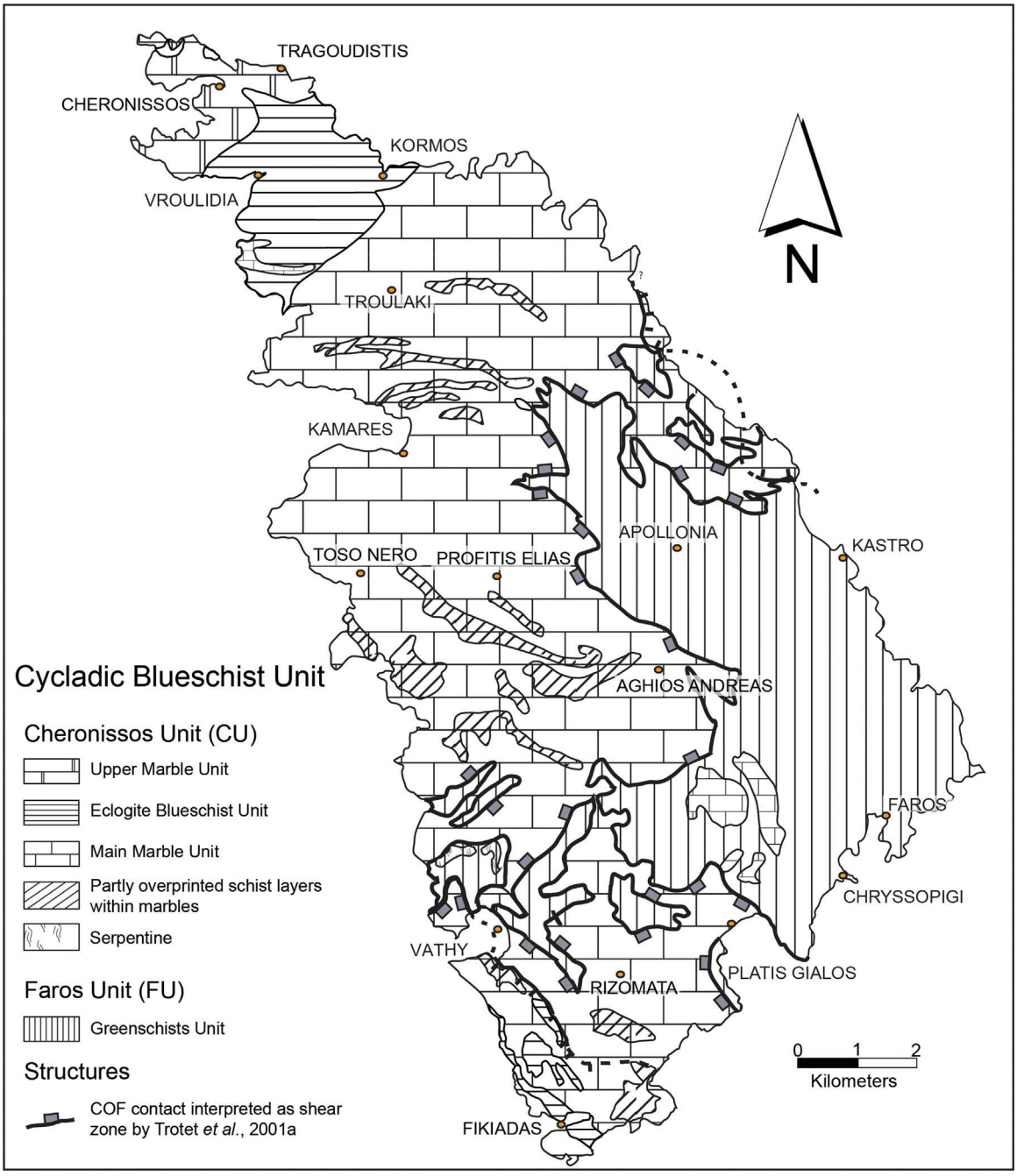

Fig. 2. Simplified geological map of Sifnos modified after Avigad (1993) and Trotet et al. (2001a,b).

Jacobshagen, 1986; Stampfli, 2000). The stratigraphic sequences of the main Hellenic nappes and their paleogeographic origin can still be recognized and correlations can be made from the mainland to the islands, despite the intensity of later post-orogenic extension (Bonneau, 1984; Jolivet et al., 2004; Van Hinsbergen et al., 2005). Secondly, since 35 Ma, the kinematics in the upper plates of the Mediterranean subduction zones has mainly been controlled by the southward retreat of the African slab (Malinverno and Ryan, 1986; Jolivet and Faccenna, 2000; Jolivet et al., 2008; Jolivet and Brun, 2010), responsible for back-arc extension. The Cyclades archipelago results from the collapse of the Hellenides-Taurides belt caused by this retreating subduction which changed the kinematic boundary conditions from compressional to extensional in the back-arc region (Fig. 1b; Lister et al., 1984; Jolivet et al., 2013).

Extension was recorded in the Rhodope Massif earlier than in the Aegean Sea. The Rhodope Massif is located in the northern part of the studied domain, south of the Balkans. The Rhodope Massif underwent a H*P* metamorphism (i.e. 12–17 kbar, 750–811 °C) with locally ultra-H*P* conditions, no later than the late Cretaceous (Liati et al., 2002; Bonev et al., 2006; Bauer et al., 2007). Then, M*T*-M*P* metamorphism (i.e. 8–10 kbar, 560–650 °C) was recorded in the Paleocene and exhumation of these rocks started in the central Rhodope massif ~55 Ma ago below top-to-the NE ductile-brittle detachments in back-arc domain (Burg et al., 1996; Bonev et al., 2006). Extension started in the Rhodope earlier than in the Cyclades, sometimes in the Eocene (Brun and Sokoutis, 2007). During the same period, syn-orogenic exhumation occurred in the Cyclades region within the Hellenic subduction zone and the CBU underwent HP metamorphism at 70–90 km depth whereas par-

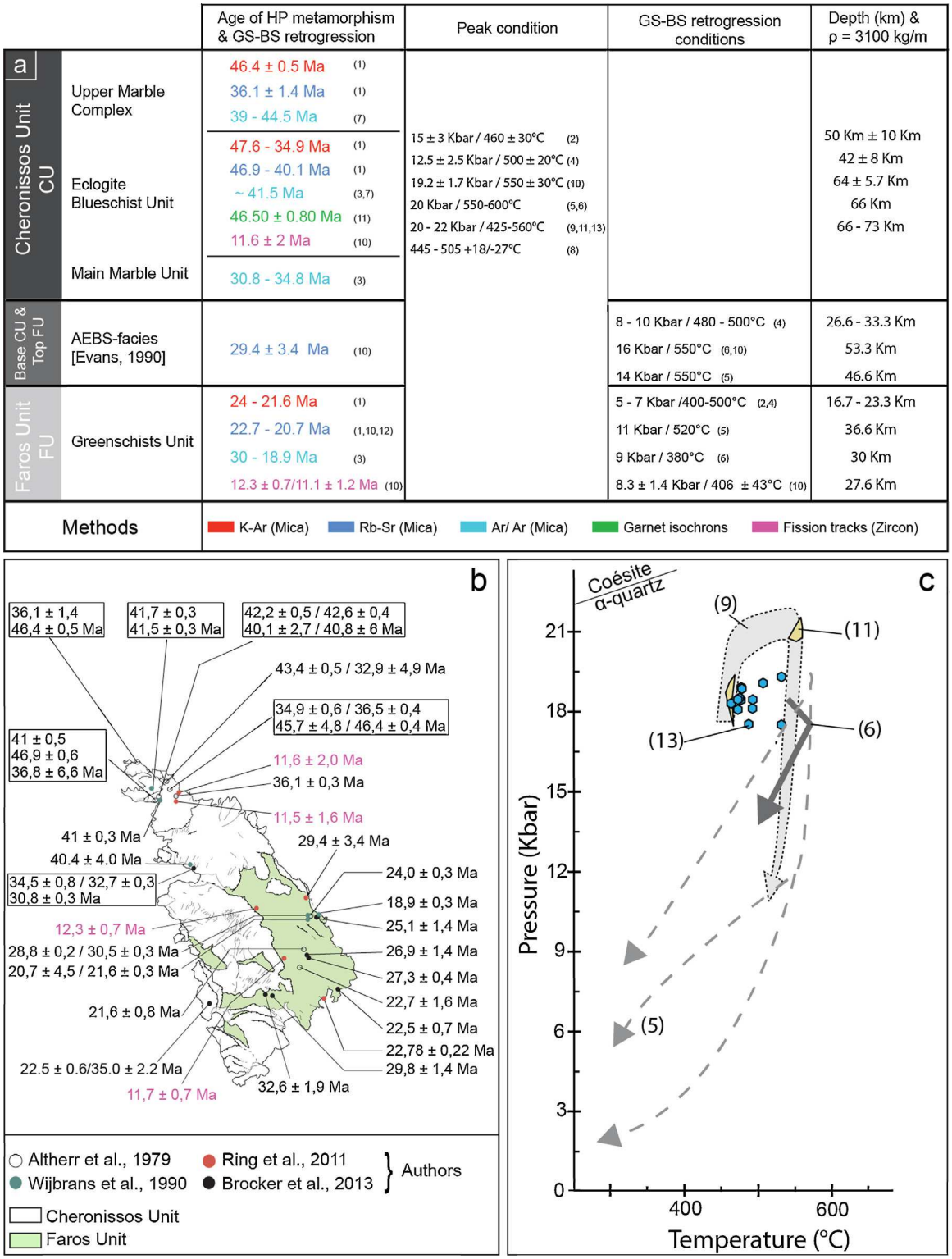

Fig. 3. P–T conditions and deformation ages within Cheronissos and Faros units.
(a) Geological pile on Sifnos showing different ages of metamorphic peak conditions, and blueschist-facies (BS) to greenschist-facies transition (GS) with the associated depths. Superscript numbers indicate the citations, 1) Altherr et al., 1979; 2) Schliestedt and Matthews, 1987; 3) Wijbrans et al., 1990; 4) Avigad et al., 1992; 5) Trotet et al., 2001a; 6) Schmadicke and Will, 2003; 7) Forster and Lister, 2005; 8) Spear et al., 2006; 9) Groppo et al., 2009; 10) Ring et al., 2011; 11) Dragovic et al., 2012; 12) Bröcker et al., 2013; 13) Ashley et al., 2014. (b) Compilation of results of K-Ar, $^{40}Ar/^{39}Ar$ and Rb-Sr ages on phengite, paragonite and fission track on zircon. (c) Detailed P-T path modified after Ashley et al. (2014), subscript numbers indicate the References.(For interpretation of the references to colour in this figure legend, the reader is referred to the web version of this article.)

tial exposure at the surface of the central Rhodope core complex occurred in the back-arc domain (Jolivet and Brun, 2010). Extension then migrated to the Cyclades some 35 Myrs ago and the Aegean Sea started to form. This new episode of extension associated with a fast migration of the magmatic arc, during slab retreat, while during the first extensional episode, the arc was more steady, suggesting

that slab retreat was quite slow (Jolivet and Brun, 2010; see also Menant et al., 2016).

2.1. Cycladic archipelago

The geology of the Cycladic archipelago is divided into three units, which are from top to bottom: the Upper Unit (UU), the Cycladic Blueschist Unit (CBU), and the Cycladic Basement Unit. In this framework, we focus on the CBU that mainly crops out in the central part of Aegean domain (Fig. 1b). This unit is correlated with the Pindos Unit in continental Greece (Bonneau, 1982, 1984) and consists of alternating marbles, metapelites, metabasites and meta-ophiolite. CBU rocks have undergone a dominant HP-LT metamorphism in the Eocene (K-Ar, ^{40}Ar-^{39}Ar and Rb-Sr on phengite after Altherr et al., 1979; Bröcker and Franz, 1998; Huet, 2010), and are particularly well exposed in the mapped area. Different parageneses display contrasting P-T-time evolutions but with the same peak P-T conditions in the eclogite-facies around 21kbar and 550 °C (Trotet et al., 2001b; Groppo et al., 2009; Dragovic et al., 2012; Ashley et al., 2014). This HP-LT metamorphism is partially overprinted by Oligo-Miocene HT-LP metamorphism (Altherr et al., 1979, 1982; Keay et al., 2001; Vanderhaeghe, 2004; Duchene et al., 2006; Bröcker et al., 2013), which took place contemporaneously with back-arc extension. The overprint is generally characterized by greenschist-facies parageneses and locally by amphibolite-facies ones, reaching partial melting conditions in Naxos, Ikaria and Mykonos (Keay et al., 2001; Denèle et al., 2011; Laurent et al., 2015; Beaudoin et al., 2015). The CBU recorded their retrograde peak temperature in the centre of the back-arc area during the Miocene, at about 20 Ma in Naxos (K-Ar, ^{40}Ar/^{39}Ar and Rb-Sr on phengite, Altherr et al., 1982; Wijbrans et al., 1990; Bröcker et al., 2013) or 16 Ma in Ikaria (Beaudoin et al., 2015). Previous studies (Lister et al., 1984; Urai et al., 1990; Gautier and Brun, 1994; Jolivet et al., 1994; Tirel et al., 2009; Jolivet and Brun, 2010; Ring et al., 2010) have shown that Miocene low-angle normal faults have accommodated the late-stage exhumation of the metamorphic core complexes during extension. As a result, several detachments were formed and are now exposed in the northern and western Cyclades, they are the NCDS (North Cycladic Detachment System) and WCDS (West Cycladic Detachment System) (Jolivet et al., 2010; Lecomte et al., 2010; Iglseder et al., 2011; Grasemann et al., 2012). Those structures are associated with top-to-the-NE and top-to-the-SW kinematic indicators, respectively (Fig. 1b). During this period the first formed MCC (Metamorphic Core Complex) were exhumed in the Oligocene and Early Miocene, and they partly escaped from the later (Middle Miocene) complete retrogression and partial melting observed in Naxos, Paros, Mykonos or Ikaria.

2.2. Sifnos Island geology

Sifnos lies in the back-arc region of the Hellenic subduction and is situated in the south-western part of the Aegean Sea between the Serifos metamorphic core complex (Iglseder et al., 2009) and the Milos Quaternary volcano (Fig. 1b). According to Ring et al. (2011), the morphology of Sifnos is partly controlled by NE- and SW-dipping normal faults, and E- or W-dipping younger faults. This island is characterized by an apparently inverse metamorphic gradient within the CBU (Schliestedt and Matthews, 1987; Wijbrans et al., 1993; Lister and Raouzaios, 1996). Indeed, blueschists found at the top of the structural pile are well preserved while the base is strongly retrograded under greenschist-facies conditions. Nevertheless, high-pressure markers are locally preserved in all units on Sifnos (Avigad et al., 1992). Two main tectonics units separated by a shallow-dipping tectonic discontinuity have been recognized (Trotet et al., 2001a): the Cheronissos and the Faros units (Fig. 2). The contact between the two units is named COF (Cheronissos Over Faros) in the following.

Cheronissos Unit (CU) lays on top and it is further divided into three lithologic subunits, which are from top to bottom, 1) the Upper Marble Complex, exposed in the north-western part of the island (mainly calcitic and dolomitic marbles with lenses of quartzites and well preserved blueschists and eclogites), 2) the Eclogite and Blueschist Unit (interbedded quartzites, metabasites, metasediments and acidic gneisses), 3) the Main Marble Unit (a succession of thick marble levels alternating with metasediments and metabasites metamorphosed in the blueschist- to greenschist-facies) (Schliestedt and Matthews, 1987; Wijbrans et al., 1990; Schmädicke and Will, 2003; Ring et al., 2011;Fig. 2). Faros unit (FU) crops out underneath Cheronissos Unit mainly in the south-eastern part of the island (Fig. 2). It is composed of metabasites and metasediments strongly retrograded in the greenschist-facies. Locally, lenses of albite- and epidote-bearing blueschists (AEBS-facies of Evans, 1990) are preserved at the base of Cheronissos Unit and the top of Faros Unit (Trotet et al., 2001a).

Two main stages have been inferred in the metamorphic evolution of Sifnos during the Eocene and Miocene. The first was characterized by HP-LT metamorphism under blueschist- to eclogite-facies conditions possibly due to the subduction of Apulia and the Pindos oceanic basin below Eurasia (Avigad, 1993) in the Eocene with peak conditions around 21kbar and 550 °C (Fig. 3a) (Trotet et al., 2001b; Groppo et al., 2009; Dragovic et al., 2012, 2015; Ashley et al., 2014). In a recent paper, Aravadinou et al. (2015) have related this tectono-metamorphic event (their D1 and D2 stages) to a top-to-the-SE shearing event. This episode has been dated around 45 Ma with different methods such as K-Ar and Rb-Sr on white micas (see compilation on Fig. 3a and b; Altherr et al., 1979; Wijbrans et al., 1990), ^{40}Ar/^{39}Ar apparent age spectra on white micas (Fig. 3a; Forster and Lister, 2005) and Sm-Nd isochrons on garnets (Fig. 3a; Dragovic et al., 2012,2015). The second stage (D3 in Aravadinou et al., 2015) overprinted the blueschist- to eclogite-facies assemblages in the greenschist- to amphibolite-facies; it ranges in age from 30 to 19 Ma based on K-Ar, Rb-Sr and ^{40}Ar/^{39}Ar dating on white micas (Fig. 3a and b; Altherr et al., 1979; Wijbrans et al., 1990; Forster and Lister, 2005; Ring et al., 2011; Bröcker et al., 2013).

2.3. Main geological controversies about Sifnos

One of the main differences of interpretation of the geological evolution of Sifnos relates to the significance of the second stage of deformation and the retrogression of the eclogite- and blueschist-facies parageneses into greenschist-facies assemblages. It has been for instance either interpreted as an extensional episode (Trotet et al., 2001b) or as a contractional episode (Aravadinou et al., 2015). In more details, the nature and origin of the contact between Cheronissos and Faros units, which can be best observed along the road from Apollonia to Vathy (Fig. 2), has been debated in the literature (Avigad, 1990,1993; Wijbrans et al., 1990; Lister and Raouzaios, 1996; Trotet et al., 2001b; Bröcker et al., 2013). This tectonic contact has been diversely interpreted as: a brittle detachment with top-to-the-northeast kinematics (Avigad 1993); a top-to-the-south thrust (Lister and Raouzaios, 1996); a top-to-the-northeast ductile shear zone (Trotet et al., 2001a) and, more recently, as a detachment marked by top-to-the-south brittle-ductile deformation (Ring et al., 2011).

Conventional thermobarometry and multiphase equilibria (Matthews and Schliestedt, 1984; Schliestedt, 1986; Schliestedt and Matthews, 1987; Avigad, 1993; Trotet et al., 2001b; Schmadicke and Will, 2003; Groppo et al., 2009; Dragovic et al., 2012, 2015), oxygen isotope thermometry (Matthews and Schliestedt, 1984), Zr-in-rutile thermometry (Spear et al., 2006) and

quartz inclusion in garnets (Ashley et al., 2014) have been used to estimate the P-T paths and the conditions of peak metamorphism for the Eclogite and Blueschist subunit in Cheronissos Unit (Fig. 3a and c). The shape of the prograde path is similar for all studies and follows a HP-LT gradient inferred from the presence of pseudomorphs of lawsonite (Trotet et al., 2001a). However, the main controversy relates to the retrograde P-T paths in Cheronissos and Faros units. Schmädicke and Will (2003) gave a similar P-T gradient of 10–12 °C/km for both units whereas Trotet et al. (2001b) proposed two different paths with a cooler one for Cheronissos Unit starting from a common peak at around 600 °C and 20kbar (Fig. 3c). Consequently, different explanations were proposed for the apparent inverse metamorphic gradient in Sifnos (eclogites and blueschists rocks overlying greenschists; Altherr et al., 1979; Matthews and Schliestedt, 1984; Schliestedt, 1986; Schliestedt and Matthews, 1987; Trotet et al., 2001b; Wijbrans et al., 1990; Avigad 1993; Groppo et al., 2009; Ring et al., 2011). It was suggested that the greenschist overprint in Faros Unit resulted from pervasive fluid infiltration (Matthews and Schliestedt, 1984; Schliestedt and Matthews, 1987), the Main Marble Unit being a relatively impermeable layer, protecting the Eclogite-Blueschist Unit from it. Wijbrans et al. (1990) assumed instead that overprinting was due to a temperature increase at the base of the metamorphic pile, fitting the younger $^{40}Ar/^{39}Ar$ ages found there (Fig. 3b). Another interpretation suggests that both Cheronissos and Faros units were derived from different structural levels and were juxtaposed next to each other by a thrust during the post-orogenic history (Lister and Raouzaios, 1996), involving a significant displacement between the two units and implying different peaks of metamorphism in the two units. Alternatively, Avigad (1993) and Trotet et al. (2001b), have proposed different cooling histories between the two units with a similar peak of metamorphism, leading to different degrees of retrogression (Fig. 3c). In order to clarify these kinds of discrepancies we focused our field study on the relations between deformation and metamorphism at different scales.

3. A new geological map of Sifnos

Our new geological and structural map at the 1:20,000 scale (Fig. 4) is entirely redrawn following field observations and satellite images analyses. Hence, a more detailed description of the 3D geometry of lithological assemblages and structure, is provided. The new data shed light on the shape of lithological boundaries and on the nature of the contact between Cheronissos and Faros units. The main occurrences of serpentinite and eclogite are reported on the map (Fig. 4). The geometry and kinematics of later normal faults have also been redrawn (Fig. 4). This map is consistent with the more detailed map recently proposed for the northern part of the island by Aravadinou et al. (2015).

3.1. Brittle deformation

The general structure of the island and the topography are controlled by a set of major normal to oblique faults that control the first-order distribution of lithologies on Sifnos (Ring et al., 2011). We carefully remapped these faults that should not be confused with the main contact between Cheronissos and Faros units (Fig. 5a). The largest of these late faults are the Kastro Fault and the Toso Nero Fault respectively along the eastern and western coast of the island, whereas the southern and central parts show a series of SW-dipping normal to oblique faults with different slicken-fibres generations such as the Kamares Fault or the Vathy Fault (see Fig. 4 for location; Fig. 5a and b). In most outcrops, the youngest brittle movement is top-to-the-SW and brittle-ductile criteria also indicate top-to-the-SW motion (Fig. 5c). One of these faults, the Vathy Fault, locally marks the COF (Fig. 5d). This high angle fault cross-cuts the contact that is parallel to the regional foliation. The fault shows a core with a thick talc-rich fault gouge and the fault plane shows slickensides (Fig. 5f) and other brittle-ductile criteria indicating top-to-the-SW and −S movements (Fig. 5e and g). A few meters away from the damage zone, the older ductile deformation, characterized by top-to-the-northeast shear is visible like in most of the island. In the far south of Sifnos, S- to SSE-dipping faults occur (Fig. 4). Their exact kinematics is not well established but their effect on the distribution of metamorphic rocks and the associated scarp show a normal component. These faults cut probably the SW-dipping faults.

3.2. Regional foliation

The intense ductile deformation is characterized by well-developed foliations and stretching lineations shown on Fig. 4. Within the same unit, foliation planes are generally parallel to each other in different lithologies. At the scale of the island, in the north, the foliation dips toward the NW, whereas in the rest of the island it dips toward the NNE with a large dip range, between 0° and 90° and

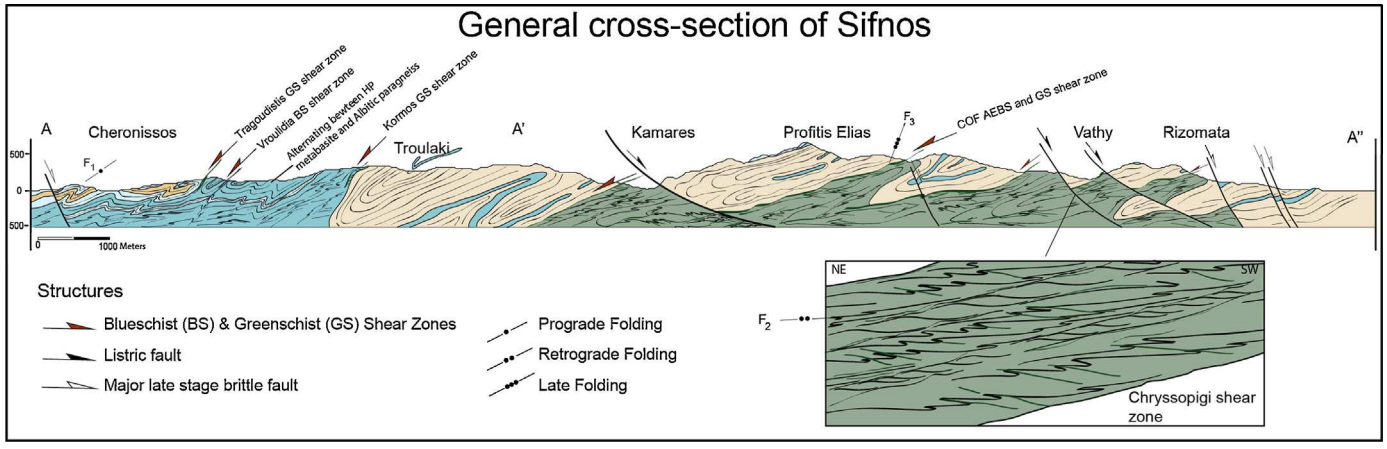

Fig. 4. Geological map of Sifnos.
New stretching lineation map of Sifnos with foliation trajectories. Lithologic contours have been defined on the basis of our field observations and satellite images. We have also included some information of Aravadinou et al., 2015. The major structures are indicated (TNF: Toso Nero Fault; KF: Katro Fault; VF: Vathy Fault; SSEF: S-SE Faults). Lineations associated with blueschist- and greenschist-facies assemblages are respectively indicated in blue and green; arrows indicate the sense of shear (top-to-the-N to −NE in different colours and top-to-the-SW in black). North–south cross-section showing the general architecture of Sifnos and relative sequence of high- and low-angle extensional faults.(For interpretation of the references to colour in this figure legend, the reader is referred to the web version of this article.)

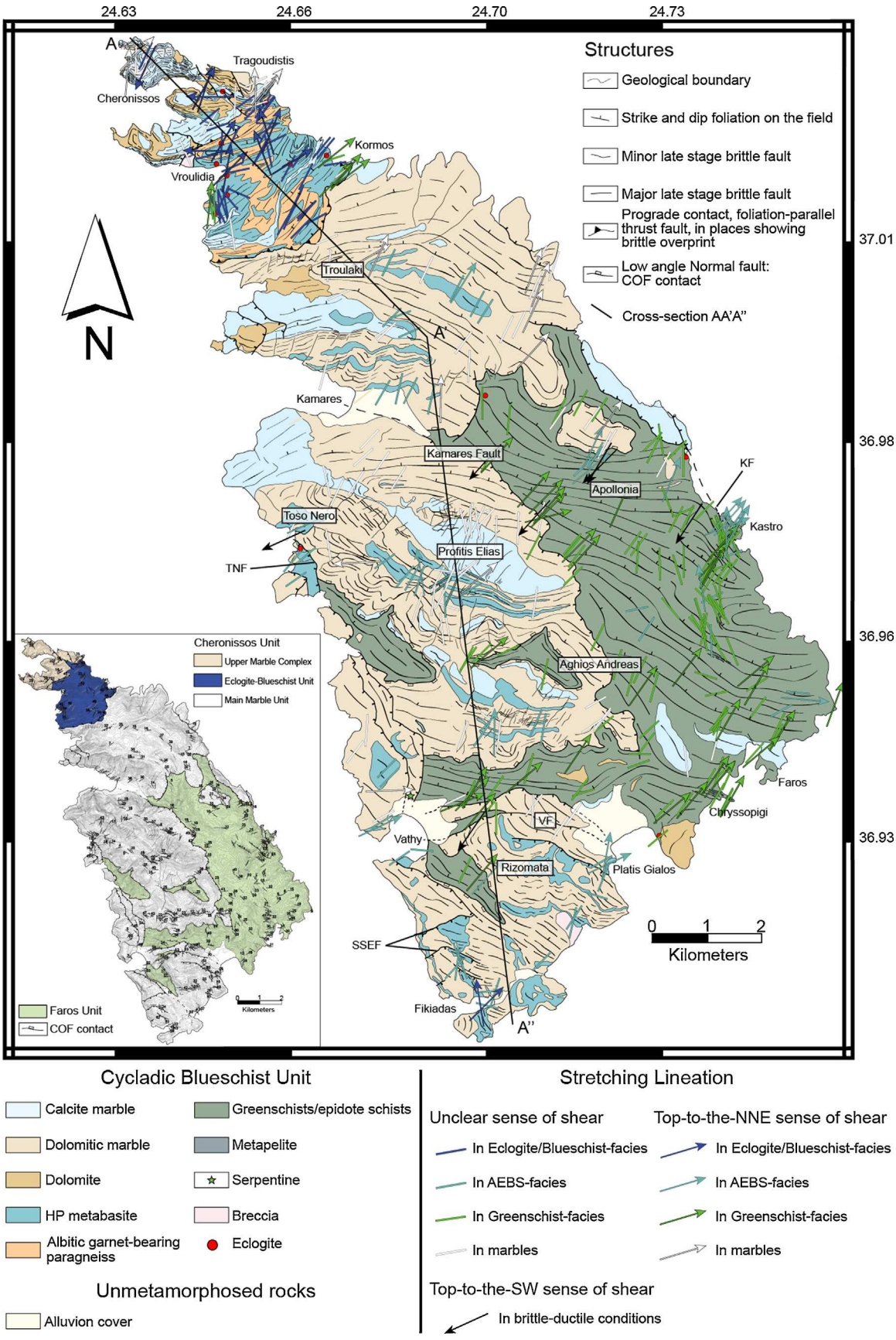

Fig. 4. (*Continued*)

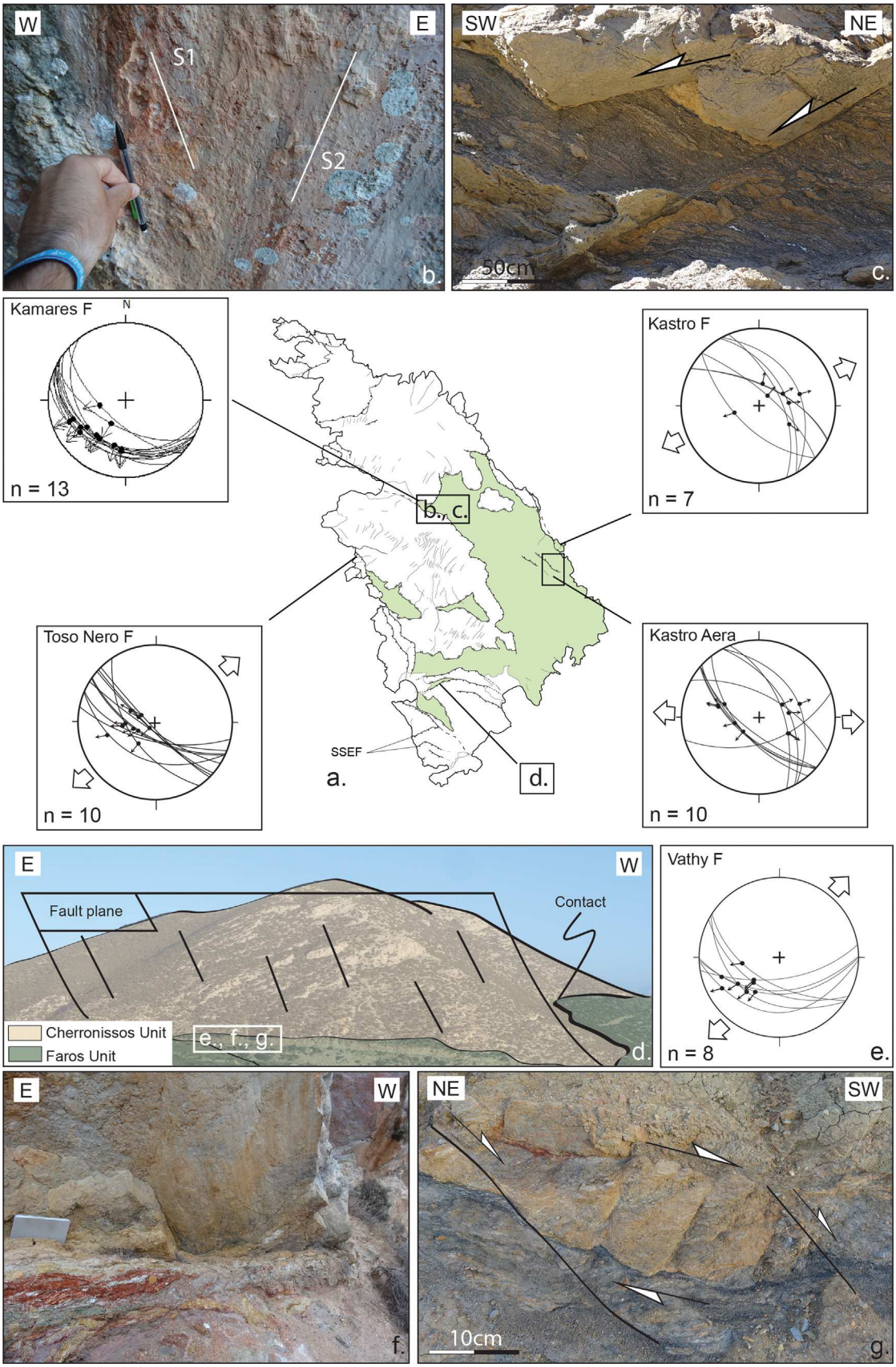

Fig. 5. Brittle deformation on Sifnos.
(a) Location of fault-slip data from high-angle normal faults. The diagrams show great circles of fault planes and the projected trace of slickenside lineations in a lower hemisphere equal-area projection. Arrows indicate extension directions from the measured fault sets (paleostress orientation patterns were calculated with the win-tensor computer-aided inversion software of Delvaux and Sperner, 2003). Readers unfamiliar with the method, or more generally with fault-slip data inversion are referred to the work of Angelier (1990). (b) Kamares Fault showing two slicken-fibre generations. (c) Top-to-the-SW brittle-ductile kinematic indicators associated with Kamares Fault. (d) Vathy SW dipping normal fault with (e) stereographic projections of striations. (f) Fault plane characterized by a few meters thick reddish fault gouge showing (g) top-to-the-SW brittle-ductile kinematic indicators. Note the consistency of the NNE-SSW to E-W direction of brittle extension all over the island.

dip increasing northward (Fig. 6a). Different families of foliation can be distinguished depending on the associated parageneses and the apparent intensity of shearing deformation (e.g. density of shear bands, intensity of stretching. . .). In the northern part of the island, the main foliation (S_2) generally strikes ENE-WSW and dips toward the NNW (Fig. 6a). An early S_1 foliation is seen as relics within garnets porphyroblasts (Trotet et al., 2001a; Aravadinou et al., 2015). In the Main Marble Unit, foliation is generally characterized by NW-SE strike and dips to the NE (Fig. 6a). At the base of Cheronissos Unit, lenses of metabasic rocks wrapped within marbles are preserved at the mesoscopic-scale. Locally, a new AEBS-facies foliation (S_3) is developed, overprinting the earlier foliations (Trotet et al., 2001a; Aravadinou et al., 2015). In Faros Unit, the main foliation (S_3) is well developed with a NNW-SSE strike, dipping toward the NNE. Finally, a later greenschist-facies foliation (S_4) is characterized by a low northward dip at the base of Faros Unit (Trotet et al., 2001a). Hence, from Cheronissos to Faros Unit, a succession of deformation from blueschist- to greenschist-facies conditions is recognized. Moreover, good exposures of the tectonic contact between Cheronissos and Faros Unit show that the foliation planes retain the same strike and dip across the contact and across major lithological contacts as well.

3.3. Stretching lineation

Stretching lineations are widespread through all lithologies and have been distinguished according to the associated mineralogy, dominant metamorphic facies, and/or intensity of deformation. In calcitic and dolomitic marbles, white micas and calcite define the lineation; in basic rocks, the elongation and boudinage of prismatic minerals (glaucophane, epidote, albite and chlorite) reflects a component of stretching, which is also locally expressed within metaconglomerates by elongated pebbles carrying pressure shadows. These lineations are projected on the map of Fig. 4. At the scale of the island and on most outcrops, stretching lineations trend consistently NE-SW (Fig. 6b), except for some local NNW-SSE-trending lineations observed in the northern part of the island (see also Aravadinou et al., 2015). The plunge of lineation is generally shallow and it rarely exceeds 40°. We have distinguished three successive generations of lineations based on the metamorphic grade coeval with deformation: 1) under blueschist-facies conditions, the trend of lineations, defined by glaucophane in most cases, shows a dispersion between N330°E and N30°E with an average around N350°E (Fig. 6b); 2) in Faros Unit, the lineation characterized by albite and chlorite, is less dispersed with an average around of N52°E (Fig. 6b); 3) close to the main contact, in AEBS-facies conditions, lineations defined by epidote, albite and rare glaucophane, trend in average around N30°E (which correspond to the average of the trend of blueschist and greenschist lineation, see stretching lineation on the map in Fig. 4).

3.4. Fold directions

Three folding events have been identified in the field. In the structurally highest and northern part of the island, early isoclinal to very tight macroscopic folds F_1 can be seen to affect thick massive dolomites alternating with calcitic marbles (Figs 7b and 7; see also Aravadinou et al., 2015). These folds are asymmetric and generally south-vergent, with an axial plane parallel to the foliation. The geometry and kinematic interpretation of these folds is detailed in Section 6. A second generation of folds F_2 is particularly well developed at small scale in both units and generally associated with an intense shearing deformation. F_2 folding is dominantly NE-vergent but characterized by variable axial trend with respect to the lineation. The axial plane of the first family is lying parallel to the foliation with the fold axis sub-parallel to the local stretching lineations. The tight to isoclinal folds are overturned toward the N or NE. These folds are mainly observed in areas where the deformation is intense such as near Vroulidia (northern part of the island, Fig. 7d) or Chryssopigi (southeast part of the island, Fig. 7e). They are best expressed in metabasites and metapelites. The second set has its axial planes dipping toward the north and the axes are roughly perpendicular to the lineation (Fig. 7f). These folds have been observed at small scale in all units. Finally, late stage F_3 folds refold the main foliation and tectonic contacts with an orientation perpendicular to the second generation. The relation between F_1, F_2, F_3 folds and the top-to-the-north or −northeast shearing deformation is discussed in Section 6.

4. Kinematic indicators and metamorphic conditions within Cheronissos Unit (CU)

4.1. Eclogite-Blueschist subunit

This unit, which outcrops in the northern part (Fig. 4), is composed by mafic and siliceous rocks. Most kinematic indicators are top-to-the-N to −NE. All lithologies are affected by asymmetric structures at various scales: 1) Decametric asymmetric folds affect the main foliation either in mafic (Fig. 8a) or in siliceous layers (e.g., quartz and phengite aggregates in Fig. 8b); 2) Meter-scale asymmetric boudinage of mafic (eclogite) layers embedded in a weaker matrix indicating a top-to-the-northeast shear sense (Fig. 8c); 3) Shear bands in all units (Fig. 8d and e). Spacing between shear bands ranges from a few millimetres to a few centimetres in the weakest levels. The angle between shear bands and foliation varies from one outcrop to another, depending on lithology. Shear bands are commonly marked by thin glaucophane coatings in mafic rocks (Fig. 8f) and quartz/mica in acidic rocks. Shear bands give rise to sigmoidal foliation at the centimetric or metric scale compatible with top-to-the-northeast sense of shear; 4) Pressure shadows within garnet porphyroblasts consisting of quartz, mica, rare glaucophane and chlorite also indicate a top-to-the-NE sense of shear (Fig. 8g and h).

4.2. Upper Marble Complex subunit and Main Marble subunit

The marbles and schist lenses composing the Upper Marble Complex and the Main Marble units display kinematic indicators showing a top-to-the-northeast sense of shear (Fig. 4) consistent with the structures described in the Eclogite-Blueschist Unit, but with a more localized distribution. In marbles, stretching is expressed by boudinage at various scales. In the northern part of the island for instance, competence contrast between calcite and dolomite results in domino and asymmetrical sigma/delta clasts indicating a top-to-the-northeast shear sense (Fig. 9b and c). Stretching is also marked by tension gashes and calcite recrystallization within marbles (Fig. 9d). Isoclinal folds overturned toward the north, with an axis generally perpendicular to the stretching lineation, are commonly observed in the Main Marble Unit (Fig. 9e). Few kinematics indicators are observed in other lithologies in these two subunits of Cheronissos Unit. They all indicate a top-to-the-northeast sense of shear (e.g., asymmetric shape of stretched carbonate pebbles in metaconglomerate layers in Fig. 9f).

4.3. Metamorphic conditions of shearing deformation in Cheronissos Unit

In the northern part of the island, Upper Marble Complex and Eclogite-Blueschist Unit are characterized by an overall good preservation of HP-LT parageneses such as fresh and very abundant glaucophane and omphacite within metabasites. Shear bands and sometimes strain shadows around garnets are often filled with glaucophane and phengites, indicating syn-HP-LT conditions for

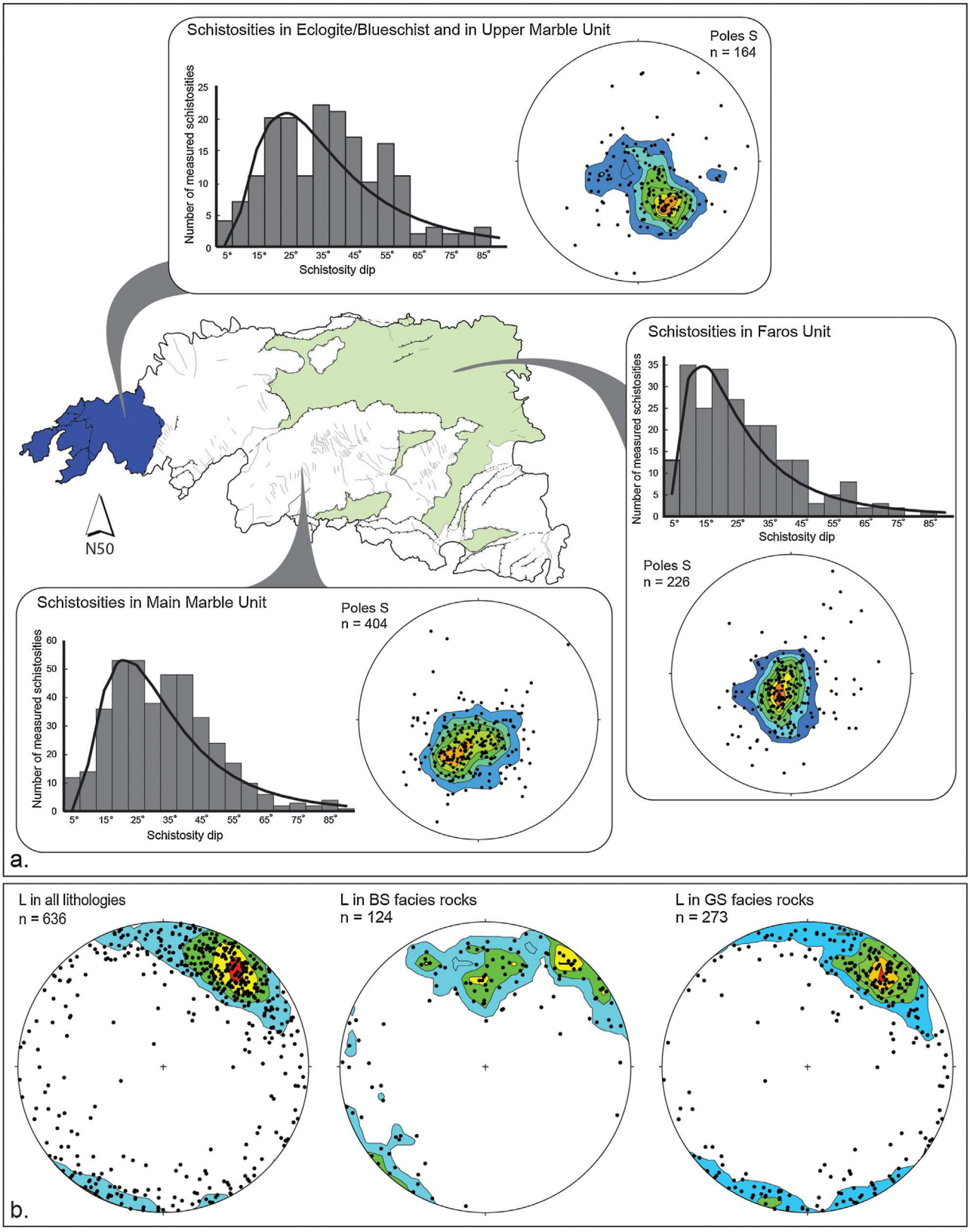

Fig. 6. Main planar fabrics and stretching lineation.
(a) Statistics of the main foliation of different units showing distribution frequency of dip schistosity and Schmidt's lower hemisphere equal-area projection of schistosity poles. (b) Statistics of the preferred orientation of stretching lineation presented in Schmidt's lower hemisphere equal-area projection. We used the 1% area contouring to define the contour lines. In our case, we used a contour interval value of 2.

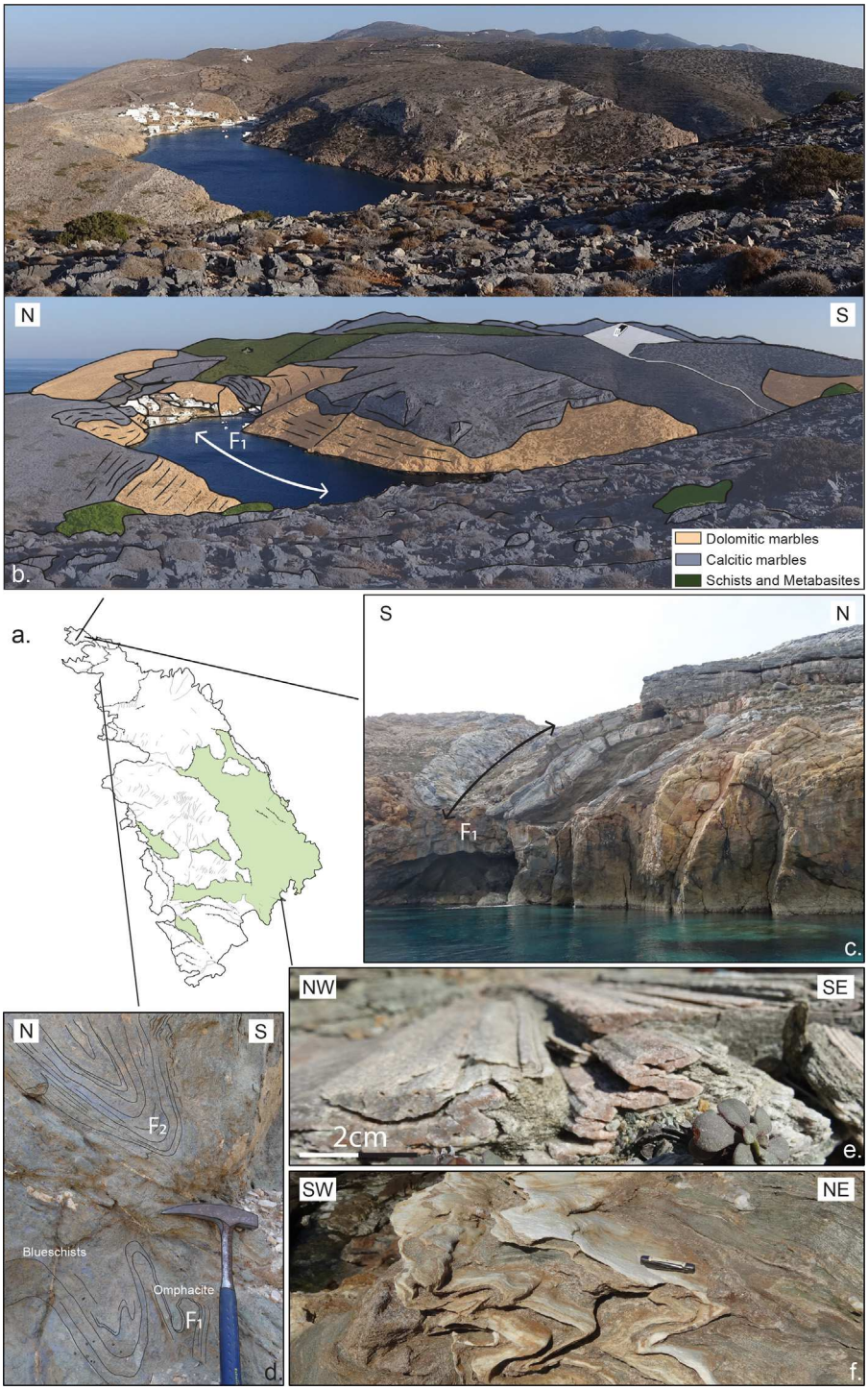

Fig. 7. Different folding phases at various scales.
(a) Location of field photographs. (b) and (c) show field evidences of folding of dolomitic marbles and calcitic marbles in the northern part of the island. (d) Syn-blueschist folding affected early folds in a metabasite. Note that F_2 fold axes are mostly perpendicular to the stretching direction. Two sets of axial planes showing, (e) axes parallel to the stretching and (f) perpendicular to the stretching lineation in the south-eastern part of the island.

the top-to-the-N to –NE shearing deformation (blue arrows on Fig. 4). In the Main Marble Unit, HP-LT parageneses are generally more retrograded when approaching the contact between Cheronissos and Faros units. In this latter unit, top-to-the-northeast kinematic indicators in metabasite lenses are associated with glaucophane, epidote, phengite and sometimes chlorite, albite characteristic of AEBS-facies P-T conditions (green/blue arrows on Fig. 4).

5. Kinematic indicators and metamorphic conditions within Faros unit

5.1. Top-to-the-NE ductile shear deformation

Top-to-the-northeast kinematic indicators are widely distributed through Faros Unit but more common in zones of strain localization. Several types of shear-derived objects are observed: 1) metric shear bands indicating top-to-the-northeast sense of shear

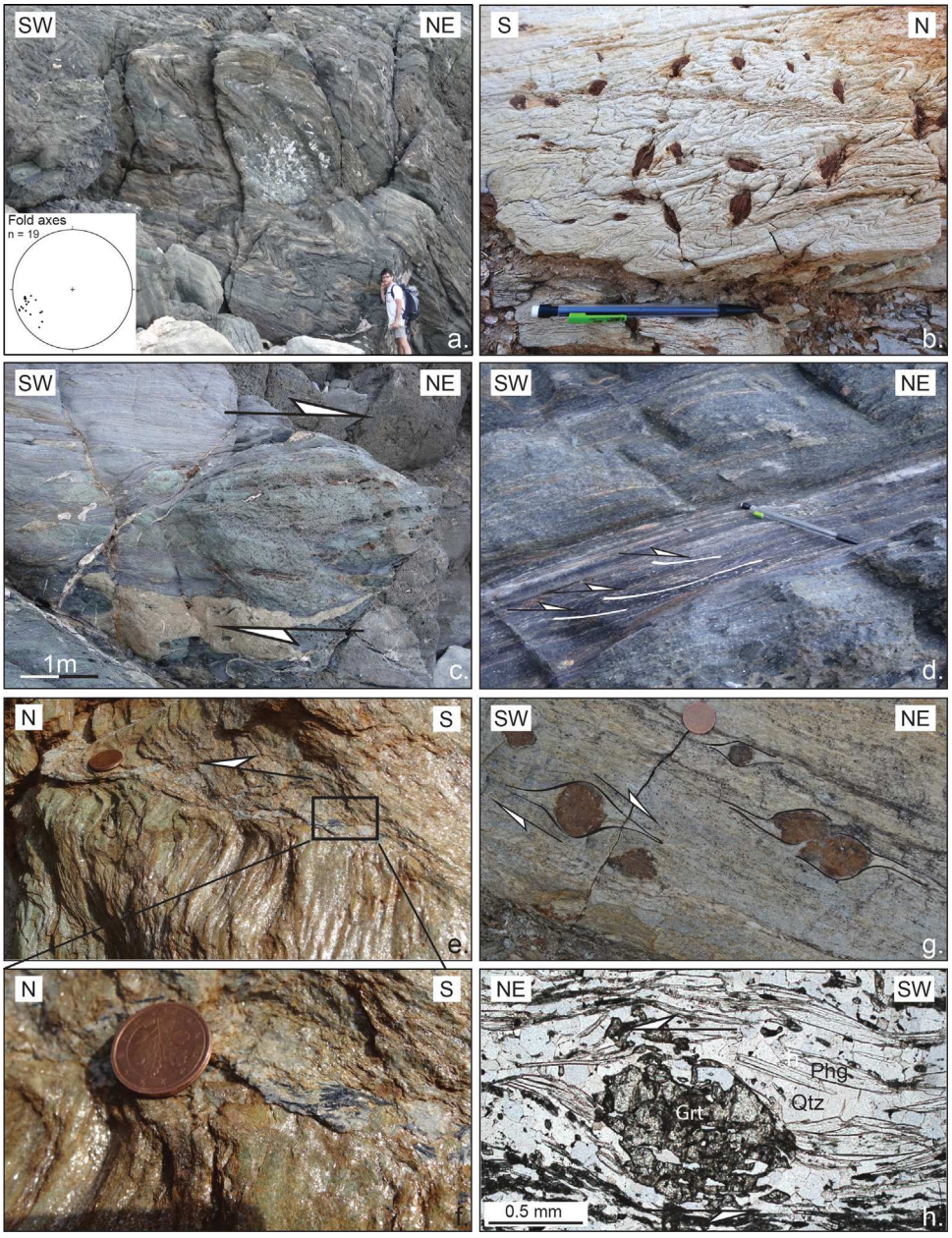

Fig. 8. Microstructures and macrostructures observed in Sifnos Eclogite-Blueschist Unit.
(a) Decametric asymmetric folds in mafic rocks close to Kormos, showing axes mostly perpendicular to the stretching direction. (b) Asymmetric folds in siliceous levels with S_1 preserved in garnets in the upper level of Eclogite-Blueschist Unit. (c) Boudinage of eclogites showing a top-to-the-NE sense of shear. (d) Top-to-the-NE shear bands affecting competent mafic rocks and (e) acidic rocks in the north of the island. (f) Details of shear bands marked by glaucophane in more acidic rocks. (g) Pressure shadow on garnet porphyroblasts in a field photograph and (h) thin section. They show top-to-the-NE sense of shear close to the contact between Eclogite-Blueschist Unit and Main Marble Unit.

near Kamares Fault (Fig. 10b); 2) asymmetric boudins of competent lithologies, such as those preserving mafic eclogite boudins (Fig. 10c); 3) sheared quartz-carbonate veins perpendicular or parallel to the main foliation showing pressure shadows filled with chlorite and albite such as near Vathy, with NE-verging shearing in greenschist-facies conditions (Fig. 10d and e); 4) syn-greenschist asymmetric folding affecting layers rich in glaucophane and epidote close to the COF (Fig. 10f). Crenulation of an earlier foliation compatible with top-to-the-northeast shearing is also frequent within Faros Unit and especially near zones of strain localization such as Chryssopigi (Fig. 10g).

Greenschist-facies ductile deformation is more localized in Faros Unit than in other units along shear zones. One spectacular example of such shear zones can be observed at the southern coast of the island (Fig. 11a). This area, located near the base of Faros Unit, shows a distinct gradient of shearing deformation. In average, the foliation strikes almost E-W and dips moderately toward the southwest. The shear zone develops within micaschists and minor marbles, displays the same overall distributed top-to-the-NE kinematic indicators occurring at various scales over the whole Faros Unit. Such kinematic indicators are also exposed near the port of Faros. The N50°E trending stretching lineation is marked by stretched micas and albite pods. The deformation strongly increases toward the northwest and the gradient is clearly visible on Chryssopigi peninsula (Fig. 11a). Approaching the peninsula, an increasing number of veins composed of quartz, chlorite, and carbonates are sheared and transposed into the main foliation (Fig. 11c). The foliation and the veins are strongly and asymmetri-

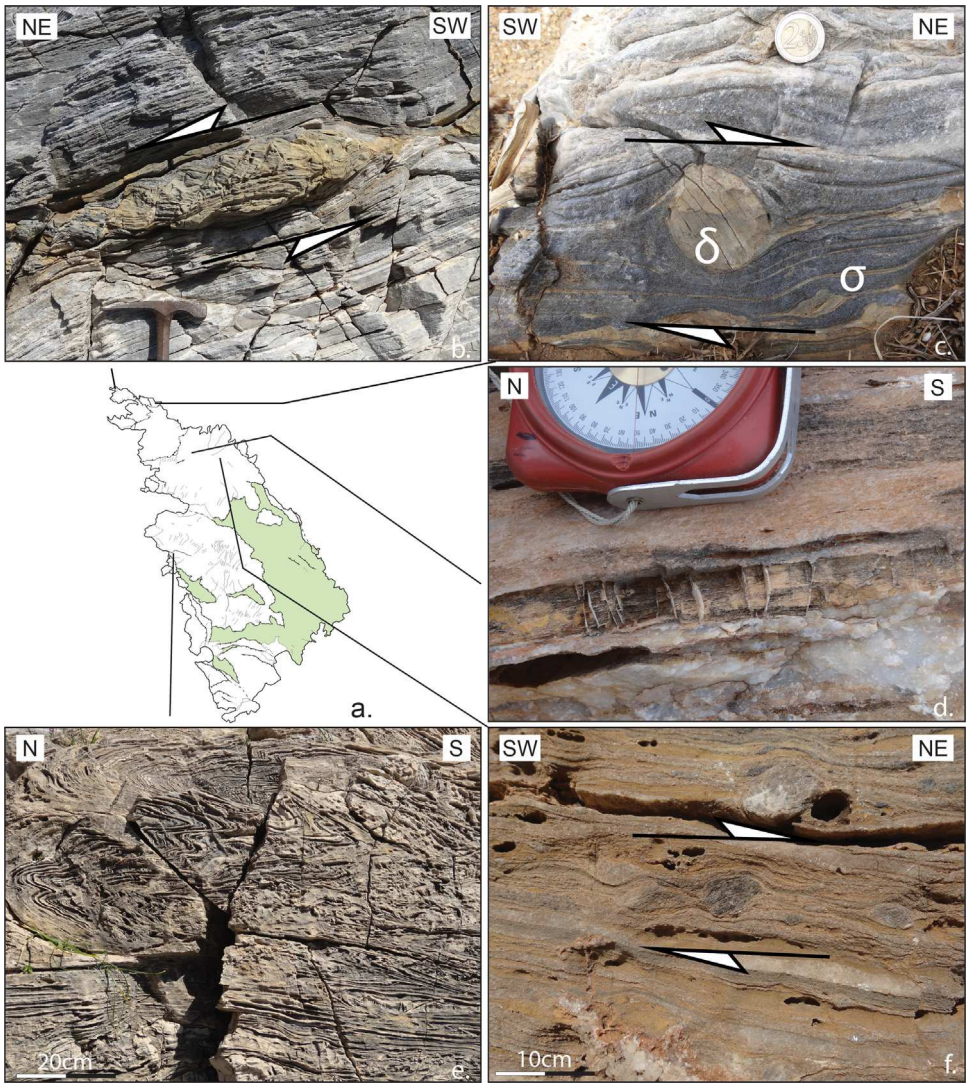

Fig. 9. Microstructures and macrostructures observed in Upper Marble Complex and Main Marble Unit.
(a) Location of field photographs. (b) Difference of competence between calcite and dolomite showing the development of dominos and (c) delta/sigma clasts indicating top-to-the-NE sense of shear. (d) North-south stretching shown by calcite recrystallization within tension gashes. (e) Centimetric folds showing axes mostly perpendicular to the stretching direction. (f) Top-to-the-NE shear sense defined by the asymmetric shape of stretched carbonate pebbles in metaconglomerate layers.

cally folded consistently with the mean shearing direction. Curved fold axes are dispersed around a direction perpendicular to the stretching lineation (Fig. 11a, number 1). Here, an axial plane crenulation cleavage develops in the hinge of these folds (Fig. 11d). Sheared lenses of metabasite, or quartz and calcite veins indicate a top-to-the-northeast sense of shear (Fig. 11e). Toward the top of the peninsula, moving upward toward the core of the shear zone, the non-coaxial deformation increases sharply. Fold axes tend to progressively rotate toward the shearing direction and are finally deflected parallel to the stretching lineation, although no clear closed eye-structure has been observed in the YZ plane (Fig. 11g). These folds are typically a-folds that show a large simple shear component in the direction of the stretching lineation (Fig. 11a, number 3). In the most deformed areas, observations of the XZ plane of the finite strain ellipsoid show a dense network of small-scale shear bands, all compatible with top-to-the-northeast sense of shear (Fig. 11f). Their spacing ranges from a few millimetres to a few centimetres and they are associated with white mica and albite. Chlorite, calcite and quartz veins are stretched and folded and totally transposed into the foliation.

5.2. Metamorphic conditions of the top-to-the-northeast deformation

In the Faros unit, metabasites that are deformed by top-to-the-NE deformation show strongly retrograded blueschist- or greenschist-facies rocks. From top to bottom 1) eclogite and blueschist lenses are locally preserved close to the COF in the northern part of the island (Fig. 10c). At macro-structural scale, the dominant paragenesis is characterized by glaucophane, epidote, phengite and albite. In this structural level, glaucophane filling of top-to-the-NE shear bands indicates that deformation has partly acted in HP-LT conditions (see Fig. 12); 2) in the middle part of Faros Unit, deformation is locally more intense and the retrogression into greenschist-facies more advanced. Chlorite-filled pressure shadows develop around quartz-calcite lenses, attesting that top-to-the-northeast deformation has also acted in greenschist-facies conditions (Fig. 10e). We have furthermore observed top-to-the-northeast shear bands filled by low-grade minerals such as chlorite and albite, leading to the same conclusion; 3) the base of Faros Unit is the most retrograded zone (e.g., Chryssopigi). Here, veins filled by calcite, chlorite and albite are mostly (or totally) trans-

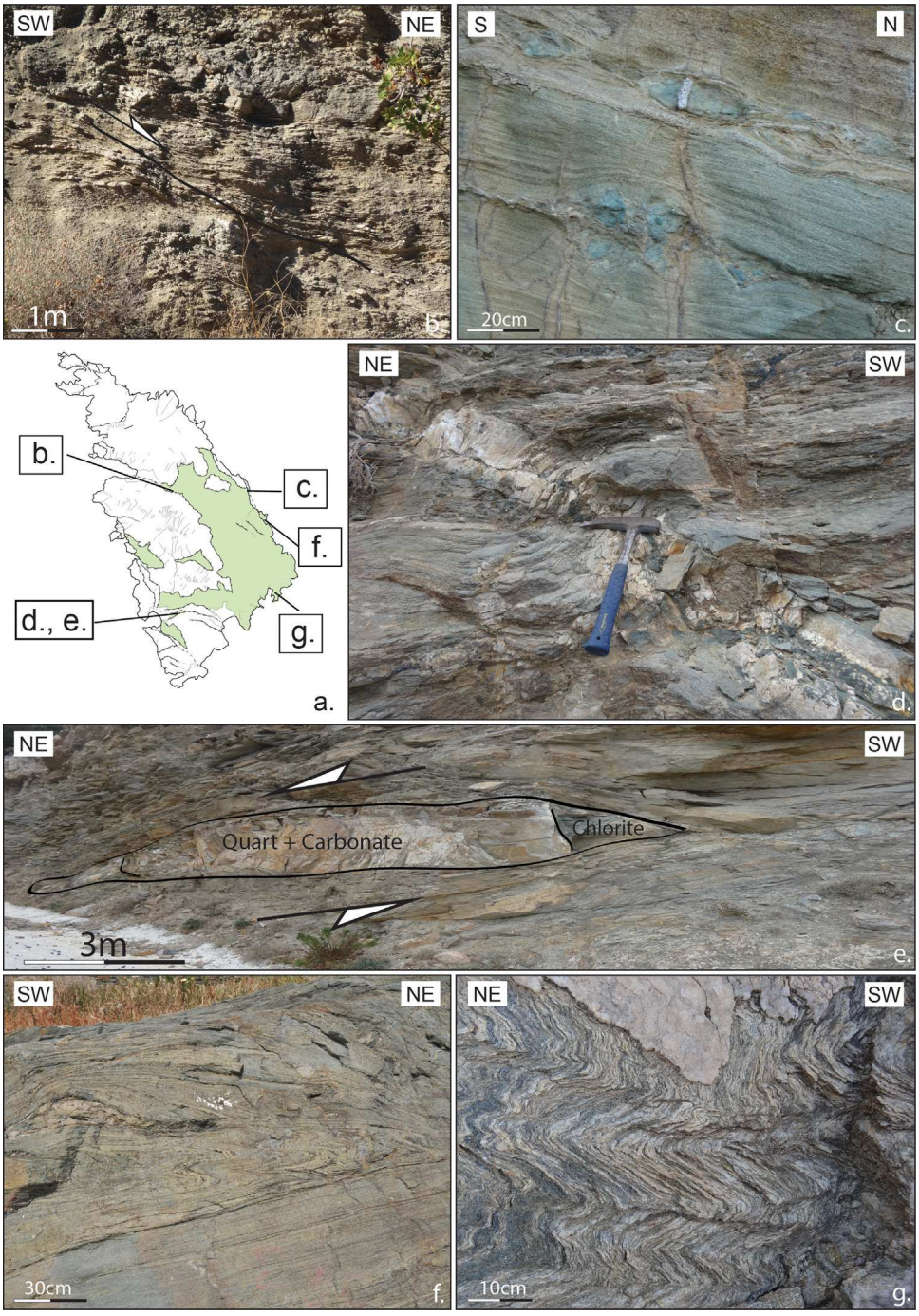

Fig. 10. Macrostructures observed in Faros Unit (FU).
(a) Location of field photographs. (b) S-C Structures with top-to-the-NE sense of shear characterized by metric shear bands in a metapelite. (c) Asymmetric mafic eclogite boudins cross cut by quartz-carbonate veins showing a north-south stretching. (d) Sheared quartz-carbonate veins cross cut the main foliation and (e) are commonly transposed in the foliation with pressure shadows filled in chlorite and albite showing top-to-the-NE sense of shear. (f) Centimetric folds showing axes mostly perpendicular to the stretching direction. (g) Axial plane crenulation cleavage associated with the hinge of folds at the base of this unit.

posed in the main foliation. At the micro-structural scale, in thin sections collected from Chryssopigi, shearing deformation is localized around syn-kinematic porphyroblasts of albite that are surrounded by quartz-mica strain shadows. These criteria attest that top-to-northeast deformation has acted during a continuum from blueschist- to greenschist-facies conditions during exhumation.

6. Kinematics of deformation in the main shear zones

6.1. Contact between Cheronissos and Faros units (COF)

The COF contact, as shown on the cross-section (Fig. 4), is folded by open folds and then later faulted by high-angle faults. This contact appears sub-parallel (or only locally slightly discordant) to

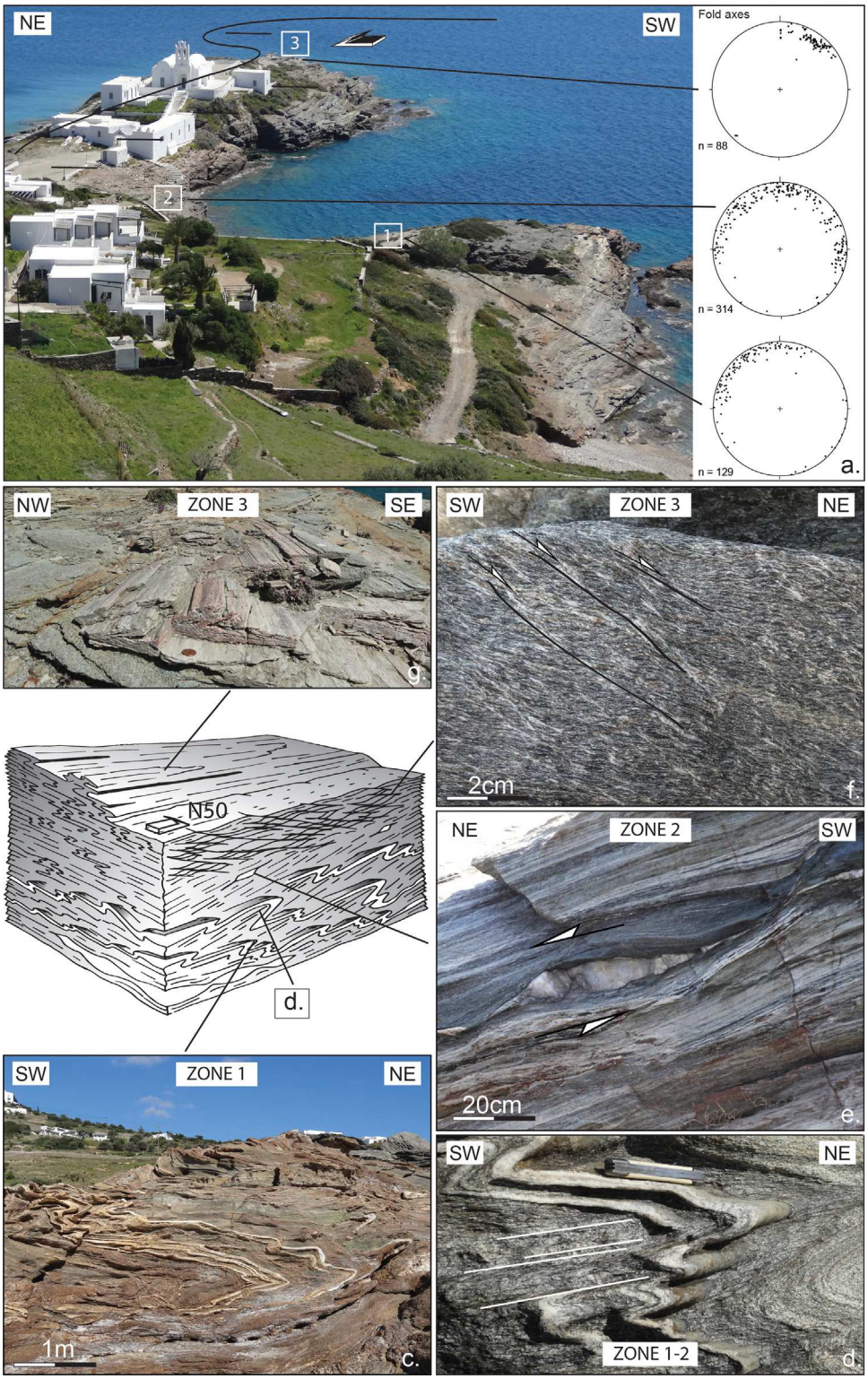

Fig. 11. Chryssopigi shear zone defined by a distinct gradient of shearing deformation.
(a) Large scale representative view of the Chryssopigi shear zone in the south-eastern part of the island. Albite pods marked the stretching lineation trending N50°E. All information is summarized with synthetic 3-D diagrams. This shear zone is divided in three areas; zone 1 corresponds to (c) an intense folding and (a) associated Schmidt's lower hemisphere equal-area projections showing fold axes dispersion; zone 2 is defined by (d) axial plane crenulation cleavage associated with the hinge of folds. (a) Fold axes tend to progressively rotate toward the shearing direction. (e) Sheared lenses of quartz and calcite showing a top-to-the-NE sense of shear; zone 3 is marked by intense non-coaxial shearing consistent with an overall top-to-the-NE kinematics. (f) Shear bands spacing ranges from few millimetres and (g) a-folds are commonly observed. Note that folds axes are now parallel to the stretching direction.

the main foliation. It is particularly well exposed in the southern part of the island along the country road that brings from Vathy to Fikiadas beach (Fig. 4). This area shows a distinct gradient of shearing deformation close to the main contact with the Cheronissos Unit and a shallow northeast-dipping foliation, sometimes strongly folded (Fig. 12d). There, sheared carbonate pebbles and

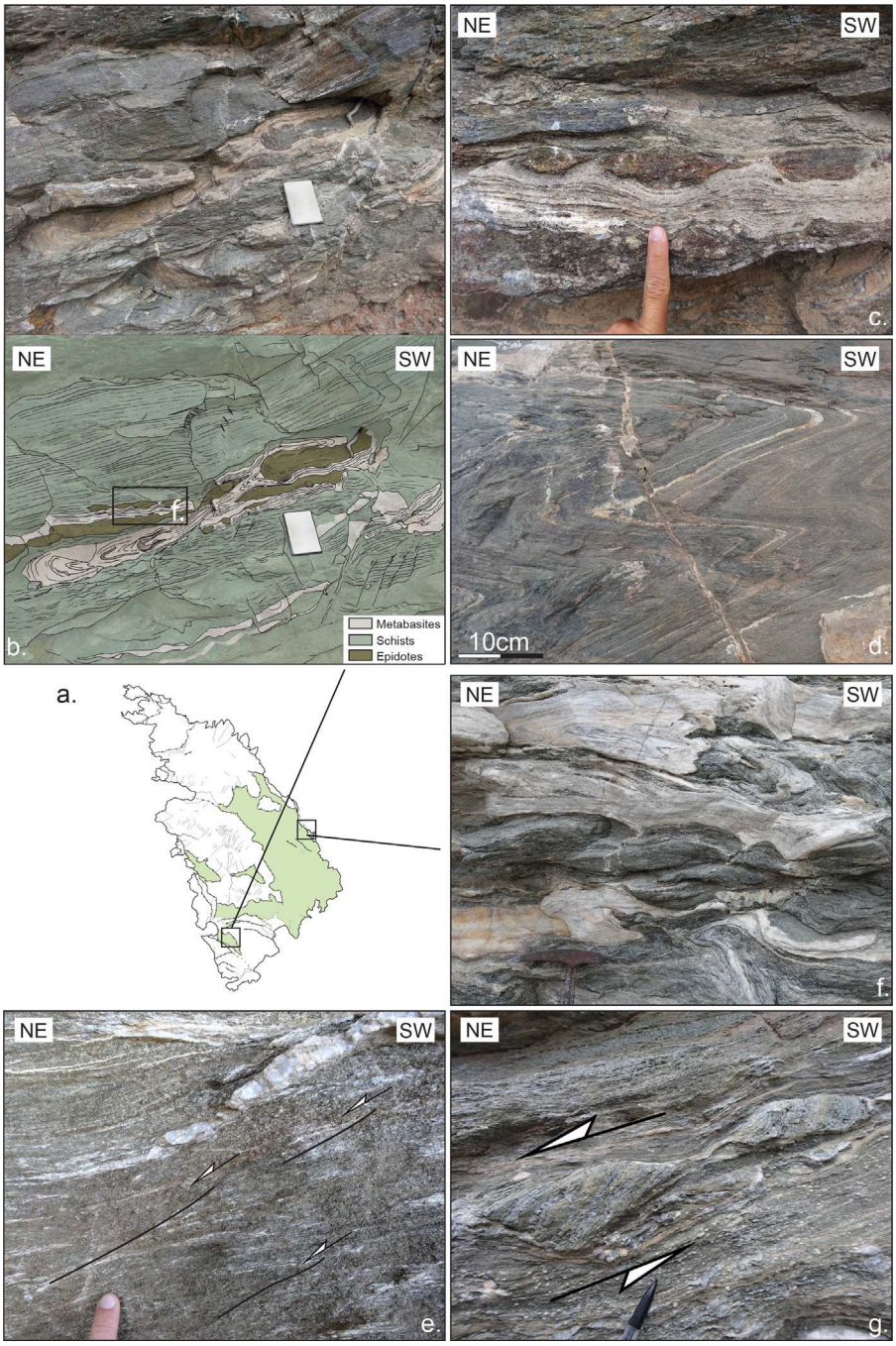

Fig. 12. COF contact.
The COF contact is well exposed (a) Intense ductile deformation shown by folding in all lithologies. Top-to-the-NE shear bands associated with glaucophane affect the foliation. (b) Asymmetric boudinage of epidotite boudins showing a top-to-the-NE shear sense. (c) Closely-spaced shear bands associated with white mica indicate top-to-the-NE sense of shear close to Vathy. (d) Similar features observed close to Kastro, just below the main contact.

asymmetric boudinage of epidotite boudins indicate a top-to-the-northeast shear sense (Fig. 12b and c) together with closely spaced shear bands associated with glaucophane and white micas. The NE-trending stretching lineation is defined by the elongation of albite spots and glaucophane needles.

The same features are observed close to Kastro, just below the main contact with the upper unit (Fig. 4). In this area the foliation strikes almost N-S and dips shallowly toward the east. The lineation is marked by epidote, glaucophane and albite. Numerous quartz lenses are transposed in the foliation and in shear bands with an asymmetry compatible with a top-to-the-northeast sense of shear (Fig. 12e and f). Asymmetric boudinage of epidotites is also well developed and indicates a top-to-the-northeast shear sense (Fig. 12g). Late veins, perpendicular to the regional stretching, filled with chlorite, quartz and hematite cutting the main foliation, suggest a continuum of stretching during more brittle conditions in greenschist-facies conditions. To summarize, the COF contact is characterized by a more intense shearing deformation and the sense of shear is clearly top-to-the-northeast, as observed within Cheronissos and Faros units. This shearing has been active during the retrogression from blueschist- to greenschist-facies conditions.

6.2. Shear zones away from the COF contact

The Eclogite-Blueschist Unit overlays the Main Marble Unit and the contact is exposed along the east coast close to Troulaki (see location on Fig. 4). The average dip of foliation is about 50°W (Fig. 13a). The stretching direction is provided by the mineral lineation (glaucophane, chlorite, albite and calcite) and the elongation of pebbles within metaconglomerate layers interleaved with metabasites and marbles. Depending on the mineral paragenesis, the trend of lineations changes from N70–80°E for the more retrograded levels to N45°E for the better-preserved blueschist-facies. In particular close to the Main Marble Unit, a metric metaconglomerate level, which mainly contains calcitic and dolomitic pebbles, shows near its base eclogite pebbles when approaching the Eclogite-Blueschist Unit (Fig. 13c). Immediately above, a pile of fully retrograded metabasites crops out (Fig. 13d). Associated with greenschist-facies parageneses, quartz veins parallel or perpendicular to the main foliation are observed (Fig. 13e). Well preserved eclogite- and blueschist-facies parageneses with pristine garnets occur just above (Fig. 13g). Kinematic indicators such as domino structures (Fig. 13b), stretched pebbles in metaconglomerates (Fig. 13c), shear bands (Fig. 13f) and asymmetrical eclogite boudins (Fig. 13g), are common in all units at all metamorphic grades and are characterized by a top-to-the-NE to −E sense of shear.

In the north-eastern part of the island, close to Cheronissos (Fig. 4), the contact between Upper Marble Complex and Eclogite-Blueschist Unit is well exposed along the coast. This contact appears similar to the previous one except for the absence of metaconglomerate level. Kinematic indicators are top-to-the-northeast in both units and the degree of retrogression seems to be the same as in the contact described above.

7. Discussion

7.1. Timing of deformation and metamorphism

Based on kinematic indicators and their relations with metamorphic parageneses described above and those reported in the literature, we propose a new metamorphic map (Fig. 14). This map is intended to display the first-order distribution of the dominant parageneses as seen in the field, keeping in mind that the peak of metamorphism was everywhere in similar P-T conditions, in the eclogite-facies. In this section, we re-evaluate the chronological evidence used to support the relative timing of tectonic and metamorphic events recorded on Sifnos.

Throughout most of Cheronissos Unit, HP-LT parageneses are particularly well preserved. In the northern part of the island, syn-kinematic minerals in shear band and pressure shadows are developed during syn-orogenic deformation. Locally, an early S_1 foliation has been observed as relics into garnet porphyroblasts but kinematic indicators related to this event are unknown. Most kinematic indicators associated with the retrograde path (under HP-LT conditions) are distributed heterogeneously in all lithologies and indicate a penetrative top-to-the-N shear sense in the upper part and top-to-the-NE to −E in the rest of this unit. Aravadinou et al. (2015) have recognized top-to-the-SE kinematic indicators in thin-sections cut in zones preserved from the bulk of retrograde deformation in northern Sifnos. If one admits that the original stretching direction has been preserved in these zones, the shear sense during the beginning of S_2 formation was top-to-the-SE. This is debatable because the folds refolding S_2 are acute and it is not sure whether the original direction of stretching direction was preserved but this is the only available information in favour of a top-SE shearing event, which could represent the early shearing related to thrusting near the peak of pressure, as proposed by Aravadinou et al. (2015), before the top-to-the-NE shearing. This second-stage shearing is instead observed all over the island and it started before the rocks had left the blueschist-facies during their exhumation. It is possible that this change of shear sense corresponds to the transition from burial to exhumation at high pressure.

Ductile deformation is locally more intense in certain areas such as in the northern part of the island at Vroulidia. This pervasive deformation is linked with the exhumation of Cheronissos Unit from its maximum burial depth and is dated around 45 Ma (Altherr et al., 1979; Wijbrans et al., 1990; Forster and Lister, 2005; Dragovic et al., 2015). At the base of Cheronissos Unit and top of Faros Unit, close to the main contact, a strong deformation gradient in AEBS-facies P-T conditions is observed near Kastro and close to Rizomata Mountain (Fig. 12). Greenschist-facies conditions are recorded in the whole Faros Unit and locally also in Cheronissos Unit close to tectonic contacts (Fig. 14), and are always associated with top-to-the-NE or −E kinematic indicators. Strain localization in Faros Unit is systematically associated with greenschist-facies conditions such as near Chryssopigi (Fig. 11). Available radiochronological data (Altherr et al., 1979; Wijbrans et al., 1990; Ring et al., 2011; Bröcker et al., 2013), obtained on rocks sampled in Faros Unit, date the greenschist-facies retrogression from the Oligocene and Miocene like on most other islands of the Cyclades (e.g., Syros Island, Maluski et al., 1987; Baldwin, 1996; Wijbrans et al., 1990; Tinos and Andros Islands, Bröcker et al., 1993; Huet, 2010).

All lithologies are affected by early isoclinal folds F_1, overturned to the SW Figs. 4 and 7b) and particularly well expressed by alternating folded calcitic and dolomitic marbles in the northern part of the island, where HP rocks are best preserved. The relation between F_1 folds and the top-to-the-north to −northeast shear deformation is debated. Avigad (1990) suggested that they were formed before the peak of metamorphism in the orogenic wedge (or subduction channel) during the subduction of the African slab involving ductile kinematic indicators top-to-the-SW, hence their overturning to the SW. Alternatively, they may have formed continuously during exhumation from blueschist- to greenschist-facies conditions during the dominant top-to-the-northeast shearing and their overturning to the SW is only apparent. Based on field observations (e.g., relationships between dolomitic marbles and marbles), we suggest that the metamorphic pile of Sifnos underwent important flattening and shearing before the peak of metamorphism. This folding could be associated with top-to-the-south deformation that was active within the subduction zone, in syn-orogenic conditions (Huet et al., 2009; Philippon et al., 2011; Aravadinou et al., 2015). The excellent preservation of eclogite- and blueschist-facies parageneses in the north of Cheronissos Unit suggests that these folds started to form within HP-LT conditions and evolved continuously during exhumation from blueschist- to greenschist-facies conditions during the dominant top-to-the-northeast shearing. A later fold generation F_3 deforms the COF contact where we have observed a certain localization of greenschist-facies deformation.

7.2. P-T-time paths of Sifnos and links to deformation

Our study shows that the intense greenschist retrogression of Faros Unit is closely associated with the deformation along the main tectonic contact between Cheronissos and Faros Unit during exhumation. Conspicuous preservation of HP-LT parageneses in Cheronissos Unit largely reflects the fact that greenschist-facies deformation localized in deeper parts of CBU and only locally affected this unit. Thus, Cheronissos Unit was already partly exhumed while Faros Unit was exhuming below it. The observation that the lower part of Faros Unit is dominated by low-pressure parageneses suggests that deformation progressively migrated downward during exhumation. The P-T estimates of Trotet et al.

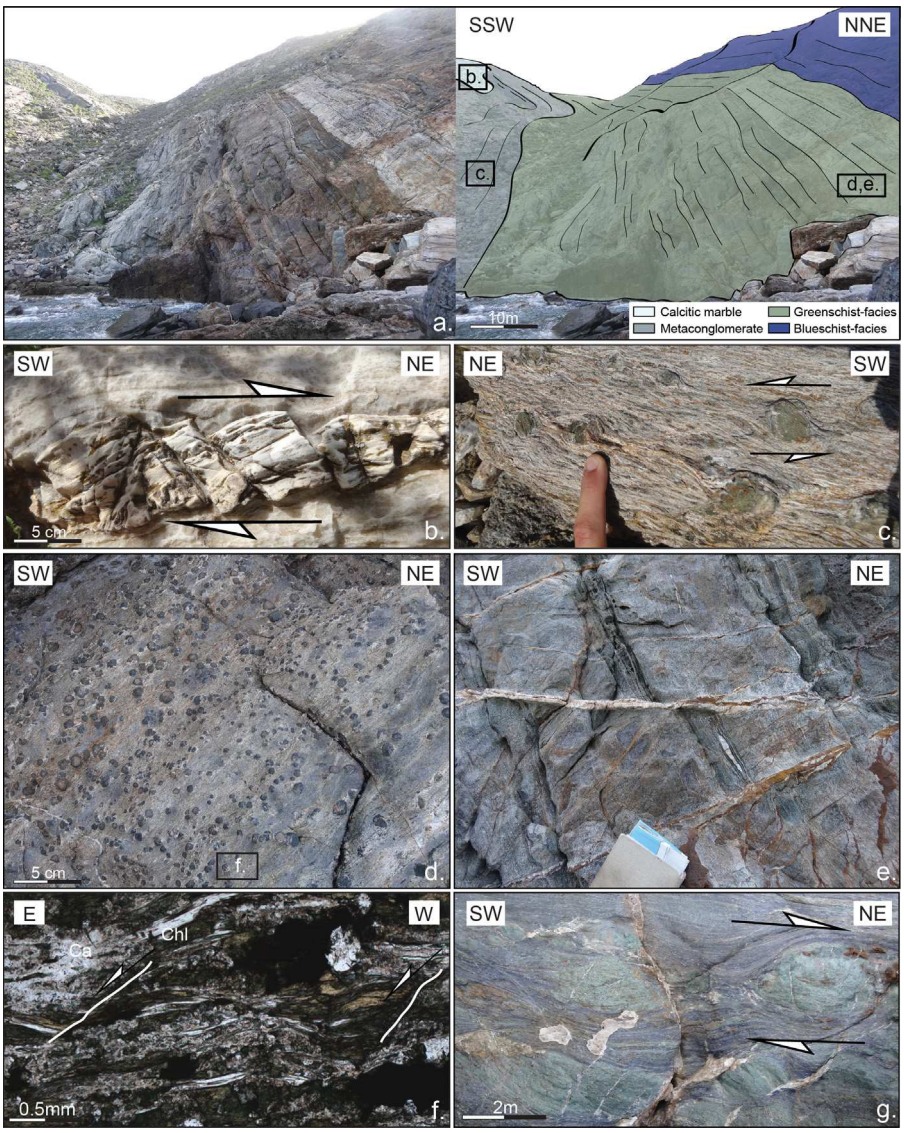

Fig. 13. Contact between the Eclogite-Blueschist Unit and Main Marble Unit (a) This contact is characterized by an average dip of the foliation is about 50° westward and showing a local greenschist-facies retrogression. All kinematic indicators indicate top-to-the-NE sense of shear. Bottom to top, (b) dominos structures in marbles and (c) asymmetric metabasite pebbles within a metaconglomerate level showing a top-to-the-NE sense of shear. (d) Metabasite fully retrograded in the greenschist-facies conditions is associated with (e) quartz-calcite veins which are parallel or perpendicular to the foliation. At micro scale, (f) millimetric shear bands filled in chlorite showing a consistent top-to-the-NE to −E sense of shear. (g) Metabasites form asymmetric pinch boudinage indicating top-to-the-NE kinematics in blueschist-facies condition.

(2001a,b) plot at slightly higher temperature (around 600 °C) than those of Groppo et al. (2009), whose peak is around 560 °C (Fig. 3c). Whether this discrepancy is due to different sampling strategies or to different petrological approaches is beyond the scope of this paper. However, the higher temperature proposed by Trotet et al. (2001b) for the greenschist-facies conditions fits quite well the HT pulse proposed around 19 Ma by Wijbrans et al. (1990) based on $^{40}Ar/^{39}Ar$ data on phengite in Faros Unit (see ages in Fig. 3a and b). Further petrological and chronological studies are needed to clarify the blueschist- to greenschist-facies transition on Sifnos.

7.3. Nature of the contact between Cheronissos and Faros units

In this study, we interpret the COF contact as a top-to-the-northeast ductile shear zone as proposed by Trotet et al. (2001a) (Figs.4 and 14). At small-scale, local brittle deformation may be observed, but not to the point of suggesting a large-scale brittle detachment. Locally, brittle or brittle-ductile kinematic indicators with a top-to-the-SW sense of shear are observed, which led Ring et al. (2011) to suggest that this contact belongs to a top-to-the-south detachment system. Our observations indicate instead that these kinematic indicators are related to the south-dipping late-stage normal faults that cut through the regional foliation.

This shear zone along the COF contact is coeval with the greenschist-facies deformation observed in the whole Faros Unit, and more locally in Cheronissos Unit, as well as along a few localized shear zones such as the Chryssopigi Shear Zone. The COF Shear Zone thus belongs to a thick strain localization zone that encompasses the whole Faros Unit with a downward gradient of strain and progressive downward localization through time, with local smaller scale shear zones where shearing has been preferentially partitioned. We then refer to this thick shear zone as the Apollonia Shear Zone.

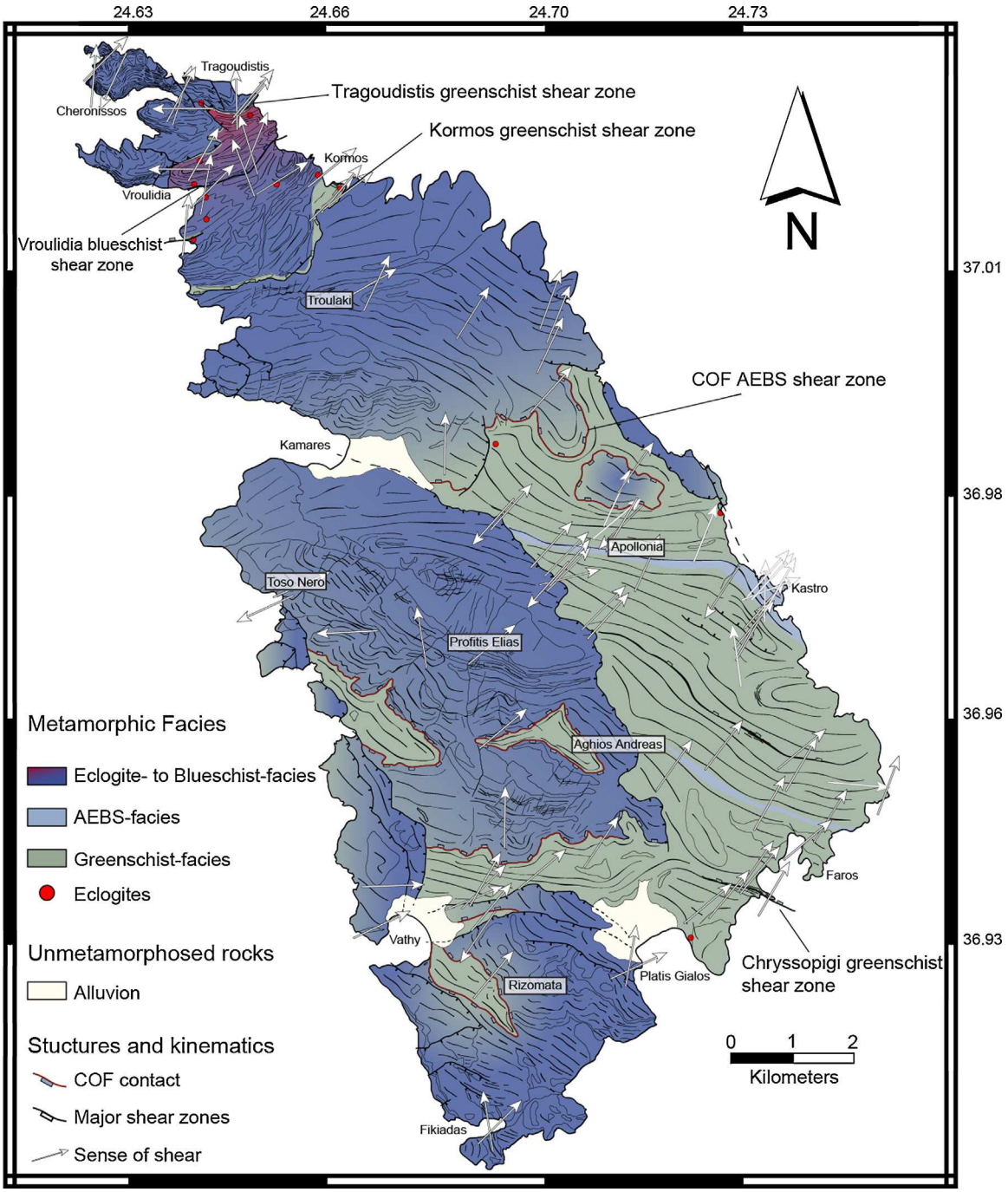

Fig. 14. A new metamorphic map of Sifnos.
Colours correspond to the dominant metamorphic facies observed in the field and colour gradients show the gradual transitions due to progressive top-to-the-NE shearing deformation and coeval retrogression (red shows dominant eclogite-facies, blue dominant blueschist-facies and green dominant greenschist-facies). The white arrows indicate the sense of shear in all units. The main shear zones are indicated in the map.(For interpretation of the references to colour in this figure legend, the reader is referred to the web version of this article.)

7.4. Evolution of shear zones and strain localization

Although some uncertainties remain on the detailed P-T evolution, we show that, from the Eocene (45 Ma) to the Miocene (19 Ma), a continuum of syn- *syn*-blueschist to syn-greenschist top-to-the-N/NE shearing along the Apollonia Shear Zone accommodated the exhumation. In the northern part of the island, peak to retrograde HP-LT deformation is locally well preserved near Vroulidia, without significant greenschist-facies retrogression nor deformation. This part of the top-to-the-north shear zone was thus deactivated early in the exhumation process. The deformation is progressively localized within the major Apollonia Shear Zone, toward the base of the CBU of Sifnos during exhumation. This large-scale structure appears to be more retrograded (from AEBS- to greenschist-facies) toward its lower part. Moreover, progressive localization of deformation is linked with a rejuvenation of apparent ages, from northern (around 47 Ma) to southern (30–19 Ma) part of the island, especially shown by $^{40}Ar/^{39}Ar$ and Rb-Sr data on phengite (see compilation on Fig. 3a and b; Altherr et al., 1982; Wijbrans et al., 1990; Ring et al., 2011; Bröcker et al., 2013). Hence, from a geodynamic point of view, we

propose that this progressive downward localization of strain first occurred at the stage of exhumation within the subduction channel (Eocene, syn-orogenic exhumation *sensu* Jolivet et al., 2003). In a later stage, strain localization occurred within the back-arc region (Oligocene to Miocene, post-orogenic exhumation). The observed shear zones, in the AEBS- or greenschist-facies, tended to localize due to rheological contrast along lithological boundaries such as the base of the Main Marble Unit. Some shear zones (e.g., Chryssopigi) are localized within a single lithological unit. Hence, the downward migration of deformation could be linked to 1) the initial lithological heterogeneity of the CBU. Shear zones were thus active during syn-orogenic and post-orogenic stages of exhumation showing that the kinematic of the Aegean extension in the Oligocene to Miocene was influenced by heterogeneities created during burial and syn-orogenic stage; 2) an intense fluid circulation which is reflected by many syn-kinematic veins; 3) increased thermal influx at the base of the metamorphic pile as suggested by various authors (Matthews and Schliestedt, 1984; Schliestedt and Matthews, 1987; Avigad, 1993; Trotet et al., 2001b). Whatever the actual cause for this downward strain localization one important consequence is that it leaves the upper part of the accretionary complex preserved from late deformation and allows it to reach the surface almost intact. This process of progressive localisation is important to explain how pristine blueschists-facies or eclogite-facies units can now be observed at the surface.

7.5. Tectono-metamorphic evolution of Sifnos

Our observations of the tectono-metamorphic evolution of the cycladic blueschists of Sifnos show that, after a phase of prograde top-to-the-SE shearing (Aravadinou et al., 2015), exhumation involved a top-to-the-NE shearing coeval with decompression and progressive localization of strain in the lower part of the tectonic pile, from the Eocene to the Early Miocene. This evolution thus encompasses both the syn-orogenic stage within the subduction zone and the post-orogenic stage in a back-arc position.

In more details the tectono-metamorphic evolution of Sifnos can be summarized in four stages (Fig. 15):

- Before 47 Ma, during the convergence between African and Eurasian plates and the subduction of the Pindos oceanic basin below the southern margin of Eurasia, the CBU of Sifnos recorded a first deformation phase in the subduction channel, creating an early foliation S_1, only preserved as inclusions in garnets, in particular in the northern part of Sifnos where HP-LT parageneses are well preserved. The sporadic preservation of S_1 structures does not allow constraining the kinematics associated with this first deformation stage. However, we interpret the large-scale folds observed in the northern part of the island as the consequence of this first ductile deformation event (Figs. 4, 7 b and c). This top-to-the-SSW kinematics may be related to the top-to-the-SE shearing described on Sifnos by Aravadinou et al. (2015) or the top-to-the-SW sense of shear described in the CBU on Syros Island by Philippon et al. (2011) and interpreted by these authors as synchronous with the prograde high-pressure deformation phase. On Sifnos, during this first stage of deformation in the mid-Eocene, the Marble Complex, Eclogite-Blueschist Unit and Main Marble Unit were respectively thrust southward on the top of Faros Unit, but the amount of displacement cannot be further constrained. All rocks of Sifnos have probably recorded this prograde top-to-the-SW kinematics that was almost completely overprinted by the later deformation phases.
- Between 47 and 30 Ma, the metamorphic rocks of Sifnos reached peak P-T conditions and started their exhumation. During this syn-orogenic exhumation period, a syn-blueschist deformation phase has resulted in the formation of the foliation in Eclogite-Blueschist Unit with top-to-the-N to –NE sense of shear (Fig. 14). Many folds have developed during this phase, some with their axes perpendicular to the transport direction; locally, a-type folds were formed indicating a strong non-coaxial shearing component.
- From 30 Ma, which corresponds to the beginning of post-orogenic extension and formation of the Aegean Sea, P-T conditions evolved from AEBS- to greenschist-facies conditions. During this phase, the deformation was mainly distributed in the whole Faros Unit, and more locally in Cheronissos Unit. Kinematic criteria indicate a top-to-the-NE sense of shear. The entire Faros Unit can be interpreted as a thick shear zone (Apollonia Shear Zone) with strain localization along the COF contact and, later, near the base of Faros Unit along discrete shear zones such as the Chryssopigi Shear Zone (Fig. 14). Extensive downward greenschist-facies overprint during this event may be related to enhance fluid circulation and increased thermal influx at the base of the metamorphic pile (Matthews and Schiestedt, 1984; Schiestedt and Matthews, 1987; Avigad, 1990; Trotet et al., 2001b).
- Between 19 Ma and Present, the timing of CBU exhumation is constrained by zircon fission track data (Ring et al., 2011). ZFT ages of 13–10 Ma suggest that Faros Unit was exhumed across the 250–300 °C isotherm during this period. The youngest ages associated with ductile deformation are those obtained on micas with the $^{40}Ar/^{39}Ar$ method (Wijbrans et al., 1990) around 19 Ma. The late folds F_3 developed during the beginning of this period and they refold both Faros and Cheronissos Unit. The southwest-dipping normal faults that offset the main COF contact are locally low-angle structures displaying brittle-ductile microstructures Fig. 5c and g). However, their throw is not large and it is difficult to say whether these structures had a significant effect on the final exhumation of Faros Unit. Therefore, the timing of the transition from top-to-the-NE ductile shearing to late brittle top-to-the-SW normal faults observed on Sifnos is not well constrained. Similar SW-dipping listric normal faults and flat-ramp system have been described respectively on Folegandros Island (Augier et al., 2015) and on Syros Island (Philippon et al., 2011). Like on Sifnos, faults crosscut there the metamorphic pile of the CBU and the greenschist-facies foliation, which are both associated with ductile top-to-the-north shear sense. The significance of these SW-dipping faults is debated. Ring et al. (2011) interpreted the contact between Cheronissos and Faros Unit as a top-to-the-SW brittle detachment, which they coined as the "Sifnos detachment" belonging to the "South Cycladic Detachment System" outcropping on the islands of Serifos, Ios and Sifnos. The top-to-the-south sense of shear previously described on Ios (Lister et al., 1984) has been reinterpreted by Huet et al. (2009) as a thrust-related shearing event, thus predating the top-to-the-north Aegean extension. In a more recent paper, Mizera and Behrmann (2015) have addressed this debate again and argued in favour of the extensional model for the Cycladic Blueschist/Basement Unit contact on Ios. They have studied the distribution of kinematic indicators and quantified the amount of stretching in the basement orthogneiss and concluded that the basement has been stretched and flattened by respectively 70% and 40%. They use the upward strain gradient in the basement to conclude that the contact was mainly extensional and they estimate the total displacement during extension to some 13 km. They also recognized that, before extension, the main contact had to be a thrust as shown by Huet et al. (2009). The main point of disagreement stems from different interpretations of the deformation in the basement. Huet et al. (2009) did not consider that the upward strain gradient in the basement was indicative of extension and we stick to their interpretation. It shows the existence of a major shear zone there, but it does not say whether it was extension or compressional. Besides, the late extension is clearly shown in the overlying cycladic

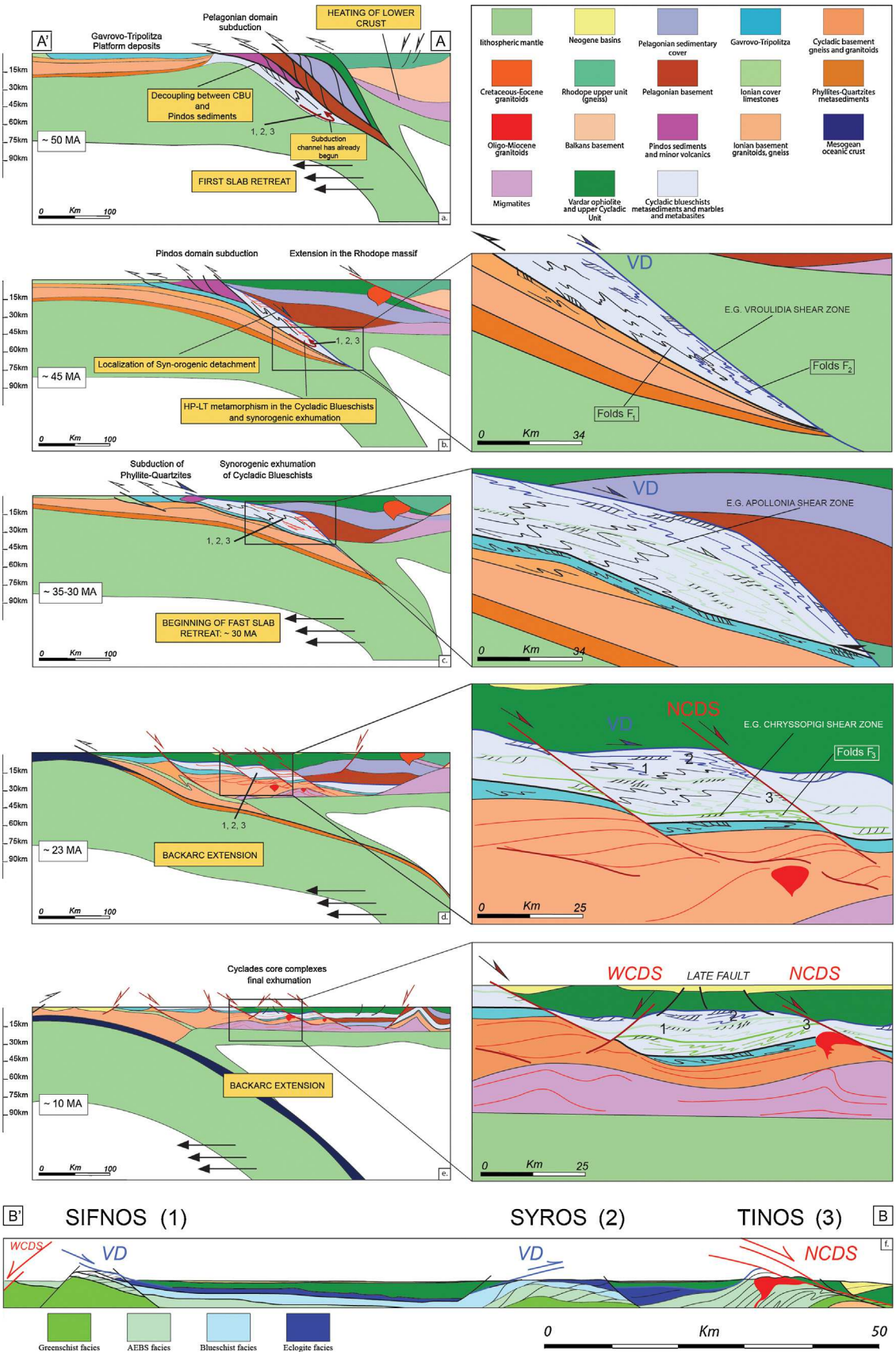

Fig. 15. Series of step-by-step north-south cross-sections of the Aegean domain from 65 Ma to 10 Ma modified after Jolivet and Brun (2010). See location in Fig. 1a. Reconstructions indicate the tectono-metamorphic evolution of Sifnos, Syros and Tinos, respectively shown by numbers 1, 2 and 3. The last cross-section, see location in Fig. 1b, showing the Present geometry of these islands. Abbreviations WCDS, VD, NCDS indicate respectively the West Cycladic Detachment System, the Vari Detachment and the North Cycladic Detachment System.(For interpretation of the references to colour in this figure legend, the reader is referred to the web version of this article.)

blueschists by retrograde top-to-the-N shear bands at all scales, while top-to-the-S syn-blueschists shearing has been preserved only in the vicinity of the main contact. Such intense top-to-the-N shearing, that Huet et al. (2009) attribute to extension is observed all over the island, also in the main contact and it is difficult to confidently say whether the top-to-the-N and top-to-the-S shear zones in the basement were coeval or not.

Grasemann et al. (2012) have described the West Cycladic Detachment System (WCDS) exposed on Kea, Kythnos and Serifos Islands. The WCDS consists in two main detachments, a ductile one intruded by a granodiorite pluton and a brittle one cutting the roof of the same pluton (see also Rabillard et al., 2015). The sense of shear on the WCDS is everywhere top-to-the-south, from Serifos all the way to Lavrion (Fig. 1b). Based on our new field observations of the deformation recorded on Sifnos and especially along the contact between Cheronissos and Faros units, we propose an interpretation significantly different from that of Ring et al. (2011) who associated Ios and Sifnos within the South Cycladic Detachment. As Augier et al. (2015) on Folegandros Island and Jolivet et al. (2015), we suggest to associate the top-to-the-SW faults that offset the COF Shear Zone to a brittle expression of the WCDS that may be extended from Serifos to offshore Sifnos. In this scenario, the N-S-trending normal faults dipping either west or east on either sides of the island are taken to reflect the latest brittle stages accommodating the end of exhumation on Sifnos.

7.6. Implications for the exhumation of the Cycladic Blueschist Unit (CBU)

Current assumptions on the tectonic and metamorphic history of the CBU need to be revised in the light of our new observations. Forster and Lister (2005) proposed a reconstruction involving the succession of several subduction/exhumation episodes with repeated inversion of the sense of motion along the main contacts. However, the exhumation of the CBU is mainly characterized by a top-to-the-N to −E ductile deformation since the Eocene with, most notably, the same metamorphic peak conditions across the whole pile. These can hardly be reconciled with the inversions hypothesized for the evolution of the CBU on Sifnos. Based on the extrusion wedge model of Chemenda et al. (1995), Ring and Reischmann (2002) suggested a decoupling of crustal units accommodated by a detachment at the top and a thrust at the base to explain a part of CBU exhumation. Brun and Faccenna (2008) proposed a similar model with an extreme localization of strain at the top and base of the CBU, their model also emphasizing the importance of slab retreat to favour exhumation. However, our field observations show the existence of several shear zones active since the Eocene during exhumation, showing that the CBU did not behave as a single coherent unit.

This study has clarified some of the uncertainties about the general structure of the CBU of Sifnos, which shows some similarities with Syros Island. Indeed, on Syros the metamorphic peak is estimated around 20kbar and 500–550 °C (Trotet et al., 2001b) and dated around 52 Ma (Lagos et al., 2007). The HP-LT parageneses are also well preserved and the syn-exhumation kinematics are characterized by top-to-the-E sense of shear active in blueschist-facies and greenschist-facies conditions (Trotet et al., 2001a,b; Laurent et al., 2016). Hence, the overall structure of Syros is very similar to that of Sifnos with the notable addition of the Vari Detachment cropping out on Syros. Both islands show the same architecture with the uppermost units below the main detachment displaying the best-preserved HP-LT parageneses with a progressive localization of deformation toward the base of the tectonic stack during exhumation (see Trotet et al., 2001a and Laurent et al., 2016 for Syros Island). However, this Eocene syn-orogenic exhumation gradient is associated with different shearing directions (E-verging on Syros, N-NE-verging on Sifnos; Trotet et al., 2001a,b). Everywhere else, the CBU shows mostly top-to-the-N or NE kinematic indicators related to syn-blueschist exhumation. These are found to vary according to their position within the arc subduction, north-directed in the front, (e.g., Ios), more east-directed on the northern side of the arc (e.g., Andros, Tinos, Fig. 1b).

The history of exhumation of the CBU thus involved a thrust at the base (seen on Ios or Sikinos), a main detachment at the top (the Vari Detachment seen on Syros; Trotet et al., 2001a; Soukis and Stöckli, 2013; Laurent et al., 2016) and a distribution of strain within the exhumed unit along a series of shear zones synthetic of the main upper detachment (top-to-the-N or −E). So the exhumation scenario should be intermediate between the extrusion mode where all the deformation is concentrated at the top and base and a subduction channel in the sense of England and Holland (1979) or Shreve and Cloos (1986) where the deformation is fully distributed. We suggest that HP units are progressively detached from the subducting lithosphere when they reach the peak of pressure by top-to-the-S syn-HP thrusts and are then exhumed within the channel, progressively sheared top-to-the-N or −NE when the approach the roof of the channel, like in Jolivet et al. (2005). Precisely dating the peak of metamorphism in the different units as well as strain localization along the main shear zone would help reaching a consensus on this question.

After the Eocene syn-orogenic episode, exhumation was completed from 35 to 30 Ma during the formation of the Aegean Sea by crustal thinning and accommodated by the NCDS (Jolivet et al., 2010), the Naxos-Paros detachment (Gautier et al., 1993) or the WCDS (Grasemann et al. (2012). This post-orogenic exhumation is characterized by a progressive localization of deformation along extensional shear zones and a consistent sense of shear during the Oligo-Miocene. It is well expressed on Tinos, marked by a NE-SW gradient of non-coaxial strain across a major extensional shear zone (Parra et al., 2002). A greenschist-facies deformation gradient, associated to the NCDS, separates the CBU from the Upper Unit. The top-to-the-north retrograde shearing deformation observed on Ios is probably related to this episode (Huet et al., 2009). Radiometric ages show that this episode is also recorded on Sifnos during the late localization of shearing toward the deep parts of the edifice.

We then suggest that south-dipping brittle normal faults are the brittle expression of the WCDS. The CBU of Sifnos are localized within the footwall of the WCDS, just as Kea, Kythnos and Serifos, but probably deeper and they did not see the intense ductile shearing associated with the WCDS, they only recorded this extension as some late brittle normal faults. Similar south-dipping normal faults are observed on Folegandros Island, further to the southeast and these are the only expression of the WCDS there. At this period, the CBU of Sifnos has undergone penetrative top-to-the-NE deformation whereas the CBU of Serifos has recorded post-orogenic deformation with top-to-the-W sense of shear. A possibility is that the main detachment (WCDS) associated with ductile deformation dies out toward the southeast or reaches the surface off the west coast of Sifnos and Folegandros Islands.

Combining our new structural observations with published petrological and geochronological data, we propose a tectonic model for the exhumation of the CBU in the Aegean domain with particular emphasis placed on evolution of the Cycladic islands of Sifnos, Syros and Tinos. The initial lithospheric scale geometry of the subduction and the disposition of the different units are taken from Jolivet and Brun (2010). Our model is presented as a series of step-by-step north-south cross-sections of the Aegean domain from 50 Ma to the present day with different numbers tracking the evolution of Sifnos (1), Syros (2) and Tinos (3) (see Fig. 15).

Early Eocene (50Ma) to Late Eocene-Early Oligocene (30–35 Ma):

Convergence between the African and Eurasian plates leads the Pindos oceanic crust and margin to reach peak pressure at 20 kbar around 52 Ma and form the CBU at depth (Fig. 15a). Relics of top-to-the-south shearing related to this episode are only locally preserved on Sifnos in the form of few kinematic indicators (Aravadinou et al., 2015) or the large F_1 folds. Top-to-the-south shearing deformation is better preserved on Ios (Huet et al., 2009) and also locally on Syros (Philippon et al., 2011). During this episode, thrusting propagates southward and leads to crustal thickening with nappe stack forming at the expense of the Pindos Ocean and Pelagonian Domain (Fig. 15a). In the early-middle Eocene, around 45 Ma, the CBU started to exhume with a cold retrograde P-T path (Trotet et al., 2001a) while the thrust at its base was still active (Huet et al., 2009). This fast exhumation is accommodated by the Vari Detachment that crops out on Syros Island, representing at this period the roof of the subduction channel (Huet et al., 2009; Jolivet and Brun, 2010; Augier et al., 2015; Laurent et al., 2016) as well as several smaller-scale coeval shear zones with the same kinematics. Just below the Vari Detachment, HP-LT parageneses are well preserved and increasingly retrograded downward with a progressive localization of deformation toward the base of the tectonic stack during exhumation (Fig. 15b). During this period, deformation proceeds mostly in the blueschist-facies with evidence of top-to-the-N to −NE sense of shear and some strain localization, in the subduction channel, as in Vroulidia (Fig. 15b) (Eocene, syn-orogenic exhumation).

Late Eocene to Late Miocene (35–10 Ma):

After a drastic change in the boundary conditions due to a second-stage of slab roll-back at 30–35 Ma (Fig. 15c; Jolivet and Faccenna, 2000; Jolivet and Brun, 2010), thrusting continues to propagate southward in the Apulian platform, whereas in the back-arc region the detachment activity increases because of enhanced rollback. At the scale of the CBU, the deformation is still mainly localized below the Vari Detachment but progressively propagates within the lower parts of the CBU. Syn-AEBS-facies shear zones associated with a top-to-the-NE asymmetric kinematic develop along lithological boundaries such as the base of the Main Marble Unit in Sifnos (COF Shear Zone) and later evolve toward greenschist-facies shear zones during exhumation (Fig. 15c). Altogether these shear zones make the Apollonia Shear Zone. During this period, slab retreat accelerates and back-arc extension is accommodated by a system of post-orogenic detachments, the NCDS and the WCDS, exhuming metamorphic core complexes of the northern and western Cyclades. Slab retreat leads to the replacement of the lithospheric root by the hot asthenosphere in this area, leading to partial melting and the progressive formation of HT core complexes as in Mykonos, Naxos (Fig. 15d; Jolivet and Brun, 2010) or Ikaria (Laurent et al., 2015; Beaudoin et al., 2015; Jolivet et al., 2015) in the Middle Miocene. In the latest stages, granodioritic plutons intrude these core complexes and detachments migrate upward in the crust.

The respective contributions of the Vari Detachment and the NCDS and WCDS in the exhumation of the CBU are not well constrained. The syn-orogenic Vari Detachment has accommodated only a part of the HP-LT rocks exhumation while post-orogenic detachments such as the NCDS crosscut or rework the Vari Detachment and accommodated the last part of rocks exhumation (Fig. 15d). Very little retrogression in greenschist-facies conditions below the Vari Detachment is observed on Syros and Tinos because most of the post-orogenic extension was accommodated on other detachments, such as the NCDS as well as on deeper shear zones such as the Apollonia Shear Zone. When the exhumed material enters the brittle-ductile transition zone, it is exhumed beneath the NCDS or WCDS and is deformed by such shear zones in the greenschist-facies and later in brittle conditions (Fig. 15d). This continuum of extensional strain from ductile-to brittle regime is also particularly well shown in the footwall of the NCDS on Tinos or Andros islands (Jolivet et al., 2004; Mehl et al., 2005, 2007).

During the post-orogenic period, the CBU followed different exhumation paths as recorded on Tinos, Syros and Sifnos. In Fig. 15e, Tinos Island (3) is localized close to the NCDS deeper in the crust whereas Syros (2) and Sifnos (1) have already been largely exhumed just below the Vari Detachment. The whole CBU on Tinos shows a much more intense retrogression in the greenschist-facies than Syros and Sifnos islands, except for those outcrops located on the south-western flank of the foliation dome (Gautier and Brun, 1994; Jolivet et al., 2004; 2010). On Sifnos and Syros, the best-preserved part of the CBU is much thicker and only the lower part is strongly retrograded. This suggests that on Tinos, closer to the NCDS, finite exhumation during the post-orogenic stage has been more important. This late exhumation shows mostly the deepest part of the CBU, strongly retrograded, with the syn-greenschist retrogression along the NCDS itself.

Early Late Miocene (10 Ma) to the present

Around 10 Ma, back-arc extension localized in the Cretan Sea giving rise to local crustal necking, whereas a constant thickness of ~26 km persisted below the hottest part of the Cyclades (Jolivet and Brun, 2010). At around 5 Ma, extension migrated in the northern part of the Aegean domain along the North Anatolian Fault and along the Corinth Rift and the Menderes grabens in western Turkey. As shown by Sanchez-Gomez et al. (2002) and Kuhlemann et al. (2004), the absence of the CBU clasts in continental Miocene basins (8–10 Ma) implies that CBU did not outcrop at this time. The end of the exhumation was accommodated by the brittle deformation that controlled the current geometry of Cycladic islands (Fig. 15f and see location of cross-section Fig. 1b). Around 10 Ma, the metamorphic domes were already formed and close to the surface.

8. Conclusion

In this study, new geological and metamorphic maps at the scale 1:20,000 have been redrawn leading us to reconsider the history of exhumation of the Cycladic Blueschist and discuss published models. The CBU of Sifnos shows several units with different degree of retrogression of HP-LT parageneses. The Cheronissos Unit, which contains well preserved eclogite and blueschist parageneses overlies the Faros Unit where retrogression in the greenschist-facies is intense and HP-LT parageneses are preserved only locally. The main retrograde deformation is associated with a top-to-the-NE sense of shear that is more intense within the Faros Unit. In particular, this unit behaved as a major top-to-the-NE large-scale shear zone (the Apollonia Shear Zone), active throughout the retrograde P-T path from AEBS- to greenschist-facies conditions. Toward the base of the tectonic pile, shearing was characterized by localization of strain along progressively more restrained volumes and therefore thinner shear zones. An earlier deformation is associated with retrograde blueschist-facies parageneses after the peak metamorphic conditions in the eclogite-facies, with a top-to-the-N to −NE sense of shear. Continuous deformation lasted with the same top-to-the-NE sense of shear from the Eocene syn-orogenic blueschist-facies to the Oligocene-Miocene post-orogenic greenschist-facies, showing that the shear zones formed during syn-orogenic exhumation were continuously deformed and/or reactivated during the formation of the Aegean back-arc (see also Gautier and Brun, 1994). Late low-angle and steeper normal faults with top-to-the-SW to −S kinematic indicators crosscut the ductile structures. In our interpretation, they may be the brittle expression of the West Cycladic Detachment System. We propose a model of progressive exhumation, first in the subduction channel of the Hellenic subduction and then in the back-arc region with the same top-to-the-NE non-coaxial component of shearing. Deformation tends to local-

ize downward through time during exhumation leaving the upper parts of the subduction complex preserved from late deformation, thus reaching the surface almost intact. The main discontinuities allowing this exhumation are the Vari Detachment cropping out on Tinos and Syros islands during the syn-orogenic period (Eocene) and then the NCDS and WCDS afterward.

Acknowledgements

We are deeply indebted to the people of Sifnos and especially our friends of Anthoussa Hotel and Kafeneio O Drakakis in Apollonia, as well as Antonios Fissas in Cheronissos. We also wish to thank the two anonymous reviewers who read a first version of the manuscript and helped us prepare a more focussed version. This work has received funding from the European Research Council (ERC) under the seventh Framework Programme of the European Union (ERC Advanced Grant, grant agreement No 290864, RHEOLITH). It is also a contribution of the Labex Voltaire (Convention n° ANR-10-LABX-100-01).

References

Agard, P., Yamato, P., Jolivet, L., Burov, E., 2009. Exhumation of oceanic blueschists and eclogites in subduction zones: timing and mechanisms. Earth Sci. Rev. 92 (1), 53–79.

Altherr, R., Schliestedt, M., Okrusch, M., Seidel, E., Kreuzer, H., Harre, W., Lenz, H., Wendt, I., Wagner, G.A., 1979. Geochronology of high-pressure rocks on sifnos (Cyclades Greece). Contr. Mineral. Petrol. 70, 245–255, http://dx.doi.org/10.1007/BF00375354.

Altherr, R., Kreuzer, H., Wendt, I., Lenz, H., Wagner, G.A., Keller, J., Harre, W., Hohndorf, A., 1982. A late oligocene/early miocene high temperature belt in the attic-cycladic crystalline complex (SE Pelagonian, Greece). Geologisches Jahrbuch E 23, 97–164.

Angelier, J., 1990. Inversion of field data in fault tectonics to obtain the regional stress-III: a new rapid direct inversion method by analytical means. Geophys. J. Int. 103, 363–376.

Aravadinou, E., Xypolias, P., Chatzaras, V., Iliopoulos, I., Gerogiannis, N., 2015. Ductile nappe stacking and refolding in the cycladic blueschist unit: insights from sifnos island (south aegean sea). Int. J. Earth Sci., 1–22.

Ashley, K.T., Caddick, M.J., Steele-MacInnis, M.J., Bodnar, R.J., Dragovic, B., 2014. Geothermobarometric history of subduction recorded by quartz inclusions in garnet. Geochem. Geophys. Geosyst. 15 (2), 350–360, http://dx.doi.org/10.1002/2013GC005106.

Aubouin, J., 1957. Essai de corrélation stratigraphique de la Grèce occidentale. Bulletin de la Société Géologique de France 7, 281–304.

Augier, R., Jolivet, L., Gadenne, L., Lahfid, A., Driussi, O., 2015. Exhumation kinematics of the Cycladic Blueschists unit and back-arc extension, insight from the Southern Cyclades (Sikinos and Folegandros Islands, Greece). Tectonics 34, http://dx.doi.org/10.1002/2014tc003664.

Avigad, D., Matthews, A., Evans, B.W., Garfunkel, Z., 1992. Cooling during the exhumation of a blueschist terrane: sifnos (Cyclades), Greece. Eur. J. Mineral. 4, 619–634.

Avigad, D., 1990. The Geodynamic evolution of the Cycladic blueschist belt (Aegean Sea, Greece)-a contribution to the study of continental collision. In: Unpublished Ph. D. Thesis. Hebrew University of Jerusalem, Israel.

Avigad, D., 1993. Tectonic juxtaposition of blueschists and greenschists in Sifnos Island (Aegean Sea)-implications for the structure of the Cycladic blueschist belt. J. Struct. Geol. 15, 1459–1469, http://dx.doi.org/10.1016/0191-8141(93)90006-V.

Baldwin, S.L., 1996. Contrasting P-T-t histories for blueschists from the western baja terrane and the aegean: effects of synsubduction exhumation and backarc extension. Subduction Top to Bottom, 135–141.

Bauer, C., Rubatto, D., Krenn, K., Proyer, A., Hoinkes, G., 2007. A zircon study from the Rhodope metamorphic complex, N-Greece: time record of a multistage evolution. Lithos 99 (3), 207–228.

Beaudoin, A., Laurent, V., Augier, R., Jolivet, L., Lahfid, A., Arbaret, L., Rabillard, A., Menant, A., 2015. The ikaria high-temperature metamorphic core complex (Cyclades, Greece): geometry, kinematics and thermal structure. J. Geodyn. 92, 18–41, http://dx.doi.org/10.1016/j.jog.2015.09.004.

Beaumont, C., Ellis, S., Hamilton, J., Fullsack, P., 1996. Mechanical model for subduction-collision tectonics of Alpine-type compressional orogens. Geology 24 (8), 675–678.

Blake, M.C., Bonneau, M., Geyssant, J., Kienast, J.R., Lepvrier, C., Maluski, H., Papanikolaou, D., 1981. A geologic reconnaissance of the Cycladic blueschist belt, Greece. Geol. Soc. Am. Bull. 92 (5), 247–254.

Bond, C.E., Butler, R.W., Dixon, J.E., 2007. Co-axial horizontal stretching within extending orogens: the exhumation of HP rocks on Syros (Cyclades) revisited. Geol. Soc. Lonon Spec. Publ. 272 (1), 203–222.

Bonev, N., Beccaletto, L., 2007. From syn-to post-orogenic Tertiary extension in the north Aegean region: constraints on the kinematics in the eastern Rhodope-Thrace, Bulgaria-Greece and the Biga Peninsula, NW Turkey. Geol. Soc. London Spec. Publ. 291 (1), 113–142.

Bonev, N., Burg, J.P., Ivanov, Z., 2006. Mesozoic–Tertiary structural evolution of an extensional gneiss dome—the Kesebir–Kardamos dome, eastern Rhodope (Bulgaria–Greece). Int. J. Earth Sci. 95 (2), 318–340.

Bonneau, M., 1982. Evolution géodynamique de larc égéen depuis le Jurassique Supérieur jusquau Miocène. Bulletin de la Societé géologique de France, 229–242.

Bonneau, M., 1984. Correlation of the Hellenide nappes in the south-east Aegean and their tectonic reconstruction. Geol. Soc. London Spec. Publ. 17, 517–527.

Bröcker, M., Franz, L., 1998. Rb-Sr isotope studies on Tinos Island (Cyclades, Greece): additional time constraints for metamorphism, extent of infiltration-controlled overprinting and deformational activity. Geol. Mag. 135, 369–382.

Bröcker, M., Kreuzer, H., Matthews, A., Okrusch, M., 1993. 40Ar/39Ar and oxygen isotope studies of polymetamorphism from Tinos Island, Cycladic blueschist belt, Greece. J. Metamorph. Geol. 11, 223–240.

Bröcker, M., Baldwin, S., Arkudas, R., 2013. The geological significance of $Ar^{39}Ar$ and Rb-Sr white mica ages from Syros and Sifnos Greece: a record of continuous (re)crystallization during exhumation? J. Metamorph. Geol. 31, 629–646, http://dx.doi.org/10.1111/jmg.12037.

Brun, J.P., Sokoutis, D., 2007. Kinematics of the southern Rhodope core complex (North Greece). Int. J. Earth Sci. 96 (6), 1079–1099.

Brun, J.-P., Faccenna, C., 2008. Exhumation of high-pressure rocks driven by slab rollback. Earth Planet. Sci. Lett. 272, 1–7, http://dx.doi.org/10.1016/j.epsl.2008.02.038.

Burg, J.P., Ricou, L.E., Ivano, Z., Godfriaux, I., Dimov, D., Klain, L., 1996. Syn-metamorphic nappe complex in the Rhodope Massif. Structure and kinematics. Terra Nova 8 (1), 6–15.

Burov, E., Jolivet, L., Le Pourhiet, L., Poliakov, A., 2001. A thermomechanical model of exhumation of high pressure (HP) and ultra-high pressure (UHP) metamorphic rocks in Alpine-type collision belts. Tectonophysics 342 (1), 113–136.

Chemenda, A.I., Mattauer, M., Malavieille, J., Bokun, A.N., 1995. A mechanism for syn-collisional rock exhumation and associated normal faulting: results from physical modelling. Earth Planet. Sci. Lett. 132 (1), 225–232.

Delvaux, D., Sperner, B., 2003. New aspects of tectonic stress inversion with reference to the TENSOR program. In: Nieuwland, D.A. (Ed.), New Insights into Structural Interpretation and Modelling., 212. Geological Society London, SPecial Publications, pp. 75–100.

Denèle, Y., Lecomte, E., Jolivet, L., Lacombe, O., Labrousse, L., Huet, B., Le Pourhiet, L., 2011. Granite intrusion in a metamorphic core complex: the example of the Mykonos laccolith (Cyclades, Greece). Tectonophysics 501, 52–70.

Dragovic, B., Samanta, L.M., Baxter, E.F., Selverstone, J., 2012. Using garnet to constrain the duration and rate of water-releasing metamorphic reactions during subduction: an example from Sifnos, Greece. Chem. Geol. 314-317, 9–22, http://dx.doi.org/10.1016/j.chemgeo.2012.04.016.

Dragovic, B., Baxter, E.F., Caddick, M.J., 2015. Pulsed dehydration and garnet growth during subduction revealed by zoned garnet geochronology and thermodynamic modeling Sifnos, Greece. Earth Planet. Sci. Lett. 413, 111–122.

Duchene, S., Aissa, R., Vanderhaeghe, O., 2006. Pressure-temperature-time evolution of metamorphic rocks from Naxos (Cyclades, Greece): constraints from thermobarometry and Rb/Sr dating. Geodinamica Acta 19, 301–321.

England, P.C., Holland, T.J.B., 1979. Archimedes and the Tauern eclogites: the role of buoyancy in the preservation of exotic eclogite blocks. Earth Planet. Sci. Lett. 44 (2), 287–294.

Evans, B.W., 1990. Phase relations of epidote-blueschists. Lithos 25, 3–23.

Forster, M.A., Lister, G.S., 2005. Several distinct tectono-metamorphic slices in the Cycladic eclogite–blueschist belt Greece. Contrib. Mineral. Petrol. 150, 523–545.

Forster, M.A., Lister, G.S., 2009. Core-complex-related extension of the Aegean lithosphere initiated at the Eocene-Oligocene transition. J. Geophys. Res. 114 (2), p36.

Gautier, P., Brun, J.-P., 1994. Crustal-scale geometry and kinematics of late-orogenic extension in the central Aegean (Cyclades and Ewia Island). Tectonophysics 238, 399–424.

Gautier, P., Brun, J.-P., Jolivet, L., 1993. Structure and kinematics of upper Cenozoic extensional detachment on Naxos and Paros (Cyclades Islands, Greece). Tectonics 12, 1180–1194.

Gerya, T.V., Stöckhert, B., Perchuk, A.L., 2002. Exhumation of high-pressure metamorphic rocks in a subduction channel: a numerical simulation. Tectonics 21 (6), 6–11.

Grasemann, B., Schneider, D.A., Stöckli, D.F., Iglseder, C., 2012. Miocene bivergent crustal extension in the Aegean: evidence from the western Cyclades (Greece). Lithosphere 4, 23–39.

Groppo, C., Forster, M., Lister, G., Compagnoni, R., 2009. Glaucophane schists and associated rocks from Sifnos (Cyclades Greece): new constraints on the P–T evolution from oxidized systems. Lithos 109, 254–273, http://dx.doi.org/10.1016/j.lithos.2008.10.005.

Huet, B., Labrousse, L., Jolivet, L., 2009. Thrust or detachment? Exhumation processes in the Aegean: insight from a field study on Ios (Cyclades, Greece). Tectonics 28, TC3007, http://dx.doi.org/10.1029/2008TC002397.

Huet, B., 2010. Rhéologie de la lithosphère continentale: lexemple de la Mer Egée. Université Pierre et Marie Curie—Paris VI.

Iglseder, C., Grasemann, B., Schneider, D.A., Petrakakis, K., Miller, C., Klötzli, U.S., Thöni, M., Zámolyi, A., Rambousek, C., 2009. I and S-type plutonism on serifos (W-Cyclades Greece). Tectonophysics 473, 69–83, http://dx.doi.org/10.1016/j.tecto.2008.09.021.

Iglseder, C., Grasemann, B., Rice, A.H.N., Petrakakis, K., Schneider, D.A., 2011. Miocene south directed low-angle normal fault evolution on kea island (West cycladic detachment system, Greece). Tectonics 30, TC4013.

Jacobshagen, V., Dürr, S., Kockel, F., Kopp, K.O., Kowalczyk, G., Berckhemer, H., Büttner, D., 1978. Structure and geodynamic evolution of the Aegean region. In: Cloos, H., Roeder, D., Schmidt, K. (Eds.), Alps, Apennines, Hellenides. IUGG, Stuttgart, pp. 537–564.

Jacobshagen, V., 1986. Geologie von Griechenland: Berlin-Stuttgart Borntraeger, 279 p.

Jolivet, L., Brun, J.-P., 2010. Cenozoic geodynamic evolution of the Aegean. Int. J. Earth Sci. (Geol Rundsch) 99, 109–138, http://dx.doi.org/10.1007/s00531-008-0366-4.

Jolivet, L., Faccenna, C., 2000. Mediterranean extension and the Africa-Eurasia collision. Tectonics 19, 1095–1106, http://dx.doi.org/10.1029/2000TC900018.

Jolivet, L., Brun, J.P., Gautier, P., Lallemant, S., Patriat, M., 1994. 3D-kinematics of extension in the Aegean region from the early Miocene to the present; insights from the ductile crust. Bull. Soc. Geol. Fr. 165, 195–209.

Jolivet, L., Faccenna, C., Goffé, B., Burov, E., Agard, P., 2003. Subduction tectonics and exhumation of high-pressure metamorphic rocks in the Mediterranean orogens. Am. J. Sci. 303, 353–409.

Jolivet, L., Famin, V., Mehl, C., Parra, T., Aubourg, C., Hébert, R., Philippot, P., 2004. Strain localization during crustal-scale boudinage to form extensional metamorphic domes in the Aegean Sea. Spec. Pap.-Geol. Soc. Am., 185–210.

Jolivet, L., Raimbourg, H., Labrousse, L., Avigad, D., Leroy, Y., Austrheim, H., Andersen, T.B., 2005. Softening trigerred by eclogitization, the first step toward exhumation during continental subduction. Earth Planet. Sci. Lett. 237 (3), 532–547.

Jolivet, L., Augier, R., Faccenna, C., Negro, F., Rimmele, G., Agard, P., Robin, C., Rossetti, F., Crespo-Blanc, A., 2008. Subduction: convergence and the mode of backarc extension in the Mediterranean region. Bulletin de la Société Géologique de France 179, 525–550.

Jolivet, L., Lecomte, E., Huet, B., Denèle, Y., Lacombe, O., Labrousse, L., Le Pourhiet, L., Mehl, C., 2010. The north cycladic detachment system. Earth Planet. Sci. Lett. 289, 87–104.

Jolivet, L., Faccenna, C., Huet, B., Labrousse, L., Le Pourhiet, L., Lacombe, O., Lecomte, E., Burov, E., Denèle, Y., Brun, J.-P., Philippon, M., Paul, A., Salaün, G., Karabulut, H., Piromallo, C., Monié, P., Gueydan, F., Okay, A.I., Oberhänsli, R., Pourteau, A., Augier, R., Gadenne, L., Driussi, O., 2013. Aegean tectonics: strain localisation, slab tearing and trench retreat. Tectonophysics 597-598, 1–33, http://dx.doi.org/10.1016/j.tecto.2012.06.011.

Jolivet, L., Menant, A., Sternai, P., Rabillard, A., Arbaret, L., Augier, R., Laurent, V., Beaudoin, A., Grasemann, B., Huet, B., Labrousse, L., Le Pourhiet, L., 2015. The geological signature of a slab tear below the Aegean. Tectonophysics 659, 166–182, http://dx.doi.org/10.1016/j.tecto.2015.08.004.

Keay, S., Lister, G., Buick, I., 2001. The timing of partial melting, Barrovian metamorphism and granite intrusion in the Naxos metamorphic core complex Cyclades, Aegean Sea, Greece. Tectonophysics 342, 275–312.

Keiter, M., Piepjohn, K., Ballhaus, C., Lagos, M., Bode, M., 2004. Structural development of high-pressure metamorphic rocks on Syros island (Cyclades, Greece). J. Struct. Geol. 26 (8), 1433–1445.

Keiter, M., Ballhaus, C., Tomaschek, F., 2011. A new geological map of the Island of Syros (Aegean Sea, Greece): Implications for lithostratigraphy and structural history of the Cycladic Blueschist Unit. Geol. Soc. Am. Spec. Pap. 481, 1–43.

Kuhlemann, J., Frisch, W., Dunkl, I., Kázmér, M., Schmiedl, G., 2004. Miocene siliciclastic deposits of Naxos Island: geodynamic and environmental implications for the evolution of the southern Aegean Sea (Greece). Geol. Soc. Am. Spec. Pap. 378, 51–65.

Kumerics, C., Ring, U., Brichau, S., Glodny, J., Monié, P., 2005. The extensional Messaria shear zone and associated brittle detachment faults, Aegean Sea, Greece. J. Geol. Soc. 162, 701–721.

Lagos, M., Scherer, E.E., Tomaschek, F., Münker, C., Keiter, M., Berndt, J., Ballhaus, C., 2007. High precision Lu–Hf geochronology of Eocene eclogite-facies rocks from Syros Cyclades, Greece. Chem. Geol. 243, 16–35.

Laurent, V., Beaudoin, A., Jolivet, L., Arbaret, L., Augier, R., Rabillard, A., Menant, A., 2015. Interrelations between extensional shear zones and synkinematic intrusions: the example of Ikaria Island (NE Cyclades, Greece). Tectonophysics 651-652, 152–171.

Laurent, V., Jolivet, L., Roche, V., Augier, R., Scaillet, S., Cardello, G.L., 2016. Strain localization in a fossilized subduction channel: insights from the Cycladic Blueschist Unit (Syros, Greece). Tectonophysics 672, 150–169, http://dx.doi.org/10.1016/j.tecto.2016.01.036.

Lecomte, E., Jolivet, L., Lacombe, O., Denèle, Y., Labrousse, L., Le Pourhiet, L., 2010. Geometry and kinematics of Mykonos detachment, Cyclades, Greece: evidence for slip at shallow dip. Tectonics 29, http://dx.doi.org/10.1029/2009tc002564.

Liati, A., Gebauer, D., Wysoczanski, R., 2002. U–Pb SHRIMP-dating of zircon domains from UHP garnet-rich mafic rocks and late pegmatoids in the Rhodope zone (N Greece); evidence for Early Cretaceous crystallization and Late Cretaceous metamorphism. Chem. Geol. 184 (3), 281–299.

Lister, G.S., Raouzaios, A., 1996. The tectonic significance of a porphyroblastic blueschist facies overprint during Alpine orogenesis: sifnos, Aegean Sea, Greece. J. Struct. Geol. 18, 1417–1435, http://dx.doi.org/10.1016/S0191-8141(96)00072-7.

Lister, G.S., Banga, G., Feenstra, A., 1984. Metamorphic core complexes of Cordilleran type in the Cyclades Aegean Sea, Greece. Geology 12, 221–225.

Malinverno, A., Ryan, W.B.F., 1986. Extension in the Tyrrhenian Sea and shortening in the Apennines as result of arc migration driven by sinking of the lithosphere. Tectonics 5, 227–245, http://dx.doi.org/10.1029/TC005i002p00227.

Maluski, H., Bonneau, M., Kienast, J.R., 1987. Dating the metamorphic events in the Cycladic area; 39 Ar/40 Ar data from metamorphic rocks of the Island of Syros (Greece). Bulletin de la Société géologique de France 3, 833–842.

Matthews, A., Schliestedt, M., 1984. Evolution of the blueschist and greenschist facies rocks of Sifnos, Cyclades, Greece. Contr. Mineral. and Petrol. 88, 150–163, http://dx.doi.org/10.1007/BF00371419.

Mehl, C., Jolivet, L., Lacombe, O., 2005. From ductile to brittle: evolution and localization of deformation below a crustal detachment (Tinos, Cyclades, Greece). Tectonics 24, http://dx.doi.org/10.1029/2004tc001767.

Mehl, C., Jolivet, L., Lacombe, O., Labrousse, L., Rimmele, G., 2007. Structural evolution of Andros (Cyclades, Greece): a key to the behaviour of a (flat) detachment within an extending continental crust. Geol. Soc. London Spec. Publ. 291, 41–73.

Menant, A., Jolivet, L., Vrielynck, B., 2016. Kinematic reconstructions and magmatic evolution illuminating crustal and mantle dynamics of the eastern Mediterranean region since the late Cretaceous. Tectonophysics.

Mizera, M., Behrmann, J.H., 2015. Strain and flow in the metamorphic core complex of Ios Island (Cyclades, Greece). Int. J. Earth Sci., 1–14.

Parra, T., Vidal, O., Jolivet, L., 2002. Relation between the intensity of deformation and retrogression in blueschist metapelites of Tinos Island (Greece) evidenced by chlorite–mica local equilibria. Lithos 63, 41–66.

Philippon, M., Brun, J.-P., Gueydan, F., 2011. Tectonics of the syros blueschists (Cyclades Greece): from subduction to aegean extension. Tectonics 30 (4).

Platt, J.P., 1993. Exhumation of high-pressure rocks: a review of concepts and processes. Terra nova 5 (2), 119–133.

Rabillard, A., Arbaret, L., Jolivet, L., Le Breton, N., Gumiaux, C., Augier, R., Grasemann, B., 2015. Interactions between plutonism and detachments during metamorphic core complex formation, serifos island (Cyclades, Greece). Tectonics (Submitted).

Ring, U., Reischmann, T., 2002. The weak and superfast Cretan detachment, Greece: exhumation at subduction rates in extruding wedges. J. Geol. Soc. 159, 225–228, http://dx.doi.org/10.1144/0016-764901-150.

Ring, U., Thomson, S.N., Bröcker, M., 2003. Fast extension but little exhumation: the Vari detachment in the Cyclades, Greece. Geol. Mag. 140, 245–252, http://dx.doi.org/10.1017/S0016756803007799.

Ring, U., Glodny, J., Will, T., Thomson, S., 2010. The Hellenic subduction system: high-pressure metamorphism, exhumation, normal faulting, and large-scale extension. Annu. Rev. Earth Planet. Sci. 38, 45–76.

Ring, U., Glodny, J., Will, T.M., Thomson, S., 2011. Normal faulting on sifnos and the south cycladic detachment system, aegean sea, Greece. J. Geol. Soc. 168, 751–768, http://dx.doi.org/10.1144/0016-76492010-064.

Rosenbaum, G., Avigad, D., Sánchez-Gómez, M., 2002. Coaxial flattening at deep levels of orogenic belts: evidence from blueschists and eclogites on Syros and Sifnos (Cyclades, Greece). J. Struct. Geol. 24, 1451–1462.

Rosenbaum, G., Ring, U., Kühn, A., 2007. Tectonometamorphic evolution of high-pressure rocks from the island of Amorgos (Central Aegean Greece). J. Geol. Soc. London 164, 425–438.

Sanchez-Gomez, M., Avigad, D., Heimann, A., 2002. Geochronology of clasts in allochthonous Miocene sedimentary sequences on Mykonos and Paros Islands: implications for back-arc extension in the Aegean Sea. J. Geol. Soc. 159, 45–60.

Schliestedt, M., Matthews, A., 1987. Transformation of blueschist to greenschist facies rocks as a consequence of fluid infiltration, Sifnos (Cyclades), Greece. Contr. Mineral. Petrol. 97, 237–250, http://dx.doi.org/10.1007/BF00371243.

Schliestedt, M., 1986. Eclogite-Blueschist relationships as evidenced by mineral equilibria in the high-Pressure metabasic rocks of sifnos (Cycladic islands), Greece. J. Petrol. 27, 1437–1459, http://dx.doi.org/10.1093/petrology/27.6.1437.

Schmadicke, E., Will, T.M., 2003. Pressure-temperature evolution of blueschist facies rocks from Sifnos, Greece, and implications for the exhumation of high-pressure rocks in the Central Aegean. J. Metamorph. Geol. 21, 799–811, http://dx.doi.org/10.1046/j.1525-1314.2003.00482.x.

Schumacher, J.C., Brady, J.B., Cheney, J.T., Tonnsen, R.R., 2008. Glaucophane-bearing marbles on Syros, Greece. J. Petrol. 49 (9), 1667–1686.

Shreve, R.L., Cloos, M., 1986. Dynamics of sediment subduction, melange formation, and prism accretion. J. Geophys. Res.: Solid Earth (1978–2012) 91 (B10), 10229–10245.

Spear, F.S., Wark, D.A., Cheney, J.T., Schumacher, J.C., Watson, E.B., 2006. Zr-in-rutile thermometry in blueschists from Sifnos, Greece. Contrib. Mineral. Petrol. 152, 375–385, http://dx.doi.org/10.1007/s00410-006-0113-4.

Stampfli, G.M., 2000. Tethyan oceans. Geological Society. London Spec. Publ. 173, 1–23, http://dx.doi.org/10.1144/GSL.SP.;1;2000.173.01.01.

Tirel, C., Gautier, P., Van Hinsbergen, D.J.J., Wortel, M.J.R., 2009. Sequential development of interfering metamorphic core complexes: numerical experiments and comparison with the Cyclades, Greece. Geolo. Soc. London Spec. Publ. 311 (1), 257–292.

Tirel, C., Brun, J.-P., Burov, E., Wortel, M.J.R., Lebedev, S., 2013. A plate tectonics oddity: caterpillar-walk exhumation of subducted continental crust. Geology 41, 555–558, http://dx.doi.org/10.1130/G33862.1.

Trotet, F., Jolivet, L., Vidal, O., 2001a. Tecto-metamorphic evolution of syros and sifnos islands (Cyclades Greece). Tectonophysics 338, 179–206, http://dx.doi.org/10.1016/S0040-1951(01)00138-X.

Trotet, F., Vidal, O., Jolivet, L., 2001b. Exhumation of Syros and Sifnos metamorphic rocks (Cyclades, Greece): new constraints on the PT paths. Eur. J. Mineral. 13, 901–902.

Urai, J.L., Schuiling, R.D., Jansen, J.B.H., 1990. Alpine deformation on naxos (Greece). Geol. Soc. London Spec. Publ. 54 (1), 509–522.

Van Hinsbergen, D., Hafkenscheid, E., Spakman, W., Meulenkamp, J.E., Wortel, R., 2005. Nappe stacking resulting from subduction of oceanic and continental lithosphere below Greece. Geology 33, 325–328.

Vanderhaeghe, O., 2004. Structural development of the Naxos migmatite dome. Geol. Soc. Am. Spec. Pap. 380, 211–227, –v.

Wijbrans, J.R., Schliestedt, M., York, D., 1990. Single grain argon laser probe dating of phengites from the blueschist to greenschist transition on Sifnos (Cyclades Greece). Contr. Mineral. Petrol. 104, 582–593, http://dx.doi.org/10.1007/BF00306666.

Wijbrans, J.R., Wees, J.D., van Stephenson, R.A., Cloetingh, S. a. P.L., 1993. Pressure-temperature-time evolution of the high-pressure, metamorphic complex of Sifnos, Greece. Geology 21, 443–446, http://dx.doi.org/10.1130/0091-7613(1993)021<0443:PTTEOT>2.3.CO;2.

Migration of geothermal fluids in extensional MCC: a long-lived hydrothermal (mineral and geothermal) system? (Annexe C)

Vincent ROCHE[1, 2, 3], Johann TUDURI[1, 2, 3], Vincent BOUCHOT[1, 2, 3], Laurent JOLIVET[1, 2, 3]

[1] *Université d'Orléans, ISTO, UMR 7327, 45071, Orléans, France*

[2] *CNRS/INSU, ISTO, UMR 7327, 45071 Orléans, France*

[3] *BRGM, ISTO, UMR 7327, BP 36009, 45060 Orléans, France*

(Je présente ici des résultats préliminaires)

In the following, we present our preliminary results from the Salihli prospect. We have provided ^{40}Ar-^{39}Ar dating on adularia to determine with precision the age of the mineralization. Although this approach provides new information on the structural control of such deposits, a detail study of fluid inclusions would be necessary. The mineral paragenetic sequence was thus only constructed on field observations and reflected light- and scanning electron microscope studies of thin sections.

1. Introduction

Subduction dynamics exerts a primary control at the lithospheric- and crustal-scale on the location of low- to high-sulphidation epithermal deposits. Although many studies constrain the physicochemical mechanisms at the origin of these deposits, especially in the domains of magmatic arcs and in collision zones [*e.g.* Groves *et al.*, 1998; Sillitoe & Hedenquist, 2003; Richards, 2005; 2009; Bertrand *et al.*, 2014], porphyry Cu-Au and related epithermal Au systems can also form in postsubduction and collisional tectonic settings such as in the Mediterranean realm [Menant *et al.*, submitted]. However, the link between post-collisional metallogenic evolution (*i.e.* porphyry-epithermal), magmatism and extension remains poorly constrained. Nevertheless, there are some examples of epithermal-like deposits that are structurally controlled by detachment faults or listric normal faults, such as the AdaTepe district in the Eastern Rhodope Mountains in Bulgaria [Marchev *et al.*, 2004], or the Lewis-Crofoot in the Basin & Range in Nevada [Ebert & Rye, 1997]. In both cases, the contribution of sub-contemporary magmatism associated with mineralization is strongly discussed. In addition, Sillitoe and Hedenquist [2003] also indicated that this type of epithermal occurrences located within the detachment was generally not mineralized in gold, and thus without economic interest. Located in the Western part of Anatolia, the Menderes Massif offers the opportunity to study this type of deposit.

The Western Anatolian metallogenic province, located from the Biga Peninsula in the north, to the Menderes Massif in the south, is well known for its distribution of (i) alkaki porphyry Au-Cu-Mo systems (*e.g.* the Au-rich Kışladağ deposit and the Cu-Au Halilağa prospect) [Yigit, 2006; 2009], (ii) skarn Fe(-Cu) and Pb-Zn(Au-Cu) ore deposits (*e.g.* the Ayazmant and Balya deposits) [Agdemir *et al.*, 1994; Oyman, 2010], (iii) large number of low- to -intermediate sulfidation epithermal Au-(Ag-Pb-Zn-Cu) deposits of various sizes and ore grades located in the Biga Peninsula and Izmir area (*e.g.* the Ağı Dağı and Sahinli prospects, and the Efemçukuru and Ovacik deposits) [Oyman, 2003; Yılmaz *et al.*, 2007; 2010], and (iv) the wide Sb-Hg-As-Au occurrences and deposits (*e.g.* the Haliköy Hg and Emirli Au-Sb deposits [Akçay *et al.*, 2006; Yigit, 2012]). In that sense, this province displays a high economic interest with several active mines and numerous recent discoveries of precious- and base-metal prospects (Fig. C.1) [Yigit, 2006; 2009; 2012]. Although most of these mineral deposits are spatially associated with extensional tectonics-related volcanic rocks from Eocene to Miocene from north to south [*i.e.* the epithermal, skarn and porphyry deposit types, respectively [Yılmaz *et al.*, 2007; 2010; Yigit, 2012;

Bozkaya *et al.*, 2016]), the Sb-Hg-As-Au ones seem to be clearly metamorphic-hosted and detachment fault-controlled (*i.e.* high-angle-normal faults and shear zones [Yigit, 2012]). For these reasons, this kind of Sb-Hg-As-Au deposits have been interpreted as orogenic deposit types [Gessner *et al.*, 2017]. They are mainly located in the Menderes Massif (Fig. C.1). This massif has recorded a complex nappe stacking during two major orogenic cycles during the Neoproterozoic-Cambrian and the Eocene, and a strong reworking during the Oligo-Miocene post-orogenic extension [*e.g.* Hetzel *et al.* 1995a; 1995b; Candan *et al.* 2001; Gessner *et al.* 2001a; 2004; Rimmele *et al.* 2003; Koralay 2015].

According to Yigit [2012], genesis of orogenic gold deposits in the Menderes Massif is due to a low temperature remobilization during the core complex formation and an epithermal mineralization related to magmatism in the back-arc domain (*i.e.* the Salihli granodiorite). However, the link between such deposits and the magmatic activity remains poorly constrained. In this study we therefore focus on the Salihli area that presents both fossil and active geothermal systems. First, we briefly present the structural control on these Au-Sb, Hg occurrences in this area, and we propose a paleo fluid flow pathways for this mineralization event and discuss the ore forming processes and then propose an ore deposit type model. Then, we compare this fossil geothermal system with active ones, and we suggest a conceptual model without magmatic source in the upper levels of the crust. This approach may bring regional- to local-scale guides for the possible discovery of new ore-deposits.

2. Geological setting

2.1. The Menderes Massif

The Menderes Massif is a tectonic window exposing metamorphic rocks in the back-arc domain of the Hellenic subduction zone in the western part of Turkey (Fig. C.1a). It is made of a "core" of augen gneisses, and a metasedimentary "cover" formed from the early Paleozoic to the Tertiary [Schuiling, 1962]. Belonging to the Anatolide-Tauride block, this massif has undergone two main tectonometamorphic events: (i) a first stage which consisted in nappe stacking and crustal thickening during the Cretaceous and the Eocene [*e.g.* Collins & Robertson, 1998; Gessner *et al.*, 2001b; Schmidt el al. 2015], and (ii) a second stage where the thickened crust of the Menderes Massif has undergone a NNE-SSW post-orogenic extension stage since the Oligo-Miocene [Bozkurt & Oberhänsli, 2001; Bozkurt *et al.*, 2011]. Extension was accommodated by three main low-angle normal faults (*i.e.* detachment faults) in the northern and central submassifs. From north to south, there are the Simav Detachment bounding to the south the Simav graben (Fig. C.1a) [Işik & Tekeli, 2001], the Alaşehir detachment (also named Gediz detachment) along the southern margin of the Alaşehir graben and the Büyük Menderes detachment along the northern margin of the Büyük Menderes graben [Fig. C.1, Hetzel *et al.*, 1995a; 1995b]. An additional distributed strike-slip tectonics has also been

recorded in the entire massif. There, high-angle N-S trending faults crosscut the Neogene sediments [Çiftçi & Bozkurt, 2010] and affect the basement of the Menderes Massif. Finally, the recent evolution of the Menderes Massif is dominated by high-angle E-W trending normal faults that affected the detachment and controlled the basin sedimentation.

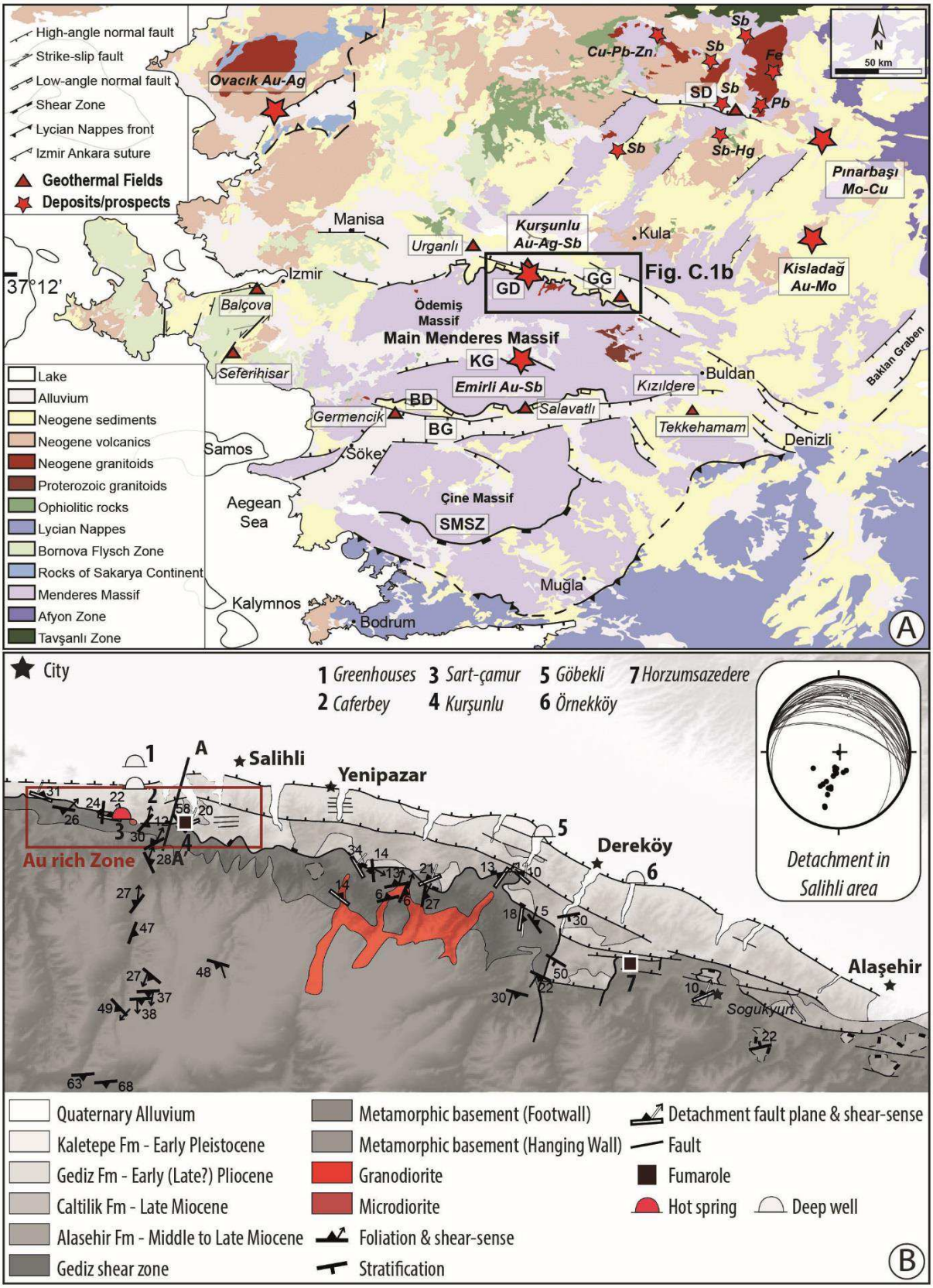

Figure C.1: Tectonic and geological maps of the area. (a) Map of the Menderes Massif showing location of mineral deposits modified after Delibas et al. [2017]. The main geothermal areas correspond to red triangles, from Faulds et al. [2010] and Kaya [2015]. Main structures and grabens: SMSZ (southern Menderes shear zone); BD (Büyük Menderes detachment); GD (Gediz detachment, i.e. Alaşehir detachment); KG (Küçük Menderes graben); SD (Simav detachment); BG (Büyük Menderes graben) and GG (Gediz graben, i.e. Alaşehir graben). (b) Tectonic and

geological map of the Salihli area showing the main structures such as the Alaşehir low-angle normal fault, E-W striking high-angle normal faults and N-S striking high strike-slip faults. The N-S cross-section (thick black line) in this area, is roughly parallel to the tectonic transport.

2.2. The Salihli district

The studied area corresponds to the northern central part of the Menderes Massif (Fig. C.1). Mineralized occurrences crop out near the locality of Salihli (Fig. C.1b), where both active and fossil hydrothermal systems occur. There, the series from the Menderes metamorphic cover crop out well. It consists of metasedimentary sequence, including shelf sediments of inferred Permo-Carboniferous age, made of graphitic schist, and quartzite with carbonate beds [*e.g.* Schuiling 1962; Gessner *et al.*, 2001b]. These metamorphic rocks were exhumed along a ductile-to-brittle extensional shear zone named the Alaşehir detachment [Hetzel *et al.*, 1995a; Bozkurt, 2001; Rossetti *et al.*, 2017]. The activity of the north-dipping Alaşehir detachment system is associated with the emplacement and ductile shearing of the Salihli granodiorite (Fig. C.1b) [Hetzel *et al.*, 1995a; Lips *et al.*, 2001; Glodny & Hetzel, 2007]. Based on U-Pb dating of allanite, Glodny and Hetzel [2007] estimated an age around 15.0 ± 0.3 Ma for this intrusion. Additional ^{40}Ar-^{39}Ar ages of biotite and muscovite indicate a cooling age around 12.2 ± 0.4 Ma [Hetzel *et al.* 1995b]. Furthermore, according to many studies, geochemical signatures of this intrusion derived from heterogeneous sub-continental lithospheric mantle sources [Dilek *et al.*, 2009; Öner *et al.*, 2010; Catlos *et al.*, 2010; Erkül & Erkül, 2012; Erkül *et al.*, 2013] with a strong crustal fingerprint [Altunkaynak *et al.*, 2012]. Thermo-barometry data suggests a shallow crustal emplacement conditions, with crystallization temperatures ranging from 700 – 800 °C over 0.2 – 0.3 GPa [Catlos et al, 2010; Erkül *et al.*, 2013]. According to Hetzel *et al.* [2013], a last event recorded at 7 ± 1 Ma close to the top of the detachment fault plane [Lips *et al.*, 2001] may be associated with the crossing through the brittle-ductile transition zone, and thus corresponds to the first increment of the brittle deformation. This brittle deformation is still active until 4 – 3 Ma [Hetzel *et al.*, 2013]. Above this major extensional structure, Neogene sediments crop out well in this area. They are controlled by E-W steeply dipping normal fault systems (Fig. C.1b). In addition to precedent fault types, steeply N-S tending strike-slip fault spaced by 2 – 5 km cut and dissect the massif.

3. New field structural data

Foliation of the basement strikes E-W with moderate dip values toward the north. Most of the ductile kinematic indicators consist of asymmetric boudinage in alternating lithologies (Fig. C.2a), metric folds in marbles levels, and centimetric shear bands in all lithologies. All these indicators show a top-to-the-NNE sense of shear (Fig. C.2). Brittle deformation is also well-exposed in this area. For instance, low- to moderate-angle normal faults frequently affect the main foliation, suggesting that

deformation appears more localized (Fig. C.2b). E-W striking veins without visible mineralization are also locally developed in competent layers, perpendicular to the main foliation (Fig. C.2c). Approaching the main fault plane (*i.e.* the Alaşehir detachment), foliation is fully transposed into a new main penetrative foliation, and thus becoming parallel to the detachment. This crustal-scale structure is clearly visible in the landscape, and the main fault plane is marked by both fault gouges and cataclases (approximately 15 meters thick). Slickenlines supported by the fault plane have a N-S trend direction (Fig. C.2d). Inversion of fault slip data was carried out using the WinTensor software of Delvaux & Sperner [2003]. Results indicate that kinematics of brittle motion is consistently with a top-to-the-northeast motion.

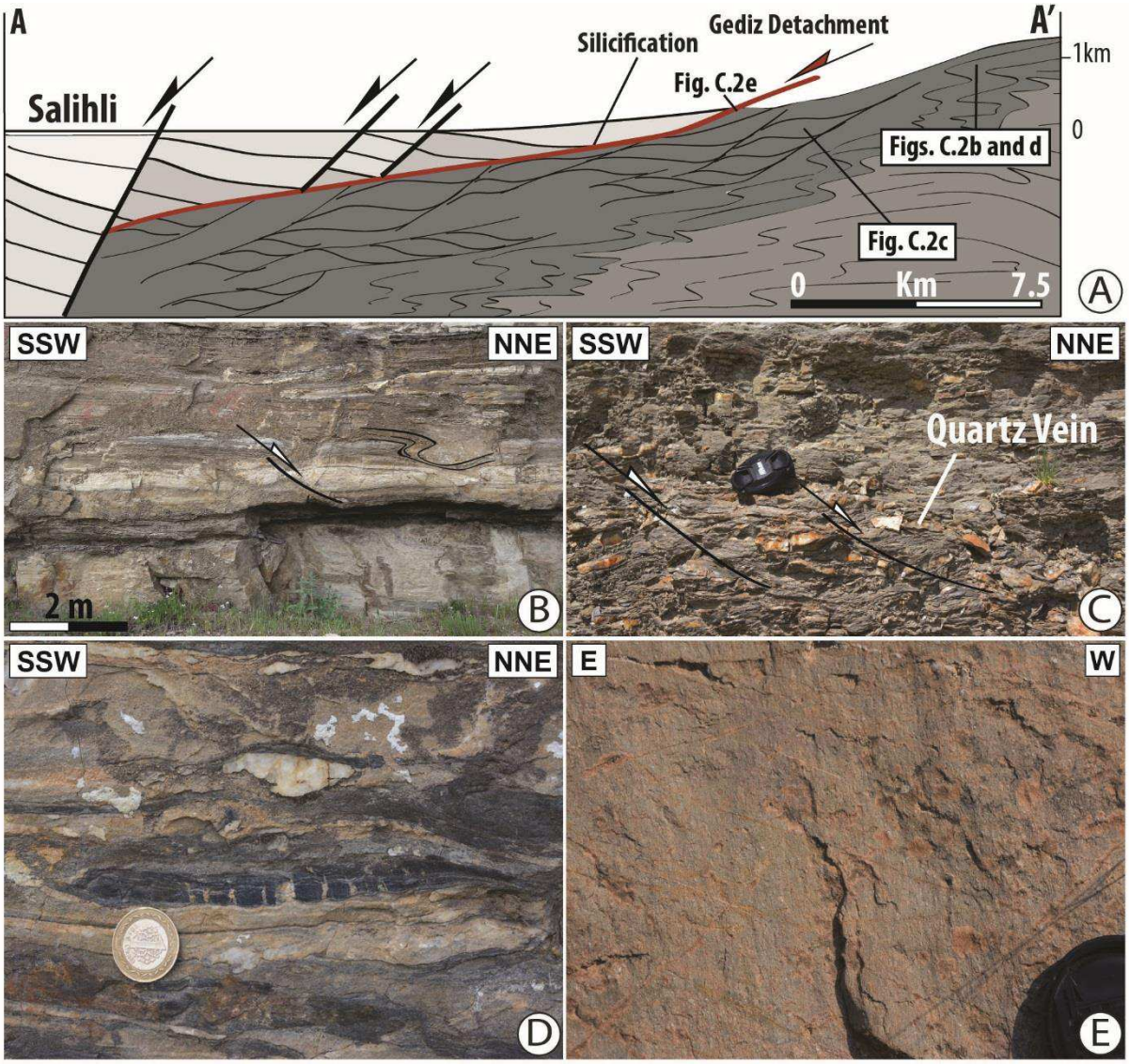

Figure C.2: Kinematics of deformation. (a) Simplified cross-section showing the continuum of deformation from ductile to brittle conditions. The location is indicated in figure C.1a. (b) Low-angle shear bands in marble levels showing a top-to-the-north shearing. (c) Moderate-angle shear bands affecting the main foliation in schists. Note also the presence of numerous quartz veins. (d) Tension gashes within dark marbles showing a N-S stretching. (e) Striae along the main fault plane of the Alaşehir detachment. Locations of pictures are indicated in figure C.2a.

Furthermore, a late brittle stage is also well-expressed in all the area. We report two main directions of faults: (i) the first one is characterized by high-angle NNE-dipping normal faults and (ii) the second one by vertical N-S strike-slip. Depending on the area, this set of faults may indicate either dextral or senestral movement with a normal component. All these faults may affect the basement and the Neogene sediments, and relationships between them in the field are ambiguous. However, kinematics of the brittle deformation is clear, and indicates an overall top-to-the-north-northeast motion such as the ductile deformation.

3.1. Fluid circulations and associated hydrothermal alteration within the Alaşehir detachment

The Alaşehir detachment crops out over a large distance (kilometric), presenting numerous evidences of paleo-circulations of hydrothermal fluids. It is noteworthy that all cataclastic levels are locally mineralized, and thus such mineralization can be followed laterally for several meters. In the field, three main mineralized occurrences are identified in the Kurşunlu valley (the silicaceous area, the breccia veins, the distal flat veins, Fig. C.3a), and only one shows Au occurrences (see below). These deposits have been observed in the elevated part of the massif, where the activity of the Alaşehir detachment is marked by a thick cataclasites zone (~ 15 meters). In addition, Larson and Erler [1993] have also reported various mineralized occurrences rich in precious metals (*e.g.* Ag, Au) in addition to As, Hg, and Sb in this prospect. Hydrothermal alteration in this area is limited and mainly occurs in the immediate vicinity of the mineralized zones within the brittle part of the detachment. From top to bottom, there is:

- a body of silicified hydrothermal (Fig. C.3b) cataclasites and breccias. It measures around 20 cm up to 1 m thick, and crops outs over large areas (*i.e.* from Salihli to Dereköy, Fig. C.1b). This pervasive silicification is part of the vein formation and produced numerous thin quartz veins and breccia infilled by quartz and chalcedony along the main fault zone. The final stage of mineralization is characterized by an argillic alteration, usually replacing minerals belonging to the previous stages.
- a pervasive silicified schists with locally cockade breccia structures (Fig. C.3c), and characterized by banded quartz-veins with adularia and carbonate ghosts. Indeed, carbonate has been locally replaced by quartz and display a lamellar texture of ghost bladded calcite (Fig. C.3d). According to Dong *et al.* [1995], such a texture indicates boiling event in a hydrothermal context. Carbonatization alteration may be locally preserved and observed ~ 20 m below the main mineralized zones associated with the top of the detachment. These veins are centimetric to multi-decimetric (max 40 cm), and lie parallel to the plane of detachment and foliation. They are characterized by rare but recurrent pull-apart textures showing opening direction in accordance with a normal kinematic. Vertical veins striking N-S to N020 °E are also observed (2 cm to 50 cm) (Fig. C.3e). They are also filled by quartz, adularia and replaced carbonate.

- a network of anastomosed veins similar to a stockwork, parallel to the main schistosity.
- numerous quartz veins within the deeper structural levels of the metamorphic rocks, suggesting a strong fluid circulation. It is noteworthy that the density of veins increases toward the fault plane.

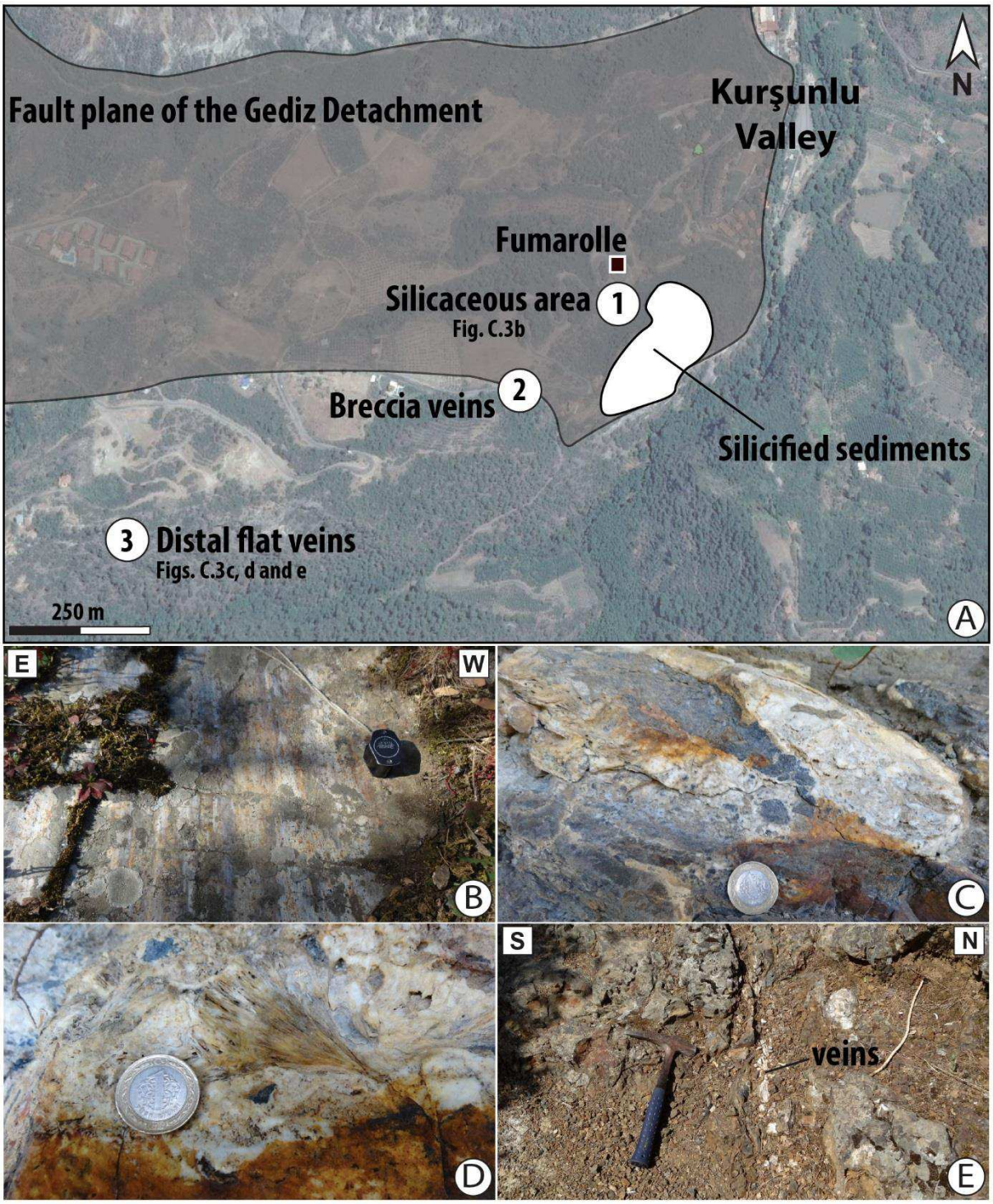

Figure C.3: (a) Sketch map of the Kurşunlu prospect showing the silicified Alaşehir detachment. (b) Striae along the main silicified fault plane. (c) Cockade breccia characterized by centimeter clast of schists. (d) Close-up view of platy calcite. (e) Centimetric quartz veins cutting across the main marbles foliation. Locations of pictures are indicated in figure C.3a.

3.2. Microstructural data and associated mineral assemblage

The silicified area is located just under the detachment fault plane in the Kurşunlu valley (Fig. C.3, number 1). At the scale of the outcrop, fluid-rock interactions along the detachment structure are responsible of a wide alteration that makes the nature of supposed host rock fragments difficult to determine. It is composed of a thick silicified breccia, which frequently host earlier sulfides (*i.e.* pyrite and arsenopyrite) remobilized, at probably low T into jarosite and scorodite (Fig. C.4a) and also by metal arsenates (*i.e.* realgar). At the micro-scale, the quartz gangue is composed of different levels. Some of them consist on irregular and compact quartz crystals without traces of deformation. However, others show two types of shear bands. Whereas some of them are characterized by low-angle faults, spaced by a few millimeters, the others have a more brittle behavior. Some minors veins cuts the foliation and contains only iron oxides (Fig. C.4a). Electrum is rare and observed in equilibrium with iron oxides (Fig. C.4b).

The brecciated veins are located few meters depths from the top of the detachment (Fig. C.3a, number 2). However, the breccia texture is well preserved in this area (Fig. C.4c). Sulfides such as pyrites and arsenopyrites, and rare occurrences of berthierite are mainly located in quartz veins but it may also be disseminated into the host rocks (Fig. C.4d). However, this dissemination is limited and does not exceed widths of few centimeters on either side of the mineralized structures. In addition, microprobe analyzes show that gold is disseminated through the pyrites.

The distal flat veins (Fig. C.3a, number 3) are located at approximately 20 meters depth below the detachment. There, the mineralization is mainly hosted by calschists and, to a lesser extent, marbles. Observations in thin sections show the presence of millimetric angular calcshists fragments preserved and cemented by quartz veinlets. Clasts vary in size from a few millimeters to a few centimeters, and are not mineralized. Nevertheless, some of them are oxidized (*i.e.* titanium oxides) and replaced by voids, suggesting that a fluid circulation event postdates the brittle stage (Fig. C.4e). Disseminated small grains of pyrite and arsenopyrite occurring within brecciated zones, filled the spaces between angular clasts of brecciated calcschist within the quartz gangue (Fig. C.4f).

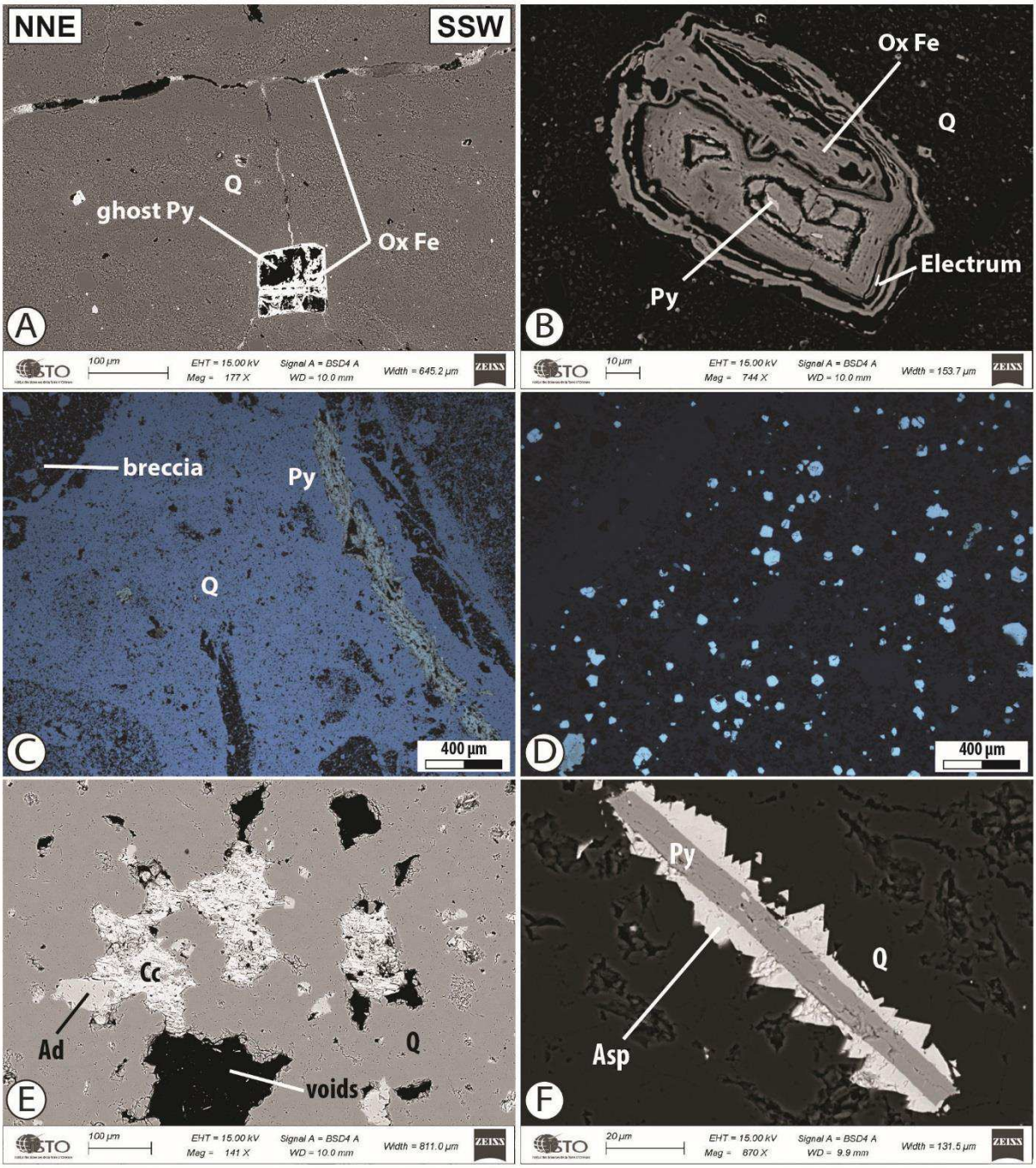

Figure C.4: Mineral assemblage. (a) Silicified breccia showing iron oxides (Ox Fe) within low-angle fractures. Note that Py (pyrite) are totally altered. Q: quartz. (b) Zoom on altered Py (pyrite) showing the presence of electrum. Q: quartz. (c) Hydrothermal vein breccia. Q: quartz; Py: pyrite. (d) Disseminated pyrite in the quartz-chalcedony gangue. (e) Hydrothermal vein breccia. Ad: adularia; Cc: calcite; Q: quartz. (f) Close-up view showing relationships between Py (pyrite) and Asp (arsenopyrite).

4. The major points that need to be discussed

4.1. A pervasive fluid circulation along the detachment

Massive fluid flows occurred approaching the Alaşehir detachment at kilometric-scale. According to Hetzel *et al.* [2013], the exhumed brittle domain of the Alaşehir detachment is still active over ~20 Ma. This major structure may provide an effective long-lived pathway for fluids circulation. Many studies focusing on fluid compositions (*e.g.* stable isotope geochemistry: H) showed that massive infiltration of meteoric water could reach depths of 10 – 15 km [*e.g.* Famin *et al.*, 2004; Gébelin *et al.*, 2017]. The currently presence of small amounts of isotopes related to CO_2, H_2S, B and He, also suggests mixing of deep thermal waters [*e.g.* Roche *et al., 2018*]. It further implies that fault systems in upper crust are connected at depth with shear zones in the lower crust, probably since the Miocene. These zones should be then relayed at depth by permeable ductile deformation where volatiles from the mantle (*e.g.* He) might have been released. Consequently, detachments could drain over a depth of several kilometers hot crustal and or mantellic fluids, and could thus control deep circulation and heat transport. Considering that the influx of cold meteoric water down to the detachment can maintain a transient geotherm over a long duration, some tectonic events such as fast exhumation, fault activity may favor the precipitation, changing the P-T conditions of reservoir.

4.2. A low sulphidation epizonal orogenic deposit without magmatism

Our preliminary study shows that gangue mineralogy from observed veins consists of quartz, chalcedony, adularia, platy-calcite, arsenopyrite, pyrite ± electrum ± berthierite. This suggest that mineralization occurs under reduced conditions and low to very low sulfidation state [Williams-Jones & Normand, 1997; Fontboté *et al.*, 2017]. Indeed, berthierite is stable only over a very narrow interval of fO_2 [Williams-Jones & Normand, 1997].

Such an ore deposit may be thus compared to orogenic deposit from the epizonal domain with a low- to very low sulfidation state in the sense of Groves *et al.* [1998; 2003]. It forms dominant open-space veins within the upper part of the shear zone, extending approximately 50 meters thick. This prospect displays thus a close temporal and spatial relationship with detachment faulting activity. Clear relationships in the field between paleo-fluids circulation and the breccia associated with the detachment activity (4 – 3 Ma K-Ar ages [Hetzel *et al.*, 2013]), suggest that fluid circulation post-dates this main brittle event. Thus, these deposits cannot be related directly to the Salihli granodiorite intrusion, for which the end of crystallization is dated at ~ 12 Ma [Rosseti *et al.* 2017]. According to Rosseti *et al.* [2017], a fast cooling/exhumation phase occurs between 3 to 2 Ma (~120° C/Ma). We suggest that the age of the deposits is probably around this period. However, ^{40}Ar-^{39}Ar ages on adularia may confirm or

not this suggestion. P-T conditions are thus strongly modified, and boiling may happens enhancing the precipitation of such deposits. Although the majority of economic hydrothermal mineral deposits have formed during crustal extension but are also associated with magmatic activity [Yigit 2006; 2009], our results show evidence for hydrothermal and structurally controlled mineralization disconnected of any magmatic activity. This type of mineralization may therefore be associated with the exhumation of the metamorphic dome induced by the detachment activity. In that sense, this deposit is similar to gold deposits described as mesothermal shear zone-hosted deposits mainly associated with metamorphic belts (Fig. C.5) [Groves *et al.*, 1998, Groves *et al.*, 2003].

To summarize, preliminary results suggest that (i) detachment controls mineralization deposits, which may be considered as epizonal (*i.e.* textures and parageneses similar to very low- to low-sulphidation states), (ii) the emplacement of the mineralization is close to the surface (<2 km) and (iii) with an age that post-dates the ductile-brittle deformation (dated at 7 Ma [Lips *et al.*, 2001]), suggesting no direct link with the Salihli granodiorite emplacement (16 – 17 Ma age U-Pb, [Rossetti *et al.*, 2017]).

4.3. Heat source and mantle dynamics

Our thesis results show that heat source at the base of the crust is controlled by slab dynamics (*i.e.* slab tearing and slab rollback). These dynamics triggered the localization of deformation (*i.e.* low-angle normal shear zone) allowing to the exhumation of the MCC. The deep heat source induces thus migmatitization and/or accumulation of magma at the base of the crust, favoring the mobilization of gold and other precious metals (Fig. C.5). In this case, the low-angle crustal normal faults control the circulation of hydrothermal fluids, and therefore the mobilization of different metals such as As-Au in the deep domains and then Au-Sb-Hg and Hg-Sb in the shallower domains (Fig. C.5). When hydrothermal fluids reach the sub-surface, their relatively low temperatures (< 200 – 250 °C) induce a very low solubility of gold, minimizing the gold transport [Fontboté *et al.*, 2017]. In addition, between 150 and 200 °C, bisulfide complexes can be transported, and thus precipitate a significant amount of Sb and Hg in the lower part of the crust [Williams-Jones & Norman, 1997]. Accordingly, the study of these paleo-systems is essential, because they bring new constraints on the current conditions of the reservoir (*e.g.* P-T, the type of alteration ...) where are located the geothermal resources.

4.4. Similitudes with HT geothermal systems

These mineralized systems display many similarities with active geothermal fields in the Menderes Massif that involve a dominant meteoric water interacting with host rocks at high-temperature conditions [*e.g.* Faulds *et al.*, 2009; Gessner *et al.*, 2017; Roche *et al.*, 2018]. According to them,

geothermal activity is not driven by magmatic sources. This geothermal Province is therefore characterized by active tectonics, where crustal-scale low-angle normal faults convey hot fluids to the surface. Although these systems are well known from surface manifestations (*i.e.* hot springs, sinter and hydrothermal breccia), direct deep data obtained from wells are scarce. Conversely, fossil hydrothermal systems can provide continuous information to depths of 2 km below the paleo-surface. In both cases, there is no magmatic source, suggesting a strong structural control on the localization of both fossil and active geothermal systems. In that sense, the same regional structural guides are applicable to the exploration of both paleo-epithermal deposits and active geothermal fields (*i.e.* the vicinity of the detachment). In addition, whereas the delay between magmatic intrusion (and volcanism) and the onset hydrothermal activity is short (around 1 m.y. to 50 K.y according to Bouchot & Genter [2009]), amagmatic systems may be considered as a long-lifetime systems where the deep heat source need time to express at the surface. This implies an episodic (*e.g.* seismic pumping) fluid circulation over several million years (Fig. C.5). However, some differences at local-scale may be noted. For instance, we show in the previous study (see *chapter II*) that strike slip faults associated with dilational structures enhance fluids circulation in the upper crustal levels. Nevertheless, no arguments have been found in the field for the mineralization.

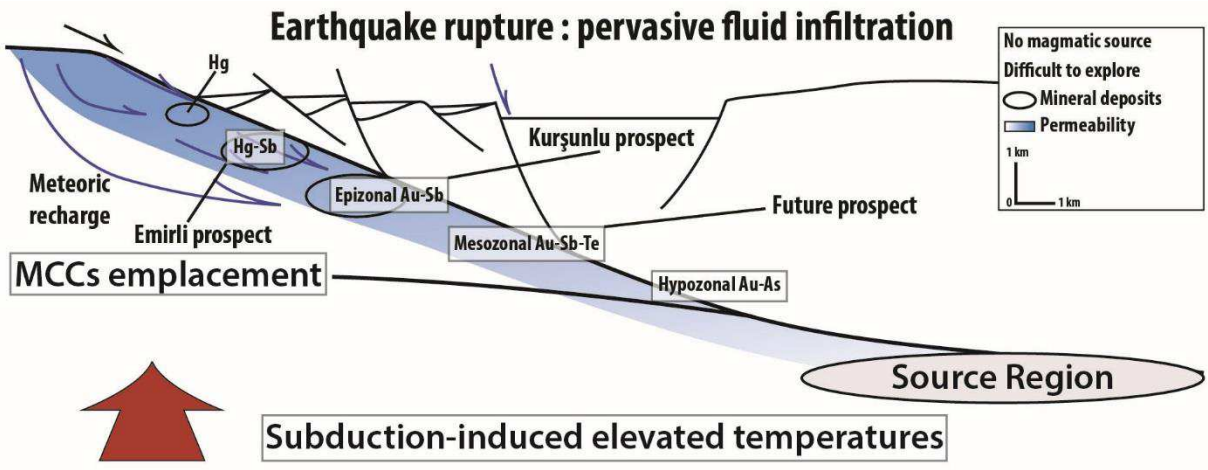

Figure C.5: Possible model for fluid circulation.

4.5. Evolution of the metallogenic province of the Menderes Massif

We can summarize the evolution of the metallogenic province of the Menderes Massif in two main stages:

(i) A first province rich in Pb-Zn-Cu (*e.g.* Pınarbaşı porphyry ore deposit [Delibaş *et al.*, 2017]) and then Au (*e.g.* Efemçukuru epithermal ore deposits [Oyman *et al.*, 2003]), has been emplaced in a back-arc context since Oligocene-Miocene mainly associated with

magmatic activity [Menant *et al.*, submitted]. This region is marked by numerous punctual events associated with the emplacement of magmatic intrusions in the upper crust. In addition, the presence of migmatites and granitoïds intrusions confirms also that slab dynamics (*i.e.* rollback and tearing events) induces and controls the spatial distribution of higher temperatures. Contemporaneous with these geothermal magmatic deposits, the entire MCC of the Menderes Massif is rapidly exhumed through many shear zones (see *Chapter V*). Associated with this dome exhumation, a regional thermal anomaly affects entirely the central part of the massif and more locally the northern part.

(ii) A second epizonal orogenic gold deposits is then recorded in the Menderes Massif (age unknown yet). Gold-pyrite-arsenopyrite-gold mineralization with elevated As and Bi contents [Erler & Larson, 1992] is controlled by detachments but also by listric faults in other places (*e.g.* Emirli [Yigit, 2006]). Crystalline metamorphic rocks including marbles, micaschists and gneisses are therefore the host-rocks for these occurrences. Such deposits result from the large-scale thermal anomalies induced by slab dynamics since ~20 Ma. Comparable examples include deposits of the Variscan orogenic belt in France [Bouchot *et al.*, 2005], and in the Carpathian–Balkan–Dinaride belts in the Rhodope Massif [Marchev *et al.*, 2003]. In these deposits, detachment-fault controlled is related to MCC exhumation rather than nearest magmatism.

5. References

Agdemir, N., Kirikoglu, M. S., Lehmann, B., & Tietze, J. (1994). Petrology and alteration geochemistry of the epithermal Balya Pb-Zn-Ag deposit, NW Turkey. Mineralium Deposita, 29(4), 366-371.

Akçay, M., Özkan, H. M., Moon, C. J., & Spiro, B. (2006). Geology, mineralogy and geochemistry of the gold-bearing stibnite and cinnabar deposits in the Emirli and Halıköy areas (Ödemiş, İzmir, West Turkey). Ore Geology Reviews, 29(1), 19-51.

Altunkaynak, Ş., Dilek, Y., Genç, C. Ş., Sunal, G., Gertisser, R., Furnes, H., ... & Yang, J. (2012). Spatial, temporal and geochemical evolution of Oligo–Miocene granitoid magmatism in western Anatolia, Turkey. Gondwana Research, 21(4), 961-986.

Bertrand, G., Guillou-Frottier, L., & Loiselet, C. (2014). Distribution of porphyry copper deposits along the western Tethyan and Andean subduction zones: Insights from a paleotectonic approach. Ore Geology Reviews, 60, 174-190.

Bouchot, V., Ledru, P., Lerouge, C., Lescuyer, J. L., & Milesi, J. P. (2005). 5: Late Variscan mineralizing systems related to orogenic processes: the French Massif Central. Ore Geology Reviews, 27(1), 169-197.

Bouchot, V., & Genter, A. (2009). Exploration guides for active high-temperature geothermal systems as modern analogs for paleo-epithermal systems. Geothermal Resources Council Transactions, 33, 447-453.

Bozkaya, Ö., Bozkaya, G., Uysal, I. T., & Banks, D. A. (2016). Illite occurrences related to volcanic-hosted hydrothermal mineralization in the Biga Peninsula, NW Turkey: Implications for the age and origin of fluids. Ore Geology Reviews, 76, 35-51.

Bozkurt, E. (2001). Neotectonics of Turkey–a synthesis. Geodinamica acta, 14(1-3), 3-30.

Bozkurt, E., & Oberhänsli, R. (2001). Menderes Massif (Western Turkey): structural, metamorphic and magmatic evolution-a synthesis. International Journal of Earth Sciences, 89(4), 679-708.

Bozkurt, E., Satır, M., & Buğdaycıoğlu, Ç. (2011). Surprisingly young Rb/Sr ages from the Simav extensional detachment fault zone, northern Menderes Massif, Turkey. Journal of geodynamics, 52(5), 406-431.

Candan, O., Dora, O., Oberhänsli, R., Çetinkaplan, M., Partzsch, J., Warkus, F., & Dürr, S. (2001). Pan-African high-pressure metamorphism in the Precambrian basement of the Menderes Massif, western Anatolia, Turkey. International Journal of Earth Sciences, 89(4), 793-811.

Catlos, E. J., Baker, C., Sorensen, S. S., Çemen, I., & Hançer, M. (2010). Geochemistry, geochronology, and cathodoluminescence imagery of the Salihli and Turgutlu granites (central Menderes Massif, western Turkey): Implications for Aegean tectonics. Tectonophysics, 488(1), 110-130.

Çiftçi, N. B., & Bozkurt, E. (2010). Structural evolution of the Alaşehir Graben, SW Turkey: temporal and spatial variation of the graben basin. Basin Research, 22(6), 846-873.

Collins, A. S., & Robertson, A. H. (1998). Processes of Late Cretaceous to Late Miocene episodic thrust-sheet translation in the Lycian Taurides, SW Turkey. Journal of the Geological Society, 155(5), 759-772.

Delibaş, O., Moritz, R., Chiaradia, M., Selby, D., Ulianov, A., & Revan, M. K. (2017). Post-collisional magmatism and ore-forming systems in the Menderes massif: new constraints from the Miocene porphyry Mo–Cu Pınarbaşı system, Alaşehir–Kütahya, western Turkey. Mineralium Deposita, 1-22.

Delvaux, D., & Sperner, B. (2003). New aspects of tectonic stress inversion with reference to the TENSOR program. Geological Society, London, Special Publications, 212(1), 75-100.

Dilek, Y., Altunkaynak, Ş., & Öner, Z. (2009). Syn-extensional granitoids in the Menderes core complex and the late Cenozoic extensional tectonics of the Aegean province. Geological Society, London, Special Publications, 321(1), 197-223.

Dong, G., Morrison, G., & Jaireth, S. (1995). Quartz textures in epithermal veins, Queensland; classification, origin and implication. Economic Geology, 90(6), 1841-1856.

Ebert, S. W., & Rye, R. O. (1997). Secondary precious metal enrichment by steam-heated fluids in the Crofoot-Lewis hot spring gold-silver deposit and relation to paleoclimate. Economic Geology, 92(5), 578-600.

Erkül, S. T., & Erkül, F. (2012). Magma interaction processes in syn-extensional granitoids: the Tertiary Menderes Metamorphic Core Complex, western Turkey. Lithos, 142, 16-33.

Erkül, F., Erkül, S. T., Ersoy, Y., Uysal, İ., & Klötzli, U. (2013). Petrology, mineral chemistry and Sr–Nd–Pb isotopic compositions of granitoids in the central Menderes metamorphic core complex: constraints on the evolution of Aegean lithosphere slab. Lithos, 180, 74-91.

Erler, A., & Larson, L. T. (1992). Genetic classification of gold occurrences of the Aegean region of Turkey. IESC in Aegean Regions: Izmir, Turkey, Proceedings, 12-23.

Famin, V., Philippot, P., Jolivet, L., and P., Agard. (2004), Evolution of hydrothermal regime along a crustal shear zone, Tinos Island, Greece. Tectonics, 23(5).

Faulds, J. E., Bouchot, V., Moeck, I., & Oguz, K. (2009). Structural controls on geothermal systems in western Turkey: a preliminary report. Geothermal Resources Council Transactions, 33, 375-382.

Faulds, J. E., Coolbaugh, M. F., Benoit, D., Oppliger, G., Perkins, M., Moeck, I., & Drakos, P. (2010). Structural controls of geothermal activity in the northern Hot Springs Mountains, western Nevada: The tale of three geothermal systems (Brady's, Desert Peak, and Desert Queen). Geothermal Resources Council Transactions, 34, 675-683.

Fontboté, L., Kouzmanov, K., Chiaradia, M., & Pokrovski, G. S. (2017). Sulfide minerals in hydrothermal deposits. Elements, 13(2), 97-103.

Gébelin, A., Jessup, M. J., Teyssier, C., Cosca, M. A., Law, R. D., Brunel, M., & Mulch, A. (2017). Infiltration of meteoric water in the South Tibetan Detachment (Mount Everest, Himalaya): When and why?. Tectonics, 36(4), 690-713.

Gessner, K., Piazolo, S., Güngör, T., Ring, U., Kröner, A., & Passchier, C. W. (2001b). Tectonic significance of deformation patterns in granitoid rocks of the Menderes nappes, anatolide belt, Southwest Turkey. International Journal of Earth Sciences, 89(4), 766–780. https://doi.org/10.1007/s005310000106

Gessner, K., Ring, U., Johnson, C., Hetzel, R., Passchier, C. W., & Güngör, T. (2001a). An active bivergent rolling-hinge detachment system: Central Menderes metamorphic core complex in western Turkey. Geology, 29(7), 611-614.

Gessner, K., Collins, A. S., Ring, U., & Güngör, T. (2004). Structural and thermal history of poly-orogenic basement: U–Pb geochronology of granitoid rocks in the southern Menderes Massif, Western Turkey. Journal of the Geological Society, 161(1), 93-101.

Gessner, K., Markwitz, V., and T., Güngör, (2017), Crustal fluid flow in hot continental extension: tectonic framework of geothermal areas and mineral deposits in western Anatolia. Geological Society, London, Special Publications, 453, SP453-7.

Glodny, J., & Hetzel, R. (2007). Precise U–Pb ages of syn-extensional Miocene intrusions in the central Menderes Massif, western Turkey. Geological Magazine, 144(2), 235-246.

Groves, D. I., Goldfarb, R. J., Gebre-Mariam, M., Hagemann, S. G., & Robert, F. (1998). Orogenic gold deposits: a proposed classification in the context of their crustal distribution and relationship to other gold deposit types. Ore geology reviews, 13(1), 7-27.

Groves, D. I., Goldfarb, R. J., Robert, F., & Hart, C. J. (2003). Gold deposits in metamorphic belts: overview of current understanding, outstanding problems, future research, and exploration significance. Economic geology, 98(1), 1-29.

Hetzel, R., Passchier, C. W., Ring, U., & Dora, Ö. O. (1995a). Bivergent extension in orogenic belts: the Menderes massif (southwestern Turkey). Geology, 23(5), 455-458.

Hetzel, R., Ring, U., Akal, C., & Troesch, M. (1995b). Miocene NNE-directed extensional unroofing in the Menderes Massif, southwestern Turkey. Journal of the Geological Society, 152(4), 639-654.

Hetzel, R., Dunkl, I., Haider, V., Strobl, M., von Eynatten, H., Ding, L., & Frei, D. (2013). Peneplain formation in southern Tibet predates the India-Asia collision and plateau uplift: REPLY. Geology, 41(9), e297-e298.

Işik, V., & Tekeli, O. (2001). Late orogenic crustal extension in the northern Menderes massif (western Turkey): evidence for metamorphic core complex formation." International Journal of Earth Sciences 89.4 (2001): 757-765.

Kaya, A. (2015). The effects of extensional structures on the heat transport mechanism: An example from the Ortakçı geothermal field (Büyük Menderes Graben, SW Turkey). Journal of African Earth Sciences, 108, 74-88.

Koralay, O. E., Candan, O., Oberhänsli, C. A., Cüneyt, A. K. A. L., Dora, O. Ö., Fukun, C. H. E. N., ... & Oberhänsli, R. (2015). The geology and geochronology of the Pan-African and Triassic metagranitoids in the Menderes Massif, Western Anatolia, Turkey.

Larson, L. T., & Erler, Y. A. (1993). The epithermal lithogeochemical signature—a persistent characterization of precious metal mineralization at Kursunlu and Örencik, two prospects of very different geology in western Turkey. Journal of Geochemical Exploration, 47(1-3), 321-331.

Erler, A., & Larson, L. T. (1992). Genetic classification of gold occurrences of the Aegean region of Turkey. IESC in Aegean Regions: Izmir, Turkey, Proceedings, 12-23.

Lips, A.L., Cassard, D., Sözbilir, H., Yilmaz, H., Wijbrans, J.R., 2001. Multistage exhumation of the Menderes Massif, western Anatolia (Turkey). Int. J. Earth Sci. 89, 781–792.

Marchev, P., Singer, B., Andrew, C., Hasson, S., Moritz, R., & Bonev, N. (2003). Characteristics and preliminary 40Ar/39Ar and 87Sr/86Sr data of the Upper Eocene sedimentary-hosted low-sulfidation gold deposits Ada Tepe and Rosino, SE Bulgaria: possible relation with core complex formation. Mineral exploration and sustainable development. Millpress, Rotterdam, 1193-1196.

Marchev, P., Raicheva, R., Downes, H., Vaselli, O., Chiaradia, M., & Moritz, R. (2004). Compositional diversity of Eocene–Oligocene basaltic magmatism in the Eastern Rhodopes, SE Bulgaria: implications for genesis and tectonic setting. Tectonophysics, 393(1), 301-328.

Menant, A., Jolivet, L., Tuduri, J., Loiselet, C., Bertrand, G., & Guillou-Frottier, L. (Under revision). 3D subduction dynamics, a first-order control of the transition from copper- to l gold-rich deposits in the Eastern Mediterranean region. Ore Geology Reviews.

Oner, Z., Dilek, Y., & Kadioglu, Y. K. (2010). Geology and geochemistry of the synextensional Salihli granitoid in the Menderes core complex, western Anatolia, Turkey. International Geology Review, 52(2-3), 336-368.

Oyman, T. (2010). Geochemistry, mineralogy and genesis of the Ayazmant Fe–Cu skarn deposit in Ayvalik,(Balikesir), Turkey. Ore Geology Reviews, 37(3), 175-201.

Oyman, T., Minareci, F., & Pişkin, Ö. (2003). Efemcukuru B-rich epithermal gold deposit (Izmir, Turkey). Ore Geology Reviews, 23(1), 35-53.

Richards, J. P. (2005), Cumulative factors in the generation of giant calc-alkaline porphyry Cu deposits, in Super Porphyry Copper & Gold Deposits: A Global Perspective, vol. 1, pp. 7–25, Porter T. M., Adelaide, Australia.

Richards, J. P. (2009). Postsubduction porphyry Cu-Au and epithermal Au deposits: Products of remelting of subduction-modified lithosphere. Geology, 37(3), 247-250.

Rimmelé, G., Jolivet, L., Oberhänsli, R., & Goffé, B. (2003). Deformation history of the high-pressure Lycian Nappes and implications for tectonic evolution of SW Turkey. Tectonics, 22(2), 1–21. https://doi.org/10.1029/2001TC901041

Roche, V., Bouchot, V., Beccaletto, L., Jolivet, L., Guillou-Frottier, L., Tuduri, J., Bozkurt, E., Oguz, K., & Bulent Tokay, B. (2018). Structural, lithological and geodynamic controls on geothermal activity in the Menderes geothermal Province (Western Anatolia, Turkey). IJES.

Rossetti, F., Asti, R., Faccenna, C., Gerdes, A., Lucci, F., & Theye, T. (2017). Magmatism and crustal extension: Constraining activation of the ductile shearing along the Alaşehir detachment, Menderes Massif (western Turkey). Lithos, 282, 145-162.

Schmidt, A., Pourteau, A., Candan, O., & Oberhänsli, R. (2015). Lu–Hf geochronology on cm-sized garnets using microsampling: New constraints on garnet growth rates and duration of metamorphism during continental collision (Menderes Massif, Turkey). Earth and Planetary Science Letters, 432, 24-35.

Schuiling, R. D. (1962). On petrology, age and structure of the Menderes migmatite complex (SW-Turkey). Bulletin of the Mineral Research and Exploration Institute of Turkey, 58, 71-84.

Sillitoe, R. H., & Hedenquist, J. W. (2003). Linkages between volcanotectonic settings, ore-fluid compositions, and epithermal precious metal deposits. Special Publication-Society of Economic Geologists, 10, 315-343.

Williams-Jones, A. E., & Norman, C. (1997). Controls of mineral parageneses in the system Fe-Sb-SO. Economic Geology, 92(3), 308-324.

Yigit, O. (2006). Gold in Turkey—a missing link in Tethyan metallogeny. Ore Geology Reviews, 28(2), 147-179.

Yigit, O. (2009). Mineral deposits of Turkey in relation to Tethyan metallogeny: implications for future mineral exploration. Economic Geology, 104(1), 19-51.

Yigit, O. (2012). A prospective sector in the Tethyan Metallogenic Belt: Geology and geochronology of mineral deposits in the Biga Peninsula, NW Turkey. Ore Geology Reviews, 46, 118-148.

Yilmaz, H., Oyman, T., Arehart, G. B., Colakoglu, A. R., & Billor, Z. (2007). Low-sulfidation type Au–Ag mineralization at Bergama, Izmir, Turkey. Ore Geology Reviews, 32(1), 81-124.

Yilmaz, H., Oyman, T., Sonmez, F. N., Arehart, G. B., & Billor, Z. (2010). Intermediate sulfidation epithermal gold-base metal deposits in Tertiary subaerial volcanic rocks, Sahinli/Tespih Dere (Lapseki/Western Turkey). Ore Geology Reviews, 37(3), 236-258.

Vincent ROCHE

Du manteau au système géothermal de haute température : dynamique de subduction et anomalies thermiques en Méditerranée orientale

Les ressources géothermales de haute température se localisent principalement le long des zones de subduction. Considérée comme amagmatique, la Province géothermale du Menderes (Turquie) offre l'opportunité d'étudier des systèmes géothermaux sans nécessairement invoquer une source de chaleur magmatique dans les premiers kilomètres de la croûte. Cette étude montre que les températures anormalement élevées dans la zone d'arrière-arc sont principalement liées à la dynamique particulière de la subduction est-méditerranéenne (*i.e.* retrait et déchirure). Les résultats de modèles numériques suggèrent que le *shear heating* et les flux mantelliques modifient temporairement la quantité du flux de chaleur à la base de croûte. Par ailleurs, des études de terrain sur l'ensemble de la région (Cyclades, Dodécanèse et Anatolie occidentale) montrent une évolution tectonique et thermique similaire depuis le Crétacé, marquée minéralogiquement par une succession d'épisodes de HP-BT puis de HT-BP. Toutefois, l'apport des données T_{RSCM} et radiochronométriques (^{40}Ar-^{39}Ar, U-Pb) souligne un évènement thermique majeur contemporain à la mise en place du dôme métamorphique du Menderes. Cet événement que l'on explique par un changement drastique de la dynamique de subduction (*i.e.* déchirure du panneau plongeant sous le Massif du Menderes), se développe au Miocène. Des structures d'échelle crustale (*i.e.* détachements) accommodent la mise en place du Massif du Menderes et contrôlent la circulation des fluides dans la croûte, depuis la zone de transition fragile-ductile jusqu'à la surface, sans nécessairement impliquer la contribution de systèmes magmatiques dans la croûte supérieure. La Province géothermale du Menderes est considérée comme une province de haute température de taille mondiale car elle résulte de la dynamique de subduction qui contrôle spatialement et temporellement l'intensité de l'anomalie thermique mais également la mise en place de structures perméables (détachements) d'échelle crustale favorisant la circulation des fluides.

Mots clés : Dynamique de subduction, Flux mantelliques, Shear heating, Province géothermale, MCCs, Métamorphisme HT-BP, Détachements, Failles de transfert

From mantle to crust: subduction dynamics and thermal anomalies in eastern Mediterranean region

High temperature geothermal resources are mainly located along subduction zones. The Menderes geothermal Province (Turkey) offers the opportunity to study amagmatic geothermal systems, without necessarily invoking a magmatic heat source in the upper crust. This study shows that high temperatures in the back-arc domain are primarily related to subduction dynamics (i.e. rollback and tearing). Numerical models suggest that shear heating and mantle flows increase temporarily the amount of heat flow at the base of the crust. Furthermore, field studies on the entire Aegean region (Cyclades, Dodecanese and Western Anatolia) show a similar tectonic and thermal evolution since the Cretaceous, characterized by a succession of episodes of HP-LT and HT-LP metamorphism. Moreover, the contribution of T_{RSCM} and radiochronometric data (^{40}Ar-^{39}Ar, U-Pb) reveals the formation of a large thermal pulse contemporaneous with the exhumation of the Menderes MCC. This event occurs in the Miocene and may be explained by a drastic change in subduction dynamics (i.e. slab tearing under the Menderes Massif). Crustal-scale structures (*i.e.* detachments) induce the emplacement of the Menderes MCC, and also control deep fluids circulation in the crust from brittle-ductile transition zone to the surface without magmatic contribution in the upper crust. As a consequence, the Menderes geothermal Province is recognized as a most important active geothermal province in the world because it results from subduction dynamics. This dynamics thus controls the spatial and temporal distribution of thermal anomaly and extension, inducing crustal-scale permeable structures (detachments) that enhance fluids circulation.

Keywords: Subduction dynamics, Mantle flows, Shear heating, Geothermal Province, MCCs, HT-LP metamorphism, Detachments, Transfer faults

UNIVERSITE D'ORLEANS

Institut des Sciences de la Terre d'Orléans
1A, rue de la Férollerie, 45071 Orléans
CEDEX 2

Géosciences pour une Terre durable
brgm